Bitlis Eren Üniversitesi
Fen Bilimleri Dergisi

Bitlis Eren University
Journal of Science

ISSN : 2147-3129
e-ISSN : 2147-3188

Cilt / *Volume*: 12 Sayı / *Number*: 3 Yıl / *Year*: 2023

Yazışma Adresi

Bitlis Eren Üniversitesi
Lisansüstü Eğitim Enstitüsü
13000, Merkez, Bitlis/TÜRKİYE
Tel: 0 (434) 2220071

https://dergipark.org.tr/tr/pub/bitlisfen

BEU FBD

Bitlis Eren Üniversitesi Fen Bilimler Dergisi

Bitlis Eren University Journal of Science

Yıl/*Year:* 2023 - Cilt/*Volume:* 12 - Sayı/*Number:* 3

Editör (Yayın) Kurulu / *Editorial Board*

Danışma Kurulu / *Advisory Board*

Dergi Hakkında / *About Journal*

Bitlis Eren Üniversitesi Fen Bilimleri Dergisi, mühendislik ve temel bilimler alanlarındaki gelişmeleri ve yenilikleri takip etmek, meslek kuruluşlarının, araştırmacıların ve bireylerin ulusal ve uluslararası gelişimlerine katkıda bulunmak ve bu alanlarda elektronik bir kaynak oluşturmak amacıyla yayımlanmaktadır. Derginin yazım dili Türkçe veya İngilizcedir. Fen Bilimleri Dergisi, Bitlis Eren Üniversitesi Lisansüstü Eğitim Enstitüsü yayını olup, 2012 yılından bu yana ücretsiz ve açık erişimli olarak yayın hayatına devam etmektedir. Mühendislik ve temel bilimlerin bilgi tabanına ve teknolojik gelişmelere ışık tutması amacıyla bu alanlarda yapılmış deneysel ve teorik ilerlemeleri konu alan özgün araştırma makalelerine yer verilmektedir. Dergiye gönderilen çalışmaların benzerlik oranı %25'i geçmemelidir. Yazım kurallarına uymayan makaleler, hakemlere gönderilmeden önce düzeltilmek üzere yazara geri gönderilir. Bu nedenle, derginin yazım kuralları dikkate alınmalıdır. Ayrıca, editörlerden yazarlara iletilen düzeltmelere veya taleplere 30 gün içerisinde cevap verilmediği takdirde ilgili makaleler reddedilir. Makaleler şekiller ve tablolar dâhil 20 sayfayı geçmemelidir. Dergiye yayın için gönderilen makaleler en az iki hakem tarafından değerlendirilir. Yazarlardan hakem önerisi talep edilmemektedir. Makalelerin dergide yayımlanabilmesi için hakemler tarafından olumlu görüş bildirilmesi gerekmektedir. Dergi Editör Kurulu, hakem raporlarını (*en aziki hakemin değerlendirmeleri geldikten sonra*) dikkate alarak makalelerin yayımlanmak üzere kabul edilip edilmemesine karar verir. Fen Bilimleri Dergisi, yılda dört defa (*Mart, Haziran, Eylül, Aralık*) yayımlanmaktadır. **Dergimiz Tübitak-Ulakbim Mühendislik ve Temel Bilimler Veri Tabanı Dergi Listesinde taranmaktadır.**

B.E.Ü. Fen Bilimleri Dergisi 12(3), 2023 / *B.E.U. Journal of Science 12(3), 2023*
İÇİNDEKİLER / *CONTENTS*

Bitlis Eren Üniversitesi Fen Bilimleri Dergisi
BİTLİS EREN UNIVERSITY JOURNAL OF SCIENCE
ISSN: 2147-3129/e-ISSN: 2147-3188
VOLUME: 12 NO: 3 PAGE: 591-595 YEAR: 2023
DOI:10.17798/bitlisfen.1197472

Investigation of Antimicrobial Effects of Some Boron Compounds

Fatih Çağlar ÇELİKEZEN[1*], İbrahim Halil ŞAHİN[2]

[1] *Bitlis Eren Üniversitesi Fen Edebiyat Fakültesi Kimya Bölümü, Bitlis, Türkiye*
[2] *Bitlis Eren Üniversitesi Sağlık Hizmetleri Meslek Yüksekokulu, Bitlis, Türkiye*
(ORCID: 0000-0001-5489-7384) (ORCID: 0000-0001-7667-9310)

Keywords: Boron, lithiummetaboratedehydrate, ammonium borate, potassiumtetraborate, antimicrobial,

Abstract

The importance of boron for human life is increasing day by day, and its usage areas are gradually expanding thanks to developing science and technology. In the present study, the antimicrobial effects of ammonium borate, lithium metaborate dehydrate, and potassium tetraborate were investigated. Kirby Bauer Disc diffusion method was used to determine the antimicrobial effect. In the study, streptomycin standard discs were used as the positive control. Boron compounds showed an antimicrobial effect on *Enterococcus faecalis* (ATCC 29212), *Streptococcus pyogenes* (ATCC 19615), *Pseudomonas aeruginosa* (ATCC 27853), *Enterobacter aerogenes* (ATCC 13048), *Escherichia coli* (ATCC 35218), *Proteus mirabilis* (ATCC 7002), *Candida tropicalis* (ATCC13803), *Citrobacter freundii* (ATCC 8090), *Bacillus subtilis* (ATCC6633), *Burkholderia cepacia* (ATCC25608). In conclusion, our results showed that these boron compounds may be used as antimicrobial agents.
.

1. Introduction

Boron, the 5th element of the periodic table, is a naturally occurring element. Boron is an essential element primarily for plants and some animals and is present in low concentrations in human and animal tissues [1]. Boron forms compounds called borates with oxygen and other elements [2]. Borates are widely used in many industries, such as electricity, computers, energy, textiles, pharmaceuticals, and cosmetics [3]**.** In addition, the effects of borates on vitamin D metabolism [1], some enzymes such as aldehyde dehydrogenase and cytochrome b5 reductase [4], hormones such as insulin, T3, T4 [5], energy substrates such as triglycerides and glucose [6] and reactive oxygen species [7] have been shown. On the other hand, boron has low toxicity for humans and is used in the treatment of some diseases, such as cancer [8]. It has been reported in studies that some bacteria synthesize boron-containing antibiotics that improve their protection systems [9]. Boromycin, Aplasmomycin, and Tartrolone are boron-containing antibiotics synthesized by bacteria, and it has been reported that Boromycin strongly inhibits HIV-1 replication as well as RNA, DNA, and protein synthesis. It has been reported that boron will have an important place in the treatment of AIDS in the future, as this antibiotic has a strong effect against HIV [10, 11, 12]. Aplasmomycin is synthesized by *Streptomyces griseus* and has been reported to be particularly effective on gram-positive bacteria [13]. Tartralone was isolated from *Streptomyces* species and showed an effect on gram-positive bacteria [14].

Today, many boron compounds are synthesized by various laboratories, and the interest shown in the biological activities of these compounds is increasing day by day. Studies examining the antimicrobial activities of boron compounds are limited in the literature. In this context, the antimicrobial effects of potassium tetraborate (PTB), ammonium borate (ABB), and lithium metaborate dihydrate (LMBDH) were investigated in the presented study.

2. Material and Method

In this study, the following bacteria and yeast isolates from the culture collection of Bitlis Eren University Medical Microbiology Laboratory were used, and

*Corresponding author: ccelikezen@beu.edu.tr
Received: 03.11.2022, Accepted: 17.06.2023

antimicrobial activities against the isolates were tested using the Kirby Bauer disk diffusion method.

2.1 Test Microorganisms and Growth Conditions

Enterococcus faecalis (ATCC 29212), *Streptococcus pyogenes* (ATCC 19615), *Pseudomonas aeruginosa* (ATCC 27853), *Enterobacter aerogenes* (ATCC 13048), *Escherichia coli* (ATCC 35218), *Proteus mirabilis* (ATCC 7002), *Candida tropicalis* (ATCC13803), *Citrobacter freundii* (ATCC 8090), *Bacillus subtilis* (ATCC6633). Bacterial isolates were activated in Mueller Hinton Broth (OXOID), and yeast fungi were inoculated into SD Broth (DIFCO) broth and incubated for 24 hours at 35±2 °C. To prepare stock solutions, a second dose was inoculated into liquid media. After 24 hours of incubation, stock solutions were obtained at 0.5 McFarland turbidity for 1-1.5 x 10^8 (CFU/ml) cells. Bacteria Mueller Hinton Agar (OXOID), and yeast fungus Sabouraud Dextrose Agar (OXOID) were left on the media with 100 µl and applied with a glass baguette and waited for 15 minutes to dry.

2.2 Disk diffusion method

20 µl of the solution prepared with 32 mg/ml distilled water of all boron compounds used in the study was absorbed into 6 mm diameter sterile paper discs (Whatman No: 3). Test microorganisms were adjusted to concentration according to McFarland 0.5 (10^8 cfu/ml) and inoculated on Mueller-Hinton Agar (Oxoid). Afterward, the discs were dried at room temperature and in a sterile environment and placed at regular intervals under aseptic conditions. Purified water was used in the preparation of boron compounds and purified water was used as negative control. Streptomycin antibiotic discs (10 µg) were used as positive control [19, 20].

2.3 Mueller- Hinton agar Media preparation

General Formula	
Peptone	17.5 g/l
Beef infusion solids	2.0 g/l
Starch	1.5 g/l
Agar	17.0 g/l
Final pH	7.3 ± 0.1 at 25 °C.

Mueller-Hinton agar was made according to the manufacturer's recipe (Scharlab). 38 g of powder was added to 1 L of distilled water and brought to a boil to dissolve the medium completely. Then, sterilize by autoclaving at 121 °C for 15 minutes.

2.4. Preparation of boron solutions

The PTB, ABB, and LMBDH were synthesized for our previous studies [15-17]. These compounds were dissolved in ultra-pure water. Concentrations were prepared at 32 mg/ml [18].

Table 1. Antimicrobial effects of PTB.

Microorganism	PTB (32mg/ml)	Zone Diameter (mm)	Streptomycin	Zone Diameter (mm)
E. faecalis	-	-	+	36
S. pyogenes	-	-	+	40
B. subtilis	+	9	+	35
P.aeruginosa	+	9	+	31
E. aerogenes	-	-	+	30
E. coli	+	10	+	34
P. mirabilis	-	-	+	35
C. freundii	-	-	+	32
C. tropicalis	+	8		31

(+ : there is a zone of inhibition , - : no zone of inhibition)

Table 2. Antimicrobial effects of AAB.

Microorganism	ABB (32mg/ml)	Zone Diameter (mm)	Streptomycin	Zone Diameter (mm)
E. faecalis	-	-	+	36
S. pyogenes	-	-	+	40
B. subtilis	+	10	+	35

P.aeruginosa	+	8	+	31
E. aerogenes	+	10	+	30
E. coli	+	9	+	34
P. mirabilis	-	-	+	35
C. freundii	+	8	+	32
C. tropicalis	+	7	+	31

(+ : there is a zone of inhibition , - : no zone of inhibition)

Table 3. Antimicrobial effects of LMBDH

Microorganism	LMBDH (32 mg/ml)	Zone Diameter (mm)	Streptomycin	Zone Diameter (mm)
E. faecalis	-	-	+	36
S. pyogenes	-	-	+	40
B. subtilis	+	9	+	35
P.aeruginosa	-	-	+	31
E. aerogenes	+	8	+	30
E. coli	-	-	+	34
P. mirabilis	-	-	+	35
C. freundii	-	-	+	32
C. tropicalis	+	10	+	31

(+ : there is a zone of inhibition , - : no zone of inhibition)

3. Results and Discussion

Boron is one of the most common elements in nature. Increasing the amount of boron may adversely affect the microflora of plants, soil, and water [21]. This can have negative consequences for the environment and public health. It has been reported in the literature that boron compounds, which are effective on microorganisms, can be used as antiseptics and disinfectants [22].

In the study, PTB at 32 mg/ml concentration was applied to standard strains of *B. subtilis, P.aeruginosa, E. coli, and C. tropicalis*; 32 mg/ml concentration of ABB on *B. subtilis, P.aeruginosa, E. aerogenes, E. coli, C. freundii, C. tropicalis* strains, and LMBDH at the same concentration on *B. subtilis, E. aerogenes*, and *C. tropicalis* standard strains was found to have an antibiotic effect (Table 1, Table 2, Table 3).

In parallel with the results obtained, some recent studies have found that diazo bore is effective against bacteria and yeasts [22, 23]. In addition, antifungal compounds containing B-N [24], boric acid, and diazoborin were found to have antibacterial effects [25]. In studies on the bacteriostatic and bacteriocidal effects of boric acid, which is also one of the boron compounds, it has been reported to have antimicrobial effects against Streptococcus sp. and Staphylococcus sp. [26, 27].

In a study conducted, it has been reported that clinical isolates of *Candida albicans* are inhibited by boric acid at a concentration of 0.4-5% by the agar dilution method and have an antifungal effect, while 500 mg of boric acid inhibits 50-90% of *C.albicans* isolates within 48 hours [28]. In another study, Peerters et al. [29] investigated the antimicrobial effect of some metal compounds (phenylmercury borate, thiomersal, mercury chloride, silver nitrate, sodium selenite, and copper sulfate) against penicillinase-producing and non-penicillinase-producing strains of *Neisseria gonorrhoeae*, which causes gonococcal ophthalmia; showed that phenylmercury borate inhibits 90% of *Neisseria gonorrhoeae* strains. In addition, Pannerselvan et al. [30], 3 amino-6-8 dibromo-2 phenyl quinazoline 4 (3H), which is one of the boron-derived compounds, was found in *Staphylococcus aureus* ATCC 914, *Staphylococcus epidermidis* ATCC-155, *Micrococcus luteus* ATCC 4698, *Bacillus cereus* ATCC 11778, *Escherichia coli* ATCC 2592. In their studies on the antibacterial and antifungal effects of *Pseudomonas aeruginosa* ATCC 2953, *Klebsiella pneumoniae* ATCC 1298 bacteria, and *Aspergillus niger* ATCC 9028, *Aspergillus fumigatus* ATCC46645 fungi according to disc diffusion and MIC (minimal inhibition concentration) methods; they stated that the inhibition amount of 3 amino-6-8 dibromo-2 phenyl quinazoline 4 (3H) compound against fungi was higher than bacteria.

On the other hand, Luan et al. [31] stated that AN0128 containing boron showed an antimicrobial effect against *Prevotella intermedia*, *Porphyromonas gingivalis*, *Eubacterium nodatum* and *Treponema denticola* bacteria that cause periodontal diseases. Similarly, AN0128 (3-hydroxypyridine-2-carbonylosi-bis (3-chloro-4-methylphenyl) borate), one of the esters of boronic acid picolinate, which is an antibacterial compound, has been reported to show both antibacterial and anti-inflammatory activity. Baker et al. [32] reported that AN0128 has an antimicrobial effect against *Staphylococcus aureus* colonizing skin and skin diseases. In a different study, it was stated that (Hea)[B(ph)2(2,3-pydc)] and (Hea)[B(ph)2(2,5-pydc)] boron compounds showed antimicrobial activity [33].

4. Conclusion and Suggestions

In conclusion, the antimicrobial effects of PTB, ABB, and LMBDH were demonstrated in the presented study. These compounds may be used as antimicrobial agents in different branches of industry. However, further research is required to fully understand the mechanism of action.

Acknowledgment

This study was supported by Bitlis Eren University Scientific Research Projects Unit as project numbered BEBAP 2013.02.

Contributions of the authors

F.Ç.Ç designed the study, wrote the article, did the experimetal studies and checked the language. İ.H.Ş did the experimental studies and contributed to the writing of the article.

Conflict of Interest Statement

There is no conflict of interest between the authors.

References

[1] C.D. Hunt, "Biochemical effects of physiological amounts of dietary boron," *J Trace Elem Med Biol* vol. 9, pp. 185–213, 1996

[2] H. Turkez, F. Geyikoglu, A. Tatar, M.S. Keles, I Kaplan, "The effects of some boron compounds against heavy metal toxicity in human blood, " *Exp Toxicol Pathol* vol. 64, pp. 93-101, 2012.

[3] N. Yenmez, "The importance of boron minerals in Turkey as a strategic mine," *İstanbul Üniversitesi Edebiyat Fakültesi Coğrafya Bölümü Coğrafya Dergisi*, vol. 19, pp.59-94, 2010.

[4] T.A. Devirian, S.L. Volpe, "The physiological effects of dietary boron," *Crit Rev Food Sci Nutr*, vol. 43, pp. 219–231, 2003.

[5] T.A. Armstrong, J.W. Spears, K.E. Lloyd, "Inflammatory response, growth, and thyroid hormone concentrations are affected by long-term boron supplementation in gilts," *JAS*, 79, pp. 1549–1556, 2001.

[6] M. Eren, G.B. Kocaoglu, F. Uyanik, N. Karabulut, "The effects of dietary boron supplementation on performance, carcass composition and serum lipids in Japanese quails," *J. Vet. Adv*, vol. 5, pp. 1105–1108, 2006.

[7] F.Ç. Çelikezen, H. Türkez, E. Aydın, "The antioxidant and genotoxic activities of $Na_2B_4O_7.10H_2O$ in vitro," *Fresenius environmental bulletin* vol. 24, no. 3, pp. 947-953, 2015.

[8] R.F. Barth, J.A. Coderre, M.G. Vicente, T.H. Blue, "Boron neutron capture therapy of cancer: current status and prospects," *Clin. Cancer Res.* Vol. 11, pp. 3987-4002, 2005.

[9] T. Rezanka and K. Sigler, "Biologically active compounds of semi-metals," *Phytochemistry*, vol. 69, pp. 585-606, 2008.

[10] R. Hutter, W. Keller-Schierlein, F. Kneusel, V. Prelog, G.C. Jr Rodgers, P. Suter, G. Vogel, W. Voser, H, "Zahner Stoffwechselprodukte von Mikroorganismen," *Helv. Chim. Acta* vol. 50, pp.1533-1539, 1967.

[11] J. Kohno, T. Kawahata, T. Otake, M. Morimoto, H. Mori, N. Ueba, A. Kinumaki, S. Komatsubara, K. Kawashima, "Boromycin, an anti-HIV antibiotic," *Biosci. Biotechnol. Biochem.*, vol. 60, pp. 1036-1037, 1996.

[12] W. Pache, H. Zahner, "Metabolic products of microorganisms. 77. Studies on the mechanism of action of boromycin," *Arch. Microbiol*, vol. 67, pp. 156-65,1969.

[13] D.H. Davies, G.L.F. Norris, "Growth promotion," *US Patent*, vol. 4, pp. 225-593,1980.

[14] P. Lewer, E.L. Chapin, P.R. Graupner, J.R. Gilbert, C. Peacock, 2003. "Tartrolone C: a novel insecticidal macrodiolide produced by Streptomyces sp. CP1130," *J. Nat. Prod*., vol. 66, pp. 143-145, 2003.

[15] F.Ç. Çelikezen, H. Turkez, B. Togar, M.S. Izgi, "DNA damaging and biochemical effects of potassium tetraborate," *EXCLI J*, vol. 30, 446-450, 2014.

[16] F.Ç. Çelikezen, B. Toğar, F.B. Özgeriş, M.S.İzgi, Türkez H, "Cytogenetic and oxidative alterations after exposure of cultured human whole blood cells to lithium metaborate dehydrate," *Cytotechnology*, vol.68, 821–827, 2016.

[17] F.Ç. Çelikezen, H. Turkez, E. Aydin, M.S. Izgi, B. Çelikezen, "Potent antioxidant and genotoxic effects of ammonium tetraborate in vitro," *Nat. Sci. Disc*., vol.1, pp. 45-49, 2015

[18] I. Aibinu, T. Adenipekun, T. Adelowotan, T. Ogunsanya, T, "Odugbemi Evaluation of the antimicrobial properties of different parts of Citrus aurantifolia (lime fruit) as used locally," *Afr J Tradit Complement Altern Med*, vol.13, no. 4(2), pp.185-90, 2006.

[19] National Committee for Clinical Laboratory Standard, "In Performance standards for antimicrobial disk susceptibility test," 6th approved standard. M2- A6, Wayne, PA, 1997.

[20] A.L. Barry, C. Thornsberry, "Susceptibility Tests: Diffusion Test Procedures," *In Lennette EH, Balows* A, Hausler WJ, Shadomy HJ (eds) Manual of Clinical Microbiology. Washington, DC: American Society. For Microbiology, pp. 978-987, 1985.

[21] M.T. Yılmaz, "Minimum inhibitory and minimum bactericidal concentrations of boron compounds against several bacterial strains," *Turk. J. Med. Sci.* Vol. 42, pp. 1423-1429, 2012.

[22] N. Surolia, S.P. Ramachandrarao, A. Surolia, "Paradigm shifts in malaria parasite biochemistry and anti-malarial chemotherapy," *Bioessays*, vol. 24: pp. 192-196, 2002.

[23] S.J. Baker, C.Z. Ding, T. Akama, Y.K. Zhang, V. Hernandez, Y. Xia, "Therapeutics potential of boron-containing compounds," *Future Med. Chem.*, vol. 1, pp. 1275-1288, 2009.

[24] V.M. Dembitsky and M. Srebnik, "Synthesis and biological activity of α-amino boronic acids, amine-carboxy boranes, and their derivatives," *Tetrahedron* vol. 59, pp. 579-593, 2003.

[25] P.J. Bailey, G. Cousins, G.A. Snow, A.J. White, "Boron-containing antibacterial agents: effects on growth and morphology of bacteria under various culture conditions," *Antimicrob. Agents Chemother*., vol. 17, pp. 549-553, 1980

[26] E.H. Ochsner, "The prevention and treatment of septic infections of the extremities," *Medical Herald* vol. 30, pp. 30-36, 1911.

[27] E.H. Ochsner, "Biochemistry of topical applications: Use of boric acid in septic infections," *JAMA* vol. 68, pp. 220-223,1917.

[28] M. Shubair, B. Larsen, "Growth inhibition of candida albicans and other medically important yeasts by vaginal contraceptive products," *Gynecol. Obstet. Invest.* vol. 29, pp. 67-70. 1990.

[29] M. Peeters, D. Vanden Berghe, A. Meheus, "Antimicrobial activity of seven metallic compounds against penicillinase-producing and non-penicillinase-producing strains of *Neisseria gonorrhoeae*," *Genitourin Med*, vol. 62, pp. 163-165, 1986.

[30] P. Panneerselvam, B.A. Rather, D.R.S. Reddy, N.R. Kumar, "Synthesis and anti-microbial screening of some Schiff bases of 3-amino-6,8 dibromo-2-Phenylquinazolin-4 (3H)-ones," *Eur. J. Med. Chem.* vol. 44, pp. 2328-2333, 2009

[31] Q. Luan, T. Desta, L. Chehab, V.J. Sanders, J. Plattner, D.T. Graves, "Inhibition of experimental periodontitis by a topical boron-based antimicrobial," *J. Dent. Res* vol. 87, pp. 148-152, 2008.

[32] S.J. Baker, T. Akama, Y.K. Zhang, V. Sauro, S.M.K. Pandit, J. Khan, J.J. Plattener, S.T. Benkoviç, V. Lee, K.R. Maples, "Identification of a novel boron-containing antibacterial agent (AN0128) with anti-inflammatory activity, for the potential treatment of cutaneous diseases," *Bioorg. Med. Chem. Lett* vol.16, pp. 5963-5967, 2006.

[33] A.T. Çolak, Y. Sahin, O.Z. Yeşilel, F. Çolak, F. Yılmaz, M. Tas, "Novel boron compounds of 2,3- and 2,5-pyridine dicarboxylic acids," *Inorganica Chim. Acta*, vol. 383,pp. 169–177, 2012.

Bitlis Eren Üniversitesi Fen Bilimleri Dergisi
BİTLİS EREN UNIVERSITY JOURNAL OF SCIENCE
ISSN: 2147-3129/e-ISSN: 2147-3188
VOLUME: 12 NO: 3 PAGE: 596-607 YEAR: 2023
DOI:10.17798/bitlisfen.1214468

Facial Expression Recognition Techniques and Comparative Analysis Using Classification Algorithms

Gamze BALLIKAYA[1*], Duygu KAYA[2]

[1] *Bitlis Eren University, Faculty of Engineering-Architecture, Department of Electrical-Electronics Engineering, Bitlis/TURKEY*
[2] *Firat University, Faculty of Engineering, Department of Electrical-Electronics Engineering, Elazig/TURKEY*
(ORCID: 0000-0001-7380-1181) (ORCID: 0000-0002-6453-631X)

Keywords: Face Expression Analysis, Feature Extraction, Deep Learning, Convolutional Neural Network, Classification.

Abstract

With the development of technology and hardware possibilities, it has become possible to analyze the changes that occur as a result of the reflection of emotional state on facial expression with computer vision applications. Facial expression analysis systems are used in applications such as security systems, early diagnosis of some diseases in the field of medicine, human-computer interaction, and safe driving. Facial expression analysis systems developed using image data consist of 3 basic stages. These are; extracting the face area from the input data, extracting the feature vectors of the data and classifying the feature vectors. In this study, a hybrid method for facial expression analysis is proposed. The method aims to combine the ability of deep learning models in feature extraction with the ability of machine learning to classify small datasets. Multi Task Cascaded Convolutional Network (MTCNN) has been used to detect the face region in the input data. The features extracted from the fully connected layer of the AlexNet model, which achieves successful results in classification problems, have been classified with K-Nearest Neighborhood (KNN), Support Vector Machine (SVM) and Linear Discriminant Analysis (LDA) algorithms. Machine learning and deep learning methods are widely used in facial expression analysis systems proposed in the literature. In this study, the performances of LDA, SVM and KNN algorithms have been analyzed using JAFFE dataset without data augmentation. With LDA, SVM and KNN algorithms, 89.2%, 88.3% and 87.8% accuracy has been achieved respectively.

1. Introduction

Facial expressions that appear as a result of the change in emotional state can variety in different cultures. However, as a result of the study achieved by Ekman and Friesen in 1971, 6 emotion expressions were universally accepted all around the world [1]. As a result of experiments in different parts of the world, the 6 basic emotions universally defined are happiness, sadness, surprise, fear, anger and disgust.

It is known that the effect of nonverbal communication tools is higher than nonverbal communication tools in interpersonal communication [2]. In addition to the importance of facial expressions in communication, it is used in research subjects such as mental health diagnosis in psychiatry, early diagnosis of autism spectrum disorder and Parkinson's diseases, behavioral analysis of delinquent people in the field of security [3]–[5]. It is used in various application areas by classifying emotions with information obtained from text data, brain wave activities, audio data or image data [6]-[8].

*Corresponding author: gballikaya@beu.edu.tr
Received: 05.11.2022, Accepted: 09.05.2023

Facial expression analysis systems using image data consist of 3 basic stages. Firstly, the face area is detected to remove the unnecessary parts. Then, the features of the face area are extracted in order to reduce the size of the data and highlight the robust features. In the last stage, the class of the test data is estimated with the extracted features. The general flow diagram of facial expression analysis systems is shown in Figure 1.

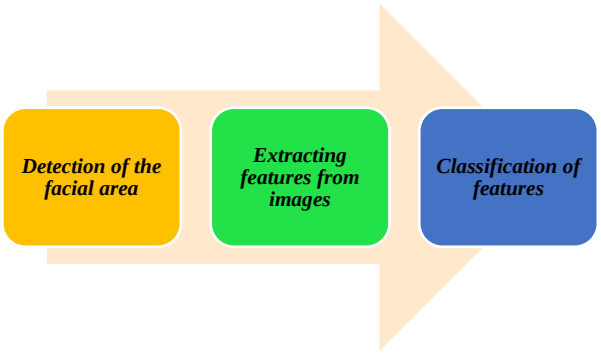

Figure 1. Main steps of facial expression analysis systems.

The systems proposed for facial expression analysis can be classified under two headings: traditional and deep learning-based. In traditional-based approaches, features are manually acquired and classified. However, in deep learning-based approaches with end-to-end learning, the network acquires the attributes of the data through its layers. Deep learning-based approaches require more training data than traditional-based approaches.

Suk et al. [9] proposed a system to classify 7 emotions. In this proposed system, Active Shape Model is used to extract feature vectors from input images, and support vector machine (SVM) is used to classify features. Extended Cohn Kanade (CK+) data set was used in the study. As a result of the study, 86% accuracy in theoretical tests and 72% accuracy in real-time applications was achieved.

Nicolai et al. [10] used image processing methods to extract features of the face area. An accuracy of 78.8% was obtained by using fuzzy logic-based approach in classification. The Japanese Female Facial Expression (JAFFE) dataset was used in the study.

Fatima Zahra et al. [11] proposed a geometric-based approach for feature extraction. In the study, in which JAFFE and Cohn Kanade (CK) datasets were used, decision trees algorithm, one of the supervised machine learning algorithms, was used. Accuracy of 89.20% for JAFFE dataset and 90.61% for CK dataset was achieved.

In the study by Ju et al. [12], emotion analysis was performed using the JAFFE dataset. Principal component analysis was used for feature extraction and random forest algorithm was used for classification of extracted features. In the study, in which 8 emotional states were classified, an average accuracy rate of 77.1% was achieved with the proposed method.

Gonzalez et al [13] proposed a system in which 6 different data sets are combined at different rates for the recognition of facial expressions and micro expressions. Convolutional neural networks (CNN) were used for feature extraction in the proposed facial expression recognition system. The proposed facial expression recognition system has achieved a success rate of 92%.

The methods that are frequently used in traditional based approaches for facial expression recognition systems are shown in Figure 2.

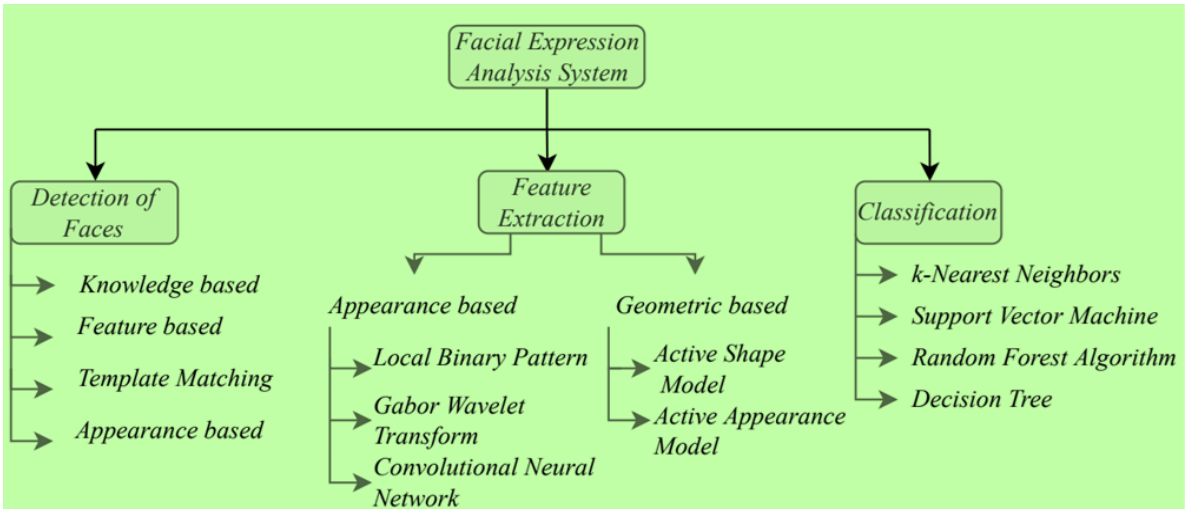

Figure 2. Approaches frequently used in facial expression analysis systems.

In recent years, following the proven success of deep learning models in classification problems [14]-[16], deep learning based methods have been proposed for facial expression analysis in addition to the traditional based approach given above.

Shervin et al. [17] proposed a deep learning-based attentive CNN model that can focus on important parts of the face with robust features. FER2013, FERG, JAFFE and CK+ datasets were used in the study, where a new visualization technique was proposed to take attention to distinct facial regions in different emotions. Accuracy values of 70.02%, 99.3%, 92.8% were obtained in the applications performed on the listed datasets, respectively.

Barman et al. [18] used landmarks to accurately detect facial expressions. In the face region, 3 points for eyebrows, 4 points for eyes, 3 points for nose and 4 points for mouth region were considered. A grid was created with these points. The distance and shape information obtained from the grid is normalized. The features obtained from the distance and shape pair were classified with a multilayer classifier. In the study performed on JAFFE, CK+, MMI and MUG datasets, accuracy between 90.1% and 100% was achieved.

Deepak et al. [19] offered suggestions to eliminate the negative effects of illumination and pose variation on facial expression recognition systems. In the study, a multi-angle optimal model-based deep learning method consisting of 5 main processes was used. After removing the background from the input image, the resulting image is isolated from illumination and pose variations. This deep learning based method achieved 74.4%, 91.34%, 84.32%, 94.62%, 86.19%, 98.7% accuracy for anger, disgust, fear, happiness, sadness and surprise expressions in the CK dataset, respectively.

In this study, 7 basic emotions such as happiness, sadness, fear, anger, surprise, disgust and normal were determined from facial images. The JAFFE dataset prepared in the laboratory environment, which is frequently used in facial expression analysis systems, was used [20]. Multistage convolutional neural networks (MTCNN) were used to detect the face area and CNN architecture was used to obtain features. In order to examine the effects on system performance, the features were classified with different supervised machine learning algorithms. In the study, the highest accuracy rate was achieved when the features extracted with the AlexNet model were classified by Discriminant Analysis.

2. Material and Method

In this study, MTCNN architecture is used to detect the faces in the JAFFE dataset. The input data were resized in accordance with the input layer of the CNN architecture. The extracted feature vectors were classified using machine learning algorithms and their performances were compared. The proposed approach is shown in Figure 3.

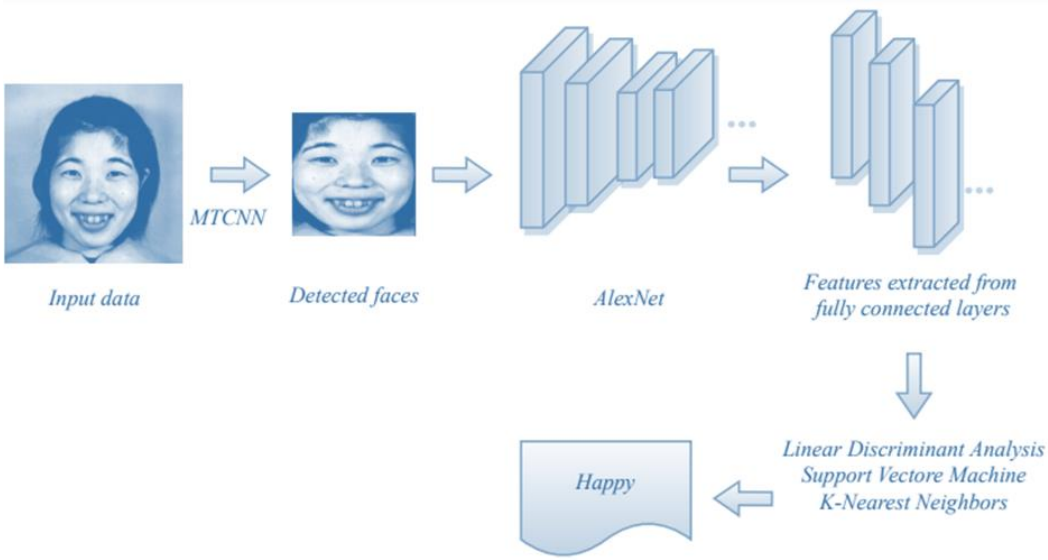

Figure 3. Proposed facial expression analysis system.

The hybrid approach of feature extraction and machine learning involves extracting valuable features from the data and then classifying them with machine learning algorithms. In the deep learning approach, multilayer neural networks are used to automatically learn from the raw data. The network is trained using large amounts of data and features are learned end-to-end.

The hybrid method preferred in this study aims to achieve the highest accuracy without augmenting the dataset. The success of the hybrid system created by combining the feature extraction success of deep learning models with machine learning algorithms is evaluated.

2.1. Dataset

For the development of facial expression analysis systems, datasets are available for researchers to perform comparative and detailed experiments [20]-[23]. In this study, the Japanese Female Facial Expression (JAFFE) dataset published by researchers from the ATR Human Computing Laboratory and the Department of Psychology at Kyushu University has been used.

Facial expression analysis systems can use deep learning models to directly classify facial expressions. However, deep learning models require more data and more computing power than machine learning. For this reason, this study examines the classification performance of a hybrid system with the JAFFE dataset containing 213 data. It is believed that considering the amount of data, the results of the study are comparable to the results obtained with deep learning-based systems in the literature. The dataset contains data on 7 different emotions: happiness, sadness, surprise, anger, fear, disgust and normal. The class distributions of the JAFFE dataset are shown in Figure 4.

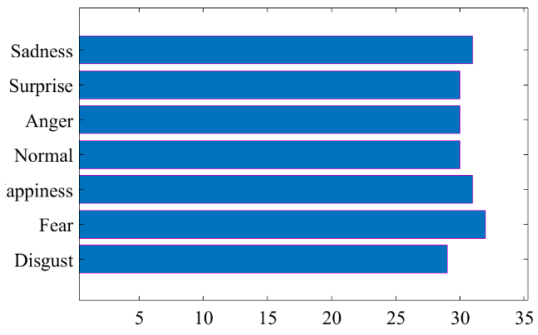

Figure 4. JAFFE dataset class distributions

2.2. Multitask Cascaded Convolutional Network (MTCNN)

Face detection has some difficulties in real-time applications. Many different methods have been proposed in the literature to overcome these difficulties. The proposed MTCNN architecture for face detection consists of 3 models: Proposal Network (P-Net), Refine Network (R-Net), Output Network (O-Net).

In the first stage, the input image is scaled and sent to P-Net. Here, the regions candidate to be faces and the bounding boxes are quickly identified. Then, R-Net rejects frames that do not contain faces from the selected candidate regions. In the third stage, the positions of some critical points on the face are determined with O-Net and the results are improved. In addition to providing the detection of the face region in the frame by obtaining the positions of the critical points of the MTCNN architecture, a solution is also offered to the face alignment problem [24].

2.3. Convolutional Neural Network (CNN)

CNN [25], one of the most basic neural network types in the field of deep learning, has been successfully applied in problems such as image classification, object identification, face recognition, autonomous vehicle technology. Researchers can solve various problems by using open-source datasets with CNNs [26,27]. Unlike machine learning algorithms, CNN does not require an additional processing step for feature extraction. CNN uses the knowledge obtained from the training set for classification due to the convolution layers it contains.

In the 2012 ImageNet Large Scale Visual Recognition Competition, the AlexNet model [16] proposed by Alex Krizhevskyi et al. has achieved significant success in object classification. The proposed model consists of 7 layers, 5 convolutional layers and 2 fully connected layers named FC6 and FC7. The convolutional layers contain 11×11, 5×5 and 3×3 filters.

The AlexNet model provides faster learning and higher accuracy rates due to the use of ReLU activation functions [16]. The model is also trained on the ImageNet dataset. Training with this very large dataset allows the model to extract features more efficiently [16]. For this reason, the AlexNet model is selected in this study in order to extract precious features from the dataset.

The feature vector obtained from the FC7 layer of the AlexNet model consists of 1000 columns. For 213 input images, 1000 feature vectors are obtained. In the feature extraction step, both valuable

features of the data are extracted and the size of the image data is reduced indirectly.

2.4. Linear Discriminant Analysis (LDA)

LDA is a technique used to classify datasets with 2 or more classes. Two different types of classification can be used: class-dependent transformation and interclass transformation. The choice of classification type depends on the type of dataset and the classification problem [28]. Class-dependent transformation aims to maximize the ratio of the variance between classes to the variance within the class, while class-independent transformation aims to maximize the ratio of the overall variance to the variance within the class. It is also used to reduce the number of features in datasets. In this process, uncorrelated features are preserved as much as possible.

2.5. Support Vector Machine (SVM)

Support vector machine is a supervised machine learning algorithm often used in classification and regression problems [29]. It can also be used in problems that cannot be linearly separated with different kernel functions. SVMs can use sigmoid, polynomial or Gaussian kernel functions.

Linear SVMs are used for datasets consisting of linearly separable classes. In the SVM algorithm, the decision boundary that separates the classes is basically created. When determining the decision boundary, the aim is to maximize the distance of the decision boundary to the samples belonging to the classes. For example, in a 2-class problem, the samples belonging to the classes can be separated from each other as in equation (1).

$$f(x) = w.x + b = 0 \quad (1)$$

2.6. K-Nearest Neighbor (k-NN)

KNN which is an easy-to-implement machine learning algorithm, is frequently used in classification and regression problems. In the algorithm, the class of the test data is decided according to the similarity between the examples in the training set [30]. Basically, the algorithm evaluates the class labels of the k samples that are nearest to the test data. The class of the test data is determined by evaluating the majority of the class labels of these samples.

In the k-NN algorithm, which is based on feature similarity, the selection of the k parameter is critical. In the classification problem given in Figure 5, if k parameter is selected 3, the decision will be made according to the class information of the 3 nearest neighbors. In this case, it will be decided that the test data belongs to class 1. On the other hand, if k parameter is selected 7, it will be decided that the test data belongs to class 2.

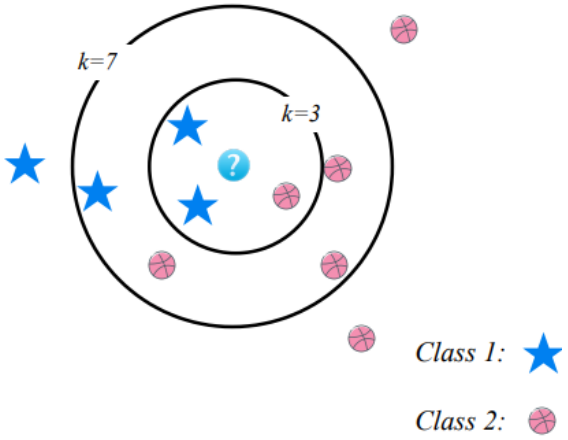

Figure 5. Selection of parameter k in k-NN algorithm.

3. Results and Discussion

The classification performances of different machine learning algorithms for emotion analysis were analyzed using image data. In this study, all experiments were performed in MATLAB R2019B environment with Intel Core CPU at 1.5 GHz, 8 GB RAM and NVIDIA GeForce MX330 graphics card. In this study, we used Classification Learner, an application used in MATLAB. This application allows the user to build classification models using the dataset and evaluate the performance of these models. The application provides various graphs and metrics to evaluate the performance of the generated models. In addition, optimizable models are used to efficiently classify the data and to find the most appropriate parameters.

Facial areas were detected using the MTCNN architecture to remove the unnecessary background in the input images and reduce the size of the image. The process is shown in Figure 6.

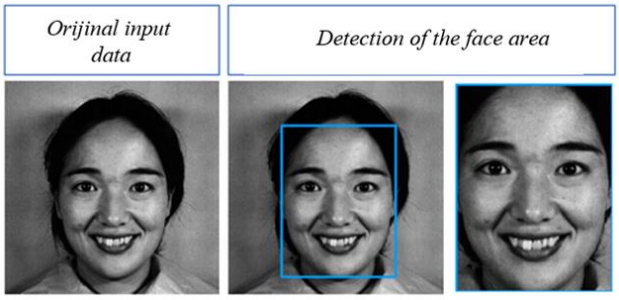

Figure 6. Face area detection from input images.

An object containing the weights and other parameters of the pre-trained AlexNet model was created and used.

Facial expression analysis using image data, LDA, SVM and KNN classifiers have been performed 50 iterations with 10-fold cross-validation technique on the JAFFE dataset. The optimized parameters of the classifiers, training times and total misclassification costs have been recorded. These values are given in Table 1 and Figure 7.

Table 1. Classification results.

	Accuracy	**Iterations**	**Training time (sec.)**	**Total misclassification cost**	**Optimized hyperparameters**	
LDA	%89,2	50	733,99	23	Discriminant type	Linear
					Optimizer type	Bayesian
SVM	%88,3		2383,8	25	Kernel function	Gaussian
					Kernel scale	151,21
KNN	%87,8		679,19	26	Number of neighbors	1
					Distance metric	Correlation

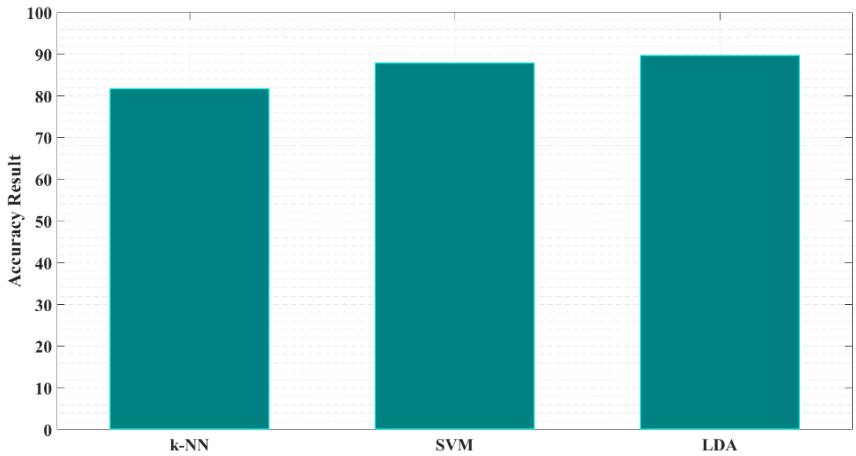

Figure 7. Accuracy scores of classifiers.

According to Table 1, the highest performance in facial expression analysis using the JAFFE dataset has been 89.2% with LDA, while the lowest performance has been 87.8% with the KNN classifier. Training time of the classifiers is analyzed and it is seen that the SVM classifier takes considerably more time compared to the other methods. During the training of the classifiers, optimal parameters are defined as the parameters with minimum error. In Figure 8, the confusion matrices of the models and Figure 9, the minimum classification error graphs of the classifiers are shown. For LDA, SVM and KNN classifiers respectively, the confusion matrix parameters and performance metrics for the emotion states are shown in Tables 2,3,4,5,6,7.

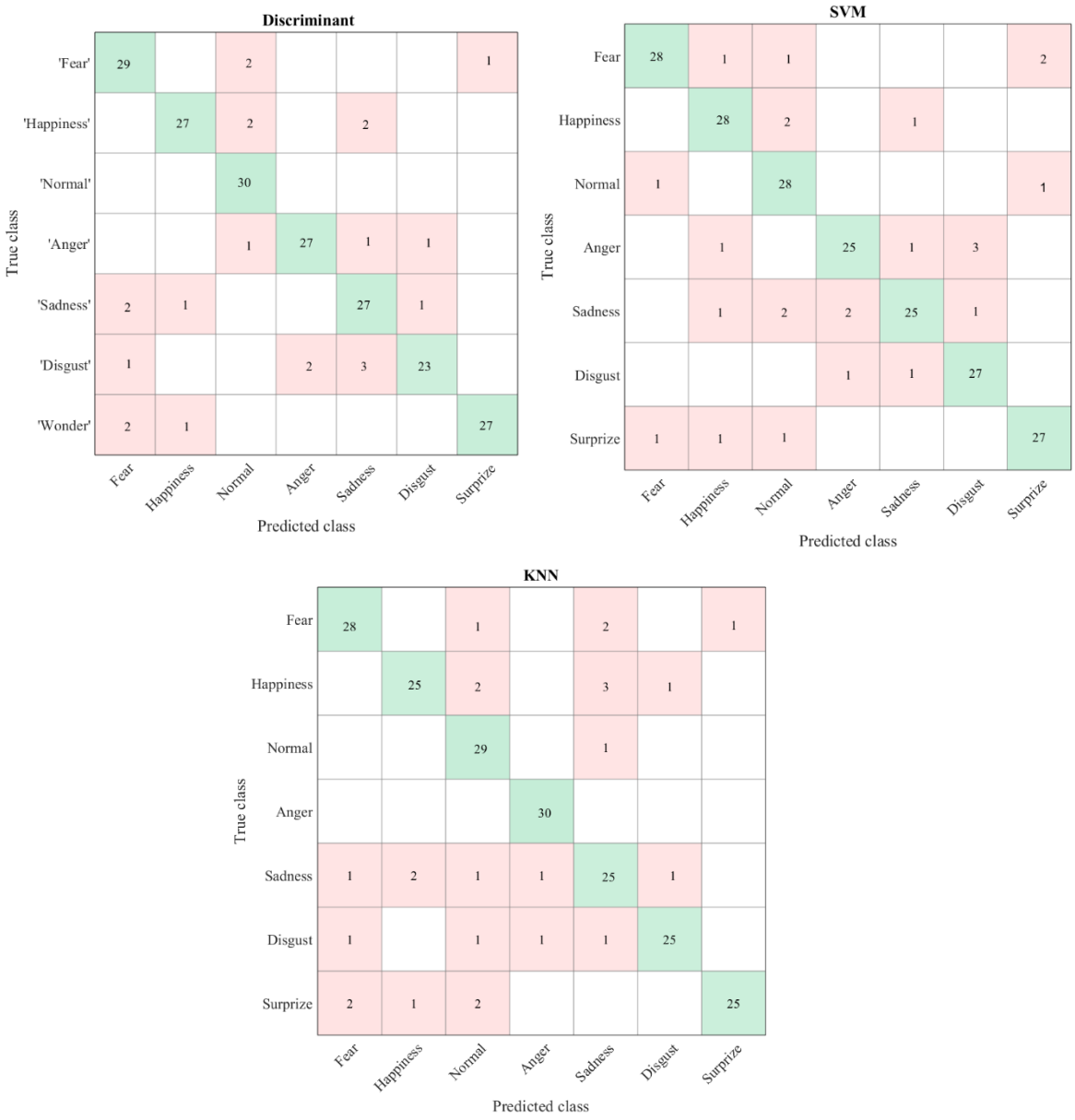

Figure 8. Confusion matrices of classifiers.

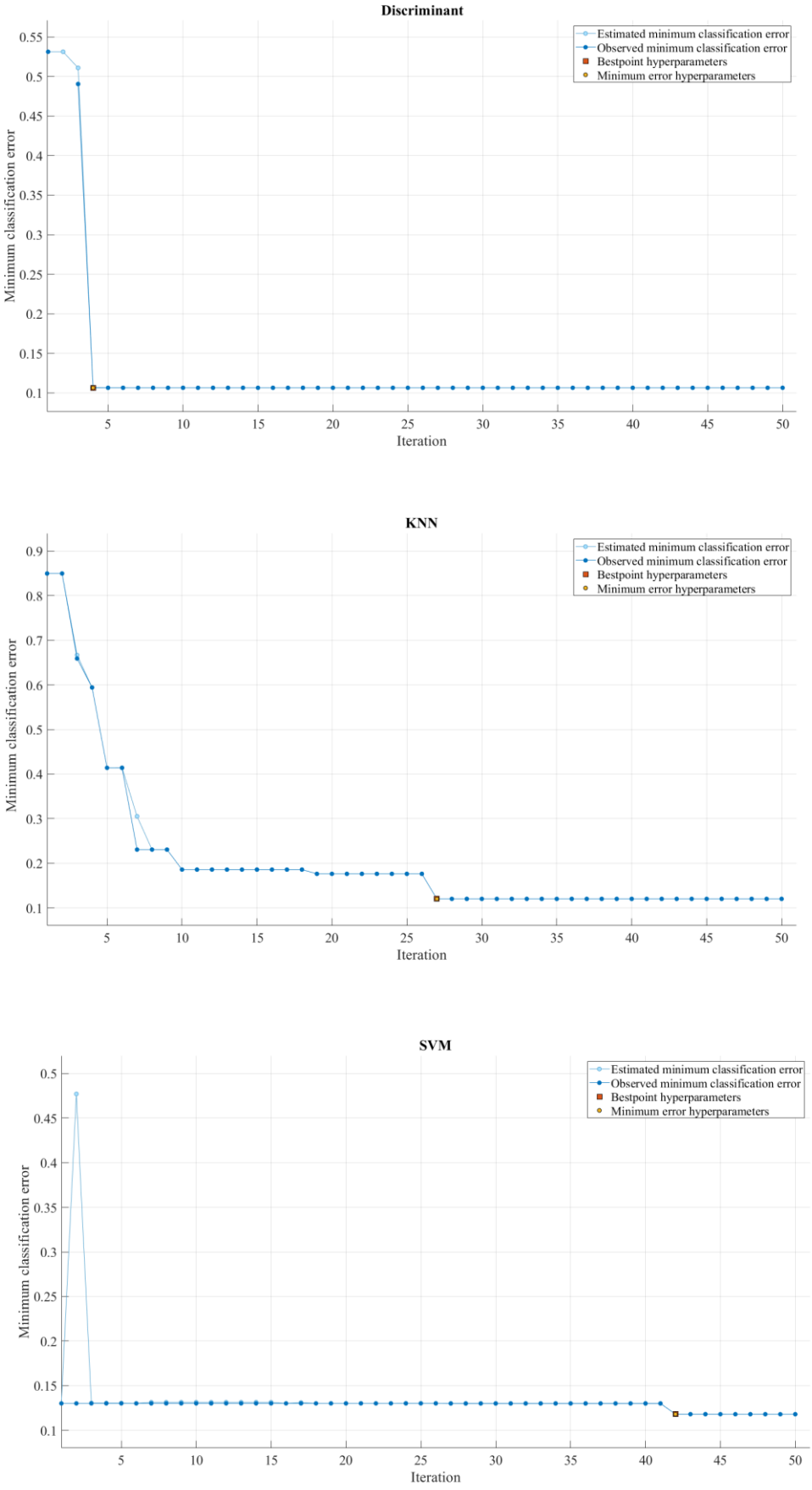

Figure 9. Minimum classification error graphs of classifiers.

Table 2. Confusion matrix parameters of emotions for AlexNet+LDA

	Fear	**Happiness**	**Normal**	**Anger**	**Sadness**	**Disgust**	**Surprise**
TP	29	27	30	27	27	23	27
TN	176	180	178	181	176	182	182
FN	3	4	0	3	4	6	3
FP	5	2	5	2	6	2	1

Table 3. Performance metrics of emotions for AlexNet+LDA

	Accuracy (%)	**Precision (%)**	**Sensitivity (%)**	**Specificity (%)**
Fear	0,96	0,85	0,91	0,97
Happiness	0,97	0,93	0,87	0,99
Normal	0,98	0,86	1,00	0,97
Anger	0,98	0,93	0,90	0,99
Sadness	0,95	0,82	0,87	0,97
Disgust	0,96	0,92	0,79	0,99
Surprise	0,98	0,96	0,90	0,99

Table 4. Confusion matrix parameters of emotions for AlexNet+SVM

	Fear	**Happiness**	**Normal**	**Anger**	**Sadness**	**Disgust**	**Surprise**
TP	28	28	28	25	25	27	27
TN	179	178	177	181	179	180	180
FN	4	3	2	4	6	2	3
FP	2	4	6	3	3	4	3

Table 5. Performance metrics of emotions for AlexNet+SVM

	Accuracy (%)	**Precision (%)**	**Sensitivity (%)**	**Specificity (%)**
Fear	0,99	0,93	0,88	0,99
Happiness	0,97	0,88	0,90	0,98
Normal	0,96	0,82	0,93	0,97
Anger	0,97	0,89	0,86	0,98
Sadness	0,96	0,89	0,81	0,98
Disgust	0,97	0,87	0,93	0,98
Surprise	0,97	0,90	0,90	0,98

Table 6. Confusion matrix parameters of emotions for AlexNet+KNN

	Fear	**Happiness**	**Normal**	**Anger**	**Sadness**	**Disgust**	**Surprise**
TP	28	25	29	30	25	25	25
TN	177	179	176	181	175	182	182
FN	4	6	1	0	6	4	5
FP	4	3	7	2	7	2	1

Table 7. Performance metrics of emotions for AlexNet+KNN

	Accuracy (%)	Precision (%)	Sensitivity (%)	Specificity (%)
Fear	0,96	0,88	0,88	0,98
Happiness	0,96	0,89	0,81	0,98
Normal	0,96	0,81	0,97	0,96
Anger	0,99	0,94	1,00	0,99
Sadness	0,94	0,78	0,81	0,96
Disgust	0,97	0,93	0,86	0,99
Surprise	0,97	0,96	0,83	0,99

The comparison of the proposed facial expression analysis system with other studies using the same dataset is presented in Table 8. When the table is analyzed, Nicolai et al. [10] achieved 78.8% accuracy with Fuzzy classifier using JAFFE dataset, Fatima Zahra et al. achieved 89.2% accuracy with decision trees in a study on JAFFE dataset, and Ju Jia et al. achieved 77.1% accuracy with SVM classifier. In the proposed study, a higher accuracy rate was achieved than the studies performed on the JAFFE dataset in the literature. It is seen that the proposed system with the features extracted with the AlexNet model and the LDA classifier from machine learning algorithms gives higher results compared to other studies using the JAFFE dataset.

Table 8. Comparison of the proposed study with studies using the same data sets.

Author	Dataset	Classifier	Success rate (%)
Nicolai at al. (2015) [10]	JAFFE	Fuzzy classification	%78,8
Fatima Zahra at al. (2016) [11]	JAFFE Cohen-Kanade	Decision tree	%89,2 %90,61
Ju Jia at al. (2016) [12]	JAFFE	Support vector machine	%77,1
Proposed system	**JAFFE**	**Linear discriminant analysis**	**%89,2**

4. Conclusion and Suggestions

In this study, a comparative analysis of the performance of machine learning techniques in expression classification from facial images has been aimed. For this reason, the JAFFE dataset, which has open source access for researchers to perform their studies, has been used. Facial expressions have been classified with LDA, SVM and KNN classifiers, which are frequently used in classification problems. The experimental results show that the LDA classifier is more successful than other methods in facial expression analysis. In addition, considering the training time of the classifiers, SVM has been the classifier which has been trained in the longest time.

The recognition of facial expressions has been used in the early diagnosis of some diseases, behavioral analysis, security systems, and safe driving. In facial expression recognition, which is a multi-class classification problem, it is possible to achieve high success with machine learning methods as well as deep learning methods. According to the results of this study, without any data augmentation, LDA has achieved 89.2% success in the classification of the JAFFE dataset.

There are many challenges in detecting the facial area in computer vision applications with facial images. In addition, many factors directly affect the success of deep learning or machine learning methods. Considering all these challenges, the research on facial expression analysis is expected to continue.

Acknowledgment

This study has been produced from the master thesis of Gamze BALLIKAYA.

Contributions of the Authors

The authors' contributions to the paper are equal.

Conflict of Interest Statement

There is no conflict of interest between the authors.

Statement of Research and Publication Ethics

The study is complied with research and publication ethics.

References

[1] P. Ekman, W. Friesen, *Facial action coding system*, Consulting Psychologists Press; 1978.

[2] A. Mehrabian, "Communication Without Words," *in communication theory*, Routledge, 2017, pp. 193–200. doi: 10.4324/9781315080918-15.

[3] G. Simcock et al., "Associations between Facial Emotion Recognition and Mental Health in Early Adolescence.," *Int J Environ Res Public Health*, vol. 17, no. 1, p. 330, Jan. 2020, doi: 10.3390/ijerph17010330.

[4] A. Wabnegger et al., "Facial emotion recognition in Parkinson's disease: An fMRI investigation," *PLoS One*, vol. 10, no. 8, p. e0136110, Aug. 2015, doi: 10.1371/journal.pone.0136110.

[5] D. S. Kosson, Y. Suchy, A. R. Mayer, and J. Libby, "Facial affect recognition in criminal psychopaths.," *Emotion*, vol. 2, no. 4, pp. 398–411, Dec. 2002, doi: 10.1037/1528-3542.2.4.398.

[6] V. V Ramalingam, A. Pandian, A. Jaiswal, and N. Bhatia, "Emotion detection from text," *J Phys Conf Ser*, vol. 1000, no. 1, p. 012027, Apr. 2018, doi: 10.1088/1742-6596/1000/1/012027.

[7] C. S. Ooi, K. P. Seng, L. M. Ang, and L. W. Chew, "A new approach of audio emotion recognition," *Expert Syst Appl*, vol. 41, no. 13, pp. 5858–5869, Oct. 2014, doi: 10.1016/J.ESWA.2014.03.026.

[8] Y. P. Lin et al., "EEG-based emotion recognition in music listening," *IEEE Trans Biomed Eng*, vol. 57, no. 7, pp. 1798–1806, Jul. 2010, doi: 10.1109/TBME.2010.2048568.

[9] M. Suk and B. Prabhakaran, "Real-Time Mobile Facial Expression Recognition System -- A Case Study," in 2014 *IEEE Conference on Computer Vision and Pattern Recognition Workshops*, IEEE, Jun. 2014, pp. 132–137. doi: 10.1109/CVPRW.2014.25.

[10] A. Nicolai and A. Choi, "Facial Emotion Recognition Using Fuzzy Systems," in 2015 *IEEE International Conference on Systems, Man, and Cybernetics*, IEEE, Oct. 2015, pp. 2216–2221. doi: 10.1109/SMC.2015.387.

[11] F. Z. Salmam, A. Madani, and M. Kissi, "Facial Expression Recognition Using Decision Trees," in 2016 *13th International Conference on Computer Graphics, Imaging and Visualization (CGiV)*, IEEE, pp. 125–130, Mar. 2016. doi: 10.1109/CGiV.2016.33.

[12] Ju Jia, Yan Xu, Sida Zhang, and Xianglong Xue, "The facial expression recognition method of random forest based on improved PCA extracting feature," in *2016 IEEE International Conference on Signal Processing, Communications and Computing (ICSPCC)*, IEEE, Aug., pp. 1–5, 2016. doi: 10.1109/ICSPCC.2016.7753643.

[13] S. M. González-Lozoya, J. de la Calleja, L. Pellegrin, H. J. Escalante, M. A. Medina, and A. Benitez-Ruiz, "Recognition of facial expressions based on CNN features," *Multimed Tools Appl*, vol. 79, no. 19–20, pp. 13987–14007, May 2020, doi: 10.1007/s11042-020-08681-4.

[14] K. He, X. Zhang, S. Ren, and J. Sun, "Deep Residual Learning for Image Recognition," in *2016 IEEE Conference on Computer Vision and Pattern Recognition (CVPR)*, IEEE, , pp. 770–778, Jun. 2016. doi: 10.1109/CVPR.2016.90.

[15] K. Simonyan and A. Zisserman, "Very Deep Convolutional Networks for Large-Scale Image Recognition," *3rd International Conference on Learning Representations, ICLR 2015 - Conference Track Proceedings*, Sep. 2014, doi: 10.48550/arxiv.1409.1556.

[16] A. Krizhevsky, I. Sutskever, and G. E. Hinton, "ImageNet classification with deep convolutional neural networks," *Commun ACM*, vol. 60, no. 6, pp. 84–90, May 2017, doi: 10.1145/3065386.

[17] S. Minaee, M. Minaei, and A. Abdolrashidi, "Deep-Emotion: Facial Expression Recognition Using Attentional Convolutional Network," *Sensors*, vol. 21, no. 9, p. 3046, Apr. 2021, doi: 10.3390/s21093046.

[18] A. Barman and P. Dutta, "Facial expression recognition using distance and shape signature features," *Pattern Recognit Lett*, vol. 145, pp. 254–261, May 2021, doi: 10.1016/j.patrec.2017.06.018.

[19] D. K. Jain, Z. Zhang, and K. Huang, "Multi angle optimal pattern-based deep learning for automatic facial expression recognition," *Pattern Recognit Lett*, vol. 139, pp. 157–165, Nov. 2020, doi: 10.1016/j.patrec.2017.06.025.

[20] M. J. Lyons, "'Excavating AI' Re-excavated: Debunking a Fallacious Account of the JAFFE Dataset", Accessed: Sep. 05, 2022. [Online]. Available: https://excavating.ai/

[21] M. Lyons, S. Akamatsu, M. Kamachi, and J. Gyoba, "Coding facial expressions with Gabor wavelets," Proceedings - *3rd IEEE International Conference on Automatic Face and Gesture Recognition*, FG 1998, pp. 200–205, 1998, doi: 10.1109/AFGR.1998.670949.

[22] O. Langner, R. Dotsch, G. Bijlstra, D. H. J. Wigboldus, S. T. Hawk, and A. van Knippenberg, "Presentation and validation of the Radboud Faces Database," http://dx.doi.org/10.1080/02699930903485076, vol. 24, no. 8, pp. 1377–1388, Dec. 2010, doi: 10.1080/02699930903485076.

[23] P. Lucey, J. F. Cohn, T. Kanade, J. Saragih, Z. Ambadar, and I. Matthews, "The extended Cohn-Kanade dataset (CK+): A complete dataset for action unit and emotion-specified expression," 2010 *IEEE Computer Society Conference on Computer Vision and Pattern Recognition - Workshops*, CVPRW 2010, pp. 94–101, 2010, doi: 10.1109/CVPRW.2010.5543262.

[24] K. Zhang, Z. Zhang, Z. Li, and Y. Qiao, "Joint Face Detection and Alignment Using Multitask Cascaded Convolutional Networks," *IEEE Signal Process Lett*, vol. 23, no. 10, pp. 1499–1503, 2016, doi: 10.1109/LSP.2016.2603342.

[25] Z. Li, F. Liu, W. Yang, S. Peng, J. Zhou, and S. Member, "A Survey of Convolutional Neural Networks: Analysis, Applications, and Prospects; A Survey of Convolutional Neural Networks: Analysis, Applications, and Prospects," *IEEE Trans. Neural Netw. Learn. Syst.*, vol. 33, no. 12, pp. 6999–7019, 2022, doi: 10.1109/TNNLS.2021.3084827.

[26] D. Kaya, "The mRMR-CNN based influential support decision system approach to classify EEG signals", *Measurement*, vol. 156 no. 107602, p.107602, 2020, http: //dx.doi.org/10.1016/j.measurement.2020.107602.

[27] D. Kaya, "Automated gender-Parkinson's disease detection at the same time via a hybrid deep model using human voice." *Concurrency and Computation: Practice and Experience*, vol. 34, no.26, 2022.

[28] S. Balakrishnama and A. Ganapathiraju, "Institute for Signal And Information Processing Linear Discriminant Analysis-A Brief Tutorial" 1998.

[29] X. Haijun, P. Fang, W. Ling, and L. Hongwei, "Ad hoc-based feature selection and support vector machine classifier for intrusion detection," Proceedings of 2007 *IEEE International Conference on Grey Systems and Intelligent Services*, GSIS 2007, pp. 1117–1121, 2007, doi: 10.1109/GSIS.2007.4443446.

[30] T. M. Mitchell, "Does machine learning really work?" *AI magazine*, vol. 18, no. 3, pp. 11–20, 1997

Bitlis Eren Üniversitesi Fen Bilimleri Dergisi
BİTLİS EREN UNIVERSITY JOURNAL OF SCIENCE
ISSN: 2147-3129/e-ISSN: 2147-3188
VOLUME: 12 NO: 3 PAGE: 608-616 YEAR: 2023
DOI:10.17798/bitlisfen.1220387

Analysis of an Inductive Coupling Wireless Power Transfer System with a Finite Element Method for Charging Applications of Electric Vehicles

Yıldırım ÖZÜPAK[1*], Mehmet ÇINAR[2]

[1]*Dicle University, Silvan Vocational School, Electrical Department, Diyarbakır, TÜRKİYE*
[2] *Bitlis Eren University, Tatvan Vocational School, Electrical Department, Bitlis, TÜRKİYE*
(ORCID: 0000-0001-8461-8702) (ORCID: 0000-0002-1542-9120)

Keywords: WPT, Inductive coupling, Ansys-Maxwell, Efficiency.

Abstract

With the development of technology, Wireless Power Transfer (WPT) systems have also started to be used in charging applications for electric vehicles. The basic methods of WPT systems are based on power transmission systems with laser, microwave, magnetic induction, and magnetic resonance. Factors such as the limited use of fossil fuels and environmental pollution have led researchers to see electric vehicles as a solution and to charge these vehicles with wireless systems. Most commercial wireless power transmission applications are currently limited to close contact transmission distances. There are challenges in increasing coverage, routing transmissions, and safely exploiting sufficiently strong electric fields. To provide power efficiently, highly directional transmitters must be used. Otherwise, with an omnidirectional transmission, only a small part of the transmitted power will reach the receiver. Especially in order to distribute power over long distances, it is often necessary to resort to radiation transfer methods that tightly combine electric and magnetic fields. In this study, important studies on WPT systems were investigated and examined. Then, a WPT transformer is modeled with the Finite Element Method based ANSYS-Maxwell-3D. The results obtained using the simulation method are presented in comparison with the research findings. Determining the efficiency of wireless power transfer used in electric vehicle charging applications is the expected result of the study.

1. Introduction

Wireless Power Transmission is the transmission of electrical energy through electric, magnetic or electromagnetic fields rather than wires or cables. Wireless power transmission can be used attractively in situations where it is dangerous or impossible to use interconnected cables. Wireless power transmission is widely used in electric vehicle charging systems, implantable medical devices such as artificial cardiac pacing, RFID tags, and many other applications. The basic concepts of wireless communication and wireless power transmission are very similar in that they use the same area and waves, but the main goal in wireless communication is to transfer data. In wireless communication, the transmitted power is not important as long as the signal-to-noise ratio of the received signal is acceptable. On the other hand, wireless power transmission aims to maximize power transmission efficiency and coverage while ensuring people's health and safety.

Most commercial wireless power transmission applications are currently limited to close contact transmission distances. There are two main challenges in increasing coverage: routing transmissions and safely benefiting from sufficiently strong electric fields. First of all, highly directional transmitters need to be applied to deliver power efficiently [1]. Otherwise, with an omnidirectional transmission, only a small part of the transmitted power will reach the receiver. Second, to distribute

*Corresponding author: yildirimozupak@gmail.com
Received: 14.02.2023, Accepted: 16.09.2023

power over long distances, it is often necessary to resort to radiation transfer methods that tightly combine electric and magnetic fields [3]-[5]. Unfortunately, prolonged exposure to large electric fields causes serious injury to living tissues. Thus, safety concerns require small electric fields, while long-distance transmissions require strong emissions of electromagnetic waves [6].

To overcome the above problems, Disney-Research engineers have recently proposed a system that can safely transfer kW-level power from a room to mobile devices. The main contribution of this research is to provide a sufficient amount of power, taking into account safety concerns. For this purpose, by simulating the resonant electromagnetic mode of a metallic room by allowing current to flow through the walls, ceiling, and floor, the researchers produced uniform magnetic fields penetrating into the room.

To separate potentially harmful electric fields from magnetic ones, Disney engineers diverted the current through some discrete capacitors. In this way, the resonant frequency of the chamber is significantly lowered so that the cavity enters the deep sub-wavelength pattern. Working in the deep sub-wavelength regime, the cavity produces magnetic fields one hundred times stronger than the electric fields produced. In conclusion, the experimental results of the new method have shown that it can successfully avoid the harmful effects of large electric fields without sacrificing the transmit power.

Wireless power transfer systems are usefully used in many areas, such as charging electric vehicles (EV), depending on the developing technological developments. Wireless power transfer offers many such advantages to the user [7]. Among the earliest records of work to use a lot of power in wireless power transfer, it is known that it provided power to electric trains running in a mine in the Soviet Union in 1980 through wireless power transfer. It is possible to control large amounts of currents, which has rapidly developed wireless power transfer innovation [8].

There are three different charching methods hat are effectively used in electric vehicles: battery replacement, wired charging, and wireless (inductive) charging [8]. The advantage of inductive power transfer is its high efficiency and high-power capacity. It has also been the most commercially successful wireless power transmission technology. Its application areas include widely integrated circuits, biomedical devices, sensor networks, portable electronic products, and electric vehicles. High efficiency can be achieved by regularly adjusting the system efficiency, circuit resonances, and energy transfer distance. The distance can be further extended using intermediate resonant coils without significantly affecting efficiency. Due to its technological features, it can be concluded that an inductive power transfer system is a good solution to realize wireless power transfer for electric vehicle charging applications. In this paper, wireless power transfer methods for electric vehicles were examined, and a wireless power transfer circuit for inductive wireless power transfer for electric vehicles was modeled in the Finite Element Method (FEM) based ANSYS-Maxwell program, and results were obtained according to the technical data of the circuit.

2. Material and Method

An inductive power transfer system uses a non-radioactive magnetic field, typically in the kHz to MHz range, to affect the power transfer. Since there are resonances in the circuit, it is also called magnetic resonance. Two planar coils form a loosely coupled transformer called a magnetic or inductive coupler to create a magnetic field. Since there is a large air gap between the coils, their magnetic coupling is relatively low [9]. The basic idea of the inductive power transfer system used in the wireless charging system is based on the well-established Ampere's law of circulation and Faraday's law of induction. The basic structure of the system is shown in Figure 1 [10].

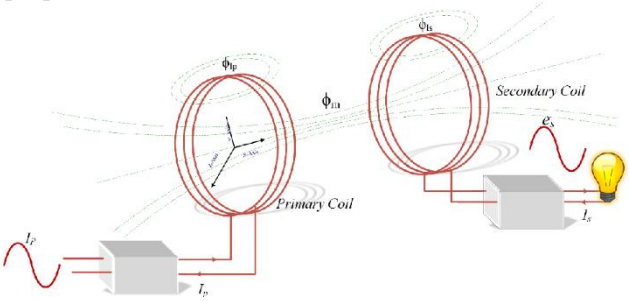

Figure 1. Structure of the inductive power transmission system

Figure 1 shows two coils connected by inductive coupling. Here, the subscript P and S denote the primary and secondary coil, respectively. The terms $\emptyset_m$, $\emptyset_{ip}$, and $\emptyset_{is}$ are mutual flux, primary leakage flux and secondary leakage flux, respectively. M, L_P and L_s are represent mutual inductance, self-inductance of primary coil and self-inductance of secondary coil, respectively. When a time varying current is applied to the primary coil, a time varying flux of the same frequency is produced in the region surrounding the primary coil. The strength of the magnetic field around a closed path is directly proportional to the current carried by the coil and can be found by Ampere's law. A generalized block

diagram of the inductive power transmission system for EV battery charging can be drawn as in Figure 2 [11].

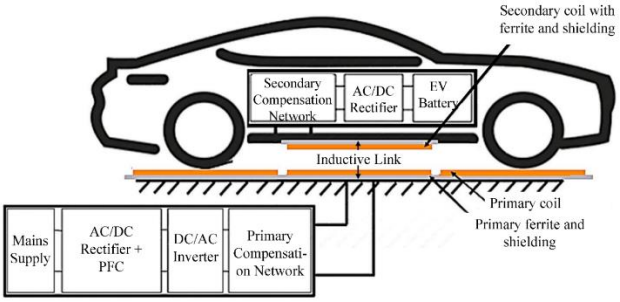

Figure 2. Block diagram of the inductive power transfer system for EV battery charging

Usually mounted under the vehicle, the receiving coil converts the oscillating magnetic flux fields into high frequency AC. The high frequency AC is then converted into a stable DC source used by the onboard batteries. Magnetic planar ferrite plates are used on both the transmitter and receiver sides to reduce any harmful leakage flux and improve the magnetic flux distribution [12]. The energy is then transferred to the vehicle side via the secondary coil, which is reciprocally connected to the primary coil via the flux produced in the air gap by the primary coil current [13]. The energy received by the secondary coil is then processed by the secondary compensation circuit, which is added to improve the power transmission capacity of the system [14]. Finally, the voltage received in this way is corrected to make it usable by the load [15].

In the case of using a magnetic induction system to wirelessly charge electric vehicles, a suitable air gap should be selected between the transmitter coil mounted on the road and the vehicle. Because of this large air gap, the leakage flux is very high, and the coupling coefficient remains constant at certain ranges. Such applications are classified as loosely coupled systems [16-19]. Weak connections in loosely coupled systems lead to poor power transmission. To improve coupling and compensate for leakage inductance, capacitive compensation is required in the primary and secondary windings.

2.1. Compensation Topologies

Compensator networks, which are capacitors, are made to resonate with the coil inductance, thereby creating a resonant inductive connection. Depending on the connection of the compensation capacitor in the primary and secondary windings, four types of resonant inductive connections can be identified. These are Serial-Serial (SS), Serial-Parallel (SP), Parallel-Serial (PS), and Parallel-Parallel (PP) connections as shown in Figure 3 [15].

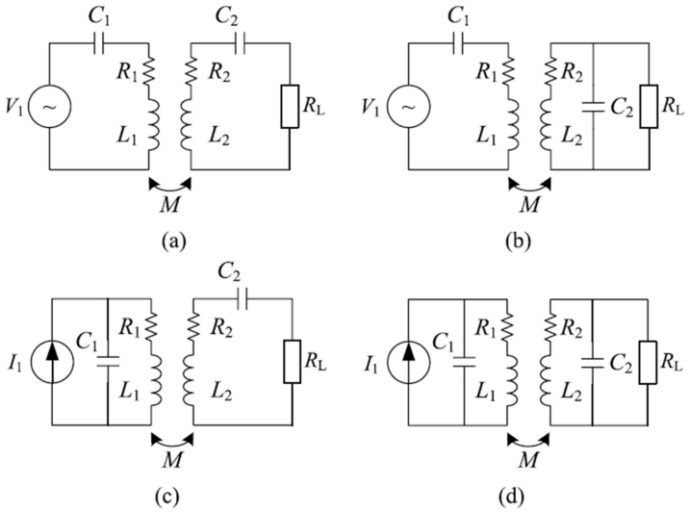

Figure 3. Compensation topologies

In this study, the Serial-Serial topology example is preferred. The Series-to-Series topology option allows selection of compensation capacitances based only on self-inductance, regardless of load and magnetic coupling. Therefore, in case of misalignments between coils, the system continues to operate under resonance despite the mutual inductance changes. Accordingly, the Serial-to-Serial topology becomes suitable for EV battery charging. A Series-Series resonant inductive connection is theoretically the best in terms of efficiency, number of components, less complexity of control, and cost, and therefore, in this study, a simulation study was carried out on a Series-Series inductively connected circuit.

The Figure 4 shows the equivalent circuit of a series-to-series compensated resonant inductive power transfer system. The primary side of the series-to-series compensated resonant inductive power transfer junction is powered by a voltage source full bridge inverter that converts direct voltage V_{DC} to high frequency alternating voltage V_{AB}. On the secondary side, a rectifier with capacitive filter C_{Cf} converts the high-frequency voltage into direct voltage V_0 and direct current I_0 required by the load R_0. The Series-Series topology acts as a current source when powered from the primary voltage source in ideal resonance condition. Therefore, a simple capacitive filter is sufficient. The full bridge inverter generates a square wave voltage V_A with an infinite number of

harmonics. However, the Series-to-Serial inductive power transmission junction acts as a bandpass filter that blocks unwanted frequency components generated from the primary-fed power electronics converter. Therefore, the current through the inductive power transmission coupling is almost sinusoidal. This allows the first harmonic approximation method to be used to calculate the parameters of the Series-to-series-inductive power transmission connection.

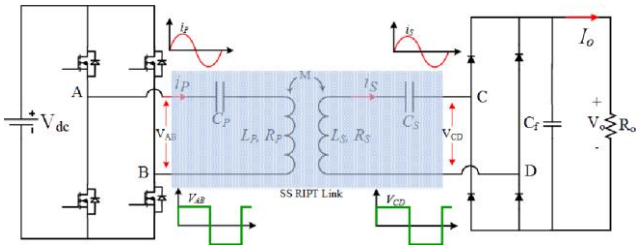

Figure 4. Equivalent circuit of Series-Series compensated resonant inductive power transfer system

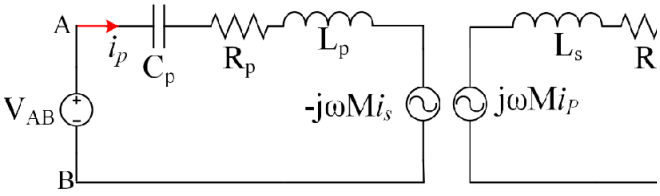

Figure 5. Simplified equivalent model of Series-Series inductive power transmission circuit

2.2. Calculation of Electrical Parameters

Figure 6 shows the block diagram and components of an SS-inductive power transfer based wireless charger. The aim is to calculate the parameters of the SS-inductive power transmission coupling (shown in the red dotted box) for a given load (battery).

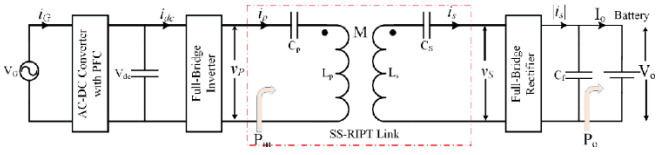

Figure 6. Block diagram of a SS-inductive power transfer based wireless charger

To simplify the calculation of the parameters of the SS-inductive power transmission coupling, the following assumptions are made:

- The efficiency of the SS-inductive power transmission link is assumed to be full. This assumption is valid since the value of the coil resistance is not known prior to the connection design and is therefore assumed to be negligible.
- Only the fundamental component of the input voltage V_P (first harmonic) and the output voltage of the SS-inductive power transmission link are taken into account, and higher order harmonics are neglected. In other words, the quality factor of the primary and secondary circuit is considered high to obtain sinusoidally varying primary and secondary currents.
- All switching elements are considered ideal with zero commutation time (instant on and off). In other words, all converters are assumed to be fully efficient.
- The magnitude of the input voltage to the SS-inductive power transmission connection, ie V_P, is considered equal to the grid (supply) voltage magnitude V_S. This assumption is valid as there is usually a power factor correction stage between the grid supply and the full bridge inverter. At this stage, the DC junction voltage of the full-bridge inverter can adjust V_{DC} so that V_P is equal to the grid voltage.
- Ideal resonance is assumed on the primary and secondary sides. Let the desired output power be P_0. Because the load is a battery pack, the charging voltage is known as defined by the manufacturer of the battery pack. If V_0 denotes rated charging voltage or output voltage, DC resistance (battery resistance) R_0 can be calculated by equation (1).

$$R_0 = \frac{V_0^2}{P_0} \tag{1}$$

The AC equivalent of a DC resistive load with a diode rectifier and a capacitive output filter can be given by equation (2). This is the value of the resistance seen from the secondary side of the SS-inductive power transmission link.

$$R_0 = \frac{\pi}{8}\frac{V_0^2}{P_0} \tag{2}$$

The secondary voltage V_S is a square wave due to the capacitive output filter. The RMS value of the principal component V_S can be given by equation (3). The RMS value of secondary current i_S, can be calculated by equation (4).

$$V_{S_{rms}} = \frac{2\sqrt{2}V_0}{\pi} \tag{3}$$

$$I_{S_{rms}} = \frac{V_{S_{rms}}}{R_L} \tag{4}$$

Assuming that V_P is equal to the mains voltage V_S, the RMS value of the primary current can be given by equation (5).

$$I_{P_{rms}} = \frac{P_{in}}{V_{P_{rms}}} \tag{5}$$

Once the values of the primary and secondary currents are known, the mutual inductance value for the desired amount of output power can be derived by applying Kirchhoff's voltage law equation on the secondary side of the SS-inductive power transmission junction. From Figure 8, it can be written as equation (6) at the resonant frequency.

$$\left| j\omega_0 M i_P \right| = R_L \left| i_S \right| \tag{6}$$

The secondary inductance is calculated from the secondary quality factor Q_S. As mentioned earlier, the value of Q_S should be chosen as a higher value may complicate the tuning of the system and will generate harmonics in a lower current and voltage waveform. Equation (7) gives the required secondary inductance value.

$$I_S = \frac{Q_S R_L}{\omega_0} \tag{7}$$

$$Q < \frac{1}{Q_S}\sqrt{1-\frac{1}{4Q_S^2}} \tag{8}$$

Equation (8) can calculate the minimum air gap between the primary and secondary coils. Also, the coupling factor must be well chosen for high efficiency. This is an important difference between a loosely coupled system, such as an SS-inductive power transmission system, and a closely coupled system, such as power transformers, if possible. Once the k value has been decided, the primary inductance value can be calculated using equation (9).

$$L_P = \frac{M^2}{L_s k^2} \tag{9}$$

2.3. Design of Rectangular WPT Transformer Model

In this section, the design of rectangular coil transformers using ANSYS-Maxwell software is explained. In this study, a unique rectangular coil arrangement is considered, as shown in Figure 7. The rectangular transformer model consists of a coil of circular cross section wound in a rectangular shape. The side lengths of the rectangular transformer model are taken to be equal to the diameter of the circular transformer model. The dimensions of the rectangular transformer model are given in Table 1.

Table 1. Dimensions of rectangular WPT transformer

Parameter	Receiver coil	Transmitter coil
Turn Number	42	24
Material thickness	2 mm	2 mm
Coil dimension	(395x395) mm	(395x395) mm

The primary and secondary winding numbers of this model are the same as the circular transformer model. Figure 7 shows the coreless circular transformer coils.

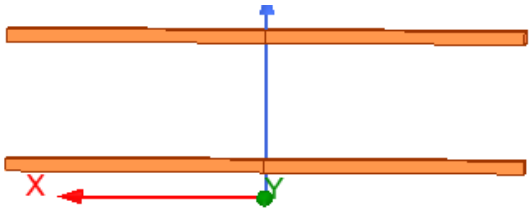

Figure 7. Coreless transformer model

3. Results and Discussion

The system's circuit was installed on the Ansys Simplorer interface, the coils were installed on the Maxwell 3D interface, and the WPT system was analyzed by simulating the two programs. The input, output power and efficiency of the system are observed. The co-simulation circuit of the WPT system is shown in Figure 8.

The ANSYS/Workbench model shown in Figure 9 was used to make the inductance calculations of the system and the analysis of the variation of the mutual inductance with respect to distance. This model calculates the input inductance of the system, the capacitance value that meets the resonance condition, and the quality factor by analyzing the mutual inductance in the desired distance range. Thus, transmission power and efficiency can be interpreted more easily.

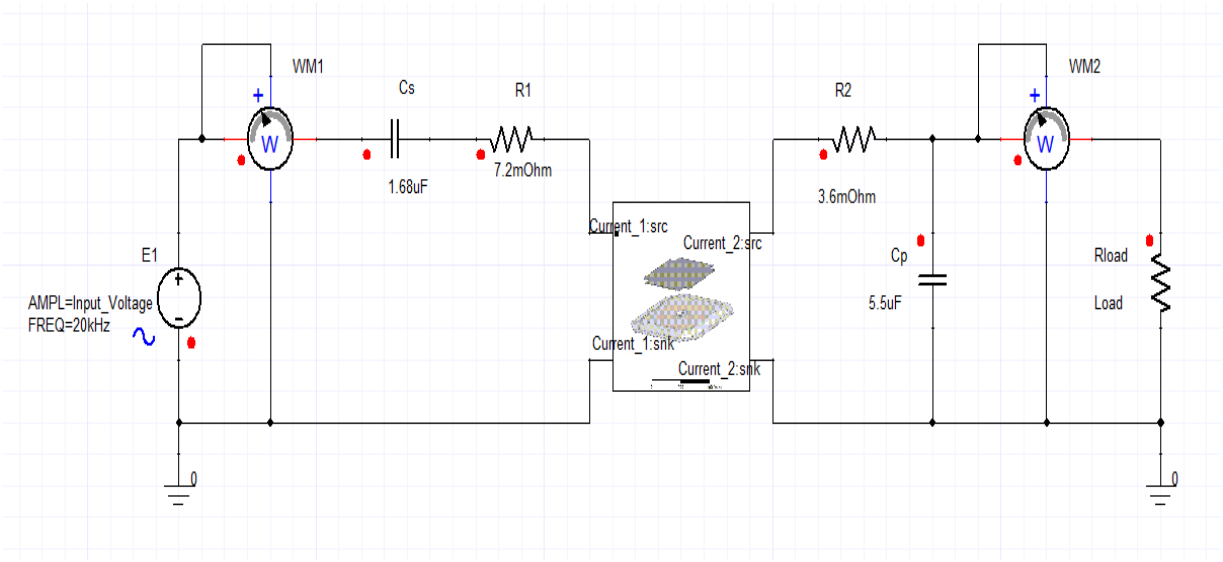

Figure 8. WPT co-simulation circuit

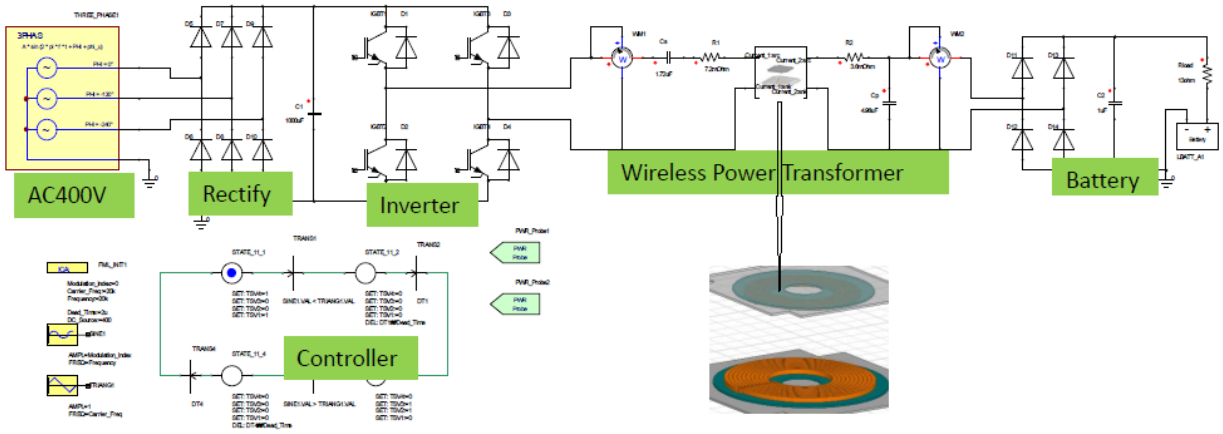

Figure 9. Inductance analysis and mutual inductance ANSYS model

The results obtained from the simulation were compared with the mathematical results. The results obtained for simulation and calculated values are presented graphically. The variation of the coupling coefficient with respect to the air gap distance is given in Figure 10.

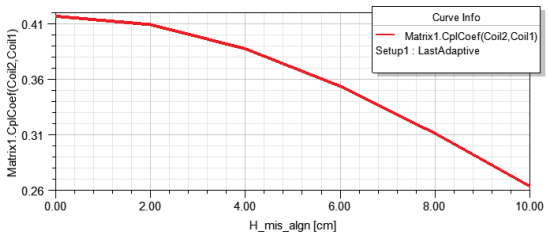

Figure 10. Coupling coefficient graph of the WPT system

The graph of the mutual inductance change is also given in Figure 11. The magnetic flux distribution between the windings is given in Figure 12. The

values of the results obtained depending on the distance variation are presented in Tables 2 and 3.

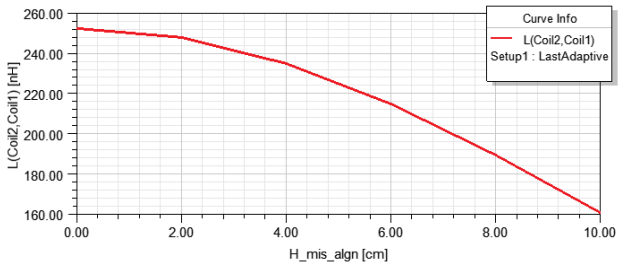

Figure 11. Variation of mutual inductance according to air gap distance

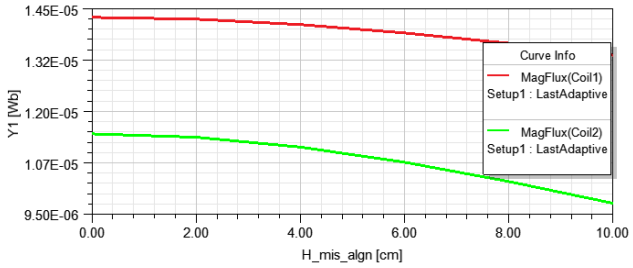

Figure 12. Magnetic flux distribution

Table 2. Coupling coefficient results

Distance (cm)	k
0	0.416
2	0.409
4	0.387
6	0.353
8	0.311
10	0.263

Table 3. Mutual inductance results

Distance (cm)	Mutual Inductance (nH)
0	252.288
2	247.851
4	234.912
6	214.867
8	189.533
10	160.946

The wireless power transfer method can be used in many different systems, including electric cars.. The simulated circuit topology is the most commonly used series-to-series topology for electric vehicles. A full-bridge inverter circuit is used to convert the rectified voltage to high-frequency AC current after the grid voltage. In this study, the efficiency obtained with a 10 cm air gap between two opposing coils at a 20 kHz operating frequency was calculated to be approximately 92.6%. In addition, the improvement of the system design is possible with the four-coil system or the compensation structures derived from the classical topologies and will increase the efficiency in common. In general, the overall performance of the circuit in terms of power and efficiency is determined by the compensation circuit on the secondary side of the topologies. Therefore, it is both experimentally and theoretically known that the efficiency decreases according to the order of Series-Series, Series-Parallel, Parallel-Serial and Parallel-Parallel. Because of its high-power output, a car to be charged is preferably charged using SS compensation or SP. In small powerful devices, generally Parallel-Parallel or Parallel-Serial topologies are preferred. In this study, the SS inductive power transmission topology was used because it is aimed to provide constant power in electric vehicles and to maximize power transfer efficiency.

4. Conclusion and Suggestions

With inductive power transfer technology, electrical power can be sent wirelessly in a safe and efficient way. Current research on Inductive Power Transfer focuses primarily on voltage source inverter technology, whereas current source technology has received very limited attention. This study also provides a comprehensive overview of compensation networks and converter topologies used in current inductive power transfer systems. Since wireless power transfer is carried out over loosely coupled windings, power transfer efficiency is expected to be low. Efficiency should be increased by using compensation topologies. In Inductive Power Transfer systems, power is transferred between the coils in the system. In inductive power transfer, the coils are not around the same core like in transformers, but there is a distance between the coils that makes the system loosely coupled. The concept of resonance is used to transfer power efficiently. There are four classical topologies, and there are also new proposed topologies derived from these topologies. It uses the series-series compensation topology, which is adequate for battery charging applications. The results obtained in the Series-Series topology show that the capacitor voltages increase very much and require special capacitors for this. In this study, WPT based on Inductive Power Transfer system was designed and analyzed. It was observed that the efficiency was high.

Acknowledgment

This study was supported by Dicle University DUBAP unit. Project number. SİLVAN-MYO.22.001.

Contributions of the authors

The contribution rate of the authors is equal.

References

[1] R. Navid, W. Jun, and Y. Xibo, "In-Situ Measurement and Investigation of Winding Loss in High-Frequency Cored Transformers Under Large-Signal Condition". *IEEE open journal Industry Applications*, Vol. 3. 2022

[2] L. Feng, L. Yanjie, Z. Siqi, C. Yifang, S. Xuan, and D. Yutong, "Wireless power transfer tuning model of electric vehicles with pavement materials as transmission media for energy conservation". *Applied Energy* 323, 119631, 2022.

[3] Y. Özüpak, "Analysis of the Model Designed for Magnetic Resonance Based Wireless Power Transfer Using FEM". *Journal of Engineering Research* , 2022, DOI: 10.36909/jer.17631.

[4] Y. Özüpak, Design and Efficiency Analysis of a Circular Coil Transformer for Wireless Power Transfer System of Electric Vehicles. *Journal of Çukurova University Engineering Faculty*, vol. 37, no. 1, pp. 209-219, 2022, DOI: 10.21605/cukurovaumfd.1095053.

[5] H. Wang, and C. K. W, Eric, A Special Magnetic Coupling Structure Design for Wireless Power Transfer Systems. *IEEE 20th Biennial Conference on Electromagnetic Field Computation (CEFC)*, pp. 1-2, doi: 10.1109/CEFC55061.2022.9940745, 2022.

[6] S.I Yahya, B.M., Alameri, Jamshidi, M., Roshani, S., Chaudhary, M.A., Ijemaru, G.K., Mezaal, Y.S. & Roshani, S. "A New Design Method for Class-E Power Amplifiers Using Artificial Intelligence Modeling for Wireless Power Transfer Applications". *Electronics* vol. 11, no. 21, p. 3608, 2022, https:// doi.org/10.3390/electronics11213608. 2022.

[7] C. S. Wong, J. Liu, L. Cao, and K. H. Loo, A SWISS-Rectifier Based Single-Stage Three-Phase Bidirectional AC-DC Inductive-Power-Transfer (IPT) Converter for Vehicle-to-Grid (V2G) Applications," in *IEEE Transactions on Power Electronics*, 2022, doi: 10.1109/TPEL.2022.3220327. 2022.

[8] M.A., Rodriguez-Otero, and E. O'Neill-Carrillo Efficient Home Appliances for a Future DC Residence". *In: Energy 2030 Conference*, 2008. ENERGY 2008. IEEE. Nov. 2008, pp. 1–6. 2008.

[9] Y. Özüpak, Design and Analysis of Different Transformer Models for Wireless Power Transfer Systems of Electric Vehicles", *DUJE (Dicle University Journal of Engineering)* vol. 13, no. 1, pp. 11-18, 2022, doi:10.24012/dumf.1079729, 2022.

[10] K. Aditya, Design And Implementation Of An Inductive Power Transfer System For Wireless Charging Of Future Electric Transportation" University of Ontario Institute of Technology Oshawa, Ontario, Canada, 2016.

[11] SAE International, (2019). Wireless Power Transfer for Light-Duty Plug-in/Electric Vehicles and Alignment Methodology. SAE J2954; SAE International: Warrendale, PA, USA, April 2019.

[12] M., Chang, X., Ma, , J., Han H., Xue, Liu, H. & Li, L. Metamaterial Adaptive Frequency Switch Rectifier Circuit for Wireless Power Transfer System," in *IEEE Transactions on Industrial Electronics*, 2022, doi: 10.1109/TIE.2022.3220908. 2022.

[13] R., Xue, K., Cheng, and M. Je, High-Efficiency Wireless Power Transfer for Biomedical Implants by Optimal Resonant Load Transformation," *IEEE Transactions on Circuits and Systems I: Regular Papers*, vol, 60, no, 4, pp, 867-874, 2013, doi: 10,1109/TCSI,2012,2209297. 2012.

[14] A., Bharadwaj, A. Sharma, and C. R. Chandupatla, A Switched Modular Multi-Coil Array Transmitter Pad With Coil Rectenna Sensors to Improve Lateral Misalignment Tolerance in Wireless Power Charging of Drone Systems," in *IEEE Transactions on Intelligent Transportation Systems*, 2022, doi: 10.1109/TITS.2022.3220793. 2022.

[15] L. Siqi, and C.C. Mi, Wireless Power Transfer for Electric Vehicle Applications. IEEE J. Emerg. Sel. Top. Power Electron, 3, 4–17. 2015.

[16] C. S. Wong, J. Liu, L. Cao and K. H. Loo, "A SWISS-Rectifier Based Single-Stage Three-Phase Bidirectional AC-DC Inductive-Power-Transfer (IPT) Converter for Vehicle-to-Grid (V2G) Applications," in *IEEE Transactions on Power Electronics*, 2022, doi: 10.1109/TPEL.2022.3220327.

[17] H. Wang and K. W. Eric Cheng, "A Special Magnetic Coupling Structure Design for Wireless Power Transfer Systems," *2022 IEEE 20th Biennial Conference on Electromagnetic Field Computation (CEFC)*, , pp. 1-2, 2022, doi: 10.1109/CEFC55061.2022.9940745.

[18] N. Mukundan, . C. M et al., "A New Multilevel Inverter Based Grid Connected Reliable Solar Power Transfer Unit with Power Quality Enhancement," *in IEEE Transactions on Industry Applications*, vol. 59, no 2, pp. 1887-1900, 2023, doi: 10.1109/TIA.2022.3218523.

[19] S. Jeong et al., "Analysis of Repetitive Bending on Flexible Wireless Power Transfer (WPT) PCB Coils for Flexible Wearable Devices," *in IEEE Transactions on Components, Packaging and Manufacturing Technology*, vol. 12, no. 11, pp. 1748-1756, 2022, doi: 10.1109/TCPMT.2022.3217291.

Bitlis Eren Üniversitesi Fen Bilimleri Dergisi
BİTLİS EREN UNIVERSITY JOURNAL OF SCIENCE
ISSN: 2147-3129/e-ISSN: 2147-3188
VOLUME: 12 NO: 3 PAGE: 617-624 YEAR: 2023
DOI:10.17798/bitlisfen.1224055

Design and Thermal Analysis of a Parabolic Collector

Cuma ÇETİNER[1*]

[1] *Harran University, Faculty of Engineering, Department of Mechanical Engineering, Şanlıurfa, Turkey*
ORCID: 0000-0002-5105-5699

Keywords: Solar energy, Parabolic collector, Thermal efficiency, Design collector

Abstract
In this study, the sun follow-up systematic parabolic collector typed collector's design and experimental study were made. The system provides sun tracking in the east-west direction. Instead of a mirror, chromium-nickel metal was used to reflect the sun's rays onto the focusing tube. Sanliurfa offers a conducive environment for conducting systematic performance evaluations through a series of thoughtfully designed experiments. These experiments aim to compare theoretical values with actual experimental results, ensuring a comprehensive analysis of the system's capabilities. It was possible to obtain 380 W of thermal power from the collector, whose area is 1.2 m^2. The thermal efficiency is high at 43% and low at 26%.

1. Introduction

The interest in continuous renewable energy sources is increasing, especially solar heating, cooling, and electricity generation are spreading. Solar concentrators are used to achieve high temperatures with solar radiation. They follow the sun on only one axis or two. There is a wide variety of solar collectors [1,2]. These are examined in two parts linear focus (Fresnel and parabolic collector type) and point (dish type and tower type) focus. The parabolic solar collector transfers the thermal energy to oil, water, and a similar flow by reflecting the sun rays with mirrors placed towards the absorber at the parabolic focal point on its surface and circulating it in the system. It is possible to reach very high temperatures using a very large parabolic surface area. Parabolic collectors work only with direct radiation and are more efficient in areas with plenty of sun throughout the year.

The flat reflector is used in Heliostat-type and Fresnel-type collectors. In the manufacture of dish-type and trough-type parabolic collectors, special manufacturing is required to use the mirror on the parabolic surface. In the manufacture of the parabola, easily shaped aluminum or chrome-nickel surface plate can be used to act as a reflector in terms of material. Venegas-Reyes designed a solar parabolic trough concentrator (PTC), 4.88 m high and 5.8 m^2 aperture area, with aluminum construction and efficiency of approximately 60% [3]. Irving Eleazar conducted a fascinating study on a parabolic field collector, measuring an impressive 2.44 m in length and 1.6 m in width, providing a collection area of approximately 3.8 m^2. The aluminum plate is used as reflective material in the parabolic collector whose construction is made of aluminum, and it is stated that its thermal efficiency is around 60% [4]. The thermal efficiency shows that the reflector, absorber material, environment, and heat carrier vary according to the fluid [5]. However, the efficiency of flat collectors is high (70%) [6].

In this study, chromium-nickel material was used as reflective material. This collector, which has 1.5 x 0.80 m dimensions and a 1.2 m^2 opening area, was circulated with a flow rate of 0.04 kg/s. The theoretical thermal efficiency of the system was compared with the experimental findings.

2. Material and Method

Figures 1 and 2 visually demonstrate the intriguing process where the sun's rays converge at the focal point, resulting in the transformation of the reflective material into a parabolic surface. The

*Corresponding author: ccetiner@harran.edu.tr
Received: 25.12.2022, Accepted: 16.09.2023

copper tube is placed inside the glass tube. The low-temperature water entering from T_{in}, shown in Figure 2, is collected in the tank, leaving the T_{out} section. The water in the tank is re-entered into the pipe with a pump and the water in the system is circulated. With the current coming from the solar ray's sensor placed on the parabolic collector, the tracking system moves the collector toward the direction of the sun's rays. The parabolic collector has a solar sensor as shown in Figure 1 and follows the sun in the east-west direction. It follows the sun automatically with the electronic card as shown in Figure 2 in the control unit. The system acts according to the radiation detected in the sun sensor. In the experiments, the inlet and outlet temperatures of the water, the ambient temperature, and the glass temperature were measured with a data logger.

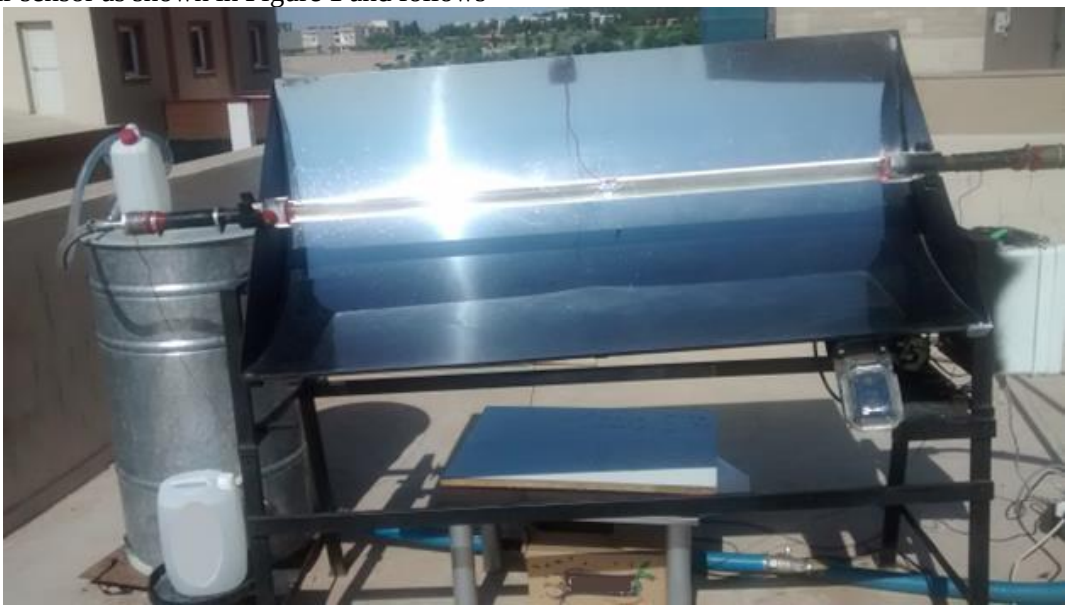

Figure 1. Inlet, outlet, glass, and ambient temperature measurements in the parabolic collector

As seen in Figure 2 and Figure 3, the length of the concentrator is 150 cm (L) with a parabolic opening of 80 cm (B). The copper outer diameter of the pipe used for the absorber is 35 mm and the inner diameter is 32 mm. A glass tube is placed inside this 42 mm diameter copper tube. The flow rate of the circulated water is 0.040 kg/sec.

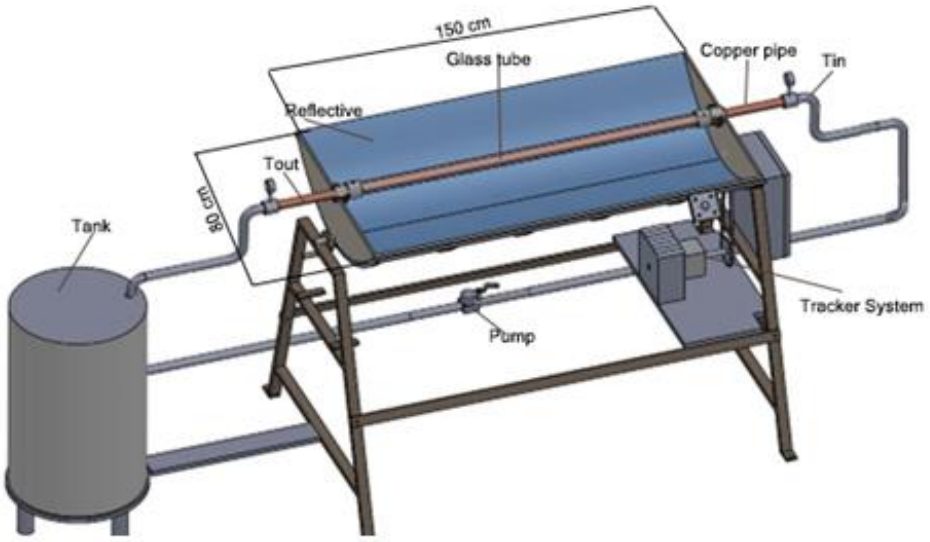

Figure 2. Parts of the parabolic collector

Equation (1) is related to the manufacture of the parabolic collector, f is the focal length (20 cm), y is the collector aperture (40 cm), x is the height (20 cm), and L is the length (150 cm). The x and y values obtained in Equation 1 for the parabolic collector designed for manufacturing are given in Table 1.

$$y = \sqrt{4\,f\,x} \tag{1}$$

Table 1. Parabolic of the collector coordinate values

X(cm)	20.0	15.8	12.1	8.9	6.2	4.0	2.2	1.0
Y(cm)	-40.0	-35.6	-31.1	-26.7	-22.2	-17.8	-13.3	-8.9

As seen in Figure 3 below, the x arm gives the height of the parabolic, and the 2y value gives the total span length of the parabolic. The focal length has been taken to be the same as the height for ease of fabrication.

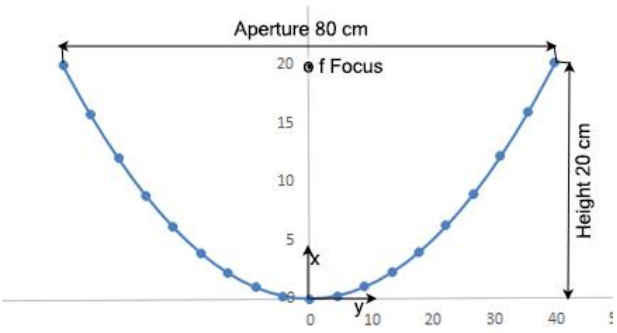

Figure 3. Height, width, and focal dimensions of the parabolic collector

3. Thermal Analysis of Parabolic Collector

While some of the amounts of radiation reaching the absorber from the condenser are thrown into the low-temperature environment due to losses, the other part is absorbed by the fluid and turns into useful energy. The useful thermal energy of the parabolic collectors transferred to the fluid in the absorber can be found in the following Hotel-Willer-Bliss equation 2 [7].

$$Q_u = A_a F_R \left[I_d \alpha \rho \gamma \tau - \frac{A_y}{A_a} U_T (T_{in} - T_a) \right] \tag{2}$$

In this equation (Q_u) is the useful heat energy, (A_a) is the aperture area, (A_y) is the absorber area, (F_R) is the heat gain factor, and (I_d) represents the amount of direct radiation falling over the unit aperture area. α is the absorption rate of the absorber material, ρ is the reflectance rate of the reflective material, γ is the intercept factor, and τ is the transmittance coefficient of the transparent cover. (U_T) is the total heat transfer coefficient given from the absorber to the environment, (T_{in}) is indicated by the fluid inlet temperature and the ambient temperature (T_a).

The thermal efficiency of the concentrator and the useful thermal power of the collector are found by the aperture area of the parabolic collector and the rate of incident direct radiation. Accordingly, the theoretical thermal efficiency is as follows [7],

$$\eta_0 = \frac{Q_u}{A_a I_d} = F_R(\tau\alpha\gamma\tau) - F_R U_T \frac{A_y (T_{in} - T_a)}{A_a I_d} \tag{3}$$

In addition, when the inlet and temperatures of the fluid and the experimental values such as the flow rate are known, the thermal power can be found from the equation given below.

$$Q_u = m\, c_p (T_{out} - T_{in}) \tag{4}$$

Here, m is the flow rate and T_{out} is the exit temperature of the fluid from the absorber. Thermal efficiency is defined as the ratio of the amount of heat transferred to the water to the direct solar energy coming to the total reflective surface. Accordingly, thermal efficiency is found equality as follows.

$$\eta = \frac{m\, c_p (T_{out} - T_{in})}{A_a I_d} \tag{5}$$

3.1 Calculation of Total Heat Transfer Coefficient

For the heat gains and losses in the parabolic collector, the total heat transfer coefficient in the pipe must be calculated. The total heat transfer coefficient U_T for conduction, convection, and radiation heat losses from the absorber to the environment can be found in equation (6) below [8].

$$U_T = \left[\frac{A_y}{A_a (h_{bc} + h_{rc})} + \frac{1}{h_w} \right]^{-1} \tag{6}$$

The losses occur by radiation and convection emitted from the outer surface of the absorber tube to the environment. As shown in the total heat transfer equation, it is necessary to calculate the radiation resistances in the pipe in terms of convection. Forced convection occurs on the outer surface of the glass pipe due to the wind in the environment. Reynold and Nusselt's values must be found because forced convective conditions

occur. Nusselt value is suitable for glass pipe in the horizontal position (Equation 7) [9].

$$Nu = \frac{\rho V D_c}{\mu} = 0.193 Re^{0.618} Pr^{0.333} \quad (7)$$

After the equation is found, the forced (h_{bc}) value is found. The radiation between the glass tube and the medium is shown in equation 8.

$$h_{rc} = \varepsilon_r \sigma (T_c + T_a)(T_c^2 + T_a^2) \quad (8)$$

The radiation coefficient occurs between the copper tube and the glass tube. Where Tc is the transparent cover temperature, Stefean-Boltzman constant, and εc is the radiation emission coefficient of the surface.

The radiation between the copper tube and the glass tube is the radiation between two parallel plates. It is found from the following equation 9 in terms of convection.

$$h_w = \frac{\sigma (T_c + T_a)(T_c^2 + T_a^2)}{\frac{1}{\varepsilon_r} + \frac{A_r}{A_a}(\frac{1}{\varepsilon_c} - 1)} \quad (9)$$

From equations 7, 8, and 9 above, the total heat loss coefficient for the absorber is found by substituting it in equation 6.

The heat gain factor F_R for the collector used in the useful power equation is derived from the following equation 10 [10].

$$F_R = \frac{\dot{m} c_p}{A_r U_T} \left[1 - exp\left(- \frac{A_y U_T F}{\dot{m} c_p} \right] \right. \quad (10)$$

Here, the collector efficiency factor F is independent of the operating conditions and is a factor dependent on the construction of the collector. This value is found in the equation 11 below.

$$F = \frac{\frac{1}{U_T}}{\frac{1}{U_T} + \frac{d_d}{h_w d_i} + \frac{d_d ln(\frac{d_d}{d_i})}{2k}} \quad (11)$$

When the values in equations 10 and 11 were put in their places, the heat gain factor F_R was found to be 0.98. An Excel file was prepared to use the formulas given above and theoretical values were obtained.

4. Results and Discussion

The experiments were carried out in Şanlıurfa (e=37.1) between 8 a.m. and 5 p.m. In the collector, which is manufactured in small sizes, water is circulated at a low flow rate. Equation 3 was used for the theoretical thermal efficiency. In the calculation made, the total heat transfer coefficient from the glass pipe to the environment is around 4.98 W/m^{2}K. Since the copper pipe is not selective, the absorption ratio of the pipe is 0.82, the transmittance coefficient of the glass pipe is 0.83, and since the reflective surface is not a mirror, the reflection ratio is 0.75 and the intercept factor is 0.95. Using these values, the theoretical thermal efficiency value was calculated as 46-48% (Figure 4). Experimental efficiency was found from equation 5 by using inlet and outlet water temperatures and flow rates in the experiment. It can be seen in Figure 4 that the curve found for the experimental experiment is closer to the theoretical thermal efficiency in the afternoon.

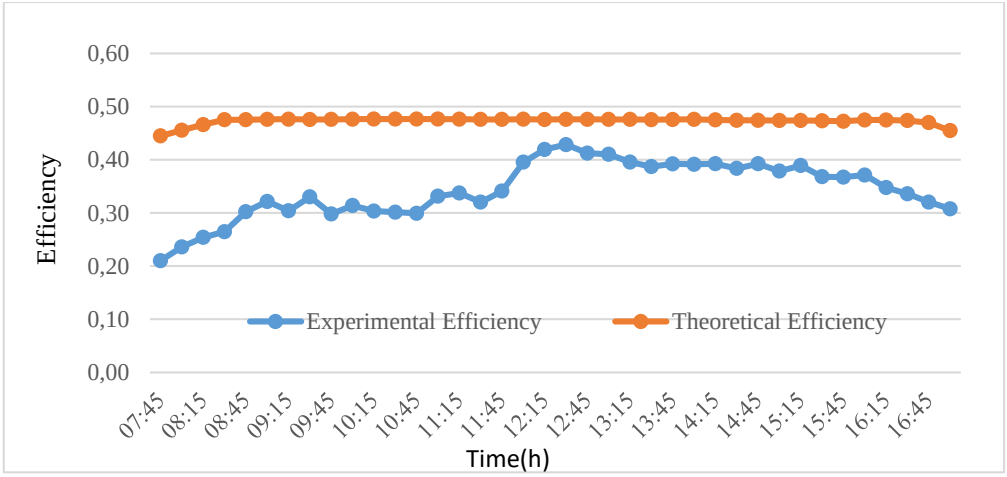

Figure 4. Theoretical and experimental thermal efficiency

The measured direct radiation value is around 600 to 800 W/m^2. Thermal efficiency calculations were made with direct radiation values (Sanliurfa, Lat 37.1). The radiation values were taken from the radiation measurement center at Harran University Engineering Faculty. The experimental section was set up at a distance of 20 m from this measurement center [11]. It was calculated that approximately 420 W of thermal power could be obtained theoretically from the parabolic collector (Figure 5). The reflectance rate, transmittance and absorption coefficient values selected in the theoretical calculation are effective. It is seen that the experimental results are closer to the useful power value at noon. In the morning and evening times, the thermal power values also decrease due to the low solar radiation intensity.

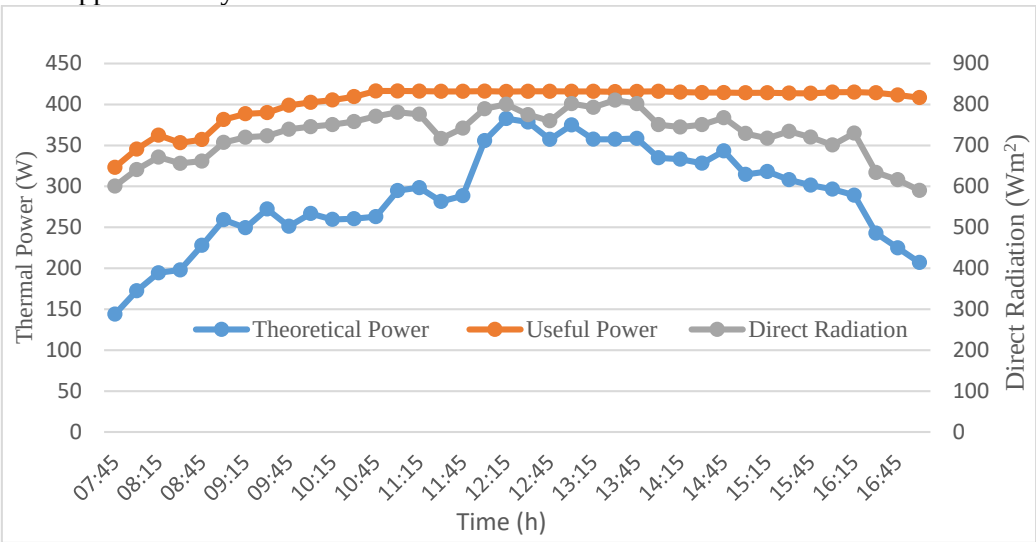

Figure 5. Theoretical and experimental thermal power and direct radiation values

Although the glass pipe temperature varies slightly in the experimental measurements in the collector, it is seen that the ambient, water inlet and outlet temperatures are in harmony (Figure 6). Since the parabolic is of small size, the difference between the inlet and outlet temperatures of the water is very small (Table 2).

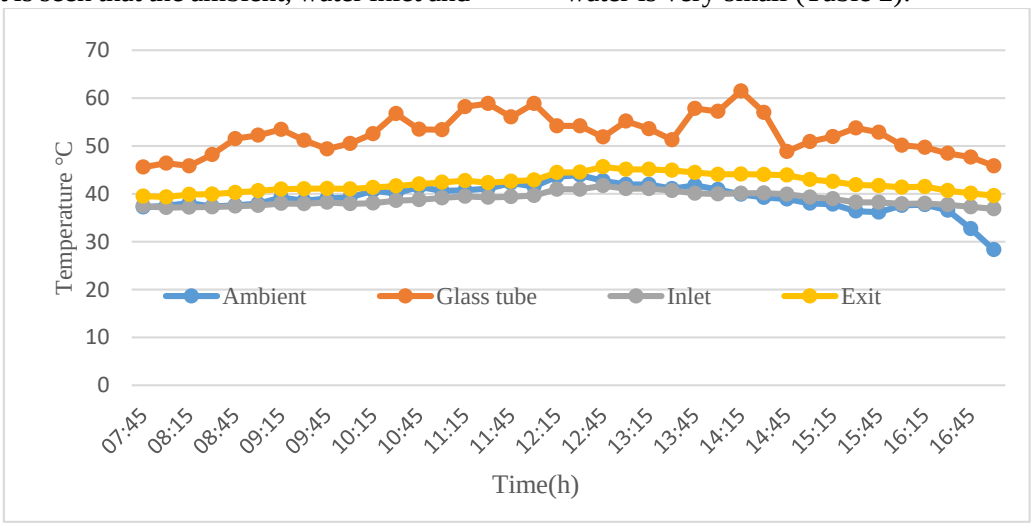

Figure 6. Ambient, glass pipe, water inlet, and outlet temperatures were measured in the parabolic collector

Table 2. Ambient, water inlet, and outlet temperatures were measured in the parabolic collector

Ambient °C	Water Inlet °C	Water Outlet °C
37,2	37,4	39,5
37,5	37,1	39,3
38,1	37,2	39,8
37,3	37,2	39,9
37,6	37,4	40,3
37,9	37,6	40,6
39,2	38,0	41,0
38,5	37,9	41,0
39,0	38,2	41,1
39,2	37,9	41,0
40,6	38,0	41,3
40,1	38,6	41,6
41,4	38,7	42,0
40,6	39,1	42,4
40,7	39,5	42,7
41,1	39,2	42,3
42,2	39,4	42,6
41,5	39,6	42,9
43,6	40,9	44,4
43,9	40,9	44,5
42,7	41,7	45,6
42,0	41,1	45,1
41,9	41,1	45,1
41,1	40,7	44,9
41,7	40,1	44,4
40,9	40,0	44,1
39,9	40,1	44,1
39,2	40,2	44,0
38,9	39,9	43,9
38,0	39,3	43,0
37,8	39,0	42,6
36,4	38,2	41,9
36,2	38,2	41,7
37,6	37,9	41,4
37,7	38,0	41,5
36,5	37,7	40,7
32,7	37,3	40,1
28,3	36,9	39,6

Figure 7 shows the graph obtained by direct radiation division of the thermal data and the inlet and ambient temperature values of the water. In this graph, the line equation for thermal efficiency shows a decreasing slope. Although the efficiency of the system is low, it is seen that it complies with the ASHRAE 93-863 standard for thermal applications [12,13,14,15].

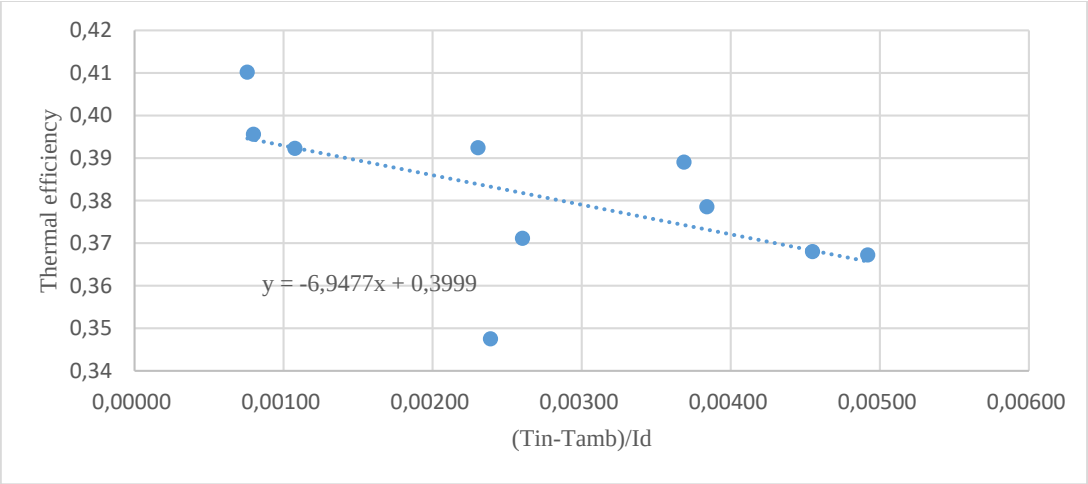

Figure 7. Thermal efficiency of the collector for hot water

6. Conclusions and Suggestions

If this collector, which is made in small sizes, can be made in larger sizes, more thermal power and high temperature can be obtained. The reason for choosing the reflective surface chrome-nickel material is that there is no ready-made mirror with a suitable parabola surface in the market. If a reflective mirror could be used, the thermal efficiency, power, and temperature would be greater. The theoretical and experimental values were close to each other. A thermal power of 380 W could be obtained from this collector with a collector area of 1.2 m^2 at noon. The thermal efficiency was the highest at 43% and the lowest at 26%.

Conflict of Interest Statement

There is no conflict of interest between the authors.

Statement of Research and Publication Ethics

The study is complied with research and publication ethics.

Symbols

A_a : Reflective surface area (m^2)

A_y : Absorber surface area (m^2)

C_p : Specific heat (kJ/kgK)

Id : Direct radiation (W/m^2)

$\dot{m}$: Fluid flow rate (kg/s)

T_{in} : Water inlet temperature °C

T_{out} : Water outlet temperature °C

T_a : Ambient temperature °C

U_T : Total heat transfer coefficient (W/m^2K)

Q_u : Useful energy (W)

γ : Intercept factor (0.95)

: Collector thermal efficiency

τ : Heat transition coefficient (0.78)

α : Absorbtion coefficient (0.82)

ρ : Reflection ratio (0.83)

References

[1] A.Z, Hafez and et al., Design analysis of solar parabolic trough thermal collectors. *Renewable and Sustainable Energy Reviews* 82, pp. 1215–1260, 2018

[2] A. Kalogirou Soteris, *Solar Energy Engineering Processes and Systems*, Second Edition, printed Elsevier, 2014

[3] E. Venegas-Reyes et al., Design, construction, and testing of a parabolic trough solar concentrator for hot water and low enthalpy steam generation, *Journal of Renewable and Sustainable Energy* 4, pp.053-103, 2012

[4] E.A Irving Eleazar and et al., Design and Construction of a Parabolic Trough Solar Collector for Process Heat Production, *Energy Procedia* 57, pp. 2149-2158, 2014.

[5] G.K Manikandan and et al., Enhancing the optical and thermal efficiency of a parabolic trough collector-A review, *Applied Energy*, 235, pp.1524-1540, 2019.

[6] K.D Ramesh and K. Suresh, Thermal performance of parabolic trough collector with absorber tube misalignment and slope error, *Solar Energy*, 184, pp. 249-259, 2019.

[7] J.A Duffie and W.A. Beckman, *Solar Energy Thermal Processes*, John Wiley and Sons, New York 1991.

[8] A. Kılıç, Solar Energy, Kipaş Yayıncılık ,1984.

[9] F.P Incropera and D.P, DeWitt, *Heat and Mass Transfer*, Literatur Publishing (translation), Istanbul 2001.

[10] J.S., Hesieh, *Solar Energy Engineering*, Prentice-Hall,1986.

[11] H.Bulut, and et al, Measurement of Global Direct Beam and Diffuse Solar Radiation for Determining the Potential of Solar Energy Application, *State-University-Industry Cooperation Symposium and Marble Works Counci*l, 24-26 January, Diyarbakır, pp.484-490, 2010

[12] P.L Singh, R.M Sarviya and J.L Bhagoria, Thermal performance of linear Fresnel reflecting solar concentrator with trapezoidal cavity absorbers, *Applied Energy*, 87, pp.541-550, 2010.

[13] H.B Kulkarni, Design, and development of prototype cylindrical parabolic solar collector for water heating application, *International Journal of Renewable Energy Development*, pp.49-55, 2016.

[14] J.K Nayak, E.Y Amer and S.M Deshpande, Comparison of three transient methods for testing solar flat-plate collector, *Energy Conversions & Management*, 4, pp.677-700, 2000.

[15] E. Y, Amer, J. K Nayak and G.K Sarma, Transient test method for flat-plate collector: review and experimental evaluation, *Solar Energy*, 60 (5) , pp.229-243, 1997.

Bitlis Eren Üniversitesi Fen Bilimleri Dergisi
BİTLİS EREN UNIVERSITY JOURNAL OF SCIENCE
ISSN: 2147-3129/e-ISSN: 2147-3188
VOLUME: 12 NO: 3 PAGE: 625-633 YEAR: 2023
DOI:10.17798/bitlisfen.1251421

Investigation of Copper-Iron Oxide Thin Film Grown by Co-Sputtering

Sevda SARİTAS[1*]

[1] *Atatürk University, Department of Electric Power Generation, Transmission and Distribution, İspir Hamza Polat Vocational College, Erzurum, Turkey.*
(*ORCID: 0000-0002-7274-3968*)

Keywords: Copper oxide, Iron oxide, Thin film, Co-sputtering,

Abstract

In this study, the iron oxide and copper oxide structures were grown with the DC magnetron and RF magnetron sputtering respectively and the $Cu_xFe_{3-x}O_4$ structure was grown with the co-sputtering. Structural optical and topographic examination of the grown thin films has been done in detail. Absorption measurements of the thin films were taken with the help of a Perkin Elmer UV/Visible Lambda 2S spectrometer at room temperature. The value of the band gap energy with the fit drawn in the $(ah\upsilon)^2$ (cm^{-1} eV^2) counter energy graph of Fe_2O_3, $Cu_xFe_{3-x}O_4$, Cu_2O thin film is grown on glass was calculated as 2.44, 2.39, 2.55 eV respectively. Also, the structural and topographic properties of thin film structures were investigated by scanning electron microscopy (SEM), atomic force microscopy (AFM), X-ray diffraction (XRD), X-ray photoelectron spectroscopy (XPS), and Raman spectroscopy. According to XPS results; the binding energies of the 2p3\2 orbital for the Fe^{3+} (Fe_2O_3) ion is 710.85 eV and for the Fe^{3+} ($Cu_xFe_{3-x}O_4$) ion is 712.49 eV. The binding energy of the 2p3\2 orbital for the Cu^{1+} (Cu_2O) ion is 933.64 eV, and for the Cu^{2+} ($Cu_xFe_{3-x}O_4$) ion is 935.58 eV. O^{2-} the binding energy of the 1s orbital of the ions are 529.95, 531.35 and 529.39 eV for Fe_2O_3, $Cu_xFe_{3-x}O_4$, and Cu_2O respectively.

1. Introduction

For a long time, extensive studies have been carried out on the optical, magnetic, and electrical properties of many nanostructures that are important for scientific, technological, environmental security, cyber security, industrial and medical applications [1], [2]. Evaluation of nano-scale events with nanotechnology and the development of similar ones with applications have created new perspectives in science. In terms of optical, magnetic, thermal, electrical and mechanical properties, nano-sized particles have quite different properties than micron-sized particles and are more advantageous [3]-[5]. These advantages include applications in different fields such as energy, environmental biology, catalyst, magnetic and gas sensors, and electromagnetic interference problems. It has a very important place in applications such as imaging, magnetic recording, magnetic cooler and magnetic printers.

Iron is the most abundant metal on earth. This element has played a role in the development of our civilization, as in Antiquity, as the basis of numerous structural materials. Corrosion processes associated with iron oxides (excluding pigment applications) and iron oxide have long been considered a nuisance. However, in recent years, iron oxides have become increasingly studied materials as extremely useful materials in various fields such as medicine, biology, catalysis, photovoltaics, and combustible gas sensors [6]-[12].

As a metal oxide, CuO attracts attention due to its low cost and intense solar absorption, which can be found in abundance in nature. However, CuO has been reported to be a profitable and promising nanomaterial for applications such as gas sensors, batteries, catalysis, semiconductor photovoltaic cells, field emission, and photocatalytic reactions. The CuO structure is grown with very different growth techniques such

*Corresponding author: sevda.saritas@atauni.edu.tr
Received: 14.02.2023, Accepted: 16.09.2023

as electrospin [13], e-beam evaporation, wet chemical methods [14]-[16], microwave heating technique [17], electropolymerization [18], and hydrothermal method [19]. CuO is an important monoclinic semiconductor with a narrow band gap in the (1.2-1.9 eV) range, an important structure used in solar cell and sensor technology. In addition, CuO is a p-type semiconductor material and worldwide research is carried out by researchers [20]-[22]. Copper oxide and iron oxide thin films are ideal materials in terms of band gap, especially in solar cell applications. The band gap of the films changes by changing the growth parameters (power, growth pressure, oxygen partial pressure, substrate temperature, etc.) [23].

Cations such as Cr, Co, Ni, Cu, Zn, and Ag can be located in interstitial sites and tetrahedral places instead of Fe cation with appropriate cation distribution in Fe_2O_3. Thus, changes can occur in the electronic and magnetic properties of maghemite [24]. Iron oxide and copper oxide structures may differ in terms of optical and structural properties, depending on the growth technique and growth parameters. Copper oxide and iron oxide thin films are ideal materials in terms of band gap, especially in solar cell applications. The band gap of the films grown by the sputter technique changes by changing the growth parameters (power, growth pressure, oxygen partial pressure, substrate temperature, etc.). The main applications of CuO are in optoelectronic and high-performance electronic devices [25]. CuO belongs to antiferromagnetic materials and has a different crystal system [17]. Besides, the bandgap is not a single value but a range of values from 1.75 eV up to 2.45eV. Copper vacancies in CuO play an important role in hole conduction [26], [27], [17], [28]. As an important semiconductor metal oxide, hematite (α-Fe_2O_3) is the most stable phase of iron oxide under ambient conditions [29]. α-Fe_2O_3, which is an n-type semiconductor with an indirect band gap of 2.2 eV, is regarded as an attractive material due to its applications in photoelectrochemical devices [30], photocatalysts [31], magnetic materials [32], pigments, anticorrosive agents and sensors [33].

Recent studies have shown the availability of Fe_2O_3/CuO composite structures [34]-[36], which aim to enhance the absorption range in solar cell research. Adjusting the band gap is crucial for numerous optical applications. In this study, our objective is to obtain three distinct structures. The first two structures are commonly used in optical and solar cell applications, while the third structure is a novel combination of the first two. This study aims to demonstrate the impact of magnification techniques on various aspects of a structure, including its structural, optical, morphological, and topographic features. Additionally, the study aims to highlight how adjusting magnification parameters can lead to the creation of more practical and beneficial structures.

So, it is aimed to show that thin films can be grown in a wide band range, especially by changing the growth parameters of the copper iron oxide structure grown by the co-sputtering technique. In this study, the iron oxide and copper oxide structures were grown with the DC magnetron, RF magnetron sputter technique respectively, and the $Cu_xFe_{3-x}O_4$ structure was grown with the co-sputtering. Structural optical and topographic examination of the grown thin films has been done in detail.

2. Material and Method

The iron oxide and copper oxide structures were grown with the DC magnetron and RF magnetron sputter technique respectively, and the $Cu_xFe_{3-x}O_4$ structure was grown with the co-sputtering.

The sputter technique is the growth of ions, atoms and molecules broken from the metal target on the heated substrate cleaned by chemical processes as a thin film with the help of inert gas. To break the material to be grown from the metal target, argon is turned into an inert gas carrier plasma with the help of an RF or DC power source and the plasma performs the detachment process by beating the surface of the target metal. The copper sputtering foil target has 2 inches (dia) x 0.005 inches (thickness) and the iron sputtering foil target has 2 inches (dia) x 0.005 inches (thickness). An iron target was placed in the DC power gun and a copper target was placed in the RF gun source. The sputter technique has been preferred because it is a reproducible, relatively low cost, and low surface roughness film growth technique that can more easily control the optical and structural properties of the grown film. In the sputter technique, due to the vacuum environment, the pollution rate is lower and higher quality binary and triple compounds are grown.

In this experimental study, an iron thin foil was attached to the DC power supply and a copper metal foil target was attached to the RF power supply part. While the DC power supply is 120 watts, the RF power supply is set to 40 watts. The glass substrates placed for the vacuum chamber up to $5*10^{-6}$ Torr pressure (base pressure) were heated up to 450 degrees. Then 100 sscm of inert argon gas

was sent in and plasma was formed. Then, 40 sscm of argon and 3 sscm of oxygen gas were given to grown pressure of $8.5*10^{-3}$ Torr and growth was made for 35 minutes. Also, the copper oxide and iron oxide films grown on glass substrates at 8 mTorr grown pressure.

In this study, the structural, optical, and topographic properties of copper iron oxide structures grown by RF-DC co-sputtering were investigated by scanning electron microscopy (SEM), atomic force microscopy (AFM), X-ray diffraction (XRD), X-ray photoelectron spectroscopy (XPS) and UV-VIS spectroscopy and Raman spectroscopy.

3. Results and Discussion

One of the most used methods to determine the optical absorption edge and band gap of semiconductors is the absorption measurement method. Absorption measurements of the thin films on the glass substrate were taken with the help of Perkin Elmer UV/Visible Lambda 2S spectrometer at room temperature. The spectrometric measurement range used is 300–900 nm. In the measurements (Figure 1a) made, information about the band gap of (Figure 1b) the material was obtained.

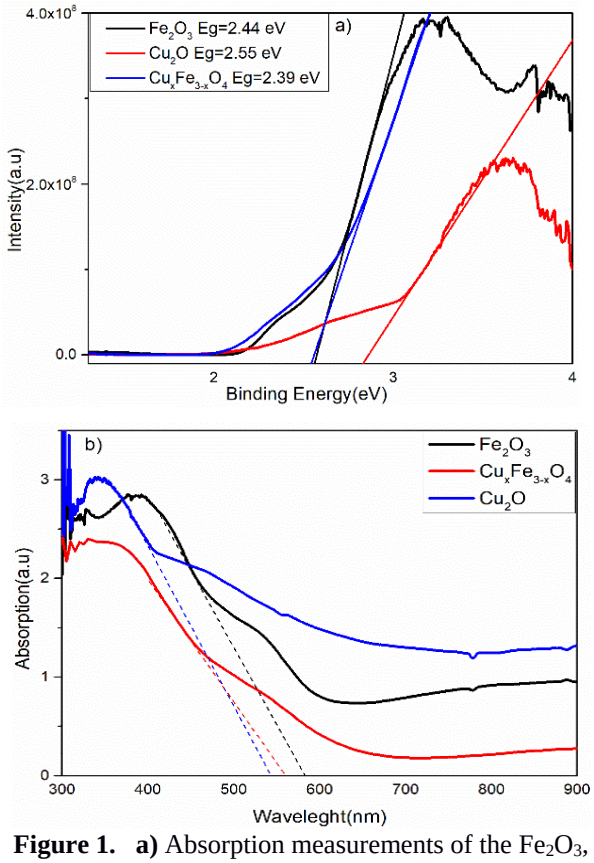

Figure 1. **a)** Absorption measurements of the Fe_2O_3, $Cu_xFe_{3-x}O_4$, Cu_2O thin films, **b)** the value of the band gap energy with the fit drawn in the $(ah\upsilon)^2$ (cm^{-1} eV^2) counter energy graph of Fe_2O_3, $Cu_xFe_{3-x}O_4$, Cu_2O

In Figure 1b, the value of the band gap energy with the fit drawn in the $(ah\upsilon)^2$ (cm^{-1} eV^2) counter energy graph of Fe_2O_3, $Cu_xFe_{3-x}O_4$, Cu_2O thin film grown on glass was calculated as 2.44, 2.39, 2.55 eV. This value of the iron oxide film is compatible with the literature for maghemite and hematite phases. While the Fe_2O_3 and Cu_2O thin films absorb at smaller wavelengths, shifts are observed at larger wavelengths as a result of doping. This may mean that the imperfections in the structure cause the energy gap to shrink, as it creates the possibility of transition at the band gab edge.

The XRD diffraction pattern of the iron oxide, structure growing on the glass substrate is given in Figure 2 and it has been determined that the structure has a tetragonal structure. The lattice constants have the values a=b=8.34 $\dot{A}$, c=25.02 $\dot{A}$ [JCPDS 39-1346]. Cu_2O (Figure 2a) has been determined that the structure has a cubic structure [JCPDS 45–0937] and the lattice constants have the values a=b=c= 4.26 $\dot{A}$ [37]. Two distinct peaks were observed, among which the characteristic maghemite and hematite peaks with orientations of 35.84 and 18.65 degrees. Also, two distinct peaks were observed, which are the characteristic cuprite peaks with orientations of 36.5° and 42.40° [JCPDS 05–0667 and 45–0937]. The values of the three peaks obtained in the XRD analysis (Figure 2a) results show that there is a polycrystalline structure for $Cu_xFe_{3-x}O_4$ thin film [38].

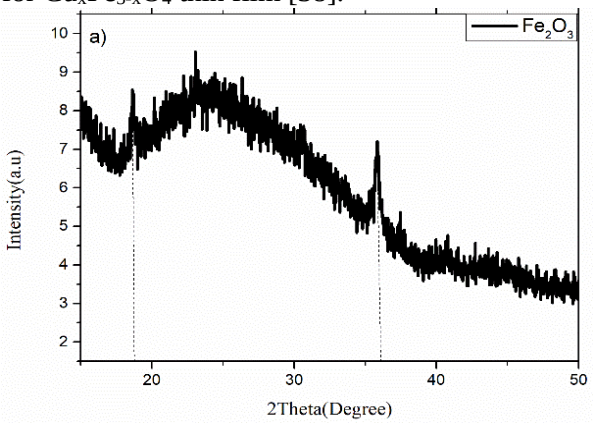

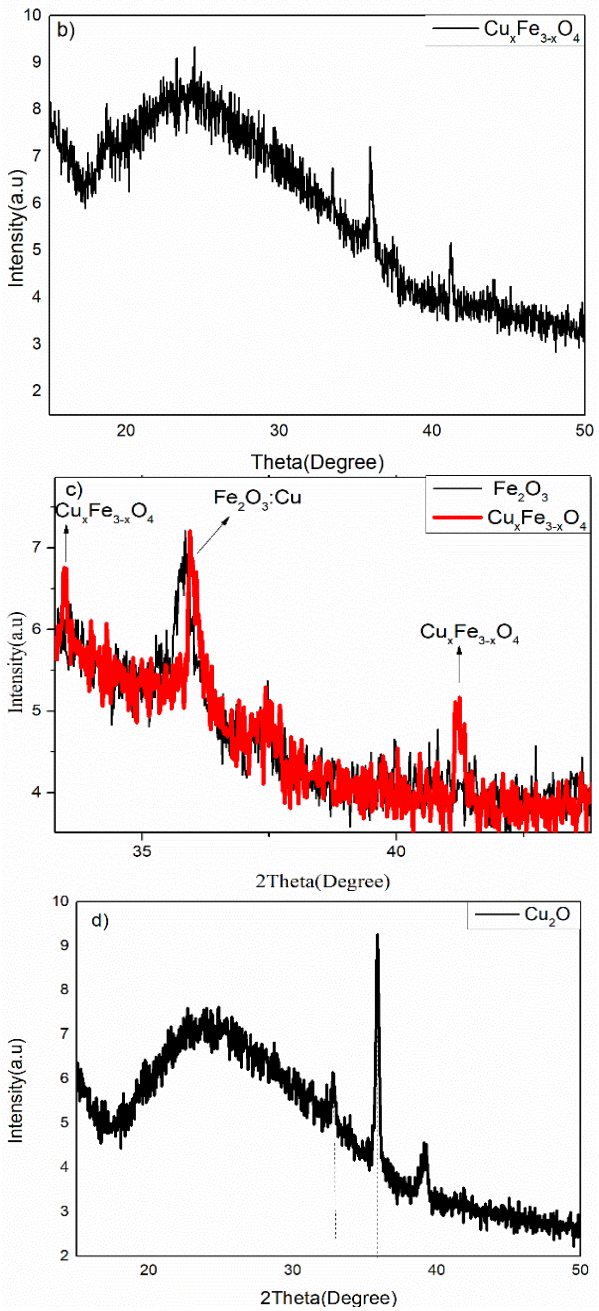

Figure 2. The XRD diffraction pattern of the **a)** Fe_2O3 b) Cu_xFe_2-xO3 **c)** $Cu_xFe_{3-x}O_4$, Fe_2O_3 and **d)** Cu_2O

In Cu cation-doped ferrites ($Cu_xFe_{3-x}O_4$), oxygen ions are replaced by Cu^{1+} and Fe^{3+} ions and have a tetragonal and cubic strong packing arrangement in two different crystallographies. In a published study, researchers tried to understand how Cu atoms change the structure properties of maghemite with Raman measurements. They revealed the active modes of five Raman spectra at room temperature, which are compatible with previous Raman spectra. The Raman active mode for Fe_2O_3 shifted (Figure 3) from 670 cm^{-1} for doped $Cu_xFe_{3-x}O_4$ to 660 cm^{-1} in the Raman spectrum with Cu doping and Cu doping density function [39], [40]. In line with their results, the researchers suggested that Cu^{1+} ions are mostly located in interstitial sites places [23].

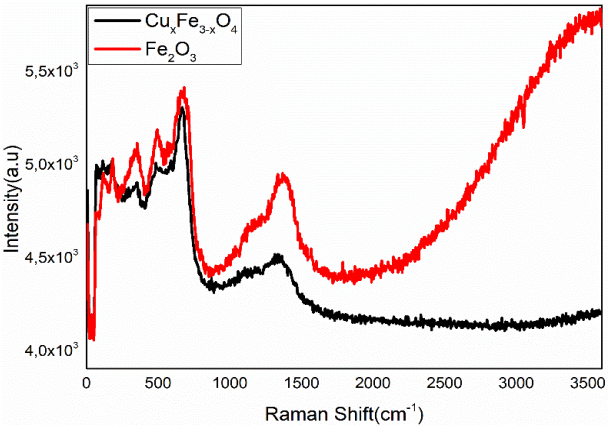

Figure 3. Raman shift graph of Fe_2O_3 and $Cu_xFe_{3-x}O_4$ structure

Figure 3 shows the stretching vibration mode of the Fe_2O_3 film. Peaks showing the Raman shift are seen. It can be said that these peaks are relatively narrow and intense and show Raman active states belonging to hematite phases [41], [42].

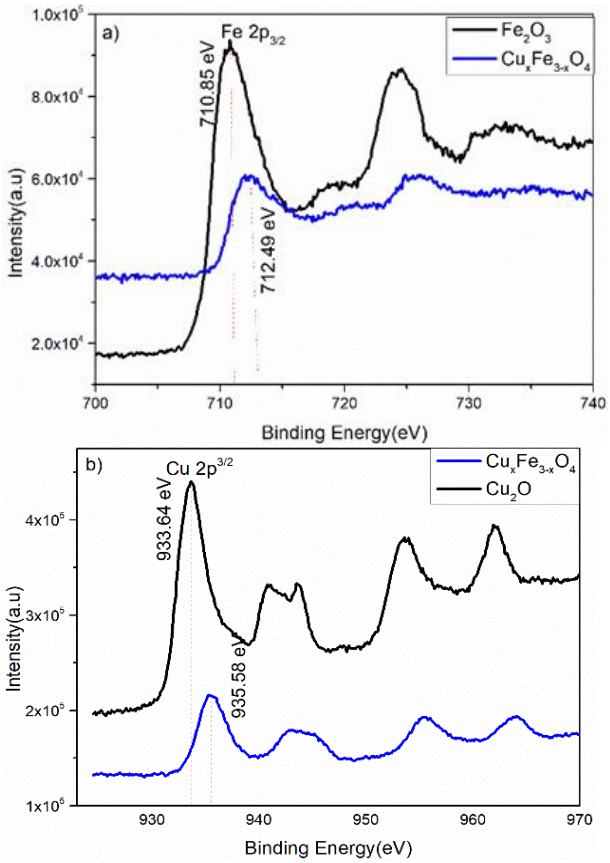

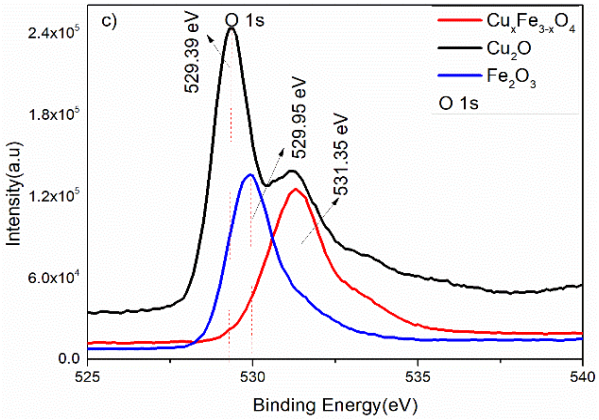

Figure 4. The binding energies of a) Fe^{3+}, b) Cu^{2+} and c) O^{-2} ions

As seen in Figure 4a, the binding energies of the 2p3\2 orbital for the Fe^{3+} (Fe_2O_3) ion are 710.85 eV and the binding energies of the 2p3\2 orbital for the Fe^{3+} ($Cu_xFe_{3-x}O_4$) ion are 712.49 eV. O^{2-} the binding energy of the 1s orbital of the ion is 529.95, and 531.35 eV for Fe_2O_3, $Cu_xFe_{3-x}O_4$ respectively. In Figure 4b, the binding energies of the 2p3\2 orbital for the Cu^{1+} (Cu_2O) ion are 933.64 eV, and the binding energies of the 2p3\2 orbital for the Cu^{2+} ($Cu_xFe_{3-x}O_4$) ion are 935.58 eV. In Figure 4c, O^{2-} the binding energy of the 1s orbital of the ion is 529.95, 531.35 and 529.39 eV for Fe_2O_3, $Cu_xFe_{3-x}O_4$, Cu_2O respectively. The peak intensities, which are an indicator of the number of bonding electrons, are very close to each other and the number of non-bonding electrons is low, which can be seen as the reason for its insulating property. In addition, we can say that its conductivity is low because the amount of oxygen and carbon with the atomic percentage of copper-iron oxide is high and it causes less oxygen vacancies that cause conductivity [41].

As seen in Figure 4(a, b, c), the graph showing the binding energies of Fe^{3+}, Cu^{2+}, and O^{2-} ions of the $Cu_xFe_{3-x}O_4$ compound, although the atomic oxygen amount is almost the same as in the Fe_2O_3 compound, there has been a decrease in the number of bonding oxygen electrons and hence the intensity of the peak. The reason for this situation can be thought that Cu may have bonded with Fe_2O_3 as well and some Cu may have bonded with O [42].

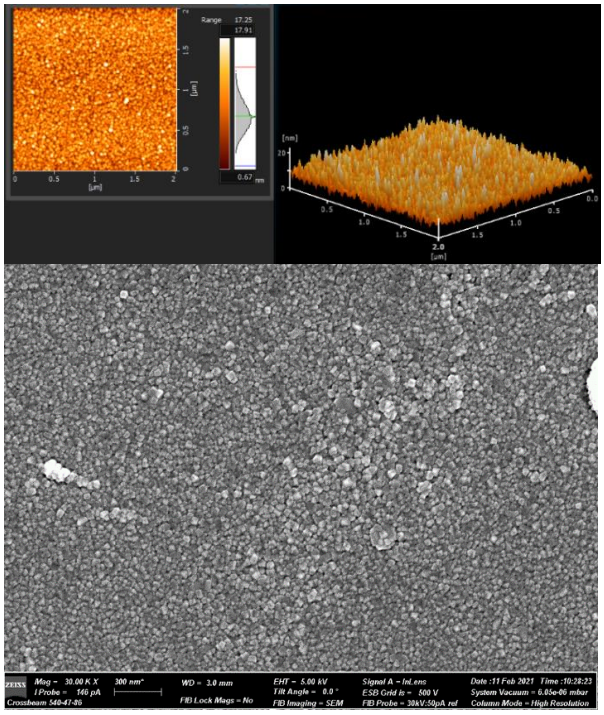

Figure 5. 2D and 3D AFM images and SEM images of the Fe_2O_3

The surface morphology of the iron oxide thin films was analyzed using the non-contact mode of AFM. Figure 5 shows 2D and 3D AFM images of the iron oxide films grown on glass substrates at 8.5 mTorr-grown pressure. The roughness values of the film are Ra= 1.88 nm and Sa=2.09 nm. In the SEM image (Fig. 5), it is seen that the structure is homogeneously distributed on the surface. In addition, a dark surface layer is observed, and under it, lighter colored structures with tetragonal shapes are observed.

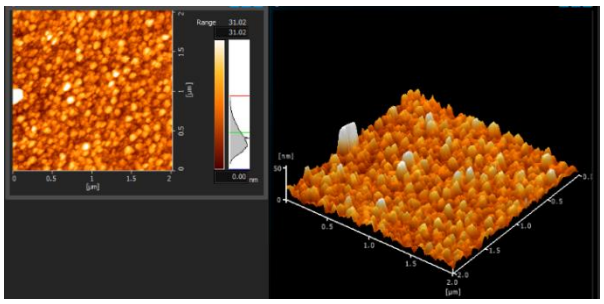

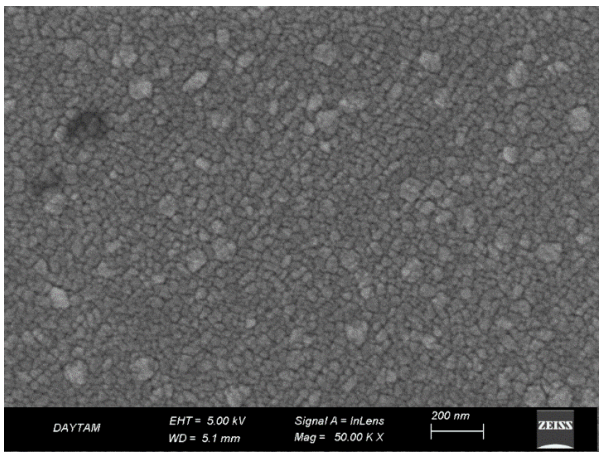

Figure 6. 2D and 3D AFM images and SEM images of the $Cu_xFe_{3-x}O_4$

The surface morphology of the copper-iron oxide thin films was analyzed using the non-contact mode of AFM. Figure 6 shows 2D and 3D AFM images of the copper-iron oxide films grown on glass substrates at 8.5 mTorr grown pressure. The roughness values of the film are Ra= 4.83 nm and Sa=4.19 nm. In the SEM (Fig. 6) image, it is seen that the structure is homogeneously distributed on the surface. In addition, a dark surface layer is seen, on which lighter colored structures are seen as lumps.

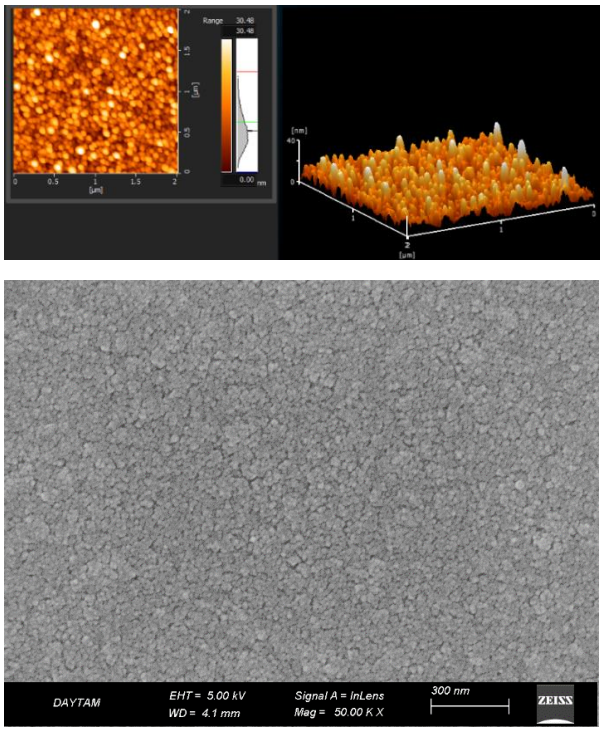

Figure 7. 2D and 3D AFM images and SEM images of the Cu_2O

The surface morphology of the copper oxide thin films was analyzed using the non-contact mode of AFM. Figure 7 shows 2D and 3D AFM images of the copper oxide films grown on glass substrates at 8 mTorr grown pressure. The roughness values of the film are Ra= 4.44 nm and Sa=4.10 nm. In the SEM image, it is seen that the structure is homogeneously distributed on the surface. In addition, relatively smaller-sized structures are observed.

Iron oxide and copper oxide structures may differ in terms of optical and structural properties, depending on the growth technique and growth parameters in terms of band gap, especially in solar cell applications. In this study, aims to show that thin films can be grown in a wide band range, especially by changing the growth parameters of the copper iron oxide structure grown by the co-sputter technique.

Structural optical and topographic examination of the grown thin films has been done in detail. The value of the band gap energy with the fit drawn in the $(ah\upsilon)^2$ ($cm^{-1}eV^2$) counter energy graph of Fe_2O_3, $Cu_xFe_{3-x}O_4$, Cu_2O thin film grown on glass was calculated as 2.44, 2.39, 2.55 eV. The binding energies of the 2p3\2 orbital for the Fe^{3+} (Fe_2O_3) ion are 710.85 eV and the binding energies of the 2p3\2 orbital for the Fe^{3+} ($Cu_xFe_{3-x}O_4$) ion are 712.49 eV. The binding energies of the 2p3\2 orbital for the Cu^{1+} (Cu_2O) ion are 933.64 eV, and the binding energies of the 2p3\2 orbital for the Cu^{2+} ($Cu_xFe_{3-x}O_4$) ion are 935.58 eV. O^{2-} the binding energy of the 1s orbital of the ion is 529.95, 531.35 and 529.39 eV for Fe_2O_3, $Cu_xFe_{3-x}O_4$, and Cu_2O respectively.

The band gap of the iron-copper oxide structure differs from that of the iron oxide and copper oxide structures and exhibits a value that falls between the two energy levels. This is consistent with the result reported in the literature, which suggests that doping induces a change in the forbidden band gap. SEM and AFM results show that the structures are homogeneously distributed across the surface. Angular or oval shapes are clearly visible. It can be observed that the contribution has taken on a new structural form. Additionally, the alteration in surface roughness reinforces this scenario. The changes in peak angles and intensities observed in the XRD results suggest the formation of a new crystal structure.

As can be seen from the XPS and Raman results, chemical bond changes in the iron oxide and copper oxide structures show that the desired thin film is grown. In all SEM images, they are seen that the structure is homogeneously distributed on the surface. The roughness values of $Cu_xFe_{2-x}O_3$

film are Ra= 4.83 nm and Sa=4.19 nm and these roughness values are bigger than others.

4. Conclusion and Suggestions

The band gap values of 2.44 and 2.55 eV in the films grown by the sputter technique. These results are different from the literature and it can be said that the growth parameters and the growth technique are quite effective. The change of the band gap (2.39 eV) of the iron copper oxide structure grown by the co-sputtering technique is a natural process, but it indicates a useful method for band gap engineering. In addition, it can be said that it is a useful method to produce materials with suitable band gaps for solar cells. Especially by combining the optical and structural properties of binary and ternary compounds, paves the way for the production of materials that will work more efficiently.

Acknowledgment

The present work was supported by Ataturk University. We would like to thank the Eastern Anatolia High Technology Application and Research Center (DAYTAM) for their support.

Conflict of Interest Statement

The authors have no relevant financial or non-financial interests to disclose. The author declare that they have no known competing financial interests or personal relationships that could have appeared to influence the work reported in this paper.

Statement of Research and Publication Ethics

The author declare that she has no conflict of interest

References

[1] C. Sanchez, B. Julián, P. Belleville, and M. Popall, "Applications of hybrid organic–inorganic nanocomposites," *J. Mater. Chem.*, vol. 15, no. 35–36, p. 3559, 2005.
[2] V. Bogush, "Application of Electroless Metal Deposition for Advanced," *Composite Shielding Materials. J. Optoelec. and Adv. Mat*, vol. 7, pp. 1635–1642, 2005.
[3] S. Kamiyama, K. Okamoto, and T. Oyama, "Study on regulating characteristics of magnetic fluid active damper," *Energy Convers. Manag.*, vol. 43, no. 3, pp. 281–287, 2002.
[4] D. D. L. Chung, "Electromagnetic interference shielding effectiveness of carbon materials," *Carbon N. Y.*, vol. 39, no. 2, pp. 279–285, 2001.
[5] L. X. Lian, L. J. Deng, and M. Han, "Microwave Electromagnetic and Absorption Properties of Nd2Fe14B/ -Fe Nanocomposites in the 0.5-18 and 26.5-40 GHz Ranges," *J. App. Phy*, vol. 101, pp. 09M – 520, 2007.
[6] U. Schwertmann and R. M. Cornell, *Iron Oxides in the Laboratory: Preparation and Characterization*, New York: Wiley, 2007.
[7] M. Vallet-Regí, C. V. Ragel, and A. J. Salinas, "Glasses with medical applications," *Eur. J. Inorg. Chem.*, vol. 2003, no. 6, pp. 1029–1042, 2003.
[8] A. N. Sukach, A. S. Lebedinskii, V. I. Grishchenko, and T. D. Lyashenko, "Effect of magnetic nanoparticles Fe3O4 on viability, attachment, and spreading of isolated fetuses and newborn rats," *Cell and Tissue Biology*, vol. 5, pp. 388–396, 2011.
[9] L. Levy, Y. Sahoo, K.-S. Kim, E. J. Bergey, and P. N. Prasad, "Nanochemistry: Synthesis and characterization of multifunctional nanoclinics for biological applications," *Chem. Mater.*, vol. 14, no. 9, pp. 3715–3721, 2002.
[10] A. Duret and M. Graetzel, "Visible light-induced water oxidation on mesoscopic α-Fe2O3 films made by ultrasonic spray pyrolysis," C*hemInform*, vol. 36, no. 48, 2005.
[11] J. Sartoretti, C. Ulmann, M. Alexander, B. D. Augustynski, and J. Weidenkaff, "Photoelectrochemical oxidation of water at transparent ferric oxide film electrodes," *Chemical Physics Letters*, vol. 376, 2005.
[12] W. B. Ingler Jr, J. P. Baltrus, and S. U. M. Khan, "Photoresponse of p-type zinc-doped iron(III) oxide thin films," *J. Am. Chem. Soc.*, vol. 126, no. 33, pp. 10238–10239, 2004.
[13] R. Sahay, J. Sundaramurthy, P.S. Kumar, V. Thavasi, S. G. Mhaisalkar, and S. Ramakrishna, "Synthesis and characterization of CuO nanofibers, and investigation for its suitability as blocking

layer in ZnO NPs based dye sensitized solar cell and as photocatalyst in organic dye degradation," *Journal of Solid State Chemistry*, 186, 261-267, 2012.

[14] Q. Liu, S. Anandan, S. H. Yang, and W. K. Ge, "Nanostructured CuO films on copper: Fabrication and application as a cathode in dye-sensitized TiO_2 solar cells," *in 2006 IEEE 4th World Conference on Photovoltaic Energy Conference* (Vol. 1, pp. 229-232). IEEE, 2006.

[15] T. Jiang, M. Bujoli-Doeuff, Y. Farré, Y. Pellegrin, E. Gautron, M. Boujtita, and F. Odobel, "CuO nanomaterials for p-type dye-sensitized solar cells," *RSC advances*, vol. 6, no. 114, pp. 112765-112770, 2016.

[16] S. Anandan, X. Wen, and S. Yang, "Room temperature growth of CuO nanorod arrays on copper and their application as a cathode in dye-sensitized solar cells," *Materials Chemistry and Physics*, vol. 93, no. 1, pp. 35-40, 2005.

[17] D. Wongratanaphisan, K. Kaewyai, S. Choopun, A. Gardchareon, P. Ruankham, and S. Phadungdhitidhada, "CuO-Cu2O nanocomposite layer for light-harvesting enhancement in ZnO dye-sensitized solar cells," *Applied Surface Science*, 474, pp. 85-90, 2019.

[18] M. Mazloum-Ardakani, and R. Arazi, "Enhancement of photovoltaic performance using a novel photocathode based on poly (3, 4-ethylenedioxythiophene)/Ag–CuO nanocomposite in dye-sensitized solar cell," *Comptes Rendus. Chimie*, vol.23, no. 2, pp. 105-115, 2020.

[19] K. Sharma, V. Sharma, and S. S. Sharma, "Dye-sensitized solar cells: fundamentals and current status," *Nanoscale research letters*, vol. 13, no. 1, pp. 1-46, 2018.

[20] S. Baturay, A. Tombak, D. Batibay, and Y. S. Ocak, "n-Type conductivity of CuO thin films by metal doping," *Appl. Surf. Sci*., vol. 477, pp. 91–95, 2019.

[21] T. Chtouki et al., "Characterization and third harmonic generation calculations of undoped and doped spin-coated multilayered CuO thin films," *J. Phys. Chem. Solids*, vol. 124, pp. 60–66, 2019.

[22] R. Jayakrishnan, A. S. Kurian, V. G. Nair, and M. R. Joseph, "Effect of vacuum annealing on the photoconductivity of CuO thin films grown using sequential ionic layer adsorption reaction," *Mater. Chem. Phys*., vol. 180, pp. 149–155, 2016.

[23] K. Akimoto, S. Ishizuka, M. Yanagita, Y. Nawa, G. K. Paul, and T. Sakurai, "Thin film deposition of Cu2O and application for solar cells," *Sol. Energy*, vol. 80, no. 6, pp. 715–722, 2006.

[24] M. Harada, M. Kuwa, R. Sato, T. Teranishi, M. Takahashi, and S. Maenosono, "Cation distribution in monodispersed MFe_2O_4 (M= Mn, Fe, Co, Ni, and Zn) nanoparticles investigated by x-ray absorption fine structure spectroscopy: implications for magnetic data storage, catalysts, sensors, and ferrofluids," *ACS Applied Nano Materials*, vol. 3, no. 8, pp. 8389–8402, 2020.

[25] C. H. Tsai, P. H. Fei, C. M. Lin, and S. L. Shiu, "CuO and CuO/graphene nanostructured thin films as counter electrodes for Pt-free dye-sensitized solar cells," *Coatings*, vol. 8, no. 1, p. 21, 2018.

[26] N. Abraham, A. Rufus, C. Unni, and D. Philip, "Dye sensitized solar cells using catalytically active CuO-ZnO nanocomposite synthesized by single step method," *Spectrochimica Acta Part A: Molecular and Biomolecular Spectroscopy*, 200, pp. 116-126, 2018.

[27] J. K. Sharma, M.S. Akhtar, S. Ameen, P. Srivastava, and G. Singh, "Green synthesis of CuO nanoparticles with leaf extract of Calotropis gigantea and its dye-sensitized solar cells applications," *Journal of Alloys and Compounds*, 632, pp. 321-325, 2015.

[28] V. S. Prabhin, K. Jeyasubramanian, N. R. Romulus, and N. N. Singh, "Fabrication of dye sensitized solar cell using chemically tuned CuO nano-particles prepared by sol-gel method," *Archives of Materials Science*, vol. 6, no. 7, pp. 5-9, 2017.

[29] H. Guo, and A. S. Barnard, "Naturally occurring iron oxide nanoparticles: morphology, surface chemistry and environmental stability," *Journal of Materials Chemistry A*, vol. 1, no. 1, pp. 27-42, 2013.

[30] H. Dotan, K. Sivula, M. Grätzel, A. Rothschild, and S. C. Warren, "Probing the photoelectrochemical properties of hematite (α-Fe_2O_3) electrodes using hydrogen peroxide as a hole scavenger," *Energy & Environmental Science*, vol. 4, no. 3, pp. 958-964, 2011.

[31] Y. H. Chen, and C. C. Lin, "Effect of nano-hematite morphology on photocatalytic activity," *Physics and Chemistry of Minerals*, 41, pp. 727-736, 2014.

[32] S. Yang, Y. Xu, Y. Sun, G. Zhang, and D. Gao, "Size-controlled synthesis, magnetic property, and photocatalytic property of uniform α-Fe2O3 nanoparticles via a facile additive-free hydrothermal route," *CrystEngComm*, vol. 14, no. 23, pp. 7915-7921, 2012.

[33] X. L. Fang, C. Chen, M. S. Jin, Q. Kuang, Z. X. Xie, S. Y. Xie, L. S. Zheng, "Single-crystal-like hematite colloidal nanocrystal clusters: synthesis and applications in gas sensors, photocatalysis and water treatment," *Journal of Materials Chemistry,* vol. 19, no. 34, pp. 6154-6160, 2009.

[34] S. K. Patel, D. Agravat, O. Alsalman, J. Surve, I. Crowe, S. Taya, and T. K. Nguyen, "Design of a broadband solar absorber based on Fe_2O_3/CuO thin film absorption structure," *Optical and Quantum Electronics*, vol. 55, no. 5, p. 430, 2023.

[35] D. Yang, C. Bai, J. Liu, S. Li, C. Tu, F. Zhu, and T. Zhang, "Construction of 3DOM Fe2O3/CuO heterojunction nanomaterials for enhanced AP decomposition," *Applied Surface Science,* 619, p. 156739, 2023.

[36] H. Alnahari, A. H. Al-Hammadi, A. Al-Sharabi, A. Alnehia, and A. B. Al-Odayni, "Structural, morphological, optical, and antibacterial properties of $CuO–Fe_2O_3–MgO–CuFe_2O_4$ nanocomposite synthesized via auto-combustion route," *Journal of Materials Science: Materials in Electronics*, vol. 34, no. 7,p. 682, 2023.

[37] M. E. Fleet, "The structure of magnetite: Symmetry of cubic spinels," *J. Solid State Chem.*, vol. 62, no. 1, pp. 75–82, 1986.

[38] D. Varshney and A. Yogi, "Structural and transport properties of stoichiometric and Cu2+-doped magnetite: $Fe_{3-x}Cu_xO_4$," *Materials Chemistry and Physics*, vol. 123, no. 2–3, pp. 434–438, 2010.

[39] F. J. Owens, and J. Orosz, "Effect of nanosizing on lattice and magnon modes of hematite," *Solid state communications*, vol. 138, no.2, pp. 95-98, 2006.

[40] A. M. Jubb and H. C. Allen, "Vibrational spectroscopic characterization of hematite, maghemite, and magnetite thin films produced by vapor deposition," *ACS Applied Materials and Interfaces*, vol. 2i no. 10, pp. 2804-2812, 2010.

[41] F. A. Akgul, G. Akgul, N. Yildirim, H. E. Unalan, and R. Turan, "Influence of thermal annealing on microstructural, morphological, optical properties and surface electronic structure of copper oxide thin films," *Mater. Chem. Phys.*, vol. 147, no. 3, pp. 987–995, 2014.

[42] A. M. Jubb and H. C. Allen, "Vibrational spectroscopic characterization of hematite, maghemite, and magnetite thin films produced by vapor deposition," *ACS Appl. Mater. Interfaces*, vol. 2, no. 10, pp. 2804–2812, 2010.

Bitlis Eren Üniversitesi Fen Bilimleri Dergisi
BİTLİS EREN UNIVERSITY JOURNAL OF SCIENCE
ISSN: 2147-3129/e-ISSN: 2147-3188
VOLUME: 12 NO: 3 PAGE: 634-641 YEAR: 2023
DOI:10.17798/bitlisfen.1258011

A Comparative Study of the Antiproliferative and Apoptotic Effects of Some Chemotherapeutic Drugs on Neuroblastoma Cells

Gurbet ÇELİK TURGUT[1*]

[1]*Pamukkale University, Faculty of Applied Sciences, Department of Organic Agriculture Management, Denizli, Türkiye (ORCID:0000-0002-2306-6972)*

Keywords: Neuroblastoma, Chemotherapeutic, Cytotoxicity, Apoptosis, IC50, Cancer.

Abstract

In this study, it was aimed to investigate the antiproliferative and apoptotic effects of nivolumab, cetuximab and gemcitabine used in the treatment of different cancer types as well as cisplatin and cyclophosphamide used in the treatment of neuroblastoma on SH-SY5Y neuroblastoma cells. The effect of each chemotherapeutic on cell viability and the individual half-maximal inhibitory concentration (IC50) values were determined by the crystal violet method. To determine their apoptotic effects, RT-PCR and Annexin V-FITC apoptosis detection technique were used. The results indicated that all the used chemotherapeutic drugs showed dose-dependent cytotoxic effects and induced apoptosis in SH-SY5Y cells. The IC50 values of cisplatin, cyclophosphamide, nivolumab, cetuximab, and gemcitabine were calculated as 10.91 µM, 0.54 µM, 30.26 µM 4.74 µM and 0.036 µM, respectively. After IC50 dose treatment of cisplatin, cyclophosphamide, nivolumab, cetuximab, and gemcitabine, apoptotic cell rates were found as 21%, 12%, 16%, 10% and 39% respectively. It was determined that statistically significant changes in mRNA expression levels in almost all apoptosis-related genes occurred after chemotherapeutic drugs treatment. In conclusion, gemcitabine showed more antiproliferative and apoptotic effects on neuroblastoma cells than the other chemotherapeutics. It is clear that further studies that will elucidate the mechanism of action of gemcitabine may contribute to the treatment of neuroblastoma.

1. Introduction

Neuroblastoma is an extracranial solid tumor of the autonomic nervous system that is frequently encountered in children [1]. It constitutes 7% of pediatric neoplasms and 10% of all pediatric deaths caused by cancer [2]. When evaluated in terms of incidence rate among pediatric cancers, it ranks third after leukemia and brain tumor [3].

Neuroblastoma is quite diverse, ranging from incidental tumors without symptoms to diffuse metastases with systemic signs. The biological variability of neuroblastoma causes it to exhibit various clinical behaviors with outcomes ranging from spontaneous regression or progression to metastasis and mortality despite extensive treatment [4]-[6]. The etiology of neuroblastoma is not known exactly, but the early diagnosis age and heterogeneity of the disease show that the main cause of neuroblastoma cases is that the development of irregular neural crest cells may cause tumors in the adrenal glands or sympathetic ganglia [7]-[9]. Familial neuroblastoma can generally result from mutations in various genes and has been associated with a poor prognosis [2], [10]. However, DNA methylation changes also appear to contribute to neuroblastoma biology and clinical behavior [11].

The age of the patient at the time of diagnosis, the stage of the disease, the tumor's histology, and the ploidy of the tumor cells are some of the factors used for stratifying the risk of the disease. Based on these variables and clinical and biological standards,

*Corresponding author: gurbetc@pau.edu.tr
Received: 28.02.2023, Accepted: 15.08.2023

patients are divided into low, medium, and high-risk groups [6], [12]. Patients in the high-risk group receive intensive, multimodal treatment including chemotherapy, surgery, immunotherapy with antibodies, radiotherapy, autologous stem cell transplantation, and myeloablative chemotherapy [6], [12], [13]. However, the disease can often exhibit a resistant picture and relapse [14], [15].

Chemotherapy for neuroblastoma usually involves a combination of drugs. Various drugs such as cyclophosphamide, cisplatin, vincristine, doxorubicin, etoposide, and topotecan are used in the treatment of the disease, but resistance to these chemotherapeutic drugs may develop [16]. Therefore, patients need new drugs to overcome chemoresistance, but drug development phases are multifaceted and complex, and there is a risk that the drug will not be successful even after many resources have been invested [17]. Developing drugs related to nervous system diseases, in particular, presents a series of difficulties that complicate the process due to the complex nature of the nervous system [18]. Therefore, there is an urgent need for *in vitro* drug screening with clinically approved drugs for the treatment of different types of cancer.

It has been established that high-risk neuroblastoma patients who develop metastatic neuroblastoma also have an immune resistance mechanism mediated by programmed death ligand 1 (PD-L1). [19]. Blocking the PD-1/PD-L axis seems important in a combined immunotherapy approach. In the treatment of neuroblastoma, nivolumab, a PD-1 inhibitor immunotherapeutic drug, stands out in terms of *in vitro* cytotoxicity. However, it is known that epidermal growth factor receptor (EGFR) expression is high in neuroblastoma tissues, suggesting that it is possible to develop treatment strategies for neuroblastoma by targeting EGFR [20]. Cetuximab is an anti-cancer agent that works by inhibiting the growth and survival of tumor cells that express EGFR. Gemcitabine, the deoxycytidine analog, works by a different mechanism than the drugs used in the treatment of neuroblastoma. In addition, it has been shown that gemcitabine is not a substrate for P-glycoprotein and some proteins associated with multidrug resistance in neuroblastoma [21].

Most of the currently used anticancer drugs direct cancer cells to apoptosis by acting on different signaling pathways. To avoid apoptosis, cells use different signal transduction pathways. A better understanding of these apoptotic signaling pathways could increase the effectiveness of cancer therapy. Therefore, in this study, it was aimed to comparatively investigate the antiproliferative and apoptotic effects of nivolumab, cetuximab, and gemcitabine used in the treatment of different cancer types as well as cisplatin and cyclophosphamide used in the treatment of neuroblastoma on SH-SY5Y neuroblastoma cells.

2. Material and Method

2.1. Cell Culture

The human neuroblastoma cell line SH-SY5Y (ATCC CRL-2266) was used in the experiments. DMEM-F12 medium supplemented with 1% antibiotic and 10% heat-inactivated fetal bovine serum (FBS) was used to grow cells at 37°C in a humidified incubator with 5% CO_2. By changing the medium every two days, cells were produced in a monolayer and grown in cell culture dishes. After the cells adhered to the culture dishes in a single layer, they were separated from the surface with Trypsin-EDTA, the cell mixture/trypan blue (1:1) was counted on the Thoma slide and made ready for cultivation [22]. All the chemicals were purchased from Sigma-Aldrich (Germany).

2.2. Determination of Cytotoxic Activity

At a density of 2×10^3 cells/ml in the culture medium, SH-SY5Y cells were seeded in 96-well plates. Cells were exposed to various chemotherapeutic drug concentrations (ranging from 0.0025 μM to 100 μM) after a 24-h incubation period prior to treatment. Cisplatin, cyclophosphamide, nivolumab, cetuximab, and gemcitabine used in the study were obtained from MCE (Sweden). Cells were incubated for 24 h at 37°C in a humidified 5% CO_2 atmosphere, either with chemotherapeutic drugs or as controls. Crystal violet solution (0.5% concentration, in 50% methanol) was added to the medium after incubation. The plates were incubated for 10 min at room temperature, washed with water, and the adsorbed dye was eluted with Na-citrate (0.1 M Na-citrate in 50 percent ethanol, pH 4.2). At 600 nm, the absorbance, a measure of cell viability, was taken. Viable cell was expressed as the percentage of viable cells compared to control cells [23].

2.3. RNA Isolation and RT-PCR

The innuPREP RNA Mini Kit 2.0 (Analytic Jena GmbH, Germany) was used to extract RNA from SH-SY5Y cells in accordance with the manufacturer's recommendations. The NanoDrop 1000 spectrophotometer (MaestroNano Micro-volume Spectrophotometer, USA) was used to measure the quantity and quality of RNA. The Easy Script cDNA

Synthesis Kit (ABM, Canada) was utilized to create cDNA. The gene-specific primer sequences used in the study are given in Table 1. RT-PCR was carried out using the CFX96 Touch Real-Time PCR Detection System (Bio-Rad, Dubai) and KiloGreen 2X qPCR Master Mix (ABM). β-actin was used as a control gene [24].

Table 1. Primer sequences of human genes associated with apoptosis

Gene	Primer sequence	
ACTB	F	TCCTCCTGAGCGCAAGTACTC
	R	CTGCTTGCTGATCCACATCTG
Bax	F	AGAGGATGATTGCCGCCGT
	R	CAACCACCCTGGTCTTGGATC
Bcl-2	F	ATGTGTGTGGAGAGCGTCAACC
	R	TGAGCAGAGTCTTCAGAGACAGCC
p53	F	ATCTACAAGCAGTCACAGCACAT
	R	GTGGTACAGTCAGAGCCAACC

2.4. V/PI Staining for the Identification of Apoptotic Cells

2×10^5 cells were plated in 6-well dishes to identify apoptotic cells. After 24 h of incubation, the cells were exposed to the half-maximal inhibitory concentration (IC50) of the tested drugs. Cells were harvested after 24 h and then treated with Annexin V-EGFP Apoptosis Detection Kit (BioVision, USA) in accordance with the manufacturer's instructions. Counting of cells was done using a NanoEnTek (USA) Arthur Novel Fluorescence Cell Counter. Calculations were made to determine the proportion of necrotic and apoptotic cells relative to the total cell population. A positive control for apoptosis was hydrogen peroxide (H_2O_2) [25].

2.5. Statistical Analysis

Minitab 13 statistical software was used to conduct the statistical analysis. The mean and standard deviation (SD) of independent experimental sets were used to express all results. The value needed for statistical significance was set at $p < 0.05$ when making comparisons between groups using the Student's t-test.

3. Results and Discussion

Neuroblastoma, a clinically heterogeneous pediatric cancer of the sympathetic nervous system, is the most common childhood tumor [14]. Although neuroblastoma has a high morbidity and mortality rate, it can sometimes disappear spontaneously [6]. Therefore, it shows a heterogeneous malignancy ranging from long-term survival to a high risk of death [26]. Mortality analyzes performed in high-risk groups have shown little success despite intensive multimodal therapy [27]. This lack of success can be explained by the fact that the etiology of the disease is not fully explained and it has a significant heterogeneity in its pathophysiology [28]. The high-risk group has the worst prognosis, and the disease may metastasize to various organs [27]. Chemotherapy and immunotherapeutic drugs are used in the treatment of the disease. All these drugs show beneficial effects on neuroblastoma symptoms. However, the treatment of the disease is limited due to the side effects of these drugs and the development of resistance to the drugs used [29], [30]. Thus, it is essential to identify novel therapeutics that can be applied to the management of neuroblastoma and to investigate their outcomes. Since drug development stages are challenging and risky processes, it is important to test the usability of various clinically approved therapeutics for the treatment of neuroblastoma. In the present study, the cytotoxic and apoptotic effects of five different drugs approved by the US Food and Drug Administration (FDA), which are used in various cancer treatments, on neuroblastoma cells were comparatively investigated. Cisplatin and cyclophosphamide were used as references because these drugs are the backbone of current clinical protocols for the treatment of neuroblastoma.

Investigation of drug candidates and/or drugs on cancer cells has become the primary strategy for discovering anti-cancer agents. For this reason, the effects of these drugs, which are effective on various cancer cells, on the viability in SH-SY5Y cells were determined and IC50 values were calculated in the present study. In all chemotherapeutic drug groups, the cell viability seemed to decrease with increasing drug concentration. The IC50 values of cisplatin and cyclophosphamide used in the treatment of neuroblastoma were determined as 10.91 μM and 0.54 μM, respectively (Table 2). These values are in agreement with the ones reported by several studies in the literature. For instance, in a study conducted to investigate the intracellular mechanisms of neurotoxicity of platinum drugs, the effect of cisplatin on SH-SY5Y neuroblastoma cell line was examined, and the IC50 value of cisplatin was calculated as 15 μM [31]. In another study investigating the effect of cyclophosphamide on the cell viability and tumor progression of neuroblastoma cell line, it was shown that the IC50 value was 0.602 μM and that the drug caused antiproliferative effects [32]. Based on the IC50 value results in the present study, it can be

suggested that cyclophosphamide has more toxic effect on SH-SY5Y cells compared to cisplatin.

The IC50 values of nivolumab, cetuximab, and gemcitabine, which are clinically approved for the treatment of other cancer types, were calculated as 30.26 μM, 4.74 μM, and 0.036 μM, respectively (Table 2). It was observed in a study that the inhibitory effect of nivolumab on ovarian cancer cells increased in a dose-dependent manner and that nivolumab at a concentration of 20 μM could play a synergistic antitumor role with cisplatin in ovarian cancer cells [33]. However, in the literature, there is no study regarding the antiproliferative activity of nivolumab in SH-SY5Y cells. On the other hand, in a study on the efficacies of several drugs, including cetuximab, and their combinations in eight different lung cancer cell lines with different genetic characteristics, the IC50 value of cetuximab in these cell lines was found at concentrations ranging from 0.05 μM to 12 μM [34]. In another study, the IC50 value of cetuximab in four different rhabdomyosarcoma cell lines was determined to be at concentrations ranging from 4.7 μM to 9.1 μM [35]. In a study investigating the effect of disulfiram and copper complex, which is used as a radiosensitizing anticancer agent, on cell cycle regulation, it was shown that approximately 50% of the SH-SY5Y cells treated with 40 nM gemcitabine did not survive [36]. Taken together, among the chemotherapeutic drugs tested in the present study, gemcitabine exhibited the most cytotoxic effect on neuroblastoma cells.

Apoptosis plays a strategic role in cancer treatment because one of the most important distinguishing features of cancer is avoidance of apoptosis. Mutations in various genes can occur in cancer cells. For this reason, it is important to know through which pathway chemotherapeutic drugs designed to induce apoptosis act in order to destroy cancer cells. In general, the pathway inhibited in cancer cells is the intrinsic pathway. Overexpression of Bcl-2 and loss of Bax are ways that cancer cells avoid apoptosis. In addition, these cells ensure that the tumor suppressor gene p53, which regulates Bax, is inhibited [37].

Table 2. The cytotoxic effects of five different drugs on neuroblastoma cell line (SH-SY5Y)

Drug	IC50 (μM), mean ± SD
Cisplatin	10.91 ± 2.23
Cyclophosphamide	0.54 ± 0.13
Nivolumab	30.26 ± 6.27
Cetuximab	4.74 ± 1.09
Gemcitabine	0.036 ± 0.009

The mRNA expressions of Bcl-2, Bax and p53 genes in SH-SY5Y neuroblastoma cells treated with cisplatin, cyclophosphamide, nivolumab, cetuximab, and gemcitabine were normalized with β-actin mRNA expression. As compared to the control group, treatment of SH-SY5Y cells with the chemotherapeutic drugs examined in the current study increased the expression of p53 mRNA; the increase in expression level was statistically significant for cisplatin, cyclophosphamide, cetuximab, and gemcitabine (4.53-fold, 4.57-fold, 3.43-fold, and 5.40-fold, respectively) but not for nivolumab (Table 3). The highest increase in p53 mRNA expression was observed after gemcitabine treatment. In contrast, all the chemotherapeutic drugs tested in the present study decreased the Bcl-2 mRNA expression compared to the control group; the decrease in expression level was statistically significant for cisplatin, cyclophosphamide, nivolumab, and gemcitabine (3.60-fold, 2.08-fold, 4.00-fold, and 3.95-fold, respectively) but not for cetuximab (Table 3). In addition, compared to the control group, the relative Bax mRNA level was statistically increased in SH-SY5Y cells treated with cisplatin, cyclophosphamide, nivolumab, cetuximab, and gemcitabine (3.07-fold, 5.58-fold, 2.23 fold, 4.47-fold, and 6.02-fold, respectively) (Table 3).

Table 3. Expression levels of Bax, Bcl-2 and p53 genes after five different drugs treatment

Drug	Bax	Bcl-2	p53
Cisplatin	3.07 ± 0.28*	−3.60 ± 0.03*	4.53 ± 0.83*
Cyclophosphamide	5.58 ± 0.72*	−2.08 ± 0.08*	4.57 ± 0.12*
Nivolumab	2.23 ± 0.24*	−4.00 ± 0.14*	1.94 ± 0.04
Cetuximab	4.47 ± 0.45*	−1.74 ± 0.02	3.43 ± 0.50*
Gemcitabine	6.02 ± 0.68*	−3.95 ± 0.62*	5.40 ± 0.65*

*Significantly different from respective control value for each gene ($p < 0.05$).

The percentage of apoptotic cells over the total cell population was calculated in the Novel Fluorescence Cell Counter after the neuroblastoma cells were stained with Annexin V/PI to determine whether they underwent apoptosis after being treated with drug. Apoptotic cell rates were 21%, 12%, 16%, 10%, and 39% after IC50 dose treatment of cisplatin, cyclophosphamide,

nivolumab, cetuximab, and gemcitabine, respectively (Figure 1). Among all drug groups, the greatest increase in apoptosis was seen in the cells treated with gemcitabine compared to the control group.

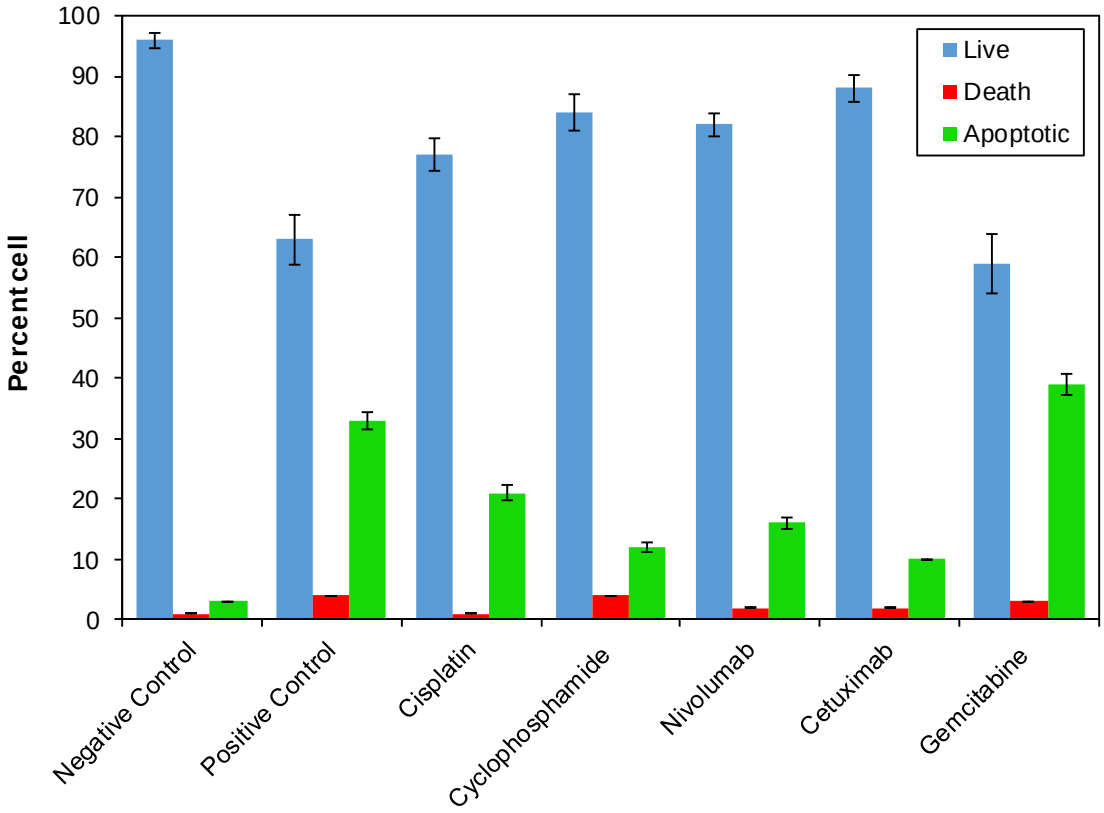

Figure 1. Apoptosis assay in SH-SY5Y cells after cisplatin, cyclophosphamide, nivolumab, cetuximab, and gemcitabine treatment. H_2O_2 was used as a positive control for cells

In a study investigating possible mechanism of cisplatin and nivolumab on platinum-resistant ovarian cancer cells, it was shown that these two drugs decreased Bcl-2 protein expression level but increased Bax protein expression level and that 50 µM cisplatin and 50 µM nivolumab induced apoptosis at a rate of 42.67% and 40.73%, respectively [33]. It was reported that p53 had an important role in cisplatin-induced apoptosis in neuroblastoma and renal tubular cells [38], [39]. Álvarez-León et al. showed that cyclophosphamide exhibited ~35% apoptotic induction and caused an increase in the apoptotic index Bax/Bcl-2 ratio, which is an indicator of caspase pathway activation in neuroblastoma cell line [32]. Moreover, gemcitabine was reported to induce p53-dependent apoptosis associated with proapoptotic proteins such as PUMA and Bax in pancreatic cancer cells [40], and cetuximab was revealed to promote apoptosis in head and neck squamous cell carcinoma cell lines [41].

4. Conclusions

Neuroblastoma, a disease with a high morbidity and mortality rate, originates from neural crest cells and is classified as an embryonal neuroendocrine tumor. Due to the serious side effects of the chemotherapeutic and immunotherapeutic drugs used in the treatment and the development of resistance to the drugs used, scientists and pharmaceutical companies have started to search for new drugs. However, due to the complex nature of the nervous system and the difficulty of drug development stages, it has revealed the necessity of *in vitro* drug screening with clinically approved drugs in the treatment of various cancer types. In conclusion, in the present study, it was determined that some cancer drugs (cisplatin, cyclophosphamide, nivolumab, cetuximab, and gemcitabine) have antiproliferative and apoptotic effects on SH-SY5Y neuroblastoma cells.

Gemcitabine was found to be more effective than the other four drugs in reducing cell viability and tending to apoptosis in neuroblastoma cells. However, it is recommended that further studies that will elucidate the mechanism of action of gemcitabine are necessary to contribute to the treatment of neuroblastoma.

Conflict of Interest Statement

There is no conflict of interest regarding the study.

Statement of Research and Publication Ethics

The study is complied with research and publication ethics.

References

[1] C. Pudela, S. Balyasny, and M. A. Applebaum, "Nervous system: Embryonal tumors: Neuroblastoma," *Atlas Genet. Cytogenet. Oncol. Haematol.*, vol. 24, no. 7, pp. 284–290, 2020.

[2] E. S. Hanemaaijer *et al.*, "Single-cell atlas of developing murine adrenal gland reveals relation of Schwann cell precursor signature to neuroblastoma phenotype," *Proc. Natl. Acad. Sci. U. S. A.*, vol. 118, no. 5, p. e2022350118, 2021.

[3] I. V. Kholodenko, D. V. Kalinovsky, I. I. Doronin, S. M. Deyev, and R. V. Kholodenko, "Neuroblastoma origin and therapeutic targets for immunotherapy," *J. Immunol. Res.*, vol. 2018, pp. 1–25, 2018.

[4] E. S.-W. Ngan, "Heterogeneity of neuroblastoma," *Oncoscience*, vol. 2, no. 10, pp. 837–838, 2015.

[5] N.-K. V. Cheung and M. A. Dyer, "Neuroblastoma: developmental biology, cancer genomics and immunotherapy," *Nat. Rev. Cancer*, vol. 13, no. 6, pp. 397–411, 2013.

[6] V. P. Tolbert and K. K. Matthay, "Neuroblastoma: clinical and biological approach to risk stratification and treatment," *Cell Tissue Res.*, vol. 372, no. 2, pp. 195–209, 2018.

[7] J. Blatt and R. L. Hamilton, "Neurodevelopmental anomalies in children with neuroblastoma," *Cancer*, vol. 82, no. 8, pp. 1603–1608, 1998.

[8] J. A. Tomolonis, S. Agarwal, and J. M. Shohet, "Neuroblastoma pathogenesis: deregulation of embryonic neural crest development," *Cell Tissue Res.*, vol. 372, no. 2, pp. 245–262, 2018.

[9] M. S. Irwin and J. R. Park, "Neuroblastoma: paradigm for precision medicine," *Pediatr. Clin. North Am.*, vol. 62, no. 1, pp. 225–256, 2015.

[10] I. Janoueix-Lerosey *et al.*, "Somatic and germline activating mutations of the ALK kinase receptor in neuroblastoma," *Nature*, vol. 455, no. 7215, pp. 967–970, 2008.

[11] S. Gómez, G. Castellano, G. Mayol, A. Queiros, J. I. Martín-Subero, and C. Lavarino, "DNA methylation fingerprint of neuroblastoma reveals new biological and clinical insights," *Genom. Data*, vol. 5, pp. 360–363, 2015.

[12] E. Sokol and A. V. Desai, "The evolution of risk classification for neuroblastoma," *Children (Basel)*, vol. 6, no. 2, p. 27, 2019.

[13] K. K. Matthay *et al.*, "Treatment of high-risk neuroblastoma with intensive chemotherapy, radiotherapy, autologous bone marrow transplantation, and 13-cis-retinoic acid. Children's Cancer Group," *N. Engl. J. Med.*, vol. 341, no. 16, pp. 1165–1173, 1999.

[14] J. M. Maris, "Recent advances in neuroblastoma," *N. Engl. J. Med.*, vol. 362, no. 23, pp. 2202–2211, 2010.

[15] H. Richard, A. Pokhrel, S. Chava, A. Pathania, S. S. Katta, and K. B. Challagundla, "Exosomes: Novel players of therapy resistance in neuroblastoma," *Adv. Exp. Med. Biol.*, vol. 1277, pp. 75–85, 2020.

[16] P. Bhoopathi, P. Mannangatti, L. Emdad, S. K. Das, and P. B. Fisher, "The quest to develop an effective therapy for neuroblastoma," *J. Cell. Physiol.*, vol. 236, no. 11, pp. 7775–7791, 2021.

[17] L. Heinonen and B. Sandberg, "Money for nothing? Risks in biopharmaceutical companies from the perspective of public financiers," *J. Commer. Biotechnol.*, vol. 14, no. 4, 2008.

[18] Y. Morofuji and S. Nakagawa, "Drug development for central nervous system diseases using in vitro blood-brain barrier models and drug repositioning," *Curr. Pharm. Des.*, vol. 26, no. 13, pp. 1466–1485, 2020.

[19] S. Zuo *et al.*, "Potential role of the PD-L1 expression and tumor-infiltrating lymphocytes on neuroblastoma," *Pediatr. Surg. Int.*, vol. 36, no. 2, pp. 137–143, 2020.

[20] S. Tamura *et al.*, "Induction of apoptosis by an inhibitor of EGFR in neuroblastoma cells," *Biochem. Biophys. Res. Commun.*, vol. 358, no. 1, pp. 226–232, 2007.

[21] M. Ogawa, H. Hori, T. Ohta, K. Onozato, M. Miyahara, and Y. Komada, "Sensitivity to gemcitabine and its metabolizing enzymes in neuroblastoma," *Clin. Cancer Res.*, vol. 11, no. 9, pp. 3485–3493, 2005.

[22] G. Celik, H. Akca, and A. Sen, "Investigation of aromotase inhibition by several dietary vegetables in human non-small cell lung cancer cell lines," *Turk. J. Bioch.*, vol. 38, no. 2, pp. 207–217, 2013.

[23] M. Sulak, G. C. Turgut, and A. Sen, "Cerium oxide nanoparticles biosynthesized using fresh green walnut shell in microwave environment and their anticancer effect on breast cancer cells," *Chem. Biodivers.*, vol. 19, no. 8, p. e202200131, 2022.

[24] I. Erdogan Orhan *et al.*, "Evaluation of anti-Alzheimer activity of synthetic coumarins by combination of in vitro and in silico approaches," *Chem. Biodivers.*, vol. 19, no. 12, p. e202200315, 2022.

[25] C. Sahin *et al.*, "New iridium bis-terpyridine complexes: synthesis, characterization, antibiofilm and anticancer potentials," *Biometals*, vol. 34, no. 3, pp. 701–713, 2021.

[26] E. Yilmaz, M. B. Samur, A. Özcan, E. Ünal, and M. Karakükçü, "Transplantation for ultra high-risk neuroblastoma patients: effect of tandem autologous stem cell transplantation," *J. Health Sci. Med.*, vol. 4, no. 6, pp. 943–948, 2021.

[27] V. Smith and J. Foster, "High-risk neuroblastoma treatment review," *Children (Basel)*, vol. 5, no. 9, 2018.

[28] A. Zafar *et al.*, "Molecular targeting therapies for neuroblastoma: Progress and challenges," *Med. Res. Rev.*, vol. 41, no. 2, pp. 961–1021, 2021.

[29] S. Mallepalli, M. K. Gupta, and R. Vadde, "Neuroblastoma: An updated review on biology and treatment," *Curr. Drug Metab.*, vol. 20, no. 13, pp. 1014–1022, 2019.

[30] N. W. Mabe *et al.*, "Transition to a mesenchymal state in neuroblastoma confers resistance to anti-GD2 antibody via reduced expression of ST8SIA1," *Nat. Cancer*, vol. 3, no. 8, pp. 976–993, 2022.

[31] E. Donzelli *et al.*, "Neurotoxicity of platinum compounds: Comparison of the effects of cisplatin and oxaliplatin on the human neuroblastoma cell line SH-SY5Y," *J. Neurooncol.*, vol. 67, no. 1/2, pp. 65–73, 2004.

[32] W. Álvarez-León, I. Mendieta, E. Delgado-González, B. Anguiano, and C. Aceves, "Molecular iodine/cyclophosphamide synergism on chemoresistant neuroblastoma models," *Int. J. Mol. Sci.*, vol. 22, no. 16, p. 8936, 2021.

[33] L.-M. Sun *et al.*, "Nivolumab effectively inhibit platinum-resistant ovarian cancer cells via induction of cell apoptosis and inhibition of ADAM17 expression," *Eur. Rev. Med. Pharmacol. Sci.*, vol. 21, no. 6, pp. 1198–1205, 2017.

[34] M. Wang and A. Yuang-Chi Chang, "Molecular mechanism of action and potential biomarkers of growth inhibition of synergistic combination of afatinib and dasatinib against gefitinib-resistant non-small cell lung cancer cells," *Oncotarget*, vol. 9, no. 23, pp. 16533–16546, 2018.

[35] Y. Yamamoto *et al.*, "Cetuximab promotes anticancer drug toxicity in rhabdomyosarcomas with EGFR amplification in vitro," *Oncol. Rep.*, vol. 30, no. 3, pp. 1081–1086, 2013.

[36] M. Tesson, G. Anselmi, C. Bell, and R. Mairs, "Cell cycle specific radiosensitisation by the disulfiram and copper complex," *Oncotarget*, vol. 8, no. 39, pp. 65900–65916, 2017.

[37] M. Hassan, H. Watari, A. AbuAlmaaty, Y. Ohba, and N. Sakuragi, "Apoptosis and molecular targeting therapy in cancer," *Biomed Res. Int.*, vol. 2014, p. 150845, 2014.

[38] K. Million *et al.*, "Differential regulation of p73 variants in response to cisplatin treatment in SH-SY5Y neuroblastoma cells," *Int. J. Oncol.*, vol. 29, no. 1, pp. 147–154, 2006.

[39] M. Jiang, X. Yi, S. Hsu, C.-Y. Wang, and Z. Dong, "Role of p53 in cisplatin-induced tubular cell apoptosis: dependence on p53 transcriptional activity," *Am. J. Physiol. Renal Physiol.*, vol. 287, no. 6, pp. F1140-7, 2004.

[40] R. Hill *et al.*, "Gemcitabine-mediated tumour regression and p53-dependent gene expression: implications for colon and pancreatic cancer therapy," *Cell Death Dis.*, vol. 4, no. 9, p. e791, 2013.

[41] H. Baysal *et al.*, "Cetuximab-induced natural killer cell cytotoxicity in head and neck squamous cell carcinoma cell lines: investigation of the role of cetuximab sensitivity and HPV status," *Br. J. Cancer*, vol. 123, no. 5, pp. 752–761, 2020.

Bitlis Eren Üniversitesi Fen Bilimleri Dergisi
BİTLİS EREN UNIVERSITY JOURNAL OF SCIENCE
ISSN: 2147-3129/e-ISSN: 2147-3188
VOLUME: 12 NO: 3 PAGE: 642-648 YEAR: 2023
DOI:10.17798/bitlisfen.1264187

Controllability of the Main Road with an On-Ramp Section in Freeway Traffic Flow

Ali HAMİDOĞLU[1*]

[1]*Mathematics Department, Bahçeşehir University, 34353, Çirağan Caddesi, No: 4-6, Beşiktaş İstanbul/Türkiye*
(ORCID:0000-0003-3584-8848)

Keywords: Control theory, Traffic flow, Kalman rank condition, Controllability, Continuous time system.

Abstract
This study examines the controllability issue pertaining to the main road with a single on-ramp segment within the context of freeway traffic flow. In this regard, a finite-dimensional nonlinear model is formulated by integrating variable speed limit (VSL) and ramp metering (RM) techniques with the controllability property of the system derived under continuous VSL and RM controllers. This allows us to simultaneously control the density of the main line and reduce the queue density of the merging sector. In the numerical experiment, numerical simulations are conducted on a sample model of a main road to investigate the null controllability of the system and validate the theoretical findings. The numerical findings suggest that it is possible to achieve a consistent queue length for the on-ramp section through the implementation of suitable VSL and RM controls. Therefore, the primary accomplishment of this study is to effectively regulate the traffic flow on the main road segment by managing the density of vehicles within a specified timeframe while also considering the queue density of the on-ramp section.

1. Introduction

Increasing mobility has been a challenging and interesting task in the last decade to provide service and maintenance in urban regions. Hence, with the growing needs of mobility, intelligent transportation systems (ITS) become an important topic in transportation research. The tools, together with applications such as dynamic traffic signaling, RM, VSL, vehicle navigation systems, cooperative driving, and so on, are the major parts of ITS that increase the quality of mobility and the level of safety. On the freeway, it is crucial to maintain the traffic flow without building unnecessary road structures like extra road lanes or ramps. For this reason, various constructions and techniques are provided for building effective control strategies to increase the safety factor and, on the other hand, decrease traffic on the road [1]. As an example, various coordinated RM approaches are investigated in [2]. Model-predictive control approaches have also been emerging for optimal coordination of VSL and RM. The integrated free-way traffic flow management scheme is applied in [3] by means of VSL to design an optimal model of controlling freeway traffic flow with minimum travel time in the network. Several RM algorithms have been used to manage the inputs to freeways from entry ramps in an effort to reduce peak-hour congestion on the roads. In [4], a freeway system made up of an entry/exit ramp and a highway segment is examined as a ramp control problem to reduce the overall system time on the freeway.
Sometimes, VSLs and RM solutions frequently fall short of the anticipated outcomes when dealing with the merging zone of a freeway or managing heavy traffic demand due to poor traffic information transfer and the inability to actively control vehicles. An integrated technique for controlling traffic flow in the expressway merging region is suggested in order to increase traffic efficiency [5].
In a variety of traffic flow models, [6] uses ramp control frameworks via cell transmission. In recent

*Corresponding author: ali.hamidoglu@eng.bau.edu.tr
Received: 13.03.2023, Accepted: 13.09.2023

years, RM and VSL controls have been used for different purposes, such as robust control [7], feedback control [8], optimal control [9], and so on. In the context of the controllability of traffic models, we refer to [10] for studying the controllability problem of traffic network models from the optimal control point of view. The exact boundary controllability problem is considered in [11] for the class of non-local conservation laws that control the traffic flow of the given system. Moreover, a novel methodology is developed in [12] for investigating the problem of controllability on a free-way traffic model by means of knowledge of routing and arcs. A controllability problem is studied in [13] for complex networks under both propagation/spill-back dynamics and drivers' behavior by means of route selection.

In this work, we investigate the controllability problem of a main road with one on-ramp sector in the freeway traffic flow. Roughly speaking, the concept of controllability means investigating whether it is possible to derive the solution of the given control system to a desired final state at the final time by means of a control [14]. More precisely, if any given final target is exactly achieved by a suitable control, then the system becomes exactly controllable. On the other hand, there are two more concepts of controllability: the system becomes null controllable whenever the solution hits zero at the final time [15], [16], and the system becomes approximate controllable whenever the solution nearly achieves the given final input at the terminal time [17]. These notions coincide in finite-dimensional space. This is because the only subspace that is dense in finite-dimensional space is the whole space itself. However, this is not the case in infinite-dimensional spaces. Here, we study the finite-dimensional controllability problem in freeway traffic flow with ramp dynamics. In this regard, we build a finite-dimensional control system via VSL control and RM control by applying the conservation law and Newtonian physics law on the main road as well as taking into account the ramp dynamics of the on-ramp sector. Once we establish the traffic model on the main road, we prove that the system is always controllable by means of continuous VSL and RM controllers.

Hence, the main contributions of the study could be briefly highlighted as follows:

- A road model is proposed, along with parameters and descriptions related to the mainstream and road dynamics.
- Controllability property is obtained for the main road with one on-ramp segment in the freeway traffic flow.
- A special case is regarded as a null controllability problem for controlling the mainstream density at critical levels and reducing the queue length of the on-ramp segment at any given final time by a continuous controller.
- A consistent queue length for the on-ramp segment and a controlled mainstream density are determined through numerical simulations conducted on a sample model of a main road within a specified time frame.

This study is presented as follows. Firstly, several notions and theorems are provided in section 2. In this part, the idea of controllability for finite-dimensional systems is explained, and the Kalman rank condition is given as a necessary and sufficient condition for the controllability property of linear finite-dimensional systems. Later, we state the problem in section 3, where the road model is proposed together with a nonlinear control system designed by means of VSL and RM controls. Here, the property of controllability is derived for the traffic model, and the existence of a continuous controller is proven for the system. In section 4, numerical experiments are conducted on a sample main road model, and the null controllability property of the system is numerically derived by means of VSL and RM controls. Finally, the paper concludes with further remarks and future work in section 5.

2. Material and Method

In this part, we provide several notions and theorems, some of which are novel in the context of matrix theory. Here, we mainly concentrate on the following control model:

$$x'(t) = Ax(t) + Bu(t) + w(t), \qquad (1)$$

with the standard assumption that $w(t)$ is continuous in $[0,T]$ where $T > 0$ stands for a final time and the linear part is provided by means of the real matrices A, B of reasonable dimensions $n \times n, n \times m$ with $n \geq m$.

On the other hand, the control model (1) is the perturbed version of the following finite-dimensional control system:

$$x'(t) = Ax(t) + Bu(t). \qquad (2)$$

Now, we define the notion of controllability for the model (1) in two directions:

Definition 1. (*Exact Controllability***)**

The system (1) is exactly controllable in finite time T if for each $t_0 \in [0,T]$ and arbitrary initial and final state $x_0, x_1 \in \mathbb{R}^n$, one can find a control input $u(\cdot)$: $[t_0,T] \to \mathbb{R}^m$ in such a way that the solution $x(t)$ hits the target at the given time T, i.e., $x(T) = x_1$.

Definition 2. (*Null Controllability***)**

The system (1) is null controllable in finite time T if for each $t_0 \in [0,T]$ and arbitrary initial $x_0 \in \mathbb{R}^n$, one can find a control input $u(\cdot)$: $[t_0,T] \to \mathbb{R}^m$ in such a way that the solution $x(t)$ satisfies $x(T) = 0$.

Theorem 1. (*Duality of Controllability in* $\mathbb{R}^n$**)**
In $\mathbb{R}^n$, the concepts of null controllability and exact controllability are equivalent.

The last theorem comes from the fact that the only affine subspace of $\mathbb{R}^n$ is the whole space itself. Next, we define Kalman rank criteria [18] for the linear control system (2):

Theorem 2. (*Kalman Rank Condition [18]***)**
The continuous time system (2) becomes controllable whenever the following rank condition satisfies

$$rank[B;\ A\,B;\ A^2B;\cdots;\ A^{n-1}B] = n. \qquad (3)$$

Now, we provide the following result [19]:

Theorem 3. (*Controllability of Perturbed System [19]*)
The control system (1) is controllable if Kalman rank condition is satisfied and the function $w(t)$ is continuous and bounded in $(0,T)$. More precisely, if $w(t)$ is bounded and continuous in a given domain, then, the perturbed system (1) is controllable on that domain. In addition, we have the following result:

Corollary 1. (*Existence of Continuous Controller [19]*)
There exists a continuous controller that makes the perturbed control system (1) controllable.

In the following sections, we investigate the problem of controllability on the main road with one on-ramp section to control the traffic flow in the mainstream. Since the concept of exact controllability coincides with the null controllability notion, we build the first-order continuous time system on the traffic density of the main road and on-ramp section in order to control the traffic flow both ways.

3. Controllability of Main Road with On-ramp Segment

In this section, we study the freeway composed of the main road and an on-ramp segment. Firstly, we start by proposing the road model and all related parameters that would be used to build the first-order nonlinear continuous time system. Then, we derive the controllability result from that system by applying the Kalman rank condition. Lastly, we investigate an application of the main result.

3.1. Road Model

In this part, we study a road model with a main road and an on-ramp shown in Figure 1. In this road model, we assume that the flow from the on-ramp sector is continuous, which means that there is no traffic congestion on the on-ramp section. More precisely, the function is assumed to be continuous in time.

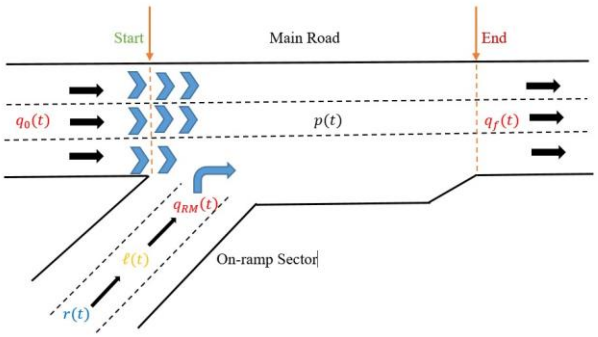

Figure 1. The free-way consisting of the main road with an on-ramp sector.

Define the following parameters for this road model:

- $\rho(t)$ as the density of the main road at the time t.
- $q_0(t)$ and $q_f(t)$ as the number of vehicles coming from the initial road segment (Start) into the main road and the main road into the final road segment (End) at a time t respectively.
- $\ell(t)$ as the queue length of the on-ramp segment at the time t.
- $q_{RM}(t)$ as the number of vehicles entering from the on-ramp into the main road at the time t respectively.
- $r(t)$ as the number of vehicles entering the on-ramp at a given time t.
- L and λ as the length and the number of lines of the main road, respectively.

From the conservation law, we have

$$\rho'(t) = \frac{q_0(t) - q_f(t) + q_{RM}(t)}{\lambda L}. \qquad (5)$$

The linear car-following model is widely used in traffic flow models, which simply depend on Newtonian physics laws. In this regard, the speed and the density are related and represented as the following piecewise function [20]:

$$v(\rho) = \begin{cases} v_f, & \rho < \rho_c \\ C\left(\frac{1}{\rho} - \frac{1}{\rho_m}\right), & \rho \geq \rho_c \end{cases}$$

where ρ_c and ρ_m represent critical density and maximum density of the traffic flow on the road,

respectively, and C is a sensitive constant [20]. Hence, by using $q(\rho) = v\,\rho$, one can get the following flow-density relationship:

$$q(\rho) = \begin{cases} v_f \rho\,, & \rho < \rho_c \\ C(1 - \dfrac{\rho}{\rho_m}), & \rho \geq \rho_c \end{cases}$$

Define, $e(t) = \rho(t) - \rho_c$, then the flow dynamics for the congested state becomes

$$q_f = C\,(1 - \tfrac{e(t)+\rho_c}{\rho_m}) \qquad (6)$$

By using (5) and (6), we finally have the following first-order nonlinear differential system for the proposed road model:

$$e'(t) = \tfrac{q_0(t) + q_{RM}(t)}{\lambda L} - \tfrac{C}{\lambda L}\,(1 - \tfrac{e(t)+\rho_c}{\rho_m}) \qquad (7)$$

with the ramp dynamics

$$\ell'(t) = r(t) - q_{RM}(t). \qquad (8)$$

To control the solutions of (7) and (8) together, we utilize VSL control as well as RM control in the following sense:

$$u_{VSL}(t) = q_0(t) - C(1 - \frac{\rho_c}{\rho_m}),$$
$$u_{RM}(t) = q_{RM}(t).$$

Now, we concentrate on the following finite-dimensional control system:

$$x'(t) = \boldsymbol{A}x(t) + \boldsymbol{B}u(t) + \boldsymbol{w}(t), \qquad (9)$$

where

$$x(t) = \begin{pmatrix} e(t) \\ \ell(t) \end{pmatrix}, u(t) = \begin{pmatrix} u_{VSL}(t) \\ u_{RM}(t) \end{pmatrix}, \boldsymbol{w}(t) = \begin{pmatrix} 0 \\ r(t) \end{pmatrix}$$

$$\boldsymbol{A} = \begin{pmatrix} \dfrac{C}{\lambda L \rho_m} & 0 \\ 0 & 0 \end{pmatrix}, \quad \boldsymbol{B} = \begin{pmatrix} \dfrac{1}{\lambda L} & \dfrac{1}{\lambda L} \\ 0 & -1 \end{pmatrix}$$

In the following section, we investigate the problem of controllability on a nonlinear first-order system (9) and obtain the main result of this work.

3.2. Controllability

In this part, we study the controllability problem for the control system (9) as follows:

Given any initial state $x_0 \in \mathbb{R}^2$ and final state $x_f \in \mathbb{R}^2$, is it possible to find a control input $u(t) \in C(t_0, t_f)^2$ that is the space of continuous functions defined in (t_0, t_f) such that the solution of the system (9), $x(t)$ satisfies $x(t_f) = x_f$. For this controllability problem, we prove the following main result of the paper:

Theorem 4. (*Main Result*)
The system (9) is exactly controllable with continuous controllers $u_{VSL}(t)$ and $u_{RM}(t)$.

Proof: Since traffic flow on the on-ramp sector is continuous on time, $\boldsymbol{w}(t)$ becomes continuous and bounded on time t, which provides that the controllability problem of the system (9) becomes the controllability problem of a perturbed version of the following linear control system:

$$x'(t) = \boldsymbol{A}x(t) + \boldsymbol{B}u(t), \qquad (10)$$

according to Theorem 3. Hence, it suffices to check the Kalman rank condition for the system (10) according to Teorem 2. Since,

$$A \times B = \begin{pmatrix} \dfrac{C}{\lambda^2 L^2 \rho_m} & \dfrac{C}{\lambda^2 L^2 \rho_m} \\ 0 & 0 \end{pmatrix},$$

which makes

$$det[B\ AB] = det \begin{vmatrix} \dfrac{1}{\lambda L} & \dfrac{1}{\lambda L} & \dfrac{C}{\lambda^2 L^2 \rho_m} & \dfrac{C}{\lambda^2 L^2 \rho_m} \\ 0 & -1 & 0 & 0 \end{vmatrix} =$$
$$= det \begin{vmatrix} 1 & 0 & 0 & 0 \\ 0 & 1 & 0 & 0 \end{vmatrix} = 2.$$

Hence, the Kalman rank condition is satisfied for the system (10) which implies that the system (9) is exactly controllable. This concludes the proof. □

3.3. An Application

As an application of Theorem 4, under any given initial data, this result provides $e(t_f) = \rho(t_f) - \rho_c = 0$ and $\ell(t_f) = 0$ under the suitable choice of continuous VSL control and RM control, which is simply the property of null controllability of the system as a result of Teorem 1. As a result, the null controllability issue, which is the special class of exact controllability, provides a way to manage the mainstream density at a critical level and to reduce the queue length of the on-ramp segment by VSL and RM continuous controllers at any given final time.

4. Numerical Results

This section presents numerical simulations conducted on a sample road model in order to provide numerical validation for the primary finding of the study. In this regard, we consider the problem of null controllability on a main road with a length $L = 100$, consisting of $\lambda = 4$ number of lines. Moreover, we assume a sensitivity constant C = 800 and a maximum road density $\rho_m = 2$. Finally, we consider the number of vehicles entering the on-ramp at time t as a nonlinear function, $r(t) = t^2$. Hence, we have the following nonlinear system:

$$\begin{pmatrix} \dot{e}(t) \\ \dot{\ell}(t) \end{pmatrix} = \begin{pmatrix} 1 & 0 \\ 0 & 0 \end{pmatrix} \begin{pmatrix} e(t) \\ \ell(t) \end{pmatrix} + + \begin{pmatrix} \frac{1}{400} & \frac{1}{400} \\ 0 & -1 \end{pmatrix} \begin{pmatrix} u_{VSL}(t) \\ u_{RM}(t) \end{pmatrix} + \begin{pmatrix} 0 \\ t^2 \end{pmatrix}, \qquad (11)$$

In the context of this particular system, we address the issue of null controllability pertaining to the road model within a time span of one hour as follows: given $\begin{pmatrix} e(0) \\ \ell(0) \end{pmatrix} = \begin{pmatrix} e^{-1} \\ 0 \end{pmatrix}$, find VSL and RM controls

$\begin{pmatrix} u_{VSL}(t) \\ u_{RM}(t) \end{pmatrix}$ such that the solution of the above system satisfies $\begin{pmatrix} e(1) \\ \ell(1) \end{pmatrix} = \begin{pmatrix} 0 \\ 0 \end{pmatrix}$. In this particular problem, the constant e represents Euler's number, while the variable time t is defined within the interval of 0 and 1. Furthermore, we make the initial assumption that there is an absence of traffic congestion by letting $\ell(0) = 0$.

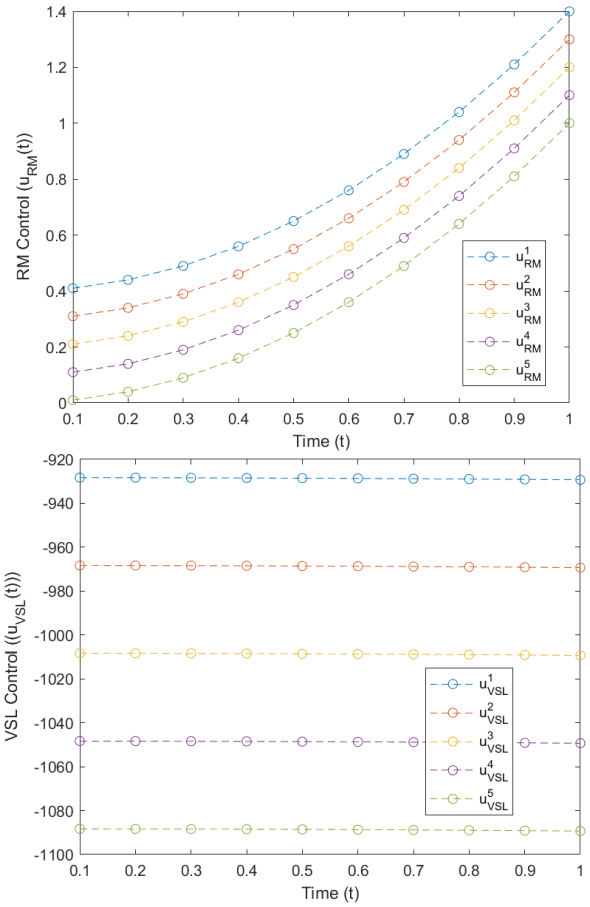

Figure 2. Five distinct VSL and RM control models numerically implemented to achieve the null controllability of the system (11) within a time span of one hour.

According to Theorem 4, it can be deduced that the system (11) fulfills the Kalman rank condition, thereby establishing the theoretical basis for the null controllability of the system (11). On the other hand, in this study, we evaluate and conduct simulations on five distinct VSL and RM control models in order to ascertain their effectiveness in achieving the null controllability outcome, depicted in Figure 2 and Figure 3. These analyses are performed using the MATLAB R2021b version toolbox.

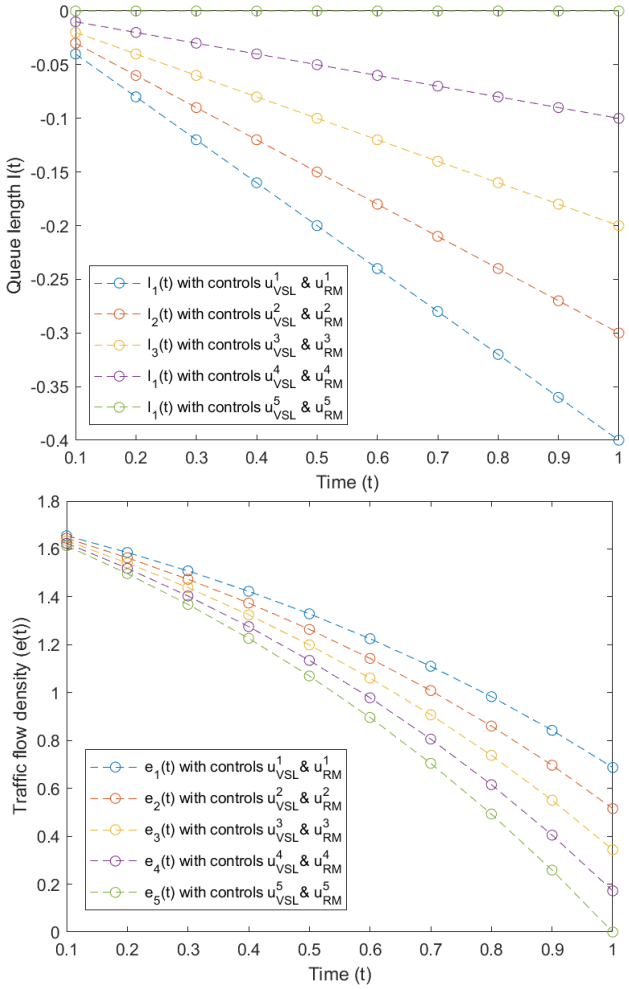

Figure 3. The numerical solutions of the system (11) under five different VSL and RM controls over a duration of one hour.

Figure 2 depicts the computed numerical values of VSL and RM controls over the course of one hour. These parameters are numerically implemented in the system (11) and their corresponding solutions are shown in Figure 3 as traffic flow density $e(t)$ and queue length $\ell(t)$ over the course of one hour.
In these numerical simulations illustrated in Figure 2 and Figure 3, we derive the fact that the green curves establish the null controllability of the system. In other words, numerical results show that the solution of the system (11) under the u_{VSL}^5 and u_{RM}^5 controls provides $e(1) = 0$ and $\ell(1) = 0$ in the final round. This outcome signifies the null controllability of the system (11).

5. Conclusion

This study focuses on the issue of controllability within the traffic model, which comprises a single main road and an on-ramp sector. The controllability is achieved through the implementation of continuous VSL control and RM control strategies. This work demonstrates that by implementing appropriate VSL

and RM controls, it is possible to effectively manage the main road density at its critical level while simultaneously reducing the queue length in the on-ramp segment. Theoretical findings are enhanced by conducting numerical simulations on a sample main road model. In this study, the concept of null controllability is derived through the implementation of VSL and RM controls. The numerical results indicate that it is feasible to maintain a constant queue length for the on-ramp segment by implementing appropriate VSL and RM controls. This can be achieved while also ensuring that the density of vehicles on the main road remains at the critical level within a specified time frame. As a future work, It would be an interesting and motivating attempt to focus on the controllability problem of a more general integrated traffic system where the road model consists of N number of main roads with N number of on-ramp segments for $N > 1$.

Statement of Research and Publication Ethics

The study is complied with research and publication ethics.

References

[1] T.V. Baby, V. Bhattacharyya, P.K. Shahri, A.H. Ghasemi, and B. HomChaudhuri, "A suggestion based fuel efficient control framework for connected and automated vehciles in heterogeneous urban traffic", *Transportation Research Part C: Emerging Technologies,* 134, 103476, 2022.

[2] S.R. Klomp, V.L. Knoop, H. Taale, and S.P. Hoogendoorn, "Ramp metering with microscopic gap detection algorithm design and empirical acceleration verification", *Transportation Research Record,* vol. 2676, no. 1, pp. 91-104, 2021.

[3] S. Li, and D. Cao, "Variable speed limit strategies' analysis with cell transmission model on freeway" *Modern Physics Letters B,* vol. 31, no. 24, 1750219, 2017.

[4] H. Zhang, S. G. Ritchie and W. W. Recker, "Some general results on the optimal ramp control problem", *Transportation Research Part C: Emerging Technologies*, vol. 4, no. 2, pp. 51-69, 1996.

[5] Y. Di, W. Zhang, H. Ding, X. Zheng, and H. Bai, "Integrated Control for Mixed CAV and CV Traffic Flow in Expressway Merge Zones Combined with Variable Speed Limit, Ramp Metering, and Lane Changing", *Journal of Transportation Engineering, Part A: Systems*, vol. 149, no. 2, 04022140, 2023.

[6] G. Gomes, and R. Horowitz, "Optimal freeway ramp metering using the asymmetric cell transmission model", *Transportation Research Part C: Emerging Technologies*, vol. 14, no. 4, pp. 244–262, 2006.

[7] C. Gu, C. Wu, Y. Wu, and B. Wiwatanapataphee, "Distributionally robust ramp metering under traffic demand uncertainty", *Transportmetrica B: Transport Dynamics*, vol. 10, no. 1, pp.652-666, 2022.

[8] C. Gu, T. Zhou, and C. Wu, "Deep Koopman Traffic Modeling for Freeway Ramp Metering", *IEEE Transactions on Intelligent Transportation Systems*, pp. 1-13, 2023.

[9] N. Yuan, M. Ma, S. Liang, W. Wang, and H. Zhang, "Optimal control method of freeway based on tollbooths lane configuration and variable speed limit control", *Physica A: Statistical Mechanics and its Applications*, vol. 603, 127801, 2022.

[10] J. Wang, Y. Zheng, Q. Xu, J. Wang, and K. Li, "Controllability analysis and optimal control of mixed traffic flow with human-driven and autonomous vehicles," *IEEE Transactions on Intelligent Transportation Systems,* vol. 22, no. 12, pp. 7445-7459, 2020.

[11] A. Bayen, J. M. Coron, N. De Nitti, A. Keimer, and L. Pflug, "Boundary controllability and asymptotic stabilization of a nonlocal traffic flow model", *Vietnam Journal of Mathematics*, vol. 49, no. 3, pp. 957-985, 2021.

[12] S. Agarwal and P. Kachroo, "Controllability and observability analysis for intelligent transportation systems", *Transportation in Developing Economies*, vol. 5, no. 1, 2, 2019

[13] M. Rinaldi, "Controllability of transportation networks", *Transportation Research Part B: Methodological*, vol. 118, pp. 381-406, 2018.

[14] A. Hamidoğlu and E. N. Mahmudov, "On construction of sampling patterns for preserving observability/controllability of linear sampled-data systems", *International Journal of Control*, vol. 95, no. 1, pp. 206-217, 2022.

[15] A. Hamidoğlu, "Null controllability of heat equation with switching controls under Robin's boundary condition", *Hacettepe Journal of Mathematics and Statistics*, vol. 45, no. 2, pp. 373-379, 2016.

[16] A. Hamidoglu, "Null controllability of heat equation with switching pointwise controls", *Transactions of NAS of Azerbaijan, Issue Mathematics, Series of Physical-Technical and Mathematical Sciences*, vol. 35, no. 4, pp. 52-60, 2015.

[17] A. Hamidoglu, "Switching lumped controls", *Proceedings of the Institute of Mathematics and Mechanics, National Academy of Sciences of Azerbaijan*, vol. 41, no. 2, pp. 83-90, 2015.

[18] E. D. Sontag, "Kalman's controllability rank condition: from linear to nonlinear", *Mathematical system theory: The influence of RE Kalman*, pp. 453-462, 1991.

[19] D. Lukes, "Global controllability of nonlinear systems", *SIAM Journal on Control*, vol. 10, no. 1, pp. 112–126, 1972.

[20] P. I. Richards, "Shock waves on the highway", *Operations research*, vol. 4, no. 1, pp. 42-51, 1956.

Bitlis Eren Üniversitesi Fen Bilimleri Dergisi
BİTLİS EREN UNIVERSITY JOURNAL OF SCIENCE
ISSN: 2147-3129/e-ISSN: 2147-3188
VOLUME: 12 NO: 3 PAGE: 649-659 YEAR: 2023
DOI:10.17798/bitlisfen.1268718

An Experimental Study of Thermoacoustic Couples

Netice DUMAN[1*], Halil İbrahim ACAR[2], Özlem KUZEY[3],Şakir KUZEY[4]

[1] *SCU. Sivas Technical Sciences Vocational School Machinery and Metal Technologies, Machine Program, Sivas*
[2] *SCU. Faculty of Engineering Department of Mechanical Engineering, Sivas*
[3] *Mayer Metal Machinery Construction Industry Trade Limited Company, Kocaeli*
[4] *KOU. Karamursel Vocational School, Electronics and Automation Department, Kocaeli*
(ORCID: 0000-0002-9926-8511) (ORCID: 0000-0003-3951-6138) (ORCID: 0000-0001-8779-7865) (ORCID: 0000-0003-3680-0862)

Keywords: Thermoacoustic, cooling system, Stack, Resonance tube, Thermoacoustic couples

Abstract
In this study, a simple thermoacoustic refrigerator system experiment set was established by using the design parameters in accordance with the relevant literature. In the experimental setup, a loudspeaker was used as an acoustic power source, and a suitable frequency value was determined for the system. Three kinds of stack materials with different thermal conductivity coefficients, respectively, mylar, cotton, and glass wool, were placed in the resonance tube. The temperature values at both ends of the stack material were measured by placed temperature gauges. In the measurements made within the same time period, the temperature differences were measured as 5.2°C for mylar, 4.7°C for cotton, and 4.3°C for glass wool, respectively. It was determined that the highest temperature difference was in the mylar material.

1.Introduction

Refrigerators are used in almost all areas. Hydrofluorocarbons (HFC) and chlorofluorocarbons (CFC) found in refrigerants used in conventional refrigerators cause harmful environmental effects such as thinning and perforation of the ozone layer. Therefore, taking harmful environmental effects into account is becoming more and more important in the design and development of cooling systems. In order to eliminate the harmful effects of refrigerants on the environment, research efforts are more focused on the development of environmentally friendly refrigerants and alternative cooling technologies. One of the alternative cooling technologies is thermoacoustic refrigerating (TAR), which produces cooling from sound. Devices that cool by using acoustic energy are called thermoacoustic coolers. The basic principle in thermoacoustic coolers is the thermoacoustic effect resulting from the interaction between the solid surface and the compressed fluid. The power of the TAR system depends on the power of the sound waves that create vibrational motion within the molecules of the working fluid.

TAR systems can be thermally or electrically operated. The first is driven by heat energy, while the second is driven by the compressor. Thermoacoustic systems working with thermal energy are used for cryogenic cooling and ambient cooling. The purpose of cryogenic thermoacoustic cooling is to achieve the lowest possible temperature, while the TAR of the other is to achieve the highest cooling effect. In conventional cooling systems, the necessary working pressure is provided by the compressor, while the required working pressure in TAR systems, loudspeakers producing sound energy, etc., is supplied with components. One of the positive effects of TAR systems on the environment is that they can also work with atmospheric air. However, the use of air as a refrigerant gas causes a slight decrease in the cooling effect compared to the use of helium and hydrogen [1].

The only disadvantage of the TAR system compared to conventional mechanical vapor

*Corresponding author: nduman@cumhuriyet.edu.tr
Received: 22.03.2023, Accepted: 14.09.2023

compression systems is that it has a lower coefficient of cooling effect. On the other hand, it has advantages such as the absence of moving parts, the use of working fluids that are not harmful to the environment, such as argon and helium, and being safer. In addition, this cooling system also protects the ecosystem by transferring energy from economic sources such as waste heat and solar energy.

The discovery of acoustic cooling dates back about 250 years. The observations made by Higgins [2] in 1777 are the first records of heat-induced oscillations, as Putnam and Dennis (1956) highlighted. Higgins [3] conducted experiments with an open glass tube in which acoustic oscillations were stimulated by the appropriate placement of a hydrogen flame, the so-called "singing flame". The concept of thermoacoustics was first used by Sondhauss (1850) and entered the literature. Later, Rayleigh (1878 and 1945) called this phenomenon the "thermoacoustic effect". About 20 years later, Rott et al. derived linear equations based on thermo-acoustic theory and presented their solutions in their article [4], [5].

A thermoacoustic cooling system consists of four basic components: a stack, hot and cold end heat exchangers, a resonance tube, and an acoustic source [6]. The heat energy is carried over the stack, which is the heart of the acoustic system. The stack is a solid component that contains pores, and its purpose is to cause the working fluid to oscillate when in contact with the solid walls. A temperature distribution occurs on the stack due to the heat carried from one end to the other by the operation of the acoustic source. With the heat exchangers mounted at both ends of the stack, cooling is done by utilizing the decreasing temperature of the stack, and waste heat is given to the outside from the heat exchanger on the side with an increasing temperature. The stack of a thermoacoustic cooler system without heat exchangers is called a thermoacoustic couple [7]. As a result of the interaction between the solid surface of the stack and the gas parcels, a temperature gradient is formed across the stack. The stack or couple temperature difference (ΔT_s) occurs from the hot end close to the pressure antinode to the cold end away from the pressure antinode. Understanding the basic thermoacoustic process that occurs in thermoacoustic couples is crucial for the design and development of thermoacoustic devices.

Experimental studies of thermoacoustic couples (TAC) usually indicate the temperature difference from one end to the other. The thermoacoustic temperature couple forming the basis of the thermoacoustic system TAC was first introduced by Wheatley et al. [8]. In their study, they measured the temperature differences using three different stack materials. The first thermoacoustic coolers were designed by Wheatley and his team and started to be used in the cooling sector. Piccolo and Cannistraro [9] carried out experimental studies on a TAC using a 7-cm-long stack of polyethylene with a thermal conductivity of about 0.11 W/mK. The experimental results were compared with the ΔT_s values predicted by the theoretical model of Atchley et al. [10]. Worlikar et al. [11] developed a numerical model to predict the temperature difference across the thermoacoustic couple. Zoontjens et al. [12] performed numerical modeling of the temperature couple of the different edge profiles of the stack plates. Terdi [13], placed photographic film as stack material inside the resonator tube and experimentally investigated acoustic cooling. In his study, Girgin used polypropylene lemonade straws with a heat transmission coefficient of 0.15 W/mK as a stack and placed the stack in a resonance tube of different sizes (10 cm, 15 cm, and 22 cm), and compared the acoustic cooling effects that occurred. Girgin conducted experiments using atmospheric air and helium as the working fluids and compared the results in both cases [14]. In another study, Somasekher et al. [15] experimentally investigated the effect of tube length on acoustic cooling by using different lengths of resonator tubes in the system.

Teja et al. [16] placed leather as stack material inside the resonator tube and wrapped the skin with nylon fishing line to create a space between the plates. In their experimental studies, acoustic cooling was investigated experimentally by using helium as a working fluid. Mergen [17] numerically investigated the effects of thermophysical properties on thermoacoustic cooling by using five different plastic-derived stack materials, namely PVC, nylon, polyethylene, polyamide, and polypropylene, in standing wave model thermoacoustic coolers. Alcock et al. [18] developed an adjustable-length resonance tube. Wang et al. [19] showed that the multi-stage thermoacoustic cooler designed for operation at room temperature has a better cooling effect than the single-stage case. İlker and Karabacak [20] used air as the working fluid and polypropylene as the stack material and carried out experiments for different sound wave types by changing the diameter of the resonator tube.

In this study, a sinusoidal sound wave with a frequency of 340 Hz was used. With the up-and-down movement of this sound wave, the air passing through the stack is compressed and expanded, and in this way, the air is heated and cooled. The temperature difference between heating and cooling of the air is equivalent to the temperature difference between the ends of the stack. Then, an experimental simple TAC system was established using the design systematics available in the literature [4], [6], [21]. In the

experimental setup, a loudspeaker capable of converting electrical power into acoustic power was used as an acoustic source. As a result of the calculations made with the determined frequency, the length of the resonance tube was found to be one quarter of the ideal wavelength. One end of the resonance tube is fixed to the loudspeaker and the speaker is enclosed in a wooden box for sound isolation.

Except for Mylar, cotton and glass wool, which have not been used before in the literature, were preferred as stacking materials. Then, the temperature difference between the two ends of the stack material was measured using temperature gauges.

2. Material and Method

In this study, a simple thermoacoustic refrigerator system experiment set was established by using the design parameters in accordance with the relevant literature. TAR design parameters can be divided into three groups. As seen in Table 1, the first group includes the geometric parameters, the second group includes the thermophysical properties of the working fluid and stack material, and the third group includes the operating parameters.

Table 1. Design parameters of TAR [22].

Geometric Parameters	Material Specific Parameters	Operating Parameters
λ- Wavelength	Working Fluid	$\dot{Q}_c$-Cooling power
L_s - Stack length	K- Thermal Conductivity	ΔT_m-Desired temperature range
x_c - Center of stack	α- Speed of sound	T_m - Average operating temperature
$2y_0$ - Stack space	μ-Dynamic viscosity	P_m-Average pressure
2l- Plate thickness	γ- Ratio of isobaric and isochoric specific heats	P_r - Pressure amplitude
A-Cross-sectional area	β- Coefficient of thermal expansion	f - Frequency
	Stack Material	
	$\rho_{s\_}$-İntensity	
	c_s - Specific heat	
	K_s-Thermal conductivity	

2. 1. Design of the system

The heat and work equations on the stack material in a thermoacoustic cooling system are given in equations (1) and (2). [4], [23]

$$\dot{\mathbf{H}}_{\mathbf{2}} = -\frac{\mathbf{1}}{\mathbf{4}}\mathbf{\Pi}\boldsymbol{\delta}_{\mathbf{k}}\left(\frac{\mathbf{T_m}\boldsymbol{\beta}\mathbf{p_1^s}\langle\mathbf{u_1^s}\rangle}{(\mathbf{1}+\boldsymbol{\varepsilon}_{\mathbf{s}})(\mathbf{1}+\boldsymbol{\sigma})\left(\mathbf{1}-\frac{\boldsymbol{\delta}_{\mathbf{v}}}{\mathbf{y_0}}+\frac{{\boldsymbol{\delta}_{\mathbf{v}}}^{\mathbf{2}}}{\mathbf{2}{\mathbf{y_0}}^{\mathbf{2}}}\right)}\right)\left[\Gamma\frac{\mathbf{1}+\sqrt{\boldsymbol{\sigma}}+\boldsymbol{\sigma}+\boldsymbol{\sigma}\boldsymbol{\varepsilon}_{\mathbf{s}}}{\mathbf{1}+\sqrt{\boldsymbol{\sigma}}}-\left(\mathbf{1}+\sqrt{\boldsymbol{\sigma}}-\frac{\boldsymbol{\delta}_{\mathbf{v}}}{\mathbf{y_0}}\right)\right]-\mathbf{\Pi}(\mathbf{y_0K}+\mathbf{lK_s})\frac{\mathbf{dT_m}}{\mathbf{dx}} \quad (1)$$

$$\dot{W}_2 = -\frac{1}{4}\Pi\delta_k\Delta x\frac{(\gamma-1)\omega({p_1}^s)^2}{\rho_m a^2(1+\varepsilon_s)}\left(\frac{\Gamma}{(1+\sigma)\left(1-\frac{\delta_v}{y_0}+\frac{{\delta_v}^2}{2{y_0}^2}\right)}-1\right)-\frac{1}{4}\Pi\delta_v\Delta x\frac{\omega\rho_m\langle{u_1}^s\rangle^2}{\left(1-\frac{\delta_v}{y_0}+\frac{{\delta_v}^2}{2{y_0}^2}\right)} \quad (2)$$

$$Q_{cn} = -\frac{\delta_{kn}D^2 sin(2x_n)}{8\gamma(1+\sigma)\Lambda}\left[\frac{\Delta T_m\tan(x_n)}{(\gamma-1)BL_{sn}}\frac{1+\sqrt{\sigma}+\sigma}{1+\sqrt{\sigma}}-\left(1+\sqrt{\sigma}-\sqrt{\sigma}\delta_{kn}\right)\right]-K_{pt}[B+(1-B)K^*]\Delta T_{mn} \quad (3)$$

$$W_n = \frac{\delta_k LD^2}{4\gamma}(\gamma-1)Bcos(x_n)^2\left(\frac{\Delta T_{mn}\tan(x_n)}{BL_{sn}(\gamma-1)(1+\sqrt{\sigma})\Lambda}-1\right)-\frac{\delta_{kn}L_{sn}D^2}{4\gamma}\frac{\sqrt{\sigma}\sin(x_n)^2}{B\Lambda} \quad (4)$$

Considering the axial heat conduction effects, these equations are dimensionless and equation (3) and equation (4) are obtained.

$\boldsymbol{\Lambda}$, $\boldsymbol{K_{PT}}$, $\boldsymbol{K^*}$ in the equation are given below.

$$\Lambda = 1 - \sqrt{\sigma}\delta_{kn} + \frac{1}{2}\sigma{\delta_{kn}}^2,$$

$$K_{PT} = \frac{KT_m}{p_m \alpha L_S},$$

$$K^* = \frac{K_s}{K}$$

2.2. Design systematic

The parameters used in the experimental study are given in Table 2.

Table2. Parameters used in the experimental study.

Parameter	Studied value
Wave Structure	Sinusoidal
Resonance tube material	PVC
Resonance tube length	0.25m
Resonant frequency	340Hz
Stack material	Mylar, glass wool and cotton
Stack length	8 cm
Working fluid	Weather

As the resonance tube in the system, a PVC pipe with a length of 25 cm and an inner diameter of 2.3 cm, which is a good insulator, was preferred instead of the glass tube since the necessary holes for the temperature gauge can be opened more easily, the necessary adjustments are made in the length, and there is no heat transfer in the system [23], [24]. The length of the resonance tube is adjusted to be one-quarter of the wavelength [17], [24].

The Length of the Resonance Tube

$$L = \frac{\lambda}{4} = \frac{1}{4} = 0.25 \text{ m} = 25 \text{ cm} \qquad (5)$$

Sound speed; $\nu \cong 340$ m/s and

$$\lambda = \frac{\nu}{f} \qquad (6)$$

From the equation (6), the operating frequency in the system is chosen as f = 340 Hz. In the experimental study, air [24], [25] was used as the working gas and three different stack materials were used in the system design. 75-micron-thick mylar [26] with a heat conduction coefficient of 0.16 W/mK was cut into parallel plates of approximately 0.3 cm width and 8 cm length, and wrapped in a tape that functions as a stack holder, and made ready for experimental study. Cotton, the next stack material used in the system with a heat conduction coefficient of 0.07 W/mK and a thickness of 50 microns, was wrapped in a diameter of 2.3 cm, which is the diameter of the resonance tube, and cut into 8 cm in length. The stack is made ready for experimental work by being wrapped in a tape that functions as a holder. The thickness of the Glass wool, which is the last stack material used in the experimental study, is 180 microns, and the heat transmission coefficient is 0.04 W/mK.

3. Experimental setup

The experimental setup, shown schematically in Figure 1, was set up using the design systematic described in the previous section.

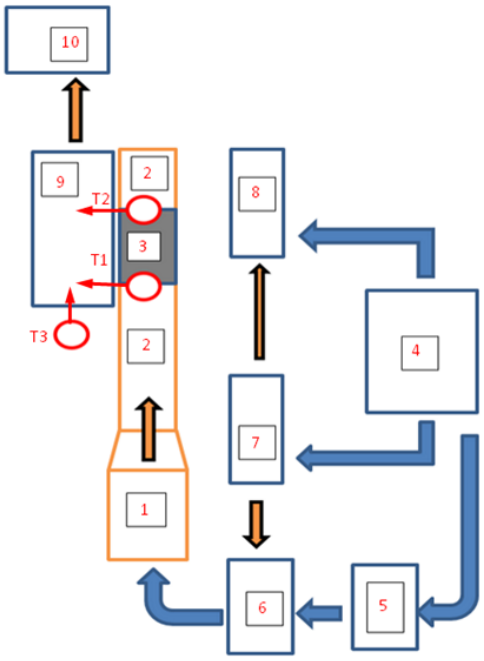

1- Loudspeaker, 2-Resonance Tube, 3-Stack, 4-Power Source, 5-DC 12V, 6-Operational Amplifier, 7-Signal Generator, 8-Oscilloscope, 9-Datalogger, 10-Computer,T_1-T_{hot},T_2-T_{col}, T_3-T_{Amb},

Figure 1. Schematic representation of the experimental setup.

Technical specifications of devices use in this study are shown in Table 3.

Table 3. Technical specifications of devices use in this study.

System Elements	Model	Technicial specifications
Loudspeaker	Suzhou YDD103-04B	Rated power: 15W Maximum power: 20W Sensitivity: 82 ± 3dB Diameter: 100mm
Signal generator	EZ Digital FG – 7005C	60V DC or 30V AC Mode: Linear Width: Variable from 1: 1 to 100: 1 Rate: 0.5 Hz to 50 Hz (20 mS to 2 S) External VCF Input: Input Voltage: 0 to 10 V Display: 6 digit green LED Frequency Range: 500 mHz to 50 MHz with Auto Range. Accuracy: ± Time base error ± 1 count Input Sensitivity: 100 mVrms Max. Power: 15W Max. Input Voltage: 250 Vpp Temperature: -20° C to +70° C Humidity: below 85% RH
Oscilloscope	EZ Digital DS – 1150	-150MHz bandwidth, 2 CH dual digitizer. -100MS/s simultaneous maximum sampling rate per channel. -200MS/s sampling rate for one channel only. -25GS/s equivalent sampling rate per channel. - 10ns peak detection for glitch capture even in ROLL mode. - Max. 400Vpk input voltage into all channels. - Direct single trigger capture function using a hot-key. - Simultaneous 5 waveform information auto measurement and FFT analysis. - Auto trigger level setting to 50%. - Saving 10 waveforms & 10 setup parameters. - Convenient inserting interface card for RS-232C, hardcopy and USB. - Operating temperature 0 C to +40 C. - Relative humidity <80%.
Digital multimeter	Fluke 87 – V	Rate: 0.1 mV to 1000 V Accuracy: ±(0.7% + 4) true-rms AC bandwidth: 20 kHz with low pass filter; 3 dB @ 1 kHz Max. Resolution: 0.1 mV -Temperature range: Indoor & Outdoor -50 ~ +70 degree (-58 ~ +158°F).
Temperature meter	HTC - 2	-Temperature measurement accuracy: ±1°C (1.8°F). -Humidity range: 10% ~ 99% RH. -Humidity accuracy: ±10% RH.

In the experimental setup, consists of three main parts: the acoustic power supply, resonance tube, and stack. In the setup, a Suzhou brand YDD103-04B model 15 W loudspeaker with a 10 cm diameter was used as an acoustic power source. The resonant tube and the loudspeaker are combined with the help of an aluminum conical piece. In order to provide sound insulation, the loudspeaker was placed in a closed wooden box, and a hole in the diameter of the resonance tube was drilled in the top cover of the box. The loudspeaker is mounted at the bottom of the hole,

and in this way, the passage of sound waves into the resonance tube is provided. On the bottom cover of the box, a small hole is made for the output of the speaker cables. The lid of the box was screwed on all four sides in order to provide good sound insulation during the experiment. According to the results of the calculations, the stack material was placed 4 cm below the top of the resonance tube. In this way, sufficient distance is left for the sound waves to return again.

In order to measure the temperatures at both ends of the stack material, HTC-2 brand temperature meters were used. In the system, one of the temperature meters was placed at the top of the stack by puncturing the plug of the resonance tube, and the other was fixed to the bottom of the stack by adjusting it to leave a gap of 12 cm (8 + 4) from the top of the resonance tube. An EZ Digital brand FG – 7005C model signal generator was used as a signal source in the system. The sinusoidal sound waves produced in the signal generator are amplified in an operational amplifier and applied to the loudspeaker. The signal is also sent to the oscilloscope so that the shape of the signal used in the system can be seen. The operational amplifier used in the experimental study is Y – 0014 model, and there are many input and output elements required for a constant symmetrical power supply, signal generator, voltmeters, and Op–Amp applications. DS – 1150 model oscilloscope is used in the system. The horizontal axis of the oscilloscope is set to 2 ms and the vertical axis ~to 5V. Fluke brand 87 – V model digital multimeter was used to clearly see the sensitivity of the 3.029 amplitude value applied in the system. The measurement was made in the AC volt range of the multimeter.

4. Experimental Results and Suggestions

Since there is no heat exchanger in the experimental setup, heat transfers between the ends of the stack and the fluid and between the stack and the surface of the resonance tube are neglected, and it is assumed that the system does not transfer heat to the environment. Since air is used at atmospheric pressure in the study, the cooling power is low. In addition, although it is very small, there is convection heat transfer with air from the ends of the stack and heat transfer by conduction between the stack and the resonance tube. Frequency and ambient temperature were kept constant in the experiments.

Initially, the temperature values at the top and bottom of the stack are the same. Temperature measurements were made every 10 minutes. The temperature difference between the ends of the stack remained constant after 140 min. Since there was no change in the temperature difference after this value, the measurement was ended. In the experimental study, three different stack materials were used: mylar, cotton, and glass wool, and test results were obtained for each case. It is given in Table 4, Table 5, and Table 6.

Table 4. Measurements with a stack of Mylar material.

	Duration (min)	**T_{hot}(°C)**	**T_{col}(°C)**	**ΔT(°C)**
1	–	24.5	24.5	0
2	10	24.6	24.5	0.1
3	20	24.7	24.5	0.2
4	30	25.1	24.4	0.7
5	40	25.1	24.2	0.9
6	50	25.2	24.0	1.2
7	60	25.3	23.9	1.4
8	70	25.4	23.7	1.7
9	80	25.4	23.3	2.1
10	90	26.2	23.0	3.2
11	100	26.2	22.6	3.6
12	110	26.3	22.4	3.9
13	120	26.7	22.3	4.4
14	130	26.8	22.1	4.7
15	140	27.1	21.9	5.2
		(+) 2.6	**(-) 2.6**	**5. 2**

As seen in Table 4, T_{hot} and T_{col} values, which were both 24.5°C at the beginning, were measured as 26.9°C, and 22.2°C, respectively, after 140 minutes. It can be seen from the table that the

temperature difference between the two ends of the stack material is 4.7°C

T_{hot} and T_{col} values, which were both 24.5°C at the beginning, were measured as 27.1°C and 21.9°C, respectively, after 140 minutes. It can be seen from the table that the temperature difference between the two ends of the stack material is 5.2°C. The results in the table are shown in figure 2 in graphic form. As can be seen from the graph, the temperature at the lower end of the stack material increased over time, and the temperature at the upper end decreased over time.

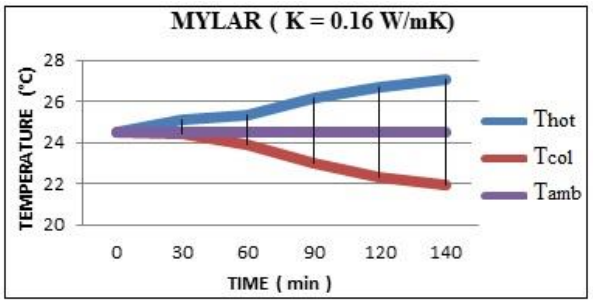

Figure 2. Temperature and time graph of stack with mylar material.

.

Table 5. Measurements with cotton material stack.

	Duration (min)	T_{hot}(°C)	T_{col}(°C)	ΔT(°C)
1	–	24.5	24.5	0
2	10	24.6	24.2	0.4
3	20	24.7	23.9	0.8
4	30	24.9	23.7	1.2
5	40	25.2	23.7	1.5
6	50	25.4	23.7	1.7
7	60	25.8	23.7	2.1
8	70	26.1	23.5	2.6
9	80	26.1	23.2	2.9
10	90	26.2	23.2	3.0
11	100	26.4	23.0	3.4
12	110	26.5	23.0	3.5
13	120	26.7	22.8	3.9
14	130	26.8	22.8	4.0
15	140	26.8	22.5	4.3
		(+) 2.3	**(-) 2.0**	**4. 3**

The results in the table are shown in the graph in Figure 3. As can be seen from the graph, the temperature at the lower end of the stack material increased with time, while the temperature at the upper end decreased with time.

As can be seen in Table 5, T_{hot} and T_{col} values, which were both 24.5°C at the beginning, were measured as 26.8°C and 22.5°C, respectively, after 140 minutes. It can be seen from the table that the temperature difference between the two ends of the stack material is 4.3°C.

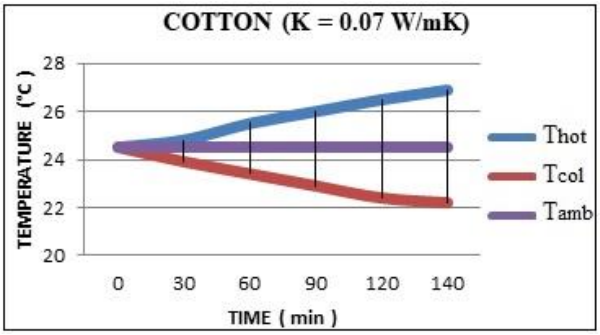

Figure 3. The temperature-time graph of the cotton material stack.

Table 6. Measurements with glass wool material stack.

	Duration (min)	T_{hot}(°C)	T_{col}(°C)	ΔT(°C)
1	–	24.5	24.5	0
2	10	24.6	24.2	0.4
3	20	24.7	23.9	0.8
4	30	24.9	23.7	1.2
5	40	25.2	23.7	1.5
6	50	25.4	23.7	1.7
7	60	25.8	23.7	2.1
8	70	26.1	23.5	2.6
9	80	26.1	23.2	2.9
10	90	26.2	23.2	3.0
11	100	26.4	23.0	3.4
12	110	26.5	23.0	3.5
13	120	26.7	22.8	3.9
14	130	26.8	22.8	4.0
15	140	26.8	22.5	4.3
		(+) 2.3	**(-) 2.0**	**4. 3**

The results in the table are shown in the graph in Figure 4. As can be seen from the graph, the temperature at the lower end of the stack material increased with time, while the temperature at the upper end decreased with time.

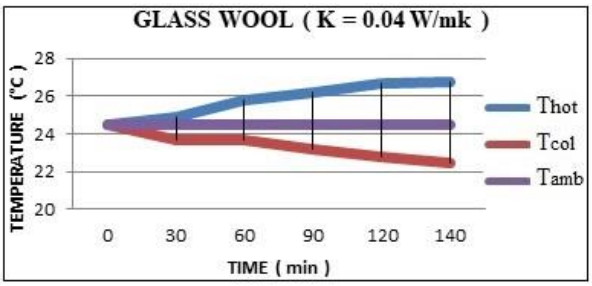

Figure 4 Temperature – time graph of the stack with Glass Wool material.

In the case of using three different stack materials, the variation of the measured temperature values at the cold end of the stack materials with respect to time can be seen comparatively in Figure 5. Initially, the values measured at the hot ends of all three stack materials were 24.5 °C. As seen in Figure 5, the cold end temperatures after 140 minutes were 21.9 °C for mylar, 22.2 °C for cotton, and 22.5 °C for glass wool. It was observed that the lowest cold-end temperature was in the mylar stack material.

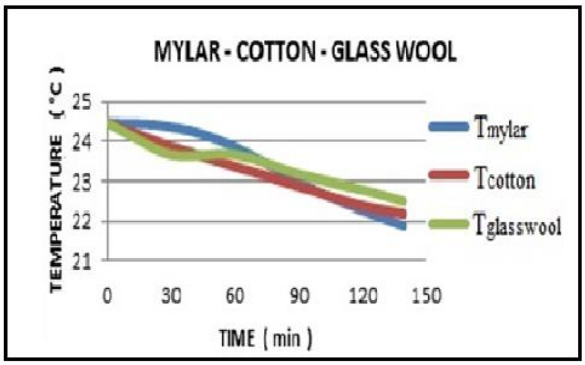

Figure 5. Temperature values at the cold end of the stack.

In Figure 6, the temperature differences between the two ends of the stack are given graphically when different stack materials are used. The highest temperature difference occurred when mylar stack material was used, followed by cotton and glass wool, respectively. With the increase in the heat transfer coefficients of these stack materials, an increase was observed in the temperature differences.

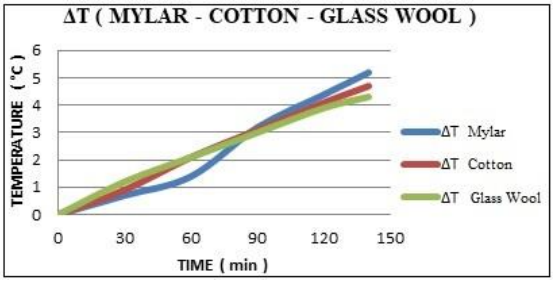

Figure 6. Comparison of temperature difference (Mylar - Cotton - Glass Wool).

5. Conclusion

As a result of the experiments, it has been observed that a temperature difference may occur due to the acoustic effect. These temperature differences are different for each stack material used. In the measurements made within the same time period, it is seen that the acoustic cooling and temperature difference obtained from the mylar material with a high heat transmission coefficient are the highest, the cotton material with a lower heat transmission coefficient than mylar has a lower acoustic cooling and temperature difference than mylar, and finally, the cotton material has the lowest heat transmission coefficient. It has been observed that the temperature difference obtained from the glass wool material, which has the lowest heat transmission coefficient, is the lowest. When the related studies are examined, it is seen that generally the same stack materials are used. In this study, unlike previous studies, glass wool and cotton were used as stack materials for the first time. The temperature differences between the two ends of the stack were compared with each other by using three different materials with different heat conduction coefficients as the stack material.

Prototype development costs are quite high since the performance of acoustic cooling systems is relatively low. For now, it is very difficult to predict whether thermoacoustic coolers will be used commercially. However, as efforts to improve performance in this area progress, the possibility of thermoacoustic coolers competing with conventional coolers will increase.

The efficiency of thermoacoustic devices is not yet at a level that can compete with commercial solutions. For this reason, many studies have been carried out to improve the design and performance of thermoacoustic coolers.

Focusing on theoretical as well as experimental analysis will facilitate the optimization of geometric parameters such as stack location, stack length, resonator length, or operating parameters such as frequency, mean pressure, and temperature gradient. The investigation of TAC between the stack ends will increase the performance of the thermoacoustic refrigerators.

Icons ındex

a	Sound velocity, acoustic velocity (m/s)	**B**	Stack fill rate
c_p	Specific heat at constant pressure (J/kgK)	f	Acoustic frequency
l	Half of the stack thickness (mm)	$\dot{H}_2$	Carried heat
k	Heat transfer coefficient (W/mK)	**I**	Current from speaker
L_s	Stack length (cm)	**L**	Resonance tube length
P	Pressure (kPa)	l_m	Dimensionless stack length
p_1	Pressure variation amplitude	$Pm\_$	Average pressure
Q	Heat (J)	p_1^s	The positive real part of the pressure amplitude
t	Time(s)	**R**	Gas constant
T_1	Acoustic temperature amplitude	s_m	Average entropy
T_s	Temperature of the stack	T_m	Average temperature
x	**x** Axis	T_{kr}	Critical temperature
u_1	Speed amplitude	ΔT_s	Temperature difference
v	y component of speed	**u**	Speed
$\dot{W}_2$	Work	u_1^s	The positive real part of the velocity amplitude
Γ	Ratio of the temperature distribution on the heap to the critical temperature distribution		
δ_k	Thermal penetration depth	y_0	Half the distance between the plates
γ	Specific heats ratio	β	Coefficient of thermal expansion
ε_s	Stack thermal capacity ratio	**Δx**	Plate (stack) length
$\varkappa$	Thermal dissipation coefficient	δ_v	Viscous penetration depth
λ	Wavelength	ε	Internal energy
ν	Kinematic viscosity	**η**	Efficiency
Σ	Viscous stress tensor	K_s	Thermal dissipation coefficient of the stack
ρ_m	Average density	μ	Dynamic viscosity
ω	Angular frequency	**Π**	The circumference of the plate
σ	Prandtl number	ρ	Intensity

Conflict of Interest Statement

There is no conflict of interest between the authors.

Statement of Research and Publication Ethics

The study is complied with research and publication ethics

References

[1] J. Chi, J. Xu, L. Zhang, Z. Wu, J. Hu, and E. Luo, "Study of a gas-liquid-coupled heat-driven room-temperature thermoacoustic refrigerator with different working gases", *Energy Conversion and Management*, vol. 246, p. 114657, Oct. 2021, doi: 10.1016/j.enconman.2021.114657.

[2] P. A. Habibbhai, M. Yadav, and K. Nagori, "Experimental analysis of thermoacoustic refrigeration with combination of different gases and stack material", *International Research Journal of Engineering and Technology* vol. 05, no. 04, Apr-2018

[3] N. Rott, "Thermoacoustics", *Advanced in Applied Mechanics*, 20, pp.135-174,1980.

[4] G. Swift, "Thermoacoustic engines", *Journal Acoustical Society of America*, 84, pp.1145-1180,1988

[5] J. Wheatley, G.W. Swift, T. Hofler, 'Heat-Driven Acoustic Cooling Engine Having No Moving Parts', *The Journal of the Acoustical Society of America*., vol.88, no. 4, pp. 2046-2048, 1990.

[6] T.J. Hofler, "Thermoacoustic Refrigerator Design and Performance (Heat Engine, Resonator, Microphone)." Doctoral dissertation, University of California, San Diego, 1986.

[7] H. Babaei and K. Siddiqui, "Modified theoretical model for thermoacoustic couples", *International Journal of Thermal Sciences*, vol. 50, no. 2, pp. 206–213, Feb. 2011, doi: 10.1016/j.ijthermalsci.2010.09.011

[8] J. Wheatley, T. Hofler, G.W. Swift, A. Migliori, "An intrinsically irreversible thermoacoustic heat engine", *The Journal of the Acoustical Society of America*, vol. 74, no. 1, pp. 153-170, 1983.

[9] A. Piccolo and G. Cannistraro, "Convective heat transport along a thermoacoustic couple in the transient regime", *International Journal of Thermal Sciences*, vol. 41, no. 11, pp. 1067-1075, 2002

[10] A.A. Atchley, T.J. Hofler, M.L. Muzzerall, M.D. Kite, "Acoustically generated temperature gradients in short plates", *The Journal of the Acoustical Society of America*, vol. 88, pp. 251-263, 1990.

[11] A.S. Worlikar, O.M. Knio, R. Klein, "Numerical simulation of a thermoacoustic refrigerator-stratified flow around the stack", *Journal of Computational Physics*, vol.144, pp. 299-324, 1998.

[12] L. Zoontjens, C. Q. Howard, A. C. Zander, and B. S. Cazzolato, "Numerical comparison of thermoacoustic couples with modified stack plate edges", *International Journal of Heat and Mass Transfer*, vol. 51, no. 19–20, pp. 4829–4840, Sep. 2008, doi: 10.1016/j.ijheatmasstransfer.2008.02.037.

[13] M Terdi, "Ses Enerjisi ile Soğutma", Master's thesis, Mimar Sinan Fine Arts University, İnstitute of Science, Department of Physics, İstanbul, 2006.

[14] İ. Girgin, "Termoakustik Soğutucu Analizi", Doctoral dissertation İstanbul Technical University, İnstitute of Science, Department of Mechanical Engineering, İstanbul, 2007

[15] T. Somasekhar, and P. Kishore, "Thermo Acoustic Refrigeration", *IOSR Journal of Mechanical and Civil Engineering* (IOSR-JMCE), 2278, 58-63, 2012.

[16] T. Teja, and V. Kumar, "Design and fabrication of thermo acoustic refrigerator", *International Journal of Advances in Engineering&Technology* (IJAET), vol. 10, no. 3, pp. 309-317, 2017.

[17] S. Mergen, "Duran Dalga Termoakustik Soğutuculardа Yığın Malzemesi Termofiziksel Özelliklerinin Termoakustik Dönüşüme Etkilerinin Sayısal Olarak İncelenmesi", Doctoral dissertation Gazi University, İnstitute of Science,Ankara, 2019.

[18] A. C. Alcock, L. K. Tartibu, and T. C. Jen, 'Design and construction of a thermoacoustically driven thermoacoustic refrigerator, *in 2017 International Conference on the Industrial and Commercial Use of Energy (ICUE)*, Cape Town, Aug. 2017, pp. 1–7. doi: 10.23919/ICUE.2017.8103430.

[19] X. Wang, Z. Wu, L. Zhang, J. Hu, and E. Luo, "Traveling-wave thermoacoustic refrigerator for room temperature application", *International Journal of Refrigeration*, vol. 120, pp. 90–96, Dec. 2020, doi: 10.1016/j.ijrefrig.2020.08.021.

[20] İ. Gökay and R. Karabacak, "Experimental investigation of the effect of different waveforms on heat transfer in a thermoacoustic cooler", *International Journal of Refrigeration*, vol. 129, pp. 259–266, Sep. 2021, doi: 10.1016/j.ijrefrig.2021.04.015.

[21] M. Tijani, "Loudspeaker-driven thermo-acoustic refrigeration". Doctoral dissertation, Eindhoven University of Tecnology, 98p, Eindhoven. 2001.
[22] J. Kajurek, A. Rusowicz, & A. Grzebielec, "Design and simulation of a small capacity thermoacoustic refrigerator". *SN Applied Sciences*, 1, pp. 1-9. 2019
[23] İ. Girgin and M. Türker, "Thermoacoustic systems as an alternative to conventional coolers". *Journal of Naval Sciences and Engineering*, vol. 8, no.1, pp. 14-32, 2012.
[24] S. H. Tasnim, S. Mahmud, and R. A. Fraser, "Effects of variation in working fluids and operating conditions on the performance of a thermoacoustic refrigerator", *International Communications in Heat and Mass Transfer*, vol. 39, no. 6, pp. 762–768, Jul. 2012, doi: 10.1016/j.icheatmasstransfer.2012.04.013.
[25] T. C. Bammann, C. Q. Howard, and B. S. Cazzolato, "Review of flow-through design in thermoacoustic refrigeration", *In Proceedings of ACOUSTICS*, pp. 9-11, 2005.
[26] A.H. Ibrahim, H. Omar, and E. Abdel-Rahman, "Constraints and challenges in the development of loudspeaker-driven thermoacoustic refrigerator", *In 18th International Congress on Sound & Vibration*, ICSV18, Rio de Janeiro, Brazil, pp. 10-14, July,2011.

Bitlis Eren Üniversitesi Fen Bilimleri Dergisi
BİTLİS EREN UNIVERSITY JOURNAL OF SCIENCE
ISSN: 2147-3129/e-ISSN: 2147-3188
VOLUME: 12 NO: 3 PAGE: 660-672 YEAR: 2023
DOI:10.17798/bitlisfen.1279496

A Novel Anthraquinone-Based Azo Compound: Synthesis, Quantum Chemical Calculations and Investigation of ADMET Properties

Mehmet ULUTÜRK[1], Çiğdem KARABACAK ATAY[2*], Bülent DEDE[3], Tahir TİLKİ[3]

[1] *TÜBİTAK Marmara Research Center, 41470, Gebze, Kocaeli, Turkey*
[2] *Burdur Mehmet Akif Ersoy University, Faculty of Education, Department of Basic Education, 15030, Burdur, Turkey*
[3] *Süleyman Demirel University, Faculty of Science & Arts, Department of Chemistry, 32260, Isparta, Turkey*
(ORCID: 0000-0003-3931-5328) (ORCID: 0000-0001-7226-9971)
(ORCID: 0000-0003-1416-7373) (ORCID: 0000-0002-1040-2375)

Keywords: Azo, Anthraquinone, DFT, ADMET, Toxicity

Abstract
This study involved the synthesis of the potential drug candidate 2-[(9,10-dioxo-9,10-dihydroanthracen-2-yl) diazenyl]-5-hydroxybenzoic acid (DHA), the elucidation of its structure using spectroscopic techniques, and the determination of the compound's lowest energy structure using the DFT/B3LYP method and the 6-311G(d,p) basis set. The compound's vibration frequencies and NMR chemical shift values were then determined using optimized geometry. The three-dimensional molecular electrostatic potential (MEP) map of the compound and the HOMOs-LUMOs and molecular orbital energies were examined using the DFT approach. The compound's ADMET properties were then determined, and its potential to usage as a drug was assessed. The predicted toxicity class and LD_{50} value for the DHA were also established. The outcomes demonstrated that by having ADMET properties, this newly synthesized compound has the potential to be a drug.

1. Introduction

Due to their high bioactivity and low toxicity, anthraquinones, which include three benzene rings wherein the keto groups are located on the central ring (9,10-anthracenedione), have been discovered to be fascinating. Due to their biological, pharmacological, and industrial potential, they are receiving greater attention today. For example, they exhibit great enzyme inhibition properties [1]-[3]. In addition to being used as dye pigments in the cosmetics, pharmaceutical, and food sectors [4], [5], its pharmacological potential also includes anticancer, antibacterial, immunosuppressive, antioxidant, antipyretic, diuretic, anti-inflammatory, and antiviral properties [6]-[9]. The compounds should exhibit both strong biological activity and minimal toxicity. In the process of developing a new drug, it is critical to assess the pharmacokinetic characteristics of newly synthesized compounds. Lipinski's rule of five, also known as the drug-similarity test, establishes the structural characteristics desired in a candidate compound that can be a drug based on the relationship between pharmacokinetic and physicochemical parameters [10]. In silico research thus enables us to understand the likelihood that a chemical may be a potentially good drug [11].

Based on all of this knowledge, a compound with a strong potential to become a drug, 2-[(9,10-dioxo-9,10-dihydroanthracen-2-yl)diazenyl]-5-hydroxybenzoic acid (DHA) based on anthraquinones, was synthesized in our work. One of the factors contributing to the preference for this molecule is the inclusion of azo and anthraquinone groups in its structure. The presence of azo groups in a compound's

*Corresponding author: ckatay@mehmetakif.edu.tr
Received: 08.04.2023, Accepted: 15.08.2023

structure is known to confer highly bioactive characteristics. There have been more studies in recent years on the synthesis of azo-containing compounds and the analysis of their in vitro and in silico characteristics. It is stated that synthesized azo molecules show significant anticancer properties against cancer cells in in vitro studies and even have the potential to become anticancer drugs as a result of in vivo and other studies [12]-[14]. Because of the biological significance of anthraquinones and azo groups in the literature, this study was designed to discover novel potential bioactive chemicals. Spectroscopic techniques were used to clarify its structure. The 6-311G(d,p) basis set and the DFT/B3LYP method were used to perform quantum chemical calculations on the molecule's molecular structure, vibrational spectroscopic data, electronic transition absorption wavelengths, HOMOs and LUMOs analyses, and molecular electrostatic potential (MEP). Absorption, distribution, metabolism, excretion, and toxicity (ADMET) parameters were calculated using the SwissADME and ProTox-II servers.

2. Material and Method

2.1. Physical measurements

Sigma&Aldrich and Merck Chemical Companies provided the chemicals and solvents used in the investigation, which were then used directly without further purification. With the use of a Perkin Elmer Frontier Spectrometer and KBr, FT-IR analysis was carried out. Utilizing a Varian 600 MHz NMR spectrometer, NMR analyses were carried out on deuterated dimethylsulfoxide (DMSO-d6), and chemical shifts are given in δ units (ppm). On a Shimadzu UV-1800 spectrophotometer, UV-Visible absorption spectra were captured at the wavelength of DHA's maximum absorption (max) in dimethylsulfoxide (DMSO). Acetone was used to produce high-resolution electrospray ionization mass spectra (HR-ESI-MS) on a Thermo Scientific Q Exactive, Orbitrap LC/HRMS system. A BÜCHI Melting Point M-565 equipment was used to determine the melting point in an open glass capillary tube.

2.2. Synthesis of 2-[(9,10-dioxo-9,10-dihydroanthracen-2-yl) diazenyl]-5-hydroxybenzoic acid (DHA)

An ice-salt bath was used to cool a solution of 558 mg (2.5 mmol, 1.00 eq) 2-aminoanthraquinone in 5 mL of concentrated HCl and 3 mL of water to (-5)-0 °C. Next, a cold solution of $NaNO_2$ (190 mg, 2.75 mmol, and 1.10 eq) in 2 mL of water was added dropwise while being constantly stirred. The diazonium salt was produced when the mixture was agitated for an hour at a temperature of 0 °C or lower. The freshly-prepared anthraquinonediazonium salt was slowly added into the solution of *m*-hydroxybenzoic acid (345 mg, 2.5 mmol, 1.00 eq) in saturated $NaHCO_3$ a.q. (150 mL) at 0-5 °C. The reaction mixture was stirred for 4 h at 0-5 °C. After adding 1M HCl solution to the resulting dark brown solution to bring the pH level to 4-5, 100 mL of ice water was added. The mixture was stirred for 1 hour at 5 °C. The precipitated material was removed through filtering, washed with cold water, and then recrystallized using a 1:1 solution of ethanol and water before being dried at 50 °C under vacuum. 2-[(9,10-dioxo-9,10-dihydroanthracen-2-yl)diazenyl]-5-hydroxybenzoic acid, (**DHA**) was obtained 720 mg as brown solid, yield is %77. **Figure 1** illustrates the synthetic method for producing DHA. **Mp** 251-253 °C; **FT-IR** (KBr): ν_{max} (cm^{-1}) = 3066, 2673, 1716, 1674, 1587, 1572, 1466, 1429, 1326, 1291, 1223, 1169, 1127, 1068, 982, 931, 896, 848, 839, 808, 780, 724, 708, 657, 635, 595, 571, 485, 471, 454; **^{1}H-NMR** (600 MHz, DMSO-d_6): δ = 13.02 (br, s, 1H), 11.30 (br, s, 1H), 8.38 (d, *J* = 2.2 Hz, 1H), 8.31 (d, *J* = 8.2 Hz, 1H), 8.19-8.14 (m, 3H), 7.91-7.88 (m, 2H), 7.73 (d, *J* = 8.7 Hz, 1H), 7.08 (d, *J* = 2.8 Hz, 1H), 7.03 (dd, *J* = 8.8, 2.6 Hz, 1H); **^{13}C-NMR** (150 MHz, DMSO-d_6): δ = 182.0, 181.8, 168.5, 161.5, 154.9, 142.2, 136.0, 134.7, 134.6, 134.5, 134.3, 133.7, 133.2, 133.1, 128.6, 127.7, 126.8, 119.9, 119.7, 117.9, 114.8; **HR-ESI-MS** ($C_{21}H_{12}N_2O_5$ Exact Mass: 372.07462): calcd for $[M + H]^+$: 373.08190, found: 373.07877 **(Figure 2)**; **UV-VIS** (DMSO): λ_{max} (Abs.) = 342 nm (1.723), 390 nm (2.161).

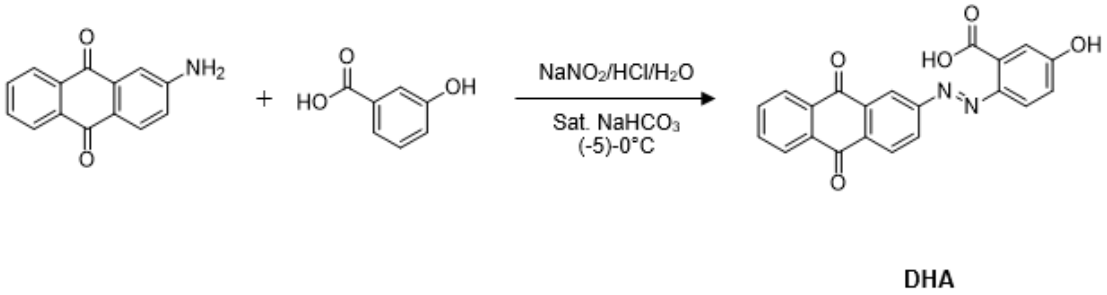

Figure 1. Synthesis of the DHA

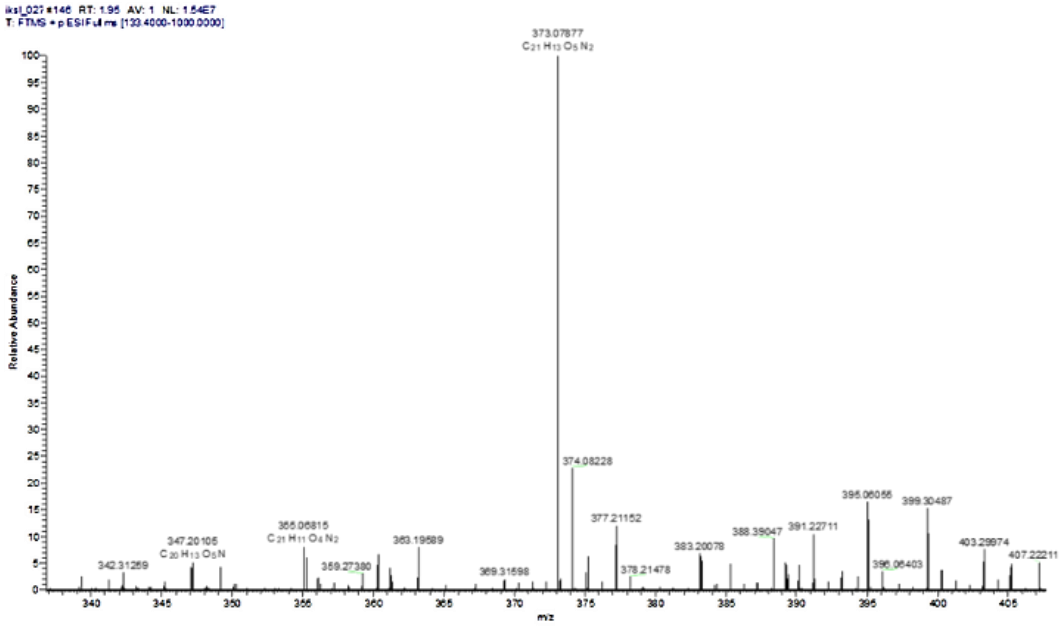

Figure 2. Experimental HR-ESI-MS spectrum of the DHA

2.3. Computational methods

Calculations for quantum chemistry were performed using the Gaussian 09 package, and visualizations were done using the GaussView 5.0.9 program [15], [16]. The molecular structure of the DHA in the ground state was calculated using the DFT method and the B3LYP functional with the 6-311G(d,p) basis set [17], [18]. Additionally, vibrational wavenumbers at the DFT/B3LYP/6-311G(d,p) level were determined. In order to avoid systematic mistakes, the calculated vibrational wavenumbers for the B3LYP/6-311G(d,p) basis set were scaled as 0.9682 for frequencies greater than 1700 cm^{-1} and 1.0119 for frequencies less than 1700 cm^{-1} [19]. The same basis set and B3LYP level of the time dependent density functional theory (TD-DFT) were used to model UV-vis spectra [20], [21]. The excitations' contribution rates were computed with GaussSum 3.0 [22]. To find the shielding factors for ^{1}H, and ^{13}C-NMR, the gauge-invariant atomic orbital (GIAO) method was used [23], [24].

2.4. ADMET predictions

The SwissADME web server calculated ADME characteristics for the DHA, including its physicochemical, pharmacokinetic, lipophilicity, and drug similarity [25]. Using the ProTox-II web server, the toxicity profile, LD50 value, and acceptable use range of DHA were discovered [26].

3. Results and Discussion

3.1. NMR spectra

The ^{1}H- and ^{13}C-NMR chemical shifts of the DHA were determined using the Gauge-Independent Atomic Orbital (GIAO) method at DFT/B3LYP/6-311G(d,p) level.

While its estimated chemical shift was determined to be 5.10 ppm, the O-H group proton H40 was found to be a singlet signal at 11.30 ppm. Although the carboxylic acid proton H39 was empirically detected as a singlet peak at 13.02 ppm, the DFT method calculated its value to be 5.90 ppm. In the expected region, aromatic protons were discovered. They were meant to be in the range of 7.04-8.79 ppm in theory, but they were actually measured empirically to be in the range of 7.03-8.38 ppm. For ease of comparison between the experimental and predicted chemical shift values of the DHA, ^{1}H-NMR values were given collectively in **Table 1**. In **Figures 3** and **4**, experimental and calculated ^{1}H-NMR spectra for the substance were displayed.

Table 1. Experimentally and theoretically obtained ^{1}H-NMR chemical shifts

H Number	Experimental	Theoretical
H35	7.73	8.79
H33	8.38	8.69
H31-H32-H34	8.19-8.14	8.52
H36	8.31	8.30
H29-H30	7.91-7.88	8.04
H37	7.03	7.40
H38	7.08	7.04
H39	13.02	5.90
H40	11.30	5.10

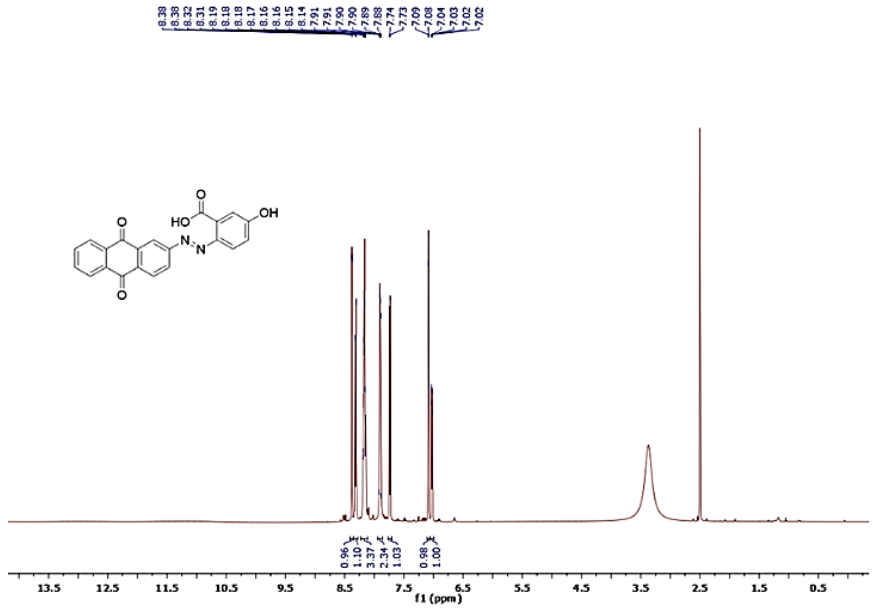

Figure 3. Experimental ^{1}H-NMR (DMSO-d6) spectrum of the DHA

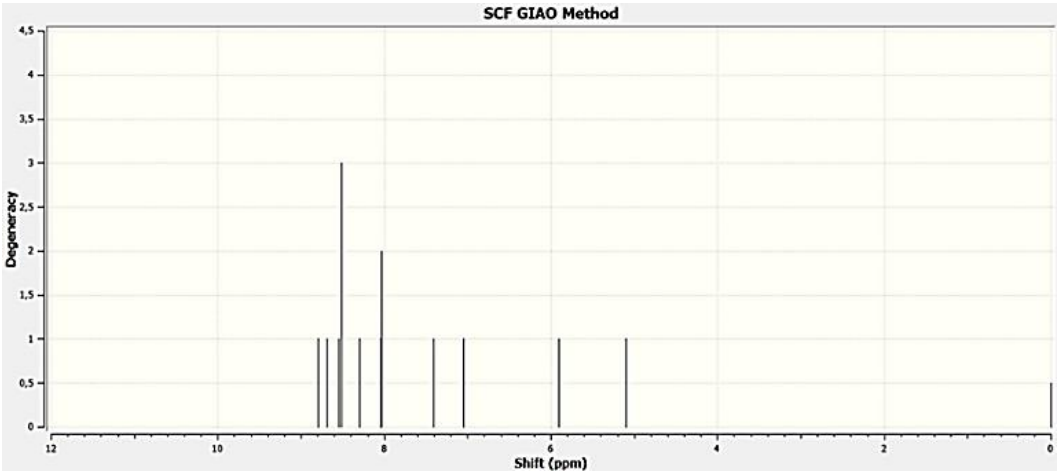

Figure 4. Theoretical ^{1}H-NMR (DMSO-d6) spectrum of the DHA

In the ^{13}C-NMR spectrum, the C22 atom associated with the O-H group was measured and logged at 161.5 ppm, while this signal was discovered at 166.4 ppm in the theoretical spectrum. The carboxylic acid group's carbon atom C25 was correlated with a signal at 168.5 ppm, and their computed chemical shift was visible at 174.1 ppm. The results are detailed in **Table 2**, and all other carbon atoms were found in the predicted area. In **Figures 5** and **6**, the compound's experimental and computed ^{13}C-NMR spectra were displayed.

Table 2. Experimentally and theoretically obtained ^{13}C-NMR chemical shifts

C Number	Experimental	Theoretical
C10	182.0	186.6
C7	181.8	185.9
C25	168.5	174.1
C22	161.5	166.4
C13	154.9	158.9
C19	142.2	151.2
C12	119.9	142.3
C20	127.7	140.6
C2	133.7	139.4
C1	134.3	139.2
C8	134.7	137.9
C9	136.0	137.6
C5	134.6	137.0
C4	134.5	136.9
C11	126.8	133.4
C6-C3	133.1	131.6
C24	117.9	127.2
C21	119.7	121.2
C23	114.8	120.7
C14	128.6	115.3

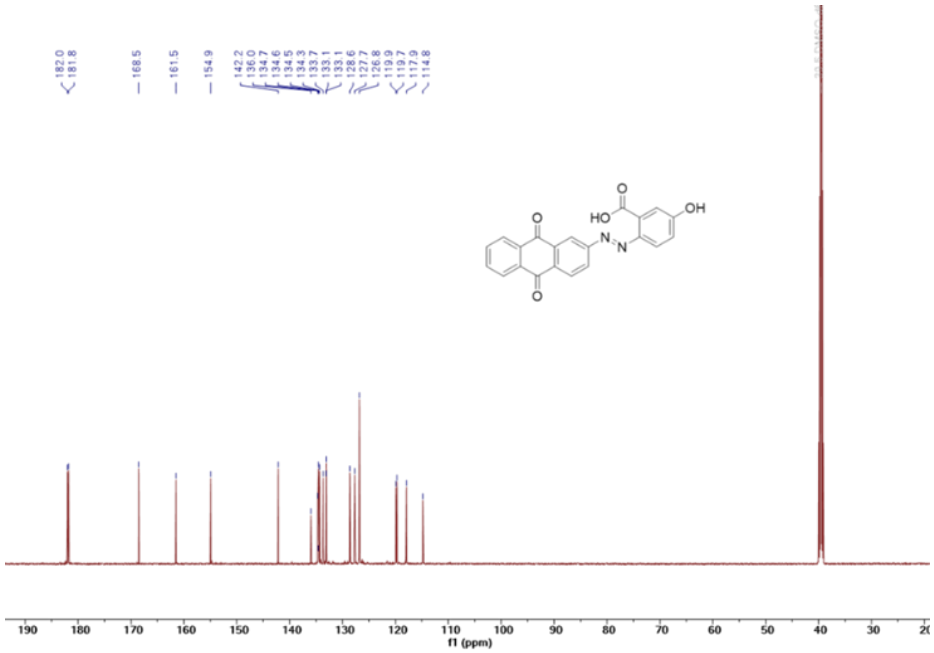

Figure 5. Experimental ^{13}C-NMR (DMSO-d6) spectrum of the DHA

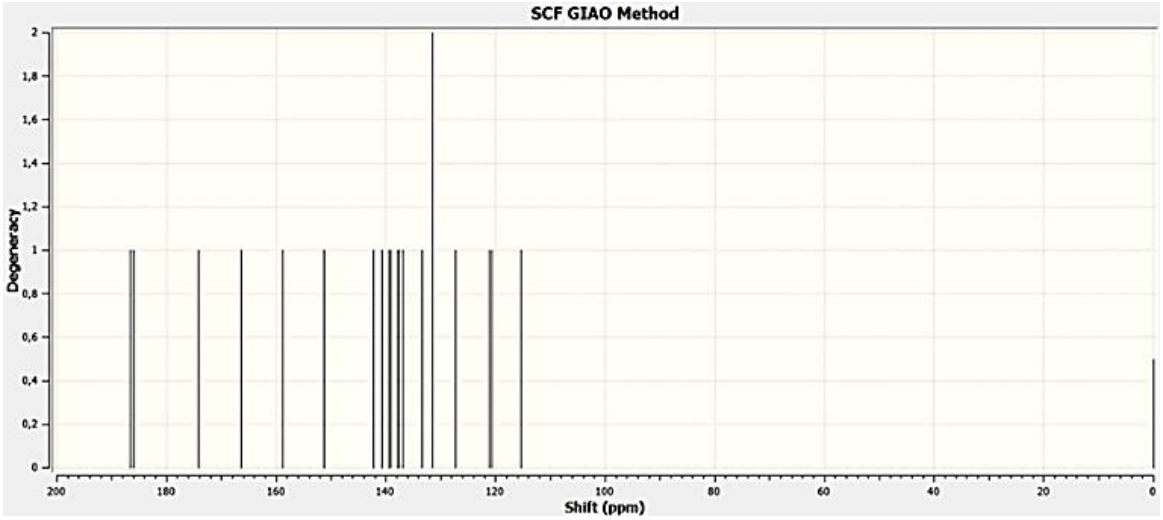

Figure 6. Theoretical ^{13}C-NMR (DMSO-d6) spectrum of the DHA

Theoretical predictions and experimental data had good agreement, according to an analysis of the correlation between theoretical and experimental NMR chemical shift values. The data from the literature and the findings that were obtained agreed [27]-[29].

3.2. FT-IR spectra

The FT-IR spectra of DHA revealed bands at 3542 cm^{-1} for phenolic -OH, 1716 cm^{-1} for C=O carbonyl, 1587 cm^{-1} for azo (N=N), and 1674 cm^{-1} for COOH carboxylic acid. The following bands were detected at B3LYP/6-311G (d,p) calculations: the azo (N=N) band at 1322 cm^{-1}, the COOH carboxylic acid band at 1667 cm^{-1}, the phenolic -OH band at 3701 cm^{-1}, and the C=O carbonyl band at 1751 cm^{-1}. The azo (-N = N-) functional group's distinctive peak confirms the synthesis of the intended molecule. Because the vibration bands are complex, there were minor differences when the results were compared [26]. **Figures 7** and **8**, respectively, show the compound's experimental and theoretical FT-IR spectra.

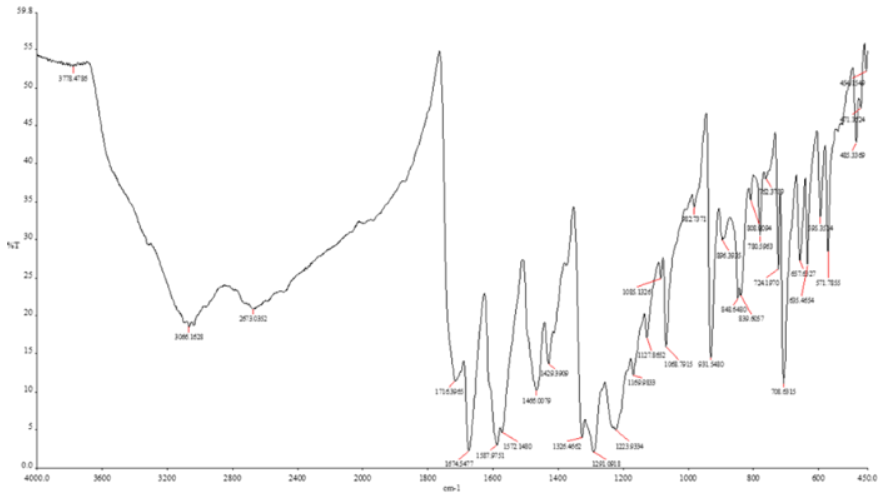

Figure 7. Experimental FT-IR spectrum of the DHA

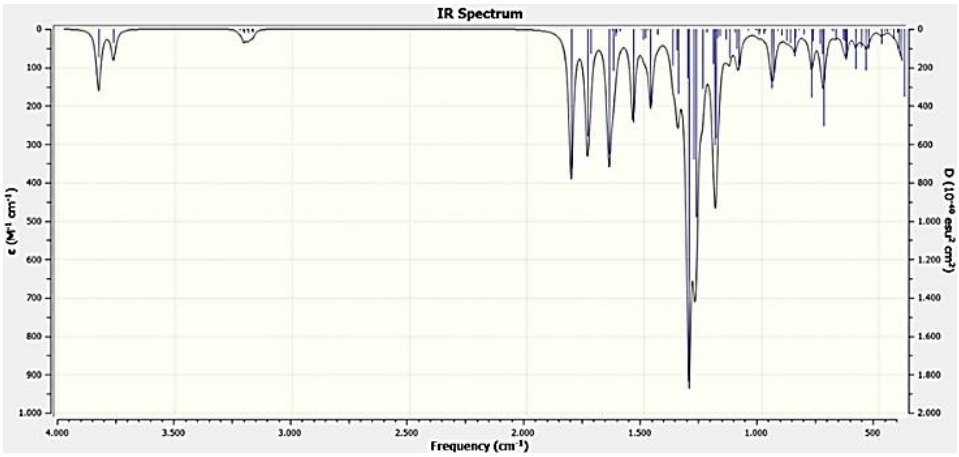

Figure 8. Theoretical FT-IR spectrum of the DHA

3.3. UV-vis spectrum and frontier molecular orbitals

Between 300 and 600 nm, the UV-vis spectra of DHA in DMSO were recorded. The electronic transition wavelengths of the DHA were computed using the TD-DFT technique and the B3LYP/6-311G (d,p) level. **Figures 9** and **10** represent the experimental and theoretical UV-vis spectra of the compounds, respectively. The experimental UV-vis spectra of the compound were detected at 390 nm and theoretically calculated to be at 351 nm. This band was caused by the π→ π* transition in DHA and contributed 61% by HOMO→ LUMO. The other band observed in the experimental spectrum belonged to the n→ π* transition and was at 342 nm. This band was calculated theoretically at 306 nm and it was determined that the HOMO→LUMO+1 transition contributed 49% to this band.

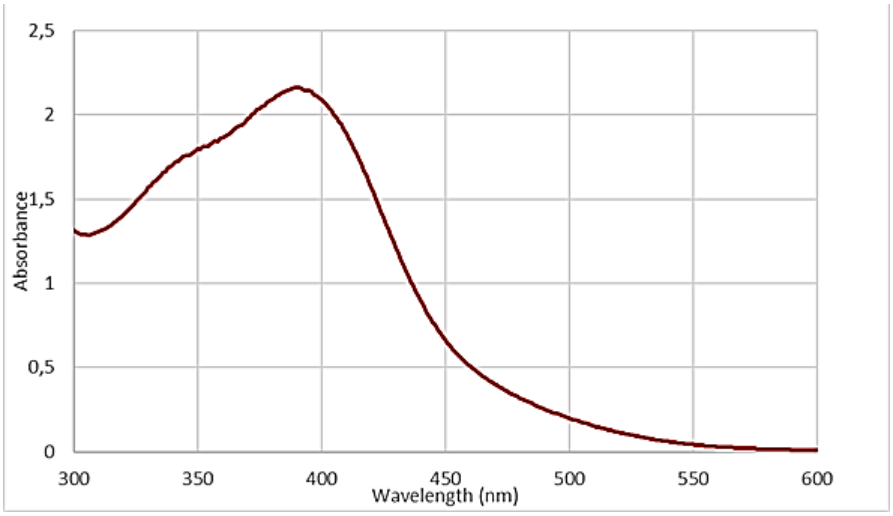

Figure 9. Experimental UV-VIS spectrum of the DHA in DMSO

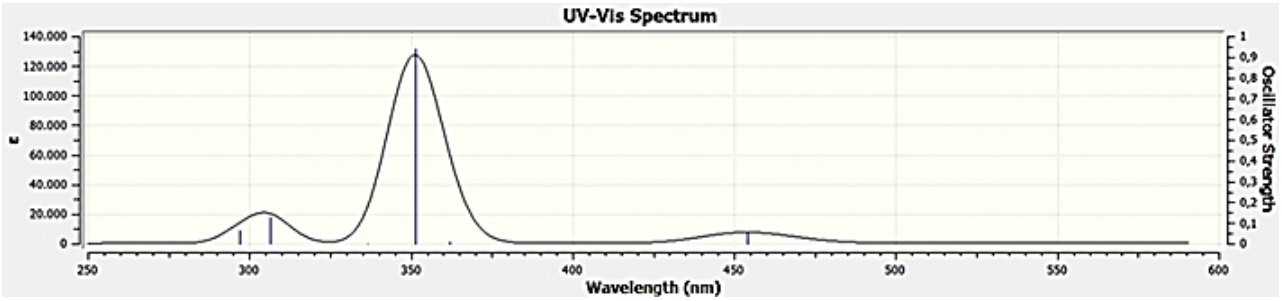

Figure 10. Theoretical UV-VIS spectrum of the DHA in DMSO

When studying the light that is released or reflected when an object is excited, the HOMO-LUMO energy gap offers crucial information about the hardness, softness, stability, and color of the compounds. The HOMOs and LUMOs of the DHA were calculated at the B3LYP/6-311G(d,p) level using the DFT method. The molecular orbital surfaces, energies, and energy difference between HOMO and LUMO of the compound were detailed in **Figure 11.**

Analysis of the HOMO-LUMO graph of DHA revealed that HOMOs clustered on the hydroxybenzoic acid moiety, whereas LUMOs clustered on the hydroxybenzoic acid and anthraquinone moieties. The DHA's HOMO and LUMO energies were determined to be -6.461 and -3.212 eV, respectively, and the energy value for the HOMO-LUMO gap was determined to be 3.249 eV.

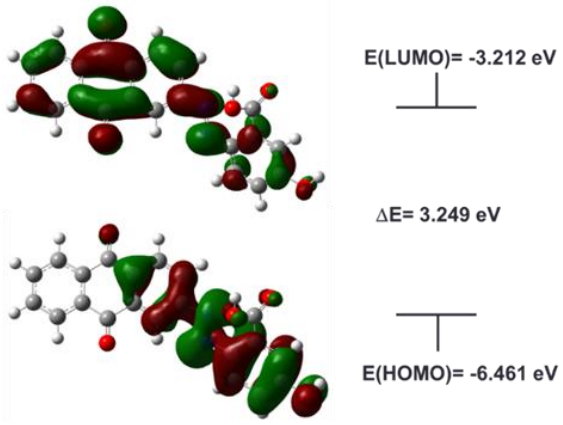

Figure 11. Molecular orbital surfaces, energies, and energy gap between HOMO and LUMO of the DHA

Some of the global reactivity characteristics identified using the HOMO-LUMO energy values of the DHA are shown in **Table 3.** The following electronic factors were created:

I (Ionization Potential) $= -E_{HOMO}$,
A (Electron Affinity) $= -E_{LUMO}$,

χ (Electronegativity) $= (I + A)/2$,
η (Chemical Hardness) $= (I - A)/2$,
S (Chemical Softness) $= 1/2\eta$

Table 3. Global reactivity descriptors for the DHA

Parameter	Value
E_{HOMO} (eV)	-6.461
E_{LUMO} (eV)	-3.212
ΔE (eV)	3.249
I (eV)	6.461
A (eV)	3.212
χ (eV)	4.836
η (eV)	1.624
S (eV^{-1})	0.308

3.4. Computational details

3.4.1. Molecular structure

To achieve the optimized geometry for the DHA, a B3LYP functional with a 6-311G(d,p) basis set was used. The complete optimized geometry of DHA, including atom numbering, is shown in **Figure 12**.

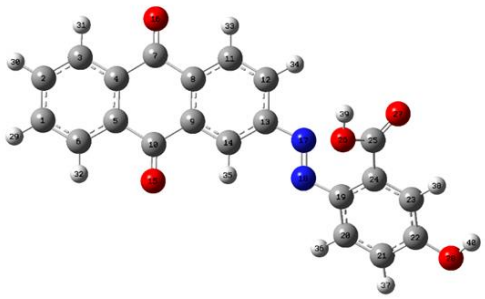

Figure 12. Optimized molecular geometry of the DHA calculated at DFT/B3LYP/6-311G(d,p) level

The values for the computed bond lengths (Å), bond angles (°), and dihedral angles (°) were shown in **Table 4,** and according to this, the shortest calculated bond length belonged to the atoms C25 and O27. After comparing the bond angles between the atoms, it was discovered that the C24-C25-O27 bond angle was a little larger. A dihedral angle equal to or close to 0° or 180° indicates that the atoms are in the same plane. C13-N17-N18-C19 had a dihedral angle of 178.4°, which indicated that these units were lying in the same plane.

Table 4. Some selected calculated bond lengths (Å), bond and dihedral angles (°) for the DHA at the B3LYP/6-311G(d,p) level.

Parameters	B3LYP/6-311G(d,p)
Bond lengths (Å)	
N17-N18	1.254
N18-C19	1.405
C22-O28	1.357
C25-O27	1.205
C25-O26	1.350
C7-O16	1.220
C10-O15	1.218
Bond angles (°)	
C4-C7-O16	121.4
C5-C10-O15	121.4
C13-N17-N18	115.0
C24-C25-O27	124.1
N17-N18-C19	114.9
C21-C22-O28	117.6
C24-C25-O26	112.4
Dihedral angles (°)	
C13-N17-N18-C19	178.4
O15-C10-C9-C8	179.5

3.4.2. Molecular electrostatic potential (MEP) diagram

The Molecular Electrostatic Potential (MEP) diagram, which is essential in distinguishing the nucleophilic and electrophilic regions of the molecule, can provide information on the value of the electrostatic potential and the distribution of charges. The MEP maps' red and blue areas, respectively, correspond to the molecule's electronically dense and deficient regions. DFT/B3LYP/6-311G(d,p) was used to compute the MEP surface diagram of the DHA, which is depicted in **Figure 13**.

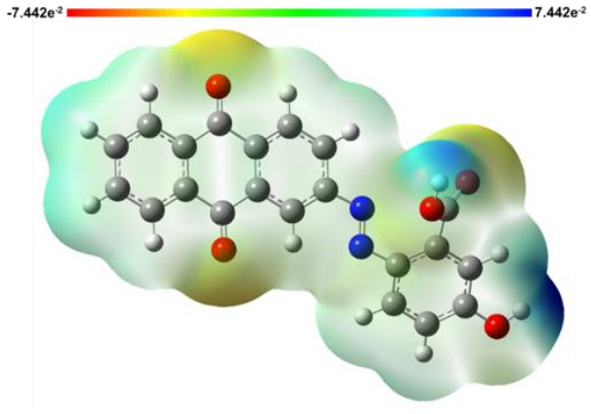

Figure 13. MEP diagram of the DHA calculated at DFT/B3LYP/6-311G(d,p) level

On the oxygen atoms in the anthraquinone group and the oxygen atom in the carboxylic acid moiety in the MEP diagram of DHA, some electron density was found. These red areas, which the high

electronegativity of oxygen caused, were the molecule's interaction sites for potential nucleophilic reactions. On the other hand, the phenolic proton and the proton linked to the carboxylic acid group were the electron-poor blue regions of DHA. Potential DHA interaction sites in electrophilic reactions were located in these blue regions.

3.5. ADMET predictions

A pharmacological molecule's creation must begin with the identification of ADMET properties. Most potential substances are rejected due to their unsuitable pharmacokinetic, druglikeness, etc. profiles.

When the physicochemical characteristics of the synthesized molecule DHA were assessed (**Figure 14**), its molecular weight was determined to be 372.33 g/mol. This value is within the limits of being a drug (150 g/mol <MW<500 g/mol). The TPSA value should be less than 140 $Å^2$ because TPSA values greater than 140 $Å^2$ make it more difficult to get through cell membranes [30]. DHA's TPSA value was determined to be 116.39 $Å^2$.

The dispersion between lipids and water is known as lipophilicity. Drug molecules must pass through numerous biological membranes, including the blood-brain barrier, the skin, and the gut, in order to reach their target areas. A chemical must therefore dissolve at specific rates in both water and oil [31]. The many types of lipophilicity shown in **Figure 14** were discovered by various researchers using various mathematical equations. The mean lipophilicity (CLogPo/w) value of DHA was calculated to be 3.18.

One of the fundamentally important features in studies on drug development is solubility. This is because the drug's molecule must be soluble to reach its target. The maximum quantity of drug that can dissolve in the given mixture is known as logSw. When **Figure 14** is examined, it is seen that DHA resolution is moderately soluble according to the first two resolution types and poorly soluble according to the last resolution type.

A pharmacokinetic analysis of the compound DHA was also conducted. The liver contains crucial enzymes called cytochrome P450 (CYP) inhibitors that are involved in the metabolism of numerous drugs. Determining whether a specific substance will be a cytochrome P450 substrate is crucial. 2D6 and 3A4 are the two main isoforms in charge of drug metabolism. Five main cytochrome isoforms (CYP1A2, CYP2C19, CYP2C9, CYP2D6, and CYP3A4) are thought to be its estimated substrates. DHA inhibits the activity of CYP2C9 isoforms, as shown by **Figure 14**.

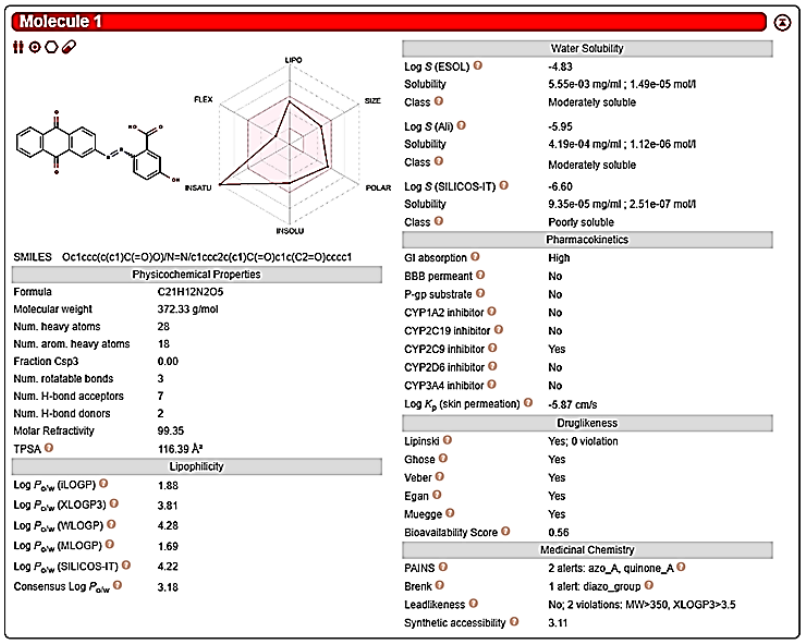

Figure 14. Physicochemical, lipophilicity, solubility, pharmacokinetics and druglikeness properties of the DHA

In **Figure 15,** DHA's BOILED-Egg graph, the ADME parameters GI (gastrointestinal absorption) and BBB (blood-brain barrier) were estimated. In this diagram, the white region contains potential GI absorption locations, while the yellow region has potential BBB permeability areas. Additionally, red dots (PGP-) show that P-gp is not a substrate, whereas blue dots (PGP+) show that P-gp is an active substrate. A red dot (PGP-) indicates that the synthesized DHA compound is not a P-gp substrate, and its presence in the white region indicates that it is predicted to have high intestinal absorption and low brain permeability [32].

The DHA compound was assessed for pharmacological similarity using five different filters, including Lipinski (Pfizer), Ghose (Amgen), Veber (GSK), Egan (Pharmacia), and Muegge (Bayer), that are commonly employed by large pharmaceutical companies to enhance the quality of their proprietary drugs. According to all of the filters, it can be shown that the compound meets all requirements.

When DHA, a medication candidate chemical, is assessed using the PAINS, Brernk, Lead-likeness, and synthetic accessibility metrics, it is discovered that it provides two warnings in PAINS, one warning in Brenk, and two warnings in Lead-likeness. A measure of how simple it is to synthesize drug-like compounds is called synthetic accessibility. A scale from 1 (easiest to make) to 10 (very difficult to make) is used to rate synthetic accessibility. The DHA compound's synthetic accessibility score was determined to be 3.11.

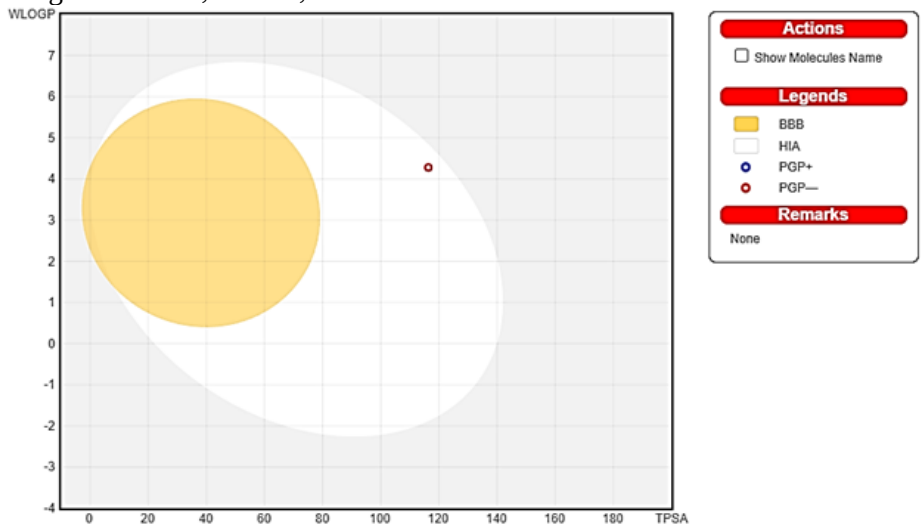

Figure 15. BOILED-Egg model of the DHA

The toxicity level and LD_{50} number of DHA were calculated using the ProTox-II web server. DHA's LD_{50} value was found to be 4000 mg/kg, and it had no immunotoxicity or mutagenicity. Additionally, the predicted toxicity classes for the compounds were established on the web server from worst to best, ranging from 1 to 6. The DHA was in the fifth class, which was made up of substances with the highest LD_{50} values due to its LD_{50} value of 4000 mg/kg (**Figure 16**).

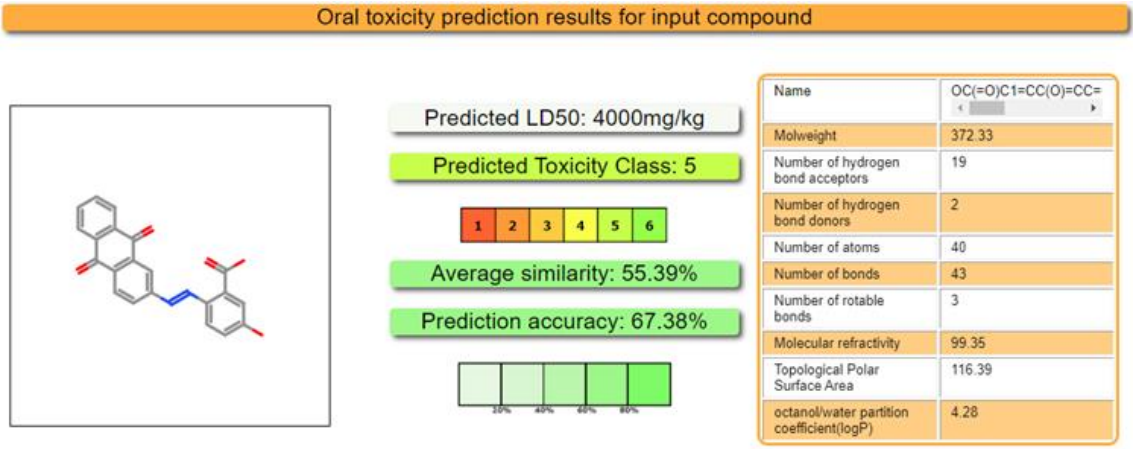

Figure 16. The predicted toxicity classes of the DHA

4. Conclusion and Suggestions

This research involved the synthesis of 2-[(9,10-dioxo-9,10-dihydroanthracen-2-yl)diazenyl]-5-hydroxybenzoic acid (DHA). HR-ESI-MS, FT-IR, ^{1}H-NMR, ^{13}C-NMR, and UV-vis spectroscopy were used to analyze the structure of the DHA. The DFT/B3LYP/6-311G(d,p) level was used to compute all of the DHA's spectral information. The characterization of the compound was helped by the fact that

all of the experimental results were in good agreement with the theoretical values. Additionally, DHA's global reactivity parameters and frontier molecular orbitals were determined. On the other side, it was found that DHA had a very high LD_{50} value (4000 mg/kg). Thus, it was determined that the compound's toxicity was extremely minimal. The DHA computed all of the ADMET and drug similarity parameters within allowable ranges. In light of this, we believe that the DHA has the potential to be applied in more extensive studies in related areas.

Acknowledgment

Conflict of Interest Statement

There is no conflict of interest between the authors.

Statement of Research and Publication Ethics

The study is complied with research and publication ethics.

References

[1] Y. Liu, M. S. T. Mapa and R. L. Sprando, "Anthraquinones inhibit cytochromes P450 enzyme activity in silico and in vitro," *J. Appl. Toxicol*., vol. 41(9), pp.1438-1445, 2021.

[2] H. Küçükbay, F. M. Parladı, F. Z. Küçükbay, A. Angeli, G. Bartolucci and C.T. Supuran, "Synthesis, antioxidant and carbonic anhydrase inhibitory properties of monopeptide-anthraquinone conjugates," *Org. Commun*., vol. 14, no.3, pp. 255-269, 2021.

[3] U. Parladı, Ü. Yılmaz, S. A. A. Noma, B. Ateş and H. Küçükbay, "Synthesis of new anthraquinone compounds and evaluation of their considerable xanthine oxidase inhibitory activities," *ARKIVOC*, vol. 2022, pp. 158-167, 2022.

[4] L. Dufossé, "Anthraquinones, the Dr Jekyll and Mr Hyde of the food pigment family," *Food Res. Int.*, vol. 65, Part B, pp. 132-136, November 2014.

[5] J. Duval, V. Pecher, M. Poujol and E. Lesellier, "Research advances for the extraction, analysis and uses of anthraquinones: A review," *Indust. Crops and Products*, vol. 94, pp. 812–833, 2016.

[6] S. C. Chien, Y. C. Wu, Z. W. Chen and W. C. Yang, "Naturally occurring anthraquinones: chemistry and therapeutic potential in autoimmune diabetes," *Hindawi Publishing Corporation Evidence-Based Complementary and Alternative Medicine*, pp. 1-13, March 2015.

[7] F. Zhao, S. Zhao, J. T. Han, Y. F. Wang, Y. N. Wang and C. H. Wang, "Antiviral anthraquinones from the roots of Knoxia valerianoides," *Phytochem. Lett.*, vol. 11, pp. 57-60, March 2015.

[8] J. Singh, Y. Hussain, S. Luqman and A. Meena, "Purpurin: A natural anthraquinone with multifaceted pharmacological activities," *Phytother. Res.*, vol. 35, no. 5, pp. 2418-2428, 2021.

[9] A. Ntemafacka, R. V. Singh, S. Ali, J. R. Kuiate and Q. P. Hassan, "Antiviral potential of anthraquinones from Polygonaceae, Rubiaceae and Asphodelaceae: Potent candidates in the treatment of SARS-COVID-19, A comprehensive review," *South African Journal of Botany*, vol. 151, Part A, pp. 146-155, December 2022.

[10] A. Daina, O. Michielin and V. Zoete, "iLOGP: A simple, robust and efficient description of n-octanol/water partition coefficient for drug design using the GB/SA approach," *J. Chem. Inform. and Model.*, vol. 54, no. 12, pp. 3284-3301, 2014.

[11] A. Daina, O. Michielin and V. Zoete, "SwissADME: A free web tool to evaluate pharmacokinetics, drug-likeness and medicinal chemistry friendliness of small molecules," *Sci. Rep.*, vol. 7, pp. 1-13, 2017.

[12] M. Gökalp, B. Dede, Ç. Karabacak Atay and T. Tilki, "Triazole based azo molecules as potential antibacterial agents: Synthesis, characterization, DFT, ADME and molecular docking studies," J. *Mol. Struct*., vol. 1212, pp. 128140, 2020.

[13] B. Sezgin, B. Dede, Ç, Karabacak Atay and T. Tilki, "Synthesis, Characterization and Theoretical Calculations of a Novel Azo Derivative with In Vitro and In Silico Biological Studies," *Arab. J. Sci. En*g., vol. 46, pp. 5567–5581, 2021.

[14] R. Sharma, R.K. Rawal, T.Gaba, N. Singla, M. Malhotra, S. Matharoo and T. R. Bhardwaj, "Design, synthesis and ex vivo evaluation of colon-specific azo based prodrugs of anticancer agents," *Bioorganic Med. Chem. Lett*., vol. 23, pp. 5332-5338, 2013.

[15] M. J. Frisch, G. W. Trucks, H. B. Schlegel, G. E. Scuseria, M. A. Robb, J. R. Cheeseman, G. Scalmani, V. Barone, G. A. Petersson, H. Nakatsuji, X. Li, M. Caricato, A. Marenich, J. Bloino, B. G. Janesko, R. Gomperts, B. Mennucci, H. P. Hratchian, J. V. Ortiz, A. F. Izmaylov, J. L. Sonnenberg, D. Williams-Young, F. Ding, F. Lipparini, F. Egidi, J. Goings, B. Peng, A. Petrone, T. Henderson, D. Ranasinghe,

V. G. Zakrzewski, J. Gao, N. Rega, G. Zheng, W. Liang, M. Hada, M. Ehara, K. Toyota, R. Fukuda, J. Hasegawa, M. Ishida, T. Nakajima, Y. Honda, O. Kitao, H. Nakai, T. Vreven, K. Throssell, J. A. Montgomery Jr, J. E. Peralta, F. Ogliaro, M. Bearpark, J. J. Heyd, E. Brothers, K. N. Kudin, V. N. Staroverov, T. Keith, R. Kobayashi, J. Normand, K. Raghavachari, A. Rendell, J. C. Burant, S. S. Iyengar, J. Tomasi, M. Cossi, J. M. Millam, M. Klene, C. Adamo, R. Cammi, J. W. Ochterski, R. L. Martin, K. Morokuma, O. Farkas, J. B. Foresman, D. J. Fox, "Gaussian 09, Revision E.01," Gaussian Inc Wallingford CT, 2016.

[16] R. Dennington, T. A. Keith, J. M. Millam, "GaussView, Revision 5.0.9," Semichem. Inc Shawnee Mission, KS, 2009.

[17] A. D. Becke, "Density-functional exchange-energy approximation with correct asymptotic behavior," *Phys. Rev. A*, vol. 38, pp. 3098–3100, 1988.

[18] C. Lee, W. Yang and R. G. Parr, "Development of the Colle-Salvetti correlation-energy formula into a functional of the electron density," *Phys. Rev. B*, vol. 37, pp. 785–789, 1988.

[19] J. P. Merrick, D. Moran and L. Radom, "An evaluation of harmonic vibrational frequency scale factors," *J. Phys. Chem. A*, vol. 111, pp. 11683-11700, 2007.

[20] R. Bauernschmitt and R. Ahlrichs, "Treatment of electronic excitations within the adiabatic approximation of time dependent density functional theory," *Chem. Phys. Lett.*, vol. 256, pp. 454–464, 1996.

[21] M. E. Casida, C. Jamorski, K. C. Casida and D. R. Salahub, "Molecular excitation energies to high-lying bound states from time-dependent density-functional response theory: characterization and correction of the time-dependent local density approximation ionization threshold," *J. Chem. Phys.*, vol. 108, pp. 4439–4450, 1998.

[22] N. M. O'Boyle, A. L. Tenderholt and K. M. Langner, "cclib: a library for package-independent computational chemistry algorithms," *J. Comput. Chem.*, vol. 29, pp. 839–845, 2008.

[23] R. Ditchfield, "Molecular orbital theory of magnetic shielding and magnetic susceptibility," *J. Chem. Phys.*, vol. 56, pp. 5688–5691, 1972.

[24] K. Wolinski, J. F. Hinton and P. Pulay, "Efficient implementation of the gauge-independent atomic orbital method for NMR chemical shift calculations," *J. Am. Chem. Soc.*, vol. 112, pp. 8251–8260, 1990.

[25] A. Daina, O. Michielin and V. Zoete, "SwissADME: a free web tool to evaluate pharmacokinetics, drug-likeness and medicinal chemistry friendliness of small molecules," *Sci. Rep.*, vol. 7, no. 1, pp. 1-13, 2017.

[26] P. Banerjee, O. A. Eckert, A. K. Schrey and R. Preissner, "ProTox-II: a webserver for the prediction of toxicity of chemicals," *Nucleic Acids Res.* (Web server issue 2018).

[27] C. Li, T. Zhang, Z. Zeng, X. Liu, Y. Zhao, B. Zhang and Y. Feng, "A New Route to Indazolone via Amidation Reaction of o-Carboxyazobenzene," *Org. Lett.*, vol. 14, No. 2, pp. 479–481, 2012.

[28] S. Riaz, A. Jabbar, Ambreen, S. Khaskheli, S. Sagheer and M. I. Choudhary, "Anthraquinone based anti-UV acid-azo dyes; a study of their synthesis, fastness, and UV-protection properties," J. *Mol. Struct.*, vol. 1272, 134219, 2023

[29] H. F. Huang, W. Ma, B. T. Tang and S. F. Zhang, "Properties of a novel acid dye 1-amino-4-[(6-nitro-2-benzothiazolyl)amino]-9,10-anthraquinone-2-sulfonic acid with anti-UV capability," *Chin. Chem. Lett.*, vol. 21 pp. 417–420, 2010.

[30] H. Pajouhesh and G. R. Lenz, "Medicinal Chemical Properties of Successful Central Nervous System Drugs, NeuroRx," *J. Am. Soc. Exp. NeuroTher*., vol. 2, pp. 541–553, October 2005.

[31] A. Mermer and S. Alyar, "Synthesis, characterization, DFT calculation, antioxidant activity, ADMET and molecular docking of thiosemicarbazide derivatives and their Cu II) complexes," *Chem.-Biol. Interact.*, vol. 351, 109742, 2022

[32] A. Daina and V. Zoete, "A boiled-egg to predict gastrointestinal absorption and brain penetration of small molecules," *ChemMedChem*, vol. 11, pp. 1117-1121, 2016

Bitlis Eren Üniversitesi Fen Bilimleri Dergisi
BİTLİS EREN UNIVERSITY JOURNAL OF SCIENCE
ISSN: 2147-3129/e-ISSN: 2147-3188
VOLUME: 12 NO: 3 PAGE: 673-685 YEAR: 2023
DOI:10.17798/bitlisfen.1281022

Inertia Weight-free Particle Swarm Optimization in Optimal Control Design for Vehicle Active Suspension Systems

Hasan BAŞAK[1*], Kadri DOĞAN[2]

[1]*Artvin Çoruh University, Faculty of Engineering, Dept. of Electrical-Electronics Eng. Artvin /TURKEY*
[2]*Artvin Çoruh University, Faculty of Engineering, Dept. of Basic Sciences, Artvin/TURKEY (ORCID:0000-0002-3724-6819) (ORCID:0000-0002-6622-3122)*

Keywords: Active suspension system, Standard PSO, Inertia-weight-free PSO, LQR, Road disturbance.

Abstract
Vehicle active suspension systems play an important role in ride comfort and driving safety. This study considers the problem of an efficient control scheme design for vehicle active suspension systems. The active suspension systems aim to get more comfortable riding and good handling for random road disturbances. The purpose of this work is to reduce the driver's entire body acceleration and thereby improve ride comfort. The inertial weight-free particle swarm optimization (PSO) method is utilized to obtain weighting matrices of the optimal control namely linear quadratic regulator (LQR) for the active suspension systems. The designed state-feedback controller is applied to the quarter-car suspension system under different road profiles. Simulation results of the inertia weight-free PSO-tuned LQR are compared with the results of the classical-tuned controller and standard PSO-tuned LQR controller to show the effectiveness.

1. Introduction

Active suspension systems in vehicles aim to ensure ride comfort, road holding, and passenger safety for different road irregularities. To utilize the potential of active suspension systems, the control algorithms should deal with changing road profiles. In the literature, various control methods have been designed for active suspension systems such as sliding mode control [1], adaptive control [2], fuzzy H_∞ control [3], fuzzy [4], machine learning-based controller [5], and PID (Proportional-Derivative–Integral) with the genetic algorithm [6]. The control objectives of active suspension systems are passenger comfort, minimum vehicle body acceleration, and road handling. The linear quadratic controller is designed to obtain optimal performance without deteriorating conflict design requirements [7-9]. A state feedback optimal control law namely Linear Quadratic Regulator (LQR) offers guaranteed stability, robustness, and a structured design method for multiple-input multiple-output systems. The LQR approach computes an optimal state-feedback gain by minimizing a quadratic performance index, which consists of the state and input variables penalized by the weighting matrices. In the spite of the potential advantages, one of LQR design difficulties is the optimal selection of the weighting matrices, which does not have an efficient procedure. Bryson's method [10] can be used to obtain the initial selection of weighting matrices. However, this method is a check-test method that is a time-consuming and tiring approach. Hence, we focus on the problem of the selection of weighting matrices for the LQR control design using inertia weight-free particle swarm optimization (PSO) approach.

In literature, several researchers have proposed swarm intelligence methods to find out the optimal weighting matrices. For instance, Kumar et al. [11] use the PSO approach to obtain the weighting matrices of LQR for a two-degrees-of-freedom helicopter system. It is reported that weighting matrices obtained with the PSO make the control law

*Corresponding author: hasanbasak@artvin.edu.tr
Received: 11.04.2023, Accepted: 13.08.2023

optimal and also eliminate the tiring manual tuning procedure. A reinforced quantum-behaved PSO is proposed in [12] to optimize the weighting matrices of the LQR controller, which is applied to an inverted pendulum system and a flight landing system. Maghfiroh et al. [13] utilize the PSO algorithm to find optimal weighting matrices for a DC motor system. The controller provides the smallest integral of absolute the error index. Karanki et al. [14] design a PSO-based state feedback controller for a unified power-quality conditioner. Shao et al. [15] propose PSO-based LQR for a model of an overhead crane system. For vehicle active suspension systems, the bat algorithm [16], artificial fish swarm algorithm [17], and adaptive predator–prey optimization algorithm [18] are employed for the selection of optimal weighting matrices of the LQR controller.

The main contribution of this work is to propose the inertia weight-free PSO algorithm tuned optimal LQR controller for an active suspension system. The inertia weight-free PSO algorithm improves the convergence speed and accuracy of the standard PSO algorithm. The simulation studies are conducted to show the effectiveness of the proposed method. The inertia weight-free PSO-tuned LQR controller is compared with the classical tuned LQR controller and the standard PSO-tuned LQR in terms of the vehicle body acceleration, suspension deflection, and tire deflection.

2. Material and Method

2.1. Model of Active Suspension System

This section gives the dynamic equations of a quarter-active suspension system. The quarter active suspension system is depicted in Figure 1. The system has two inputs (control input F and the road surface position, z_r). The vehicle body displacement and the tire displacement are denoted by z_s and z_{us} from the ground respectively.

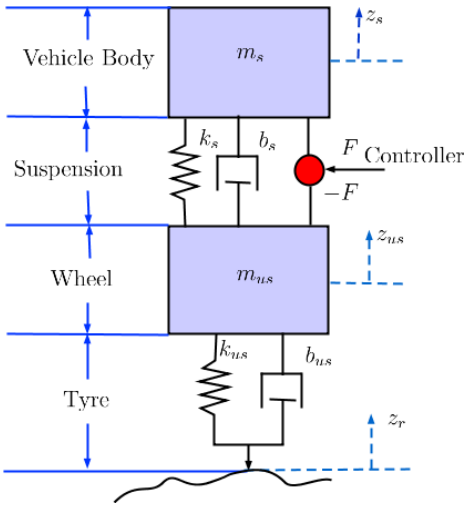

Figure 1. Diagram of the quarter active vehicle suspension system

The quarter active suspension system equation of motion are derived in [16] using the Newton law as follows:

$$\begin{aligned} m_{us}\ddot{z}_{us} = &-b_{us}\dot{z}_{us} - b_s\dot{z}_{us} - F + b_s\dot{z}_s \\ &+ b_{us}\dot{z}_r - (z_{us} - z_s)k_s \\ &- (z_{us} - z_r)k_{us} \end{aligned} \quad (1)$$

$$m_s\ddot{z}_s = b_s\dot{z}_{us} + F - b_s\dot{z}_s - (z_s - z_{us})k_s \quad (2)$$

Equations (1)-(2) can be given in the state–space realization as:

$$\begin{aligned} \dot{x}(t) &= \mathcal{A}x(t) + \mathcal{B}u(t) \\ y(t) &= \mathcal{C}x(t) + \mathcal{D}u(t) \end{aligned} \quad (3)$$

where the state variable vector is $x = [(z_s - z_{us})\ \dot{z}_s\ (z_{us} - z_r)\ \dot{z}_{us}]^T$ and the input vector is $u = [\dot{z}_r\ F\ ]^T$ and the output vector is $y = [\ (z_s - z_{us})\ \ddot{z}_s\ ]^T$. $(z_s - z_{us})$ and $(z_{us} - z_r)$ are the suspension and tire deflections, $\dot{z}_s$ and $\dot{z}_{us}$ are the body and the tire vertical velocities respectively. Matrices $\mathcal{A}, \mathcal{B}, \mathcal{C}$ and $\mathcal{D}$ are obtained as follows:

$$\mathcal{A} = \begin{bmatrix} 0 & 1 & 0 & -1 \\ \frac{-k_s}{m_s} & \frac{-b_s}{m_s} & 0 & \frac{b_s}{m_s} \\ 0 & 0 & 0 & 1 \\ \frac{k_s}{m_{us}} & \frac{b_s}{m_{us}} & \frac{-k_{us}}{m_{us}} & -\frac{(b_s+b_{us})}{m_{us}} \end{bmatrix},$$

$$\mathcal{B} = \begin{bmatrix} 0 & 0 \\ 0 & \frac{1}{m_s} \\ -1 & 0 \\ \frac{b_{us}}{m_{us}} & -\frac{1}{m_{us}} \end{bmatrix}, \quad (4)$$

$$\mathcal{C} = \begin{bmatrix} 1 & 0 & 0 & 0 \\ \frac{-k_s}{m_s} & \frac{-b_s}{m_s} & 0 & \frac{b_s}{m_s} \end{bmatrix}, \ \mathcal{D} = \begin{bmatrix} 0 & 0 \\ 0 & \frac{1}{m_s} \end{bmatrix}$$

Table 1 gives the parameters of the quarter active suspension system.

Table 1. Model parameters [16].

Symbol	Value	Definition
$\mathbf{m_s}$	2.45 kg	Sprung mass
$\mathbf{m_{us}}$	1 kg	Unsprung mass
$\mathbf{k_s}$	900 N/m	Suspension stiffness
$\mathbf{k_{us}}$	1250 N/m	Tire stiffness
$\mathbf{b_s}$	7.5 Ns/m	Suspension damping coefficient
$\mathbf{b_{us}}$	5 Ns/m	Tire inherent damping coefficient

2.2. Performance Requirements

The performance requirements of the active suspension system are given in [8, 9] as:

1) Ride comfort: The vehicle body acceleration, $\ddot{z}_s$ must be reduced by the active suspension system.
2) Suspension deflection: The active suspension system has to maintain the suspension deflection within the allowable interval to avoid vehicle damage.$|(z_s - z_{us})| \leq \bar{z}$, $\bar{z}$ is the greatest acceptable suspension deflection.
3) Road handling: The wheel assembly has to stay in firm contact with the road to ensure passenger safety. Therefore, the tire's dynamic load has to be smaller than its static load $(|k_s(z_{us} - z_r)| \leq (m_s + m_{us})g)$.

2.3. Problem Description

Consider the following linear time-invariant system:

$$\begin{aligned} \dot{x}(t) &= \mathcal{A}x(t) + \mathcal{B}u(t), \qquad x(0) = x_0 \\ y(t) &= \mathcal{C}x(t) + \mathcal{D}u(t) \end{aligned} \tag{5}$$

in which $x(0)$ is the initial condition. The purpose is to find the optimal control law, $u(t)$ which can drive the state variables of the dynamics to demand state by optimizing the following quadratic objective function:

$$J = \int_0^\infty x^T(t)Qx(t) + u^T(t)\mathcal{R}\,u(t)dt, \tag{6}$$

Here Q is the positive semi-definite state and $\mathcal{R}$ is the positive-definite weighting matrices respectively. Diagonal weighting matrices are generally selected. The order of Q and $\mathcal{R}$ matrices equals the number of states and the number of inputs. Assume that $(\mathcal{A}, \mathcal{B})$ is stabilisable and $(\mathcal{A}, \mathcal{C})$ is observable, then the LQR controller computes as follows:

$$u(t) = -Kx(t) \tag{7}$$

in which K is the optimal state-feedback gain computed by $K = \mathcal{R}^{-1}\mathcal{B}^T\mathcal{P}$ that is called the Lagrange multiplier based on optimization. The positive definite-matrix, $\mathcal{P}$ is obtained from the solution of the following algebraic Riccati equation:

$$\mathcal{A}^T\mathcal{P} + \mathcal{P}\mathcal{A} + Q - \mathcal{P}\mathcal{B}\mathcal{R}^{-1}\mathcal{B}^T\mathcal{P} = 0 \tag{8}$$

The design of the LQR control approach has a challenging issue in selecting the weighting matrices. The selection of weighting matrices Q and $\mathcal{R}$ affect the speed of state variables and control effort [17]. Hence, the weighting matrices can be determined by using the inertial weight-free PSO in this work. The model of the active suspension system is given as a fourth-order system. Therefore, the weighting matrix Q is set to be a 4x4 diagonal semidefinite matrix $(Q = \text{diag}([q_1\ q_2\ q_3\ q_4])$. The system has a control input, F thereby a scalar, $\mathcal{R}$ is considered as $\mathcal{R} = r_1$. The corresponding J to be minimized is given as follows:

$$\begin{aligned} J = \int_0^\infty & \begin{bmatrix} x_1 \\ x_2 \\ x_3 \\ x_4 \end{bmatrix}^T \begin{bmatrix} q_1 & 0 & 0 & 0 \\ 0 & q_2 & 0 & 0 \\ 0 & 0 & q_3 & 0 \\ 0 & 0 & 0 & q_4 \end{bmatrix} \begin{bmatrix} x_1 \\ x_2 \\ x_3 \\ x_4 \end{bmatrix} \\ & + u_1 r_1 u_1 dt \\ = \int_0^\infty & (q_1 {x_1}^2 + q_2 {x_2}^2 + q_3 {x_3}^2 + q_4 {x_4}^2 \\ & + r_1 {u_1}^2) dt \end{aligned} \tag{9}$$

in which q_1, q_2, q_3 and q_4 are scalar weights of state variables. r_1 is the scalar weight of the controlled force. LQR weighting matrices are optimized using the PSO algorithm whose fitness function is given by the following integral of the time-weighted absolute error (ITAE):

$$\mathrm{ITAE} = \int_0^{\infty} t|e|dt \qquad (10)$$

where e $= \boldsymbol{e}_{(z_s - z_{us})} + \boldsymbol{e}_{\dot{z}_s} + \boldsymbol{e}_{(z_{us} - z_r)} + \boldsymbol{e}_{\dot{z}_{us}}$ and $\boldsymbol{e}_{(z_s - z_{us})}$, $\boldsymbol{e}_{\dot{z}_s}$, $\boldsymbol{e}_{(z_{us} - z_r)}$ and $\boldsymbol{e}_{\dot{z}_{us}}$ are tracking errors of state variables for the given road profile.

2.4. Inertia Weight-free Particle Swarm Optimization

Many realistic optimization issues demand costly computation-based assessments in order to find the optimal solution. The optimization method should be carried out speedily and it should not be overly complicated [17] due to various limits in research such project time needs and computer resource constraints. Performances of optimization techniques are evaluated using different benchmark fitness functions. These algorithms often provide acceptable results by utilizing their unique information transmission methods in conjunction with a variety of first-candidate solutions in various fitness evaluations. These procedures frequently run-time and resource-intensive computer resources since they evaluate each potential resolution. The study and creation of effective optimization algorithms for assessing a small number of functions is therefore an expanding research topic. Several novel ideas have been proposed and published recently. These techniques with constrained function evaluations have produced some pleasing results [17-19].

Wilson [20] first put out the swarm idea in 1975. Each member of a swarm may use the discoveries and experiences of the others to escape from predators and find food. Each bird in a swarm can identify where it is within the swarm. Every individual will observe neighbouring individuals' flight motions to modify their own flight trajectory, giving the impression that a single entity is in charge of the whole swarm. The positions of two or three of its neighbours, as well as the flight path of the entire swarm, are the three features that each bird must see [21]. Reynolds [22] established a distributed behavioural model in light of this.

Kennedy and Eberhart [23] first developed the stochastic population-based technique known as particle swarm optimization (PSO), which was inspired by some animals' intelligent group behaviour. This technique is a unique evolutionary technique, first motivated by the specific social behaviours of fish schools and bird flocks. PSO blends evolutionary calculations with social psychology concepts from socio-cognition agents. It uses a swarm of particles to represent the potential solutions to the objective issue when applied for optimization processes. Each particle will move in the direction of the problem's probable solution after a search has started, based on its own and the partner particles' investigations. The easy implementation and the limited number of adjustable parameters of PSO are its two main benefits. Inertia weight (*w*), one of PSO's parameters, to strike a balance between the features of exploration and exploitation. Since the parameter's inception, several ideas for various approaches to calculating the value of inertia weight throughout the duration of a run have been made.

The standard PSO contains the following four items:

1. Determine the objective function.

2. Set parameters.

The basic parameters of the PSO include:

(i) Space dimension

(ii) Particle swarm size

(iii) Location constraint

(iv) Velocity constraint

(v) Number of iterations

(vi) Inertia weight

(vii) Learning factor: The ranges of the independent variables should be considered while determining the learning factor. Particle and particle swarm learning factors are the two different categories of learning factors. Typically, a value between 0 to 5 can be used.

3. Initialize particle swarm.

4. Update velocity and location.

Updating velocity and position is the essence of the standard PSO. The function velocity and position, which is called the PSO algorithm, is as follows:

$$\begin{aligned} v^{k+1}(m,n) = {} & wv^{k}(m,n) \\ & + r_1 c_1 \left(xp^{k}(m,n) \right. \\ & \left. - x^{k}(m,n) \right) \\ & + r_2 c_2 \left(xg^{k}(n) \right. \\ & \left. - x^{k}(m,n) \right) \end{aligned} \qquad (11)$$

$$x^{k+1}(m,n) = x^{k}(m,n) + v^{k+1}(m,n)$$

Where $v^{\mathrm{k}}(m,n)$ is the velocity of the m^{th} particle for the n^{th} dimension at the k^{th} iteration, $x^{\mathrm{k}}(m,n)$ is the current position of the m^{th} particle for the n^{th} dimension at the k^{th} iteration. $xp(m,n)$ represents the

position of the best solution that the m^{th} particle has achieved so far, for the n^{th} dimension of the problem. $xg(n)$ is the current global best obtained so far by the particle swarm optimization for the n^{th} dimension of the problem. w, c_1, c_2 and r_1, r_2 are defined as inertia weight, single particle's learning factor, particle swarm's learning factor and random values in [0,1], respectively [24]. The hybrid optimization algorithm is an effective combination of a metaheuristic optimization algorithm with another optimization algorithm that can exhibit more stable behaviour and greater flexibility against complicated and difficult problems. Local search algorithms use a well-specified neighborhood mechanism to recursively explore the search space for a better answer than an already existing one. Metaheuristics are made up of iterative processes that successfully integrate many sub-heuristics to find a search space. To locate global optimal areas, certain learning algorithms are employed. Natural approaches known as population-based metaheuristics investigate the search space by manipulating the population, and the outcomes heavily depend on these particular manipulative techniques. Compared to other trajectory approaches, which are easily impacted by local optima, population-based metaheuristics methods are better at characterizing local optima. Because of this, metaheuristic hybrids that effectively combine the advantages of population-based and trajectory approaches are typically quite effective and successful [25-26].

During the early search phase, the standard PSO technique often converges quickly before slowing down. It frequently has slow convergence and becomes locked in local minima. Moreover, the inertia weight, w and the pair of learning factors (c_1, c_2) are important variables affecting the standard PSO convergence. The way each particle updates are the main difference between the inertia weight-free PSO and the standard PSO algorithm. In this work, the inertia weight-free means that PSO algorithm does not have adjustable parameters of w, c_1 and c_2.The following equations show the calculation of particle positions and velocity in the inertia weight-free PSO algorithm [27]:

$$\begin{aligned} v^{k+1}(m,n) = {} & (2r_1 - 0.5)v^k(m,n) \\ & + (2r_2 - 0.5)\Big(xp^k(m,n) \\ & - x^k(m,n)\Big) \\ & + (2r_3 - 0.5)(xg^k(n) \\ & - x^k(m,n)) \end{aligned} \tag{12}$$

$$\begin{aligned} u^{k+1}(m,n) = {} & (2r_4 - 0.5)\Big(xg^k(n) \\ & - xp^k(m,n)\Big) \\ & + (2r_5 - 0.5)\Big(xg^k(n) \\ & - x^k(m,n)\Big) \end{aligned} \tag{13}$$

$$\begin{aligned} x^{k+1}(m,n) = {} & xp^k(m,n) \\ & + (2r_6 - 0.5)v^{k+1}(m,n) \\ & + (2r_7 - 0.5)u^{k+1}(m,n) \end{aligned} \tag{14}$$

where, r_1, r_2 , r_3 r_4 r_5 r_6 and r_7 are defined as random values in [0,1]. Figure 1 illustrates the flowchart of the inertia weight-free PSO algorithm.

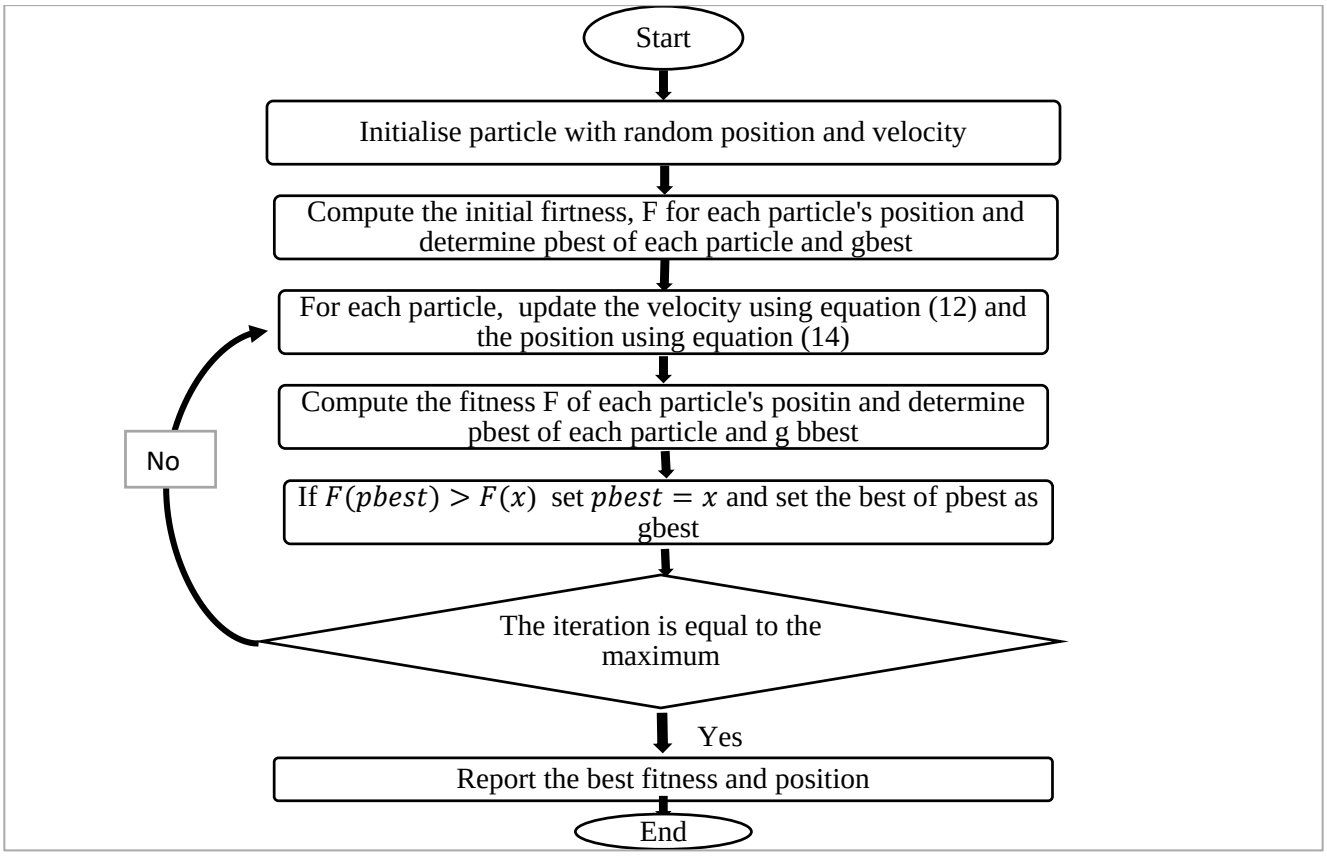

Figure 2. Flowchart of the inertia weight–free PSO algorithm

The process of LQR controller design through the inertia weight-free PSO algorithm can be summarized as follows: A state-feedback gain is computed using with Matlab lqr() command for the pair of system matrices (A,B) from equation (4) and matrices Q and R are found by the inertia weight-free PSO algorithm. For each iteration, the closed-loop system is simulated to calculate ITAE (fitness) given in equation (10). Obtained ITAE values are compared. As a result, the lowest ITAE value and corresponding matrices Q and R are recorded at the final iteration. Simulation results will be given in next section.

3. Simulation Results and Discussion

In this section, simulation results are given to show the effectiveness of the active suspension system with the designed LQR controller against random road disturbances. A square shape (with an amplitude of 0.01 m and frequency of 0.3 Hz) and a bumpy shape (with an amplitude of 0.1 m and 0.175 Hz) signals are taken into consideration as random road disturbances. Classical-tuned LQR, standard PSO-tuned LQR, and inertia weight-free PSO-tuned LQR are tested under random road disturbances.

The parameters of the standard PSO and the inertia weight–free PSO are given in Table 1. The number of the optimized parameter is five which consists of four states and a control variable. The range of weighting matrices Q and R are set between 0.01 and 500. Both the standard PSO and weight–free PSO have 60 particles and 50 iterations. The standard PSO has an inertia weight and a cognitive constant but the weight-free PSO algorithm does not have these critical weight and cognitive constants.

For both the standard PSO and the inertia weight-free PSO, the convergence of the fitness function is shown in Figure 3. It can be seen that the weight-free PSO reaches the minimum fitness value faster than the standard PSO. The standard PSO approach typically converges rapidly during the initial search period and then slows. It has the tendency of being trapped in local minima and slow convergence. Furthermore, inertia weight w, c1 and c2 are critical factors that affect the convergence of the PSO. The inertia weight–free PSO algorithm overcomes these problems. The inertia weight-free PSO takes 27 iterations to find the minimum fitness value whereas the standard PSO obtains the minimum fitness value with 34 iterations. The resulting weighting matrices and gains of state-feedback controllers are reported in Table 2.

Table 1. Parameters of the standard PSO and the inertia weight-free PSO

Parameters	Standard PSO	Inertia weight-free PSO
Iterations	50	50
Particles	60	60
Variables	5	5
Inertia weight	0.9	-
Cognitive constants	2	-

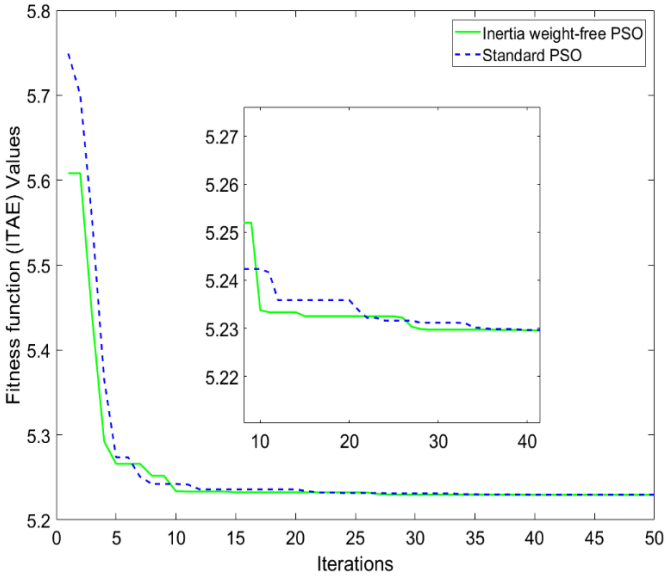

Figure 3. Comparison of fitness function values

Table 2. State feedback gains and weighting matrices

	State-feedback gain	Weighting matrices
Classical-tuned LQR [8]	$K = \begin{bmatrix} 469.4581 \\ 52.2394 \\ -179.95 \\ -12.35 \end{bmatrix}^T$	$Q = \text{diag}(692.52, 0.16, 652.52, 0.16)$ $\mathcal{R} = 0.00065$
Standard PSO-tuned LQR	$K = \begin{bmatrix} 0.0006 \\ 73.96 \\ -347.90 \\ -13.6843 \end{bmatrix}^T$	$Q = \text{diag}(0.0100, 53.5209, 1.2415, 14.0084)$ $\mathcal{R} = 0.01$
Inertia weight-free PSO-tuned LQR	$K = \begin{bmatrix} 0.00060 \\ 116.9200 \\ -494.5004 \\ -13.6274 \end{bmatrix}^T$	$Q = \text{diag}(0.0101, 136.7950, 204.8922, 19.2798)$ $\mathcal{R} = 0.01$

Figure 4 compares the vehicle body acceleration closed-loop responses for the square road profile. The inertia weight-free PSO-tuned LQR controller (black line) provides lower body acceleration than other controllers do. Figures 5 and 6 display the vehicle body and tire positions respectively. It can be seen from plots that the inertia weight-free PSO-tuned LQR controller achieves better road profile tracking. However, the classical-tuned LQR controller (green line) has an oscillatory response that might damage the vehicle. To void structural damage, the absolute value of the suspension deflection should be less than 0.038 m ($|(z_s - z_{us})| \leq 0.038$ m) [8]. The results of suspension deflections with all designed controllers are given in Figure 7. It can be seen that $|(z_s - z_{us})| \leq 0.02$ m which is within the acceptable range. The tire deflection responses are plotted in Figure 8. For road handling requirements, the tire's dynamic load has to be smaller than its static load ($((m_s + m_{us})g = 33.84\ N$). All controllers satisfy this performance requirement. The active suspension system with the classical tuned LQR controller has tire's dynamic load, $|k_s(z_{us} - z_r)| = 17.16\ N$ and with the standard PSO-tuned LQR controller has tire's dynamic load $|k_s(z_{us} - z_r)| = 17.12\ N$. Although, the inertia weight-free PSO-tuned LQR controller has a less dynamic load

($|k_s(z_{us} - z_r)| = 17.07$ N) within the permissible range.

Similarly, closed-loop responses are given in Figures 9, 10, 11, 12 and 13 under the bumpy road profile. Vehicle body acceleration plots are given in Figure 9 to evaluate the passenger ride comfort. It is clearly seen that the inertia weight-free PSO-tuned LQR controller improves the ride comfort better than other controllers do. Figures 10 and 11 show that the vehicle body and the tire positions are tracked well with the inertia weight-free PSO-tuned LQR controller so passenger safety is ensured. Figure 12 indicates the suspension deflection under the bumpy road profile. The inertia weight-free PSO-tuned LQR controller increases the suspension deflection to improve ride comfort. The maximum value of the suspension deflection is 0.0124 m with the inertia weight-free PSO-tuned LQR controller, which is less than the permissible travel range of 0.038 m. Lastly, the tire deflection is depicted in Figure 13. The dynamic loads with the classical tuned LQR, the standard PSO-tuned LQR and the inertia weight-free PSO tuned LQR controllers are 3.049 *N*, 2.755 *N*, and 2.62 *N* respectively which are lower than the tire's static load. Furthermore, the closed-loop response with the inertia weight-free PSO-tuned LQR controllers has the best tire deflection amongst all designed controllers. ITAE values under different road profiles are reported in Table 3. Closed-loop response with the inertial weight-free PSO-tuned LQR controller has the lowest ITAE index. The above discussion and figures show that the inertial weight-free PSO-tuned LQR controller outperforms the other controllers and enhances ride comfort without an important deterioration in suspension deflection.

Table 3. ITAE values of controllers in the different road conditions.

Road Profile	Controller	ITAE values
Square road profile	Classical tuned LQR	12.7569
	Standard PSO-tuned LQR	5.2322
	Inertia weight-free PSO-tuned LQR	**5.2296**
Bumpy road profile	Classical tuned LQR	8.9835
	Standard PSO-tuned LQR	8.3998
	Inertia weight-free PSO-tuned LQR	**7.9868**

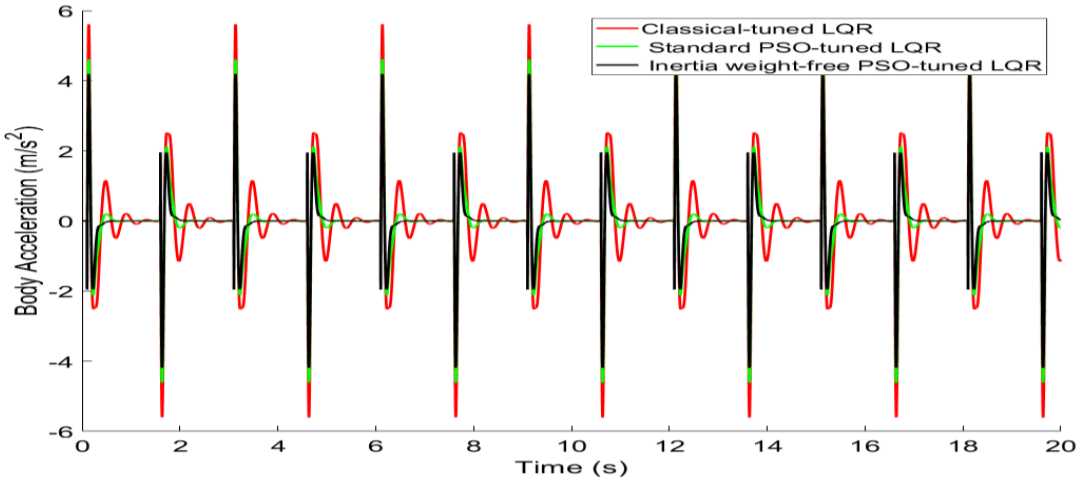

Figure 4. The vehicle body acceleration under the square road disturbance

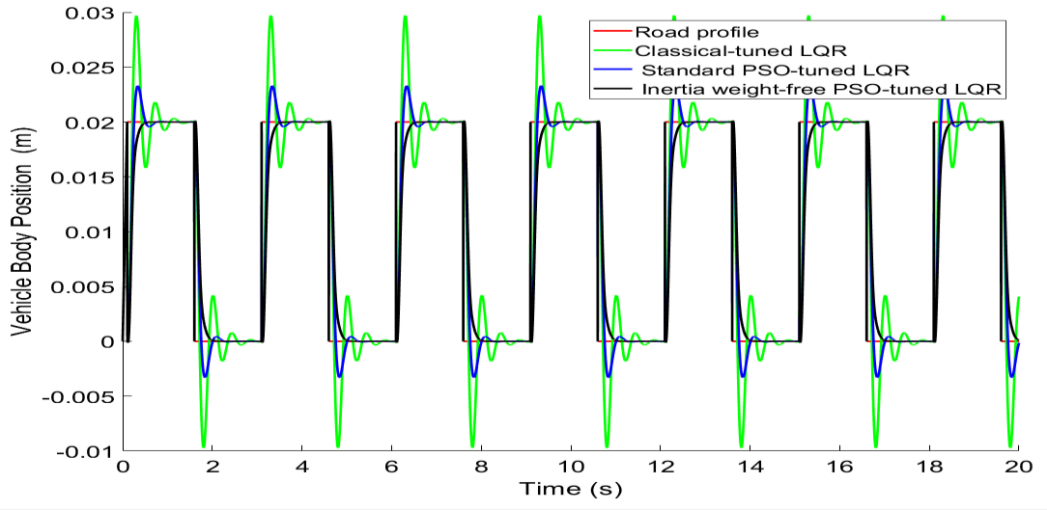

Figure 5. The vehicle body position under the square road disturbance

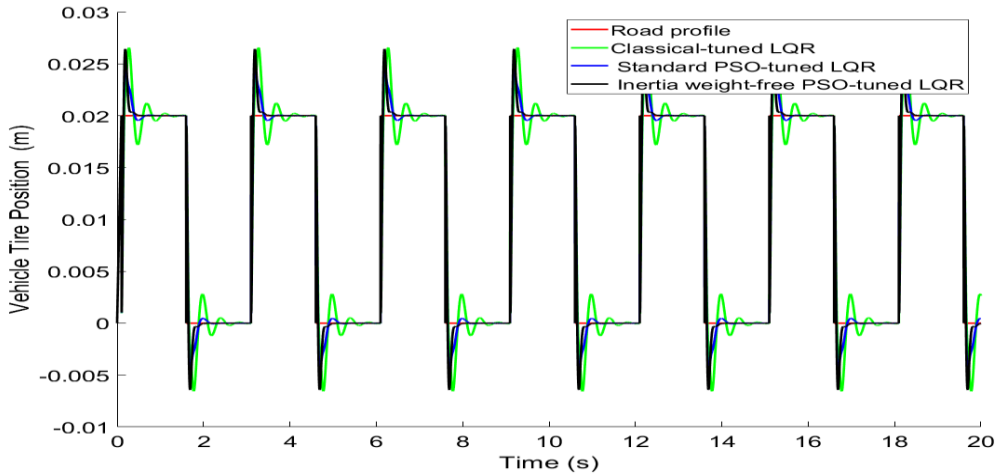

Figure 6. Vehicle tire position under the square road

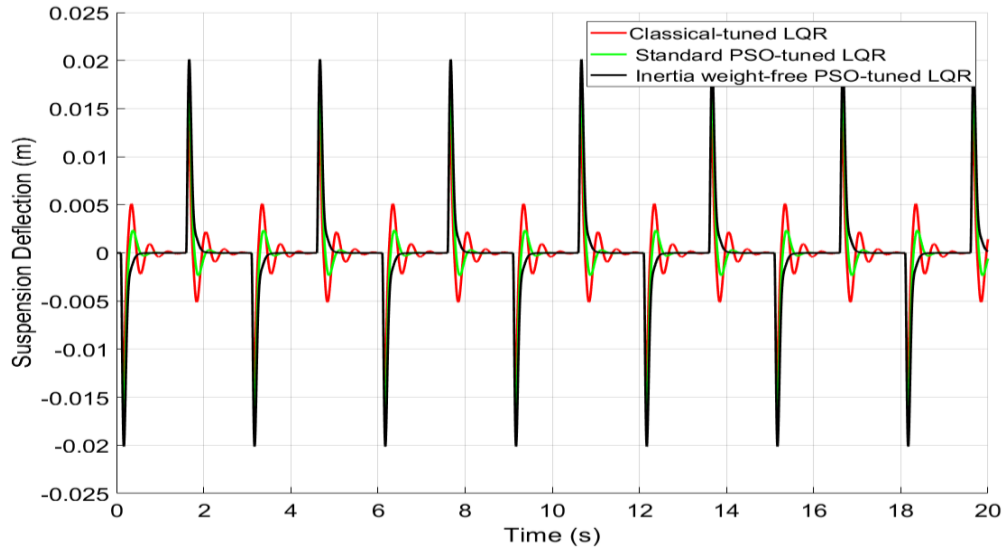

Figure 7. Suspension deflection under the square road

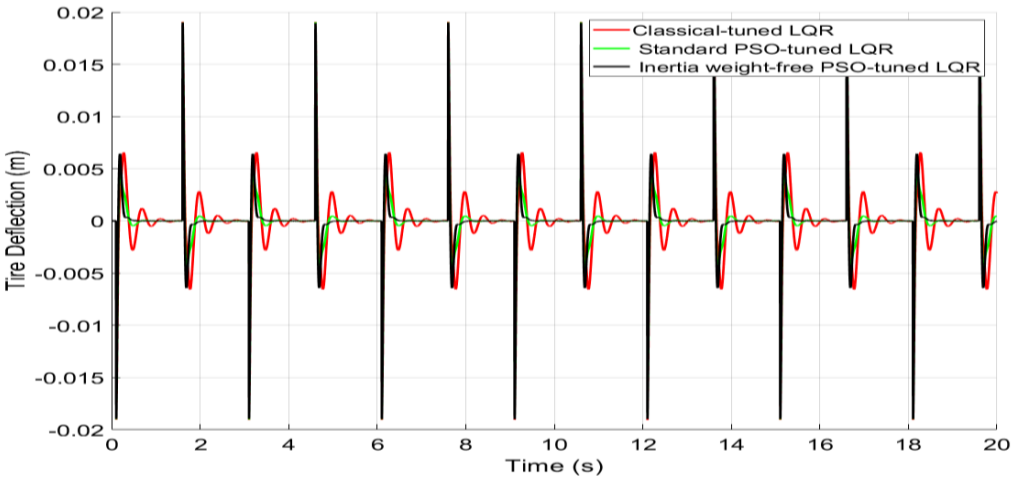

Figure 8. Tire deflection under the square road

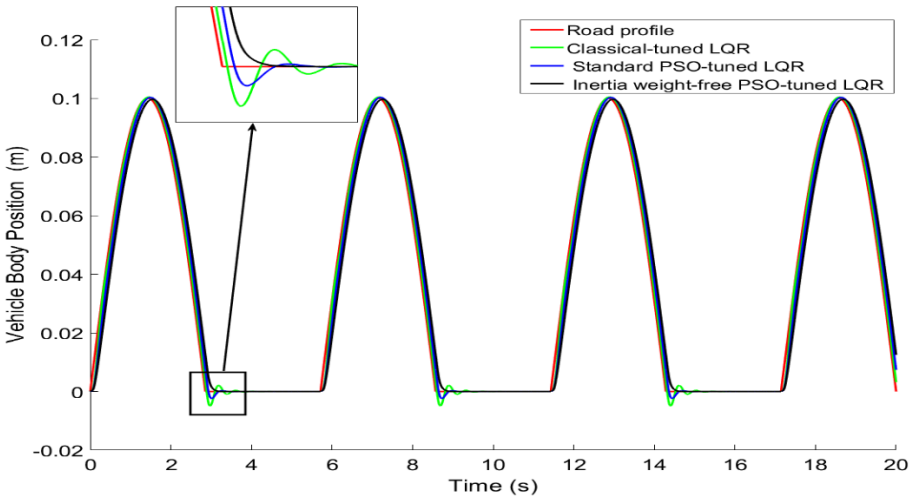

Figure 9. Vehicle body position under the bumpy road

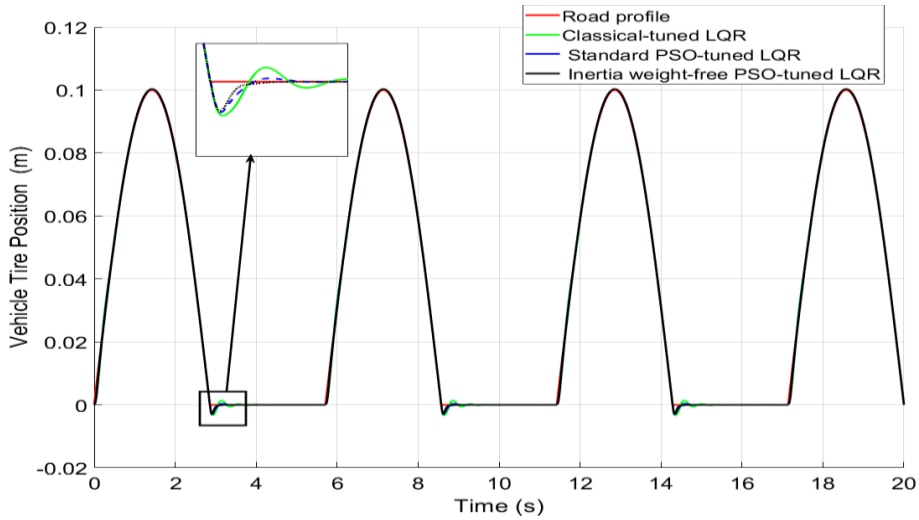

Figure 10. Tire position under the bumpy road

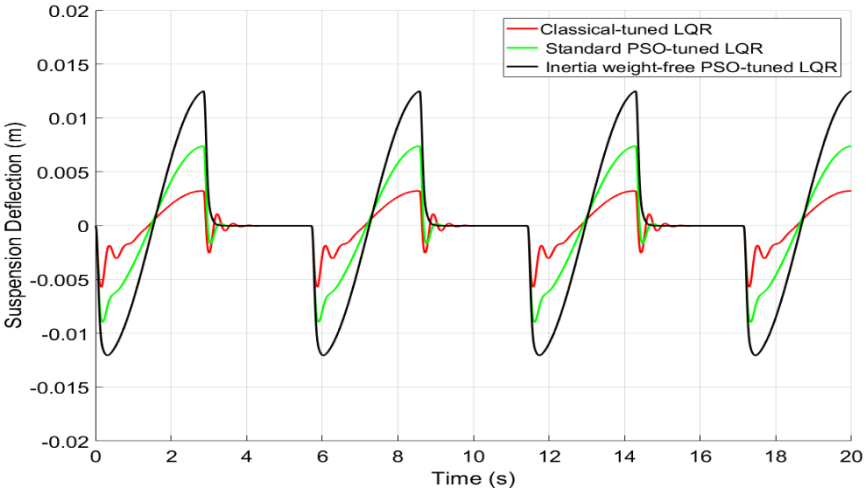

Figure 11. Suspension deflection under the bumpy road

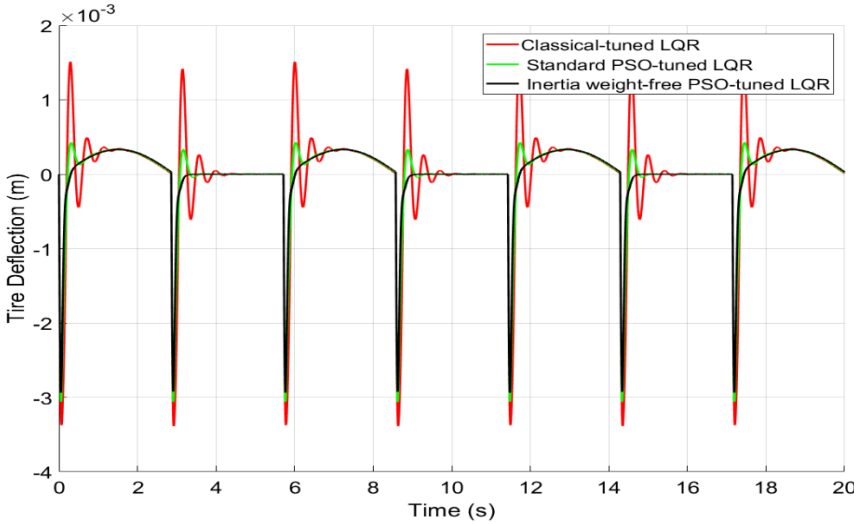

Figure 12. Tire deflection under the bumpy road

4. Conclusions

In this paper, the efficiency of a quarter-active suspension system has been investigated under different road profiles with the optimal control law. To improve ride quality, the inertia weight-free PSO-tuned LQR control law is proposed. Here, the inertia weight-free PSO finds the optimal weighting matrices of the LQR controller so as to satisfy conflicting performance requirements for the quarter-active suspension system. A comparative simulation study is carried out for inertia weight-free PSO-tuned LQR, the standard PSO-tuned LQR controller and the classical-tuned LQR controller. The simulation results demonstrate that the inertia weight-free PSO-tuned LQR controller provides well body and tire position tracking performances and reduces the vehicle body acceleration with the permissible suspension deflection.

Conflict of Interest Statement

There is no conflict of interest between the authors.

Statement of Research and Publication Ethics

The study is complied with research and publication ethics

References

[1] V. S. Deshpande, B. Mohan, P. D. Shendge, and S. B. Phadke, "Disturbance observer based sliding mode control of active suspension systems," *J. Sound Vib.*, vol. 333, no. 11, pp. 2281–2296, 2014.

[2] I. Fialho and G. J. Balas, "Road adaptive active suspension design using linear parameter-varying gain-scheduling," *IEEE Trans. Control Syst. Technol.*, vol. 10, no. 1, pp. 43–54, 2002.

[3] X. Shao, F. Naghdy, and H. Du, "Reliable fuzzy H∞ control for active suspension of in-wheel motor driven electric vehicles with dynamic damping," *Mech. Syst. Signal Process.*, vol. 87, pp. 365–383, 2017.

[4] J. Cao, P. Li, and H. Liu, "An interval fuzzy controller for vehicle active suspension systems," *IEEE Trans. Intell. Transp. Syst.*, vol. 11, no. 4, pp. 885–895, 2010.

[5] A. R. Kaleli and H. İ. Akolaş, "Aktif araç süspansiyon sistemi İçin makine Öğrenimi tabanlı kontrol sisteminin geliştirilmesi," *Bitlis Eren Üniversitesi Fen Bilimleri Dergisi*, vol. 11, no. 2, pp. 421–428, 2022.

[6] M. P. Nagarkar, Y. J. Bhalerao, G. J. Vikhe Patil, and R. N. Zaware Patil, "GA-based multi-objective optimization of active nonlinear quarter car suspension system—PID and fuzzy logic control," *Int. J. Mech. Mater. Eng.*, vol. 13, no. 1, 2018.

[7] A. Unger, F. Schimmack, B. Lohmann, and R. Schwarz, "Application of LQ-based semi-active suspension control in a vehicle," *Control Eng. Pract.*, vol. 21, no. 12, pp. 1841–1850, 2013.

[8] S. Manna *et al.*, "Ant colony optimization tuned closed-loop optimal control intended for vehicle active suspension system," *IEEE Access*, vol. 10, pp. 53735–53745, 2022.

[9] J. S. David Reddipogu and V. K. Elumalai, "Hardware in the loop testing of adaptive inertia weight PSO-tuned LQR applied to vehicle suspension control," *J. Control Sci. Eng.*, vol. 2020, pp. 1–16, 2020.

[10] A. E. Bryson, "*Control of spacecraft and aircraft* (Vol. 41)". Princeton: Princeton university press, 1993.

[11] H. Maghfiroh, M. Nizam, M. Anwar, and A. Ma'Arif, "Improved LQR control using PSO optimization and Kalman filter estimator," *IEEE Access*, vol. 10, pp. 18330–18337, 2022.

[12] K. Hassani and W.-S. Lee, "Multi-objective design of state feedback controllers using reinforced quantum-behaved particle swarm optimization," *Appl. Soft Comput.*, vol. 41, pp. 66–76, 2016.

[13] E. Vinodh Kumar, G. S. Raaja, and J. Jerome, "Adaptive PSO for optimal LQR tracking control of 2 DoF laboratory helicopter," *Appl. Soft Comput.*, vol. 41, pp. 77–90, 2016.

[14] S. B. Karanki, M. K. Mishra, and B. K. Kumar, "Particle swarm optimization-based feedback controller for unified power-quality conditioner," *IEEE Trans. Power Deliv.*, vol. 25, no. 4, pp. 2814–2824, 2010.

[15] X. Shao, J. Zhang, and X. Zhang, "Takagi-Sugeno fuzzy modeling and PSO-based robust LQR anti-swing control for overhead crane," *Mathematical Problems in Engineering*, vol. *2019*, p. 14, 2019.

[16] T. Yuvapriya, P. Lakshmi, and V. K. Elumalai, "Experimental validation of LQR weight optimization using bat algorithm applied to vibration control of vehicle suspension system," *IETE J. Res.*, pp. 1–11, 2022.

[17] R. R. Das, V. K. Elumalai, R. Ganapathy Subramanian, and K. V. Ashok Kumar, "Adaptive predator–prey optimization for tuning of infinite horizon LQR applied to vehicle suspension system," *Appl. Soft Comput.*, vol. 72, pp. 518–526, 2018.

[18] Quanser, Active Suspension System: User Manual, Quanser Corporation, Ontario, Canada, 2009.

[19] Q. Chen, B. Liu, Q. Zhang, J. J. Liang, P. N. Suganthan, and B. Y. Qu, "Problem definitions and evaluation criteria for CEC 2015 special session on bound constrained single-objective computationally expensive numerical optimization," *Al-roomi.org*. [Online]. Available:https://alroomi.org/multimedia/CEC_Database/CEC2015/RealParameterOptimization/ExpensiveOptimization/CEC2015_ExpensiveOptimization_TechnicalReport.pdf. [Accessed: 05-Apr-2023].

[20] M. R. Tanweer, S. Suresh, and N. Sundararajan, "Improved SRPSO algorithm for solving CEC 2015 computationally expensive numerical optimization problems," in *2015 IEEE Congress on Evolutionary Computation (CEC)*, 2015.

[21] J. L. Rueda and I. Erlich, "MVMO for bound constrained single-objective computationally expensive numerical optimization," in *2015 IEEE Congress on Evolutionary Computation (CEC)*, 2015

[22] E. O. Wilson, *Sociobiology: The New Synthesis*, 25th ed. London, England: Harvard University Press, 2000.

[23] W. Zhang, *Selforganizology: The science of self-organization*. WORLD SCIENTIFIC, 2016.

[24] C. W. Reynolds, "Flocks, herds and schools: A distributed behavioral model," *Comput. Graph. (ACM)*, vol. 21, no. 4, pp. 25–34, 1987.
[25] J. Kennedy and R. Eberhart, "Particle swarm optimization," in *Proceedings of ICNN'95 - International Conference on Neural Networks*, 2002.
[26] W. J. Zhang, "Particle swarm optimization: A Matlab algorithm," *Iaees.org*. [Online]. Available:http://www.iaees.org/publications/journals/selforganizology/articles/2022-9(3-4)/particle-swarm-optimization-Matlab-algorithm.pdf. [Accessed: 05-Apr-2023].
[27] C. Blum, M. J. B. Aguilera, A. Roli, and M. Sampels, Eds., *Hybrid metaheuristics: An emerging approach to optimization*. Berlin, Heidelberg: Springer Berlin Heidelberg, 2008.
[28] I. H. Osman and G. Laporte, "Metaheuristics: A bibliography," *Ann. Oper. Res.*, vol. 63, no. 5, pp. 511–623, 1996.
[29] M. Jaberipour, E. Khorram, and B. Karimi, "Particle swarm algorithm for solving systems of nonlinear equations," *Comput. Math. Appl.*, vol. 62, no. 2, pp. 566–576, 2011.

Bitlis Eren Üniversitesi Fen Bilimleri Dergisi
BİTLİS EREN UNIVERSITY JOURNAL OF SCIENCE
ISSN: 2147-3129/e-ISSN: 2147-3188
VOLUME: 12 NO: 3 PAGE: 686-703 YEAR: 2023
DOI:10.17798/bitlisfen.1282555

Geotechnical and Structural Investigations in Malatya Province after Kahramanmaraş Earthquakes on February 6, 2023

Özgür YILDIZ[1], Ceren KINA[1*]

[1]*Malatya Turgut Ozal University, Faculty of Engineering and Natural Sciences, Department of Civil Engineering, Malatya, Türkiye*
(ORCID: 0000-0002-3684-3750) (ORCID: 0000-0002-2054-3323)

Keywords: Kahramanmaraş earthquake, Reinforced concrete buildings, Collapse, Damage, Earth structures, Geotechnical investigation.

Abstract
Two earthquakes with moment magnitudes of 7.7 and 7.6 occurred on February 6, 2023, at 04:17 a.m. (with local time, GMT+3) in Kahramanmaraş-Ekinözü Pazarcık and at 13:24 p.m. (with local time, GMT+3) in Kahramanmaraş-Elbistan, respectively, in Türkiye. The earthquake was felt in a wide area within Türkiye and caused structural destruction and heavy damage to buildings, especially in eleven cities, including Adana, Adıyaman, Diyarbakır, Gaziantep, Hatay, Kahramanmaraş, Kilis, Malatya, Osmaniye, Şanlıurfa and Elazığ. The aim of this study was to present a detailed field investigation in Malatya province, which was one of the most affected cities in the region. The strong ground motion records have been analyzed, and PGA distribution maps were presented. Structural, design, and manufacturing defects in damaged and collapsed buildings were examined. The performance of soil structures was examined, and the defects demonstrated were evaluated in the context of the geological environment. The study is essential in terms of evaluating the damage and possible causes of the building stock in Malatya city center and its districts after the earthquake. In this sense, a holistic evaluation has been carried out, which can be a useful resource for Anatolian cities with typical building characteristics.

1. Introduction

On February 6, 2023, at 04:17 local time (GMT +03:00) in Ekinözü Pazarcık Kahramanmaraş (Lat: 37.288, Longitude: 37.043) and at 13:24 (GMT +03:00) in Elbistan Kahramanmaraş (Lat: 38.089), Longitude: 37.239), two earthquakes with moment magnitudes of Mw 7.7 and Mw 7.6 occurred at a depth of 7.7 and 8.6 km, respectively. The earthquake was felt in a wide geography within the borders of Türkiye, especially in Adana, Adıyaman, Diyarbakır, Gaziantep, Hatay, Kahramanmaraş, Kilis, Malatya, Osmaniye, Şanlıurfa and Elazığ, and in Syria as well as in Türkiye, and caused significant structural destruction. Between February 6 and 9, when the earthquake took place, more than 3000 aftershocks, varying in magnitude between M 4 and M 6.6, occurred within a radius of 350 km in Pazarcık and Elbistan epicenters [1]. The settlements in the impact area of both earthquakes are located in the East Anatolian Fault Zone (EAFZ). The fault mechanism of earthquakes is left lateral strike-slip.

Various levels of destruction, loss of life and property, and injuries occurred in 11 city centers and districts within the impact area of the earthquakes. According to the Türkiye Earthquake Recovery and Reconstruction Assessment Report published by the Presidency of Strategy and Budget and the findings of the Ministry of Treasury and Finance, the total amount of material damage caused by earthquakes is 1.6 trillion ₺. It is recorded that the material and financial total cost of the earthquake was 103.6 billion dollars. Housing damages constitute the most important component of the total financial burden created by the earthquake on the Turkish economy, with 54.9 percent (i.e., 1,073.9 billion Turkish liras (₺)/56.9 billion dollars). Demolitions in public infrastructure and service buildings are considered the second-ranked damages in terms of financial burden (i.e., 242.5 billion Turkish liras (₺)/12.9 billion dollars). According to current field data, Malatya city

*Corresponding author: ceren.kina@ozal.edu.tr
Received: 13.04.2023, Accepted: 07.08.2023

center and its districts have 5,393 collapsed buildings that urgently need to be demolished.

The epicentral distances of 105 and 170 km from the epicenters of the Pazarcık (Mw 7.7) and Elbistan (Mw 7.6) earthquakes and other parameters caused significant destruction in Malatya city center and its districts (Fig. 1). When both earthquakes are evaluated from a technical point of view, he stated that the Pazarcık (Mw 7.7) earthquake undoubtedly caused demolition and structural damage, but a significant part of the destruction observed in Malatya city center occurred with the subsequent Elbistan (Mw 7.6) earthquake. Among many other parameters, epicentral distance is considered to be highly influential on the intensity of structural destruction. Official figures indicate that 8365 buildings were collapsed or heavy damaged and 9905 were moderately and slightly damaged based on the first post-earthquake damage observations carried out by the Ministry of Environment, Urbanization and Climate Change.

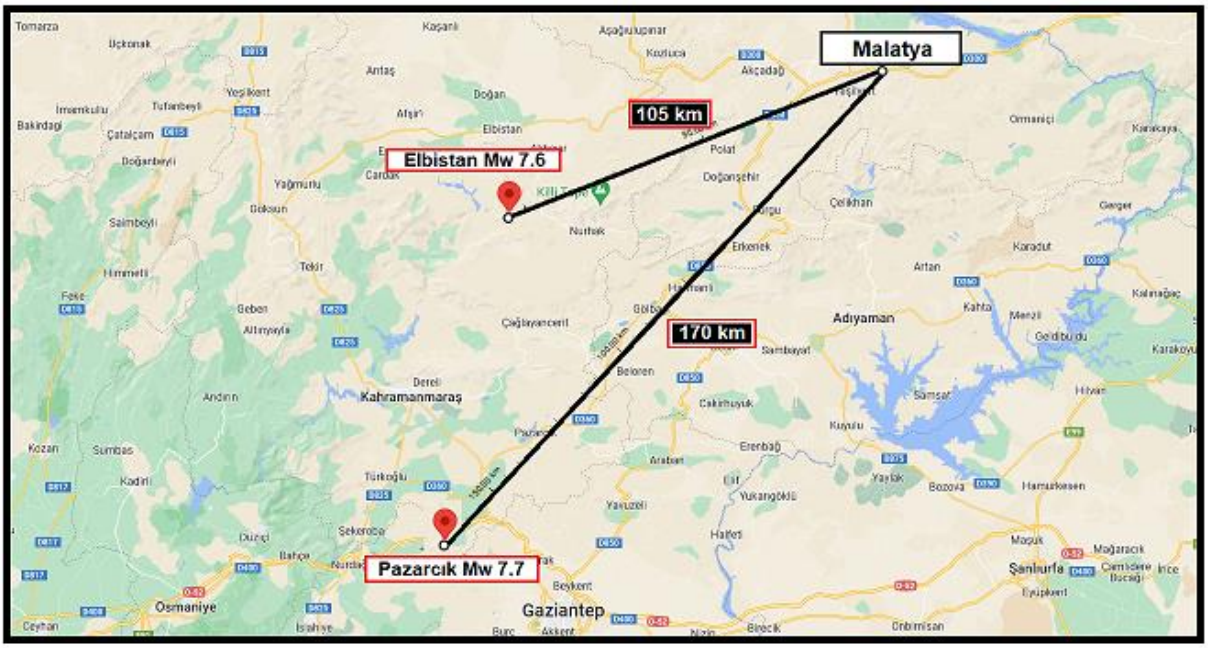

Figure 1. Distance from Malatya to the epicenter of the Pazarcık (Mw 7.7) and Elbistan (Mw 7.6) earthquakes

In general, damage is defined as a stability problem that arises during the life of a building exceeds the tolerance limits. Structural damage, on the other hand, can be defined as the complete or partial loss of the standard or defined features of a building or building element for any reason during use and the loss of its service function. Historical earthquakes show that earthquakes are the primary cause of structural damage in these buildings [2]. The probability of damage to buildings that are not taken care of during design and construction varies depending on the magnitude of the earthquake [3]. Although the destruction in residential areas is mostly in the foreground due to the loss of life it causes, the types of collapse and damage to other civil structures are also important in terms of both affecting the continuation of civil life and making engineering evaluations necessary.

There are some studies in the literature related to the damage to buildings caused by the earthquakes in the different seismic regions. Nemutlu et al. [4], Sayın et al. [5], and Işik et al. [6] investigated the structural damages of masonry and reinforced concrete buildings after 2020 Elazığ-Sivrice earthquake. Bilgin et al. [7] carried out a detailed field survey after the 2019 Albania earthquake and evaluated the performance and damages of masonry buildings. Işık et al. [8] studied the time-dependent seismicity model of the North Anatolian Fault Zone earthquakes. Nemutlu et al. [9] investigated the assessment of earthquake preparedness of existing buildings in Bingöl province, and in another work [10], they estimated the probabilistic hazard for Bingöl province. In the study of Işık [11], the seismic parameters were obtained for M $\geq$6 earthquakes in Türkiye after 1900, and the measured and current peak ground acceleration values were compared. The structural damages to masonry buildings, mosques, and minarets in Adıyaman after the Kahramanmaraş earthquakes were also investigated by the studies of Işık et al. [12], [13]. Besides, Kocaman [14] investigated the influence of Kahramanmaraş earthquakes on historical masonry minarets and mosques.

In this study, the damage and collapse of the structures in Malatya center and its districts caused by the earthquakes on February 6 are evaluated. Inferences are presented as a result of field observations and examinations carried out in 8 districts, two of which are central districts. Earthquake damages are examined in relation to local soil properties and other earthquake parameters. The structural damage caused by these two major earthquakes in the historical period is revealed, and the local construction practices are criticized.

2. Seismicity and Site Description

The EAFZ, which lies between Bingöl Karlıova and Antakya, consists of six segments from northeast to southwest between Karlıova-Bingöl, Palu-Hazar Lake, Hazar-Sincik, Çelikhan-Gölbaşı, and Gölbaşı-Türkoğlu. In the historical period, the Eastern Anatolian Fault System formed an earthquake series that started with the 1822 Antakya earthquake. Erdik [15] reports two devastating earthquakes in CE115 and 526 that claimed more than 500.000 lives. A devastating earthquake was produced by Karlıova-Bingöl segment in 1866, and in 1872, another damaging earthquake was propagated by the Türkoğlu-Antakya segment. The other destroyed earthquakes occurred on the Palu-Hazar Lake and Hazar Lake-Sincik segments in 1874 and 1875, respectively. The last earthquake on the EAFZ occurred in 1893 on Çelikhan-Gölbaşı segment. The 1905 earthquake destroyed many villages between Çelikhan and Pütürge towns. In the last century, except for the 1971 Bingöl and 2020 Sivrice earthquakes, the Eastern Anatolian Fault System entered a quieter period and did not produce an earthquake large enough to cause a surface rupture. The EAFZ System, with a total length of 600 km and consisting of 6 different segments with lengths ranging from 50 to 145 km, dates back to BC 17-1900 in the historical period (Fig. 2). 30-AD 100; M.S. 700's; M.S. 1100's, M.S. It produced five main series of earthquakes in the 1500s and 1800s. Since EAFS has a very low shear rate of 5-8 mm/year, earthquakes with a magnitude of 7.0-7.5 are repeated at very long intervals [16]. The province of Malatya is located in the east of Türkiye, with an area of 12,313 km^2 and a population of approximately 800,000, in a geography surrounded by this intense tectonic activity. As can be seen in the active fault map of Türkiye, Doğanşehir-Surgu Faults are located in the south, and the part of the EAFZ passing through Pürge-Doğanyol and the Malatya Fault are tectonic structures that affect the city significantly. Coulomb stress transfer studies carried out after the Sivrice (Mw 6.8) earthquake indicated that the seismic potential of the Palu-Hazar and Çelikhan-Gölbaşı segments increased [17]. According to the 1996 Earthquake Zones Map published by the Türkiye Ministry of Public Works and Settlement General Directorate of Disaster Affairs, Malatya and its districts are located in the I to III degree earthquake zones. Malatya PGA is defined as 475 (years) in the earthquake hazard map of Türkiye, and the maximum acceleration value varies between 0.2g and 0.7g [18]. Considering the geology of the Malatya, detailed simulations were performed to assess the seismic response of the local soils under recent earthquakes [19], [20].

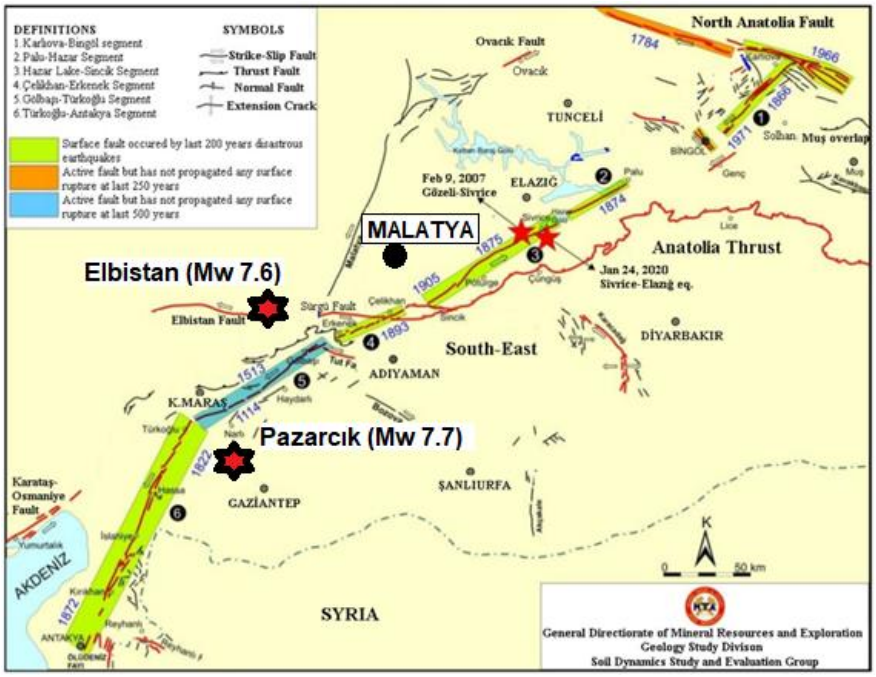

Figure 2. Main segments of the East Anatolian Fault Zone and damaging earthquakes [18]

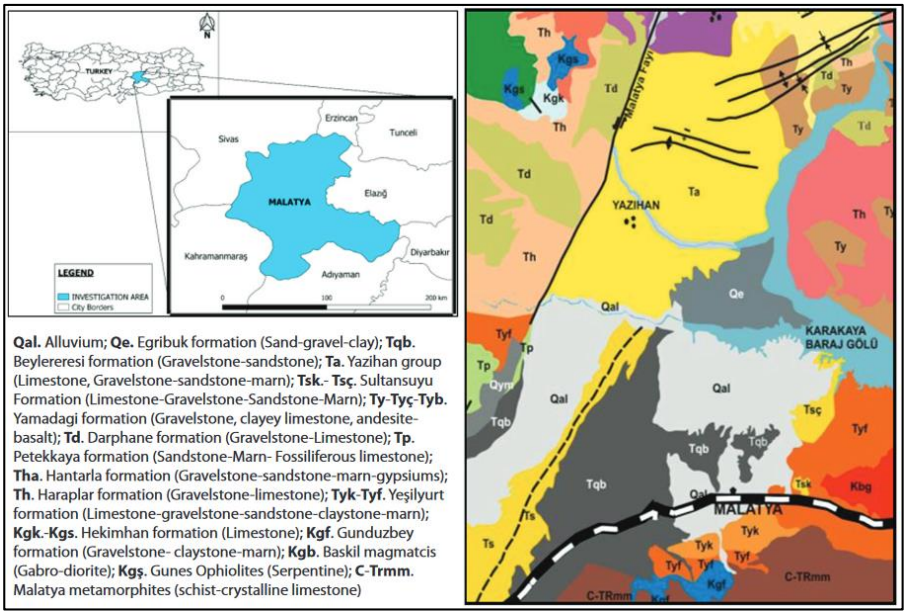

Figure 3. Site location and general geological map of the region [21]

The general geological map of Malatya is presented in Fig. 3. The geological units on which the city center is built can be evaluated in two categories: the south and north of the highway extending on the east-west axis. The northern part of the city consists mostly of the Beylerderesi formation, where alluvial units and conglomerate-sandstone units are stacked. In the south, the lithology is represented by limestone-conglomerate-marl units known as Yeşilyurt formation. The eastern side of the city was built on units where magmatic rocks were stacked.

3. Ground Motions

The acceleration records of the February 6 earthquakes were downloaded from the 'General Directorate of Disaster Affairs' (i.e., AFAD) official site on February 11. The measured instrumental peak ground acceleration of the Pazarcık (Mw 7.7) earthquake was recorded at TK4614 Kahramanmaraş station, with 1966.74 cm/s^2 (2.00 g) belonging to the EW component (Fig. 4a, b). The activity depth was 8.6 km, and the Vs_{30} shear wave velocity of the station location was reported as 671 m/s. The epicentral distance to the focal point of the

earthquake was recorded at 31.42 km. According to the 5% damping ratio, the dominant period of the spectral acceleration was found to be in the range of 0.1-0.2 s. The peak velocity value was calculated as 0.552 m/s and the maximum displacement as 0.186 m. The significant duration of the earthquake was calculated as 24.06 s between 39.71 and 63.77 s. The acceleration time history and response spectra of the NS component of the motion are presented in Figs.4c, d. The highest measured instrumental peak ground acceleration of the north-south (NS) component was recorded as 1948,767 cm/s^2 (1.99 g). It was observed that the dominant period of the spectral acceleration occurs in the range of 0.1-0.2 s, according to the 5% damping ratio. The peak velocity value was calculated as 0.818 m/s and the maximum displacement was calculated as 0.232 m, respectively. The significant duration of the earthquake was calculated as 23.15 s between 39.81 and 62.96 s. The peak acceleration of the vertical component of the earthquake (UD) was recorded as 1352.510 cm/s^2.

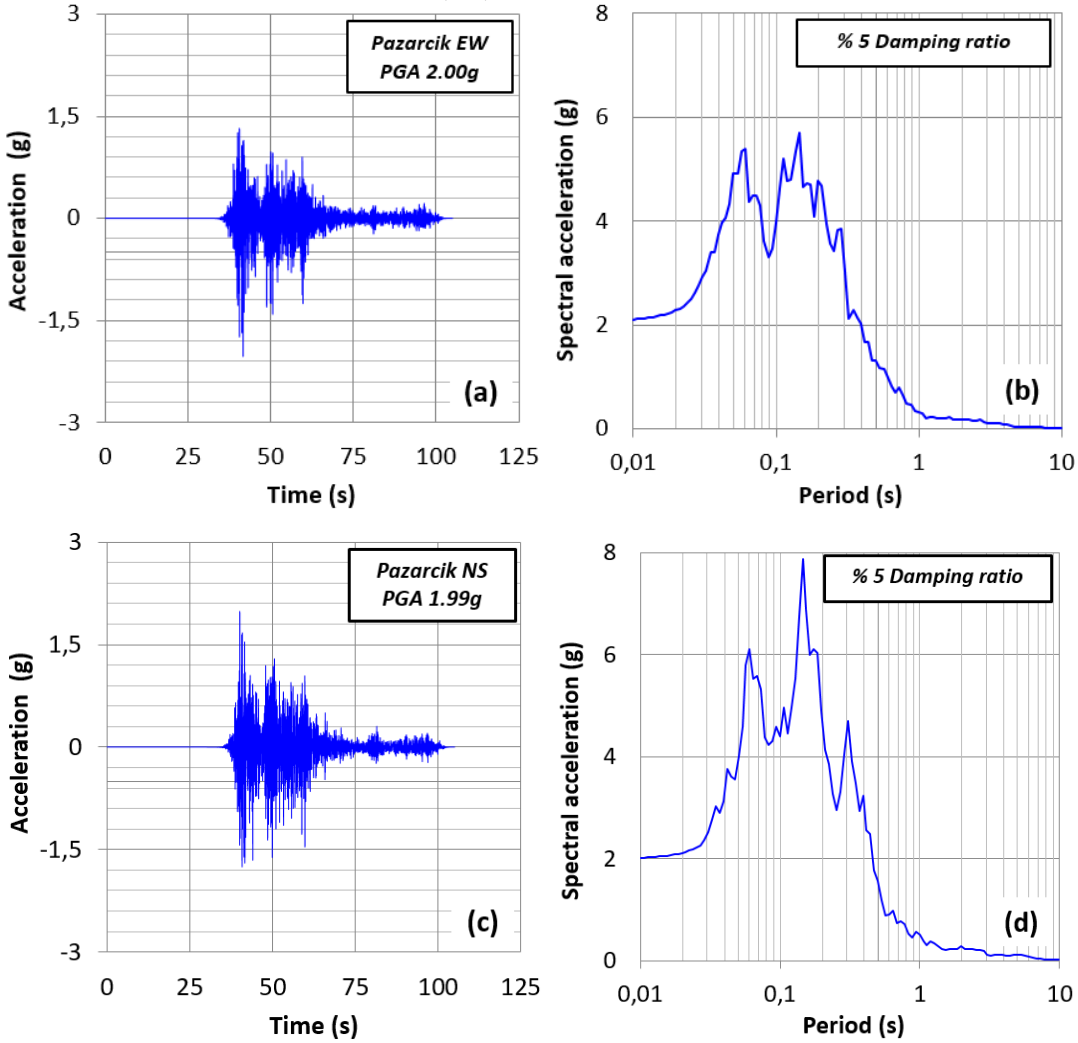

Figure 4. Acceleration-time history and response spectra of Pazarcık earthquake (Mw 7.7); (a, b) EW and (c, d) NS components

The highest acceleration record of the east-west (EW) component of the Elbistan (Mw 7.6) earthquake that occurred during the period following the Pazarcık (Mw 7.7) earthquake was at TK4612 Göksun station at 520.662 cm/s^2 (0.531 g), (Fig. 5a). The dominant period of the spectral acceleration was recorded as 0.4 s according to the 5% damping ratio (Fig. 5b). The activity depth is 7 km, and the Vs_{30} shear wave at the station location is reported as 246 m/s. The epicentral distance to the focal point of the earthquake was calculated at 66.68 km. The peak velocity value was calculated as 0.725 m/s, and the maximum displacement was calculated as 0.574 m. The significant duration of the earthquake was calculated as 25.9 s between 30.60 and 56.50 s. The peak acceleration value of the vertical component of the earthquake was recorded as 430.195 cm/s^2. The highest acceleration record of the north-south (NS) component was measured at 627.184 cm/s^2 (0.64g) (Fig. 5c). The dominant period was recorded as 0.5 s according to the 5% damping ratio (Fig.5d). The peak velocity value was

calculated as 1.707 m/s, and the maximum displacement was calculated as 0.679 m. The significant duration of the earthquake was calculated as 20.14 s between 30.99 and 51.13 s**.** The spectra obtained from the EW and NS components of Elbistan earthquake (#4406 Akçadağ station) are quite above the elastic design spectra defined by Turkish Building Earthquake Code [22], which corresponds to the DD-2 earthquake level with a 10% probability of exceedance in 50 years (Fig. 6)

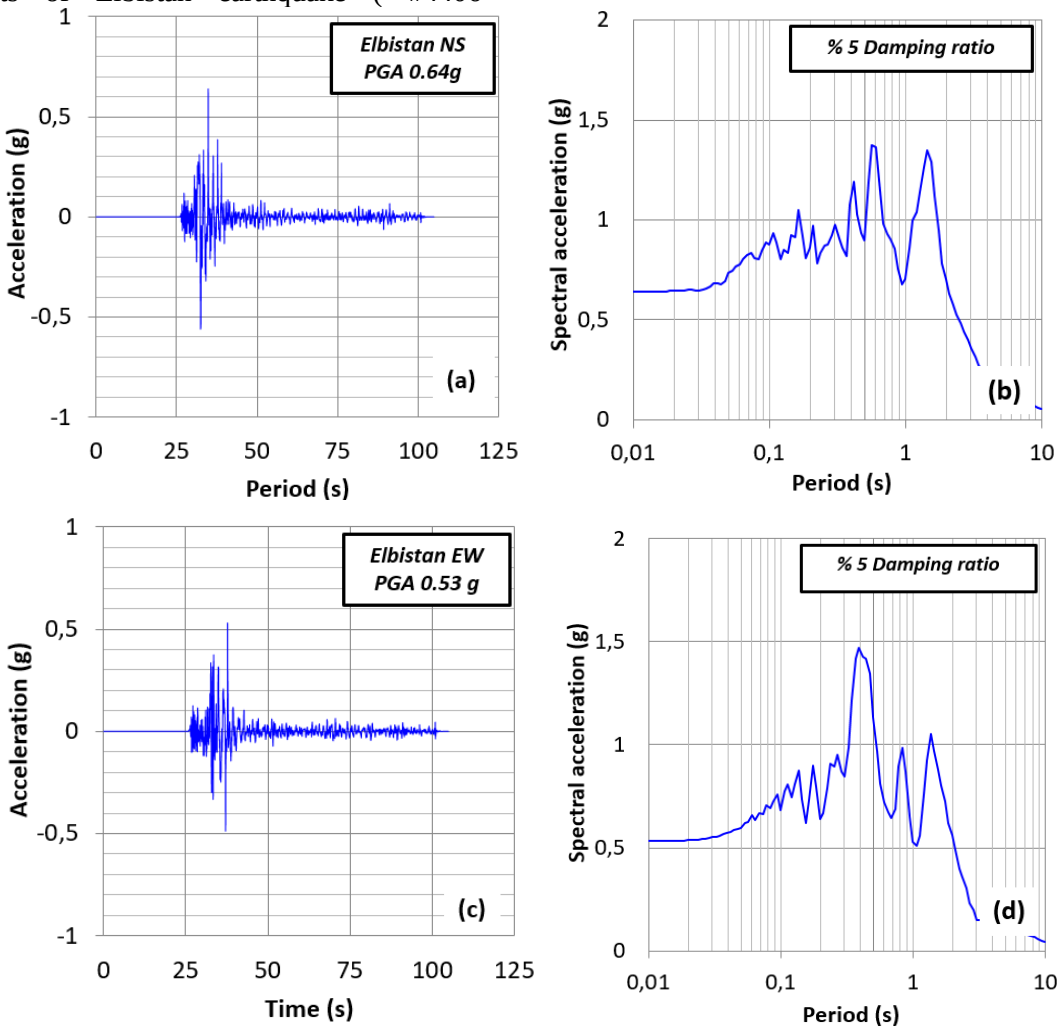

Figure. 5 Acceleration-time history and response spectra of Elbistan earthquake (Mw 7.7); (a, b) NS and (c, d) EW components

The damages and destruction caused by the Pazarcık and Elbistan earthquakes occurred as a result of many parameters. The intensity distribution of the earthquake in Malatya city center and its districts, with distances of 105 and 170 km, respectively, is shown on maps. It is observed that the intensity of the Pazarcık (M_W 7.7) earthquake increases from the city center to the southwest as expected (Fig. 7). While the earthquake was felt in the city center with a magnitude of MMI 7-8, it caused damage and destruction in buildings with low construction quality. It is seen that MMI 6 is felt as one moves north from the city center (i.e., in the direction of Darende and Akçadağ in the north and in the direction of Kale in the east). Instant investigations on the effects of the Elbistan earthquake (Mw 7.6), which took place within the hours following the Pazarcık (Mw 7.7) earthquake (i.e., approximately nine hours later), showed that a significant part of the destruction occurred as a result of the Elbistan earthquake. This situation also coincides with the Elbistan earthquake intensity distribution map. In fact, the effects of the earthquake in the city center correspond to much greater intensities (Fig. 8). In general, intensity distribution maps largely reflect post-earthquake observations in the area.

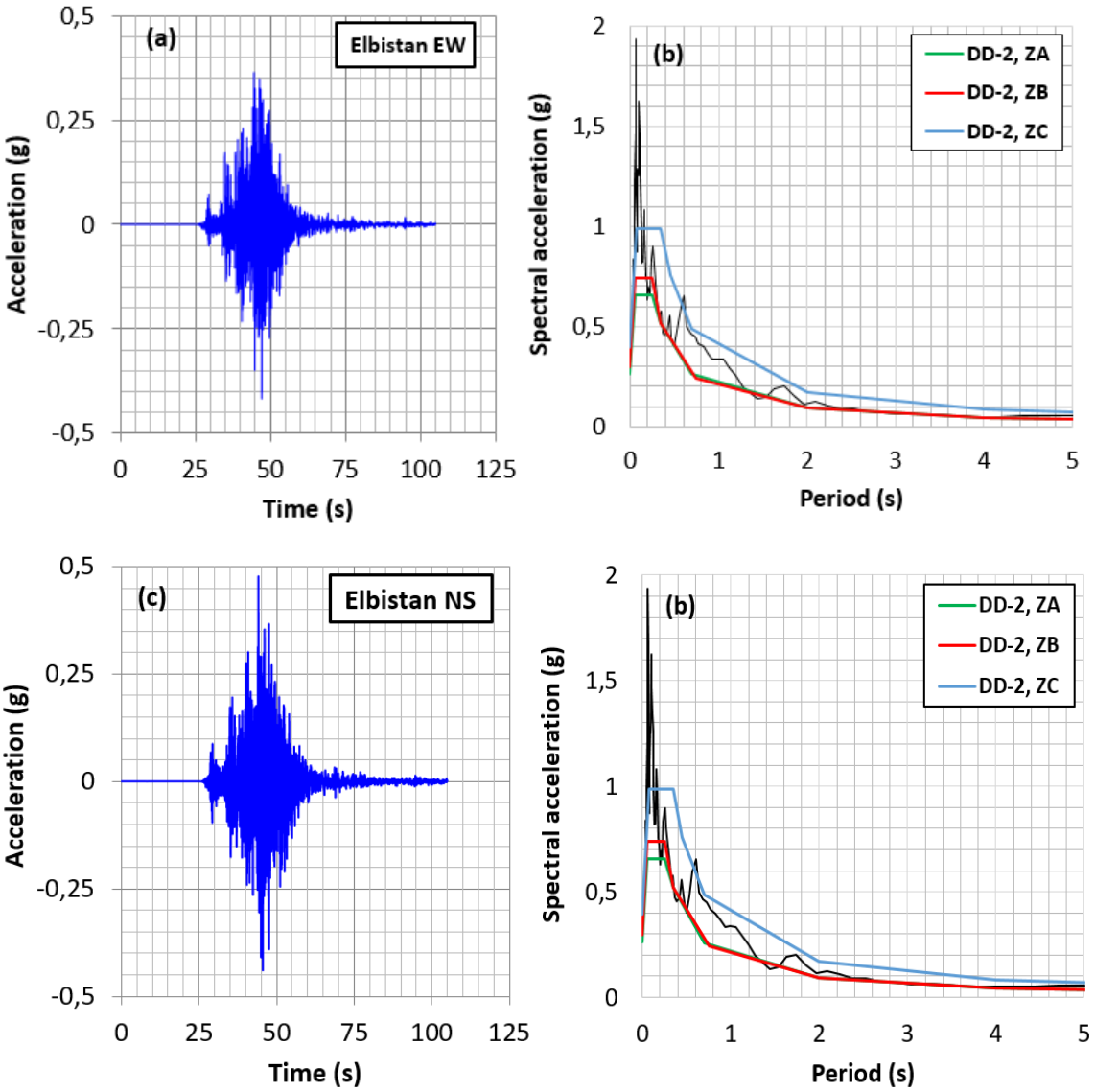

Figure. 6 Acceleration-time history and response spectra of Elbistan earthquake (Mw 7.6); (a, b) EW and (c, d) NS components (#4406 station)

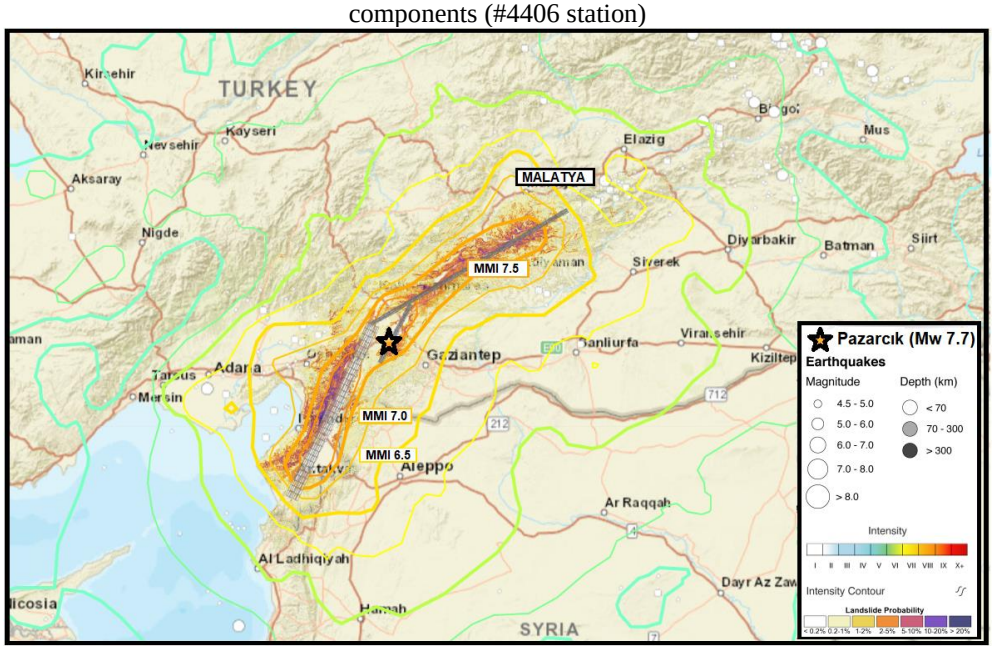

Figure 7. The intensity distribution map of Pazarcık (Mw 7.7) earthquake

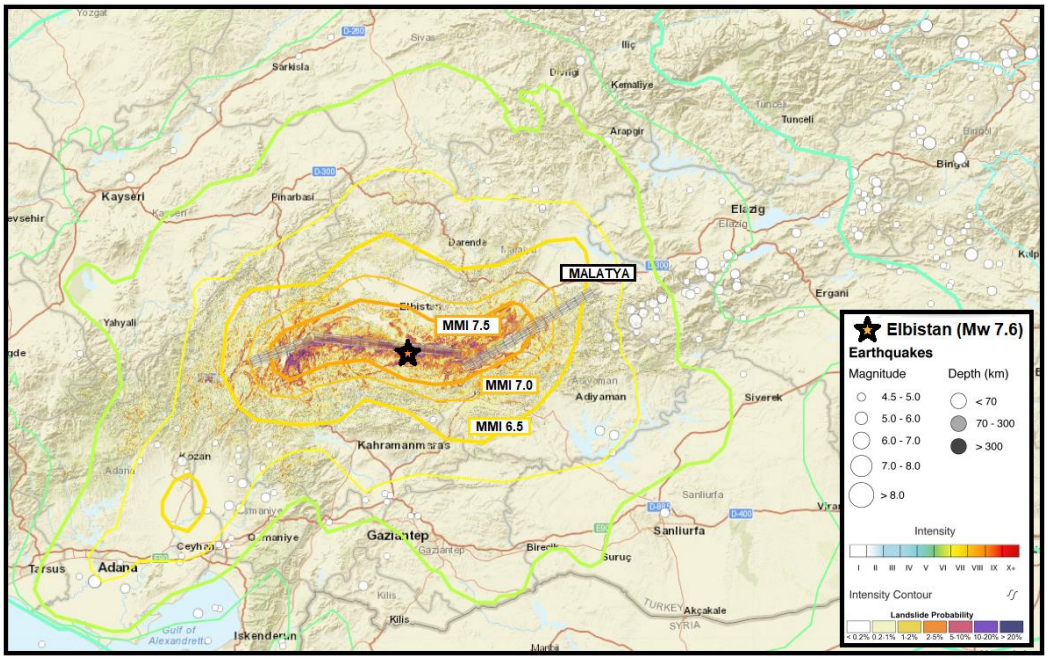

Figure 8. The intensity distribution map of Elbistan (Mw 7.6) earthquake

4. Distribution of Structural Damages

The building stock of the city center of Malatya involves generally reinforced concrete buildings and masonry buildings in rural areas. In the city center and in the countryside of Doğanşehir, Akçadağ, and Darende villages of Malatya, structural and non-structural damage as well as collapses were observed in most of the buildings, resulting in more than 1000 deaths.

The population of Malatya is nearly 815.000, and there are 32.344 buildings in the city center. According to the first post-earthquake damage observations carried out by the Ministry of Environment, Urbanization, and Climate Change, the damage distribution in Malatya province was shown in Fig 9.

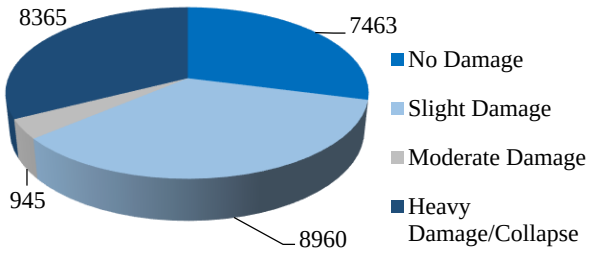

Figure 9. Ministry of Environment, Urbanization and Climate Change damage detection findings on February 16, 2023

4.1. Structural Properties of the Building Stock

The quality of the buildings in the city center of Malatya shows variations. In the building stock, there are old and newly built reinforced concrete buildings with up to 15 stories and also lots of masonry buildings in the rural areas. It is seen that the buildings in the very center of the city, especially in the region where commercial enterprises are concentrated, were generally built before the year 2000. The building inspection was arranged and legally regulated after the earthquakes on August 17 and November 12, 1999, in Kocaeli and Düzce. As a result of these earthquakes, awareness of seismic resistance increased, and a new reinforced concrete design requirement (TS500) [23] was started to be used, so buildings built prior to the year 2000 can be defined as uncontrolled buildings. According to the observations, these old adjacent reinforced concrete structures with no separation distance exhibited heavy damage and many of them even collapsed.

There have been many major earthquakes in the history of Türkiye, resulting in a great deal of destruction and death. After these tragic events, the earthquake regulations of Türkiye have been revised many times, and some vital practical and conceptual changes have occurred. One of the most striking improvements from the Turkish Building Earthquake Code-1975 [24] to Turkish Building Earthquake Code-2018 [22] was the change in column and column-beam connection sections. In

Malatya region, there are many buildings built before the Turkish Building Earthquake Code-2007 [25]. However, the collapsed and heavily damaged buildings were generally built before 2000. The most important drawbacks of these buildings were the use of non-deformed bars, the insufficiency of stirrups, and not using ready-mixed concrete.

4.2. Damages in Reinforced Concrete Buildings

- *The damage in old buildings (prior to 2000)*

The building stock in the very center of the city, especially in the region where commercial enterprises are concentrated, is commonly old and adjacent structures with no or not enough dilatation. These buildings, which were generally built prior to 2000, are mid-rise with infill walls. A modern reinforced concrete design guide (TS 500) [22] was issued on October 12, 2000, and it mandated the use of ready-mixed concrete and ductile low-carbon steel. Besides, this guide improved the detailing of the steel bars and banned the use of non-deformed bars. It was observed that most of the buildings built prior to 2000 were collapsed, immediately demolished, or heavily damaged (Fig. 10). The main defects in these buildings were the use of non-deformed bars, the inadequacy of stirrups, and the low strength properties of concrete due to the use of hand-mixed concrete.

Figure 10. Totally collapsed buildings in Malatya

Figure 11. The observed damages in the old buildings in the city center, caused by the insufficiency in stirrups and the use of non-deformed steel bars

Observing Fig. 11, the longitudinal bars buckled due to the wide stirrup spacing, so the bond strength of the concrete-steel bar could not be achieved and the concrete was crushed. Besides, it is also striking that the bond strength of concrete-steel bars was not provided due to the use of non-deformed steel bars.

- *Pounding effect*

As mentioned above, the old building stock in the city center was commonly built as adjacent structures with no or not enough seismic gaps. For these kinds of structures, in order to exhibit the least damage caused by the earthquake motion, a sufficient seismic gap element should be placed or a seismic gap should be left between the buildings. Based on the code, the minimum seismic gap should be 30 mm up to 6 m in height. Moreover, a minimum of 10 mm should be added for every 3 m of height increase. In the opposite case, a pounding effect can cause harm to the structural elements of buildings. Another defect observed in the collapsed or damaged reinforced concrete buildings can be explained by the fact that they were built at different times as adjacent buildings, and they damaged each other's load-bearing elements due to the lack of or insufficient seismic gap. Considering Fig. 12, the pounding of the adjacent structural elements of two buildings induced damages due to an insufficient seismic gap or element.

Figure 12. Pounding effect in adjacent reinforced concrete buildings caused by the lack of seismic gap

- *Inadequate reinforcement detailing*

The load-bearing capacity of the elements and their connection zones in the structures must have the required ductility and strength to provide the structural safety of the buildings built in the earthquake zones. Within this scope, in the structural system, the most vital and critical areas are the column-beam connections during an earthquake. Turkish Building Earthquake Code-2018 [22] includes some rules and restrictions on structural element design. For example, the spacing of stirrups must be reduced in the confinement area, and at their ends, the ties must have hooks with a bent of 135 degrees. It can minimize the damage in the connection areas during the earthquake caused by the use of insufficient stirrups. According to the present code [22], for columns, the minimum transverse reinforcement spacing is 5 cm and the maximum spacing is 1/3 of the smaller cross-section dimensions. Besides, it shall not be higher than ¼ of the beam depth and eight times of the minimum diameter of longitudinal reinforcement for beams. In Fig. 13, the defects in the structural elements caused by the lack of stirrups in the columns and column-beam connections were depicted. As shown, sufficient stirrup spacing was not applied in the columns, and the distance between the stirrups was also widened due to insufficient anchoring. Therefore, the longitudinal bars were buckled by the effect of both vertical load and moment, and thus, severe damage occurred in the core of the concrete.

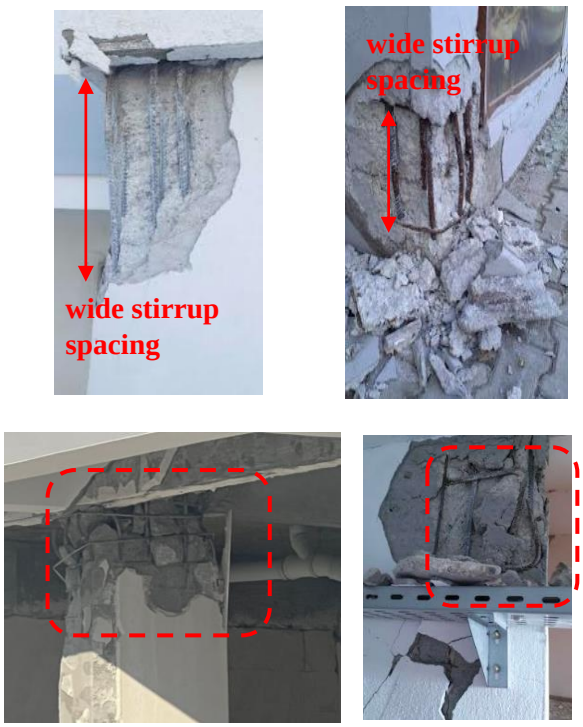

Figure 13. Improper stirrup spacing and 90-degree hook bends

During observations, some mistakes were also detected due to straight hooks bent 90 degrees at their ends. Considering Fig. 13, the improper 90-degree hook bends could not provide a sufficient confinement effect. In some cases, ruptures in the stirrups were also observed due to the insufficient detailing of the transverse reinforcements, as shown in Fig. 14. It was seen that in some buildings, especially in the lower parts of the columns, the stirrup spacing was so high that there was no stirrup in those parts. Besides, when the columns were subjected to a high axial load, the longitudinal reinforcements buckled, resulting in the spalling of the cover concrete (Fig. 14). This fact can also be attributed to the use of wide stirrup spacing, insufficient concrete strength, and column-cross section dimensions.

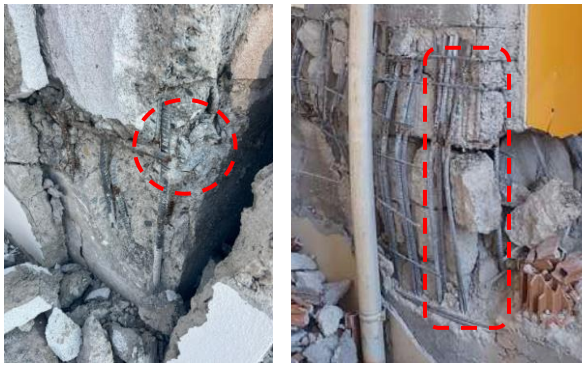

Figure 14. Rupture in stirrup and buckling of longitudinal reinforcement

- *Workmanship defects*

The workmanship defects can also cause tragic damage to the buildings during an earthquake. One of the main defects is the poor placement of concrete in the buildings. In some columns, coarse aggregates were observed and a homogeneous distribution was not achieved, so segregation took place. In these load-bearing structural elements, the reinforcement bars were also seen on the surface of the members, which can be due to the use of insufficient concrete cover around the longitudinal reinforcement (Fig. 15). Therefore, the bond strength between the reinforcement and concrete could not be achieved. Besides, it was seen that, in one of the beam elements, wood and large stone pieces mixed with the concrete during concrete pouring prevented the concrete from entering the mold, resulting in gaps between the reinforcements (Fig 16). The voids in the column and beam elements where concrete was not well placed showed faults in workmanship.

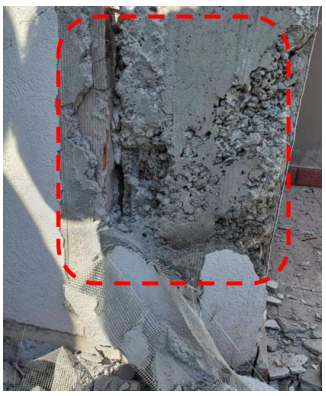

Figure 15. Insufficient concrete cover, concrete settlement problems and segregation

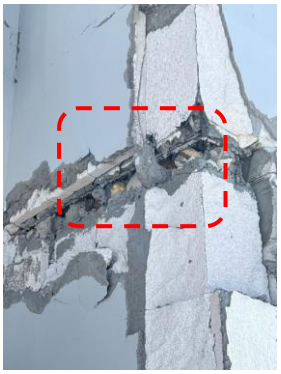

Figure 16. Foreign materials in concrete

- *Damaged staircase*

Staircases are one of the most important load-bearing structural elements and should not be damaged during an earthquake in order to ensure the safe evacuation of people from the buildings. The seismic damages in the joints of the staircase and landing were observed, as shown in Fig. 17. The spalling of the concrete cover occurred both on the landing and staircase-landing joint parts. Besides, on some staircases of buildings, splitting cracks were also observed on the concrete elements.

Figure 17. Damages in staircase

- *Defects in beam-column joint*

According to the earthquake regulations, it is aimed at absorbing the energy caused by the earthquake in the buildings by the beam elements and keeping the columns undamaged. Therefore, columns must be designed to be stronger than beams. A design implemented in this way will allow plastic hinges to form on the beam elements so that most of the energy will be absorbed in the damaged areas that will occur on the beams. The fact that the columns remain undamaged under the effects of an earthquake also prevents the structure from experiencing stability problems. However, from the observations, it was seen that there were structures that did not comply with this design principle. Observing Fig. 18, in some structures, the beams remained undamaged, and plastic hinges were formed at the lower and upper ends of the column elements. This situation led to the deterioration of the building's stability.

Figure 18. Stability problem due to weak column-strong beam situation

- *Shear damages in shearwalls and columns*

Shear damages caused by insufficient shear strength were observed in columns and shearwalls. Observing Fig. 19, cracks with a slope of 45 degrees were formed. This brittle type of damage can be considered heavy damage. The shearwalls were damaged due to the inability of the lateral reinforcement in the web of the element to meet the shear force caused by the earthquake. It caused the spalling of the concrete cover and crushed the concrete.

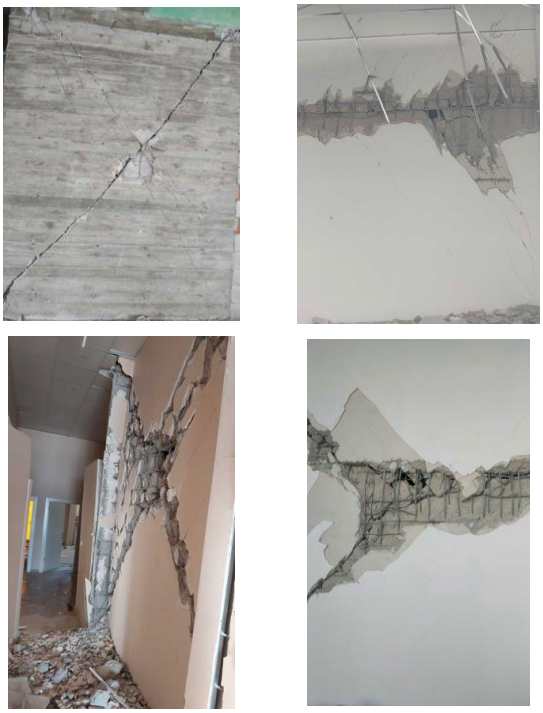

Figure 19. Shear damages in the shearwalls and columns

- *Shear cracks at the beams*

In the Turkish Building Earthquake Code, there are some restrictions that must be obeyed in the design of the end sections of the structural elements. According to this code, the reduction in the spacing of stirrups in the confinement area causes an increase in the energy consumption of this region. The shear cracks in the beam elements shown in Fig. 20 formed due to the increase in shear stress near the beam-column joint section. This type of damage can be due to the use of wide spacing between the stirrups in the beam-column joint section and inadequate transverse reinforcement. It was seen that the lack of reinforcement in the beam and beam-column joint sections caused critical damage.

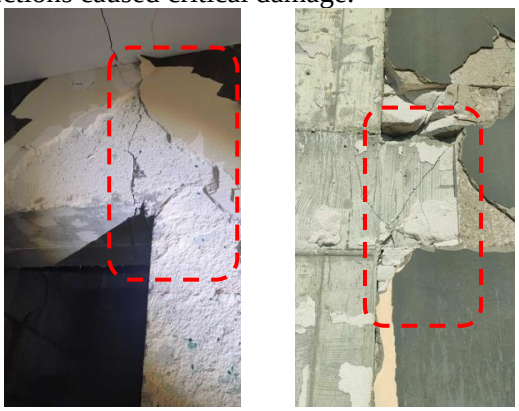

Figure 20. Shear cracks at the beams

- *Nonstructural damages*

The non-structural elements are the components such as curtain walls, chimneys, walls, cladding, etc. that are not in the load-bearing system of the building. Such damages can cause interruptions in the use of buildings after the earthquake. As seen in Fig. 21, cracks have formed on the outer surface of almost all buildings, and plaster and paint spills have been observed.

Figure 21. Cracks and plaster spills observed on the exterior of the buildings

Although the load-bearing capacities of the infill walls are ignored, they contribute to the lateral strength of the structure. The damages in the brick wall show the insufficiency of the lateral stiffness of the structure. The shear cracks were observed because of the inadequate rigidity of the structural system and as a result of the reversed cyclic lateral loading during an earthquake. Lots of shear cracks in the form of X were observed on both the interior and exterior walls of the buildings, as seen in Fig. 22.

In some buildings, the damages caused by the deflection of the walls in an out-of-plane direction due to the strong ground motion were observed. This type of damage can be due to inadequate adhesion between the walls and structural elements. Besides, it was observed that during lateral motion, the frame with no adequate lateral stiffness caused shear damage in the infill walls (Fig 23). In order to reduce this type of damage, in Turkish Building Earthquake Code-2018 [22], the use of elastic materials between the infill walls and structural system has been advised.

Figure 22. Shear cracks in walls

Figure 23. Out-of-plane toppling of walls and frame-wall separations

- *Soft storey irregularity*

As the brick infill walls used on the upper floors of the buildings are not continued on the ground floors due to the presence of shops or stores, a sudden decrease in rigidity occurs on these floors. This causes the formation of ‘soft storey’ irregularities. The presence of mezzanines on the ground floors of the buildings, which makes the floor height higher than the other floors, also causes a sudden decrease in rigidity. In this case, the lateral displacements between the ground and first floors of the buildings reach relatively high levels, and the stability of the building deteriorates. Especially in the district of Doğanşehir, many buildings were heavily damaged due to the formation of soft storey irregularities, and the ground floors were completely demolished (Fig. 24).

Figure 24. Collapsed structures due to sudden stiffness changes on the ground floor.

4.3. Damages in Masonry Buildings

The rural buildings in the countryside of Doğanşehir, Akçadağ, and Darende villages of Malatya have been heavily damaged, and it was observed that many masonry buildings constructed by their users without any engineering services collapsed (Fig. 25). These rural buildings in the villages were built with local materials found in the close vicinity, such as stone and adobe. In general, they are in the form of a one or two storey masonry structure.

In the villages of Doğanşehir, Akçadağ, and Darende, it was observed that the bearing walls were built using mud mortar as a binder. However, according to Turkish Building Earthquake Code-2007 [25], the use of lime mortar supported with cement or cement mortar was suggested as a binder in load-bearing walls. The minimum compressive strength of mortar for masonry buildings should be higher than 5 MPa, so the use of mud mortar as a binder could cause deficiencies. Besides, their flooring includes beams made of wood and plank decking. The wooden logs were placed in one direction, parallel to the walls. No mechanical connection between the wall sections was observed, so during the earthquake motion, the walls separated. The out-of-plane failures were observed in some buildings, as shown in Fig. 26. The quality of the workmanship of these buildings was so poor such that there were no horizontal bonding timber beams inside the bearing walls.

Figure 25. Collapsed structures in the rural areas

Figure 26. Wall damages in Gündüzbey and Akçadağ

It was observed that the loads formed during the earthquake caused the formation of shear cracks on the walls of the masonry structure (Fig. 27). In order to prevent this type of damage, during the construction of the building, continuous beams should be placed at certain heights that surround the structure.

Vertical cracks have occurred in the corners of the masonry buildings due to the effect of ground movement. With the growth of these cracks, the walls separated from the building were partially demolished, as seen in Fig. 28. This damage can be avoided by installing corner joints during the construction of the masonry structure.

Figure 27. Shear cracks in masonry buildings

Figure 28. Corner collapses due to vertical cracks in Akçadağ

5. Performance of Earth Structures and Geotechnical Evaluations

The dense construction in Malatya's city center makes it difficult to observe the surface traces created by the earthquake. However, in rural areas, data that allow observational evaluation, such as surface fractures, ground traces, and slope movements, can be encountered. Surface ruptures (i.e., ground rupture or ground displacement) occur as the apparent slip of the ground surface when an earthquake rupture affects the ground surface along a fault. Those ruptures, which pose a great risk for structures built along a fault belt that may be active, were observed in Akçadağ, the district of Malatya on the western border. The slit width reaches 1.5 m, and the height reaches 80 cm. The observed surface crevices were formed in a rural area with no settlement. Therefore, no structural effects were noticed (Fig. 29).

Figure 29 View of surface ruptures in Akçadağ district

Significant asphalt pavement damages were observed on the roads between Yeşilyurt and Gündüzbey districts, on the border of the city of Adıyaman in the south. It was observed that the deformation and cracks on the surface are deduced by the movement in the earth retaining structures supporting the road, which have an approximate height of 4 m. The lateral movement of the retaining structure supporting the road and the ground structure has also caused the movement of the abutment structure on the upper side. Rock masses broken off from the backfill caused significant deformations on the asphalt pavement (Fig, 30). Again, in this region, where the superstructure damage density is quite high, displacements and settlements have occurred on the highways supported by the retaining walls. Due to the lateral movement of the bearing structure, fractures and displacements of up to 40 cm occurred at the asphalt pavement level (Fig. 31).

Figure 30. The asphalt pavement cracks due to the lateral movement of retaining wall in Yeşilyurt district

Figure 31. The slided pavement due to lateral movement of retaining wall

Figure 32. Retaining wall failures and flow of backfill material

Even in small magnitude earthquakes, lateral displacement of retaining walls can be expected within certain limits. The movements of massive, weighted walls built on rock are more limited. The performance of the reinforced earth structures against these earthquakes has been observed to be quite successful. It has been concluded that this is largely due to the flexibility provided by the strip reinforcements used. Local and global failures were observed in the load-bearing structures built, especially in regions where soil amplification effects are observed. It is also considered that wall height is an important parameter of structural performance. Vegetation and afforestation, which correspond to significant surcharge loads in the abutment structures at the border of the public parcels, especially in the backfills, triggered the effects on wholesale collapses (Fig. 32).

6. Conclusion and Discussion

The aim of this study was to reveal the detailed field investigation in Malatya province after Kahramanmaraş Earthquakes on February 6, 2023. The field investigations showed that alluvial units in Malatya city center consist of unconsolidated gravel, sand, schist, and clays. This situation indicates that soil augmentation is effective in the damages that occur, especially in the city centre of Malatya (Bostanbaşı, Fahri Kayhan, Yüzakı, Battalgazi, Eski Malatya, Orduzu, and Fuzuli locations) where these units are stacked. In the region where commercial enterprises are concentrated, the building stock consists of relatively older buildings (built prior to 2000). It has been determined that significant destruction occurred in these structures, especially after the Elbistan (M_w 7.6) earthquake. While significant structural damages and destruction are observed in Doğanşehir, Akçadağ, and Yeşilyurt districts, the density of structural damage is lower in the districts of Kale, Hekimhan, and Yazıhan.

There are major problems with the way buildings were made, such as soft storey formations at the ground and normal storey levels, not enough dilatation joints between buildings, problems with concrete settling at column-beam junctions, not connecting transverse reinforcements as required, and damage caused by not having enough anchorage lengths. According to the local soil conditions, soil amplification affects a sizable portion of the buildings. However, no liquefaction or ground settlements due to liquefaction were observed in the building stock. The absence of soil liquefaction despite high acceleration earthquake loads and groundwater levels is attributed to the high content of fine materials in the soil layers. Cracks, swellings, and collapses on asphalt pavements have been observed at different widths and levels in the city and on the ring road.

Turkish Building Earthquake Code-2018 [22], which determines the necessary design and construction rules for buildings to be earthquake resistant and to minimize the damage caused by earthquakes, imposes building height restrictions depending on the building usage class and earthquake design classes, taking into account the standard. It was determined in the field investigations that the relevant criteria of the

regulation were not complied with, especially in multi-storey and newly constructed buildings with high damage levels. In the field investigations, it was observed that the buildings were heavily damaged and collapsed due to design and construction errors. The buildings designed according to Turkish Building Earthquake Code-2007 [25] and Turkish Building Earthquake Code-2018 [22] survived the Pazarcık and Elbistan earthquakes with less damage. In general, the main construction defects are the low quality of concrete in the structural elements constituting the load-bearing systems of the structures built before the implementation of Turkish Building Earthquake Code-2007 [25], the arrangement of the reinforcements without considering the ductile design principles, and the failure to use suitable stirrups. In addition, it was determined that the structural irregularities that should have been taken into account in the design were not complied with. In masonry buildings, the use of low-strength wall materials, incorrect wall connections, and a lack of maintenance were determined to be the main construction defects. The settlements were selected and the structures were built without considering the amplification effects of the local soil characteristics during the earthquake.

Acknowledgment

The data and pictures used in the study were partially compiled from the project final report supported by the TUBITAK 1002C program.

Contributions of the authors

All authors contributed equally to the study.

Conflict of Interest Statement

There is no conflict of interest between the authors.

Statement of Research and Publication Ethics

The study is complied with research and publication ethics

References

[1] https://deprem.afad.gov.tr/event-catalog)., "AFAD." .

[2] İ. Yüksel, "Betonarme Binaların Deprem Sonrası Acil Hasar Değerlendirmeleri," *Erciyes Üniversitesi Fen Bilimleri Enstitüsü Dergisi*, vol. 24, no. 1–2, pp. 260–276, 2008.

[3] Z. Celep, *Deprem Mühendisliğine Giriş ve Depreme Dayanıklı Yapı Tasarımı*. 2015.

[4] Ö. F. Nemutlu, B. Balun, and A. Sarı, "Damage assessment of buildings after 24 January 2020 Elazığ-Sivrice earthquake," *Earthquake and Structures*, vol. 20, no. 3, pp. 325–335, 2021, doi: 10.12989/eas.2021.20.3.325.

[5] E. Sayın, B. Yön, O. Onat, M. Gör, M. E. Öncü, E. T. Tunç, D. Bakır, M. Karaton, and Y. Calayır, "24 January 2020 Sivrice-Elazığ, Turkey earthquake: geotechnical evaluation and performance of structures," *Bulletin of Earthquake Engineering*, vol. 19, no. 2, pp. 657–684, 2021, doi: 10.1007/s10518-020-01018-4.

[6] E. Işik, M. C. Aydin and A. Büyüksaraç, "24 January 2020 Sivrice (Elaziğ) earthquake damages and determination of earthquake parameters in the region," *Earthquake and Structures*, vol. 19, no. 2, pp. 145–156, 2020, doi: 10.12989/eas.2020.19.2.145.

[7] H. Bilgin, N. Shkodrani, M. Hysenlliu, H. Baytan Ozmen, E. Isik, and E. Harirchian, "Damage and performance evaluation of masonry buildings constructed in 1970s during the 2019 Albania earthquakes," *Engineering Failure Analysis*, vol. 131, 2022, doi: 10.1016/j.engfailanal.2021.105824.

[8] E. Işik, Y. L. Ekinci, N. L. Sayil, A. Büyüksaraç, and M. C. Aydin, "Time-dependent model for earthquake occurrence and effects of design spectra on structural performance: a case study from the north anatolian fault zone, Turkey," *Turkish Journal of Earth Sciences*, vol. 30, no. 2, pp. 215–234, 2021, doi: 10.3906/yer-2004-20.

[9] O. F. Nemutlu, B. Balun, and A. Sari, "Assessment of Earthquake Preparedness of Existing Buildings: Example of Bingöl Province," *Turk Deprem Arastirma Dergisi*, vol. 3, no. 1, pp. 92–109, 2021, doi: 10.46464/tdad.932452.

[10] B. Balun, Ö. F. Nemutlu, A. Benli, and A. Sari, "Estimation of probabilistic hazard for Bingol province, Turkey," *Earthquake and Structures*, vol. 18, no. 2, pp. 223–231, 2020, doi: 10.12989/eas.2020.18.2.223.

[11] E. Işık, "Comparative investigation of seismic and structural parameters of earthquakes ($M \geq 6$) after

1900 in Turkey," *Arabian Journal of Geosciences*, vol. 15, no. 10, 2022, doi: 10.1007/s12517-022-10255-7.

[12] E. Işık, F. Avcil, A. Büyüksaraç, R. İzol, M. H. Arslan, C. Aksoylu, E. Harirchian, O. Eyisüren, E. Arkan, M. Ş. Güngür, M. Günay, and H. Ulutaş, "Structural damages in masonry buildings in Adıyaman during the Kahramanmaraş (Turkiye) earthquakes (Mw 7.7 and Mw 7.6) on 06 February 2023," *Engineering Failure Analysis*, vol. 151, 2023, doi: 10.1016/j.engfailanal.2023.107405.

[13] E. Işık, F. Avcil, E. Arkan, A. Büyüksaraç, R. İzol, and M. Topalan, "Structural damage evaluation of mosques and minarets in Adıyaman due to the 06 February 2023 Kahramanmaraş earthquakes," *Engineering Failure Analysis*, vol. 151, 2023, doi: 10.1016/j.engfailanal.2023.107345.

[14] İ. Kocaman, "The effect of the Kahramanmaraş earthquakes (Mw 7.7 and Mw 7.6) on historical masonry mosques and minarets," *Engineering Failure Analysis*, vol. 149, 2023, doi: 10.1016/j.engfailanal.2023.107225.

[15] M. Erdik, "Earthquake risk in Turkey," *Science*, vol. 341, no. 6147, pp. 724–725, 2013, doi: 10.1126/science.1238945.

[16] R. Demirtaş and C. Erkmen, "Doğu Anadolu Fay Sistemi Deprem Etkinliği- Gelecek Deprem Potansiyeli," no. March, 2019.

[17] H. Alkan, A. Büyüksaraç, Ö. Bektaş, and E. Işık, "Coulomb stress change before and after 24.01.2020 Sivrice (Elazığ) Earthquake (Mw = 6.8) on the East Anatolian Fault Zone," *Arabian Journal of Geosciences*, vol. 14, no. 23, 2021, doi: 10.1007/s12517-021-09080-1.

[18] MTA, "http://www.mta.gov.tr." .

[19] Ö. Yıldız, "Seismic site characterization of Battalgazi in Malatya, Turkey," *Arabian Journal of Geosciences*, vol. 15, no. 9, 2022, doi: 10.1007/s12517-022-10170-x.

[20] Ö. Yildiz, "Influence of input motion and surface layer properties on seismic site response: A stochastic simulation method–based MLR model," *Near Surface Geophysics*, 2023, doi: 10.1002/nsg.12255.

[21] Ö. Yıldız and Ç. Ceylan, "Geotechnical characterization of zeolite-sand and bentonite-sand mixtures," *Acta Geotechnica Slovenica*, vol. 2, pp. 15–32, 2022.

[22] Turkish Seismic Code (TSC-2018), "Building earthquake code of Turkey," Ankara, 2018.

[23] Turkish Standard (TS500), "Requirements for design and construction of reinforced concrete structures," Ankara, 2000.

[24] Turkish Seismic Code (TSC-1975), "Regulations for the structures to be built in disaster areas," Ankara, 1975.

[25] Turkish Building Earthquake Code (TSC-2007), "Regulations for the buildings to be built in earthquakes areas," Ankara, 2007.

Bitlis Eren Üniversitesi Fen Bilimleri Dergisi
BİTLİS EREN UNIVERSITY JOURNAL OF SCIENCE
ISSN: 2147-3129/e-ISSN: 2147-3188
VOLUME: 12 NO: 3 PAGE: 704-711 YEAR: 2023
DOI:10.17798/bitlisfen.1285270

Secure Handover Management Against False Base Station Attacks

Yerdos AMİRBEKOV[1], Elif BOZKAYA[2*]

[1]*National Defence University, Istanbul, Türkiye*
[2]*National Defence University Turkish Naval Academy, Istanbul, Türkiye*
(ORCID: 0000-0001-8117-3373) (ORCID: 0000-0001-6960-2585)

Keywords: False Base Stations, Measurement Report, Handover, 5G Networks, Man-in-the-Middle Attack.

Abstract
False Base Station attack raises concerns about data privacy during handover process in 5G networks. Broadcasting of measurement reports unveils the need for security assessment since a false base station can send a stronger signal to the User Equipment (UE) to establish a connection with itself. This may cause the leakage of information. Thus, a fundamental solution is to protect measurement reports with encryption algorithms. In this paper, we identify the security vulnerabilities of handover process and simulate a scenario, where a false base station is deployed and UEs can be connected to it during handover process. To prevent this, we propose a secure handover scheme to protect measurement reports by using two encryption algorithms; (i) Advanced Encryption Algorithm (AES)-256, and (ii) Rivest Cipher 4 (RC4) Algorithm. Then, we analyze the computation time and show the secure connection to a legitimate base station during the handover process.

1. Introduction

With the development of wireless networks, the traffic volume and the number of devices have been significantly increased. Consequently, new technologies, e.g., Software Defined Networks (SDN) [1], Network Function Virtualization (NFV) [2], edge computing [3], have become effective ways to meet the ever-increasing needs of mobile users. The radio communication Sector of ITU (ITU-R) has defined three usage scenarios for 2020 and beyond [4]: (i) Enhanced Mobile Broadband to focus on the increased data rates, a high number of users, and high traffic requests for hotspots (ii) Ultra Reliable and Low Latency Communications to meet Quality of Service (QoS) requirements such as latency, reliability, throughput, etc., and (iii) Massive Machine Type Communications to connect a large number of Internet of Things devices with low cost and long battery life.

To meet these stringent requirements of the new services and applications, 5G networks offer high QoS, higher data rates, and latency of less than one millisecond with the deployment of a large number of Access Points. In this case, one of the most important issues is the handover management for such ultra-dense networks due to user mobility. The handover procedure is the transfer of an ongoing service from one base station to another without interruption and with minimum delay. To facilitate this process, the Third Generation Partnership Project (3GPP) has proposed a measurement report containing frequency and power measurements to decide whether handover is necessary and which transmission is required [5]. Handover management is mainly based on the measurement report of the User Equipment (UE). The source base station triggers the handover procedure and sends it to the target base station. When the target base station receives and confirms the handover request, the source base station initiates the handover procedure. However, measurement reports are vulnerable to attacks, and the handover management is challenging due to the authentication complexity and requires high bandwidth.

Man-in-the-middle attack is one of the critical attacks that targets data confidentiality and integrity and can cause service interruption [6]. In this attack,

*Corresponding author: ebozkaya@dho.edu.tr
Received: 19.04.2023, Accepted: 18.09.2023

a false base station can enter between two base stations and force UEs to connect to themselves. To implement this, a false base station transmits more power than the legitimate base station, and service interruption can occur during the handover process.

False Base Station can perform passive and active attacks against the UEs over the Radio Access Networks (RAN). In 5G networks, base stations periodically broadcast information about the network. The UEs listen to these broadcast messages and select a suitable cell to connect. Due to practical difficulties, broadcast messages are not protected for confidentiality, authenticity, or integrity. Therefore, broadcast messages are prone to spoofing. 3GPP 5G Release also addresses the detection of false base stations [5]. Accordingly, the Received Signal Strength Indicator (RSSI) and location information in measurement reports can be used for detection. This can be accomplished by detecting inconsistency between the information on the broadcast information and the base station deployment information. The 5G system has already made significant improvements against false base stations such as mutual authentication, integrity protected signaling, and secure algorithm negotiations [7]. However, there are still challenges due to the computation complexity and requiring high bandwidth.

In this respect, we simulate a scenario, where a false base station is deployed and users can be connected to it during handover process. Then, we show the steps of how an attack can be prevented and, propose a solution to protect broadcast messages with two fundamental encryption algorithms; AES-256 Algorithm and RC4 Algorithm.

As a result, the main contributions of this paper are as follows:

- We describe the handover procedure in 5G networks and give a threat model.
- We simulate a false base station attack and analyze the security of the proposed system model.
- Then, we observe the handover procedure in different radio access technologies and propose to encrypt the measurement reports showing the computation time.

The rest of the paper is organized as follows. Section 2 reviews the most relevant studies related to the handover process and false base station attacks. Section 3 describes the system model during the handover process and gives our proposed solution in a simulation environment. Section 4 evaluates the performance of the proposed solution. Finally, we give our conclusions in Section 5.

2. Related Work

A false base station can collect user information or prevent users from accessing the service. Due to the difficulty of detecting false base stations, many researchers have investigated the handover procedure [8]. In this section, we give the security weakness of the handover process and false base station attacks.

In [9], the authors focus on estimating the location of false base stations and propose a network-based localization method. The proposed method is based on the analysis of Reference Signal Received Power (RSRP) and UE location information in the measurement reports. Measurement reports are used to check for any inconsistencies in the network topology since the reports contain information about both the false base station and the legitimate base stations. This method is based on estimating the UE locations where measurement reports are sent to identify the locations of false base stations. In [10], the authors consider the International Mobile Subscriber Identity (IMSI) catcher device to simulate a false base station. The IMSI catcher can obtain the IMSI number sent by the UEs within the coverage area and capture the data traffic [11]. It is emphasized that the IMSI catcher can eavesdrop on calls, intercept messages, and obtain UE locations. Thus, an IMSI catcher detection mechanism is proposed against the possible attacks and a location-based cell print algorithm is presented. However, both of these methods assume that the UEs are legitimate and already known and the measurement reports are not filtered for malicious traffic.

In addition, the authors in [12] investigate the false base station attack and propose location awareness-based methods since UE can receive multiple signals from the nearby base stations and a false base station can send the strongest signal to the UE to establish a connection with itself. In this regard, the received signal strength is checked according to the location of UE and legitimate base station. This method can effectively mitigate the false base station attack, but this process is time-consuming for a mobile network as malicious traffic can be generated for network congestion. In [13], the authors aim to detect false base stations and prevent denial of service attacks. To achieve this, the authors use automatic neighbor relations in self-organizing networks to prohibit UEs from establishing a connection with the false base station. The authors classify the base stations as false and legitimate according to the measurement reports and send each UE a list of false base stations. However, updating the list and sending it to each UE inevitably consumes resources (e.g. time, bandwidth). In [14], [15], the authors identify

the unique RF characteristics of the transmitter to distinguish legitimate base stations from false base stations. The authors only investigate the measurements of false base stations, but the measurements of legitimate base stations are also an important factor for detection criteria. In [16], the authors propose an identification protocol to verify the base stations and protect user privacy. The authors use the measurement reports of UEs in different positions so that they estimate the power and position of the real base stations. When a new base station is included in the topology, its position and power are verified by a cloud server. After the verification process, the UEs can be connected to the base stations. However, this method requires a database to check legitimate base stations, which may cause a change in the current LTE procedure.

Frequent handovers between base stations cause security vulnerabilities and potential threats. Although 3GPP has determined the new security functionalities [7], secure handover is still a critical issue, in particular, against false base station, and denial of service attacks. In [17], the authors propose a secure handover authentication protocol between neighbor base stations by using the Chinese remainder theory. It is aimed to enable mutual authentication between UE and the network so that after the UE has completed the authentication with the current base station, a handover process can happen. Then, mutual authentication is executed with the target base station. However, the attackers can implement more volumes of malicious traffic, and the handover procedure may be much more complicated and time consuming, especially in latency sensitive applications resulting in lower QoS. In [18], the authors investigate the challenges of the false base station, denial of service attack, and high network complexity and, then propose authentication and key agreement process for handover in 5G networks. However, this work does not take into consideration the characteristics of false base station attacks, and cannot be implemented for specific attack scenarios related to measurement reports.

In [19], the authors present an Elliptic curve cryptography-based authentication model to both confirm the validity of the node and design handover schemes. In the study, by using the cryptography-based solution, the main-in-the-middle attack is prevented. When the malicious node receives the user authentication request, the node needs to master the private key to confirm its identity, thus the malicious node cannot send back the legitimate response message. However, the proposed secure method can be challenging for UEs due to the limited storage and energy capabilities, and extensive computation. Thus, the solution should be a distributed security solution and constantly monitor the measurement reports to detect false base station attacks. Similarly, in [20], the authors present a secure handover authentication scheme based on the certificateless public-key cryptography technique. In this technique, a key generator center generates the partial public key and private key and the user obtains the complete public key and private key by combining the partial keys and a random number by itself. Thus, in the proposed model, privacy is preserved with an authentication scheme and three-handshake during handover in the mobility scenarios. In [21], the authors also address the problems of authentication mechanisms and introduce a robust handover authentication protocol for 5G heterogeneous networks. A mutual authentication with the key procedure is presented. Although certificateless public-key cryptography and key procedure method can support secure handover with reduced computation time, the complicated procedure associated with UEs is still concerning.

These approaches mainly consume a lot of resources of UEs leading to the decrease in application performance to detect false base stations. On the other hand, this work is motivated to provide a cryptography-based solution for the handover procedure by diminishing the overall computation time in addition to restricting the communication with measurement reports between UEs and base stations. This is important for the handover authentication procedure.

3. System Model and Proposed Solution

This section describes the 5G handover system model and threat model. As illustrated in Fig. 1, 5G networks basically consist of two components: Core Network (CN) and Radio Access Network (RAN). CN includes the Access and Mobility Function (AMF), User Plane Function, Session Management Function (SMF), and Authentication Server Function (AUSF). In the 5G RAN, there are g-Node BSs (gNBs) communicating with the UEs. If a UE requests to connect to the 5G CN, the AMF first offers the AUSF to perform mutual authentication with the UE.

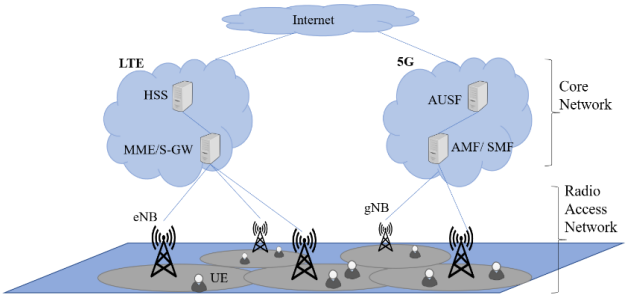

Figure 1. The illustration of handover for 5G networks.

In a cellular network, UE is configured to send the measurement reports to the gNBs to which it is connected. Measurement reports include power and frequency measurements collected from nearby gNBs. All information necessary for the UE to measure is available in the gNB's system information block (SIB) and main information block (MIB) broadcast messages. After receiving the messages, the serving gNB evaluates the measurement reports and decides whether a handover procedure is required. In particular, if the communication with the serving gNB deteriorates and/or another neighboring gNB at a different frequency becomes better than the serving gNB, then the handover procedure may be performed from the serving gNB to the neighbor gNB. In addition, the Reference Signal Received Power (RSRP), the Reference Signal Received Quality (RSRQ), and Signa

Interference and Noise Ratio (SINR) are considered when making the handover decision. The handover decision and these measurement reports are standardized by 3GPP [22].

3.1. Thread Model

In this paper, we simulate the Man-in-the-Middle attack through the scenario of eavesdropping, changing, and retransmitting messages. As seen in Fig. 2, we focus on a scenario, where an active attacker can deploy a false base station with the same capabilities as the legitimate base station. Specifically, a false base station could impersonate a legitimate base station, thereby forcing UE to connect itself. This may occur by broadcasting MIB and SIB messages of the false base station with a higher signal strength than the legitimate base station to which it is connected. We also assume that an attacker could intercept the MIB and SIB messages of legitimate BSs by listening to open channels.

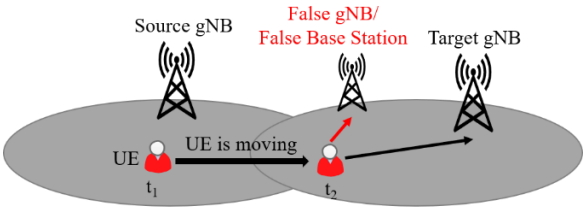

Figure 2. The illustration of the threat model.

3.2. Proposed Solution and Simulation Environment

In this subsection, we give our scenario to simulate a false base station with the presented threat model and analyze the security of the proposed model using discrete-event network simulator NS-3.

In our experiment, we simulate two scenarios, where a UE is in a Radio Resource Control (RRC)-connected state and transmits video data while interacting with the network. In the first scenario, the UE moves randomly choosing different directions. In the second scenario, the UE moves along a certain trajectory.

As shown in Fig. 3, our first scenario consists of a 4G/5G core network, two eNB/gNB representing the legitimate base station, a malicious/false eNB/gNB used for attacks, and several UEs. Two legitimate eNB/gNBs are connected to the core network via S1 in 5G and N2 in 4G. In addition, legitimate eNB/gNBs are interconnected via interface Xn in 5G and X2 in 4G, and their cellular interfaces are configured according to the NS3 documentation.

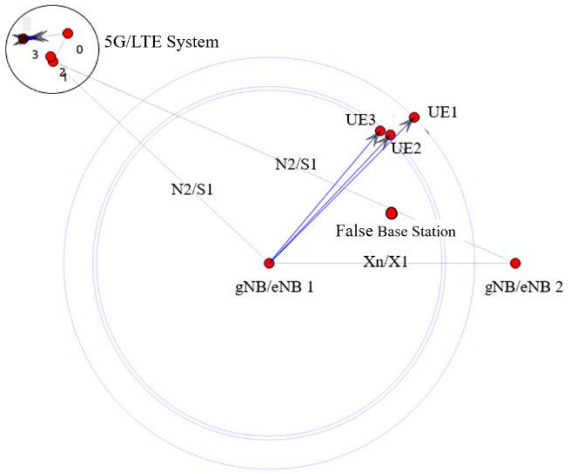

Figure 3. The implementation of scenario 1 in NS-3.

To simulate the handover procedure, we increase the signal strength of the false base station and reduce the signal strength of eNB_1/gNB_1. Unaware of cell 2's existence, the UE reports a strong signal from the false base station to cell 1 via

measurement report. Figs. 4 and 5 show examples of malicious measurement reports with false power measurements on LTE and 5G, respectively. The UE is eventually forced to disconnect from the legitimate base station and connect to the false base station.

```
Message: Measurement Report

Data:

{
  message c1: measurementReport: {
    criticalExtensions c1: measurementReport-r8: {
      measResults {
        measId 3,
        measResultPCell {
          rsrpResult 53,
          rsrqResult 33
        },
        measResultNeighCells measResultListEUTRA: {
          {
            physCellId 2,
            measResult {
              rsrpResult 59,
              rsrqResult 26
            }
          }
        }
      }
    }
  }
}
```

Figure 4. Malicious measurement report on LTE.

```
Message: Measurement report

Data:

{
  message c1: measurementReport: {
    criticalExtensions measurementReport: {
      measResults {
        measId 3,
        measResultServingMOList {
          {
            servCellId 0,
            measResultServingCell {
              physCellId 500,
              measResult {
                cellResults {
                  resultsSSB-Cell {
                    rsrp 39,
                    rsrq 61,
                    sinr 52
                  }
                }
              }
            }
          }
        },
        measResultNeighCells measResultListNR: {
          {
            physCellId 501,
            measResult {
              cellResults {
                resultsSSB-Cell {
                  rsrp 72,
                  rsrq 66,
                  sinr 71
                }
              }
            }
          }
        }
      }
    }
  }
}
```

Figure 5. Malicious measurement report on 5G.

Then, we observe the handover procedure in different radio access technologies and evaluate the results of the handover between the 4G system and the 5G system. We consider that the UE is located at base station 1 and the UE is moving to the coverage area of base station 2, thus a handover is required between base stations 1 and 2. Here, in the simulation environment, BS_1 operates on 4G and BS_2 operates on 5G. At the same time, the attacker tries to abuse the handover by impersonating BS_2. In Fig. 6, eNB CellId 4 represents the malicious BS.

Figure 6. Handover Report.

In the second scenario, where the UE moves from point A to point B along a given path at a speed of 50 m/s, it connects to BS_1 and transmits data to the network as seen in Fig. 7. At initial 16 seconds of the simulation, the UE sends a measurement report to the serving BS_1, triggers the BS_2, but connects to malicious/false BS_3 as shown in Fig. 8. UE connecting to a malicious BS is under attack for 3 seconds. In the 19th second, it reestablishes the connection with the BS_2 and receives the available services from the network.

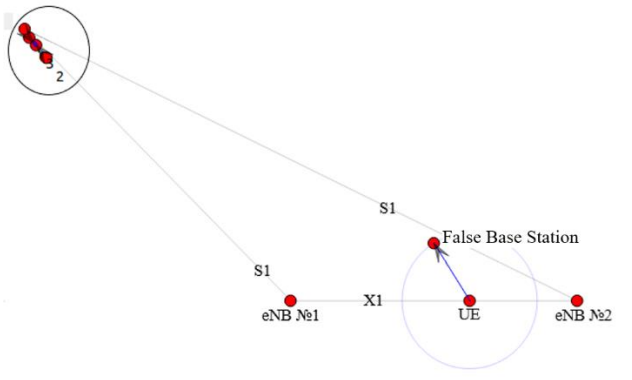

Figure 7. The implementation of scenario 2 in NS-3.

```
+15.920001000s -1 A2A4RsrqHandoverAlgorithm:EvaluateHandover(): [LOGIC] Best neighbour cellId 2
+15.920001000s -1 A2A4RsrqHandoverAlgorithm:EvaluateHandover(): [LOGIC] Trigger Handover to cellId 2
+15.920001000s -1 A2A4RsrqHandoverAlgorithm:EvaluateHandover(): [LOGIC] target cell RSRQ 31
+15.920001000s -1 A2A4RsrqHandoverAlgorithm:EvaluateHandover(): [LOGIC] serving cell RSRQ 14
+16.000001000s -1 A2A4RsrqHandoverAlgorithm:DoReportUeMeas(0x5644395dc6f0, 1, 2)
+16.000001000s -1 A2A4RsrqHandoverAlgorithm:UpdateNeighbourMeasurements(0x5644395dc6f0, 1, 3, 31)
+16.000001000s -1 A2A4RsrqHandoverAlgorithm:UpdateNeighbourMeasurements(0x5644395dc6f0, 1, 2, 18)
/NodeList/7/DeviceList/0/LteUeRrc/ConnectionEstablished UE IMSI 1: connected to CellId 3 with RNTI 1
/NodeList/6/DeviceList/0/LteEnbRrc/ConnectionEstablished eNB CellId 3: successful connection of UE with IMSI 1 RNTI 1
```

Figure 8. Handover to a Malicious BS.

4. Performance Evaluation

Traditional detection mechanisms such as mobile applications or network sniffers cannot prevent handover attacks because the UE cannot implement security measures against a false base station on its own and the attack will likely be detected after completion. Therefore, we propose to use the AES-256 and RC4 encryption algorithms to encrypt the identification number of the base stations to prevent false stations and, then we evaluate the performance of our cryptographic-based solution.

The cryptography-based methods have significantly improved secure communication, but it is still time-consuming for most applications. Similar to our work, in [20], the authors also propose a cryptography-based handover scheme for the mobile UEs in LTE-A networks. However, due to the mobility of UEs, a secure handover mechanism should be designed to make it available to the battery-limited UEs. Although the proposed method in [20] can support secure handover with reduced computation time, the complicated procedure associated with UEs is still concerning. This approach mainly consumes a lot of resources of UEs leading to the decrease in QoS [23]. Therefore, we simulate a false base station attack and analyze the security of the proposed solution in terms of computation overhead.

The cell ID is a 28-bit value that contains the ID of a base station. Initially, we assume that base station identifiers are encrypted and transmitted over broadcast channels. During the handover process, the source base station will decrypt the target base station ID received by measurement reports from the UE.

Fig. 9 shows the computation time to decrypt the base station identifier using the AES-256 and RC4 algorithms concerning the number of UEs. As seen in the figure, while the AES-256 algorithm provides higher security, it offers more computation time. On the other hand, the RC4 algorithm provides a less computation time, but a less reliable solution. Both AES-256 and RC4 algorithms are symmetric-key algorithms. In particular, as the number of UEs increases, more processing time is required for encryption and decryption for a more secure solution. While the RC4 algorithm encrypts data independently of each other, either bit by bit or byte by byte, and offers fast processing capability, the AES-256 algorithm encrypts data in 128-bit blocks using a 256-bit key and the latency is higher as the data is processed in blocks.

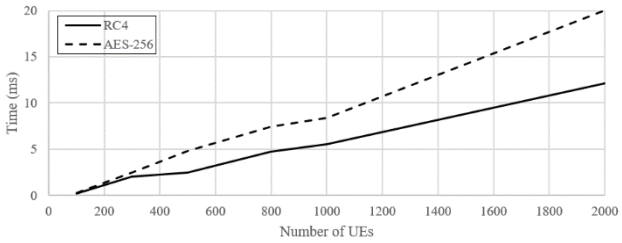

Figure 9. Computation time for AES and RC4 algorithms.

In Fig. 10, we show the secure handover solution after the cell ID of the base station is encrypted. As seen in the figure, according to the measurement reports, the UE is triggered for handover to cell ID number 2 since the Reference Signal Received Quality (RSRQ) from the target cell is better than the serving cell. Thereby, the UE connects to the legitimate base station by encrypting the cell ID.

```
+15.920001000s -1 A2A4RsrqHandoverAlgorithm:EvaluateHandover(): [LOGIC] Best neighbour cellId 2
+15.920001000s -1 A2A4RsrqHandoverAlgorithm:EvaluateHandover(): [LOGIC] Trigger Handover to cellId 2
+15.920001000s -1 A2A4RsrqHandoverAlgorithm:EvaluateHandover(): [LOGIC] target cell RSRQ 31
+15.920001000s -1 A2A4RsrqHandoverAlgorithm:EvaluateHandover(): [LOGIC] serving cell RSRQ 14
+16.000001000s -1 A2A4RsrqHandoverAlgorithm:DoReportUeMeas(0x5644395dc6f0, 1, 2)
+16.000001000s -1 A2A4RsrqHandoverAlgorithm:UpdateNeighbourMeasurements(0x5644395dc6f0, 1, 3, 31)
+16.000001000s -1 A2A4RsrqHandoverAlgorithm:UpdateNeighbourMeasurements(0x5644395dc6f0, 1, 2, 18)
/NodeList/7/DeviceList/0/LteUeRrc/ConnectionEstablished UE IMSI 1: connected to CellId 2 with RNTI 1
/NodeList/6/DeviceList/0/LteEnbRrc/ConnectionEstablished eNB CellId 2: successful connection of UE with IMSI 1 RNTI 1
```

Figure 10. Triggering the handover and connection to a legitimate base station.

As explained in the previous section, measurement reports include power and frequency measurements collected from nearby base stations. All information necessary for the UE is available in the SIB and MIB broadcast messages. In addition to encrypting the identity of a base station, we also consider increasing data size to be able to encrypt fields such as tracking area code, scheduling information list, and radio resource configuration in SIB messages for a more secure solution [24]. Thus, we set the number of UEs to 500, also consider the AES-128 algorithm, which uses a 128-bit key, and compare the computation time to observe the results more clearly. As seen in Table 1, the computation overhead increases as the data size increases. AES-128 and AES-256 algorithms have longer computation time but are still suitable for latency sensitive traffic in a 128-bit data size because according to the 5G and beyond 5G Key Performance Indicator (KPI), it is assumed that the end-to-end latency requirement should be under 5 ms [25].

Table 1. Computation time overhead for different data sizes

Data size:	28 bits	128 bits	160 bits
RC4 Algorithm	3.33 ms	3.72 ms	4.25 ms
AES-128 Algorithm	3.97 ms	4.65 ms	5.02 ms
AES-256 Algorithm	4.42 ms	4.97 ms	5.36 ms

5. Conclusion

In this paper, we proposed a secure handover process to prevent the Man-in-the-Middle attack, i.e., the false base station. We simulated a false base station and defined the security vulnerabilities in different radio access technologies. We also proposed to encrypt the cell ID of the base station, which is sent with the measurement reports. We demonstrated the steps of handover triggering and handover process in a simulation environment. It is shown that the computation time is acceptable and a secure connection can be established between UE and a legitimate base station.

Contributions of the authors

The system model and proposed solution were developed by Yerdos AMİRBEKOV and Elif BOZKAYA. Performance evaluation was carried out by Yerdos AMİRBEKOV and Elif BOZKAYA commented on the results obtained from the study. All authors contributed to the writing of the article.

Conflict of Interest Statement

There is no conflict of interest between the authors.

Statement of Research and Publication Ethics

The study is complied with research and publication ethics.

References

[1] D. Kafetzis, S. Vassilaras, G. Vardoulias and I. Koutsopoulos, "Software-Defined Networking Meets Software-Defined Radio in Mobile ad hoc Networks: State of the Art and Future Directions", *in IEEE Access*, vol. 10, pp. 9989-10014, 2022, doi: 10.1109/ACCESS.2022.3144072.

[2] P. Xue and Z. Jiang, "SecRouting: Secure Routing for Network Functions Virtualization (NFV) Technology*", in IEEE Transactions on Circuits and Systems II: Express Briefs*, vol. 69, no. 3, pp. 1727-1731, March 2022, doi: 10.1109/TCSII.2021.3119938.

[3] D. Zhao, Z. Yan, M. Wang, P. Zhang, B. Song, "Is 5G Handover Secure and Private: A Survey", *IEEE Internet of Things Journal* vol. 8, no.16, pp. 12855–12879, 2021. doi:10.1109/JIOT.2021.3068463.

[4] IMT Vision-Framework and Overall Objectives of the Future Development of IMT for 2020 and Beyond, Recommendation ITU-R M.2083-0 (09/2015).

[5] 3GPP TS 33.501, "Security Architecture and Procedures for 5G System (version 15.4.0 release 15)", Technical specification (2019).

[6] M. Conti, N. Dragoni, V. Lesyk, "A Survey of Man in the Middle Attacks*", IEEE Communications Surveys & Tutorials* vol. 18, no. 3 pp. 2027–2051, 2016. doi:10.1109/COMST.2016.2548426.

[7] 3GPP TR 33.809 v0.20.0, "Study on 5G Security Enhancement Against False Base Stations (FBS) (Release 18)", Technical specification (2022).

[8] V. Sharma, I. You, F. Leu, M. Atiquzzaman, "Secure and Efficient Protocol for Fast Handover in 5G Mobile Xhaul Networks", *Journal of Network and Computer Applications*, vol.102, pp. 38-57, 2018.

[9] L. Karaçay, Z. Bilgin, A. B. Gündüz, P. Çomak, E. Tomur, E. U. Soykan, U. Gülen, F. Karakoç, "A Network-based Positioning Method to Locate False Base Stations", *IEEE Access* vol. 9, pp.111368–111382, 2021. doi:10.1109/ACCESS.2021.3103673.

[10] H. Alrashede and R. A. Shaikh, "IMSI Catcher Detection Method for Cellular Networks", i*n 2019 2nd International Conference on Computer Applications & Information Security (ICCAIS)*, Riyadh, Saudi Arabia, 2019, pp. 1-6, doi: 10.1109/CAIS.2019.8769507.

[11] S. Park, A. Shaik, R. Borgaonkar, and J. Seifert. "Anatomy of Commercial IMSI Catchers and Detectors", *in Proceedings of the 18th ACM Workshop on Privacy in the Electronic Society (WPES'19).* Association for Computing Machinery, New York, NY, USA, pp. 74–86, 2019. https://doi.org/10.1145/3338498.3358649.

[12] K.-W. Huang, H.-M. Wang, "Identifying the Fake Base Station: A Location Based Approach", *IEEE Communications Letters* vol. 22, no. 8, pp. 1604–1607, 2018. doi:10.1109/LCOMM.2018.2843334.

[13] J. Shin, Y. Shin, J.-G. Park, "Network Detection of Fake Base Station Using Automatic Neighbour Relation in Self-organizing Networks", *in 13th International Conference on Information and Communication Technology Convergence (ICTC)*, 2022, pp. 968–970. doi:10.1109/ICTC55196.2022.9952901.

[14] A. Ali, G. Fischer, "Symbol Based Statistical RF Fingerprinting for Fake Base Station Identification", *in 29th International Conference Radioelektronika (RADIOELEKTRONIKA)*, pp. 1–5, 2019. doi:10.1109/RADIOELEK.2019.8733585.

[15] A. Ali, G. Fischer, "The Phase Noise and Clock Synchronous Carrier Frequency Offset based RF Fingerprinting for the Fake Base Station Detection", *in IEEE 20th Wireless and Microwave Technology Conference (WAMICON)*, pp. 1–6, 2019. doi:10.1109/WAMICON.2019.8765471.

[16] A. Mazroa, M. Arozullah, "Detection and Remediation of Attack by Fake Base Stations in LTE Networks", *International Journal of Soft Computing and Engineering (IJSCE)*, vol.5, no. 2, 2015.

[17] X. Yan, M. Ma, "A Lightweight and Secure Handover Authentication Scheme for 5G Network Using Neighbour Base Stations", *Journal of Network and Computer Applications* vol. 193, p. 103204, 2021. https://doi.org/10.1016/j.jnca.2021.103204.

[18] A. Sharma, I. Sharma and A. Jain, "A Construction of Security Enhanced and Efficient Handover AKA Protocol in 5G Communication Network", *in 10th International Conference on Computing, Communication and Networking Technologies (ICCCNT)*, Kanpur, India, pp. 1-6, 2019. doi: 10.1109/ICCCNT45670.2019.8944569.

[19] J. Guo, Y. Du, Y. Zhang, M. Li, "A Provably Secure ECC-based Access and Handover Authentication Protocol for Space Information Networks", *Journal of Network and Computer Applications* vol. 193, 2021. 103183. https://doi.org/10.1016/j.jnca.2021.103183.

[20] R. Ma, J. Cao, D. Feng, H. Li, Y. Zhang, X. Lv, "PPSHA: Privacy Preserving Secure Handover Authentication Scheme for All Application Scenarios in LTE-A Networks", *Ad Hoc Networks* vol. 87, pp. 49–60, 2019. https://doi.org/10.1016/j.adhoc.2018.11.012.

[21] Y. Zhang, R. H. Deng, E. Bertino and D. Zheng, "Robust and Universal Seamless Handover Authentication in 5G HetNets," *in IEEE Transactions on Dependable and Secure Computing*, vol. 18, no. 2, pp. 858-874, 1 March-April 2021, doi: 10.1109/TDSC.2019.2927664.

[22] 3GPP TS 36.331 – "Evolved Universal Terrestrial Radio Access (E-UTRA); Radio Resource Control (RRC); Protocol Specification (Release 8)", Technical Specification (2013).

[23] Y. Y. Deng, C. L. Chen, J. Shin and K. H. Wang, "Cryptanalysis of Yang et al.'s Handover Authentication Scheme for Mobile Network Environment," *in 2017 International Symposium on Computer Science and Intelligent Controls (ISCSIC)*, Budapest, Hungary, pp. 152-157, 2017. doi: 10.1109/ISCSIC.2017.43.

[24] V. A. Vasudevan, M. Tayyab, G. P. Koudouridis, X. Gelabert, and I. Politis, "An Integrated Approach for Energy Efficient Handover and Key Distribution Protocol for Secure NC-enabled Small Cells", *Computer Networks*, vol.206, 2022. https://doi.org/10.1016/j.comnet.2022.108806.

[25] W. Saad, M. Bennis and M. Chen, "A Vision of 6G Wireless Systems: Applications, Trends, Technologies, and Open Research Problems", *in IEEE Network*, vol. 34, no. 3, pp. 134-142, May/June 2020, doi: 10.1109/MNET.001.1900287.

Bitlis Eren Üniversitesi Fen Bilimleri Dergisi
BİTLİS EREN UNIVERSITY JOURNAL OF SCIENCE
ISSN: 2147-3129/e-ISSN: 2147-3188
VOLUME: 12 NO: 3 PAGE: 712-724 YEAR: 2023
DOI:10.17798/bitlisfen.1288561

Enhancing Deep Learning-Based Sentiment Analysis Using Static and Contextual Language Models

Khadija MOHAMAD[1], Kürşat Mustafa KARAOĞLAN[2*]

[1,2]*Karabük University, Faculty of Engineering, Department of Computer Engineering, 78050, Karabük, Türkiye*
(ORCID: 0009-0005-2741-3897) (ORCID: 0000-0001-9830-7622)

Keywords: Deep learning, Sentiment analysis, Static language models, Contextual language models, BERT, ELMo.

Abstract
Sentiment Analysis (SA) is an essential task of Natural Language Processing and is used in various fields such as marketing, brand reputation control, and social media monitoring. The various scores generated by users in product reviews are essential feedback sources for businesses to discover their products' positive or negative aspects. However, it takes work for businesses facing a large user population to accurately assess the consistency of the scores. Recently, automated methodologies based on Deep Learning (DL), which utilize static and especially pre-trained contextual language models, have shown successful performances in SA tasks. To address the issues mentioned above, this paper proposes Multi-layer Convolutional Neural Network-based SA approaches using Static Language Models (SLMs) such as Word2Vec and GloVe and Contextual Language Models (CLMs) such as ELMo and BERT that can evaluate product reviews with ratings. Focusing on improving model inputs by using sentence representations that can store richer features, this study applied SLMs and CLMs to the inputs of DL models and evaluated their impact on SA performance. To test the performance of the proposed approaches, experimental studies were conducted on the Amazon dataset, which is publicly available and considered a benchmark dataset by most researchers. According to the results of the experimental studies, the highest classification performance was obtained by applying the BERT CLM with 82% test and 84% training accuracy scores. The proposed approaches can be applied to various domains' SA tasks and provide insightful decision-making information.

1. Introduction

Sentiment Analysis (SA) identifies and extracts a text's underlying sentiment or opinion. As a result of the increase in textual data available on the internet, SA has become helpful in various applications, like market analysis, brand reputation management, social media monitoring, and news articles [1]. Deep Learning-based approaches have shown promising results in SA tasks [2], mainly using Static and Contextual Language Models. Static Language Models (SLMs), such as Word2Vec and GloVe, represent each word in a fixed-dimensional vector space based on its co-occurrence statistics. Contextual Language Models (CLMs), such as Embeddings from Language Models (ELMo) and Bidirectional Encoder Representations from Transformers (BERT), generate word representations that capture the context and meaning of the entire sentence [3].

SA studies, whose use has increased in recent years, are widely used in many areas, such as using SA in political analysis [4], [5], and social media monitoring [6]. In addition, studies to detect sentiment in social media are also presented in the literature [7], [8]. At the same time, in the marketing field, some studies detect sentiment in the reviews of

* Corresponding author: kkaraoglan@karabuk.edu.tr
Received: 27.04.2023, Accepted: 08.09.2023

customers or their feedback [9]. The role of SA also played a lot during the Corona pandemic period, as many researchers analyzed the feelings and emotions of people towards this disease during this period [10], [11].

Deep Learning has a significant role in Natural Language Processing (NLP) projects in multiple areas, such as entity recognition [12], [13], question answering [14], [15], and SA [16]. It has been observed that sentiment in the text can be detected using the Convolutional Neural Network (CNN) model [17], [18]. A Long Short-Term Memory (LSTM) [19], [20], on the other hand, is a neural network developed as a solution to the disappearing gradient problem that complicates the training of this data. In addition, there is research based on the Transformer Model to achieve this task. For example, emotions are classified using BERT as a Transformer-based Deep Learning model. It was found that it is possible to obtain a high classification accuracy of 88% [21], [22]. In addition, machine learning has a significant role in applying this task; for example, Support Vector Machine can be used to perform SA [23], [24]. In addition, some of the experiments resorted to linguistic analysis features, which showed beneficial results in the fields of text classification and context understanding [25].

As for the representation of words, research in this field has been numerous and varied to achieve this task. Some of them followed SLMs, and some of them followed CLMs; examples of SLMs are following FastText to represent words, which is the famous language model (word embedding) [26], and Word2Vec [27], but CLM refers to the process of representing words or phrases in a sentence based on their surrounding context, such as BERT [28], and Robustly Optimized BERT Pre-Training Approach (RoBERTa) [29], which uses Deep Learning techniques to generate CLMs by processing text in a way that takes into account the words that come before and after each word being analyzed. Multiple experiments that combined two methods of word embedding, such as combining GloVe and FastText, showed promising results from their combination [30].

Several studies have been conducted in the literature on SA. One study utilized [26] FastText for feature extraction and CNN as the classifier model to analyze sentiment in the Movie Reviews dataset, achieving exceptional accuracy. In another study [27], SA was performed using hotel reviews in Indonesia. In the given study, Word2Vec was used for feature extraction, LSTM was used as a classifier model, and high accuracy scores were obtained. Another study [20] used Residual Long Short-Term Memory and obtained acceptable accuracy scores for SA. In addition to the above studies, the Amazon dataset used in this study contains a wide variety of data and covers a wide range of diversity. Thus, this dataset is valuable for researchers to evaluate model performance. The literature [31] presents a hybrid approach combining SVM and k-Means to perform SA tasks on the Amazon dataset. Another study [32] focuses on cell phone reviews on Amazon dataset to perform SA tasks with the BERT language model. A similar study [33] applied a CNN-based SA approach using Word2Vec in text representation for SA on cell phone reviews. Other work in the literature [34], which uses TF-IDF for feature extraction and LSTM as a classifier model, also produces effective performance results on the Amazon dataset. These studies contribute to SA research in different areas by developing or using various feature extraction techniques and classifier models.

It is also worth noting that different studies have adopted different labeling approaches when working with the dataset in question. For example, in one study in the literature [32], comments with 1 and 2 stars were classified as negative, while comments with three stars were considered neutral, and comments with 4 and 5 stars were considered positive. In contrast, another study [35] turned the classification task into a binary problem by treating (1 and 2) stars as negative and (4 and 5) stars as positive, effectively excluding three-star reviews.

This simplified binary classification achieved higher accuracy than the more complex task of classifying the sentiment into five different categories, which is the approach adopted in our study. Moreover, several studies have extensively studied the SA of customer reviews from different sources. In one notable study [36], researchers collected customer reviews on “We Chat” for three years. These comments were associated with ratings ranging from 1 to 5 stars, where ratings of 1 and 2 were considered negative comments, 3 represented neutral feedback, and 4 and 5 indicated positive comments.

This paper addresses the growing need for robust, state-of-the-art SA models that accurately classify sentiments across various domains. The exponential growth of online reviews and customer feedback emphasizes the importance of understanding emotions expressed in textual data. However, obtaining accurate sentiment classification remains a significant challenge in this context. To address this challenge, in this study, we propose a Deep Learning-based SA approach that uses SLMs

and CLMs to effectively classify sentiments in textual data. This study examines the effectiveness of a multi-layer CNN architecture as a Deep Learning model for sentiment classification. The objective is to classify input data according to sentiments such as "very satisfied", "satisfied", "neutral", "unsatisfied", or "very unsatisfied". To evaluate the performance of our approaches, we conduct assessments using Amazon data, a publicly available SA dataset that includes a customer review dataset.

The main objectives of this paper are:

- Introducing a novel approach to SA: The study proposes new approaches using Deep Learning-based methodologies that utilize SLMs and CLMs. These approaches are evaluated on the Amazon dataset, which is publicly available for SA and is considered by most researchers as a benchmark dataset.
- Comparing the performance of static and contextual language models: This study compares the performance of SLMs such as Word2Vec and GloVe with CLMs such as ELMo and BERT for SA purposes.
- Development of a CNN for SA: The paper proposes CNN models that can use static or contextual representations of texts as input. The CNN models are trained to predict labels based on user-generated ratings in review texts.
- Obtaining high accuracy for SA: Among the proposed approaches, the BERT CLM-based approach achieves high classification results with 82% test accuracy and 84% training accuracy.
- Providing insights for decision-making: The proposed approach provides insightful decision-making information for various areas where SA is required, such as marketing, brand reputation control, and social media monitoring. And for businesses facing high user populations, it allows them to use user reviews and satisfaction scores to discover the positives or shortcomings of their products.

This paper is structured in 6 sections to present the research. Section 1 introduces the objectives of the study and lays the foundation for the following sections by providing a comprehensive literature review on neural network-based word representation models and SA analysis. Section 2 summarizes the specific research objectives by highlighting the pool of problems addressed in the study. Section 3 details the methodologies for this work and describes the specific approaches and techniques applied and developed to perform the experiments. Section 4 presents information about the dataset used in the study, the performance metrics applied, and the hyperparameters identified during the CNN model training process. Furthermore, the results obtained from the experiments are presented in detail in Section 4. In Section 5, a comprehensive description of the findings of the experimental studies is presented along with analysis and discussion. In the same chapter, key insights and observations from the experimental results are also presented. Finally, in Section 6, discussions and conclusions are given. In this section, the main findings of the study are summarized, and the performance results are discussed. Furthermore, this section concludes the paper by summarizing potential work for future research and advancements in the field of SA and word representation.

2. Research Objectives

This research aims to achieve the following objectives:

- Performing precise text pre-processing with NLP techniques without distorting the meaning and structure of the input texts
- Performing labeling operations to prepare model labels based on the customer score, considering the semantics of the review texts
- Generating vectors of review texts with contextual features using SLMs and pre-trained CLMs and ensuring that the inputs to the deep network model are transformed into the appropriate form
- Developing a CNN model for sentiment classification, and optimizing the fine-tuning of hyperparameters to improve the performance of the models
- Conducting experimental studies to measure the performance of the realized language models and evaluating the results of experimental studies.

To achieve the research goals outlined in this chapter, we conducted experiments using state-of-the-art contextual word representation models (CLMs) as input and CNN-based approaches. The experiments aim to compare static representation models with contextual models and test their performance evaluations. Through these experiments, we demonstrate the effectiveness of contextual word representation models over static models in category-based multi-class in SA tasks.

3. Methodology

In this section, the main steps we follow to create our SA system are explained, including language models for the representation of textual reviews and the Deep Learning model used in customer review

classification. Section 3.1 presents the data pre-processing, Section 3.2 gives the pre-trained models as language models used in this study, and Section 3.3 provides an overview of the architecture of the applied learning model.

3.1. Pre-processing

Applying measures like text cleaning or preprocessing is crucial for enhancing the performance of our approaches, and it constitutes an essential step in any NLP project. Removing ineffective words or punctuation marks must be executed precisely, ensuring the preservation of sentence structure, integrity, or opinion while aligning with the intended scenario [37].

Punctuation, URLs (https:// or www.), numbers, and symbols (#tags, mentions, and emojis) were all removed from the reviews as they do not convey sentiment. Subsequently, the reviews underwent processes such as lowercasing, lemmatization, and tokenization. Tokenization was performed using the tokenizer from the NLTK package. Finally, stop words were dropped from the text using the NLTK package to obtain the refined list.

3.2. Static and Contextual Language Models

Word representations are numerical representations of words that capture their semantic and syntactic information. These embeddings are used as inputs to Deep Learning-based SA models. This paper uses two types of embeddings: static embeddings with Word2Vec and GloVe as SLMs and contextual embeddings with BERT and ELMo as CLMs.

SLMs are pre-trained on a large corpus of text and represent each word in a fixed-dimensional vector space based on its co-occurrence statistics. These models detect the distributive properties of words and are useful for capturing semantics at the word level. There are several SLMs, such as Word2Vec and GloVe. Word2Vec is a neural-based model that learns embedding vectors by predicting the surrounding words in a context [38]. GloVe, on the other hand, is a count-based model that uses the co-occurrence matrix of words to generate embeddings [39]. We choose 100 as the vector dimension to represent each word in the case of SLMs.

CLMs are generated by Deep Learning models that consider the context and meaning of the entire sentence. These models are beneficial for detecting the nuances of language, such as irony and negation. Two popular models for generating contextual embeddings are ELMo and BERT. ELMo uses a bi-directional LSTM to generate an embedding vector that captures the context of the sentence [40]. BERT uses a transformer-based architecture to generate embeddings that capture the sentence's syntax and semantics [41]. From BERT models, we chose the $BERT_{large\text{-}uncased}$ model (BERTM) for creating vectors. The vector dimension we have in the case of CLMs is 1024 to represent each review in our dataset.

3.3. Multi-layer Convolutional Neural Network

CNN, one of the Deep Neural Network models, is usually used in computer vision and image recognition tasks, but it has also been successfully applied in SA and other NLP tasks. The network architecture of a CNN comprises several layers, such as convolutional, pooling, and fully connected layers. The input data for a CNN is typically a two-dimensional matrix. The convolutional layers apply a series of learnable filters to the input data to produce feature maps that indicate the existence of particular patterns and features in the data. The feature maps are then down-sampled by the pooling layers to make them smaller while preserving the most crucial data. The fully connected layers produce the network's ultimate output after they have processed the pooling layers' flattened output.

A CNN can capture the local context and relationships between words in a sentence in the context of SA. Convolutional layers can be used to create feature maps that show the presence of particular word or phrase combinations in the input text by applying them to the pre-trained word embedding vectors of the input words. The fully connected layers can then process the pooling layers' flattened output to provide the input text's final sentiment prediction. At the same time, the pooling layers can down-sample the feature maps to collect the most crucial information. CNNs are potent tools for SA tasks because they are good at catching local and global correlations between words in the text.

In this study, a multi-layer CNN model was created and trained for various epochs according to the language model and cross-validated using k-fold 5. Since the task involves multiple classifications, the loss function was set to categorical cross-entropy. The CNN model architecture and hyper-parameters used in the study are presented in Table 2. These values were obtained by optimizing through experience to achieve acceptable accuracy while at the same time taking into account overfitting and underfitting.

In order to take into account the multi-label classification included in this study, the SoftMax

function was chosen as the output function. The formulas applied to the ReLU and SoftMax functions are presented in equations (1) and (2).

$$ReLU(x) = \max(0, x) \quad (1)$$

$$SoftMax(z_i) = \frac{e^{z_i}}{\sum_{j=1}^{n} e^{z_j}} \quad (2)$$

Where x is the input value, n is the number of classes, and zi is the value of the input vector to the SoftMax function.

3.4. Architecture of the Proposed Approaches

In constructing the architecture of the proposed approaches, the initial step involved aligning the input data to the model inputs, and ensuring data quality and consistency through data preprocessing techniques applied to the reviews. Semantic vectors were then constructed using SLMs and CLMs to extract rich semantic information from the processed data, allowing the underlying meaning and context of the reviews to be effectively captured. A CNN-based classification model was employed based on semantic vectors, chosen for its capability to leverage the hierarchical representation of features in semantic vectors.

To mitigate the risks of overfitting and underfitting, a rigorous k-fold cross-validation methodology was utilized to optimize the model's performance, with k set to five, enabling iterative training and validation of the model using different subsets of the training data. By employing k-fold cross-validation, the model's generalization ability was enhanced, allowing it to perform well on unseen data. Throughout the iterative training and validation process, consideration was given to addressing overfitting and underfitting issues. Overfitting ensues when the model performs exceptionally well on the training data but fails to generalize to new, untouched data. In contrast to overfitting, underfitting ensues when the model's sophistication is insufficient to capture the underlying patterns in the data, resulting in poor performance.

In addition to the above overfitting and underfitting checks, the K-fold cross-validation process analyzed the model's performance on both the training and validation sets and fine-tuned the hyperparameters to ensure the optimal configuration of the model. After the training phase, the performance of the trained model was evaluated on the test data, and fundamental and valid performance metrics measured the outputs. These metrics, such as accuracy, precision, recall, and F_1-score, produced quantitative analyses of the model's effectiveness in capturing desired patterns and predicting the precision of reviews or other relevant aspects. Figure 1 shows the architecture for implementing the proposed approaches and their detailed components.

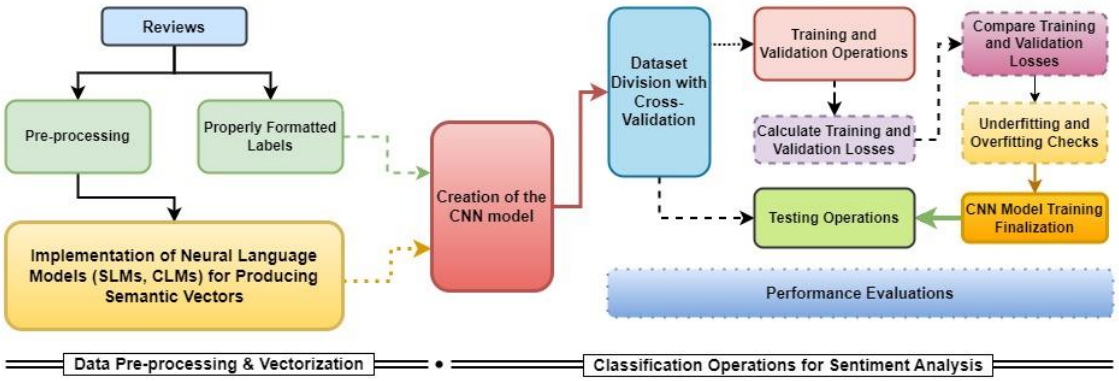

Figure 1. The architecture with components for the execution of the proposed approaches

4. Experimental Study

This section summarizes the experimental studies, covering the dataset and training hyperparameters. The results are then presented using various performance metrics. Specifically, Section 4.1 provides detailed information about the dataset employed, classifier hyperparameters, and performance metrics utilized in the experimental settings. Afterward, Section 4.2 offers a comprehensive analysis of the experimental results, including performance comparisons.

4.1. Experimental Settings

4.1.1. Dataset

In this subsection, information about the data set used in the experimental studies is described in

detail. The experiments were conducted using Amazon datasets comprising mobile phone reviews totaling 30,000 customer reviews, each accompanied by a corresponding rating value. Prior to the initiation of the training process, the dataset was divided into Train and Test sets. Notably, cross-validation was applied to parse the data, a technique utilized to ensure the robustness and reliability of our results.

Table 1 presents descriptive statistical information about the dataset utilized in our study. For example, the table indicates that there are 16,251 reviews labeled as "very satisfied," as these reviews received a rating of 5. Our classification scheme categorizes 1-star reviews as "very unsatisfied," 2-star reviews as "unsatisfied," 3-star reviews as "neutral," 4-star reviews as "satisfied," and 5-star reviews as "very satisfied". The table provides a comprehensive overview of the sentiment label distribution based on the corresponding customer ratings.

Table 1. Statistical descriptive information about the dataset used

Total number of reviews	30000				
Shortest review	1 word				
Longest review	250 words				
Average word count	30				
Number of labels	5				
Distribution of each class	very satisfied	satisfied	neutral	unsatisfied	very unsatisfied
	16251	4300	2290	1910	5249

4.1.2. Evaluation Metrics

Various metrics used to evaluate multiple classifications are presented in the literature, including micro, macro, and example-based average metrics. Micro metrics [42] have been widely adopted in the literature to assess multiple classifications on large-sized data, showcasing their effectiveness in handling multiple classes. Additionally, alternative metrics can be employed to evaluate different systems.

In this study, a comprehensive set of metrics was employed to assess the performance of our Deep Learning model, encompassing Accuracy (3), Recall (4), Precision (5), and F_1-score (6), Learning curves, and Receiver Operating Characteristic (ROC). These metrics allow for a holistic evaluation of the model's effectiveness in capturing relevant patterns and predicting sentiment sensitivity in the reviews.

$$Accuracy = \frac{TP + TN}{TP + TN + FP + FN} \quad (3)$$

$$Recall = \frac{TP}{TP + FN} \quad (4)$$

$$Precision = \frac{TP}{TP + FP} \quad (5)$$

$$F1 - score = 2 * \frac{(Precision * Recall)}{(Precision + Recall)} \quad (6)$$

Whereas "TP" denotes the number of True Positives, "TN" denotes the number of True Negatives, "FP" denotes the number of False Positives, and "FN" denotes the number of False Negatives.

4.1.3. Training Hyperparameters of Deep Learning Approaches

The user-specified parameters employed to train the Deep Learning model are referred to as hyperparameters. Hyperparameters govern the model's behavior and significantly affect its performance. Configuring these values is crucial for achieving optimal results in the model training process [43].

In our study, the hyperparameter settings were carefully fine-tuned, and the selected values are presented in Table 2. The table presents a comprehensive overview of the determined hyperparameters, facilitating the fine-tuning of the model for enhanced performance and effective learning during training. These hyperparameter settings are essential in ensuring that the model's behavior aligns with the specific requirements of the task, producing reliable and accurate results.

Table 2 presents the hyperparameters utilized in our study, encompassing various essential aspects of the model configuration. The hyperparameters include the number of epochs, batch size, loss function, activation function, learning rate, CNN activation function, filter size,

kernel size, dropout rate, training approach, and optimizer. The number of epochs represents the frequency with which the training dataset is used during the training process. Batch size, however, denotes the number of samples fed into the model at once for each iteration.

The loss function measures the discrepancy between predicted and actual sentiment labels. The activation function generates a probability distribution over the output classes, enabling the model to make effective predictions.

Table 2. Hyperparameters settings for the applied CNN model

Hyperparameters	**Properties**			
Number of epochs	BERTM	ELMo	Word2Vec	GloVe
	48	53	29	25
Batch size	256			
Loss function	Categorical Cross-entropy			
Activation functions	Softmax			
Learning rate	0.0001			
Activation function of CNNs	RelU			
Filter size of CNN_1	50			
Filter size of CNN_2	100			
Filter size of CNN_3	200			
Kernel size of CNNs	3			
Dropout of CNNs	0.2			
Train Approach	Cross-validation			
Optimizer	Adam			

Meanwhile, the learning rate governs the step size during the optimization process, impacting the convergence and stability of the model. Additionally, the CNN activation function applies explicitly to the convolutional layer, enhancing the feature extraction capability of the model.

The CNN filter size determines the number of filters employed in the convolutional layer, while the kernel size indicates the dimensions of the kernel used in the convolutional layer. A dropout technique is employed to prevent overfitting, reducing the likelihood of the model relying too heavily on specific features during training. Furthermore, our training approach involves cross-validation, ensuring our results' reliability and generalization. As for optimization, the Adam optimizer is employed, aiding in the efficient convergence of the model during the training process.

4.2. Experimental Results with Performance Comparison

The learning curves serve as essential diagnostic tools for evaluating the model's convergence and identifying potential issues such as overfitting or underfitting. They provide a comprehensive understanding of the model's behavior during training, enabling researchers to fine-tune the hyperparameters and optimize the model's performance.

Figure 2 displays the learning curves of the training and validation phases, utilizing BERTM as the word representation model. These learning curves provide valuable insights into the model's performance over time, allowing a comprehensive assessment of its convergence and generalization capabilities. Similarly, Figure 3 visually represents the learning curves for training and validation, showing the model's behavior when employing ELMo as the word representation model. Likewise, Figure 4 showcases the learning curves for training and validation using Word2Vec, presenting a detailed advancement of the model's performance throughout the training process. Lastly, Figure 5 displays the learning curves for GloVe as the word representation model, facilitating a thorough comparison of its performance during the training and validation phases.

Table 3 presents the performance results of SA classification approaches developed using SLMs and CLMs according to various metrics. The values indicate the performance quality of each model according to the experimental studies performed.

Table 3. Performance metrics results of approaches developed according to SLMs and CLMs

Metrics	BERTM	ELMo	Word2Vec	GloVe
Accuracy	0.82	0.80	0.75	0.78
Precision	0.82	0.79	0.72	0.76
Recall	0.81	0.80	0.75	0.78
F_1-score	0.81	0.79	0.73	0.77

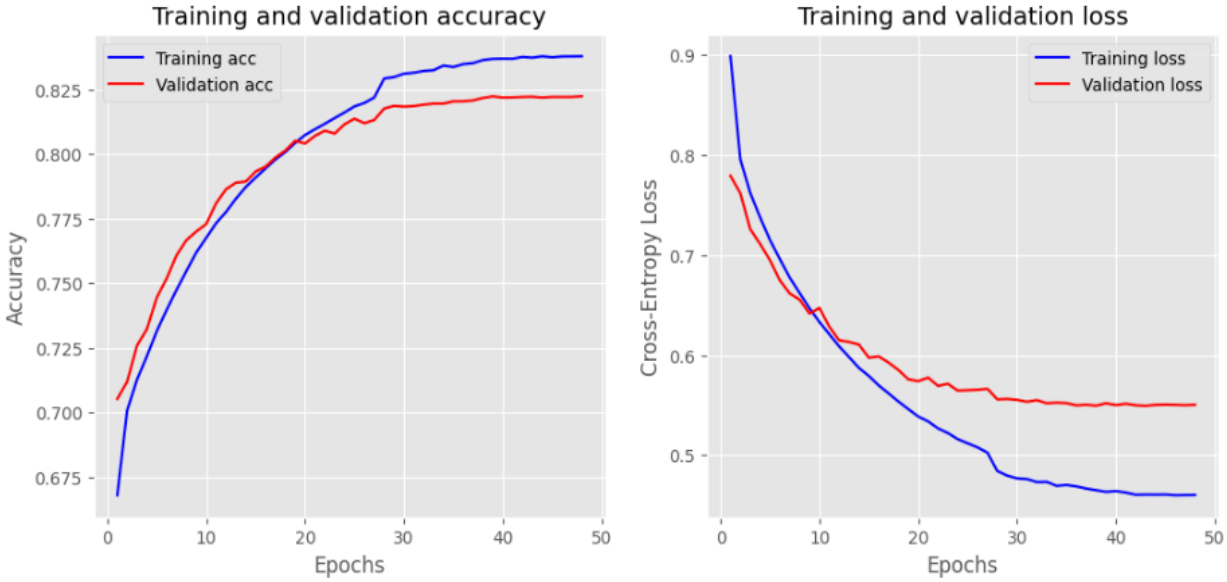

Figure 2. Learning curves of training and validation of SA with the BERTM

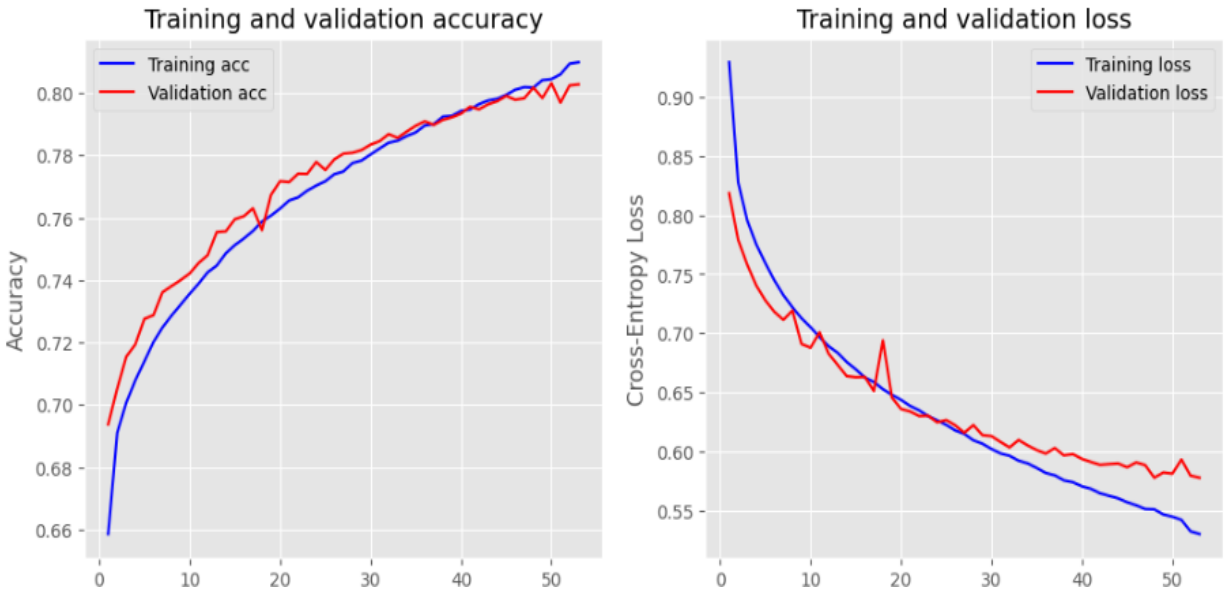

Figure 3. Learning curves of training and validation of SA with the ELMo model

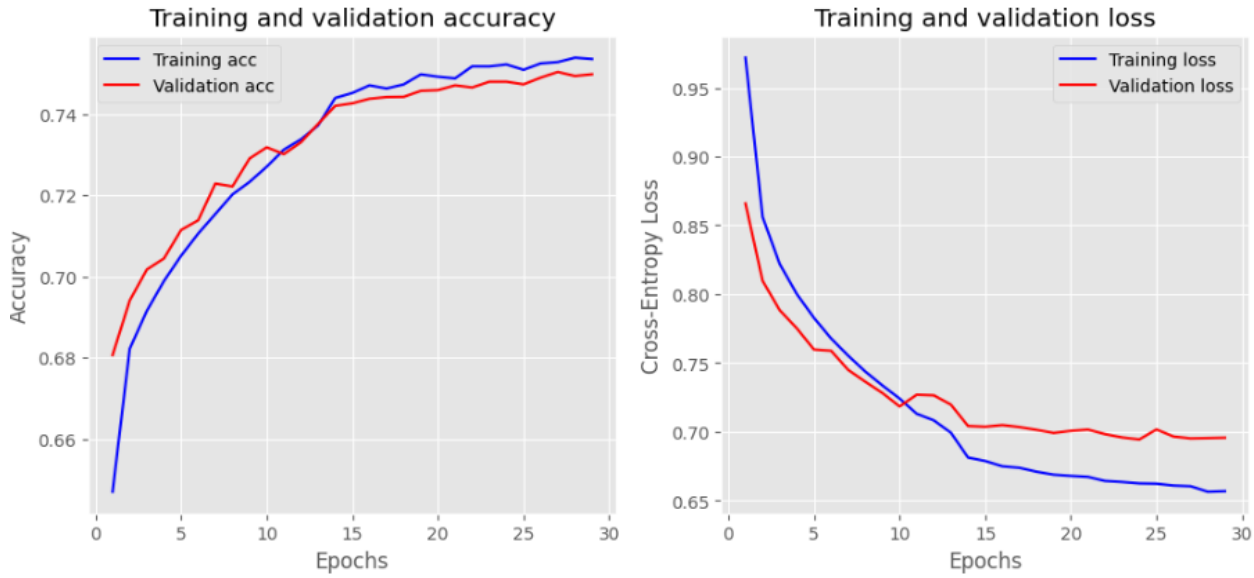

Figure 4. Learning curves of training and validation of SA with the Word2Vec model

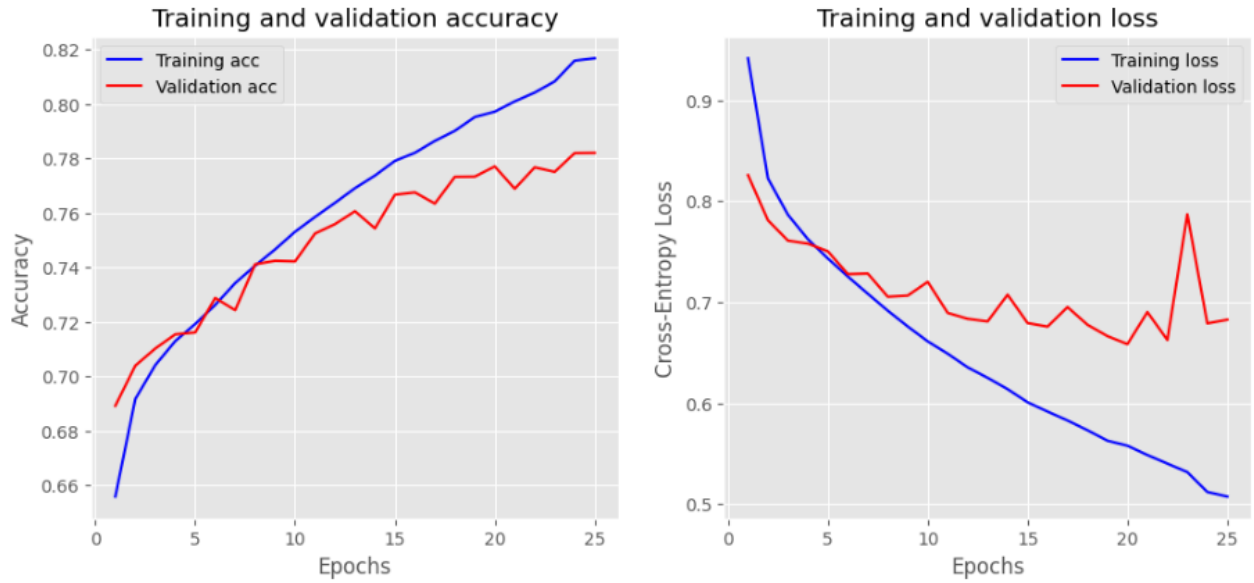

Figure 5. Learning curves of training and validation of SA with the GloVe model

Figure 6 illustrates the ROC curve plots obtained for each neural-based language model, presenting a more precise and comprehensive evaluation of the performance quality in the experimental studies. The ROC curves showcase the model's ability to discriminate between different sentiment classes, allowing for a visual comparison of their respective classification performances.

5. Discussion and Results

This section presents our understanding of the performance of both SLMs and CLMs. It describes the challenges the proposed SA approaches face in attempting to classify more than just positive or negative categories.

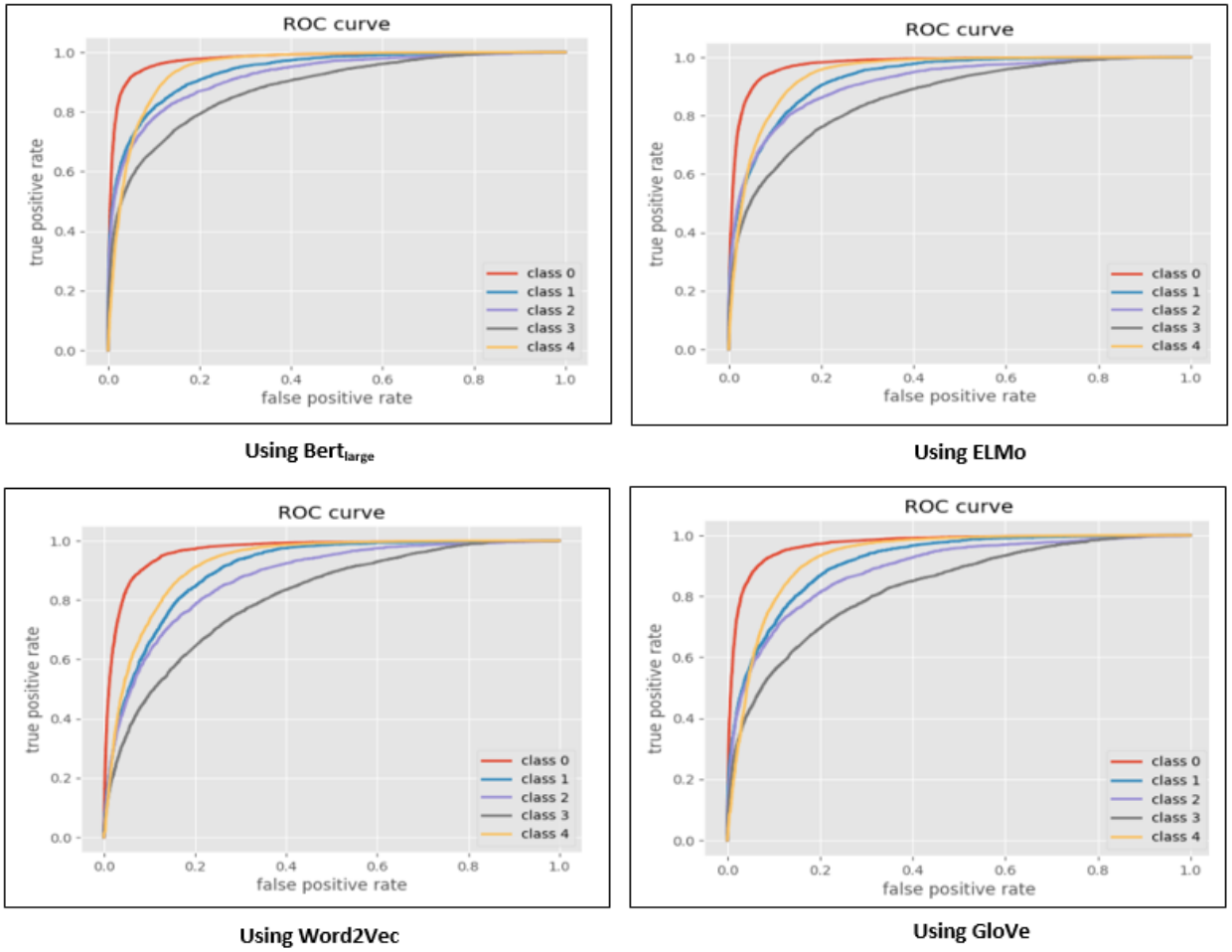

Figure 6. ROC curve plots showing the classification performance of the applied language models.

Based on the ROC curves, it is evident that categorizing classes with ratings of 1 (unsatisfied), 2 (neutral), and 3 (satisfied) poses a significant challenge. Their classification accuracy is lower compared to categories with ratings of 0 (very unsatisfied) and 4 (very satisfied). On the other hand, classes belonging to categories 0 and 4 are easily classified with higher accuracy.

The study reveals that BERTM outperforms other commonly utilized language models with remarkable accuracy and recall values of 0.82. Additionally, when ELMo is employed as the language model, elevated levels of accuracy are achieved. Fundamentally, higher accuracy and performance are attained by utilizing CLMs instead of SLMs. However, classifying feelings into multiple classes, as in our case with five classes, presents challenges due to the closeness in meaning and confusion between emotions. For instance, classes classified as 2 and 3 exhibit similarities in feelings and opinions, making their differentiation difficult. The same issue applies between classes with a classification of 1 and 2, as evident from all the ROC curves in Figure 6. Regarding hyperparameters, several settings were experimented with during the training of the CNN model before obtaining the result. Instances of decreased accuracy were observed when the number of training epochs was set to 10.

Selecting the appropriate number of epochs is a crucial and meticulous task in training Deep Learning models. In our proposed model, we initially selected an epoch of 60, and then, for each language model, we carefully determined the suitable epoch number by observing the learning rate curves. Ultimately, the last suitable epoch number was determined through experimentation, as presented in Table 3. Through our experimentation, we observed that using GloVe as the language model, an overfitting problem occurs when the number of epochs exceeds 25. Similarly, when using Word2Vec, an overfitting problem arises when the number of epochs exceeds 29. For BERTM, the critical threshold is 48 epochs, beyond which overfitting becomes a concern. Lastly, when

utilizing ELMo, an overfitting problem occurs when the number of epochs exceeds 53.

Based on the findings of the experimental study, it has been observed that neural network-based word representation models, such as SLMs, exhibit limited precision in considering the specific context of words. In contrast, contemporary pre-trained approaches like CLMs demonstrate the ability to generate distinctive vector representations that can encompass a greater number of features by incorporating the context of a word within its originating sentence. Consequently, CLMs have the capacity to capture the intricate nuances of a word's meaning within its particular context. This implies that the rich vectors produced by CLMs outperform those of SLMs.

6. Conclusion

This paper proposes high-performance SA approaches in which Deep Learning and pre-trained sentence representation models are applied. In these approaches, four state-of-the-art pre-trained models are used to represent the input text data, including BERTM, ELMo as CLM, and Word2Vec and GloVe as SLM.

In conclusion, it was demonstrated that the semantic meaning and context of words in the text can be effectively captured, and the performance of SA systems can be improved by utilizing Deep Learning architectures in conjunction with language models. The superiority of modern language models like BERTM and ELMo over traditional word embeddings as SLMs was established in this study, as evidenced by their higher accuracy and superior performance in the task. Furthermore, the investigation highlighted the significance of hyperparameters in influencing model accuracy. Overall, the limitations of SA across multiple categories were underscored, emphasizing the advantages of employing CLMs that consider the specific context in which a word is employed. Furthermore, this study has shown that the performance of language models with different architectures and training sets significantly affects the classification operations when contextualizing input texts and vectorizing them according to a semantic and distributed space. It is also essential that the features stored in the semantic vectors transformed from texts are not lost and that their valuable aspects are strengthened and included in the learning algorithms. In this context, the performance of the CNN model as a classifier is evaluated in this study. Although the classification model proposed in this study offers high performance, it is thought that with Deep Learning models with attention mechanisms and advanced CNN architectures to be developed by considering fine-tuning optimizations, high applicability, and higher performance results can be obtained.

In the future, we plan to use our experience in this study to test the classification performance of the attention-learning models on state-of-the-art pre-trained language models, as well as to increase the resolution of feature extraction by combining the contextual vectors obtained from language models. In addition to the above, we also plan to classify the semantic vectors in SA by vectorizing them with different data types (e.g. audio, video, and text).

Contributions of the authors

This study benefited from the diverse expertise of its authors.

Karaoğlan's contributions encompassed conceptualization, research design, editing, supervision, project management, critical review, and final approval. Mohamad's role focused on literature review, data collection, data analysis, and manuscript composition.

Conflict of Interest Statement

There is no conflict of interest between the authors.

Statement of Research and Publication Ethics

The study is complied with research and publication ethics.

References

[1] J. Hartmann, M. Heitmann, C. Siebert, and C. Schamp, “More than a feeling: Accuracy and application c sentiment analysis”, *Int. J. Res. Mark.*, vol. 40, no. 1, pp. 75–87, 2023.

[2] H. T. Phan, N. T. Nguyen, and D. Hwang, “Aspect-level sentiment analysis: A survey of grap convolutional network methods”, *Inf. Fusion*, vol. 91, pp. 149–172, 2023.

[3] F. Lin, S. Liu, C. Zhang, J. Fan, and Z. Wu, "StyleBERT: Text-audio sentiment analysis with Bi-direction Style Enhancement", *Inf. Syst.*, vol. 114, no. 102147, p. 102147, 2023.

[4] M. M. Hasan and H. Jiang, "Political sentiment and corporate social responsibility", *Br. Account. Rev.*, vo 55, no. 1, p. 101170, 2023.

[5] D. Antypas, A. Preece, and J. Camacho-Collados, "Negativity spreads faster: A large-scale multilingu Twitter analysis on the role of sentiment in political communication", *arXiv [cs.CL]*, 2022.

[6] A. R. Rahmanti *et al.*, "Social media sentiment analysis to monitor the performance of vaccination coverag during the early phase of the national COVID-19 vaccine rollout", *Comput. Methods Programs Biomed* vol. 221, no. 106838, p. 106838, 2022.

[7] R. Haque, N. Islam, M. Tasneem, and A. K. Das, "Multi-class sentiment classification on Bengali soci media comments using machine learning", *International Journal of Cognitive Computing in Engineerin* vol. 4, pp. 21–35, 2023.

[8] C. Qian, N. Mathur, N. H. Zakaria, R. Arora, V. Gupta, and M. Ali, "Understanding public opinions o social media for financial sentiment analysis using AI-based techniques", *Inf. Process. Manag.*, vol. 5 no. 6, p. 103098, 2022.

[9] H.-C. K. Lin, T.-H. Wang, G.-C. Lin, S.-C. Cheng, H.-R. Chen, and Y.-M. Huang, 'Applying sentime analysis to automatically classify consumer comments concerning marketing 4Cs aspects', *Appl. So Comput.*, vol. 97, no. 106755, p. 106755, 2020.

[10] D. Sunitha, R. K. Patra, N. V. Babu, A. Suresh, and S. C. Gupta, "Twitter sentiment analysis using ensembl based deep learning model towards COVID-19 in India and European countries", *Pattern Recognit. Let* vol. 158, pp. 164–170, 2022.

[11] N. Leelawat *et al.*, "Twitter data sentiment analysis of tourism in Thailand during the COVID-19 pandem using machine learning", *Heliyon*, vol. 8, no. 10, p. e10894, 2022.

[12] M. Bhattacharya, S. Bhat, S. Tripathy, A. Bansal, and M. Choudhary, "Improving biomedical named entit recognition through transfer learning and asymmetric tri-training", *Procedia Comput. Sci.*, vol. 218, p 2723–2733, 2023.

[13] A. Goyal, V. Gupta, and M. Kumar, "A deep learning-based bilingual Hindi and Punjabi named entit recognition system using enhanced word embeddings", *Knowl. Based Syst.*, vol. 234, no. 107601, 107601, 2021.

[14] Q. Qiu, M. Tian, K. Ma, Y. J. Tan, L. Tao, and Z. Xie, "A question answering system based on miner exploration ontology generation: A deep learning methodology", *Ore Geol. Rev.*, vol. 153, no. 105294, 105294, 2023.

[15] A. Al-Sadi, M. Al-Ayyoub, Y. Jararweh, and F. Costen, "Visual question answering in the medical domai based on deep learning approaches: A comprehensive study", *Pattern Recognit. Lett.*, vol. 150, pp. 57–7 2021.

[16] N. Sharm, T. Jain, S. S. Narayan, and A. C. Kandakar, "Sentiment analysis of Amazon smartphone review using machine learning & deep learning", in *2022 IEEE International Conference on Data Science an Information System (ICDSIS)*, 2022.

[17] D. Maity, S. Kanakaraddi, and S. Giraddi, "Text sentiment analysis based on multichannel convolution neural networks and syntactic structure", *Procedia Comput. Sci.*, vol. 218, pp. 220–226, 2023.

[18] W. Li, L. Zhu, Y. Shi, K. Guo, and E. Cambria, "User reviews: Sentiment analysis using lexicon integrate two-channel CNN–LSTM family models", *Appl. Soft Comput.*, vol. 94, no. 106435, p. 106435, 2020.

[19] Y. Zhang, J. Wang, and X. Zhang, "Conciseness is better: Recurrent attention LSTM model for documen level sentiment analysis", *Neurocomputing*, vol. 462, pp. 101–112, 2021.

[20] D. O. Oyewola, L. A. Oladimeji, S. O. Julius, L. B. Kachalla, and E. G. Dada, "Optimizing sentime analysis of Nigerian 2023 presidential election using two-stage residual long short term memory", *Heliyo* vol. 9, no. 4, p. e14836, 2023.

[21] A. Patel, P. Oza, and S. Agrawal, "Sentiment analysis of customer feedback and reviews for airline service using language representation model", *Procedia Comput. Sci.*, vol. 218, pp. 2459–2467, 2023.

[22] M. P. Geetha and D. Karthika Renuka, "Improving the performance of aspect based sentiment analys using fine-tuned Bert Base Uncased model", *International Journal of Intelligent Networks*, vol. 2, pp. 64 69, 2021.

[23] A. Borg and M. Boldt, "Using VADER sentiment and SVM for predicting customer respons sentiment", *Expert Syst. Appl.*, vol. 162, no. 113746, p. 113746, 2020.

[24] T. H. Jaya Hidayat, Y. Ruldeviyani, A. R. Aditama, G. R. Madya, A. W. Nugraha, and M. W. Adisaputr "Sentiment analysis of twitter data related to Rinca Island development using Doc2Vec and SVM an logistic regression as classifier", *Procedia Comput. Sci.*, vol. 197, pp. 660–667, 2022.

[25] M. Bibi *et al.*, "A novel unsupervised ensemble framework using concept-based linguistic methods an machine learning for twitter sentiment analysis", *Pattern Recognit. Lett.*, vol. 158, pp. 80–86, 2022.

[26] I. N. Khasanah, "Sentiment classification using fastText embedding and deep learning model", *Procedi Comput. Sci.*, vol. 189, pp. 343–350, 2021.

[27] P. F. Muhammad, R. Kusumaningrum, and A. Wibowo, "Sentiment analysis using Word2vec and lon short-term memory (LSTM) for Indonesian hotel reviews", *Procedia Comput. Sci.*, vol. 179, pp. 728–73 2021.

[28] K. Kaur and P. Kaur, "BERT-CNN: Improving BERT for requirements classification usin CNN", *Procedia Comput. Sci.*, vol. 218, pp. 2604–2611, 2023.

[29] M. Siddharth and R. Aarthi, "Blended multi-class text to image synthesis GANs with RoBerTa and Mas R-CNN", *Procedia Comput. Sci.*, vol. 218, pp. 845–857, 2023.

[30] N. Badri, F. Kboubi, and A. H. Chaibi, "Combining FastText and glove word embedding for offensive an hate speech text detection", *Procedia Comput. Sci.*, vol. 207, pp. 769–778, 2022.

[31] K. Korovkinas, P. Danėnas, and G. Garšva, "SVM and k-means hybrid method for textual data sentimer analysis", *Balt. J. Mod. Comput.*, vol. 7, no. 1, 2019.

[32] A. S. M. AlQahtani, "Product Sentiment Analysis for Amazon Reviews", *Int. J. Comput. Sci. Inf. Technol* vol. 13, no. 3, pp. 15–30, 2021.

[33] S. A. Aljuhani and N. Saleh, "A comparison of sentiment analysis methods on Amazon reviews of mobil phones", *Int. J. Adv. Comput. Sci. Appl.*, vol. 10, no. 6, 2019.

[34] Sangeetha and Kumaran, 'Sentiment analysis of amazon user reviews using a hybrid approach', *Measu Sens.*, vol. 27, no. 100790, p. 100790, 2023.

[35] B. Bansal and S. Srivastava, "Sentiment classification of online consumer reviews using word vecto representations", *Procedia Comput. Sci.*, vol. 132, pp. 1147–1153, 2018.

[36] L. Zhang, K. Hua, H. Wang, G. Qian, and L. Zhang, "Sentiment analysis on reviews of mobil users", *Procedia Comput. Sci.*, vol. 34, pp. 458–465, 2014.

[37] K. M. Karaoğlan and O. Fındık, "Extended rule-based opinion target extraction with a novel text pre processing method and ensemble learning", *Appl. Soft Comput.*, vol. 118, no. 108524, p. 108524, 2022.

[38] A. K. Sharma, S. Chaurasia, and D. K. Srivastava, "Sentimental short sentences classification by usin CNN deep learning model with fine tuned Word2Vec", *Procedia Comput. Sci.*, vol. 167, pp. 1139–114 2020.

[39] A. Pimpalkar and J. R. Raj R, "MBiLSTMGloVe: Embedding GloVe knowledge into the corpus usin multi-layer BiLSTM deep learning model for social media sentiment analysis", *Expert Syst. Appl.*, vo 203, no. 117581, p. 117581, 2022.

[40] M. Affi and C. Latiri, "BE-BLC: BERT-ELMO-based deep neural network architecture for English name entity recognition task", *Procedia Comput. Sci.*, vol. 192, pp. 168–181, 2021.

[41] A. Zhao and Y. Yu, "Knowledge-enabled BERT for aspect-based sentiment analysis", *Knowl. Based Syst* vol. 227, no. 107220, p. 107220, 2021.

[42] F. Gargiulo, S. Silvestri, M. Ciampi, and G. De Pietro, "Deep neural network for hierarchical extrem multi-label text classification", *Appl. Soft Comput.*, vol. 79, pp. 125–138, 2019.

[43] Z. A. Sejuti and M. S. Islam, "A hybrid CNN-KNN approach for identification of COVID-19 with 5-fol cross validation", *Sens. Int.*, vol. 4, no. 100229, p. 100229, 2023.

Bitlis Eren Üniversitesi Fen Bilimleri Dergisi
BİTLİS EREN UNIVERSITY JOURNAL OF SCIENCE
ISSN: 2147-3129/e-ISSN: 2147-3188
VOLUME: 12 NO: 3 PAGE: 725-731 YEAR: 2023
DOI:10.17798/bitlisfen.1289067

New Solutions for the Resonant Nonlinear Schrödinger Equation with Anti-Cubic Nonlinearity

Ebru CAVLAK ASLAN[1*], Leyla GÜRGÖZE[1]

[1] *Firat University, Science Faculty, Department of Mathematics, Elazığ*
(ORCID: 0000-0002-2291-4044) (ORCID: 0000-0002-8316-5366)

Keywords: Soliton, Optical Soliton, NLS equation, RNLS equation, JEF method, NPD equations.

Abstract
In this work, the resonant nonlinear Schrödinger equation (RNLSE) with anti-cubic nonlinearity is considered. The Jacobi elliptic function method (JEFM) has been employed on the RNLSE. The many new forms of dark, dark-bright, singular, combo-singular, bright-singular solitons and periodic solutions for governing model are reached. Furthermore, the graphics of solutions are presented.

1. Introduction

The main topic of many scientific studies especially in mathematical physics and engineering is related to the nonlinear equations (NLEs).The NLEs exist in all research fields, such as fluid mechanics, plasma physics, biology, chemistry, and so on. The solitons are obtained by dissolving nonlinear structures. Solitons have been theoretically predicted for more than 50 years. Solitons preserves their shape and speed and continue to maintain these properties after any interaction moment. The optical solitons which are the basis of optical fiber are the most important branches of study in the field of soliton [1]. Optical fibers are commonly used in telecommunication, broadcasting, medical field, defense industry have many commercial and scientific applications. Optical Soliton solutions including bright and dark solitons are a class of exact solutions that have diverse applications in the wide areas of applied sciences from sciences to engineering. The nonlinear Schrödinger equations (NLSE) are one of the basic equations from which optical solitons are derived [2]. Several approaches have been deployed on NLSE to G'/G expansion method [3], Fan sub-equation method [4], generalized projective Riccati equation method [5], the Sub-ODE method [6], the exp-function method [7], the F-expansion method [8], Kudryashov method [9]-[10], modified extended tanh expansion method [11] and so on. One of these analytical techniques, the JEFM with a history of 20 years is an effective method in finding optikal soliton solutions of NLSE [12]-[14].

In this work, we consider the RNLSE having anti-cubic nonlinearity

$$i\Psi_t + \beta\Psi_{xx} + (\delta_1|\Psi|^{-4} + \delta_2|\Psi|^2 + \delta_3|\Psi|^4)\Psi + \sigma\frac{|\Psi|_{xx}}{\Psi}\Psi = 0 \quad (1)$$

here $\Psi(x,t)$ is a wave profile by complex value. σ is the coefficient of resonant term, β is the coefficient the group velocity dispersion (GVD). δ_1, δ_2 and δ_3 are the coefficients of anti-cubic, cubic and quintic terms, respectively [15]-[16].

The aim of the current work is to find some new soliton solutions of the equation (1) by JEFM. In accordance with this purpose, this paper is organized as follows. In section 2, a detailed description of the JEFM is presented. Section 3 is devoted to the applications of the proposed method to the RNLSE with anti-cubic nonlinearity. Section 4 contains discussion and results. Also, Figures of optical

*Corresponding author: ebrucavlak@hotmail.com
Received: 28.04.2023, Accepted:02.08.2023

solitons obtained with technique are shown. Consequently, Section 5 contains Conclusion.

2. Material and Method

Let us take up a nonlinear partial differential equation (NPDE) unknown function u and free variable (x,t);

$$N(u,u_x,u_t,u_{xx},...)=0 \tag{2}$$

and by considering the travelling wave transformation

$$u(x,t)=U(\xi),\xi=x-vt \tag{3}$$

[17]. Putting (3) into (2) give in an ODE of the form

$$N(U,U',U'',U''',...)=0. \tag{4}$$

After that, we received general form of (4) as follow

$$U(\xi)=\sum_{i=0}^{n}\alpha_i\phi^i(\xi) \tag{5}$$

where α_i are the constans and $\varphi(\xi)$ satisfies the following auxiliary ODE,

$$\phi'(\xi)=\sqrt{\ell\phi^4(\xi)+\wp\phi^2(\xi)+\varsigma} \tag{6}$$

where $\ell,\wp$ and ς are the real constans. The value of n is found using the balancing principle of homogeneity in (4).

Substitting (5) into (4), we get a polynomial of $\varphi(\xi)$. Equating each coefficient of polynomial to zero. We derived a system of algebraic equations which can be solved by the aid of Mathematica program [18].

It is well-known that (6) has families of Jacobi elliptic functions (JEFs) solutions. In this $sn(\xi,m),ns(\xi,m),sc(\xi,m)$ and so on are the same types of JEFs. In this, m denotes the modulus of JEFs, where $0<m<1$. The JEFs degenerate into hyperbolic function when $m\to 1$ and turn into trigonometric functions $m\to 0$ [19].

2.1. Application of Method

We consider the following wave transformation for the conservation of (1) in to the nonlinear ODE,

$$\Psi(x,t)=\hat{g}(\xi)e^{i\varphi},\xi=x-vt,\varphi=-\kappa x+\omega t+\Theta \tag{7}$$

where $\hat{g}$ is the functional form of the complex wave profile. Substituting (7) into (1), and we get the following forms of the imaginary and real parts as below

$$-v\hat{g}'-2\kappa\beta\hat{g}'=0 \tag{8}$$

and

$$(\beta+\sigma)\hat{g}''+(-\omega-\kappa^2\beta)\hat{g}+\delta_1\hat{g}^{-3}+\delta_2\hat{g}^3+\delta_3\hat{g}^5=0. \tag{9}$$

The imaginary part of (1) yields

$$v=-2\kappa\beta. \tag{10}$$

In real part, by balancing $\hat{g}''$ with $\hat{g}^5$ in (9), we come up $n=1/2$. So

$$\hat{g}(\xi)=\tau(\xi)^{1/2}. \tag{11}$$

By putting (11) into (9) and multiplying by $4\tau^{3/2}$, we obtain the following ODE

$$2(\beta+\sigma)\tau\tau''-(\beta+\sigma)\tau'^2+4(-\omega-\kappa^2\beta)\tau^2+4\delta_1+4\delta_2\tau^3+4\delta_3\tau^4=0. \tag{12}$$

Now balancing $\tau\tau''$ with τ', we get $n=1$. So from (5)

$$\tau(\xi)=\alpha_0+\alpha_1\phi(\xi) \tag{13}$$

where α_0 and α_1 are constans and $\alpha_1\neq 0$.

Substituting (13) and its necessary derivatives into (12) and collecting all same powers terms of $\phi(\xi)$. So we acquire the following system

$$4\delta_1-4\omega\alpha_0^2-4\beta\kappa^2\alpha_0^2+4\delta_2\alpha_0^3+4\delta_3\alpha_0^4-\varsigma\beta\alpha_1^2-\varsigma\sigma\alpha_1^2=0$$

$$-8\omega\alpha_0\alpha_1+2\wp\beta\alpha_0\alpha_1-8\beta\kappa^2\alpha_0\alpha_1+2\wp\sigma\alpha_0\alpha_1+12\delta_2\alpha_0^2\alpha_1+16\delta_3\alpha_0^3\alpha_1=0$$

$$-4\omega\alpha_1^2+\wp\beta\alpha_1^2-4\beta\kappa^2\alpha_1^2+\wp\sigma\alpha_1^2+12\delta_2\alpha_0\alpha_1^2+24\delta_3\alpha_0^2\alpha_1^2=0$$

$$4\ell\beta\alpha_0\alpha_1+4\ell\sigma\alpha_0\alpha_1+4\delta_2\alpha_1^3+16\delta_3\alpha_0\alpha_1^3=0$$

$$4\ell\beta\alpha_1^2+3\ell\sigma\alpha_1^2+4\delta_3\alpha_1^4=0.$$

Solving the algebraic equations with the Mathematica, and so results as following

$$\alpha_0=\frac{4\omega-\wp\beta+4\beta\kappa^2-\wp\sigma}{3\delta_2},\alpha_1=\frac{\sqrt{-3\ell(\sigma+\beta)}}{2\sqrt{\delta_3}}$$

$$\omega = \frac{1}{32\delta_3}(-9\delta_2^2 + 8\wp\beta\delta_3 - 32\beta\delta_3\kappa^2 + 8\wp\sigma\delta_3)$$

$$\sigma = \frac{1}{96\ell\wp\delta_3^2}(9\wp\delta_2\delta_3 - 96\ell\wp\beta\delta_3^2 + \sqrt{3}\sqrt{27\wp^2\delta_2^4\delta_3^2 - 108\ell\wp\delta_2^4\delta_3^2 - 16384\ell\wp\delta_2\delta_3}).$$

Putting these values in (13), we have solution function of $\tau(\xi)$. Subsequently, considering that (11), exact solution form (1) as follow

$$\Psi(x,t) = \left(\frac{1}{6\delta_2}\left(8\omega - 2\wp\beta + 8\beta\kappa^2 + \frac{3\sqrt{3}\delta_2\sqrt{-\ell(\sigma+\beta)}}{\sqrt{\delta_3}}\right)\phi(\xi)\right)^{1/2} e^{i\varphi}. \quad (14)$$

Considering the JEFs for $\phi(\xi)$, the optical soliton, trigonometric function and singular solutions of (1) are obtained.

Case 1: If $\ell = m^2, \wp = -(1+m^2), \varsigma = 1$, then $\phi(\xi) = sn\xi$. JEF solution

$$\hat{g}(\xi) = \left(\frac{4\omega + \beta + m^2\beta + 4\beta\kappa^2 + \sigma + m^2\sigma}{3\delta_2} + \frac{\sqrt{3}\sqrt{-m^2(\beta+\sigma)}}{2\sqrt{\delta_3}}sn(\xi)\right)^{1/2}. \quad (15)$$

We can obtain the dark optical soliton solution $m \to 1$

$$\Psi(x,t) = \left(\frac{4\omega + 2\beta + 4\beta\kappa^2 + 2\sigma}{3\delta_2} + \frac{\sqrt{3(-\beta-\sigma)}}{2\sqrt{\delta_3}}\tanh(x-vt)\right)^{1/2} e^{i\varphi}. \quad (16)$$

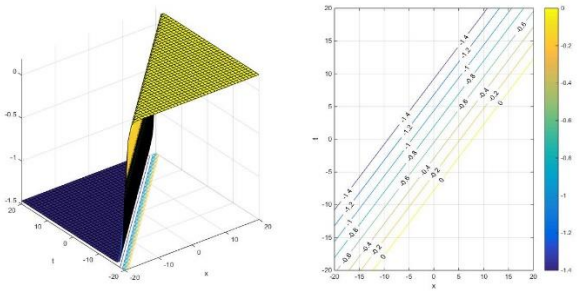

Figure 1. The 3D plot and contour plot for solution of Eq. (16). Values chosen are $\delta_1 = -0.1, \delta_2 = 2,$ $\delta_3 = 1, \kappa = 1$ and $\beta = -1$.

Case 2: If $\ell = 1, \wp = -(1+m^2), \varsigma = m^2$, then $\phi(\xi) = ns\xi$. So, we get the following Jacobi elliptic function solution

$$\hat{g}(\xi) = \left(\frac{1}{6\delta_2}\left(8\omega + 2\beta + 2m^2\beta + 8\beta\kappa^2 + 2\sigma + 2m^2\sigma + \frac{3\sqrt{3}\delta_2\sqrt{(-\beta-\sigma)}}{\sqrt{\delta_3}}ns(\xi)\right)\right)^{1/2}. \quad (17)$$

We can obtain the singular solution $m \to 1$

$$\Psi(x,t) = \left(\frac{4\omega + 2\beta + 4\beta\kappa^2 + 2\sigma}{3\delta_2} + \frac{\sqrt{3(-\beta-\sigma)}}{2\sqrt{\delta_3}}\coth(x-vt)\right)^{1/2} e^{i\varphi}. \quad (18)$$

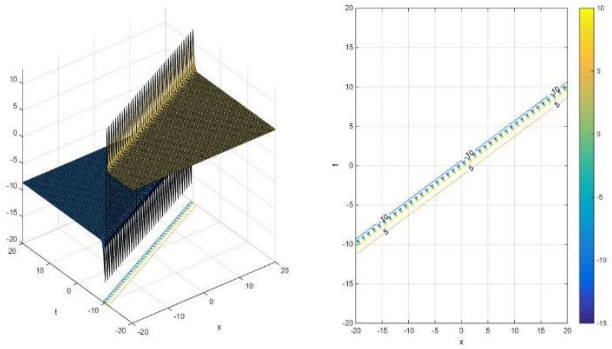

Figure 2. The 3D plot and contour plot for solution of Eq. (18). Values chosen are $\delta_1 = -0.1, \delta_2 = 5,$ $\delta_3 = 1, \kappa = 1$ and $\beta = -1$.

Case 3: If $\ell = 1 - m^2, \wp = 2 - m^2, \varsigma = 1$, then $\phi(\xi) = sc\xi$. So, we get

$$\hat{g}(\xi) = \left(\frac{1}{6\delta_2}\left((8\omega + 2\beta)(-2 + m^2 + 4\kappa^2) + 2\sigma(-2 + m^2) + \frac{3\sqrt{3}\delta_2\sqrt{(m^2-1)(\beta+\sigma)}}{\sqrt{\delta_3}}sc(\xi)\right)\right)^{1/2}. \quad (19)$$

We obtain the travelling wave solution including of a trigonometric function when $m \to 0$

$$\Psi(x,t) = \left(\frac{1}{6\delta_2}\left(2(4\omega + \beta(-1 + 4\kappa^2) - 2\sigma) + \frac{3\sqrt{3}\delta_2\sqrt{-\beta+\sigma}}{\sqrt{\delta_3}}\tan(x-vt)\right)\right)^{1/2} e^{i\varphi}. \quad (20)$$

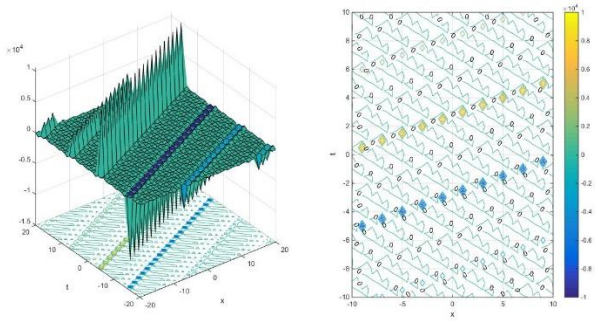

Figure 3. The 3D plot and contour plot for solution of Eq. (20). Values chosen are $\delta_1 = 1, \delta_2 = 2,$ $\delta_3 = -2, \kappa = 2$ and $\beta = -1.$

Case 4: When $\ell = 1, \wp = 2 - m^2, \varsigma = 1 - m^2,$ then $\phi(\xi) = cs\xi$. So, from (14)

$$\hat{g}(\xi) = \left(\frac{1}{6\delta_2} \left(2(4\omega + \beta(-2 + m^2 + 4\kappa^2) + \sigma(-2 + m^2)) + \frac{3\sqrt{3}\delta_2\sqrt{(-\beta-\sigma)}}{\sqrt{\delta_3}} cs(\xi) \right) \right)^{1/2}. \tag{21}$$

If $m \to 0,$ we can obtain the travelling wave solution function

$$\Psi(x,t) = \left(\frac{1}{6\delta_2} \left(8\omega - 4\beta + 8\beta\kappa^2 - 4\sigma + \frac{3\sqrt{3}\delta_2\sqrt{-\beta-\sigma}}{\sqrt{\delta_3}} \cot(x - vt) \right) \right)^{1/2} e^{i\varphi}. \tag{22}$$

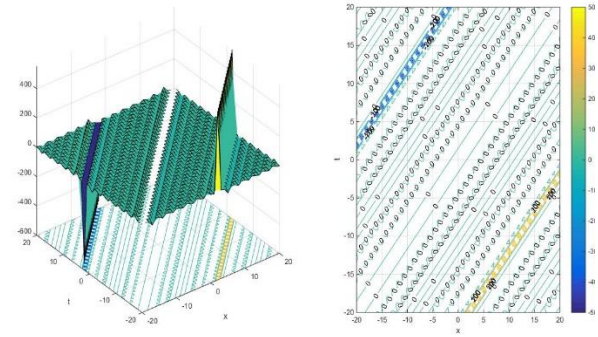

Figure 4. The 3D plot and contour plot for solution of Eq. (22). Values chosen are $\delta_1 = 1, \delta_2 = 2,$ $\delta_3 = -2, \kappa = 2$ and $\beta = -1.$

Case 5: When $\ell = \frac{1-m^2}{4}, \wp = \frac{1+m^2}{2}, \varsigma = \frac{1-m^2}{4},$ then $\phi(\xi) = nc\xi \pm sc\xi$. So, from (14)

$$\hat{g}(\xi) = \left(\frac{1}{6\delta_2} \left(8\omega - (1+m^2)\beta + 8\beta\kappa^2 - \sigma(1+m^2) + \frac{3\sqrt{3}\delta_2\sqrt{(-1+m^2)(\beta+\sigma)}}{2\sqrt{\delta_3}} (nc\xi \pm sc\xi) \right) \right)^{1/2}. \tag{23}$$

If $m \to 0,$ we can obtain the travelling wave solution function

$$\Psi(x,t) = \left(\frac{1}{6\delta_2} \left(8\omega - \beta + 8\beta\kappa^2 - \sigma + \frac{3\sqrt{3}\delta_2\sqrt{-\beta-\sigma}}{2\sqrt{\delta_3}} (\sec(v - vt) \pm \tan(x - vt)) \right) \right)^{1/2} e^{i\varphi}. \tag{24}$$

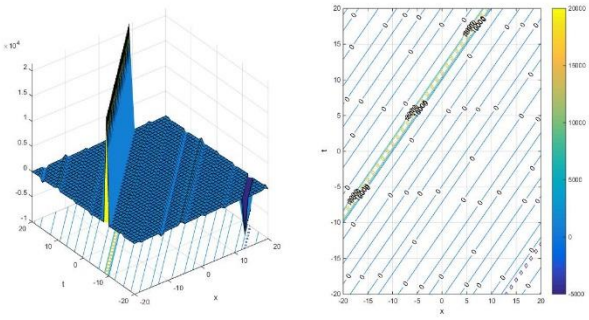

Figure 5. The 3D plot and contour plot for solution of Eq. (24). Values chosen are $\delta_1 = 2,$ $\delta_2 = 2, \delta_3 = -2, \kappa = 0.1$ and $\beta = -5.$

Case 6: If $\ell = \frac{1}{4}, \wp = \frac{m^2 - 2}{2}, \varsigma = \frac{m^2}{4},$ then $\phi(\xi) = ns\xi \pm ds\xi$. So, from (14)

$$\hat{g}(\xi) = \left(\frac{1}{6\delta_2} \left(8\omega + (2 - m^2 + 8\kappa^2)\beta - \sigma(-2 + m^2) + \frac{3\sqrt{3}\delta_2\sqrt{(-\beta-\sigma)}}{2\sqrt{\delta_3}} (ns\xi \pm ds\xi) \right) \right)^{1/2}. \tag{25}$$

So, while $m \to 1,$ we can obtain the combo singular soliton solution

$$\Psi(x,t) = \left(\frac{1}{6\delta_2} \left(8\omega + \beta(1 + 8\kappa^2) + \sigma + \frac{3\sqrt{3}\delta_2\sqrt{-\beta-\sigma}}{2\sqrt{\delta_3}} (\coth(v - vt) \pm \operatorname{csch}(x - vt)) \right) \right)^{1/2} e^{i\varphi}. \tag{26}$$

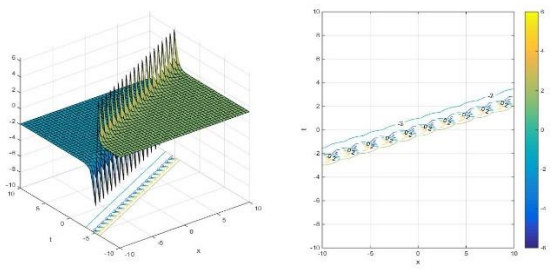

Figure 6. The 3D plot and contour plot for solution of Eq. (26). Values chosen are $\delta_1 = 2, \delta_2 = 2, \delta_3 = -2, \kappa = 0.1$ and $\beta = -5$.

Case 7: If $\ell > 0, \wp < 0, \varsigma = \dfrac{m^2\wp^2}{(1+m^2)^2\ell}$, and this conditions, $\phi(\xi) = \sqrt{-\dfrac{m^2\wp}{(1+m^2)^2\ell}}\, sn\left(\sqrt{\dfrac{-\wp}{1+m^2}}\xi\right)$. So, from (14)

$$\hat{g}(\xi) = \left(\left(\frac{8\omega+\beta+4\beta\kappa^2\sigma}{3\delta_2} + \frac{\sqrt{3}\sqrt{(-\beta-\sigma)}}{2\sqrt{\delta_3}}\right)\left(\sqrt{-\frac{m^2\wp}{(1+m^2)^2\ell}}\, sn\left(\sqrt{\frac{-\wp}{1+m^2}}\xi\right)\right)\right)^{1/2}. \tag{27}$$

Specially, if $\ell > 0, \wp < 0$ and $m \to 1$, we can obtain the dark optical soliton solution as follow

$$\Psi(x,t) = \left(\frac{4\omega+\beta+4\beta\kappa^2+\sigma}{3\delta_2} + \frac{\sqrt{3}\sqrt{(-\beta-\sigma)}}{2\sqrt{2\delta_3}}\tanh\left(\frac{x-vt}{\sqrt{2}}\right)\right)^{1/2} e^{i\varphi}. \tag{28}$$

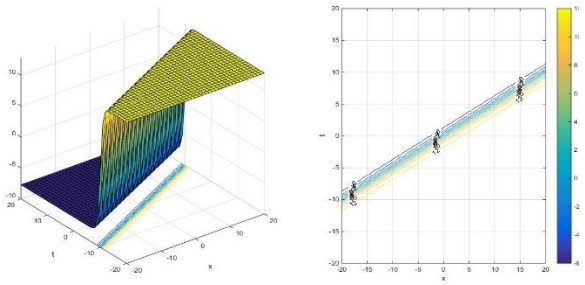

Figure 7. The 3D plot and contour plot for solution of Eq. (28). Values chosen are $\delta_1 = 2, \delta_2 = 2, \delta_3 = -1, \kappa = 0.5$ and $\beta = -2$.

Case 8: If $\ell = 1, \wp = m^2 + 2, \varsigma = 1 - 2m^2 - 4m^4$, and this conditions, $\phi(\xi) = \dfrac{dn\xi cn\xi}{sn\xi}$. So, we get the following function

$$\hat{g}(\xi) = \left(\frac{1}{6\delta_2}\left(8\omega - (2+2m^2)\beta + 8\beta\kappa^2 - 2\sigma(2+m^2) + \frac{3\sqrt{3}\delta_2\sqrt{(-\beta-\sigma)}}{\sqrt{\delta_3}}\left(\frac{dn\xi cn\xi}{sn\xi}\right)\right)\right)^{1/2}. \tag{29}$$

In this, if $m \to 1$, we can obtain the bright-singular optical soliton solution as follow

$$\Psi(x,t) = \left(\frac{1}{6\delta_2}\left(8\omega - 6\beta + 8\beta\kappa^2 - 6\sigma + \frac{3\sqrt{3}\delta_2\sqrt{(-\beta-\sigma)}}{\sqrt{\delta_3}}\left(\operatorname{sech}(x-vt)\operatorname{csch}(x-vt)\right)\right)\right)^{1/2} e^{i\varphi}. \tag{30}$$

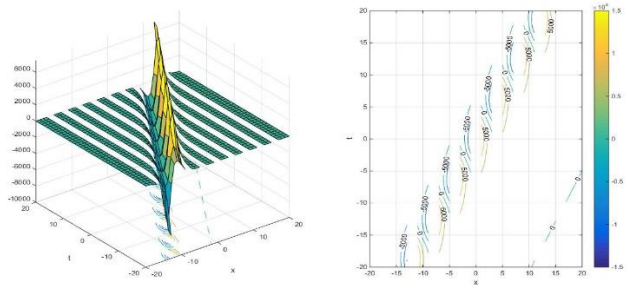

Figure 8. The 3D plot and contour plot for solution of Eq. (30). Values chosen are $\delta_1 = 2, \delta_2 = 3, \delta_3 = -2, \kappa = 0.2$ and $\beta = -2$.

Case 9: When $\ell = \dfrac{1}{4}, \wp = \dfrac{1-2m^2}{2}, \varsigma = \dfrac{1}{4}$, and $\phi(\xi) = \dfrac{sn\xi}{1 \pm cn\xi}$. So, we get the following function

$$\hat{g}(\xi) = \left(\left(\frac{8\omega+\beta(-1+2m^2+8\kappa^2)+(2m^2-1)\sigma}{6\delta_2} + \frac{\sqrt{3}\sqrt{(-\beta-\sigma)}}{4\sqrt{\delta_3}}\right)\left(\frac{sn\xi}{1\pm cn\xi}\right)\right)^{1/2}. \tag{31}$$

If $m \to 1$, we can obtain the dark-bright optical soliton solution as follow

$$\Psi(x,t) = \left(\frac{1}{6\delta_2}\left(8\omega + \beta + 8\beta\kappa^2 + \sigma + \frac{3\sqrt{3}\delta_2\sqrt{(-\beta-\sigma)}}{2\sqrt{\delta_3}}\left(\frac{\tanh(x-vt)}{1\pm\operatorname{sech}(x-vt)}\right)\right)\right)^{1/2} e^{i\varphi}. \tag{32}$$

Also here, while $m \to 0$, we get travelling wave solution with the including of trigonometric function

$$\Psi(x,t) = \left(-\frac{1}{6\delta_2}\left(-8\omega + \beta - 8\beta\kappa^2 + \sigma - \frac{3\sqrt{3}\delta_2\sqrt{(-\beta-\sigma)}}{2\sqrt{\delta_3}} \tan\left(\frac{x-vt}{2}\right)\right)\right)^{1/2} e^{i\varphi}. \quad (33)$$

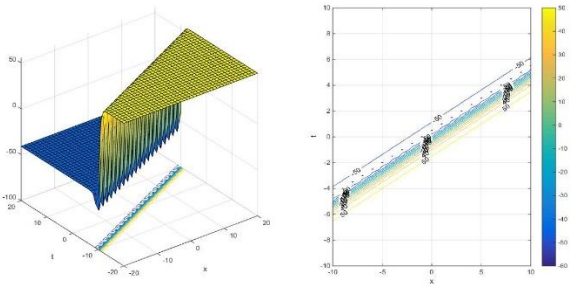

Figure 9. The 3D plot and contour plot for solution of Eq. (33). Values chosen are $\delta_1 = 2, \delta_2 = 1,$ $\delta_3 = -2, \kappa = 1$ and $\beta = -1.$

Case 10: When

$\ell = \frac{2-m^2-2\sqrt{1-m^2}}{4}, \wp = \frac{m^2}{2} - 1 - 3\sqrt{1-m^2},$

$\varsigma = \frac{2-m^2-2\sqrt{1-m^2}}{4}$, and

$\phi(\xi) = \frac{m^2 sn\xi cn\xi}{sn^2\xi(1+\sqrt{1-m^2}\,dn\xi - 1 - \sqrt{1-m^2})}$. So, we get the following function

$$\hat{g}(\xi) = \left(\frac{1}{12\delta_2}\left(16\omega + 2\beta(2-m^2+6\sqrt{1-m^2}+8\kappa^2) + (2m^2-1)\sigma + \frac{\sqrt{3}\sqrt{(-\beta-\sigma)}}{4\sqrt{\delta_3}}\right)\left(\frac{sn\xi}{1\pm cn\xi}\right)\right)^{1/2}. \quad (34)$$

If $m \to 1$, we can obtain the dark-bright optical soliton solution as follow

$$\Psi(x,t) = \left(\frac{1}{6\delta_2}\left(8\omega + \beta + 8\beta\kappa^2 + \sigma + \frac{3\sqrt{3}\delta_2\sqrt{(-\beta-\sigma)}}{\sqrt{\delta_3}}\left(\frac{\tanh(x-vt)}{1\pm \sec h(x-vt)}\right)\right)\right)^{1/2} e^{i\varphi}. \quad (35)$$

Also here, while $m \to 0$, we get travelling wave solution with the including of trigonometric function

$$\Psi(x,t) = \left(-\frac{1}{6\delta_2}\left(-8\omega + \beta - 8\beta\kappa^2 + \sigma - \frac{3\sqrt{3}\delta_2\sqrt{(-\beta-\sigma)}}{\sqrt{\delta_3}} \tan\left(\frac{x-vt}{2}\right)\right)\right)^{1/2} e^{i\varphi}. \quad (36)$$

3. Results and Discussion

This section contain the graphical representation of some new exact traveling wave solutions of the equation (1). The software Mathematica is used to describe the behavior of wave solutions. These solutions include dark solitons, singular soliton, trigonometric function solutions, combo singular soliton, bright-singular soliton and dark-bright optical solitons. The 3D and contour plots for different wave solutions of (1) are demonstrated in Figs. 1-9. $|\Psi(x,t)|^2$ received while drawing figures. Also, $\beta\kappa < 0$ and $\delta_1\delta_3 < 0$ are necessary conditions for all waves to occur. Under these basic conditions, figures are drawn by appropriate selection of the values of arbitrary parameters.

In Fig. 1, (16) shows dark optical soliton. Fig. 2 represents the graph of solution given in (18), which is singular soliton. In Figs. 3,4 and 5, the graphs for (20), (22) and (24) illustrating trigonometric function solutions are shown. Fig.6 represents the graph of solution given in (26), which is a combo singular soliton solution. In Figs. 7 and 8, the graphs for (28) and (30) illustrating dark and bright- singular soliton solutions respectively are shown. Similarly in Fig. 9, the graph for (32) is presented dark-bright optical soliton solutions.

4. Conclusion and Suggestions

In this work, we investigate the optical soliton and wave solutions of the RNLSE with anti-cubic nonlinearity throughthe use of the JEFM. The approach is very powerful scheme that first transforms the NLSE to an ODE through a complex wave transformation. So the coefficients of equal power and compared in the obtained ODE's. Finally, the obtained algebraic equation system is solved in Mathematica. The 3D and contour plots of dark solitons, singular soliton solutions, periodic solutions, combo singular solutions, bright-singular soliton and dark-bright soliton solutions are also provided along with suitable choice of values of arbitrary parameters. As a result of the calculations, it has been seen that $\beta\kappa < 0$ and $\delta_1\delta_3 < 0$ are necessary conditions for the formation of soliton and periodic waves. The results presented in this research are novel and can be a valuable addition in the literature.

Acknowledgment

This study is related to the Msc thesis of the second author.

Conflict of Interest Statement

There is no conflict of interest between the authors.

Statement of Research and Publication Ethics

The study is complied with research and publication ethics

References

[1] Y. S. Kivshar and G. P. Agrawal, *Optical solitons: From fibers to photonic crystals*. Elsevier Science & Technology, 2003

[2] A. Biswas and S. Konar, *Introduction to non-Kerr law optical solitons*. London, England: CRC Press, 2020.

[3] E. Ulutas, "Travelling wave and optical soliton solutions of the Wick-type stochastic NLSE with conformable derivatives," *Chaos Solitons Fractals*, vol. 148, no. 111052, p. 111052, 2021.

[4] N. Cheemaa and M. Younis, "New and more general traveling wave solutions for nonlinear Schrödinger equation," *Waves Random Complex Media*, vol. 26, no. 1, pp. 30–41, 2016.

[5] A. M. Shahoot, K. A. E. Alurrfi, I. M. Hassan, and A. M. Almsri, "Solitons and other exact solutions for two nonlinear PDEs in mathematical physics using the generalized projective Riccati equations method," *Adv. Math. Phys.*, vol. 2018, pp. 1–11, 2018.

[6] M. Mirzazadeh, R. T. Alqahtani, and A. Biswas, "Optical soliton perturbation with quadratic-cubic nonlinearity by Riccati-Bernoulli sub-ODE method and Kudryashov's scheme," *Optik (Stuttg.)*, vol. 145, pp. 74–78, 2017.

[7] K. Ayub, M. Y. Khan, and Q. Mahmood-Ul-Hassan, "Solitary and periodic wave solutions of Calogero–Bogoyavlenskii–Schiff equation via exp-function methods," *Comput. Math. Appl.*, vol. 74, no. 12, pp. 3231–3241, 2017.

[8] W. B. Rabie and H. M. Ahmed, "Cubic-quartic solitons perturbation with couplers in optical metamaterials having triple-power law nonlinearity using extended F-expansion method," *Optik (Stuttg.)*, vol. 262, no. 169255, p. 169255, 2022.

[9] N. A. Kudryashov, "Method for finding highly dispersive optical solitons of nonlinear differential equations," *Optik (Stuttg.)*, vol. 206, no. 163550, p. 163550, 2020.

[10] N. A. Kudryashov, "Highly dispersive solitary wave solutions of perturbed nonlinear Schrödinger equations," *Appl. Math. Comput.*, vol. 371, no. 124972, p. 124972, 2020.

[11] A. Zafar, M. Raheel, and A. Bekir, "Exploring the dark and singular soliton solutions of Biswas–Arshed model with full nonlinear form," *Optik (Stuttg.)*, vol. 204, no. 164133, p. 164133, 2020.

[12] N. Z. Petrović and M. Bohra, "General Jacobi elliptic function expansion method applied to the generalized (3 + 1)-dimensional nonlinear Schrödinger equation," *Opt. Quantum Electron.*, vol. 48, no. 4, 2016.

[13] T. A. Khalil, N. Badra, H. M. Ahmed, and W. B. Rabie, "Bright solitons for twin-core couplers and multiple-core couplers having polynomial law of nonlinearity using Jacobi elliptic function expansion method," *Alex. Eng. J.*, vol. 61, no. 12, pp. 11925–11934, 2022.

[14] A. Biswas, A. Sonmezoglu, M. Ekici, A. S. Alshomrani, and M. R. Belic, "Highly dispersive singular optical solitons with Kerr law nonlinearity by Jacobi's elliptic ds function expansion," *Optik (Stuttg.)*, vol. 192, no. 162954, p. 162954, 2019.

[15] A. U. Awan, H. U. Rehman, M. Tahir, and M. Ramzan, "Optical soliton solutions for resonant Schrödinger equation with anti-cubic nonlinearity," *Optik (Stuttg.)*, vol. 227, no. 165496, p. 165496, 2021.

[16] K. S. Nisar, K. K. Ali, Mustafa Inc, M. S. Mehanna, H. Rezazadeh, and L. Akinyemi, "New solutions for the generalized resonant nonlinear Schrödinger equation," *Results Phys.*, vol. 33, no. 105153, p. 105153, 2022.

[17] S. Tarla, K. K. Ali, R. Yilmazer, and M. S. Osman, "New optical solitons based on the perturbed Chen-Lee-Liu model through Jacobi elliptic function method," *Opt. Quantum Electron.*, vol. 54, no. 2, 2022.

[18] L. Gürgöze, "Exact Solutions With Jacobi Elliptic Function Method of Some Nonlineer Equations," Firat University, 2022.

[19] E. M. E. Zayed, R. M. A. Shohib, A. Biswas, Y. Yıldırım, F. Mallawi, and M. R. Belic, "Chirped and chirp-free solitons in optical fiber Bragg gratings with dispersive reflectivity having parabolic law nonlinearity by Jacobi's elliptic function," *Results Phys.*, vol. 15, no. 102784, p. 102784, 2019.

Bitlis Eren Üniversitesi Fen Bilimleri Dergisi
BİTLİS EREN UNIVERSITY JOURNAL OF SCIENCE
ISSN: 2147-3129/e-ISSN: 2147-3188
VOLUME: 12 NO: 3 PAGE: 732-745 YEAR: 2023
DOI:10.17798/bitlisfen.1290095

Geo-Environmental Analysis on Specifying Solar Energy Power Plant (SEPP) Fields by GIS and Different Fuzzy AHP Methods

Deniz ARCA[1*], Hülya KESKİN ÇITIROĞLU[2]

[1] *DEU Izmir Vocational School Department of Architecture and Urban Planning, 35360, Buca Izmir, Türkiye*
[2] *Directorate of Investment Monitoring and Coordination, YIKOB, 09020 Aydın, Türkiye*
(ORCID: 0000-0002-0439-4938) (ORCID: 0000-0002-2999-9570)

Keywords: Solar energy power plant (SEPP), Solar Radiation, Fuzzy Analytic Hierarchy Process (FAHP), Geographic Information Systems (GIS), Fuzzy Multiple Criteria Decision Making (FMCDM), Yalova.

Abstract
The use of solar energy among renewable energy sources has started to become widespread due to its potential, the practicality of use and environmental friendliness. In assessing the installation sites of solar energy power plants (SEPPs) economic, social and environmental elements should be taken into consideration, and cultural and paleontological heritage areas should not be damaged. In order for decision-makers to show their own predilections in some ways, the subject of this research is to specify the convenient fields for SEPP installation in Yalova province with all its districts using different methods of fuzzy analytical hierarchy processes (FAHP) together with Geographic Information Systems (GIS). Buckley (1985) found that the geometric mean approach achieved an accuracy rate of 24.99% for the combination of high and medium susceptibility levels. On the other hand, using the extent analysis method proposed by Chang (1996), an accuracy rate of 7.82% was obtained. The results indicate that the Geometric mean approach by Buckley (1985) provides more realistic results compared to the extent analysis method by Chang (1996). According to the results obtained, it has been seen that Yalova province has convenient fields for SEPP sites in the center and east, including the Central and Çiftlikköy districts.

1. Introduction

The requirement for energy is increasing continuously due to population growth, industrialization, increase in welfare and technological developments. This increase is mostly direct action to the level of the development of the countries. This increase is also in question in Türkiye and this rate will rise even more in the oncoming future. In this case, energy needs mostly met by conventional methods. Conventional methods refer to the production of energy consequences of fire fuels. This case poses many economic and environmental problems. The use of sustainable and renewable energy sources for mineral fuels is of great importance in the production of sustainable electricity [1]. Through the utilization of renewable sources, it is possible to both meet the electricity need and help avoid climate change globally. Therefore, widespread use of renewable energy sources is a necessity. In this sense, solar energy can be considered as an important different energy source for future generations [2]. Being a clean energy source and operating at a low cost after installation increases the value of solar energy [3].

Considering the world electricity production, it is seen that sources of renewable energy have an important space. Renewable resources account for 29% of the total global electricity production [4]. The share of electricity generation from solar power plants (SEPP) in global electricity generation is 2.8 percent [5]. In terms of electricity generation in Türkiye, natural gas and coal resources are superior to other opportunities. While 40.7 percent of aggregate electricity generation is derived from renewable resources, the proportion of solar energy in aggregate

*Corresponding author: deniz.arca@deu.edu.tr
Received: 30.04.2023, Accepted: 10.09.2023

electricity generation is 3.7 percent. When analyzing the distribution of electricity generation from renewable energy sources in Türkiye, it is seen that solar energy has a share of 9.1 percent [6]. This share increased by 2 percent compared to the previous year. Solar panels have started to be used to benefit from solar energy in Türkiye as well as all over the world. Solar energy has gained global importance due to its clean nature and wide availability [7]. Nowadays, source of solar power is utilized as remedies to eliminate the environmental problems produced by mineral source fuels, mostly in developed countries. Among the usage areas of solar energy, hot water and electricity production, heating of greenhouses, heating and cooling of places and heat energy for industrial establishments can be listed [3].

The choice of location is also a major factor in reducing the cost of the SEPP installation and obtaining the maximum efficiency during operation [8]. The determination of SEPP locations depends on many factors such as economics, technical and environmental. Since these criteria are mostly spatial, accurate results can be easily obtained with analyses in the Geographic Information Systems (GIS) environment. In this respect, many studies have been carried out in the GIS environment by using different multiple-criteria decision making (MCDM) methods. In the analytical hierarchy process (AHP) method, which is frequently used in MCDM mechanisms, the selection processes are made according to the predetermined criterion scoring during the decision-making phase, and focus groups affect the result [9]. Uyan [10] determined 5 criteria as environmental and economic, for the Karapınar region of Konya, he weighted these criteria using AHP and as a result of analyzes made in the GIS environment, it was detected that 40.34% of the Konya province was suitable for the setup of SEPP, and 59.66% was unsuitable. Potić et al. [11], in research to assessment the potency of solar energy of Knjazevac area in eastern Serbia, were defined 4 criteria as solstice, topography, climate and land use. Land use was obtained as 6 classes with the datum as an end of the surveys of Landsat 8 satellite images. The resulting map was created using AHP and GIS. For the purpose of defining the sites where SEPP will be installed in Iran, 11 criteria were determined in research carried out by Noorollahi et al. [12]. Fuzzy Analytical Hierarchy Process (FAHP) was used for weighting since the superiority of the factors relative to each other was not certain and SEPP suitability map for Iran was formed using GIS. Additionally, considering the 1057 regions of the country, the optimal areas for SEPP were defined. Consequence of research by Al Garni and Awasthi [13] handling GIS and AHP for the Saudi Arabia, it has been determined that the optimal regions for SEPP are the northern and northwestern locations of the Saudi Arabia. In research carried out by Asakereh et al. [14], the sites where SEPP will be installed were determined in Khuzestan, Iran use GIS and FAHP. Thanks to research, it has been determined that Khuzestan has a high potency. In research carried out by Merrouni et al. [15], 4 main and 8 sub-criteria were defined to determine the locations where SEPP will be installed in the east of Morocco, and a compatibility map was formed handling GIS and AHP. The study revealed that 19% of eastern Morocco is highly suitable for SEPP settlement. In the literature research, it has been defined that AHP and FAHP methods are common and widely used in the preparation of the suitability map with GIS. Analysis with fuzzy logic ensures a more flexible decision environment for the decision maker. For this reason, the GIS-based FAHP process was utilized to create the suitability map for the SEPP installation in Yalova, which is the subject of this research, located in the Marmara Region of Türkiye.

The first study in the field of Fuzzy AHP was conducted by Yager in 1978. In this study, a method that would facilitate decision-making in multi-criteria problems under conditions of uncertainty and fuzziness was introduced to the literature [16]. In studies conducted with Fuzzy AHP in the literature, various methods are employed to determine the importance values. However, in most studies, it has been observed that methods such as geometric mean [17] and extent analysis [18] are frequently used for ranking fuzzy numbers and determining criterion weights. For this reason, in this research, geometric mean [17] and extent analysis [18] methods found in the literature as FAHP were used. To raise the electricity production installed power of Yalova province and the proportion of SEPP in this established power, it is purposed to determine convenient SEPP fields for benefitting from solar energy in Yalova. For this purpose, suitable site selection for potential SEPPs in Yalova province was formed with the GIS-based MCDM process because it is composed of a solution system for the management of multiple solution criteria. One of the innovations of this research is that, for the first time, it identified optimal locations for installing SEPPs in an area requiring clean energy. In this context, as data layers; certain factors such as solar radiation, slope, distance to power distribution centers (PDCs), land use, distance to fault lines, lithology, distance to stream, distance to lake, distance to road line, aspect and distance to residential areas have been used. Although solar radiation has not been used as an analysis parameter in other similar studies, Kırcalı

and Selim [19] emphasized that solar radiation is the most important criterion for site selection and used it as a parameter in their studies. The innovative aspects of the research are the consideration of solar radiation and lithology factors as criteria for evaluation. All criteria placed in the research were formed in raster environment by GIS software, and pairwise comparison matrix fuzzy numbers and fuzzy number equivalents were produced. The weight values of each criterion were defined by the different FAHP methods. Later, the criterion maps classified by consolidation analysis were combined and a convenience consequent map was obtained displaying the optimal fields for SEPP. This research also introduces a new aspect, highlighting the utilization of GIS-based FMCDM (Fuzzy Multi-Criteria Decision Making) and FAHP (Fuzzy Analytical Hierarchy Process) methods for preliminary studies in potential locations. These methods prove to be highly effective in creating location suitability maps. Upon the establishment of solar energy production plants (SEPPs) in Yalova, it is expected that at least the energy demands of residential areas will be fulfilled using solar energy, leading to a significant advantage in terms of obtaining a clear and more cost-effective power supply for the province. In addition, this study is expected to it is expected that this study will guide the determination of SEPP installation areas in cities other than Yalova.

The next part belongs to the researched area, in section 3 the data and the method used in the study are explained. In section 4 the Application are reported, section 5 belongs to the results and discussion and section 6 is the conclusion.

2. Researched Area

The Solar Energy Potential Atlas of Türkiye (GEPA) has been presented by the Energy and Natural Resources Ministry in order to determine the potential in electricity production from solar power and to utilize solar power effectively. When the GEPA regional solar energy parameter values are examined, it is seen that almost every point in Türkiye has the opportunity to directly or indirectly benefit from solar energy [20]. The research area is Yalova province, which is spotted in the Marmara region and on the coast of the Marmara Sea. Yalova province is located between 39-40 North latitude and 28-29 East longitude [21], has an area of 826 km2 together with its districts. The Marmara Sea is located in the west and north of the province, Kocaeli in the east, Gemlik Bay and Bursa province in the south are located. Yalova province has a total of 6 districts, namely Armutlu, Çınarcık, Altınova, Çiftlikköy, Termal and Central districts (Figure 1).

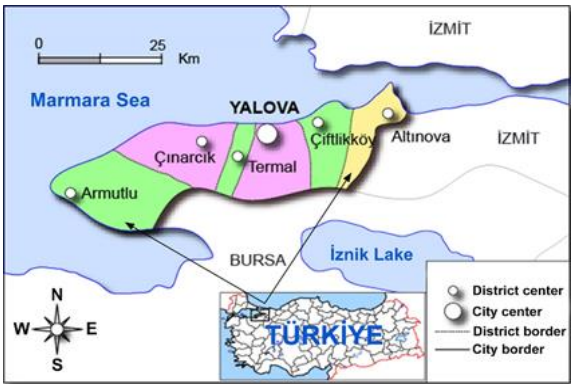

Figure 1. Location map [22]

Considering the population registration system data, it has been seen that the total population of Yalova, which was 270976 in the previous year, increased and reached 276050 people. Considering the distribution of the population by districts; the central district consists of 149330, Altınova district 30780, Armutlu district 9901, Çınarcık district 34699, Çiftlikköy district 44808 and Termal district 6532 people and it is seen that most of the population lives in the city center [23]. Approximately 5% of Yalova province is covered with forests and its climate is a transition between Mediterranean and Black Sea climates. Summers in the province are dry and hot, and winters are rainy and warm [24]. The total annual solar radiation of Yalova with its districts is between 1400-1450 KWh m^{-2}. It has been determined that the values of global radiation of all Yalova with its districts are the highest in June. It is observed that the mean density of daily radiation is about 3.7 kWh m^{-2} day^{-1}, and the annual mean value of total global radiation is about 1351 kWh m^{-2} $year^{-1}$. Additionally, the monthly and annual average daily sunshine durations in Central, Termal, Çiftlikköy and Altınova districts of Yalova are approximately 6.6 and 2409 hours and in Çınarcık and Armutlu districts, it is approximately 6.7 and 2446 hours [25]. Considering the sunshine duration, it is seen that there is an increase of approximately 1.5% in the sunshine duration toward the west of Yalova.

Kiliç et al. [26] in their research where they handed annual wind speeds and solar radiation to supply the electric load need of the University campus in Yalova, performed hybrid energy production simulations. Gül and İzgi [27], analyzed low voltage panels and wind-solar hybrid energy systems separately in order to select the hybrid system configuration for an industrial facility to be established in Yalova-Esadiye Village. A notation

based upon geographical and meteorological data has been enhanced by Sözen et al. [28] in order for assessment the potential of solar energy by taking Artificial Neural-Networks (ANNs) in 18 places in Türkiye, including Yalova province. On the other hand, Türkdoğan et al. [29] set up a hybrid power order in a farmhouse placed on the Erikli Plateau by utilizing wind and sun and they emphasized that this research will encourage the engage of renewable sources in the field of agriculture-livestock farming. There are total of 7 power plants in Yalova, 1 thermal, 5 wind and 1 SEPP completed by the Yalova Wastewater and Sewerage Infrastructure Facilities Management Association (YASKİ), producing approximately 327 GWh of electricity annually. Among these power plants, the rating of SEPPs with a total installed capacity of 294 MWe is only 1 MWe [30]. The construction of capacity power plants started in 2009 in Armutlu district, which was deemed suitable for the operating of wind energy facilities [31]

3. Material and Method

3.1. Location Specification and Identification of Restriction Sites

SEPP site specification parameters directly affect the activities from the setting cycle to the running cycle of power facilities and the costs of electricity generation. While choosing the location, legal regulations, efficiency status and environmental impact assessment criteria are taken into consideration. In the development process, efficiency comes to the fore in general, and environmental effects are unfortunately relatively ignored. However, it is important in this process to examine laws and regulations in terms of restrictions and incentives [32]. Environmental, technical and economic parameters have an impact on the area of SEPP installation [33]. Certain conditions must be met in order for a SEPP to be established in a region. These conditions vary according to the purpose and region of the study. In order to determine the restriction regions in this research, five conditions specific to the researched location were used in the direction of the literature research [12]-[14], [32]. These conditions are listed below:

- Not to be proximate than 500 m to areas of settlements, prohibited and protection,
- Not to be proximate than 400 m to lakes and streams,
- Not to be in locations with a slope of more than 11%,
- Not to be in forest fields,
- Not to be proximate than 100 m to motorways.

It is also not correct to establish SEPP or any power generation facility in cultural and paleontological heritage sites or in their immediate surroundings. The work from the building state to the production stage of such facilities negatively affects these areas. At the same time, ignoring these locations will adversely impress the SEPP establishment period. Therefore, the SEPP installation is not allowed in these areas [34]. Considering the determined criteria, a separate buffer zone analysis was carried out for each parameter. Thus, restriction fields were defined and these fields were united in the second step. In this unitization process; if an area is restricted in terms of any criteria, it is considered to be restricted in terms of other criteria. Then, the process of determining the suitability degrees for the areas deemed suitable was started.

3.2. Criteria Specification

The experiences gained so far in choosing a suitable place have led to the formation of some criteria [32]. In this research, as a result of the literature and field work, certain factors such as solar radiation, slope, proximity to PDCs, land use, proximity to fault lines, lithology, proximity to stream, lake and road line, aspect and proximity to residential areas were used and the suitable fields where SEPP will be established have been determined. It is possible to see ducks and many bird species in Hersek Lagoon located in Altınova district of Yalova and separated from the Marmara Sea by a narrow coastline [35]. Hersek Lagoon, which is the habitat of 206 bird species and is on the migratory bird route, in the analysis, it was evaluated within the distance to the lake parameter due to the fact that it remains on the edge of the research area, and proximity to the emigration ways factor is not evaluated owing to the migratory bird route passes through the shore of Lake Iznik [36].

Modeling, achievement survey and design of solar power systems adhere data of solar radiation [2], [37]. The most vital parameter for the performance of systems working with solar power is the radiation reflected in that area. For this reason, information of solar radiation was utilized as a criterion in research, and the map of solar radiation utilized is presented in Figure 2a.

One of the most vital parameters in determining the location of SEPPs is the slope criterion. Generally, regions above 11% are considered unsuitable. A slope of 4% or less is considered quite suitable. Efficiency may be affected as excessive inclination will cause the solar panels to

dark each other. In addition, the rise of slope raises the establish price of the SEPP [12]. The slope input of the research field was created from the numerical elevation pattern of the area. The produced inclination map is parted into 5 grades (Figure 2b).

The distance to PDC is an important economic factor. As the act far from the head, the transfer of the generated electricity to the centers will be more cost. In the studies, it is not desired that the distance of the areas where the facility will be established to the PDCs exceeds 10 km [38]. The distance from the PDC to the research field was assessed under five grades (Figure 2c).

Land use refers to settlements and locations of restricted and protected. SEPPs are required to be at a certain distance from these areas. Because the settlements are growing day by day. In the long term, there is a possibility that SEPPs will remain within these areas. Since the establishment of SEPP will affect the wildlife there, facility should be at a definite space from the conservation regions. In addition, land use is an important criterion, because the natural vegetation in the area to be selected for the SEPP can increase shading and this can reduce productivity. In this respect, areas covered by trees, maquis, bushes and reeds, where natural vegetation can create an obstacle, are not primarily preferred in site selection. In addition, cleaning these areas causes additional costs [32]. Therefore, it is generally accepted that SEPPs should be located at distance greater than 500 m from these zones. In the research land use was examined in 9 grades, namely heathland, lakes, chestnut, pasture, forest, farming area, non-farming area, olive grove and meadow [39]. The land use map of the research field is shown in Figure 2d.

Regions that are earthquake-prone should not be decided in site selection for SEPP installation. When approaching active faults, it is inevitable that the earthquake effect will increase. Therefore, the information of fault line was procured by numerical the map of Fault proffered on the MTA General Directorate web area [40], [41] and total five dissimilar tampon space were built at 2500 m gaps (Figure 2e).

One of the parameters used in the determination of installation site alternatives is the lithological structure of the land [38]. The lithological structure of the field where the SEPP will be established directly affects the structure cost [41]. Moreover, the ground must be suitable for hammer mounting systems. The lithological units outcropping in the research area are listed stratigraphically from the oldest to the youngest as follows: Precambrian gneiss and schists (gsa), Precambrian-Palaeozoic schists (s), Cambrian-Ordovician schist and phyllite (s1), Permian marble (mr), Permian-Triassic terrestrial detritics (pt), Upper Cretaceous meta detritics and meta carbonates (f) with detritics and carbonates (k2s), Paleocene-Eocene detritics and carbonates (pn2e), Eocene granitoid (?7) and unallocated volcanites (en), Miocene terrestrial detritics (m2-3) and Upper Miocene terrestrial detritics (m3pl). Quaternary unallocated alluvium (Qal) is the youngest member of the research field [40]. Alluvium, due to its uncemented granular unit feature and its unallocated nature in the research field, it can be convenient for SEPP installation on condition that the fitting system with hammered is applied and the framework is reducted under the alluvium. Elsewise it will not be safe for SEPP installation. Carbonate units, on the other hand, require detailed field work in the SEPP installation, as they are suitable for the formation of karstic structures. Other lithological units in the research area, especially units containing volcanic rocks, provide a suitable environment for SEPP installation. The lithological map of the research field is seen in Figure 2f.

Due to conditions such as seasonal changes in rivers, possible floods, increase in flow and displacements in the river bed, the distance factor to the streams is between the major elements affecting the selection of SEPP construction sites. SEPPs should be at least 400 m far from streams in order to prevent SEPPs from being affected by floods and to provide easy access to the energy facility [8]. The closeness to the stream factor regarding the researches field was handled under 5 grades (Figure 2g).

Due to the fact that the lake volumes change at different times of the year, it is requested that the SEPPs should be at least 400 m away from the lakes in order to prevent environmental pollution and for the safety reasons to be taken against the negative effects of the floods to be experienced because of the lakes. The proximity to lakes regarding the researches field was evaluated under 5 grades (Figure 2h).

Being close to the roads at the first installation of the SEPP plant ensures low cost in infrastructure works. In addition, since there will be no need to open new roads for transportation purposes, also prevents possible damages that may result in damage to the surrounding lands [38]. However, since the wastes caused by vehicle traffic passing will unfavorable impress the panels and cause serious problems in terms of safety. It has been accepted in the literature that SEPPs should be distance than 100 m to the ways [8]. The proximity parameter to the roads regarding the research field was assessed under 6 grades (Figure 2i).

Aspect is very essential factor for SEPP. On the locations of SEPP will be formed, fields with no elevations to shade between south, west and east directions should be determined. Flat and southern fields are convenient for selection of SEPP sites. South oriented locations supply plentiful sun angle [34]. The aspect map of the research field has been handled in a way a total of 10 grades, ranging from -1 to 360 degrees (Figure 2j).

The produced energy transmission by SEPP to distant depletion areas cause loss of energy. Energy loss in transmission also reduces efficiency. For this reason, locations that are too far from residential areas, industry and working areas should not be preferred for SEPP field choice [32]. However, it is also obligatory to consider the possibility of SEPPs staying in the middle of residential lands eventually [8]. Therefore, in this research, the proximity to lands of residential has been assessed under 5 grapes (Figure 2k)

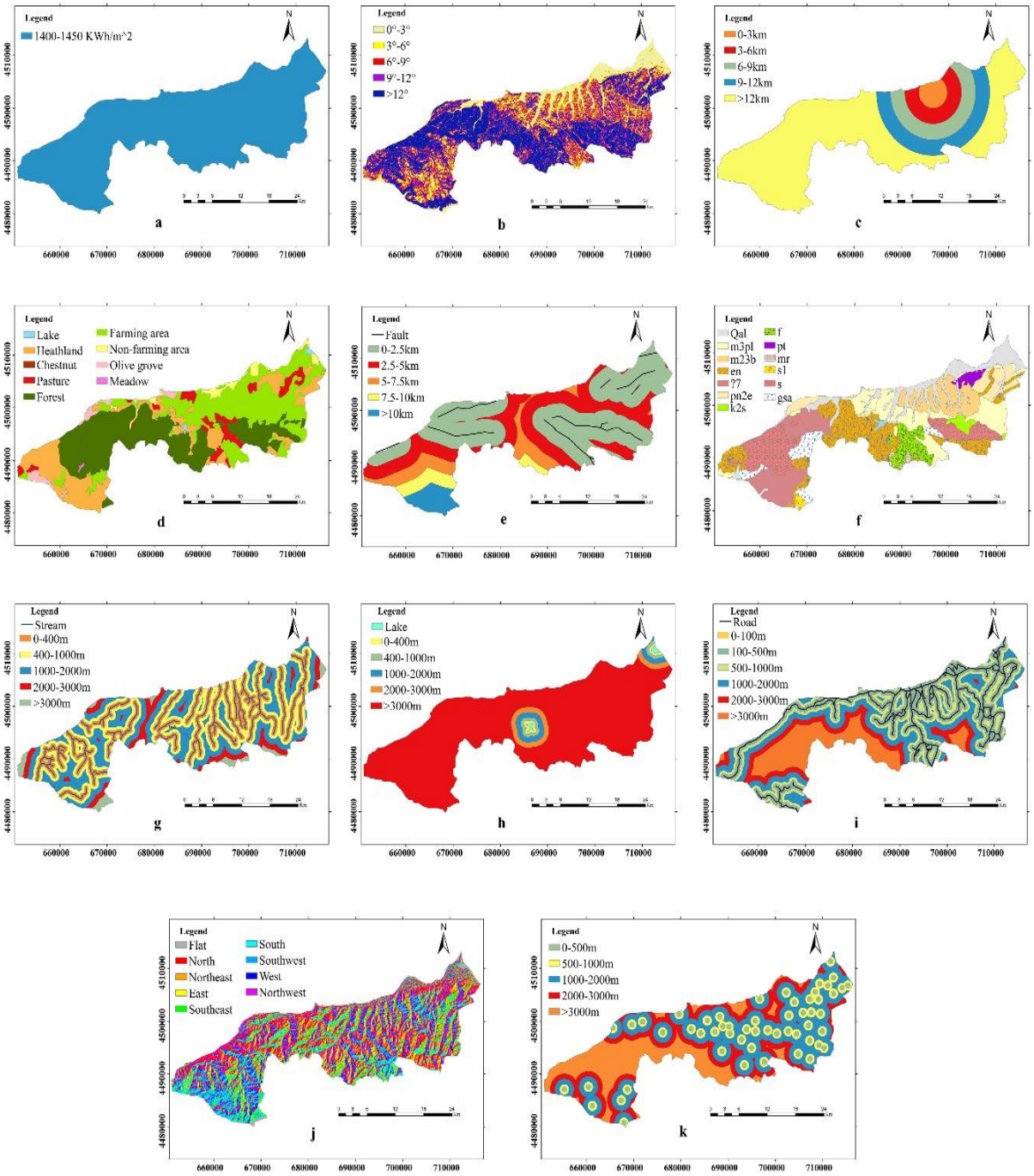

Figure 2. The criteria. a radiation, b slope, c closeness to PDCs, d land use, e closeness to fault line, f lithology, g closeness to stream, h closeness to lake, i closeness to road line, j aspect and k closeness to residential locations

3.3. Method of the Research

3.3.1 Fuzzy Logic and Fuzzy Decision Making

Fuzzy logic can be applied in situations where uncertainty exists or optimal decisions need to be reached with incomplete information. Decision making is the definition of the option or options that are determined to give the most suitable result by evaluating all aspects of one or a series of problems that must be solved at every management level [43]. Uncertainty in decision processes may also arise from the presence of verbal information and may occur in models involving subjective thoughts. In this case, eliminating the uncertainties or accepting the existence of uncertainty and adapting the analysis accordingly provides more effective results.

Analytical solution analyze with fuzzy logic supply a more flexible determination environment to the decision maker. By applying fuzzy logic, the verbally put forward information is inclusive in the resolution by acquiring its scalar provisions. Survey results and personal opinions into the model, cause the best solution to diverge to the change in the defendant personal. In this case, the decision accepted as optimal may change in the next application, or even if the decision maker remains the same, changing in the judgments of the experts whose opinions are taken may affect the suitable determination [44]. Moreover, the assessments acquired may not always include certain and fulfill knowledge. In such determination samples, analyzes can be applied with approach of fuzzy logic. In determination matters assessed by fuzzy logic, it is purposed to arrive the "best" determination that is not fuzzy as in usual matters. But the determination handled as a result of fuzzy theory does not claim to be an optimal decision and goals to indicate in which possibility each vary choice can be suitable [45]. Samples of Fuzzy were put forward as a different way by Zadeh [46] because there are certain and stable regulations in the demands and quantifiability of factors in numerical models. Fuzzy logic, which has gained increasing importance since this date, is identified as a certain array founded for the term of uncertainties and working with uncertainties [45].

3.3.2 Fuzzy Multiple Criteria Decision Making (FMCDM)

In the actual applications of MCDM models, it is seen that decision makers verbally state their judgments. AHP, one of the MCDM methods, founded pairwise matchings. Comparison weights should be treated neutrally, thinking how much more one major option is than the other. The subjective remarks are seen as a benefit of the AHP, apart from the criteria that can be measured quantitatively [47]. This individuality makes the results inadequate. In this case, the FAHP application is preferred. FAHP was first advertised by Laarhoven Van and Pedrycz [48]. In the research decisions and impacts are stated with numbers of triangular fuzzy. Buckley [17] used fuzzy logic in the normal equations of weights and suggested that a sole remedy cannot always be achieved in the study of [48] and they practiced with numbers of trapezoidal fuzzy based on the numerical process of fuzzy numbers. Their research [17] used fuzzy numbers to specify the emphasis classes of nuclear energy, hydroelectric energy, fossil energy and solar energy. In the after periods, many works have been performed, especially in industry and production in which the comparison scale was taken as fuzzy. Unlike these, Lee et al. [49] begun the notion of interspace for pairwise comparisons and they introduced a new method based on probabilistic optimization for consistency and fuzzy collations. Zhu et al. [50], further advanced the method developed by Chang [18] using synthetic grades and they introduced their new methods by applying oil exploration for China under nine main criteria and fifteen blocks determined. Kahraman et al. [51], compared three catering companies under three main elements and eleven sub-elements using FAHP. Csutora and Buckley [52], used a fuzzy comparison matrix, taking payment, benefits, placement, co-workers and promotion opportunities as criteria for new graduates' job selection. Kwong and Bai [53], established the FAHP model on the quality function expansion regarding production planning. They identified customer demands with FAHP and solved three main criteria and seven sub-criteria and nineteen second-degree sub-criteria models to ensure customer satisfaction. Enea and Piazza [54], in them research to select the best one out of three project alternatives, under four criteria, stated that they achieved more realistic results by applying FAHP. Mikhailov and Tsvetinov [55], in a problem with three alternatives with three main elements and six sub-elements, specified the optimal service provider using FAHP, and compared the results with the classical AHP results. Çanlı and Kandakoğlu [56], developed a model by applying FAHP in air power comparison. Firstly, in FAHP the question is stated in a hierarchical quality [57]. Secondly a scalar contact is founded among the aim and the parameters. In this research, geometric mean method [17] and the Extended Analysis Method [18] have been practiced.

In Table 1 the triangular fuzzy scale performed in research has been established.

Table 1. The scale of fuzzy AHP pair-wise comparison [58]

Fuzzy triangular	Reciprocal fuzzy	Definition
(1, 1, 1)	1, 1, 1	Equally important
(1, 2, 3)	1/3, 1/2, 1/1	Mediate amount between 1 and 3
(2, 3, 4)	1/4, 1/3, 1/2	lightly significant
(3, 4, 5)	1/5, 1/4, 1/3	Mediate amount between 3 and 5
(4, 5, 6)	1/6, 1/5, 1/4	Significant
(5, 6, 7)	1/7, 1/6, 1/5	Mediate amount between 5 and 7
(6, 7, 8)	1/8, 1/7, 1/6	Severely significant
(7, 8, 9)	1/9, 1/8, 1/7	Mediate amount between 7and 9
(8, 9, 9)	1/9, 1/9, 1/8	Highly significant

After the fuzzy synthesis figures are deliberated, these figures are matched to each other and the preference figures of the parameters are set. With the normalization of the vector, the exact preference vector is achieved.

4. Application

The literature review conducted shows that the choice of the parameters to be handled in MCDM issues in the renewable energy area also requires the method to be used [59]. The common feature of decision-making issues is uncertainty, and FAHP allows decision-performers to state own choices in proximate or proper practices [60,61]. Moreover, usual MCDM practices cannot sufficiently show the uncertainty of human thinking [62]. Researches on renewable energy sources are very valuable for urban energy planning [63]. Hereby the FAHP method was practiced in this research. The fuzzy number equivalents of the linguistically expressed criteria were determined by the specialists and literature review, and the pairwise comparisons of the criteria obtained with the specialists and literature review opinions are shown in the pairwise comparison matrix given in Table 2.

Table 2. Pairwise comparison matrix for FAHP (a radiation, b slope, c closeness to PDCs, d land use, e closeness to fault line, f lithology, g closeness to stream, h closeness to lake, i closeness to road line, j aspect and k closeness to residential locations)

	a	b	c	d	e	f	g	h	i	j	k
a	1 1 1	1 2 3	2 3 4	7 8 9	7 8 9	6 7 8	6 7 8	6 7 8	5 6 7	2 3 4	6 7 8
b	1/3 1/2 1	1 1 1	1/4 1/3 1/2	1 2 3	5 6 7	3 4 5	4 5 6	4 5 6	3 4 5	2 3 4	4 5 6
c	1/4 1/3 1/2	4 3 2	1 1 1	3 4 5	7 8 9	5 6 7	6 7 8	6 7 8	4 5 6	1 2 3	5 6 7
d	1/9 1/8 1/7	1/3 1/2 1	1/5 1/4 1/3	1 1 1	4 5 6	3 4 5	3 4 5	3 4 5	2 3 4	1/5 1/4 1/3	3 4 5
e	1/9 1/8 1/7	1/7 1/6 1/5	1/9 1/8 1/7	1/6 1/5 1/4	1 1 1	1/3 1/2 1	1/3 1/2 1	1/3 1/2 1	1/4 1/3 1/2	1/6 1/5 1/4	2 3 4
f	1/8 1/7 1/6	1/5 1/4 1/3	1/7 1/6 1/5	1/5 1/4 1/3	1 2 3	1 1 1	1/4 1/3 1/2	1/4 1/3 1/2	1/3 1/2 1	1/5 1/4 1/3	1 2 3
g	1/8 1/7 1/6	1/6 1/5 1/4	1/8 1/7 1/6	1/5 1/4 1/3	1 2 3	2 3 4	1 1 1	1 1 1	1/4 1/3 1/2	1/4 1/3 1/2	1 2 3
h	1/8 1/7 1/6	1/6 1/5 1/4	1/8 1/7 1/6	1/5 1/4 1/3	1 2 3	2 3 4	1 1 1	1 1 1	1/4 1/3 1/2	1/4 1/3 1/2	1 2 3
i	1/7 1/6 1/5	1/5 1/4 1/3	1/6 1/5 1/4	1/4 1/3 1/2	2 3 4	1 2 3	2 3 4	2 3 4	1 1 1	1/7 1/6 1/5	3 4 5
j	1/4 1/3 1/2	1/4 1/3 1/2	1/3 1/2 1	3 4 5	4 5 6	3 4 5	2 3 4	2 3 4	5 6 7	1 1 1	3 4 5
k	1/8 1/7 1/6	1/6 1/5 1/4	1/7 1/6 1/5	1/5 1/4 1/3	1/4 1/3 1/2	1/3 1/2 1	1/3 1/2 1	1/3 1/2 1	1/5 1/4 1/3	1/5 1/4 1/3	1 1 1

The fuzzy weights and weights for the criteria used the geometric mean practice proposed by Buckley [17] are given in Table 3.

Since the extent analysis practice that will be applied, needed to work the worth of fuzzy synthetic extent as far the i th factor [18] shown in Eq.1. S_i are synthetic extent value and $M_{g_i}^j$ are triangular fuzzy numbers in Equation 1.

$$S_i = \sum_{j=1}^{3} M_{g_i}^j \odot \left[\sum_{i=1}^{7}\sum_{j=1}^{3} M_{g_i}^j\right]^{-1} \quad (1)$$

where all the $M_{g_i}^j$, j=1,2,3 are triangular fuzzy numbers located in Table 2.

$$S_1 = (49,59,69) \odot \left(\frac{1}{318.10}, \frac{1}{257.43}, \frac{1}{201.57}\right)$$
$$= (0.154, 0.229, 0.342)$$

Table 3. The fuzzy weights and weights for the criteria in accordance with Buckley (1985) [17] practice

i	Factors	Fuzzy weights ($\widetilde{w}_i$)	Weights (w_i)
1	Radiation	0.176; 0.270; 0.420	0.270
2	Slope	0.086; 0.140; 0.239	0.145
3	PDC	0.136; 0.199; 0.298	0.197
4	Land Use	0.049; 0.076; 0.128	0.078
5	Closeness to fault	0.014; 0.023; 0.039	0.023
6	Lithology	0.015; 0.026; 0.046	0.027
7	Closeness to river	0.021; 0.033; 0.055	0.034
8	Closeness to lake	0.021; 0.033; 0.055	0.034
9	Closeness to road	0.030; 0.048; 0.081	0.049
10	Aspect	0.069; 0.131; 0.193	0.122
11	Closeness to residential fields	0.012; 0.020; 0.035	0.021

The triangular membership function is defined with three parameters. If these parameters are taken as l, m, and u, the equation of the triangular membership function is given below [18].

$$V(S_i \geq S_j = \begin{cases} 1, & if\ m_i \geq m_j \\ \left(\dfrac{u_{,} - l_j}{u_i - m_i) + (m_j - l_j)}, \right. & if\ l_j \leq u_i \\ 0, & Others, \end{cases}$$

The fuzzy synthetic extent figures and normalized weights for the factors are seen in Table 4.

Table 4. The fuzzy synthetic extent figures and weights for the factors are in accordance with Chang (1996) [18] practice

i	Factors	Synthetic extent values ($\tilde{S}_i$)	Weights (w_i)
1	Radiation	0.154, 0.229, 0.342	0.37
2	Slope	0.087, 0.139, 0.221	0.16
3	PDC	0.133, 0.192, 0.280	0.28
4	Land Use	0.062, 0.101, 0.163	0.09
5	Closeness to fault	0.015, 0.026, 0.047	0.00
6	Lithology	0.015, 0.028, 0.051	0.00
7	Closeness to river	0.022, 0.040, 0.069	0.00
8	Closeness to lake	0.022, 0.040, 0.069	0.00
9	Closeness to road	0.037, 0.067, 0.111	0.00
10	Aspect	0.075, 0.121, 0.193	0.10
11	Closeness to residential fields	0.010, 0.016, 0.030	0.00

5. Results and Discussion

As a result of the weighting made with FAHP, the parameter of radiation has the ultimate weight, then, it was calculated that this was followed by the closeness to the PDCs, slope, aspect, land use, closeness to road line, stream and lake, lithology, closeness to fault line and residential fields. Thinking the weights of the criteria calculated with FAHP, the maps in Figure 2 were unified and the restricted lands were distracted from this map and the optimal SEPP sites map was handled for the research field (Figure 3).

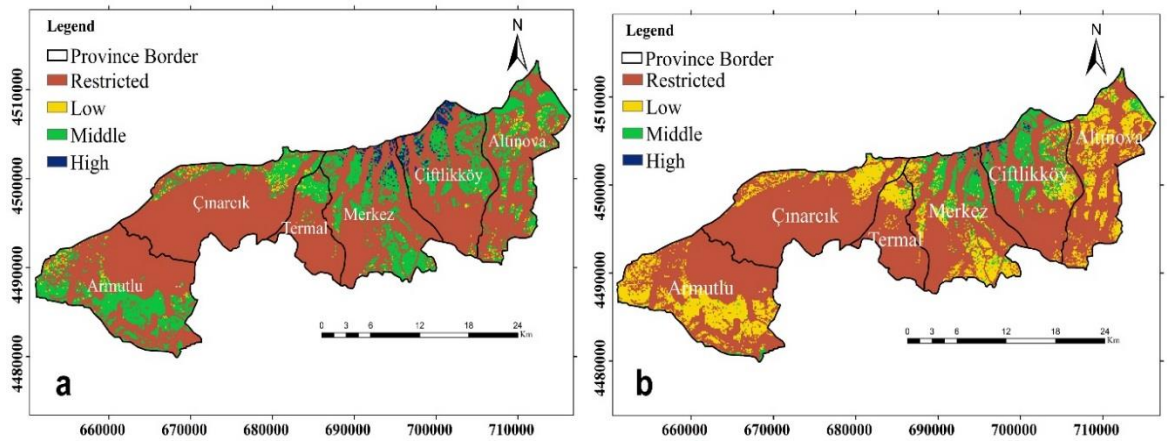

Figure 3. Susceptibility map generated for SEPPs sites. a. the geometric mean practice by Buckley [17], b. the extent analysis practice by Chang [18]

This resulting map obtained is expressed with four values as restricted, low, middle and high. The susceptibilities obtained as a result of the analyze performed are found as in Table 5.

Table 5. Percentage and area values of susceptibility

Susceptibility	Geometric mean practice by Buckley (1985)		Extent analysis practice by Chang (1996)	
	%	km^2	%	km^2
Restricted	72.84	601.66	72.84	601.66
Low	2.17	17.92	19.34	159.75
Medium	23.34	192.79	7.59	62.69
High	1.65	13.63	0.23	1.90

21.41% of the research area is covered by Armutlu district, 21.16% by Çınarcık district, 6.70% by Termal district, 18.63% by Central district, 16.45% by Çiftlikköy district and 15.65% by Altınova district. When the produced SEPP conformity map is considered on the basis of districts, while high suitability was observed in Çiftlikköy and Central districts, the most unsuitable value was obtained in Çınarcık and Armutlu districts (Table 6). The fact that Çınarcık district has dense forests has reduced the potential of receive sunlight. Since Armutlu district is deemed suitable for the installation of wind energy facilities [30], district is currently considered as another renewable energy type wind facilities area.

Table 6. SEPP compliance level values of Yalova districts

District	Restricted (%)		Low (%)		Middle (%)		High (%)	
	Buckley (1985)	Chang (1996)	Buckley (1985)	Chang (1996)	Buckley (1985)	Chang (1996)	Buckley (1985)	Chang (1996)
Armutlu	20.31	20.31	23.93	26.26	26.11	2.98	0.00	0.00
Çınarcık	25.19	25.19	25.62	10.80	9.67	2.67	0.00	0.00
Termal	7.61	7.61	6.38	12.76	4.36	3.84	0.00	0.00
Central	17.15	17.15	5.58	16.26	23.45	32.05	32.81	30.40
Çiftlikköy	15.39	15.39	3.89	8.18	17.32	49.95	67.19	69.60
Altınova	14.35	14.35	34.60	25.74	19.09	8.51	0.00	0.00

In our research, the results have been compared with various recent studies in the literature concerning the criteria employed and their respective weights [64,65,66].

Arca and Keskin Citiroglu [64] have produced the most suitable areas for SPP in Karabük using Geographic Information Systems (GIS) and Analytical Hierarchy Process (AHP). In their studies, they utilized the following factors: solar radiation, slope, aspect, distance to the road, distance to the river, distance to fault lines, lithology, land use, distance to settlement areas, and distance to PDCs. For all the models the most effective factors were determined as solar radiation, distance to PDCs and slope. Colak et al. [65] applied the Analytical Hierarchy Process method to calculate the weights of the 10 evaluation criteria. Solar energy potential was identified as the most critical factor, accounting for 22% of the weight in the areas suitable for Solar Power Plants (SPP). The land cover was ranked as the second most significant factor with a weight of 20%, followed by the aspect, which held the third most important position with a weight of 14%. The distribution of criterion weights in these two studies is similar to our study. Demir [66] used GIS Analyses and the AHP Method to identify areas with the potential for solar power plant installation in the Kars province. The study utilized 7 parameters, which included solar radiation, temperature, land slope, aspect, land cover and use, distance to energy transmission lines, and distance to road transportation network. In the study, the most effective factors were determined to be land cover and use, aspect, and distance to energy transmission lines. However, the distribution of criteria weights in our study differs from that in this work.

6. Conclusion

MCDM methods and GIS are tools that allow choosing the optimum option among different

choices in location choice works. One of the frequently preferred decision making methods in fuzzy sets is FAHP. In this research, different FAHP approaches were used in GIS environment to assess the sites where SEPP can be installed in Yalova. Since the outcomes of the study are immediately related to the determinate parameters, eleven different criteria were used in research. FAHP should be choosen to ahead of state oral ambiguity in the process of making resolution by pairwise comparison, so that determine the importance of one parameter with regard to another parameter by the decision-maker. It is advised to apply the FAHP practice, in case of the high number of pairwise comparisons, fuzziness in the mind of the decision maker, and in cases where transactions take too long. Extended Analysis Method selects the very small weights of the criteria as zero and eliminates some values that may actually have a significant effect when calculating the result by combining the weights of the criteria. For example, if we look at the normalized weights of the main parameters, the weight of the "lithology" parameter, which takes a very small value compared to the geometric mean method, is taken as zero by Extended Analysis Method. As one of the results of this research, we can say that it is more appropriate to use Extended Analysis Method with a different sorting method.

For numerical statements of oral significations in social, economic and environmental factors and sub-factors, concretion with fuzzy connection is essential in achieving more certain outcomes. Utilizing SEPP to supply the energy necessities of Yalova province, which is close to major industrial cities such as Istanbul, Kocaeli and Bursa and has sea tourism opportunities, will contribute to the supply of both inexpensive, fresh, sustainable and renewable energy. The resulting SEPP convenience map can be utilized for anterior assessment for financiers. The center and east of Yalova province have sites convenient for SEPPs. With the increase of the criteria, it can be stated that investment areas can be determined much more precisely and contribution can be made to feasibility studies. It is hoped that the outcomes achieved from this research will support decision-makers in future research researches in field administration in the research field.

Contributions of the authors

D.A.: Investigation, Methodology, Visualization, Data curation, Conceptualization, Software, Formal analysis, Writing–review. H.K.C.: Supervision, Investigation, Methodology, Data curation, Original draft preparation and Editing.

Conflict of Interest Statement

There is no conflict of interest between the authors.

Statement of Research and Publication Ethics

The study is complied with research and publication ethics

References

[1] E. Can, “Analysis of risks that are based on the aerial photography used in photogrammetric monitoring maps for environmental wind power energy plant projects,” *Environmental Monitoring and Assessment*, vol. 191, no. 746, 2019. https://doi.org/10.1007/s10661-019-7944-8

[2] H. Bulut, and O. Büyükalaca, “Simple model for the generation of daily global solar-radiation data in Turkey,” *Applied Energy*, vol. 84, no. 5, pp. 477-491, 2007. https://doi.org/10.1016/j.apenergy.2006.10.003

[3] MENRT, “Information center, energy, solar. Ministry of Energy and Natural Resources of Türkiye,” 2021a. https://enerji.gov.tr/bilgi-merkezi-enerji-gunes [Accessed: June, 02, 2021].

[4] REN21, “Renewables 2021global status report,” Paris: REN21 Secretariat, Renewable Energy Policy Network for the 21st century Paris, France, pp: 371, 2021. https://www.ren21.net/wp-content/uploads/2019/05/GSR2021_Full_Report.pdf [Accessed: June, 24, 2021].

[5] REN21, “Renewables 2020 global status report,” Paris: REN21 Secretariat, Renewable Enerji Policy Network for the 21st century Paris, France, pp:367, 2020. https://www.ren21.net/wp-content/uploads/2019/05/gsr_2020_full_report_en.pdf [Accessed: Sept. 24, 2020].

[6] TEIAŞ, "Turkish electricity transmission company 2020 annual report," pp.101, https://www.teias.gov.tr/tr-TR/faaliyet-raporlari [Accessed: June, 24, 2021].

[7] P. K. Dash, I. Majumder, N. Nayak, and R. Bisoi, "Point and interval solar power forecasting using hybrid empirical wavelet transform and robust wavelet kernel ridge regression," *Natural Resources Research*, vol. 29, no. 5, pp. 2813–2841, 2020. https://doi.org/10.1007/s11053-020-09630-6

[8] M. Uzar, and H. Koca, "Analysis of classical and fuzzy-logic based methods to generate suitability maps for solar power plants: The case of Menemen," *Journal of Geodesy and Geoinformation*, vol. 7, no. 1, pp. 11-28, 2020. https://doi.org/10.9733/JGG.2020R0002.T

[9] M. Uzar, and E. F. Asılhan, "An alternative approach supported by decision support systems and geographical information system for producing internet_based map: competition method," *Journal of Geodesy and Geoinformation*, vol. 6, no. 1, pp. 47-60, 2019. https://doi.org/10.9733/JGG.2019R00601004.T

[10] M. Uyan, "GIS-based solar farms site selection using analytic hierarchy process (AHP) in Karapinar region, Konya/Turkey," *Renewable and Sustainable Energy Reviews*, vol. 28, pp. 11-17, 2013. https://doi.org/10.1016/j.rser.2013.07.042

[11] I. Potić, R. Golić, and T. Joksimović, "Analysis of insolation potential of Knjaževac Municipality (Serbia) using multi-criteria approach," *Renewable and Sustainable Energy Reviews*, vol. 56, pp. 235-245, 2016. https://doi.org/10.1016/j.rser.2015.11.056

[12] E. Noorollahi, D. Fadai, M. Akbarpour Shirazi, and S. Ghodsipour, "Land suitability analysis for solar farms exploitation using GIS and fuzzy analytic hierarchy process (FAHP)—a case study of Iran," *Energies*, vol. 9, no. 8, no. 643, 2016. https://doi.org/10.3390/en9080643

[13] H. Z. Al Garni, A. Awasthi, "Solar PV power plant site selection using a GIS-AHP based approach with application in Saudi Arabia," *Applied Energy*, vol. 206, pp. 1225-1240, 2017. https://doi.org/10.1016/j.apenergy.2017.10.024

[14] A. Asakereh, M. Soleymani, and M. J. Sheikhdavoodi, "A GIS-based Fuzzy-AHP method for the evaluation of solar farms locations: Case study in Khuzestan province, Iran," *Solar Energy*, vol. 155, pp. 342-353, 2017. https://doi.org/10.1016/j.solener.2017.05.075

[15] A. A. Merrouni, F. E. Elalaoui, A. Mezrhab, A. Mezrhab, and A. Ghennioui, "Large scale PV sites selection by combining GIS and Analytical Hierarchy Process. Case study: Eastern Morocco," *Renewable Energy*, vol. 119, pp. 863-873, 2018. https://doi.org/10.1016/j.renene.2017.10.044

[16] E. Ekin, İ.G.Cesur, "Evaluation of Services Provided in the Consulting Sector with the Fuzzy AHP and TOPSIS Method Based on the Extended Analysis Method," Journal of Academic Researches and Studies, vol. 15, no.28, pp. 12-34, 2023. https://doi.org/10.20990/kilisiibfakademik.1231038

[17] J. J. Buckley, "Fuzzy hierarchical analysis," *Fuzzy Sets and Systems*, vol. 17, no. 3, pp. 233–247, 1985. https://doi.org/10.1016/0165-0114(85)90090-9

[18] D. Y. Chang, "Applications of the extent analysis method on Fuzzy AHP," *European Journal of Operational Research*, vol. 95, no. 3, pp. 649-655, 1996. https://doi.org/10.1016/0377-2217(95)00300-2

[19] Ş. Kırcalı, and S. Selim, "Site suitability analysis for solar farms using the geographic information system and multi‑criteria decision analysis: the case of Antalya, Turkey," *Clean Technologies and Environmental Policy*, vol. 23, pp. 1233–1250, 2021. https://doi.org/10.1007/s10098-020-02018-3

[20] MENRT, "Solar energy potential atlas (GEPA)," Ministry of Energy and Natural Resources of Türkiye, 2021b. https://gepa.enerji.gov.tr/MyCalculator/ [Accessed: June, 02, 2021].

[21] Provincial Directorate of EUCC, "Report of Yalova Province 2019 environmental status," Yalova Governorship Provincial Directorate of Environment, Urbanization and Climate Change, EIA and Environmental Permits Branch Office, pp133, 2019.

[22] CoğrafyaHarita, "Türkiye province maps," Geography map, 2021. http://cografyaharita.com/turkiye_mulki_idare_haritalari5.html [Accessed: Oct. 07, 2021].

[23] Turkish Statistical Institute, "Address based population registration system results," Turkish Statistical Institute (TUIK), 2021. https://biruni.tuik.gov.tr/medas/?kn=95&locale=tr [Accessed: August, 01, 2021].

[24] Municipality of Yalova Province (2021). About Yalova. Viewed 30 July 2021, https://www.yalova.bel.tr/kent-rehberi/yalova-hakkinda

[25] MENRT, "Solar energy potential atlas (GEPA) Yalova. Ministry of Energy and Natural Resources of Türkiye," 2021c. https://gepa.enerji.gov.tr/MyCalculator/pages/77.aspx [Accessed: June, 02, 2021].
[26] G. A. Kiliç, K. Al, E. Dağtekin, and Ü. Ünver, "Technical, economic and environmental ınvestigation of grid-ındependent hybrid energy systems applicability: a case study," *Energy Sources, Part A: Recovery, Utilization, and Environmental Effects*, Ahead-of-print, pp. 1-16, 2020. https://doi.org/10.1080/15567036.2020.1825565
[27] S. E. Gül, and E. İzgi, "Analysis of an industrial plant with intelligent or convensional panels connected to wind and solar energy systems," *Conference on Power Systems*, 15-16 November 2018, Ankara. pp. 59-63, 2018. https://doi.org/ 10.5281/zenodo.1482565
[28] A. Sözen, E. Arcaklioğlu, M. Özalp, and E. G. Kanit, "Solar-energy potential in Turkey," *Applied Energy*, vol. 80, issue. 4, pp. 367-381, 2005. https://doi.org/10.1016/j.apenergy.2004.06.001
[29] S. Türkdoğan, S. Dilber, and B. Çam, "Economic and technical investigation of the feasibility of off-grid hybrid energy systems for a farmhouse," *Sinop Uni J Nat Sci*, vol. 3, no. 2, pp. 52-65, 2018. https://doi.org/10.33484/sinopfbd.382391
[30] Energy Atlas, "Yalova electric plants," 2021. https://www.enerjiatlasi.com/sehir/yalova/ [Accessed: July, 30, 2021].
[31] MEUCCT, "Türkiye environmental status report," Ministry of Environment, Urbanization and Climate Change of Türkiye, General Directorate of EIA Permit Inspection, pp. 354, 2021. https://www.trakyaka.org.tr/upload/Node/33134/xfiles/Turkiye_Cevre_Durum_Raporu_2011_.pdf [Accessed: Sept. 13, 2021].
[32] İ. Şenlik, "Choosing the location of solar power plants," *Electrical Engineering Journal*, vol. 462, pp. 94-98, 2017. (in Turkish).
[33] Y. Charabi, and A. Gastli,). "PV site suitability analysis using GIS-based spatial fuzzy multi-criteria evaluation," *Renew. Energy*, vol. 36, no. 9, pp. 2554-2561, 2011. https://doi.org/10.1016/j.renene.2010.10.037
[34] N. Sarsıcı, "Determination of the areas where solar energy power plant (SPP) can be established in Karabük with multi-criteria decision making analysis," MSc Thesis. Karabük University Graduate Education Institute Geography Department, 193 pp. Karabük, Türkiye, 2020.
[35] District Governorship of Altınova, "Hersek lagoon," 2021. http://www.altinova.gov.tr/hersek-lagunu [Accessed: Oct. 19, 2021].
[36] Biyologlar, "Road map of migratory birds," 2021. https://www.biyologlar.com/gocmen-kuslarin-yol-haritasi [Accessed: Oct. 19, 2021].
[37] K. Kaygusuz, and T. Ayhan, "Analysis of solar radiation data for Trabzon, Turkey," *Energy Convers Manage*; vol. 40, no. 5, pp. 545–56, 1999.
[38] M. Uyan, "GIS-Supported mapping of solar power plant sites using AHP method," *Pamukkale University Journal of Engineering Sciences*, vol. 23, no. 4, pp. 343-351, 2017. https://doi.org/10.5505/pajes.2016.59489
[39] M. A. Özdemir, and M. Bahadır, "Timely change (1992-2007) of land use in Yalova Province," *Journal of Geography*, vol. 17, pp. 1-15, 2008.
[40] MTA, "Earth sciences map viewer and drawing editor," General Directorate of Mineral Research and Exploration, MTA, 2021. http://yerbilimleri.mta.gov.tr/anasayfa.aspx [Accessed: Oct. 03, 2021].
[41] AFAD, "Earthquake data," Disaster & Emergency Management Authority, Presidential of Earthquake Department, 2021. http://www.deprem.gov.tr/sarbis/Shared/Default.aspx [Accessed: Oct. 03, 2021].
[42] H. Eroğlu, "The suitability map determination for solar power plants: A case study," *Iğdır University Journal of the Institute of Science and Technology*, vol. 8, no. 4, pp. 97-106, 2018. https://doi.org/10.21597/jist.430615
[43] T. Harcar, *Silahlı Kuvvetlerde Karar Verme,* First edition, pp: 9-12, Ankara, Türkiye, KHO publications, 1992.
[44] Ö. Aydın, "Hospital Location for Ankara with Fuzzy AHP," *Dokuz Eylül University Faculty of Economics and Administrative Sciences Journal*, vol. 24, no. 2, pp. 87-104, 2009.
[45] G. J. Klir, and B. Yuan, *Fuzzy Sets and Fuzzy Logic*, USA, Prentice Hall PTR, 574pp, 1995.
[46] L. A. Zadeh, "Fuzzy sets," Inf Control, vol. 8, no. 3, pp. 338–353, 1965.
[47] D. R. Anderson, D. J. Sweeney, and T. A. Williams, *Quantitative Methods for Business 7e, Ohio*: International Thomson Publishing, 1997.

[48] P. J. M. Laarhoven Van, and W. Pedrycz, "A fuzzy extension of Satty's Priority Theory," *Fuzzy Sets and Systems*, vol. 11, pp. 229–241, 1983. https://doi.org/10.1016/S0165-0114(83)80082-7

[49] M. Lee, H. Pham, and X. Zhang, "A methodology for priority setting with application to software development process," *European Journal of Operational Research*, vol. 118, pp. 375-389, 1999.

[50] K.-J. Zhu, Y. Jing, and D.- Y. Chang, "A discussion on extent analysis method and applications of fuzzy AHP," *European Journal of Operational Research*, vol. 116, pp. 450-456, 1999. https://doi.org/10.1016/S0377-2217(98)00331-2

[51] C. Kahraman, U. Cebeci, and Da. Ruan, "Multi-attribute Comparison of catering service companies using Fuzzy AHP: The case of Turkey," *International Journal of Production*, vol. 87, no. 2, pp. 171-184, 2004. https://doi.org/10.1016/S0925-5273(03)00099-9

[52] R. Csutora, and J. J. Buckley, "Fuzzy Hierarchical Analysis: The Lambda-Max method," *Fuzzy Sets and Systems*, vol. 120, no. 2, pp. 181-195, 2001. https://doi.org/10.1016/S0165-0114(99)00155-4

[53] C. K. Kwong, and H. Bai, "A Fuzzy AHP approach to the determination of importance weights of customer requirements in quality function deployment," *Journal of Intelligent Manufacturing*, vol. 13, pp. 367-377, 2002.

[54] M. Enea, and T. Piazza, "Project selection by constrained Fuzzy AHP," *Fuzzy Optimization and Decision Making*, vol. 3, pp. 39-62, 2004. https://doi.org/10.1023/B:FODM.0000013071.63614.3d

[55] L. Mikhailov, and P. Tsvetinov, "Evaluation of services using a Fuzzy Analytic Hierarchy Process," *Applied Soft Computing*, vol. 5, pp. 23-33, 2004. https://doi.org/10.1016/j.asoc.2004.04.001

[56] H. Çanlı, and A. Kandakoğlu, "A Fuzzy AHP model for air force comparison," *JAST*, vol. 3, no. 1, pp. 71-82, 2007.

[57] A. Awasthi, K. Govindan, and S. Gold, "Multi-Tier sustainable global supplier selection using a Fuzzy AHP-VIKOR Based Approach," *International Journal of Production Economics*, vol. 195, pp. 106-117, 2018.

[58] F. T. S. Chan, and N. Kumar, "Global supplier development considering risk factors using fuzzy extended AHP based approach," *Omega*, vol. 35, no. 4, pp. 417-431, 2007.

[59] J. J. Wang, Y. Y. Jing, C. F. Zhang, and J. H. Zhao, "Review on MultiCriteria Decision Analysis aid in sustainable energy decision-making," *Renewable and Sustainable Energy Reviews*, vol. 13, no. 9, pp. 2263-2278, 2009. https://doi.org/10.1016/j.rser.2009.06.021

[60] D. Güler, and T. Yomralıoğlu, *GIS and Fuzzy AHP based area selection for electric vehicle charging stations*, The International Archives of the Photogrammetry, Remote Sensing and Spatial Information Sciences, Volume XLII-4, 249–252. ISPRS TC IV Mid-term Symposium on 3D Spatial Information Science –The Engine of Change, Delft, 1–5 October 2018, Delft, The Netherlands, 2018. https://doi.org/10.5194/isprs-archives-XLII-4-249-2018

[61] A. I. Karabulut, B. Yazici-Karabulut, P. Derin, M. I. Yesilnacar, and M. A. Cullu, "Landfill siting for municipal solid waste using remote sensing and geographic information system integrated analytic hierarchy process and simple additive weighting methods from the point of view of a fast-growing metropolitan area in GAP area of Turkey," *Env. Sci. Pol. Res.*, vol. 29, pp. 4044–4061, 2022. https://doi.org/10.1007/s11356-021-15951-7

[62] F. Ecer, "An integrated Fuzzy AHP and ARAS Model to evaluate mobile banking services," *Technological and Economic Development of Economy*, vol. 24, no. 2, pp. 670-695, 2018. https://doi.org/10.3846/20294913.2016.1255275

[63] V. Adjiski, G. Kaplan, and S. Mijalkovski, "Assessment of the solar energy potential of rooftops using LiDAR datasets and GIS based approach," *International Journal of Engineering and Geosciences*, vol. 8, no. 2, pp. 188-199, 2023. https://doi.org/10.26833/ijeg.1112274

[64] D. Arca and H. Keskin Citiroglu, "GIS-Based analysis of sites determination for solar power plant (SPP) by multi-criteria decision analysis method: A case study in Karabük," *Journal of Geomatics*, vol. 7, no. 1, pp.17-25, 2022. https://doi.org/10.29128/geomatik.803200

[65] H. Ebru Colak, Tugba Memisoglu and Yasin Gercek, "Optimal site selection for solar photovoltaic (PV) power plants using GIS and AHP: A case study of Malatya Province, Turkey," *Renewable Energy*, vol. 149, no. 2020, pp. 565-576, 2020. https://doi.org/10.1016/j.renene.2019.12.078

[66] M. Demir, "Determination of Areas with Solar Power Plant Installation Potential in Kars Province by Using GIS Analysis and AHP Method," *Journal of Geography*, vol.46, no.2023, pp. 93-109, 2023.

Bitlis Eren Üniversitesi Fen Bilimleri Dergisi
BİTLİS EREN UNIVERSITY JOURNAL OF SCIENCE
ISSN: 2147-3129/e-ISSN: 2147-3188
VOLUME: 12 NO: 3 PAGE: 746-763 YEAR: 2023
DOI:10.17798/bitlisfen.1294417

CNNTuner: Image Classification with A Novel CNN Model Optimized Hyperparameters

Halit ÇETİNER[1*], Sedat METLEK[2]

[1]*Isparta University of Applied Sciences, Vocational School of Technical Sciences, Isparta, Turkey*
[2]*Burdur Mehmet Akif Ersoy University, Vocational School of Technical Sciences, Burdur, Turkey*
(ORCID: 0000-0001-7794-2555) (ORCID: 0000-0002-0393-9908)

Keywords: CNN, Deep learning, F-MNIST, Keras Tuner, Parameter optimization.

Abstract

Today, the impact of deep learning in computer vision applications is growing every day. Deep learning techniques apply in many areas such as clothing search, automatic product recommendation. The main task in these applications is to perform the classification process automatically. But, high similarities between multiple apparel objects make classification difficult. In this paper, a new deep learning model based on convolutional neural networks (CNNs) is proposed to solve the classification problem. These networks can extract features from images using convolutional layers, unlike traditional machine learning algorithms. As the extracted features are highly discriminative, good results can be obtained in terms of classification performance. Performance results vary according to the number of filters and window sizes in the convolution layers that extract the features. Considering that there is more than one parameter that influences the performance result, the parameter that gives the best result can be determined after many experimental studies. The specified parameterization process is a difficult and laborious process. To address this issue, the parameters of a newly proposed CNN-based deep learning model were optimized using the Keras Tuner tool on the Fashion MNIST (F-MNIST) dataset containing multi-class fashion images. The performance results of the model were obtained using the data separated according to the cross-validation technique 5. At the same time, to measure the impact of the optimized parameters on classification, the performance results of the proposed model, called CNNTuner, are compared with state-of-the-art (SOTA) studies.

1. Introduction

The fashion industry is an industry that operates in many important areas, from unworn waste clothes to the creation of online store catalog images, especially in the field of sustainable fashion, which is the development of useful products. Deep learning approaches are used in different problems such as pose estimation, portrait graphic creation, garment segmentation, and garment recognition in the field of fashion [1]–[3]. Since these methods are more successful in automatic feature extraction and obtaining strong distinctive features, unlike classical machine learning methods, there is a tendency towards these methods. Security forces also have difficulties in recognizing and classifying clothes in suspicious situations where there is no clue [1]. In addition, trainable clothing search and classification systems can be created in accordance with the account profile in e-commerce-based systems, which are quite common today [3]. With the help of the specified features, it is aimed to create strong marketing

*Corresponding author: halitcetiner@isparta.edu.tr
Received: 09.05.2023, Accepted: 13.08.2023

strategies by automatically bringing the dresses suitable for the account profile. Along with these purposes and motivations, it becomes important to automatically classify clothes according to their types and shapes in line with very different purposes and targets. The problem of classifying fashion dresses is a complex task because of the multiplicity of labels characterizing the garment type, the richness of the garment features, and the similarity of the garments. Differences in camera shooting angle, lighting, and background differences are effective in deepening the classification problem [4]. In addition, high similarities in similar clothing classes such as trousers and tights make classification difficult. Although clothes recognition and classification, which is easy for humans, can be performed automatically by a computer with high performance, algorithms that work with high accuracy are needed.

Computer algorithms, on the other hand, are getting stronger day by day with powerful artificial intelligence libraries such as Tensorflow to extract meaningful information from the ever-increasing volume of images through search engines and social networks. In addition to supporting the Central Processing Unit (CPU), these libraries also support graphics processing units with high computing power, such as the Graphics Processing Unit (GPU). GPU-based codes enable rapid processing of thousands of images. Due to the limitations of classical machine learning algorithms in processing large amounts of image data, there has been a trend towards deep neural networks such as CNNs [1], [5]. There is also an increase in electronic transactions, where most transactions are carried out electronically and most of them are controlled in real time over the internet. Time series created in electronic transactions are analyzed through statistical and mathematical analysis. However, manual adjustment of the algorithm parameters used in the analysis is a difficult, tedious, laborious, and time-consuming problem. In this problem, the layer adjustments of the proposed deep learning architectures should be made automatically for the automatic classification of clothing images. In this article, the Keras Tuner tool has been used to automatically adjust the parameters of the model called CNNTuner.

Recognition and classification of images in the field of fashion using models based on deep learning architectures have many different advantages. Using these methods, users will be able to perform many different tasks in a short period of time, such as searching for related clothing and identifying the suspect type of clothing. Performing these tasks by hand is a tedious, time-consuming and exhausting process. New classification methods based on deep learning can be proposed to improve the performance of experts in searching for clothes and finding related clothes.

There are a number of issues that need to be considered when using deep learning methods for clothing classification. Firstly, due to differences in perspective, the same outfit can be described as different and different outfits as the same [1]. Secondly, clothes can be deformed as a result of washing, stretching or folding after washing [2], [3]. The third is the camera angle, lighting differences, diffuse background and shadows that are generally encountered in computer vision methods [12]. In this study, a dataset consisting of images with regular backgrounds, taken from the same angles and undeformed was determined by investigating the three main problems mentioned. In multiclass classification, which is used instead of binary classification, it is a difficult task to reduce the classification error [1]. In this study, parameter optimization of the proposed CNN model was carried out in order to reduce the multiclassification error. In order to determine the effect of parameter optimization on classification, it was compared with non-optimized parameters. In multiclass classification problems, it can be difficult to distinguish similar classes. In multiclass classification problems, the softmax activation function used in the last layer of CNN models shows the probability value of each category. In multiclass classification, the difference between these probability values may be small.

The main contributions of this article to the literature are given below.

- A new CNN model named CNNTuner has been proposed for garment classification with multiple classification problems.

- Determining the best parameters with experimental studies is a long and tiring process. This process has been accelerated by CNNTuner.

- By providing parameter optimization of the CNNTuner model, the multiple classification error has been reduced.

The remainder of the article is organized as follows. In the second section, detailed information is given about the selected dataset and the proposed CNN model. In the third section, the effect of parameter optimization on the proposed CNN model is introduced together with the performance criteria. In the last section, the article concluded by giving information about future studies.

2. Literature Review

In the literature, classification tasks have been performed with optimized parameters using different convolution-based architectures on the F-MNIST dataset [13]. Two different CNN models have been developed by Greeshma and Sreekumar to classify fashion garments [13]. The first is a model with two convolutional layers, while the second is a model with four convolutional layers. The studies show that the training process is performed with 40 and 60 epoch steps. The Adam and Adadelta optimisation algorithms used 128 and 64 values as the batch size. It was found that the best parameter optimisation result was obtained from the model with the four-convolution layer Adam optimisation algorithm and a batch size value of 64. In terms of epochs, it achieved the best test accuracy value of 60 epochs. The specified epoch value is a very high value. In this article, an attempt is made to obtain better results using the model with the best optimisation parameter with a lower epoch value.

Bhatnagar et al. developed three different CNN models to defend the F-MNIST dataset [14]. The most successful models they have developed have used residual skip connections. It is stated that the learning process is accelerated by combining these connections with the batch normalization connections.

3. Material and Methods

3.1. Material

The F-MNIST database contains 70,000 fashion images with a width and height of 28 pixels [15]. All images are in grayscale image and there are 10 categories. Each category contains 7,000 images. The training set consists of 60,000 images, while the test set consists of 10,000 images. The 10 categories are "T-shirt/top", "Trouser", "Pullover", "Dress", "Coat", "Sandal", "Shirt", "Sneaker", "Bag", "Ankle boot". Examples of images for each of these categories are shown in Figure 1. Since the separated training data were balanced, no data augmentation or balancing method was applied.

3.2. Evaluation Metrics

This section presents the model evaluation metrics constructed by performing parameter optimization. The metrics of precision, recall, F1 score, F2 score, specificity and accuracy were used to evaluate the model. False Negative (FN), True Negative (TN), False Positive (FP), True Positive (TP) markers were used in the formulation of these metrics. TP represents the accuracy of the proposed model's predicted class output and actual class output. FP means that the predicted value of the proposed model is correct while in reality it is incorrect. The FN marker represents that the proposed model predicts an incorrect output while the actual output is correct. Finally, TN means that the proposed model predicts the wrong output, while in the actual situation it is wrong [16].

$$Accuracy = \frac{TP+TN}{TP+TN+FP+FN} \quad (1)$$

$$F1 = 2x\frac{PrecisionxRecall}{Precision+Recall} \quad (2)$$

$$Precision = \frac{TP}{TP+FP} \quad (3)$$

$$Recall\ (Sensitivity) = \frac{TP}{TP+FN} \quad (4)$$

$$F2 = \frac{5xPrecisionxRecall}{4x(Precision+Recall)} \quad (5)$$

$$Specificity = \frac{TN}{TN+FP} \quad (6)$$

The accuracy metric shown in Equation 1 is the ratio of the predicted accuracy of the proposed model divided by the total predictions. Equation 2 shows the harmonic mean of the precision and recall metrics expressed in Equation 3 and Equation 4. The precision metric in Equation 3 is the number of correct predictions of the proposed model divided by the total number of predictions. In Equation 4, the recall formula shows the successful prediction status. Equation 5 increases the importance of recall performance while decreasing precision.

Equation 6 shows how effective the proposed model is in identifying negative tags.

3.3. Keras Tuner

Keras is a deep learning library that runs on top of artificial intelligence libraries such as Tensorflow. Optimization algorithms help to maximize performance by minimizing the objective function [13]. There are two separate processes in deep learning models: training and testing. In the training process, a low number of losses is a measure of whether performance is good or not [17]. The lower the losses, the more successful the proposal. The Adam optimization method is used to optimize the training of the proposed model [18].

3.4. CNN

CNN algorithms are widely used for classification of image data [19]–[21]. CNN consists of interconnected layers with different characteristics. These layers go from the input layer to the classification layer. The layers contain neurons that learn different parameters such as weights. The architecture of the CNN is not fully interconnected as in classical neural networks. Only the last layer is fully connected, partially avoiding the problem of over-fitting and the waste of full connections. Simultaneously, CNN has specialized layers for classical machine learning data reduction and feature extraction steps. While the feature mapping is performed by convolution layers, the dimensionality reduction of the feature maps is performed by the pooling layer. The task of understanding and classifying the values in the feature map is performed by the fully connected layer and the classification layer with activation function [22]. In general, binary classification tasks are performed with the sigmoid activation function, while the softmax activation function is used for multiple classification problems.

Popular CNN algorithms are known as AlexNet, ZFNet, VGGNet, GoogleNet and ResNet. AlexNet consists of 5 convolutional layers, pooling, dropout and 3 fully connected layers [23]. In addition to the classification layer, it uses the ReLU function for non-linear functions. ZFNet is designed to improve the performance of the AlexNet architecture [24].

Figure 1. Sample images from classes in the dataset

The main reason why it is better is seen in the size of its parameters and filters [24]. Parameter optimization is also important in the development of popular CNN architectures, and was one of the main motivations for writing this paper. Instead of using windows with a width and height of 11 pixels, ZFNet uses windows with a width and height of 7 pixels, allowing more information to be retained. VGGNet, uses filters with a width and height of 3 pixels. In the pooling layer, it uses windows with a width and height of 2 pixels. To increase the volume depth, VGGNet has doubled the number of filters after each pooling layer [25]. GoogleNet is capable of processing at a number of different scales in parallel, with filters of different sizes [26]. It implements maximum pooling in window sizes with the same width and height for each of its

parallel connections. The network consists of three convolutional layers, followed by 9 inception layers, including two convolutional layers and one fully connected layer. It has a total of 22 layers. ResNet includes shortcut module connections with an identity connection that can bypass the weight layers designed to solve the gradient problem [26], [27]. Popular CNN architectures can be used as a basis to provide suitable solutions for different problems, or, as in this study, models can be constructed by combining basic CNN layers with optimized parameters.

3.5. Proposed Model

Deep learning methods are widely used in the literature to solve a wide variety of problems [6]–[8]. Pre-trained weighted datasets such as ImageNet and COCO have helped explore the power of deep learning. The COCO dataset is a large dataset consisting of 381 thousand images that can be used in 91 different object detection and segmentation tasks [9]. ImageNet, on the other hand, is a dataset with 1.2 million training sets with 1000 object categories [10]. CNN algorithms, which have been used since 1980, have increased their popularity in ImageNet competitions [11]. Because CNN architectures can provide solutions for different problems and features with high distinctiveness, it formed the basis of the model proposed in this study. For these reasons, the automatic classification of fashion clothing images is carried out with a model called CNNTuner. At the same time, the parameters of this model are determined automatically, preventing the time spent on parameter determination.

The proposed model is a new 15-layer architecture developed on the basis of convolutional layers. Keras Tuner tool, one of the popular parameter optimization algorithms, is integrated into this architecture. In order for this tool to work with different filtering and activation options, each step has been controlled and run. The parameters of each convolution, maximum pooling and activation functions used in the model were determined by the Keras Tuner tool instead of being randomly selected. In the CNNTuner model, the details of which are given below, in order for the layers to work harmoniously with each other, any parameter selected at each step should not prevent the model from being compiled. For this purpose, many different experimental studies have been carried out and the results are presented in the study. The proposed model is detailed in the next step of the article.

A new CNN model called CNNTuner is proposed to measure the effect of optimized CNN parameters on classification. Fashion images with dimensions of 28x28x1 pixels were used as input for the classification of the F-MNIST dataset. Grayscale image was used as the input color format. Some of the images in the format used are shown in Figure 1. Figure 2 shows the tested hyperparameters and layers of the CNNTuner model. The aim of this article is to optimize the parameters in the CNNTuner model structure in order to obtain the best performance results, without having to be tested by constantly changing them. In the model realized for this purpose, 28x28x1 pixels dimensions images are taken as input in the first layer. In the 2nd layer, the parameter of the convolution layer is set as one of 8 filters from 32 filters to 256 filters. At the same time, instead of using a fixed window size, the optimizing algorithm will prefer to use one of the 3 or 5 pixel window sizes. In the 3rd layer, one of the frequently used ReLU, eLU, seLU, tanh activation functions are defined to be selected.

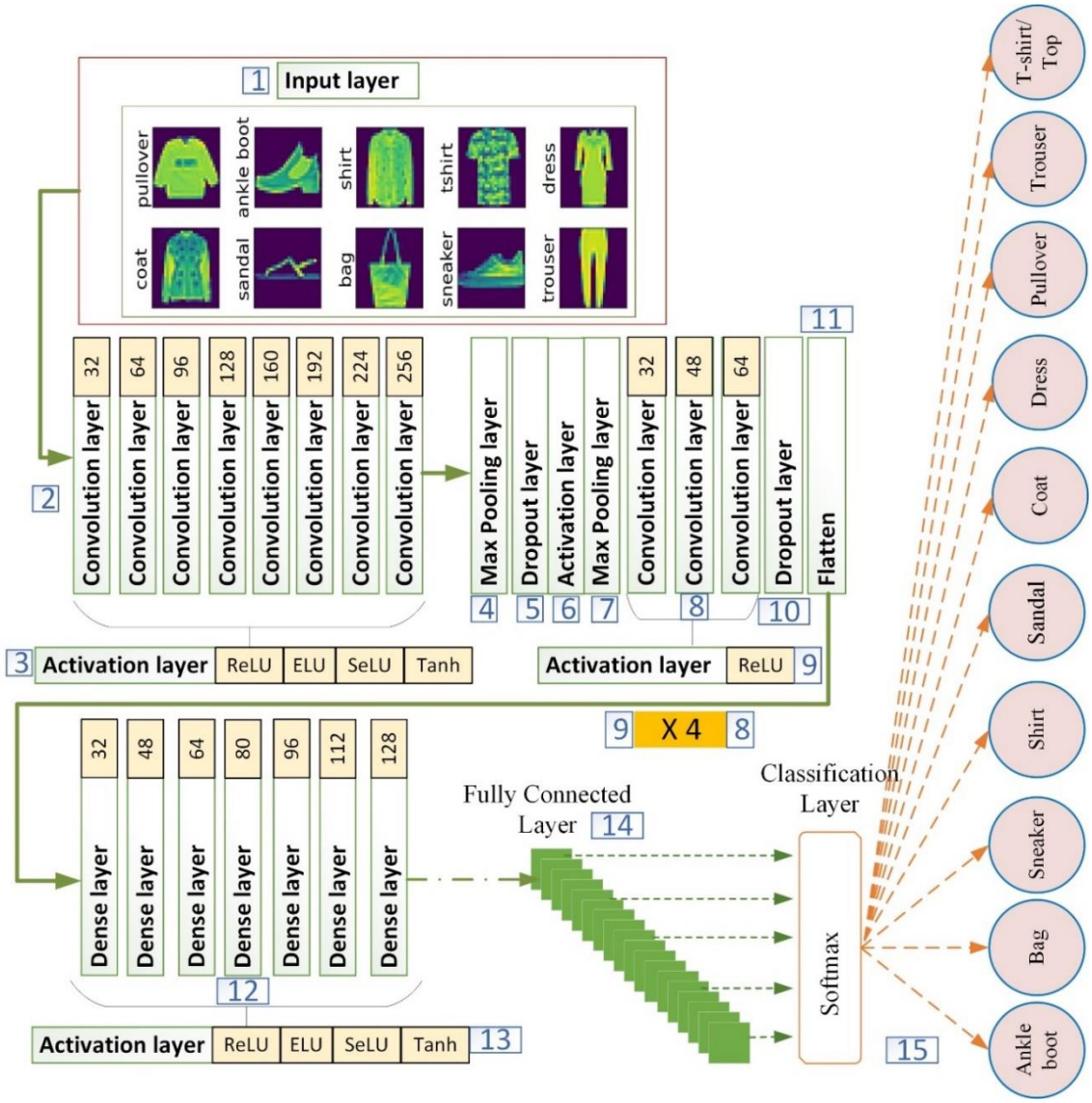

Figure 2. Proposed model with hyperparameter tested

In the 4th layer of the proposed model, a maximum pooling layer with a width and height value of 1 pixel is defined. At this point, since the number of filters coming from the previous layers is not clear, a layered structure has been created that differs from the usual fixed-definition CNN architecture. No matter what convolution filter comes, a model has been created in which the deep learning model will be built without errors. In the 5th layer, the dropout layer, which performs the neuron dropout process that prevents overlearning at a rate of 0.9, is applied.

A constant ReLU activation function is defined in the 6th layer. A maximum pooling layer with a width and height of 2 pixels is defined in the 7th layer of the proposed model. In layers 8 and 9, the convolution layer and the ReLU activation function layers are repeated together 4 times. In layer 8, one of the 8 filters from 32 filters to 256 filters is determined as the parameter of the convolution layer. A window size of 3 pixels in width and height has been applied to the selected convolution layer. The ReLU activation function was used in the 9th layer. In the 10th layer, a dropping layer was added, which causes neurons to drop out at a rate of 0.9. In the 11th layer, the Flatten layer has been applied, which reduces the data from the layers to a single dimension. In the 12th layer, a dense layer is defined, which increases by 16 neurons from 32 neurons to 128 neurons. The optimization algorithm has selected one of the specified parameters. In the 13th layer, one of the activation functions ReLU, eLU, seLU

and tanh is defined to be selected. The 14th layer is a fully connected layer, which provides a full connection to the features from the previous layers. In the 15th layer, the model is completed with a classification layer with a softmax activation function with a total of 10 classes from the F-MNIST dataset.

In this paper, one of the most important points to emphasize is the selection of one of the many different layer parameter options. The Keras Tuner optimization tool was used instead of manual selection. The best parameters were determined through 100 different iterations. Thanks to the optimization method, which increases the efficiency of the proposed model, the best result is obtained both in terms of time and performance. Both accuracy and confusion matrix information are presented to measure the performance of the results. A total of 8 different filters were applied in the 2nd layer of the proposed model. Another point to emphasize is that the resulting layered structure should be adjusted so that there is no size mismatch. It is very important to set the application to work regardless of the number of filters selected. A detailed representation of the above parameters is shown in Figure 2. If desired, the model applied to the F-MNIST dataset can be tested on a variety of datasets with a low success rate in the literature. In this case, however, it may be necessary to modify the proposed model. Not all problems can be solved with a single deep learning model.

4. Results

Parameter optimization saves the researcher the lengthy process of determining appropriate parameters. In this context, the present study makes a unique contribution to the literature on the subject. In CNN models, there are pre-trained architectures as well as structures formed by convolution, pooling, batch normalization, dropout, fully connected, classification layers coming one after another in a certain shape and structure. There are two different ways to build CNN-based deep learning models. In this study, the second type of CNN structure is targeted by combining the basic layers of the CNN structure. In such models, researchers use experimental studies to determine parameters such as the number of filters, kernel size, and number of layer repetitions to achieve optimal training and testing performance. These procedures will speed up the parameter determination processes of the researchers due to the convenience they provide in determining the parameters. According to the cross validation method, recall, F1 score, F2 score, specificity, accuracy performance values were also examined in detail. At this stage, the training data of each Fold number of cross validation were tested separately. The Fold values of cross validation are Fold1, Fold2, Fold3, Fold4, and Fold5, respectively.

Table 1 shows the performance results that were obtained according to the Fold1 option on a class basis in the F-MNIST database. The results of each class with precision, recall, F1 score, F2 score and specificity metrics are shown. While the Trouser and Bag classes give the highest results, the results obtained from the Shirt and Coat classes are the lowest performance results. In addition to the performance results given in Table 1, the accuracy results obtained using the accuracy formula are shown in Figure 3. Class-wise accuracy values are given as well as the classification accuracy obtained collectively. According to the Fold1 option, the proposed model has an average accuracy of 95.84%.

Table 1. Fold1 performance result of the proposed model

Class name	Precision	Recall	F1 Score	Specificity	F2 score
T-shirt/top	0.94	0.96	0.95	0.95	0.96
Trouser	1.00	1.00	1.00	1.00	1.00
Pullover	0.93	0.93	0.93	0.94	0.94
Dress	0.94	0.97	0.95	0.98	0.96
Coat	0.90	0.93	0.91	0.97	0.93
Sandal	1.00	0.99	0.99	0.99	1.00
Shirt	0.92	0.84	0.88	0.85	0.91
Sneaker	0.97	0.99	0.98	0.99	0.99
Bag	1.00	1.00	1.00	1.00	1.00
Ankle boot	0.99	0.98	0.98	0.99	0.99

Table 2 presents the performance results obtained according to the Fold2 option on a class basis in the F-MNIST database. While the class of Trousers and the class of Sandals give the highest results, the results obtained from the class of pullover and the class of shirt are the lowest performance results. Figure 4, which is shared in integration with the performance metrics given in Table 2, shows the confusion matrix values obtained according to the same Fold value. According to the class-based accuracy values shown in Figure 4, accuracy values of 98.26%, 99.79%, 93.99%, 98.57%, 95.99%, 100%, 94.29%, 99.58%, 99.78%, 98.83% were achieved in T-shirt/top, Trouser, Pullover, Dress, Coat, Sandal, Shirt, Sneaker, Bag, Ankle boot classes.

Table 3 presents the performance results obtained according to the Fold3 option on a class basis. Trouser, Sandal, Sneaker, Bag and Ankle boot classes gave higher results than the other classes. In this Fold3 option, there was no class with low results in general. In addition to the performance results given in Table 3, the accuracy results obtained using the accuracy formula are shown in Figure 5. Class-wise accuracy values are given as well as the classification accuracy obtained collectively. According to the Fold3 option, the proposed model has an average accuracy of 99.13%.

According to the Fold3 results given in Figure 5, T-shirt/top, Trouser, Pullover, Dress, Coat, Sandal, Shirt, Sneaker, Bag, Ankle Boot classes reached 98.62%, 100%, 98.29%, 98.60%, 97.38%, 100%, 98.47%, 99.79%, 99.78%, 100% accuracy values respectively. It is seen that the highest error is obtained from the Coat class.

Figure 6 shows the confusion matrix results obtained according to the Fold4 option. T-shirt/top, Trouser, Pullover, Dress, Coat, Sandal, Shirt, Sneaker, Bag, Ankle boot classes reached 98.05%, 99.79%, 95.24%, 98.83%, 98.62%, 99.78%, 96.16%, 100%, 99.78%, 99.79% accuracy values respectively. It is seen that the highest error is obtained from the Pullover class.

Table 2. Fold2 performance result of the proposed model

Class name	Precision	Recall	F1 Score	Specificity	F2 score
T-shirt/top	0.98	0.98	0.98	0.99	0.99
Trouser	1.00	1.00	1.00	1.00	1.00
Pullover	0.94	0.96	0.95	0.98	0.97
Dress	0.99	0.97	0.98	0.98	0.99
Coat	0.96	0.96	0.96	0.97	0.98
Sandal	1.00	1.00	1.00	1.00	1.00
Shirt	0.94	0.96	0.95	0.97	0.97
Sneaker	1.00	0.99	0.99	1.00	1.00
Bag	1.00	0.99	0.99	1.00	1.00
Ankle boot	0.99	1.00	0.99	1.00	1.00

Table 3. Fold3 performance result of the proposed model

Class name	Precision	Recall	F1 Score	Specificity	F2 score
T-shirt/top	0.99	0.99	0.99	0.99	1.00
Trouser	1.00	1.00	1.00	1.00	1.00
Pullover	0.98	0.98	0.98	0.98	0.99
Dress	0.99	0.99	0.99	0.99	1.00
Coat	0.97	0.99	0.98	1.00	0.99
Sandal	1.00	1.00	1.00	1.00	1.00
Shirt	0.98	0.96	0.97	0.96	0.98
Sneaker	1.00	1.00	1.00	1.00	1.00
Bag	1.00	1.00	1.00	1.00	1.00
Ankle boot	1.00	1.00	1.00	1.00	1.00

Figure 3. Fold1 confusion matrix results

Figure 4. Fold2 confusion matrix results

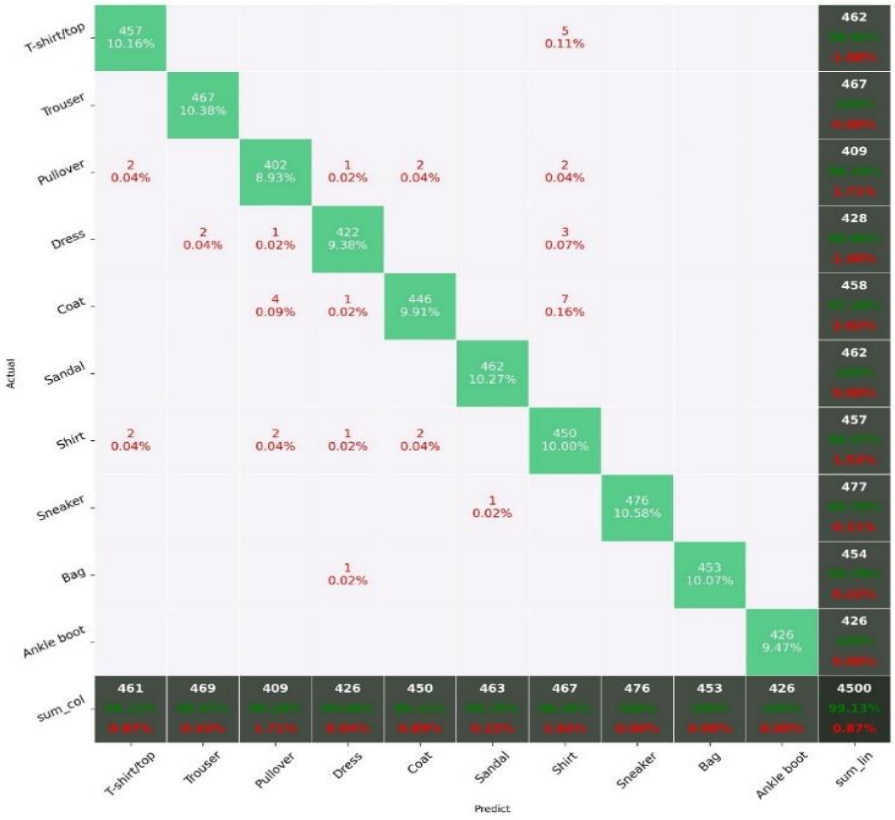

Figure 5. Fold3 confusion matrix results

Figure 6. Confusion matrix results obtained according to the Fold4 option

Table 4 shows the performance results obtained according to the Fold4 option. Although it is similar to Fold3 results, there was no class with low results. The classes with very good results are Trouser, Sandal, Sneaker, Bag, Ankle boot. The confusion matrix results obtained according to the Fold5 option are given in Figure 7. According to these results, T-shirt/top, Trouser, Pullover, Dress, Coat, Sandal, Shirt, Sneaker, Bag, Ankle boot classes gave 97.85%, 100%, 98.05%, 99.30%, 98.68%, 100%, 98.69%, 99.79%, 99.34%, 100% accuracy performance results. Among the classes, the T-shirt/top class gave the highest error. When the results are analyzed, it is determined that Fold5 provides superior performance than other Fold values. This is shown in Table 6.

Table 4. Fold4 performance result of the proposed model

Class name	Precision	Recall	F1 Score	Specificity	F2 score
T-shirt/top	0.98	0.98	0.98	0.99	0.99
Trouser	1.00	1.00	1.00	1.00	1.00
Pullover	0.95	0.98	0.97	0.99	0.98
Dress	0.99	0.99	0.99	0.99	1.00
Coat	0.99	0.95	0.97	0.95	0.99
Sandal	1.00	1.00	1.00	1.00	1.00
Shirt	0.96	0.97	0.96	0.98	0.98
Sneaker	1.00	1.00	1.00	1.00	1.00
Bag	1.00	1.00	1.00	1.00	1.00
Ankle boot	1.00	1.00	1.00	1.00	1.00

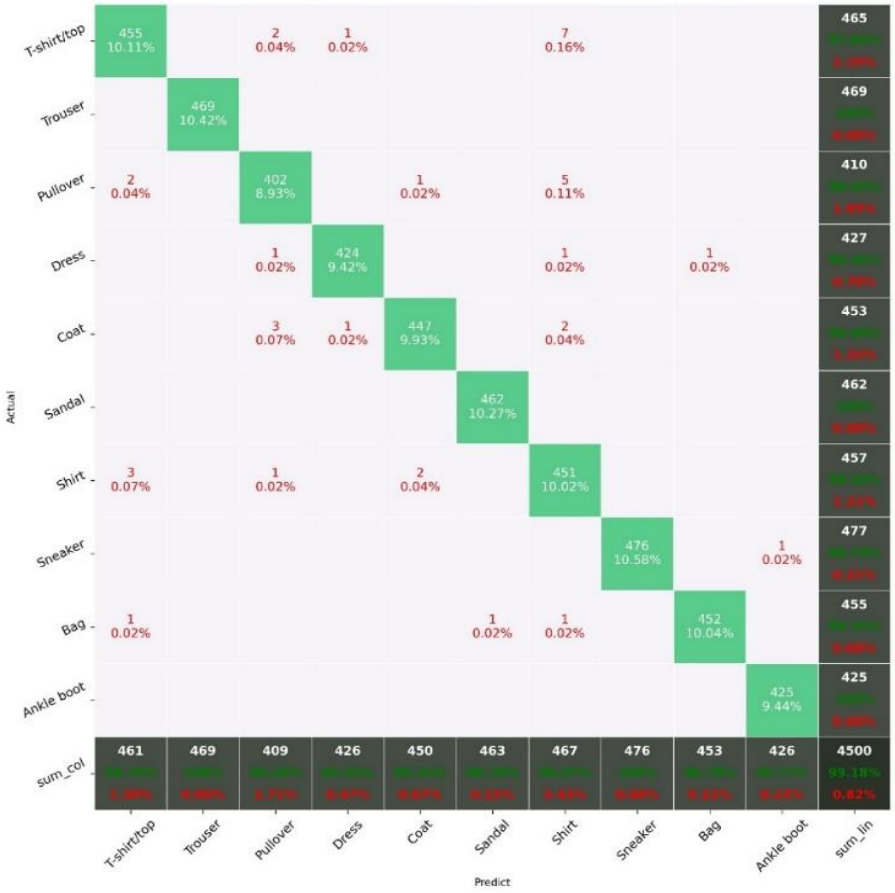

Figure 7. Confusion matrix results according to Fold5 option

Table 5. Fold5 performance result of the proposed model

Class name	Precision	Recall	F1 Score	Specificity	F2 score
T-shirt/top	0.98	0.99	0.98	0.99	0.99
Trouser	1.00	1.00	1.00	1.00	1.00
Pullover	0.98	0.98	0.98	0.98	0.99
Dress	0.99	1.00	0.99	0.99	1.00
Coat	0.99	0.99	0.99	0.99	0.99
Sandal	1.00	1.00	1.00	1.00	1.00
Shirt	0.99	0.97	0.98	0.98	0.99
Sneaker	1.00	1.00	1.00	1.00	1.00
Bag	0.99	1.00	1.00	1.00	1.00
Ankle boot	1.00	1.00	1.00	1.00	1.00

The results shown in Table 6 are different representations of the confusion matrix results given between Figure 3 and Figure 7. In addition to these, the performance results obtained are reinforced with graphical outputs.

Table 6 presents the training and validation results for each Fold value. Fold5 is preferred because the difference in success rate between the training and validation results is quite small. The model performance graphs plotted over Fold5 are presented below.

Figure 8-11 show the train accuracy, train loss, validation accuracy, validation loss graphs of the proposed model respectively. They have been zoomed in to make the graphs between the fold values clearer and closer together. In each model performance graph, the graph outputs between the last two epochs are zoomed and shown in a separate box. Train accuracy performance graphs of all Fold values are shown in Figure 8. According to the graph features shown in Figure 8, the Fold5 accuracy value is superior to the other Fold values. The difference between Fold1 train accuracy performance graph and Fold5 is higher than other Fold values. In Figure 9, the loss graphs of the Fold values whose train accuracy values are given in Figure 8 are plotted. At 20 epochs, the smallest loss value obtained was 0.0080.

Figure 10 shows the validation accuracy performance graphs. There is a significant difference between the Fold values. The most successful result is obtained from Fold5, while the lowest result is obtained from Fold1. In the same parallel, the highest loss is obtained from Fold1, while the lowest loss is obtained from Fold5.

Table 6. Performance results of train and validation of the proposed model

	Train		Validation	
	Accuracy	Loss	Accuracy	Loss
Fold1	0.9590	0.1111	0.9584	0.1241
Fold2	0.9942	0.0186	0.9793	0.0856
Fold3	0.9995	0.0023	0.9913	0.0213
Fold4	0.9949	0.0149	0.9862	0.0246
Fold5	0.9999	0.0080	0.9918	0.0189

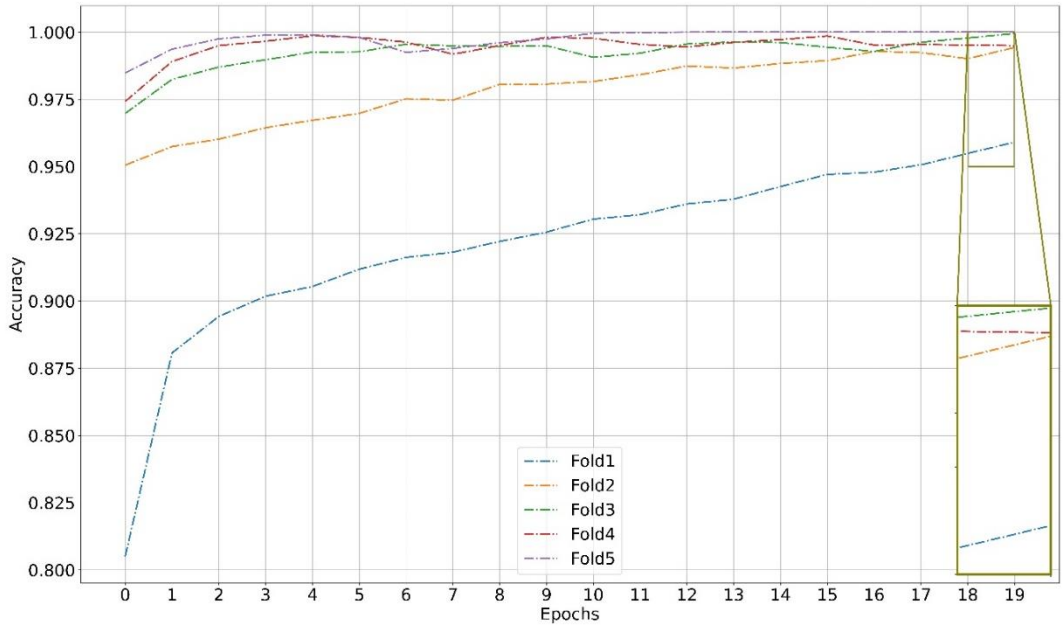

Figure 8. Train accuracy performance graph of the proposed model

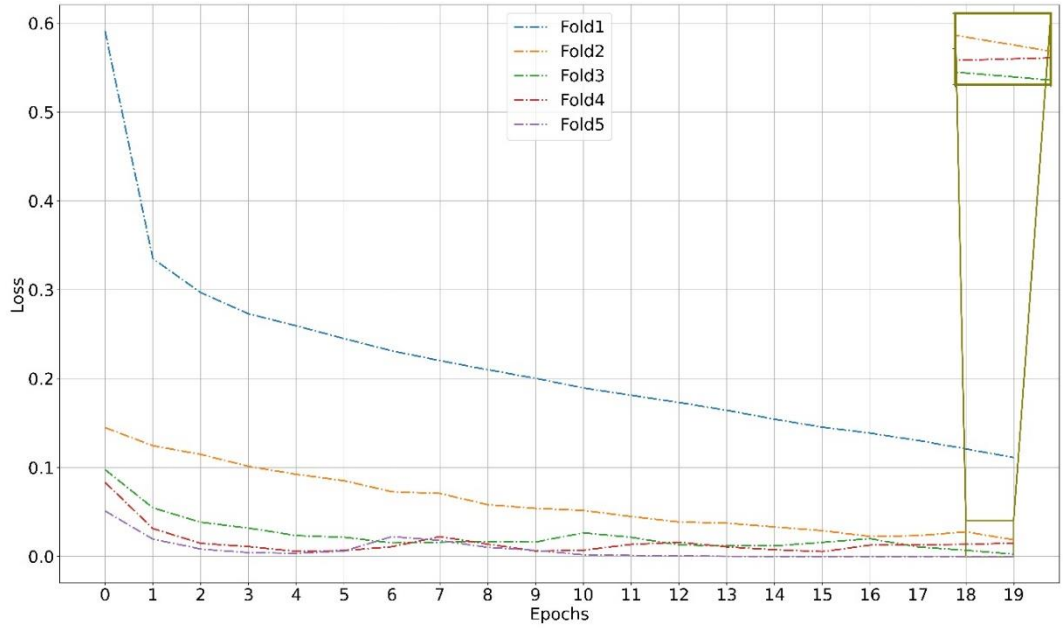

Figure 9. Graph of the performance of the proposed model for train losses

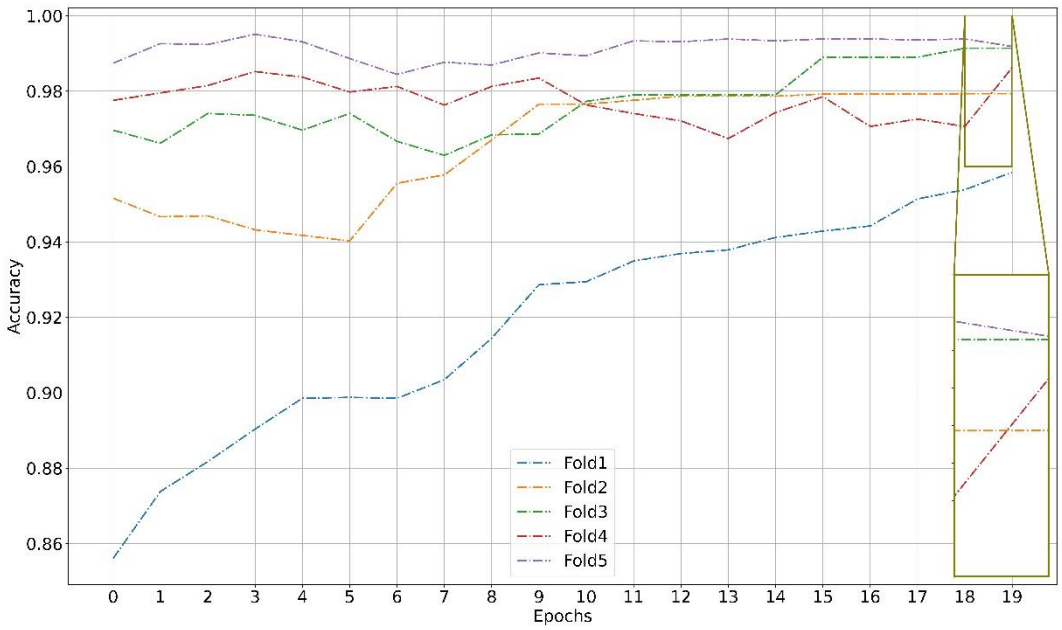

Figure 10. Graph showing the proposed model's performance in validating accuracy

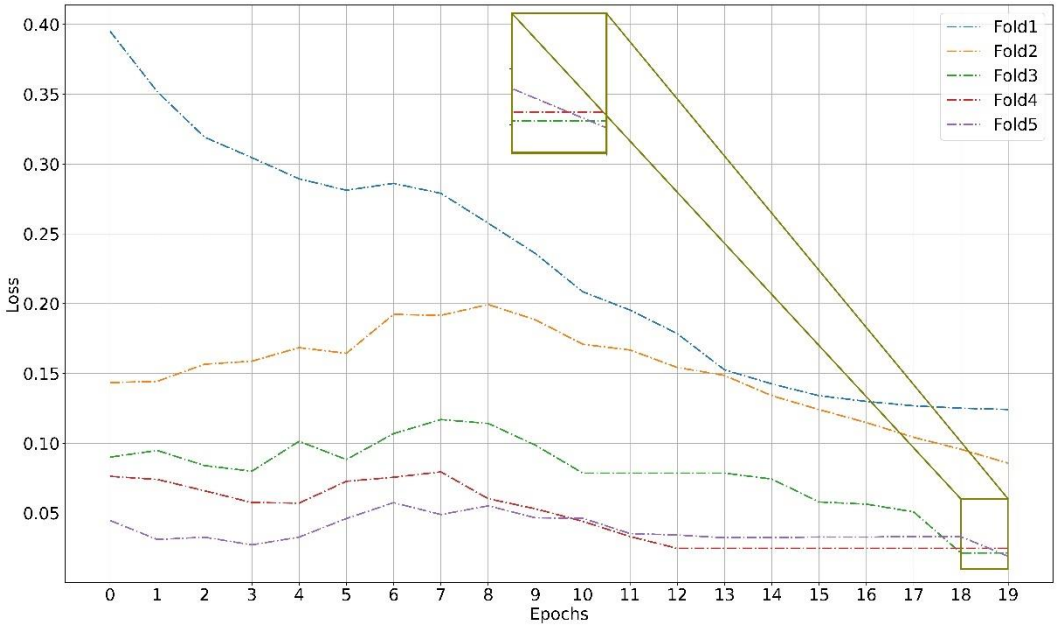

Figure 11. Validation loss performance graph of the proposed model

5. Discussion

In this section, state-of-the-art (SOTA) studies using the same dataset are discussed and compared. In terms of mean accuracy, recall, precision, F1 score, F2 score, and specificity metrics, recent studies on the F-MNIST dataset were compared with CNNTuner.

The proposed model should work in harmony with different filter and activation options. In order for this to be adjusted and the proposed model to work with the Keras Tuner tool, the layer output sizes are provided to work without error. Experimental studies have been carried out more than once in the realization of this. As a result of the evaluations, options other

than the parameters selected by the Keras Tuner tool were selected and the performance results were examined. When these results were evaluated, a performance difference between 4% and 10% was determined.

The comparison in Table 7 shows that, in general, the effect of a new activation function or the contribution of residual connections to classification is observed. Although residual connections and activation functions are effective in model performance, this study shows that the performance impact of an accurate deep learning model with appropriate parameters is higher. The abbreviation DNN in Table 7 stands for Deep Neural Network. The DeDNN-oReLU model is parameter optimized by genetic algorithm with oReLU activation function [28]. DNN-ReLU, Residual DNN, DNN-NOM models, like DNN-oReLU, consist of combining different activation types with the DNN method [29].

oReLU represents the nonlinear activation function [28]. The DNN-NOM model, using the keyword Nonlinear Optical Materials (NOM), represents a neural network based on nonlinear optical materials. The Diffractive Processing Unit (DPU) represents the diffractive processing unit that can be configured into different types of models on a large scale.

Bhatnagar et al. developed the Support Vector Classifier (SVC), CNN+BatchNorm, CNN+BatchNorm+Skip and CNN2 models [14]. Each model has different aspects. SVC is used as a classifier in the SVC model. The model called CNN2 represents the CNN model with 2 convolutional layers. Skip in CNN+BatchNorm+Skip refers to skip connection structures. Shan et al. conducted experimental studies on the LeNet-DRLU model with DRLU activation function developed based on the ReLU activation function using the F-MNIST database [32]. Residual Capsule Network (RCNet) is a vector-based network that combines the capsule network structure with residual hops, and the F-MNIST dataset is used to measure the performance of the study. It is seen that 92.91% accuracy rate was achieved in the experimental studies performed on the specified dataset. Figure 12 shows the prediction results obtained using random images on the test data. When examining these results, the actual class label of the model given as input is shown on the y-axis, while the predicted class of the model is shown at the top of the axis.

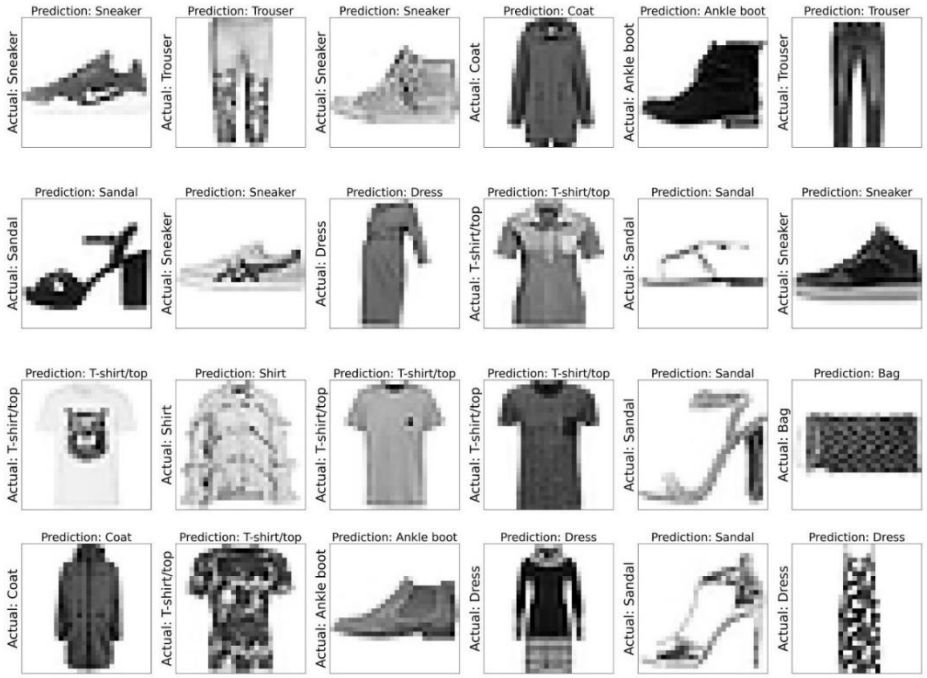

Figure 12. Prediction results of the CNNTuner model

Table 7. SOTA studies in the literature using the same dataset

References	Model	F1 score	Recall	Precision	Specificity	F2 score	Accuracy (%)
[28]	DNN-oReLU	-	-	-	-	-	87.85
[29]	DNN-ReLU	-	-	-	-	-	85.05
[30]	DPU	-	-	-	-	-	84.60
[31]	Residual DNN	-	-	-	-	-	88.40
[29]	DNN-NOM	-	-	-	-	-	88.26
[14]	SVC	-	-	-	-	-	89.70
[14]	CNN2+Batch Norm	-	-	-	-	-	92.22
[14]	CNN2+ BatchNorm+Skip	-	-	-	-	-	92.54
[14]	CNN2	-	-	-	-	-	91.17
[32]	LeNet-DRLU	-	-	-	-	-	92.00
[33]	RCNet	-	-	-	-	-	92.91
Our method	CNNTuner	0.99	0.99	0.99	0.99	0.99	99.18

6. Conclusion

CNN structures with convolution-based automatic feature extraction capability of deep learning can be effectively used in garment retrieval, automatic garment labeling and garment classification. With this motivation, a model called CNNTuner was proposed to be used on a publicly available dataset to classify clothing images. The classification process was applied to the grayscale F-MNIST dataset consisting of 10 classes of 28x28 pixel size with 50,000 training and 10,000 test images. The parameters of each convolution, maximum pooling and activation functions used in the model are determined by the Keras Tuner tool instead of being randomly selected.

The training and test data separated according to the cross validation 5 technique resulted in Fold1, Fold2, Fold3, Fold4 and Fold5. Among these values, the Fold with higher accuracy and lower loss was selected and test predictions were obtained. The search for the right parameter in deep learning models can be a time-consuming process. Parameters selected using the Keras Tuner tool should work seamlessly on the model. When either the activation or filter options are selected, the next layer selected must be compatible with the filter dimensions. For these reasons, the model has been designed to ensure this compatibility.

In future studies, optimized parameters can be used to improve the performance of image segmentation algorithms such as Mask RCNN, UNET and YOLO, which have a long training process. The purpose of this study is to contribute to the literature in this area.

Contributions of the authors

All authors contributed equally to the study.

Conflict of Interest Statement

There is no conflict of interest between the authors.

Statement of Research and Publication Ethics

The study is complied with research and publication ethics.

References

[1] Y. Seo and K. Shin, "Hierarchical convolutional neural networks for fashion image classification," *Expert Syst. Appl.*, vol. 116, pp. 328–339, 2019, doi: 10.1016/j.eswa.2018.09.022.

[2] S. G. Eshwar, G. G. P. J, A. V Rishikesh, N. A. Charan, and V. Umadevi, "Apparel classification using Convolutional Neural Networks," in *2016 International Conference on ICT in Business Industry & Government (ICTBIG)*, 2016, pp. 1–5. doi: 10.1109/ICTBIG.2016.7892641.

[3] K. Hara, V. Jagadeesh, and R. Piramuthu, "Fashion apparel detection: The role of deep

convolutional neural network and pose-dependent priors," in *2016 IEEE Winter Conference on Applications of Computer Vision (WACV)*, pp. 1–9, 2016. doi: 10.1109/WACV.2016.7477611.

[4] M. Kayed, A. Anter, and H. Mohamed, "Classification of garments from fashion MNIST dataset using CNN LeNet-5 architecture," in *2020 International Conference on Innovative Trends in Communication and Computer Engineering (ITCE)*, pp. 238–243, 2020,. doi: 10.1109/ITCE48509.2020.9047776.

[5] S. Metlek, "A new proposal for the prediction of an aircraft engine fuel consumption: a novel CNN-BiLSTM deep neural network model," *Aircr. Eng. Aerosp. Technol.*, vol. 95, no. 5, pp. 838–848, Jan. 2023, doi: 10.1108/AEAT-05-2022-0132.

[6] A. Kishwar and A. Zafar, "Fake news detection on Pakistani news using machine learning and deep learning," *Expert Syst. Appl.*, vol. 211, p. 118558, 2023, doi: 10.1016/j.eswa.2022.118558.

[7] M. S. Khan, N. Tafshir, K. N. Alam, A.R. Dhruba, M. M. Khan, A. A. Albraikan, and F. A. Almalki, "Deep learning for ocular disease recognition: an ınner-class balance," *Comput. Intell. Neurosci.*, vol. 2022, 2022.

[8] H. Çetiner and B. Kara, "Recurrent neural network based model development for wheat yield forecasting," *J. Eng. Sci. Adiyaman Univ.*, vol. 9, no. 16, pp. 204–218, 2022, doi: 10.54365/adyumbd.1075265.

[9] J. Reizenstein, R. Shapovalov, P. Henzler, L. Sbordone, P. Labatut, and D. Novotny, "Common objects in 3d: large-scale learning and evaluation of real-life 3d category reconstruction," in *Proceedings of the IEEE/CVF International Conference on Computer Vision*, pp. 10901–10911, 2021.

[10] O. Russakovsky, J. Deng, H. Su, J. Krause, S. Satheesh, S. Ma, Z. Huang, A. Karpathy, A. Khosla, M. Bernstein, A. C. Berg, and L. Fei-Fei, "ImageNet large scale visual recognition challenge," *Int. J. Comput. Vis.*, vol. 115, no. 3, pp. 211–252, 2015, doi: 10.1007/s11263-015-0816-y.

[11] M. A. Morid, A. Borjali, and G. Del Fiol, "A scoping review of transfer learning research on medical image analysis using ImageNet," *Comput. Biol. Med.*, vol. 128, p. 104115, 2021, doi: 10.1016/j.compbiomed.2020.104115.

[12] X. Wang and T. Zhang, "Clothes search in consumer photos via color matching and attribute learning," in *Proceedings of the 19th ACM international conference on Multimedia*, pp. 1353–1356, 2011.

[13] K. V Greeshma and K. Sreekumar, "Hyperparameter optimization and regularization on fashion-MNIST classification," *Int. J. Recent Technol. Eng.*, vol. 8, no. 2, pp. 3713–3719, 2019.

[14] S. Bhatnagar, D. Ghosal, and M. H. Kolekar, "Classification of fashion article images using convolutional neural networks," in *2017 Fourth International Conference on Image Information Processing (ICIIP)*, pp. 1–6, 2017. doi: 10.1109/ICIIP.2017.8313740.

[15] H. Xiao, K. Rasul, and R. Vollgraf, "Fashion-mnist: a novel image dataset for benchmarking machine learning algorithms," *arXiv Prepr. arXiv1708.07747*, 2017.

[16] H. Çetiner, "Cataract disease classification from fundus images with transfer learning based deep learning model on two ocular disease datasets," *Gumushane University Journal of Science and Technology*, vol. 13, no. 2, pp. 258–269, Jan. 2023, doi: 10.17714/gumusfenbil.1168842.

[17] S. Suganyadevi, V. Seethalakshmi, and K. Balasamy, "A review on deep learning in medical image analysis," *Int. J. Multimed. Inf. Retr.*, vol. 11, no. 1, pp. 19–38, 2022, doi: 10.1007/s13735-021-00218-1.

[18] D. Kingma and J. Ba, "Adam: a method for stochastic optimization," *Int. Conf. Learn. Represent.*, Dec. 2014.

[19] Vijayalakshmi A and Rajesh Kanna B, "Deep learning approach to detect malaria from microscopic images," *Multimed. Tools Appl.*, vol. 79, no. 21–22, pp. 15297–15317, Jun. 2020, doi: 10.1007/s11042-019-7162-y.

[20] S. Zhang, W. Huang, and C. Zhang, "Three-channel convolutional neural networks for vegetable leaf disease recognition," *Cogn. Syst. Res.*, vol. 53, pp. 31–41, 2019, doi: 10.1016/j.cogsys.2018.04.006.

[21] S. Zhang, S. Zhang, C. Zhang, X. Wang, and Y. Shi, "Cucumber leaf disease identification with global pooling dilated convolutional neural network," *Comput. Electron. Agric.*, vol. 162, pp. 422–430, 2019, doi: 10.1016/j.compag.2019.03.012.

[22] N. Saxena, V. Sharma, R. Sharma, K. K. Sharma, and S. Gupta, "Design, modeling, and frequency domain analysis with parametric variation for fixed-guided vibrational piezoelectric energy harvesters," *Microprocess. Microsyst.*, vol. 95, p. 104692, Nov. 2022, doi: 10.1016/j.micpro.2022.104692.

[23] A. Krizhevsky, I. Sutskever, and G. E. Hinton, "Imagenet classification with deep convolutional neural networks," *Adv. Neural Inf. Process. Syst.*, vol. 25, 2012.

[24] M. D. Zeiler and R. Fergus, "Visualizing and understanding convolutional networks," in *European conference on computer vision*, pp. 818–833, 2014.

[25] K. Simonyan and A. Zisserman, "Very deep convolutional networks for large-scale image recognition," *arXiv Prepr. arXiv1409.1556*, 2014.

[26] C. Szegedy, S. Ioffe, V. Vanhoucke, and A. A. Alemi, "Inception-v4, inception-resnet and the impact of residual connections on learning," 2017.

[27] K. He, X. Zhang, S. Ren, and J. Sun, "Deep residual learning for image recognition," in *2016 IEEE Conference on Computer Vision and Pattern Recognition (CVPR)*, pp. 770–778, Jun. 2016. doi: 10.1109/CVPR.2016.90.

[28] C. Dong, Y. Cai, S. Dai, J. Wu, G. Tong, W. Wang, Z. Wu, H. Zhang, and J. Xia, "An optimized optical diffractive deep neural network with OReLU function based on genetic algorithm," *Opt. Laser Technol.*, vol. 160, p. 109104, 2023, doi: 10.1016/j.optlastec.2022.109104.

[29] Y. Sun, M. Dong, M. Yu, L. Lu, S. Liang, J. Xia, and L. Zhu, "Modeling and simulation of all-optical diffractive neural network based on nonlinear optical materials," *Opt. Lett.*, vol. 47, no. 1, pp. 126–129, 2022, doi: 10.1364/OL.442970.

[30] T. Zhou, X. Lin, J. Wu, Y. Chen, H. Xie, Y. Li, J. Fan, H. Wu, L. Fang, and Q. Dai, "Large-scale neuromorphic optoelectronic computing with a reconfigurable diffractive processing unit," *Nat. Photonics*, vol. 15, no. 5, pp. 367–373, 2021, doi: 10.1038/s41566-021-00796-w.

[31] H. Dou, Y. Deng, T. Yan, H. Wu, X. Lin, and Q. Dai, "Residual D2NN: training diffractive deep neural networks via learnable light shortcuts," *Opt. Lett.*, vol. 45, no. 10, pp. 2688–2691, 2020, doi: 10.1364/OL.389696.

[32] C. Shan, A. Li, and X. Chen, "Deep delay rectified neural networks," *J. Supercomput.*, vol. 79, no. 1, pp. 880–896, 2023, doi: 10.1007/s11227-022-04704-z.

[33] J. Zhang, Q. Xu, L. Guo, L. Ding, and S. Ding, "A novel capsule network based on deep routing and residual learning," *Soft Comput.*, 2023, doi: 10.1007/s00500-023-08018-x.

Bitlis Eren Üniversitesi Fen Bilimleri Dergisi
BİTLİS EREN UNIVERSITY JOURNAL OF SCIENCE
ISSN: 2147-3129/e-ISSN: 2147-3188
VOLUME: 12 NO: 3 PAGE: 764-772 YEAR: 2023
DOI:10.17798/bitlisfen.1297654

Preparation of Transparent ZIF-8/TiO_2 Nanocomposite Thin Films for Photocatalytic Applications

Onur İLOĞLU[1], Hüsnü Arda YURTSEVER[1*]

[1]*Adana Alparslan Türkeş Science and Technology University, Faculty of Engineering, Department of Materials Science and Engineering, Adana, Türkiye*
(ORCID: 0000-0003-3410-1072), (ORCID: 0000-0002-1920-8149)

Keywords: Photocatalysis, Thin film, Nanocomposite, ZIF-8, TiO_2.

Abstract
Transparent ZIF-8/TiO_2 nanocomposite thin films were prepared by a two-stage dip-coating method. TiO_2 was first deposited on glass substrates by sol-gel dip-coating. Heat treatment temperature, number of layers, and doping metal type or level were optimized in the first step. In the next step, ZIF-8 was grown by solvent-based crystallization method on TiO_2 layers. Cu, Ce, Fe, or Zn-doped TiO_2 thin films were prepared in order to increase the photocatalytic performance of the ZIF-8/TiO_2 nanocomposite. The highest photocatalytic methylene blue degradation activities were obtained with the ZIF-8/TiO_2 nanocomposite thin films prepared by using 1% Cu or 1% Ce-doped TiO_2 thin films as the substrates. Both films exhibited 19% dye removal in 1 hour under 254 nm LED light irradiation, whereas the dye removal efficiencies were 36% and 29% , respectively, in 1 hour under 365 nm LED light irradiation.

1. Introduction

Scientific studies report that by 2050, energy and clean water demand will increase by 80% and 55%, respectively, due to an increase in the world population to 9.7 billion people [1]. Using clean and renewable energy sources and implementing new water treatment technologies with low energy requirements and high efficiencies are of great importance in ensuring a sustainable environment. Photocatalysis stands out as a promising method for the generation of clean hydrogen from water and the oxidation of water pollutants by the utilization of solar energy, which is abundant and free. Photocatalyst design and preparation, which are at the center of photocatalysis, are the most important steps that determine the efficiency of any photocatalytic process. Metal-organic frameworks (MOFs), which have been frequently used in photocatalysis in recent years, are promising materials due to their microporous structure and high surface area. ZIF-8 (Zeolitic imidazolate framework-8), which consists of zinc and 2-methyl imidazole building blocks and is in the zeolitic imidazolate family, has a high surface area (1500-2500 m^2/g), high thermal stability, and an appropriate surface structure for the adsorption of organic pollutant molecules in water [2]. ZIF-8 also has chemical resistance to aqueous alkaline solutions and organic solvents [3].

ZIF-8 is a semiconductor material with a high band gap energy (5.2 eV) and was used in the form of a nanocomposite with zinc, copper, iron, cadmium, bismuth, or carbon-based materials to improve its photocatalytic properties [4] in pollutant oxidation, heavy metal, and CO_2 reduction, NO removal, conversion of nitrogen to ammonia, or adsorption [5]-[16]. It was revealed that these nanocomposite structures showed higher photocatalytic activities in the specified applications compared to their pure form. ZIF-8 was also doped to improve its photocatalytic activity [17], [18]. Studies have shown that when ZIF-8 is used in combination with different semiconductor materials, the light absorption edge can be reduced to the visible light region. The reason for the higher activities obtained with doped or nanocomposite ZIF-8 compared to undoped or non-

*Corresponding author: husnuarda@gmail.com
Received: 16.05.2023, Accepted: 18..09.2023

composite structures was reported to be the faster transport and separation of electron-hole pairs due to heterojunctions formed on the photocatalyst surface. Studies have shown that photocatalytic activity does not only depend on light absorption properties but also on the presence of heterojunctions or structural defects in the structure [13], [19].

TiO_2 is a widely used photocatalyst due to its high activity and high chemical and photochemical stability [20]. ZIF-8 was prepared together with TiO_2 in nanocomposite form for the degradation of organic pollutants or for reduction reactions [19], [21]-[25]. The effects of the use of ZIF-8 together with TiO_2 in nanocomposite form were mostly investigated in powder form. A limited number of studies on ZIF-8 films were conducted in which different substrates were used, such as ITO/FTO [26], [27], functionalized glass [28], Au [29], [30], copper [31], or Si [32] surfaces. Those studies were on the synthesis and characterization of ZIF-8 films, and the activities of the prepared films in photocatalysis were not investigated. The use of photocatalyst films is more convenient due to the ease of application, which mostly doesn't require a photocatalyst recovery step, and the use of fewer amounts of valuable photocatalytic material compared to bulk powder form.

The aim of this study was to prepare ZIF-8/TiO_2 nanocomposite thin films and to increase the photocatalytic activity of bare ZIF-8, which is quite low compared to TiO_2. An optimization was conducted by varying parameters such as heat treatment temperature, number of layers, and amount and type of metal doping in order to find the appropriate TiO_2 support on which ZIF-8 crystals would be grown.

2. Materials and Method

2.1. Thin Film Preparation

The first step in the preparation of transparent ZIF-8/TiO_2 thin films was the optimization of the TiO_2 layer on which ZIF-8 crystallites would be grown. In these studies, the heat treatment temperature, number of TiO_2 layers, dopant metal type, and concentration were optimized by considering the photocatalytic activities. Undoped and doped TiO_2 sols were prepared with titanium:water:acid molar ratios of 1:2:0.057. Titanium tetraisopropoxide (TTIP, Aldrich 97%) was used as the titanium precursor; copper nitrate trihydrate (99.5%, Merck), cerium nitrate hexahydrate (99.5%, Alfa Aesar), iron nitrate nonahydrate (99%, Merck), and zinc nitrate hexahydrate (98%, Aldrich) were used as the dopant precursors; ethanol (absolute Aldrich), nitric acid (HNO_3, 65%, Merck) and ultra-pure water were used as solvents. Undoped TiO_2 sols were prepared by the dropwise addition of an ethanolic solution of water and nitric acid (0.555 mL H_2O, 0.065 mL HNO_3 and 50 mL ethanol) to an ethanolic solution of TTIP (5 mL TTIP and 50 mL ethanol). Metal-doped TiO_2 sols were prepared by the same procedure and recipe in which the ethanolic solution of water and nitric acid contained predetermined amounts of metal precursors. Due to the aqueous nature of the metal salts, the water originating from these salts was subtracted from the water in the main recipe to ensure a titanium:water molar ratio of 2. The sols were aged at room temperature for 15 minutes before coating.

TiO_2 thin films were coated on a 7.5x2.5 cm borosilicate glass substrate by using the dip-coating technique. A clean surface is of great importance for homogeneous and continuous glass surface coating. For this reason, the glass substrates were first soaked in detergent water, then soaked in water, acetone, and ethanol in an ultrasonic bath, then washed with ethanol and dried with nitrogen. Cleaned substrates were then coated with TiO_2 by the dip-coating method. Substrate removal rates were optimized before the preparation of TiO_2 and ZIF-8/TiO_2 nanocomposite thin films. The dipping rate was set to 200 mm/min. A removal rate of 200 mm/min, which was determined in the optimization studies, was used in the preparation of TiO_2 and ZIF-8/TiO_2 thin films.

In the first step, undoped TiO_2 thin films were prepared, dried at room temperature, and then heat treated at 400, 450, 500, and 550^{o}C for 3 hours. In the next step, metal-doped TiO_2 thin films were prepared and heat-treated at 400^{o}C. Cerium, iron, copper, and zinc-doped TiO_2 thin films with doping amounts ranging from 1-10 mol% were then prepared, and ZIF-8 was coated on these TiO_2 thin films. Zinc nitrate and 2-methylimidazole (Hmim, 99%, Aldrich) were used for the formation of ZIF-8 crystals on TiO_2 surfaces. The final molar ratios of Zn^{2+}:Hmim:methanol were set to 1:8:700, which is typical for ZIF-8 synthesis [17]. Zinc nitrate and 2-methylimidazole were stirred in 45 mL of methanol in separate beakers (50 mL) at room temperature. These solutions were added simultaneously to a beaker (100 mL) in which TiO_2 thin film-coated glass substrates were vertically immersed, and the final solution was stirred for 30 minutes at room temperature. The immersion time was optimized based on preliminary experiments. The transparency and homogeneity of the film grown for 30 minutes were better compared to the films grown for 15, 45, and 60 minutes, whereas the photocatalytic activities were similar. The coated films were washed

consecutively with methanol and ethanol and dried at 80°C for 24 hours. For comparison, bare ZIF-8 film on a glass substrate was also synthesized. The glass substrate was first functionalized by silanization. The cleaned glass substrate was kept immersed in a 2% (by volume) methanolic solution of trimethoxymethylsilane (Aldrich, 98%) for 4 hours. The glass substrate was then washed consecutively with methanol and ethanol and dried before coating. The procedure and recipe used in growing ZIF-8 crystals on TiO_2 thin films were used for the preparation of bare ZIF-8 film on a glass substrate.

2.2. Characterization

The optical characterization of the prepared films was carried out by an Agilent Cary60 UV-Vis Spectrophotometer. The light transmittances of the films were recorded in the 300-800 nm wavelength range. Surface morphology and film thickness were investigated by Scanning Electron Microscopy (SEM) with the FEI Quanta 650 Field Emission. Thickness and average grain size were calculated by using SEM images.

2.3. Photocatalytic Tests

The photoreaction system was constructed as shown in Figure 1. An 11 cm high and 10.5 cm wide Plexiglas box was used, and a glass container with a diameter of 4.8 cm and a height of 2.4 cm was placed at the bottom. A LED lamp with its maximum emission at 254 nm or 365 nm was placed on top of the box. Glass slides were cut so that the active surface area of a thin film was 2.5x2.0 cm^2. The films were placed horizontally (perpendicular to the light from the LED lamp) at the bottom of the glass container. Methylene blue solution (2 ppm, 5 mL) was used as the model dye solution. The samples withdrawn after 1-hour irradiation were analyzed by a UV-Vis spectrometer (Agilent, Cary60 UV-VIS Spectrophotometer). Dye removal (%) was calculated according to the following equation:

$$\text{Dye removal (\%)} = ((I_o\text{-}I) / I_o) * 100 \quad (1)$$

where I is the absorbance of the methylene blue solution sample and I_o is the absorbance of 2 ppm methylene blue solution. The absorbance value at the maximum absorption wavelength (664 nm) was used in the calculations. The performances of the films were also investigated under 365 nm light in order to show the interaction of ZIF-8 and TiO_2 with regard to the light absorption characteristics. The same setup was used. The only differences in these experiments were that 25 mL of methylene blue solution was used and that the solution was agitated continuously during the experiments. Photocatalytic activity determination experiments were carried out in duplicate runs.

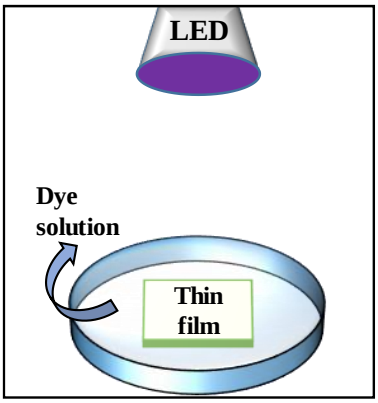

Figure 1. A schematic representation of the photocatalytic reaction setup.

3. Results and Discussion

3.1. Characterization

3.1.1. Optimization of Dip-coating Process

Dip-coating was carried out using removal rates in the range of 20-400 mm/min. Since the films will become thinner as the removal rate decreases, lower rates were also tried, but a wavy structure through the films was observed. At rates of 200 mm/min and above, it was found that this wavy structure did not exist and films of sufficient thinness were formed (no lifting from the surface or visible cracks were observed after heat treatment). Therefore, a removal rate of 200 mm/min was used in the subsequent studies. The photographs of the prepared TiO_2 thin films are shown in Figure 2.

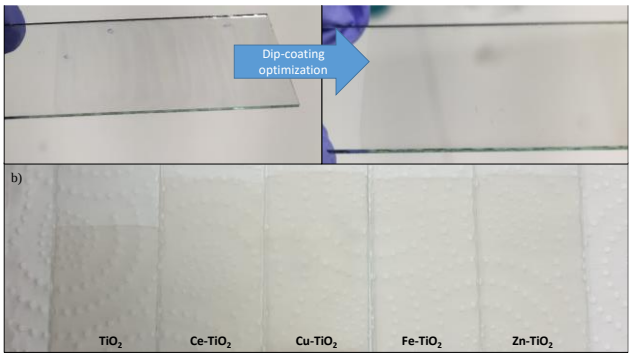

Figure 2. a) The photographs of TiO_2 thin films prepared in the optimization studies, b) Photographs of as-deposited undoped/doped TiO_2 thin films on glass substrates.

3.1.2. Morphologies of TiO_2 and ZIF-8/TiO_2 Nanocomposite Thin Films

The surface and cross-section morphology of the thin films were investigated by SEM analysis. SEM images of ZIF-8 uncoated and coated 1% Cu-doped TiO_2 and 1% Fe-doped TiO_2 thin films heat treated at 400°C are given in Figures 3 and 4, respectively. SEM images (Figures 3a and 4a) showed that ZIF-8 uncoated Cu and Fe doped TiO_2 thin films were homogeneously deposited on glass substrates. The average grain sizes of these films were determined to be 23 nm and 29 nm for 1% Cu-doped TiO_2 and 1% Fe-doped TiO_2, respectively.

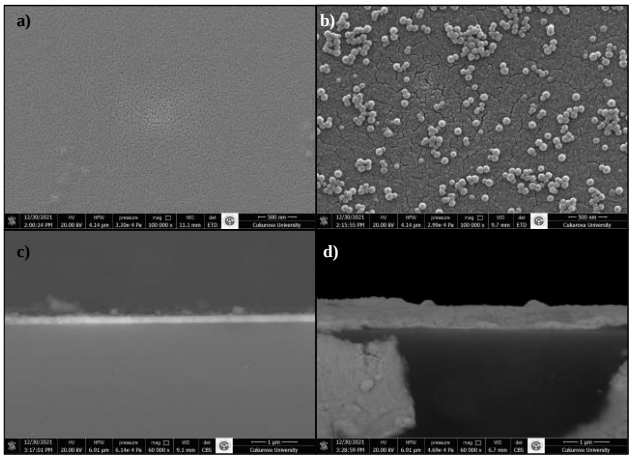

Figure 3. Surface and cross-section SEM images of 1% Cu doped TiO_2 thin films (a, c) and ZIF-8 / 1% Cu doped TiO_2 thin films (b, d).

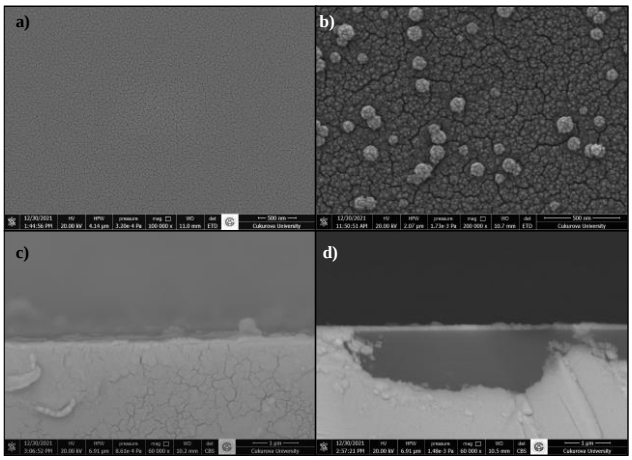

Figure 4. Surface and cross-section SEM images of 1% Fe doped TiO_2 thin films (a, c) and ZIF-8 / 1% Fe doped TiO_2 thin films (b, d).

It was observed that ZIF-8 particles grown on doped TiO_2 thin films were not homogeneously distributed on the surface (Figures 3b and 4b). ZIF-8 particles have spherical shapes, and the average grain sizes of the ZIF-8-coated thin films were determined to be in the 90-100 nm range. There were no significant differences between the average thicknesses of the uncoated and ZIF-coated thin films due to the inhomogeneity of ZIF-8 films. The average thicknesses were found to be in the 0.15-0.17 µm range.

3.1.3. Light Absorption Properties of TiO_2 and ZIF-8/TiO_2 Nanocomposite Thin Films

The light absorption properties of undoped and doped TiO_2 thin films, bare ZIF-8, and ZIF-8-coated TiO_2 thin films were determined by evaluating their UV-Vis transmittance spectra between 300 and 800 nm wavelength. The light transmission curves of these films are given in Figure 5. As seen in Figure 5a, the transmittance curve of undoped TiO_2 thin film heat treated at 400°C shifted to lower wavelengths when higher heat treatment temperatures were applied. This showed that the film heat-treated at 400°C has a higher light absorption capacity compared to the other films. The transmittance curves of Ce-doped TiO_2 thin films heat-treated at 400°C are shown in Figure 5b.

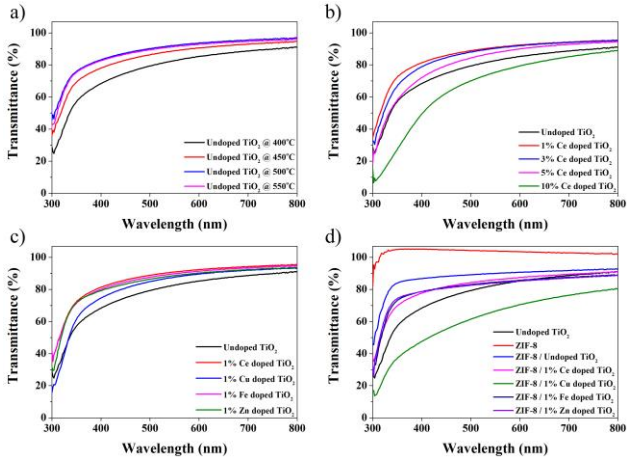

Figure 5. UV-Vis transmittance spectra of a) Undoped TiO_2 thin films heat treated at different temperatures, b) Ce Doped TiO_2 thin films heat treated at 400 °C, c) various metals doped TiO_2 thin films heat treated at 400 °C and d) ZIF-8, ZIF-8 coated various metals doped TiO_2 thin films heat treated at 400 °C.

It was observed that the transmittance curve of TiO_2 shifted to lower wavelengths at low doping levels (1, 3, 5%) and to higher wavelengths at high doping levels (10%). This finding showed that the light absorption of TiO_2 increased when doped with Ce at high doping levels. The transmittance curves of TiO_2 doped with different metals are shown in Figure 5c. It can be stated that the curve mainly shifted to

lower wavelengths when TiO_2 was doped with Ce, Cu, Fe, or Zn at a 1% doping level. Among the doped TiO_2 thin films, Cu-doped TiO_2 showed higher light absorption capacity compared to Ce, Fe, or Zn doped TiO_2 since the absorption edge of this film is at a higher wavelength. The transmittance curves of bare ZIF-8 and ZIF-8-coated TiO_2 thin films doped with different metals are shown in Figure 5d. ZIF-8-coated Cu-doped TiO_2 thin films showed higher light absorption capacities than the other ZIF-8-coated TiO_2 thin films and bare ZIF-8. The higher light absorption capacity of Cu-doped TiO_2 thin films may lead to higher photocatalytic activity than the other films. These findings indicated that the light absorption capacity and, as a result, the photocatalytic activity of bare ZIF-8 film may be increased when undoped or doped TiO_2 thin films are used as supports to grow ZIF-8 crystals.

3.2. Photocatalytic Performances of TiO_2 and ZIF-8/TiO_2 Nanocomposite Thin Films

Figure 6a shows how well dyes are removed by adsorption and photocatalysis from thin films of undoped TiO2 that have been heated at different temperatures. Photocatalytic removal efficiencies were higher than adsorptive removal efficiencies. This is an indication that photocatalytic degradation was achieved with the prepared films. The highest removal efficiencies by adsorption and photocatalysis were obtained with the film heat-treated at 400°C. With this film, 37% and 56% of the dye were removed by adsorption and photocatalysis, respectively. The film heat-treated at 400°C showed better photocatalytic performance than the films heat treated at 450, 500, and 550°C under 254 nm irradiation. Therefore, 400°C was chosen as the heat treatment temperature for further studies. After determining the optimum heat treatment temperature, the effect of the number of TiO_2 layers on the photocatalytic activity was investigated. Undoped TiO_2 thin films containing 1-4 layers were prepared, and their photocatalytic performances were evaluated. Figure 6b shows how well different numbers of layers of undoped TiO2 thin films treated at 400°C remove dye through photocatalysis. The photocatalytic performances are slightly different, as can be seen from Figure 6b. The photocatalytic dye removal efficiencies of monolayer and multilayer undoped TiO_2 thin films varied between 50 and 61%. In light of these results, it was decided to use monolayer TiO_2 thin films as a basis for the preparation of ZIF-8/TiO_2 nanocomposite thin films due to their ease of preparation.

TiO_2 thin films doped with Ce in the range of 1-10 mol% were prepared, and their photocatalytic performances were determined, in order to investigate the effect of doping level on the photocatalytic dye removal efficiency of TiO_2 and to find a suitable TiO_2 support on which ZIF-8 crystals will be grown.

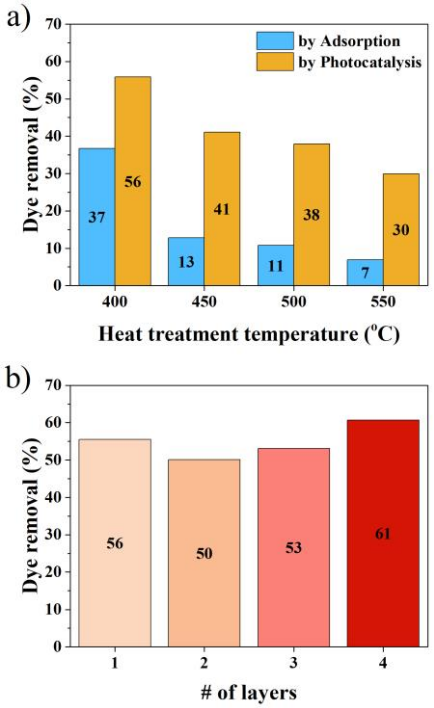

Figure 6. a) Dye removal efficiencies by adsorption and photocatalysis with undoped TiO_2 thin films heat treated at different temperatures, b) Photocatalytic dye removal efficiencies of undoped TiO_2 thin films heat treated at 400°C with different number of layers.

Before starting the photocatalytic performance determination experiments, a direct photolysis experiment was first performed to determine the contribution of spontaneous degradation of methylene blue under 254 nm light. The experiment was carried out in the absence of a photocatalyst film. It was found that 5% of the dye spontaneously self-degraded in 1 hour under 254 nm light. The photocatalytic dye removal efficiencies of Ce-doped TiO_2 thin films and dye removal by direct photolysis are given in Figure 7a. The highest activity was obtained with 1% Ce-doped TiO_2 thin films and a decrease in the photocatalytic activity was observed as the doping level increased. The photocatalytic dye removal efficiencies of TiO_2 thin films doped with various metals are given in Figure 7b. The highest activities were obtained with Ce and Fe-doped TiO_2 thin films. Zn doping had no significant effect on the photocatalytic activity, while Cu doping decreased the activity of TiO_2 under these conditions. Interaction with light is one of the parameters affecting photocatalytic activity. It is thought that photocatalytic activity will increase with an increase

in light absorption capacity. However, other parameters- such as the interaction of dye molecules with the surface and the separation efficiency of electron-hole pairs, also have significant effects on the activity. As can be seen in Figure 5, a red shift is observed in the metal-doped films only at the 10% doping level. However, when the photocatalytic activity results were analyzed (Figure 7), it was found that 1% of metal-doped films showed higher photocatalytic activity. Therefore, it can be interpreted that electron-hole pair separation and the interaction of dye molecules with the surface may be more efficient in 1% metal doped films compared to other films.

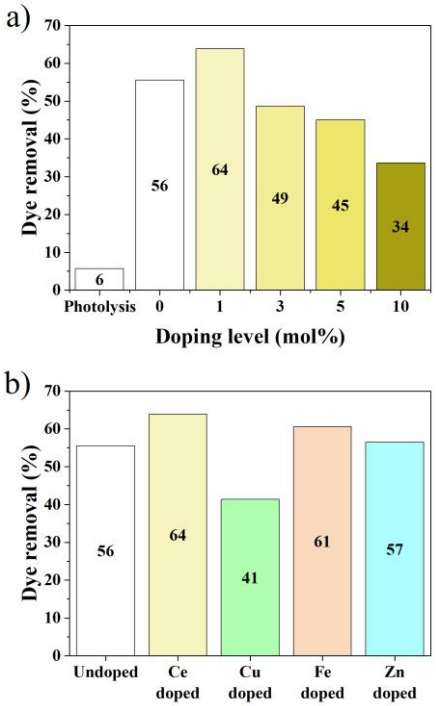

Figure 7. Photocatalytic dye removal efficiencies of a) Ce doped TiO_2 thin films and b) 1% various metals doped TiO_2 thin films.

In the final part, ZIF-8 was grown on 1% TiO2 thin films doped with various metals, and their photocatalytic performances were evaluated under both 254 nm and 365 nm LED light irradiation. The results are given in Figures 8a and 8b, respectively. The photocatalytic dye removal efficiencies of bare ZIF-8 film on glass substrate under both 254 nm and 365 nm LED irradiation are also given in Figure 8 for comparison.

The photocatalytic activity decreased when ZIF-8 was coated on TiO_2 films, according to Figures 7 and 8. The reason may be that ZIF-8 has a higher band gap energy than TiO_2, and the TiO_2 surface was blocked by ZIF-8 crystals, which prevented the interaction of TiO_2 with light. However, it should be noted that the activity of ZIF-8 increased when ZIF-8 was coated on TiO_2 films, which was the main aim of this study. According to Figure 8, ZIF-8/TiO_2 nanocomposite thin films obtained with 1% Ce and 1% Cu doped TiO_2 thin films showed higher activity in the photocatalytic removal of the dye under both 254 nm and 365 nm LED irradiation when compared to 1% Fe and 1% Zn doped TiO_2 thin films. In general, ZIF-8 grown on TiO_2 thin films showed better photocatalytic dye removal efficiencies compared to bare ZIF-8 grown on the glass substrate.

The highest photocatalytic activity was obtained with the ZIF-8 coated-, 1% Cu-doped TiO_2 film, which may be due to the formation of more efficient ZIF-8/TiO_2 heterojunctions and better light interaction. As seen in Figure 5d, a slue shift was observed in ZIF-8 coated films compared to the uncoated film, and among the ZIF-8 coated films, ZIF-8 coated Cu-doped TiO_2 thin film showed higher light absorption capacity compared to other films.

These results indicated that the photocatalytic activity of ZIF-8 could be improved when metal-doped TiO_2 substrates were used as supports for the growth of ZIF-8 crystals. According to these results, the photocatalytic activity of ZIF-8 can be enhanced by using TiO_2 thin film supports doped with low amounts of Ce, Cu, Fe, or Zn and heat treated at relatively low temperatures (400^{o}C).

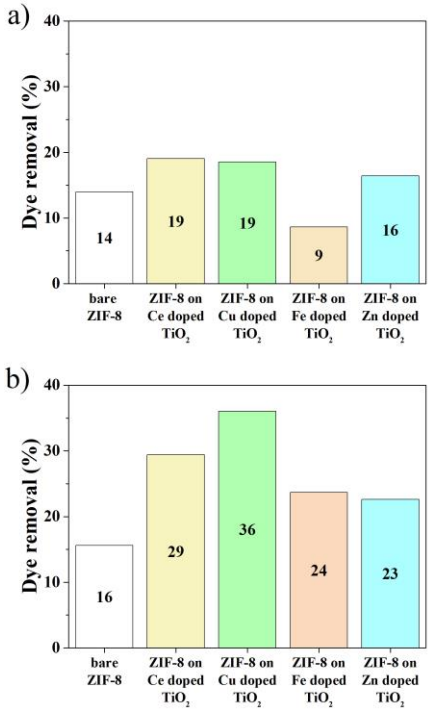

Figure 8. Photocatalytic dye removal efficiencies of bare ZIF-8 and ZIF-8/TiO_2 nanocomposite thin films: a) under 254 nm LED irradiation and b) 365 nm LED irradiation.

4. Conclusion and Suggestions

In this study, the optimization of TiO_2 support properties for the preparation of transparent ZIF-8/TiO_2 nanocomposite thin films was performed by evaluating their photocatalytic performances. According to the results, it was found that the photocatalytic dye removal efficiencies of ZIF-8/TiO_2 nanocomposite thin films prepared by 30-min ZIF-8 growth on 1% Ce, Cu, Fe, and Zn doped TiO_2 thin films heat treated at 400^{o}C were higher than those of bare ZIF-8 thin films grown on glass substrates. The highest photocatalytic dye removal efficiencies were obtained with ZIF-8/TiO_2 nanocomposite thin films prepared with 1% Ce and 1% Cu-doped TiO_2 thin films. The order of magnitude of the photocatalytic dye removal efficiencies did not change with the change of irradiation source (254 nm or 365 nm LED lamps) used in this study. The ZIF-8-coated 1% Cu and 1% Ce-doped TiO_2 films removed 19% of the dye under a 254 nm LED light in 1 hour. Their dye removal efficiencies under 365 nm LED light increased to 36% and 29%, respectively. All ZIF-8/TiO_2 nanocomposite thin films showed higher activities than the bare ZIF-8 film, indicating that the activity of ZIF-8 can be enhanced when grown on TiO_2 surfaces doped with 1% Ce, Cu, Fe, or Zn metals. These findings indicate that a nanocomposite structure containing ZIF-8 and TiO_2 can be prepared as transparent thin films, and the photocatalytic activity of ZIF-8 can be improved by the optimization of TiO_2 support.

Acknowledgment

This study was supported by Adana Alparslan Türkeş Science and Technology University Scientific Research Coordination Unit, Türkiye. Project Number: 20303001. Onur İloğlu was supported by the TÜBİTAK-BİDEB 2210-C National Scholarship in Priority Fields in Science Program for MSc students.

Contributions of the authors

Onur İloğlu: literature review, investigation, evaluation of data, writing/reviewing/editing.

Hüsnü Arda Yurtsever: conceptualization, literature review, evaluation of data, writing/reviewing/editing.

Conflict of Interest Statement

There is no conflict of interest between the authors.

Statement of Research and Publication Ethics

The study is complied with research and publication ethics.

References

[1] B. L. Loeb, "Water-Energy-Food Nexus," *Ozone: Science & Engineering,* vol. 38, no. 3, pp. 173-174, 2016, doi: 10.1080/01919512.2016.1166029.

[2] H. Dai *et al.*, "Recent advances on ZIF-8 composites for adsorption and photocatalytic wastewater pollutant removal: Fabrication, applications and perspective," *Coordination Chemistry Reviews,* vol. 441, p. 213985, 2021, doi: 10.1016/j.ccr.2021.213985.

[3] K. S. Park *et al.*, "Exceptional chemical and thermal stability of zeolitic imidazolate frameworks," *PNAS,* vol. 103, no. 27, pp. 10186-10191, Jul 5 2006, doi: 10.1073/pnas.0602439103.

[4] H.-P. Jing, C.-C. Wang, Y.-W. Zhang, P. Wang, and R. Li, "Photocatalytic degradation of methylene blue in ZIF-8," *RSC Advances,* vol. 4, no. 97, pp. 54454-54462, 2014, doi: 10.1039/c4ra08820d.

[5] A. Chakraborty, D. A. Islam, and H. Acharya, "Facile synthesis of CuO nanoparticles deposited zeolitic imidazolate frameworks (ZIF-8) for efficient photocatalytic dye degradation," *Journal of Solid State Chemistry,* vol. 269, pp. 566-574, 2019, doi: 10.1016/j.jssc.2018.10.036.

[6] A. Liu *et al.*, "Construction of $CuInS_2$@ZIF-8 nanocomposites with enhanced photocatalytic activity and durability," *Materials Research Bulletin,* vol. 112, pp. 147-153, 2019, doi: 10.1016/j.materresbull.2018.12.020.

[7] N. M. Mahmoodi, S. Keshavarzi, M. Oveisi, S. Rahimi, and B. Hayati, "Metal-organic framework (ZIF-8)/inorganic nanofiber (Fe_2O_3) nanocomposite: Green synthesis and photocatalytic degradation using LED irradiation," *Journal of Molecular Liquids,* vol. 291, p. 111333, 2019, doi: 10.1016/j.molliq.2019.111333.

[8] Y. Liu *et al.*, "Photostable core-shell CdS/ZIF-8 composite for enhanced photocatalytic reduction of CO_2," *Applied Surface Science,* vol. 498, p. 143899, 2019, doi: 10.1016/j.apsusc.2019.143899.

[9] J. Qiu *et al.*, "Constructing $Cd_{0.5}Zn_{0.5}S$@ZIF-8 nanocomposites through self-assembly strategy to enhance Cr(VI) photocatalytic reduction," *Journal of Hazardous Materials,* vol. 349, pp. 234-241, May 5 2018, doi: 10.1016/j.jhazmat.2018.02.009.

[10] X. Wei, Y. Wang, Y. Huang, and C. Fan, "Composite ZIF-8 with CQDs for boosting visible-light-driven photocatalytic removal of NO," *Journal of Alloys and Compounds,* vol. 802, pp. 467-476, 2019, doi: 10.1016/j.jallcom.2019.06.086.

[11] J. Liu *et al.*, "Photocatalytic conversion of nitrogen to ammonia with water on triphase interfaces of hydrophilic-hydrophobic composite $Bi_4O_5Br_2$/ZIF-8," *Chemical Engineering Journal,* vol. 371, pp. 796-803, 2019, doi: 10.1016/j.cej.2019.03.283.

[12] H.-T. Wang *et al.*, "Design and synthesis of porous C–ZnO/TiO_2@ZIF-8 multi-component nano-system via pyrolysis strategy with high adsorption capacity and visible light photocatalytic activity," *Microporous and Mesoporous Materials,* vol. 288, p. 109548, 2019, doi: 10.1016/j.micromeso.2019.06.010.

[13] Z. Li *et al.*, "Preparation of flexible PAN–C_3N_4–ZIF-8 photocatalytic nanofibers and visible light catalytic properties," *Optical Materials,* vol. 132, p. 112762, 2022, doi: 10.1016/j.optmat.2022.112762.

[14] T. Qiang, S. Wang, L. Ren, and X. Gao, "Novel 3D Cu_2O/N-CQD/ZIF-8 composite photocatalyst with Z-scheme heterojunction for the efficient photocatalytic reduction of Cr(VI)," *Journal of Environmental Chemical Engineering,* vol. 10, no. 6, p. 108784, 2022, doi: 10.1016/j.jece.2022.108784.

[15] D. Sajwan, A. Semwal, J. Rawat, H. Sharma, and C. Dwivedi, "Synthesis of CdSe QDs decorated ZIF-8 composite for visible light assisted degradation of methylene blue," *Materials Today: Proceedings,* 2022, doi: 10.1016/j.matpr.2022.10.008.

[16] J. Wu, Y. Jin, D. Wu, X. Yan, N. Ma, and W. Dai, "Well-construction of Zn_2SnO_4/SnO_2@ZIF-8 core–shell hetero-structure with efficient photocatalytic activity towards tetracycline under restricted space," *Chinese Journal of Chemical Engineering,* vol. 52, pp. 45-55, 2022, doi: 10.1016/j.cjche.2022.04.016.

[17] H. A. Yurtsever, M. Y. Akgunlu, T. Kurt, A. S. Yurttaş, and B. Topuz, "Photocatalytic activities of Ag^+ doped ZIF-8 and ZIF-L crystals," *Journal of the Turkish Chemical Society, Section A: Chemistry,* vol. 3, no. 3, 2016, doi: 10.18596/jotcsa.10970.

[18] G. Fan, J. Luo, L. Guo, R. Lin, X. Zheng, and S. A. Snyder, "Doping Ag/AgCl in zeolitic imidazolate framework-8 (ZIF-8) to enhance the performance of photodegradation of methylene blue," *Chemosphere,* vol. 209, pp. 44-52, Oct 2018, doi: 10.1016/j.chemosphere.2018.06.036.

[19] H. A. Yurtsever and A. E. Çetin, "Fabrication of ZIF-8 decorated copper doped TiO_2 nanocomposite at low ZIF-8 loading for solar energy applications," *Colloids and Surfaces A: Physicochemical and Engineering Aspects,* vol. 625, p. 126980, 2021, doi: 10.1016/j.colsurfa.2021.126980.

[20] N. Madkhali *et al.*, "Recent update on photocatalytic degradation of pollutants in waste water using TiO_2-based heterostructured materials," *Results in Engineering,* vol. 17, p. 100920, 2023, doi: 10.1016/j.rineng.2023.100920.

[21] R. Chandra, S. Mukhopadhyay, and M. Nath, "TiO_2@ZIF-8: A novel approach of modifying micro-environment for enhanced photo-catalytic dye degradation and high usability of TiO_2 nanoparticles," *Materials Letters,* vol. 164, pp. 571-574, 2016, doi: 10.1016/j.matlet.2015.11.018.

[22] E. Pipelzadeh, V. Rudolph, G. Hanson, C. Noble, and L. Wang, "Photoreduction of CO_2 on ZIF-8/TiO_2 nanocomposites in a gaseous photoreactor under pressure swing," *Applied Catalysis B: Environmental,* vol. 218, pp. 672-678, 2017, doi: 10.1016/j.apcatb.2017.06.054.

[23] R. Li, W. Li, C. Jin, Q. He, and Y. Wang, "Fabrication of ZIF-8@TiO_2 micron composite via hydrothermal method with enhanced absorption and photocatalytic activities in tetracycline degradation," *Journal of Alloys and Compounds,* vol. 825, p. 154008, 2020, doi: 10.1016/j.jallcom.2020.154008.

[24] X. Qi, F. Shang, T. Wang, Y. Ma, and Y. Yan, "In situ coupling of TiO_2(B) and ZIF-8 with enhanced photocatalytic activity via effective defect," *CrystEngComm,* vol. 22, no. 25, pp. 4250-4259, 2020, doi: 10.1039/d0ce00595a.

[25] W.-L. Zhong, C. Li, X.-M. Liu, X.-K. Bai, G.-S. Zhang, and C.-X. Lei, "Liquid phase deposition of flower-like TiO_2 microspheres decorated by ZIF-8 nanoparticles with enhanced photocatalytic

activity," *Microporous and Mesoporous Materials,* vol. 306, p. 110401, 2020, doi: 10.1016/j.micromeso.2020.110401.

[26] C. Hou, Q. Xu, J. Peng, Z. Ji, and X. Hu, "(110)-oriented ZIF-8 thin films on ITO with controllable thickness," *Chemphyschem,* vol. 14, no. 1, pp. 140-144, Jan 14 2013, doi: 10.1002/cphc.201200677.

[27] G. Genesio, J. Maynadié, M. Carboni, and D. Meyer, "Recent status on MOF thin films on transparent conductive oxides substrates (ITO or FTO)," *New Journal of Chemistry,* vol. 42, no. 4, pp. 2351-2363, 2018, doi: 10.1039/c7nj03171h.

[28] K. Kida, K. Fujita, T. Shimada, S. Tanaka, and Y. Miyake, "Layer-by-layer aqueous rapid synthesis of ZIF-8 films on a reactive surface," *Dalton Transactions,* vol. 42, no. 31, pp. 11128-11135, Aug 21 2013, doi: 10.1039/c3dt51135a.

[29] O. Shekhah and M. Eddaoudi, "The liquid phase epitaxy method for the construction of oriented ZIF-8 thin films with controlled growth on functionalized surfaces," *Chemical Communications,* vol. 49, no. 86, pp. 10079-10081, Oct 3 2013, doi: 10.1039/c3cc45343j.

[30] J. A. Allegretto, J. Dostalek, M. Rafti, B. Menges, O. Azzaroni, and W. Knoll, "Shedding Light on the Dark Corners of Metal-Organic Framework Thin Films: Growth and Structural Stability of ZIF-8 Layers Probed by Optical Waveguide Spectroscopy," *The Journal of Physical Chemistry A,* vol. 123, no. 5, pp. 1100-1109, Feb 7 2019, doi: 10.1021/acs.jpca.8b09610.

[31] R. L. Papporello, E. E. Miró, and J. M. Zamaro, "Secondary growth of ZIF-8 films onto copper-based foils. Insight into surface interactions," *Microporous and Mesoporous Materials,* vol. 211, pp. 64-72, 2015, doi: 10.1016/j.micromeso.2015.02.049.

[32] O. L. Rose *et al.*, "Thin Films of Metal-Organic Framework Interfaces Obtained by Laser Evaporation," *Nanomaterials,* vol. 11, no. 6, May 21 2021, doi: 10.3390/nano11061367.

Bitlis Eren Üniversitesi Fen Bilimleri Dergisi
BİTLİS EREN UNIVERSITY JOURNAL OF SCIENCE
ISSN: 2147-3129/e-ISSN: 2147-3188
VOLUME: 12 NO: 3 PAGE: 773-782 YEAR: 2023
DOI:10.17798/bitlisfen.1297952

Deep Learning-Based Automatic Helmet Detection System in Construction Site Cameras

Adem KORKMAZ[1*], Mehmet Tevfik AĞDAŞ[2]

[1] *Bandırma Onyedi Eylül University, Gonen Vocational School, Department of Computer Technology*
[2] *Munzur University, Cemisgezek Vocational School, Department of Computer Technology*
(ORCID: 0000-0002-7530-7715) (ORCID: 0000-0002-5608-6240)

Keywords: Helmet detection, Object detection, YOLOv8, Personal protective equipment.

Abstract
Ensuring worker safety in high-risk environments such as construction sites is paramount. Personal protective equipment, particularly helmets, is critical in preventing severe head injuries. This study aims to develop an automated helmet detection system using the state-of-the-art YOLOv8 deep learning model to enhance real-time safety monitoring. The dataset used for the analysis consists of 16,867 images, with various data augmentation and preprocessing techniques applied to improve the model's robustness. The YOLOv8 model achieved a 96.9% mAP50 score, outperforming other deep learning models in similar studies. The results demonstrate the effectiveness of the YOLOv8 model for accurate and efficient helmet detection in construction sites, paving the way for improved safety monitoring and enforcement in the construction industry.

1. Introduction

The construction industry is one of the high-risk working environments where employee safety is a priority. Construction sites are inherently hazardous, with high accident and injury potential. Strict adherence to safety regulations, including the mandatory use of personal protective equipment (PPE), is crucial to ensuring employee safety and minimizing risks. Helmets are critical in protecting workers from head injuries that can have serious consequences, including permanent disability and even death. The rapid development of information technologies impacts every aspect of our lives and various business processes. Their automatic and quick response in detection, recognition, and decision-making processes has become integral to data management. In this era of rapidly increasing data, deep learning algorithms are essential for decision-making and process management.

Construction sites are inherently hazardous environments with high accident and injury potential [1]. Strict adherence to safety regulations, including the mandatory use of personal protective equipment (PPE), is important to ensure worker safety and minimize risks [2]. Helmets are critical in protecting workers from head injuries that can lead to serious consequences, including permanent disability and death [3]. Inadequate site inspections and low safety awareness among construction workers can lead to accidents. Real-time detection of helmet use is crucial for rapid action and prevention of such incidents [4].

As computer technology has advanced, automatic visual detection has become increasingly prevalent. The growth of deep learning-based computer vision technologies has opened new possibilities for enhancing safety monitoring and enforcement across various sectors, including construction [5]. Deep learning-based object detection algorithms, such as Convolutional Neural Networks (CNN) and YOLO architectures, have demonstrated promising outcomes in diverse areas like traffic monitoring, pedestrian detection, and facial recognition [6], [7]. Numerous studies have focused on detecting helmet usage [8]- [17]. The ongoing progress in deep learning-based computer vision technologies continues to enhance safety

*Corresponding author: ademkorkmaz@bandirma.edu.tr
Received: 16.05.2023, Accepted: 19.09.2023

monitoring and enforcement within the construction sector and beyond.

In the study by Hayat & Morgado-Dias [3], they employed a benchmark dataset of 5,000 helmet images, divided into 60%, 20%, and 20% portions for training, testing, and validation, respectively. The findings revealed that the YOLOv5x architecture was the top performer, achieving an impressive average accuracy (mAP) of 92.44%. This demonstrates the model's effectiveness in detecting safety helmets, even under challenging low-light conditions.

In a study by Yung et al. [18], the researchers evaluated the performance of three deep learning algorithms (YOLOv5, YOLOv6, and YOLOv7) in detecting safety helmets through a series of three tests. YOLOv6s and YOLOv7 models demonstrated superior performance in low light conditions compared to the YOLOv5s model. However, it was noted that only some models could differentiate between regular and safety helmets. Ultimately, YOLOv7 emerged as the best performer, achieving the highest mAP of 89.6% in detecting protective helmets.

In a study by Otgonbold et al. [19], the researchers developed a helmet detection model using a dataset of six classes: helmet, head, helmeted head, helmeted person, helmetless person, and face. The study employed several algorithms, including YOLOv3 (YOLOv3, YOLOv3-tiny, and YOLOv3-SPP), YOLOv4 (YOLOv4 and YOLOv4pacsp-x-mish), YOLOv5-P5 (YOLOv5s, YOLOv5m, and YOLOv5x), Faster Region-Based Convolutional, and YNOL. The results showed that Faster-RCNN (Region-based Convolutional Neural Network) achieved the lowest mAP of 36.89, while the YOLOR model attained the highest mAP value of 88.28.

In a study by Chen et al. [20], the researchers aimed to achieve real-time and efficient helmet-wearing detection by utilizing a developed YOLOv4 algorithm. The results revealed that the algorithm achieved an accuracy of 92.98%, a model size of 41.88 M, and a detection speed of 43.23 images per second. Compared to the original YOLOv4, there was an increase in accuracy by 0.52%, a reduction in model size by approximately 83%, and an 88% improvement in detection speed.

Table 1. Success rates of Yolo and DL applications for helmet classification

Authors	Dataset	Applied Models	Results (mAP50-%)
[14]	13,000 images	SSD, Faster R-CNN, YOLOv3, and Improved YOLOv3	77.2, 94.3, 82.3 and 93.1
[12]	3261 images	SSD-MobileNet	36.8
[21]	13620 images	AT-YOLO + DIOU	96.5
[22]	1365 images	YOLOv2	98,52
[17]	2580 images	SCM-YOLO	93.19
[23]	5000 images	YOLO	97.12
[24]	7008 images	YOLO	95
[25]	7581 images	YOLOv5	93
[26]	3000 images	Faster R-CNN, SSD, YOLO v3, YOLO v4 and YOLO v4-HelMask	70.62, 89.72, 90.54, 93.19 and 95.51

This recent literature review underscores the effectiveness of various object detection models across diverse datasets. Studies [14, 12, 21, 22, 17, 23, 24, 25, 26] employed a range of models from SSD and Faster R-CNN to multiple versions of YOLO, including standard and modified variants such as AT-YOLO, YOLOv2, SCM-YOLO, and YOLOv4-HelMask. Despite the varying dataset sizes (ranging from 1,365 to 13,620 images), the results in terms of mAP50%, a standard metric indicating the model's precision, were generally high. YOLO and its variations consistently performed well, with a notably high mAP50% of 98.52 achieved by YOLOv2 on a dataset of 1,365 images [22]. SSD-MobileNet yielded the lowest mAP50% of 36.8 [12], possibly due to various factors, including dataset size and task complexity. These findings underscore the potency of YOLO and its variants in object detection tasks and suggest that considerations of dataset size, data quality, model selection, and task complexity are critical to optimizing model performance.

Conventional manual monitoring methods can be labor-intensive, subject to human error, and often inadequate for covering extensive construction

sites. To address these drawbacks, this study investigates the use of deep learning approaches to create an automatic helmet detection system. This system aims to detect workers wearing helmets effectively and accurately in real-time, using cameras at construction sites.

2. Material and Method

In this study, deep learning approaches and image processing methods are used to ensure human safety by detecting whether a person is wearing a helmet. The deep learning-based image processing method is the YOLOv8 (You Only Look Once) model, a state-of-the-art object detection algorithm known for its real-time processing capabilities and accuracy. The weights of the YOLOv8 model were pre-trained using millions of images from the ImageNet dataset, providing a solid foundation for transfer learning and fine-tuning the model for the specific helmet detection task.

2.1. Data Set

This study aims to identify the presence of helmets and verify if individuals are wearing them to enhance safety on construction sites. A dataset of 7036 images was used to accomplish this objective, featuring categories such as humans, human heads, and helmets [27]. These images were gathered from the Mendeley [27] websites and underwent preprocessing to ensure they were appropriate for use in the research. An example view of the dataset is given in Figure 1.

Figure 1. Sample images of the dataset.

Features of the dataset used include:

• A total of 7036 images, upscaled to 16867 images using various data augmentation techniques.

• Images accessible to everyone were selected for the data set.

• The target classes of images in the dataset were selected from different lighting conditions and environments to provide a more robust model.

• Various preprocessing techniques were applied to each image in the dataset, focusing on data augmentation, resulting in a threefold increase in dataset size.

• The dataset is divided into 14674 training images, 1349 validation images, and 844 test images for use in experimental studies.

Data set augmentation studies:

• Set to 3 printouts per training sample. In other words, three images were obtained from each image.

• Horizontal directional flip operation has been performed.

• Crop: 0% Minimum Zoom, 20% Maximum Zoom applied.

• Rotation: Applied from -10° to +10°.

• Grayscale: Applied to 10% of images.

• Hue: Applied between -20° and +20°.

• Saturation: -25% to +25% applied.

• Brightness: -20% to +20% applied.

• Exposure: -20% to +20% applied.

• Blur: Applied up to 1 pixel.

• Cutting: 6 boxes of 3% size each were created.

• As a result of magnification, 21108 images were targeted, while 16867 images were obtained. This decrease in the number of images seen is because some images obtained because of processing will not fully serve experimental studies.

2.2. YOLOv8 Model

YOLOv8 is a recently developed, highly effective model using the YOLO (You Only Look Once) architecture. It was developed by Ultralytics, known for its work on the YOLOv8, YOLOv3 and YOLOv5 models. Object detection, sample positioning, and image classification can be made in this model, as in the YOLOv7 and YOLOv6 models. The YOLOv8 model also uses the Pytorch library like YOLOv7-v6. It can run on both CPU and GPU units as working hardware.

YOLOv8 can achieve strong accuracy in COCO object classification. For example, the mid-model YOLOv8m can reach 50.2% MAP when measured in COCO. YOLOv8 scores significantly better than YOLOV5 when evaluated against Roboflow 100, a dataset that evaluates model performance in various areas specific to the desired tasks.

In addition, YOLOv8 includes developer convenience features. Unlike other models that can split into many different Python files in the execution of tasks, YOLOv8 does this with a CLI that makes model training more intuitive. The architecture of the YOLOv8 model is given in Figure 2 below. The date of this article study is the only article study of the YOLOv8 model. The architecture of the YOLUv8 model, shown in Figure 2, was visualized by GitHub website users [28].

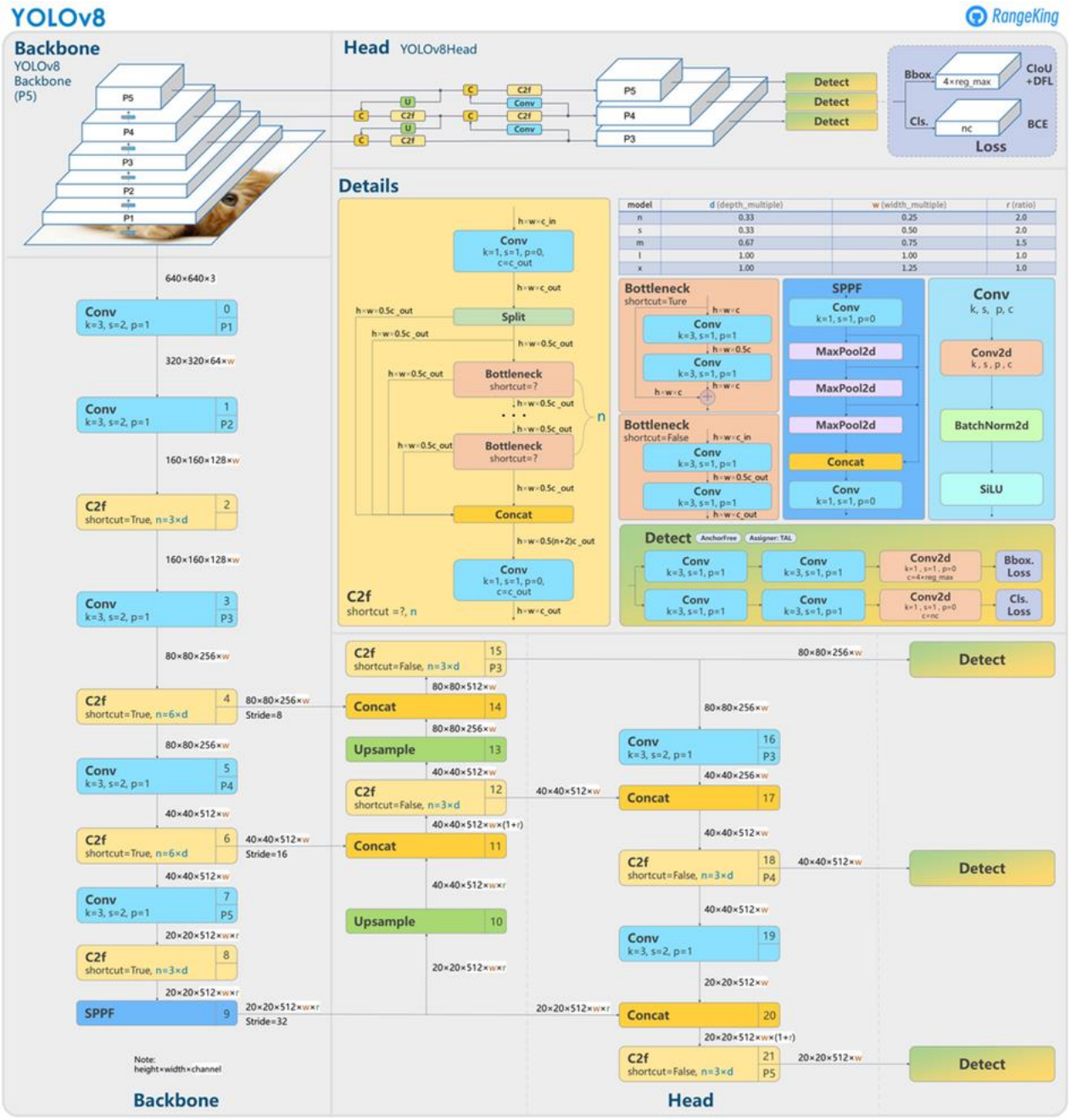

Figure 2. YOLOv8 Architecture [28]

3. Results and Discussion

Experimental studies were conducted with the study's deep learning-based YOLOv8 model. In experimental studies, it was aimed to determine three classes with image processing techniques. These classes are designated as helmet detection (helmet), head detection (head), and both head and helmet detection (all). In the working model, the batch value is eight, and the epoch value is 50 as a parameter. The numerical results of the experimental study are given in Table 2.

Table 2. Numerical results of the experimental study.

Class	Precision	Recall	mAP50	mAP50-95
All	0,938	0,933	0,969	0,642
Head	0,923	0,918	0,956	0,639
Helmet	0,952	0,947	0,971	0,646

Table 2 provides metrics evaluating the model's performance in terms of precision, recall, mAP50, and mAP50-95 for two categories: 'Head' and 'Helmet.'

Precision refers to the proportion of true positive predictions (correctly identified heads or

helmets) among all positive predictions made by the model. An accuracy of 0.923 for 'Head' and 0.952 for 'Helmet' means the model is highly accurate when it predicts the presence of a head or helmet in an image.

Recall measures the proportion of actual positives (real heads or helmets in images) that the model correctly identified. A recall of 0.918 for 'Head' and 0.947 for 'Helmet' suggests the model is proficient at detecting most instances of heads or helmets when they are present.

The mAP50 (mean average precision at 50% Intersection over Union - IoU) is a commonly used metric for object detection tasks. It considers both precision and recall calculating an overall performance score. A score of 0.956 for 'Head' and 0.971 for 'Helmet' indicates excellent performance, with the model correctly identifying and accurately placing bounding boxes around heads and helmets in most cases.

The mAP50-95 is another version of the mAP score, but it averages scores over a range of IoU thresholds from 0.5 to 0.95. This stricter metric can provide a more comprehensive view of the model's performance. The scores of 0.639 for 'Head' and 0.646 for 'Helmet' are significantly lower than the mAP50 scores, suggesting the model's performance decreases at higher IoU thresholds.

The 'All' category provides the average of the metrics across both the 'Head' and 'Helmet' categories. The overall mAP50 score of 0.969 indicates that the model performed very well across all classes in the dataset.

The confusion matrix outputs are given in Figure 3.

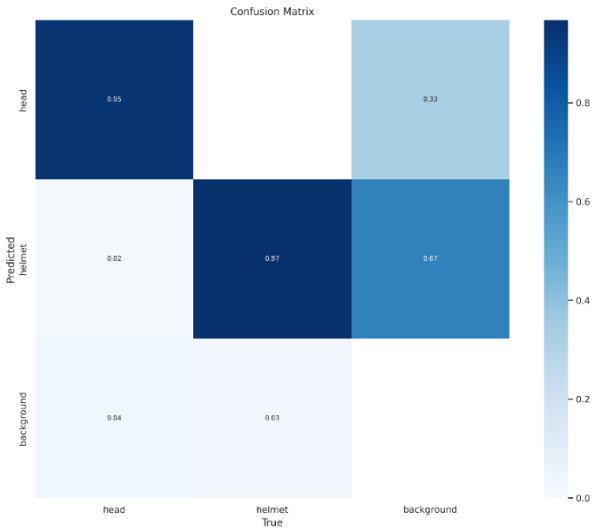

Figure 3. Confusion Matrix Output of the Study.

Predicted labels (head, helmet, background) are marked in rows, while actual titles are listed in columns. When the model predicted the "head" label, it was correct 95% of the time. He never mistakenly defined "helmet" as "head." For the "helmet" predictions, the model was right 97% of the time, sometimes misclassifying "head" as "head" (2% of the time). Misclassified "head" as "background" 4% of the time and "helmet" as "background" 3% of the time. It is clear from these results that the model performs exceptionally well in the 'head' or 'helmet' prediction but needs help in accurately identifying the 'background,' leading to a high rate of misclassification.

In Figure 4, the output values of the study are given graphically.

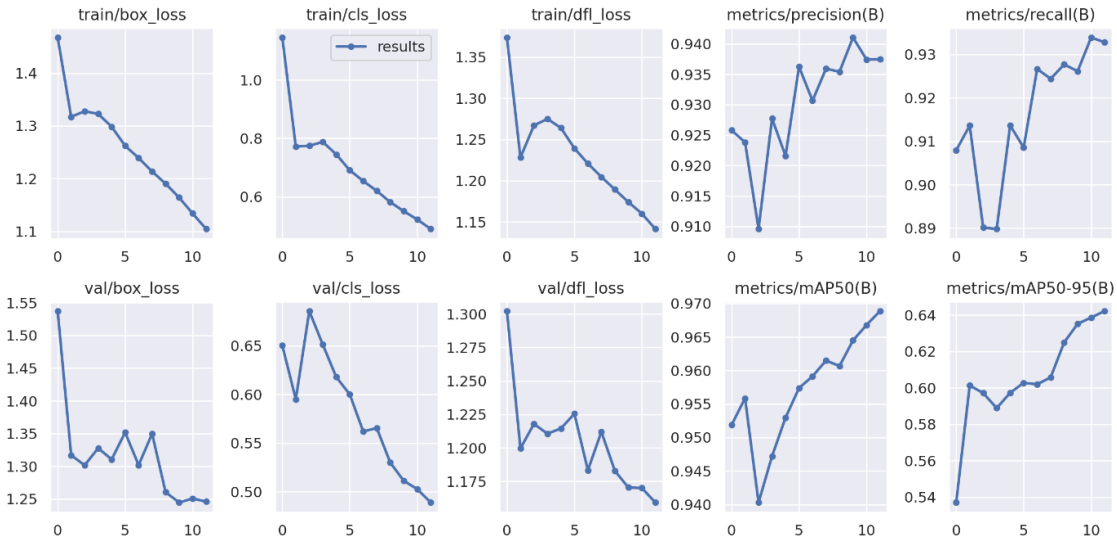

Figure 4. Graphical Representation of Experimental Study Analysis.

The test samples of the fixation system obtained from the experimental studies are given in Figure 5.

Figure 5. Example Helmet/Head Detection Ratio.

The data set used has been the subject of other scientific studies before. The table below gives this study's comparative results with similar data sets and similar studies.

Table 3. Comparison of experimental studies on automatic helmet detection with similar. Datasets.

Author	Model	mAP50 (%)
[14]	SSD, Faster R-CNN, YOLOv3, and Improved YOLOv3	77.2, 94.3, 82.3 and 93.1
[12]		36.8
[29]	SSD	96.0
[11]		68.5
[30]	YOLOv5s, YOLOv5m, YOLOv51 and YOLOv5x	93.6, 94.3, 94.4 and 94.7
[4]	YOLOv5 and Improved YOLOv5	92.1 and 95.7
[18]	YOLOv5s, YOLOv6s and YOLOv7	83.7, 83.5 and 89.6

Our Study	YOLOv8	96.9

Table 3 showcases a variety of studies, each utilizing different models for helmet detection and reporting the corresponding mAP50 scores achieved by each model. This comparison demonstrates the general improvement in the accuracy of helmet detection tasks with the evolution of the YOLO model from version 3 to version 8, keeping in mind that the different studies may have used different datasets and evaluation methods. The YOLOv8 model from this study achieved the highest mAP50 score of 96.9%, outperforming all other models tested in similar studies. This indicates that YOLOv8 is highly effective in helmet detection compared to other deep-learning models.

4. Conclusion and Suggestions

In this study, a system that performs automatic helmet control in areas where human life is in danger in common working and living environments such as construction and factories, especially in areas where there is a possibility of falling off an object harmful to the head, has been proposed. Studies have been done. In experimental studies, it has been possible to determine whether people automatically wear helmets on their heads with image processing techniques.

When Table 3 is examined, it is seen that the highest performance score among similar data sets and similar study samples is 96.9% with this study. The previous research with the highest success rate was Tan et al. [4]. It obtained a success value of 95.7%.

In addition, 98.1% for automatic helmet detection with computer vision and an average of 95.6% for human head detection (mAP50) were obtained in the study. In this and similar studies, it has been observed and suggested that YOLOv8, one of the deep learning-based models, gives more successful results than other models.

Potential directions for future work include enhancing the variety of the dataset by incorporating images from different industries where helmets are used, capturing various types of helmets, and considering diverse lighting and weather conditions. Real-time implementation of the helmet detection system in an actual construction site or other relevant industry could offer invaluable insights into its real-world effectiveness and the challenges that might arise in such a context. The scope of the study could also be extended to include the detection of other forms of Personal Protective Equipment (PPE), such as safety vests, gloves, and safety glasses, contributing to a more comprehensive safety monitoring system. Additionally, integrating the helmet detection system with an alarm or notification system could serve as an immediate alert mechanism for supervisors or safety officers when a worker is detected without a helmet. While the YOLOv8 model has demonstrated promising results, other emerging models should be explored for helmet detection, ensuring continuous evaluation of new models and techniques to remain at the forefront of technology. A deeper investigation into the causes of false positives and negatives in the current model could lead to enhanced accuracy, involving a detailed analysis of the cases where the model fails and implementing strategies to rectify these inaccuracies. Lastly, developing lightweight models suitable for real-time applications, which minimally compromise accuracy but significantly reduce computational requirements, could be a key direction for future research. This would enable on-site deployment on edge devices for instant alerts and actions.

Contributions of the authors

Corresponding author: writing (original draft, review & editing) and investigation.
Coauthor: Methodology and experimental study.

Conflict of Interest Statement

There is no conflict of interest between the authors.

Statement of Research and Publication Ethics

The study is complied with research and publication ethics

References

[1] X. Huang and J. Hinze, “Analysis of construction worker fall accidents,” *J. Constr. Eng. Manag.*, vol. 129, no. 3, pp. 262–271, 2003.

[2] R. A. Haslam et al., “Contributing factors in construction accidents,” *Appl. Ergon.*, vol. 36, no. 4, pp. 401–415, 2005.

[3] A. Hayat and F. Morgado-Dias, "Deep learning-based automatic safety helmet detection system for construction safety," *Appl. Sci. (Basel)*, vol. 12, no. 16, p. 8268, 2022. https://doi.org/10.3390/app12168268

[4] S. Tan, G. Lu, Z. Jiang, and L. Huang, "Improved YOLOv5 network model and application in safety helmet detection," *in 2021 IEEE International Conference on Intelligence and Safety for Robotics (ISR)*, 2021. https://doi.org/10.1109/ISR50024.2021.9419561

[5] Y. LeCun, Y. Bengio, and G. Hinton, "Deep learning," *Nature*, vol. 521, no. 7553, pp. 436–444, 2015. doi:10.1038/nature14539

[6] J. Redmon and A. Farhadi, "YOLOv3: An Incremental Improvement," arXiv [cs.CV], 2018.

[7] R. Girshick, J. Donahue, T. Darrell, and J. Malik, "Rich feature hierarchies for accurate object detection and semantic segmentation," *in 2014 IEEE Conference on Computer Vision and Pattern Recognition*, 2014.

[8] P. Doungmala and K. Klubsuwan, "Helmet wearing detection in Thailand using Haar like feature and circle Hough transform on image processing," *in 2016 IEEE International Conference on Computer and Information Technology (CIT)*, 2016.

[9] W. Zhang, C.-F. Yang, F. Jiang, X.-Z. Gao, and X. Zhang, "Safety helmet wearing detection based on image processing and deep learning," *in 2020 International Conference on Communications, Information System and Computer Engineering (CISCE)*, 2020.

[10] S. H. Kim, C. Wang, S. D. Min, and S. H. Lee, "Safety helmet wearing management system for construction workers using three-axis accelerometer sensor," *Appl. Sci. (Basel)*, vol. 8, no. 12, p. 2400, 2018.

[11] X. Long, W. Cui, and Z. Zheng, "Safety helmet wearing detection based on deep learning," *in 2019 IEEE 3rd Information Technology, Networking, Electronic and Automation Control Conference (ITNEC)*, 2019.

[12] Y. Li, H. Wei, Z. Han, J. Huang, and W. Wang, "Deep learning-based safety helmet detection in engineering management based on convolutional neural networks," *Advances in Civil Engineering*, vol. 2020, pp. 1–10, 2020.

[13] H. Wang, Z. Hu, Y. Guo, Z. Yang, F. Zhou, and P. Xu, "A real-time safety helmet wearing detection approach based on CSYOLOv3," *Appl. Sci. (Basel)*, vol. 10, no. 19, p. 6732, 2020.

[14] L. Huang, Q. Fu, M. He, D. Jiang, and Z. Hao, "Detection algorithm of safety helmet wearing based on deep learning," *Concurr. Comput.*, vol. 33, no. 13, 2021.

[15] G. Han, M. Zhu, X. Zhao, and H. Gao, "Method based on the cross-layer attention mechanism and multiscale perception for safety helmet-wearing detection," *Comput. Electr. Eng.*, vol. 95, no. 107458, p. 107458, 2021.

[16] K. Han and X. Zeng, "Deep Learning-Based Workers Safety Helmet Wearing Detection on Construction Sites Using Multi-Scale Features," *in IEEE Access*, vol. 10, pp. 718-729, 2022, doi: 10.1109/ACCESS.2021.3138407.

[17] B. Zhang, C.-F. Sun, S.-Q. Fang, Y.-H. Zhao, and S. Su, "Workshop safety helmet wearing detection model based on SCM-YOLO," *Sensors (Basel)*, vol. 22, no. 17, p. 6702, 2022.

[18] N. D. T. Yung, W. K. Wong, F. H. Juwono, and Z. A. Sim, "Safety helmet detection using deep learning: Implementation and comparative study using YOLOv5, YOLOv6, and YOLOv7," *in 2022 International Conference on Green Energy, Computing and Sustainable Technology (GECOST)*, 2022. doi:10.1109/GECOST55694.2022.10010490

[19] M.-E. Otgonbold et al., "SHEL5K: An extended dataset and benchmarking for Safety HELmet detection," *Sensors (Basel)*, vol. 22, no. 6, p. 2315, 2022. Doi:10.3390/s22062315

[20] J. Chen, S. Deng, P. Wang, X. Huang, and Y. Liu, "Lightweight helmet detection algorithm using an improved YOLOv4," *Sensors (Basel)*, vol. 23, no. 3, p. 1256, 2023. doi:10.3390/s23031256

[21] Q. Zhou, J. Qin, X. Xiang, Y. Tan, and N. N. Xiong, "Algorithm of helmet wearing detection based on AT-YOLO deep mode," *Comput. Mater. Contin.*, vol. 69, no. 1, pp. 159–174, 2021.

[22] Y. Jamtsho, P. Riyamongkol, and R. Waranusast, "Real-time license plate detection for non-helmeted motorcyclist using YOLO," *ICT Express*, vol. 7, no. 1, pp. 104–109, 2021.

[23] N. K. Anushkannan, V. R. Kumbhar, S. K. Maddila, C. S. Kolli, B. Vidhya, and R. G. Vidhya, "YOLO algorithm for helmet detection in industries for safety purpose," *in 2022 3rd International Conference on Smart Electronics and Communication (ICOSEC)*, 2022.

[24] J. Li, Y. Li, J. F. Villaverde, X. Chen, and X. Zhang, "A safety wearing helmet detection method using deep leaning approach," *J. Opt.*, 2023.

[25] J. Fang, X. Lin, F. Zhou, Y. Tian, and M. Zhang, "Safety Helmet Detection Based on Optimized YOLOv5," *in 2023 Prognostics and Health Management Conference (PHM)*, IEEE, 2023, pp. 117–121.

[26] Z. Zhang, Y. Tang, Y. Yang, and C. Yan, "Safety Helmet and Mask Detection at Construction Site Based on Deep Learning," *in 2023 IEEE 3rd International Conference on Information Technology, Big Data and Artificial Intelligence (ICIBA)*, vol. 3, IEEE, 2023, pp. 990–995.

[27] M. Gochoo, "Safety helmet wearing dataset." Mendeley, 2021. doi: 10.17632/9rcv8mm682.1

[28] RangeKing, (2023), Brief Summary of YOLOv8 Model Structure, URL: https://github.com/ultralytics/ultralytics/issues/189 date of access: 01/05/2023.

[29] A. Kamboj and N. Powar, "Safety helmet detection in industrial environment using deep learning," *in 9th International Conference on Information Technology Convergence and Services (ITCSE 2020)*, 2020.

[30] F. Zhou, H. Zhao, and Z. Nie, "Safety helmet detection based on YOLOv5," *in 2021 IEEE International Conference on Power Electronics, Computer Applications (ICPECA)*, 2021.

Bitlis Eren Üniversitesi Fen Bilimleri Dergisi
BİTLİS EREN UNIVERSITY JOURNAL OF SCIENCE
ISSN: 2147-3129/e-ISSN: 2147-3188
VOLUME: 12 NO: 3 PAGE: 783-796 YEAR: 2023
DOI:10.17798/bitlisfen.1301546

Single and Binary Performance Comparison of Data Compression Algorithms for Text Files

Serkan KESKİN[1*], Onur SEVLİ[2], Ersan OKATAN[3]

[1] *Burdur Mehmet Akif Ersoy University, Institute of Science and Technology, Department of Computer Engineering, Burdur*
[2] *Burdur Mehmet Akif Ersoy University, Faculty of Engineering and Architecture, Department of Computer Engineering, Burdur*
[3] *Burdur Mehmet Akif Ersoy University, Gölhisar School of Applied Sciences, Department of Computer Technologies and Information Systems, Burdur*

(ORCID: 0000-0001-9404-5039) (ORCID: 0000-0002-8933-8395) (ORCID: 0000-0001-6511-3450)

Keywords: Text Compression, Data compression, Binary Compression, Deflate, BWT

Abstract
Data compression is a technique used to reduce the size of a file. To reduce the size of a file, unnecessary information is removed or parts that repeat the same information are stored once. Thus a lossless compression is achieved. The extracted file has all the features of the compressed original file and can be used in the same way. Data compression can be done using different techniques. Some of these techniques are Huffman coding, Lempel-Ziv-Welch coding and Burrows-Wheeler Transform. Techniques such as Huffman coding, Lempel-Ziv-Welch coding and Burrows-Wheeler Transform are some of them. Which technique to use depends on the type and size of the data to be compressed. Huffman, Lempel-Ziv-Welch, Burrows-Wheeler Transform and Deflate algorithms are the most widely used techniques for text compression. Each algorithm uses different approaches and can produce different results in terms of compression ratios and performance. In this study, different data compression techniques were measured on specific data sets by using them individually and in pairs on top of each other. The most successful result was obtained with the Deflate algorithm when used alone and the achieved compression ratio was 29.08. When considered in the form of stacked pairs, the compression ratio of the Burrows-Wheeler Transform and Deflate gave the best result as 57.36. In addition, when compression is performed in pairs, which algorithm is applied first and which algorithm is applied afterwards can make a significant difference in the compression ratio. In this study, the performance measurements obtained by applying the algorithms in different orders are compared and suggestions are presented to obtain optimum performance.

1. Introduction

The vast amount of data generated every moment is the basic building block of the digital world. Any information that can be measured and recorded can be referred to as data. This information can be in a wide variety of forms such as text, graphics, numbers, video, images and audio recordings. From personal files to the data centers of large companies, the amount of data collected and generated is enormous. Data can be obtained from a variety of sources [1]. For example, it can be entered as user input or collected automatically by software, sensors and devices. This collected data can be used for analysis and decision making. Information can often be stored on different platforms. Some are saved on the hard drive of computers, while others are stored on servers in cloud infrastructure [2].

* Corresponding author: serkankeskin@isparta.edu.tr
Received: 24.05.2023, Accepted:04.09.2023

In the 21st century, data is of great importance. Data is crucial for businesses, researchers, government agencies and even individuals.

However, storing and transmitting data comes with a number of disadvantages, such as increased volume and high costs [3]. As data capacities increase, storage and transmission costs also increase. This has led to the development of data compression techniques to reduce the data footprint. Data compression techniques have been developed to minimize storage space and reduce costs. It has also positively affected processing and analysis times. Data compression techniques encode information by compressing data into smaller formats, effectively reducing data size. The focus should be on using techniques to compress data in a performant way, thus making storage and transmission less costly [4]. This paves the way for faster and easily manageable transmission.

There are numerous approaches to data compression, determined by the degree of similarity between the compressed and original data, as well as the compression ratio. The history of compression techniques dates back to the advent of electronic digital computers. Early techniques were based on basic mathematical algorithms such as Huffman coding [5]. As technology advanced, lossless and lossy compression techniques emerged in the 1970s and 1980s. Later on, various techniques such as number-length coding, arithmetic coding and wavelet compression were developed. In addition to its effectiveness in storage and data transmission, compression has also become effective in data backup and data recovery. It has enabled the reduction of storage space for backups. Data compression is a widely used technique for archiving purposes. It has facilitated the storage of very large data for long periods of time while requiring minimal space.

1.1. Literature Review

There are different studies on data compression using many techniques to date. In a study conducted by Hasan in 2011, a compression study was carried out using Huffman and then Lempel-Ziv-Welch (LZW) techniques. A compression value of 3.25 was achieved on the data. When only one technique was applied, compression did not exceed 2.55 [3]. In another study conducted in the same year, the average compression ratio in multiple applications of the Huffman technique was 5.27 [6]. In the study conducted by Rahman and Hamada, the compression ratio of LZW technique was 1.28, Gzip technique was 1.5, LZMA technique was 1.32 and Brotli technique was 1.66. The original transform-based compression technique proposed in this study was found to be more successful than the other techniques with a compression ratio of 1.88 [7]. In another study conducted on texts based on LZW compression technique, it was concluded that the compression ratio remained at 1.33 [8]. In a study using Burrows-Wheeler Transform (BWT) and RLE techniques, the compression ratio remained at 2.48 [9]. In a study with Hybrid Sym6- Huffman coding, the compression ratio was 1.70 [10]. In a study comparing LZW, wavelet tree and compressed wavelet tree techniques, the compressed wavelet tree reduced a 200 KB file with a compression ratio of 4.65 [11]. In a study comparing the compression performance of Huffman and Unary coding on text files, Unary coding was found to be more successful. The compression ratio of the Unary code remained at 2.64 [12]. In a study by S. Kumar, a comparison was made between RLE (Run-length encoding) and ASCII encoding. The experimental study resulted in an average compression ratio of 2.53 [13]. A.Rahman compared Bzip2, Gzip, LZMA, Brotli and his proposed compression algorithms on 10 data sets. As a result of the comparison, Bzip2 algorithm was the most successful technique with a compression ratio of 2.91 [14]. P.Sarker, who performed compression with another text compression technique, achieved a compression ratio of 1.49 with his proposed technique [15]. S Haldar-Iversen performed binary compression with ASCII compression modulus+GZIP and obtained a compression ratio of 3.00 [16]. In a study on compression of dictionaries in different languages using the LZW algorithm, an average compression rate of 3.33 was obtained [1]. In a binary compression study with Chinese Remainder Theorem and Huffman algorithms, a success rate of 1.56 was achieved in license.txt text file [17]. In the study conducted by Ibrahim and Gbolagade, 4 different algorithms were used and the LZW algorithm with a compression ratio of 7.91 gave more successful results [18]. In the compression process performed with the help of a matrix table using the Huffman algorithm, a compression ratio of 2.94 was achieved in the

artificial text 1.txt text file [19]. In a study conducted by Rincy and Rajesh to examine the performance of the LZW algorithm with ASCII characters, a compression ratio of 4.23 was obtained [20]. In another study where the compression algorithm was constructed by utilizing long distance correlations between words, the compression ratio remained at 1.80 [21]. In this study, a new Karhunen-Loeve transform based algorithm for lossy image compression is developed, which presents a simple algorithm where images are only subsampled and KLT is applied. While most other image compression studies use hybrid methods, this study presents an approach based solely on KLT[22]. Ince et al. present the proposed LDR-DCT method as an alternative to the conventional DCT method when compression is unnecessary. It is also claimed that if the method is designed with quantisation tables, it can achieve the same JPEG image quality as the traditional DCT method and provide higher compression ratios [23]. In the study where data compression is performed by text clustering, the Compression Ratio Index (CRI), which can be calculated faster than internal methods such as Silhouette, Calinski-Harabasz and Davies-Bouldin indices, is developed. This study showed that SOI, an alternative clustering performance measure, gives consistent results with traditional internal and external methods [24].

1.2. Basic Principles of Data Compression

The process of reducing the footprint of electronic data is commonly known as data compression. Data compression is usually performed by two different techniques. These are redundancy removal and statistical coding techniques. These techniques help to optimize the storage of data on electronic devices. It is also possible to divide data compression into two parts: lossy and lossless.

1.2.1. Redundancy Removal

Redundancy removal is a valuable technique for removing repetitive or predictable data from datasets. In this technique, unnecessary spaces or characters are identified and removed, and is often used to compress text documents. This can minimize file size, save storage space and speed up data transfer [25]. There are three main methods for redundancy removal. The first is spatial redundancy, where similar or identical data is repeated within the same file. For example, the same pixels in a photo do not need to be repeated more than once. It is enough to save them once to reduce the file size. Redundancy can also be eliminated based on time. This relates to situations where the same or similar data is repeated at different points in time. For example, the same images appearing multiple times in a single video is redundant and requires more storage space. To avoid this, video sizes can be reduced by recording repetitive images once. The third and final redundancy removal technique is encoding redundancy. Encoding redundancy occurs when the same data uses more than one bit or symbol. By eliminating these redundancies, storage requirements can be reduced.

1.2.2. Statistical Coding

Statistical coding is based on the fact that some symbols or characters are more common than others in the dataset. There are two types of statistical coding. Entropy coding is a type of statistical coding that uses probability to assign variable length codes to symbols or characters. Lexical coding is a type of coding that replaces repeated words in a dataset with references to a dictionary or a table [5].

1.2.3. Lossless Data Compression

Lossless data compression is a technique used to compress data to take up less space. In this technique, no data is lost during the compression process. This means that the compressed data is exactly equal to the original data. Lossless compression algorithms usually compress by identifying duplicate parts of the data. These parts can significantly reduce the size of the data. For example, multiple repeated words or sentences in a text document can be recognized by lossless compression algorithms and stored in a smaller footprint. The most common use of lossless compression algorithms are file compression programs [19]. These programs save storage space by compressing particularly large files or multiple files together. Since compressed data has a smaller amount of data than the original data, there are fewer errors during data transmission. This form of compression is especially important in critical systems where there is no fault tolerance during data transmission. The most

common lossless compression algorithms are Huffman Coding, LZ77 and LZ78, BWT.

1.2.4. Lossy Data Compression

When less memory or disk space is available to store information, lossy data compression is used to reduce the size of large data sets. However, this technique has a disadvantage. There is a possibility that some data may be lost during the compression process. Because of this potential loss, it is called lossy. This technique becomes more useful when working with multimedia files and other large data sets that require a significant amount of space to store and share. The size of files can be significantly reduced using lossy data compression techniques. Lossy compression is a technique that accelerates data compression by allowing efficient data storage and sharing. It can affect data quality while reducing storage requirements. Appropriate algorithm selection and proper configuration are required to achieve optimal results [26].

Different techniques are used in lossy data compression. Among the most important are volume-based, frequency-based and predictive techniques. Volume-based techniques evaluate the density and volume of data, such as how undetectable frequencies or low-density data can be bypassed by MP3 compression for audio files. Frequency-based techniques focus on frequency components using low frequency components to preserve essential information, such as JPEG compression that groups similar colors together and uses averages. Finally, predictive techniques identify recurring patterns in the data and efficiently reconstruct it using minimal information for patterns. For example, the GIF format can reduce the size of images by reusing similar colors in an image [18].
In short, lossless compression preserves all the original data, while lossy compression sacrifices some of the original data to achieve higher compression ratios. Lossless compression is typically used for text and data files, while lossy compression is typically used for image, audio and video files.

1.3. Areas Where Data Compression Is Used

1.3.1. File Compression

The technique used to reduce file size is called file compression. Compression reduces the size of files on disk. Smaller files are easier to download, share and send. This allows users to save time, internet resources and storage space. File compression algorithms such as RAR, 7z, ZIP, GZIP are commonly used file compression applications.

1.3.2. Video Compression

Video compression is the process of reducing the volume and flow rate of data and is used in direct relation to the term bandwidth. This compression technique works in the same way that a video camera captures each frame and converts it to JPEG format. If these frames are played back on a surveillance computer at 25 frames per second, you get moving video. This compression aims to provide high image quality. However, it also results in high bandwidth and storage overhead. Video compression algorithms are H.264, H.265, MPEG, HEVC, VP9, etc.

1.3.3. Audio Compression

Audio compression is the process of fitting digitally recorded audio signals into a smaller volume with or without loss. FLAC, MP3, Ogg Vorbis, AAC are examples of popular audio compression algorithms.

1.3.4. Image Compression

Image compression is a technique used to reduce the footprint of large image files. Generally, digital compression algorithms are used. These techniques are used to compress complex images such as photographs. JPEG, PNG, GIF are among the prominent ones of these techniques. In addition, high performance compression is performed with the discrete cosine transform (DCT) method. In order to minimise rounding errors and information loss, it is necessary to reduce the dynamic range of the DCT coefficients. In this way, a lower range of weights can be obtained according to frequency levels during DCT calculations [23].

2. Material and Method

2.1. Huffman Coding

Huffman coding is a commonly used technique in data compression. This technique reduces the data size by encoding frequently repeating symbols using fewer bits. This allows data to be

transmitted faster and uses less storage space. This algorithm first calculates the frequency of frequently repeated symbols and assigns shorter codes to these symbols. Rarely used symbols are assigned longer codes. In this way, the encoding of frequently used symbols uses fewer bits, while the encoding of infrequently used symbols uses more bits [27].

For Huffman coding, the symbols of the data are first identified and the frequencies of these symbols are calculated. These frequencies allow the symbols to be represented in a tree structure. Then, left branches in the tree structure are coded as 0 and right branches as 1. Since frequently used symbols will take shorter codes, the coding of these symbols will use fewer bits [15].

For example, if Huffman coding is done for the sentence "HELLO WORLD", the frequencies of the symbols of the text are first calculated. The letter "H" appears 1 time, "E" 1 time, "L" 3 times, "O" 2 times, "W" 1 time, R" 1 time and "D" 1 time. A Huffman tree is constructed according to the frequencies of these symbols [19]. First, the two lowest frequency symbols (here "E" and "R") are merged to form a node whose frequency is equal to the total frequency of the two symbols. This process continues according to the frequencies of the other symbols, and the tree structure is formed with the most frequently used symbol at the top. In this tree structure, a code is generated for each symbol. Frequently used symbols are assigned shorter codes, for example the symbol "L" is assigned a short code, while rarely used symbols are assigned longer codes. The Huffman coding for the sentence "HELLO WORLD" can be coded as shown in Table 1

Table 1. Huffman algorithm frequency and codes assigned to each symbol

Symbol	Frequency	Code
E	1	000
H	1	001
D	1	010
R	1	011
W	1	100
O	2	101
L	3	11

Table 1 shows the frequency of each symbol, the code assigned to the symbol and its path in the Huffman tree. For example, the code assigned to the symbol "L" is "11" and this symbol is located two nodes down the Huffman tree. Thanks to this coding technique, frequently used symbols in the text will receive shorter codes and the size of the text will be significantly reduced. For example, when Huffman encoding is used for the sentence "HELLO WORLD", the size of the text will decrease from 44 bits to 23 bits. This means that text can be transmitted and stored faster and using less storage space.

2.2. Lempel-Ziv-Welch

Among the data compression techniques currently in use, the LZW (Lempel-Ziv-Welch) algorithm is often preferred. It is a lossless technique. This means that no information is lost during the compression process. Basically, the algorithm identifies repeating patterns in the data and replaces them with shorter codes, resulting in compressed data [28]. Text files, graphics files and compressed data are typical applications of the LZW algorithm. Briefly summarizing the steps of the LZW algorithm: Initially, a dictionary is created by the algorithm consisting of codes for individual symbols such as "a", "b", "c", etc.

- During the compression process, individual data units are analyzed and the longest recurring pattern, also known as a word, is found. If the word is not found in the dictionary, it is given a code number and integrated into the dictionary.

- The word represented by the code number is added to the compressed data.
- Whenever a compressed data set contains a new term, the dictionary is immediately reviewed and a unique code number is assigned to the newly added word.
- This process continues in full until the piece of data is completely finished.
- The file format stores both the compressed data and a dictionary that allows the compressed data to be restored.

Using a window to identify patterns during compression, the LZW algorithm examines the data to detect repetition. The window size governs the pattern size for the search. For example, with a window size of 12 bits, the algorithm can identify up to 4096 unique words. The larger the window size, the longer patterns the algorithm can identify. However, this increases the complexity [20].
The LZW algorithm is particularly useful when dealing with data that contains repeating patterns, such as text files. In fact, it has proven effective in cases like "LLLLLLLLLLLLLLLLLLLLLLLLLLLLZ".
Instead of encoding "LLLLLLLLZ" every time it appears, the word is encoded only once and then represented by the corresponding code number each time it is repeated.

The LZW algorithm compresses the input data by replacing repeated patterns with shorter codes stored in a dictionary. The output of the algorithm consists of a set of indices corresponding to the codes in the dictionary. When the compressed data is decompressed, the dictionary is reconstructed using the same algorithm and the indices are replaced by the corresponding symbols in the dictionary [28].

As part of the compressed file, the LZW algorithm includes a table for code search. Overall, this table consists of 4,096 entries. The codes 0-255 in the table are assigned to represent individual bytes found in the input file. Before the initialization of the algorithm, only the first 256 entries of the table are filled, while the remaining entries are left blank. Basically, by default the first 256 codes are assigned to the standard character set. As the compression process evolves, the remaining codes are allocated to the sequences. During encoding initialization, the algorithm detects duplicate sequences in the data and adds them to the code table. It thus expands its content. In the context of file compression, codes between 256 and 4,095 are used to symbolize sequences of multiple bytes.

2.3. Burrows-Wheeler Transformation

The Burrows-Wheeler Transform (BWT) is an algorithm for text compression. This algorithm performs compression by identifying repetitive characters within a text. It is also based on the use of varying orderings of data based on their consecutive characters [9]. The stages of the BWT algorithm can be summarized as follows:

- Adding an EOF character at the end of the text: An EOF character is added at the end of the text.
- Creating all loops: All loops after the EOF character are created. Loops are created by shifting each character of the text to the right.
- Ordering of loops: All loops are sorted according to the lexicographic order of the characters in them.
- Creation of the BWT matrix: From each loop, the last character (except EOF) and all previous characters are copied into a matrix.
- BWT encoding: The characters of each column in the matrix are combined and used as the encoded representation of the compressed text. The key used during BWT encoding is the index of the last character in the original text. In this way, the compressed text can be reconstructed before it is encoded.

The BWT algorithm does not directly compress the data. Instead, it increases the compressibility of the data. The word "the" is most frequently used in the English text. Therefore, when the word "the" is encountered in the converted text, it is represented as "he". This feature has proven to be quite advantageous for various transformation algorithms, including Move-To-Front Transform [29]. When applying the BWT to an array, the resulting output of the Move Forward transform will consist mainly of smaller values that can be compressed efficiently using entropy encoding. We can rank the existing compression methods based on BWT in four different stages. The first stage includes the implementation of BWT, which serves as the core component of the compression algorithm. This operation increases the compressibility of the array. The next stage is known as global structure transformation (GST). At this stage, Burrows and Wheeler applied the Move Forward transformation as part of the list update algorithm [29]. The first version of the Burrows and Wheeler compression algorithm does not include a third step. However,

they introduced a concept that uses a code to symbolize the length of a string of zeros. In a later study, string length coding was applied as a tool to encode zero sequences and provided a commendable level of compression [30]. The final stage, the fourth stage, includes entropy encoding, which can be obtained through Huffman coding or arithmetic coding to compress the output of the previous stage.

The BWT algorithm performs compression by identifying repeating patterns. For example, in the text "bababababac", similar repeated characters could be "baba" and "c". The BWT algorithm creates blocks grouping the same characters and compresses by changing the order of the blocks. This can result in a significant reduction in data size.

The BWT algorithm is highly efficient for compressing data. However, in order to return the compressed data to its original format, the algorithm needs to know the index of the last character in the source text [31]. Furthermore, the compression efficiency of the algorithm may lag behind other existing algorithms in certain scenarios.

2.4. Deflate Coding

In mid-1990, Phil Katz developed a data compression format that preserves all original data, called lossless compression. This new algorithm is a combination of Huffman coding and LZ77 algorithms [24]. Deflate algorithm is a lossless compression algorithm used in compression programs such as gzip, PNG and WinZip. Data is compressed in consecutive blocks. Each block is compressed using Huffman coding and the LZ77 algorithm. The size of the compressible blocks varies and when the Huffman tree becomes too large for efficient coding, the Deflate algorithm terminates that block. It then starts a new block by creating a new Huffman tree. Each block consists of two parts. These parts are the compressed data and the Huffman code trees representing the data. In particular, the Huffman tree of each block is independent of the previous and the next block. The compressed data at the beginning of each block is preceded by Huffman trees compressed using Huffman coding. The LZ77 algorithm relies on a search buffer spanning 32,768 bytes and can refer to a string from the previous block as long as it stays within these limits. However, the length of the repeating character or forwarding buffer in this algorithm is limited to 258. The length of 256 different character numbers between 3 and 258 is represented as 1 byte. The 32,768-byte size search buffer is represented by 15 bits, while 1 bit is used for the flag representing the uncompressed data, so it is represented by 3 bytes.

2.5. Data Compression Performance

There are two parameters in data compression performance. These are data compression ratio and speed. Data compression ratio is expressed as the ratio of original data to compressed data. Take a 10 MB text or video file. Let the size of this file be 2 MB after compression. The compression ratio of this file is 5. An increase in the compression ratio means the direct success of the algorithm used. The other parameter, speed, refers to the compression time. As the speed increases, the time taken in the compression process will decrease. There is an inverse relationship between speed and compression ratio. As the speed increases, the compression ratio decreases. For this, it is important to achieve balance. The compression ratio is expressed by Equation (1).
Compression Ratio=original file/compressed file (1)

2.6. Data Set

In this study, 4 different data sets were used. The first data set is a text file named "pi.txt" consisting of the first one million digits of pi after the comma. This data set consists only of numbers and its size is 997 kilobytes. The second data set is a text file of the book "Alice's Adventures in Wonderland". It consists only of letters. The name of the data set is "alice.txt" and its size is 149 kilobytes. The third data set is a text file of firewall logs. This data set consists of 50% letters and 50% numbers. This data set is named "log.txt" and its size is 4.38 megabytes. The last data set is an Excel document. Like the log file, this document has a 50/50 ratio of letters and text. The size of the data set is 5.44 MB and is named "list.xls". "Alice.txt" was taken from the public domain [32]. The other datasets used were created by us.

3. Results and Discussion

Huffman coding, Deflate coding, LZW and BWT algorithms were used for data compression. With the algorithms, data compression operations were performed singly and sequentially in pairs. This data compression process was applied on 4 different data sets. Single compression rates and compression times are given in Table 2 and Table 3 respectively.

Table 2. Single data compression ratios

Compression Ratios								
Data Set	Pi Dataset (996,19 kilobyte)		Alice Dataset (148,52 kilobyte)		Log Dataset (4283,64 kilobyte)		List Dataset (5578.72 kilobyte)	
Algorithm	Compression The post File size	Compression Ratio	Compression The post File size	Compression Ratio	Compression The post File size	Compression Ratio	Compression The post File size	Compression Ratio
Huffman	466,57	2,13	91,13	1,62	2732,83	1,57	5231.19	1.06
LZW	468,74	2,12	64,38	2,30	638,75	6,70	8042.12	-1.69
BWT	444,73	2.24	48,18	3,08	577,45	7,41	1510.34	3.69
Deflate	486,06	2,03	53,66	2,76	147,3	29,08	1851.05	3.01

As seen in Table 2, the BWT algorithm is generally the most successful in single compression. This is due to the fact that it groups the same character blocks in the data sets and changes their order, which results in more successful results than other algorithms. The fact that the Deflate algorithm is more successful than the BWT algorithm on the log dataset can be explained by the fact that the dataset is more suitable for this algorithm. The negative result of the LZW algorithm on the list dataset is an indication that the algorithm cannot compress Excel files. It could not detect any similarity in the list dataset, thus increasing the character count instead of decreasing it.

Table 3. Single data compression times

Compression Times (milliseconds)				
Data set/ Algorithm	Pi Dataset	Alice Dataset	Log Dataset	List Dataset
Huffman	313	187	1390	2492
LZW	157	78	267	802
BWT	4478	446	29540	40845
Deflate	120	86	98	198

Table 3 shows the compression times in milliseconds. The most successful algorithm in terms of compression time is the deflate algorithm. The reason why the deflate algorithm is more successful is that the compression is done by recording the initial position and length of the pattern. This data is written to the buffer as part of the compressed data. Thus, the algorithm compresses faster than other algorithms.

Although the BWT algorithm is more successful in single compression, it can be said that the deflate algorithm is more successful if we evaluate it together with the compression time. The compression time of the BWT algorithm is 206 times higher than the deflate algorithm for the list dataset, 301 times higher for the log dataset, 5 times higher for the alice dataset and 37 times higher for the pi dataset. The differences in compression ratios are not large. Based on the size of the datasets used, compression with BWT can be used for small datasets. However, for larger data sets, the BWT algorithm may take more time to compress. Considering the compression ratios and times together, it can be said that the deflate algorithm is more successful.

The binary compression results are detailed in Table 4 and Table 5.

Table 4. Compression ratios before and after Binary Compression

Data Set	Pi Dataset		Alice Dataset		Log Dataset		List Dataset	
Algorithm	1.Compression ratio	2.Post-compression ratio	1.Compression ratio	2.Post-compression ratio	1.Compression ratio	2.Post-compression ratio	1.Compression ratio	2.Post-compression ratio
Huffman+LZW	2,135	1,634	1.629	1.390	1.567	2.410	1.066	0.767
Huffman+BWT	2,135	2.180	1.629	1.932	1.567	9.176	1.066	1.865
Huffman+Deflate	2,135	2.202	1.629	1.921	1.567	10.906	1.066	1.720
LZW+Huffman	2.125	2.100	2.306	2.274	6.706	6.664	0.693	0.770
LZW+BWT	2.125	2.123	2.306	2.310	6.706	18.704	0.693	2.427
LZW+Deflate	2.125	2.126	2.306	2.351	6.706	18.037	0.693	1.643
BWT+Huffman	2.239	2.243	3.082	3.159	7.418	29.499	3.693	4.375
BWT+LZW	2.239	1.631	3.082	2.395	7.418	44.950	3.693	3.501
BWT+Deflate	2.239	2.262	3.082	3.281	7.418	57.368	3.693	4.754
Deflate+Huffman	2.049	2.006	2.767	2.713	29.080	28.520	3.013	2.958
Deflate+BWT	2.049	2.048	2.767	2.753	29.080	29.214	3.013	3.013
Deflate+LZW	2.049	1.420	2.767	1.872	29.080	20.270	3.013	2.092

Table 5. File sizes in Kilobytes before and after binary compression

Data Set	Pi Dataset (1020100 KiloByte)		Alice Dataset (152089 KiloByte)		Log Dataset (4386450 KiloByte)		List Dataset (5712605 KiloByte)	
Algorithm	1.File size after compression	2.File size after compression	1.File size after compression	2.File size after compression	1.File size after compression	2.File size after compression	1.File size after compression	2.File size after compression
Huffman+LZW	477767	624275	93321	109355	2798420	1819681	5356740	7444115
Huffman+BWT	477767	467909	93321	78696	2798420	478030	5356740	3061738
Huffman+Deflate	477767	463181	93321	79163	2798420	402183	5356740	3319809
LZW+Huffman	479988	485702	65931	66870	654076	658156	8235129	7417408
LZW+BWT	479988	480316	65931	65815	654076	234514	8235129	2353460
LZW+Deflate	479988	479776	65931	64668	654076	243180	8235129	3476828
BWT+Huffman	455408	454766	49345	48140	591313	148695	1546586	1305441
BWT+LZW	455408	625273	49345	63481	591313	97585	1546586	1631568
BWT+Deflate	455408	450954	49345	46350	591313	76461	1546586	1201640
Deflate+Huffman	497729	508283	54948	56059	150839	153801	1895478	1931159
Deflate+BWT	497729	498057	54948	55226	150839	150148	1895478	1895806
Deflate+LZW	497729	717965	54948	81240	150839	216396	1895478	2730094

In Table 4, the compression ratios of the first and second compression results of the experimental study with binary compression are given in three digits after the dot. Table 5 shows the size of the first and second compression files in kilobytes. In both tables, the most successful ones are bolded. In both tables, compression was performed using the two algorithms in succession. As a result of the compression process, the most successful result was obtained when using the BWT and Deflate algorithms respectively. The pi dataset, which is numeric data, exceeded the initial compression measurement by 0.97%. In the alice dataset, which consists only of letters, binary compression is better than the pi dataset. The Alice dataset shows an increase of 6.06% over the initial compression rate. For the List dataset, which is an Excel file, the situation is better. There is an increase of 22.3% over the initial compression ratio. In the Log dataset, which has the highest compression ratio, an increase of 87.06% over the initial compression ratio was realized. This is because the first compression increased the similarity and the second compression reduced more characters.

In the pi and alice datasets, the similarity was significantly reduced in the first compression. As a result, the second compression resulted in a low compression ratio due to low similarity. In the list dataset, the similarity was not reduced in the first compression and was compressed slightly more in the second compression.

The main issue here is the compression order. BWT-Deflate and Deflate-BWT do not have the same compression ratios. All compression algorithms ultimately achieve a certain amount of compression. However, when subjected to a second compression process, the two algorithms give different results. This is because the BWT algorithm sorts repeated characters as consecutive variables. This compresses to a certain extent. The Deflate algorithm compares the data in the buffer with the data in the window. If there is a pattern between the data in the window and the data in the buffer, it compresses that pattern. The data that was compressed in the first compression with BWT is made suitable for compression again with Deflate. This results in an increase in the compression ratio. However, when dual compression is performed as Deflate-BWT, the second compression cannot reduce the number of characters as a sequential variable, which is required by the BWT algorithm. Thus, the order of compression is important. This will also be valid for other algorithms. Table 6 shows the binary compression times.

Table 6. Binary compression times (milliseconds)

Data Set	Pi Dataset		Alice Dataset		Log Dataset		List Dataset	
Algorithm	1.Compression time	2.Compression time	1.Compression time	2.Compression time	1.Compression time	2.Compression time	1.Compression time	2.Compression time
Huffman+LZW	313	49	187	14	1390	192	2492	514
Huffman+BWT	313	1696	187	318	1390	17617	2492	48597
Huffman+Deflate	313	37	187	12	1390	31	2492	132
LZW+Huffman	157	333	78	115	267	459	802	2994
LZW+BWT	157	1796	78	220	267	1897	802	67963
LZW+Deflate	157	22	78	11	267	32	802	211
BWT+Huffman	4478	230	446	126	29540	115	40845	541
BWT+LZW	4478	47	446	7	29540	16	40845	120
BWT+Deflate	4478	23	446	16	29540	12	40845	48
Deflate+Huffman	120	348	86	110	98	242	198	1108
Deflate+BWT	120	1789	86	172	98	496	198	13240
Deflate+LZW	120	59	86	6	98	17	198	297

Table 6 shows the binary compression times in milliseconds. In general, the Deflate-LZW binary compression algorithm performs the best in terms of binary compression times. If we look at the compression ratios, we can see that this has an inverse ratio. If we look at the BWT-Deflate binary compression algorithm, we can see that it has the highest compression time. From this we can conclude the following. The more compression, the more time it will take. Another aspect of compression time that we should not ignore is the type of data set. Text, numeric or text and numeric data also have different compression times.

As can be seen from Table 4 and Table 5, ranking in binary compression makes a big difference in both compression ratio and compression time. This is clearly seen in the experimental study. In general, the most successful result is obtained when BWT-Deflate algorithms are used consecutively.

In Table 7, the results of the study are tabulated in comparison with other studies in the literature.

Table 7. Similar Studies in the Literature

Study Name	Algorithm Used	Compression Ratio
Hasan, 2011 [3]	Huffman+LZW	3.25
Hasan, 2011 [3]	LZH	2.55
Rahman and Hamada, 2020 [7]	Proposed Method	1.88
Barua et al, 2017 [8]	MLZW	1.33
Fruchtman et al, 2023 [9]	BWT+RLE	2.48
Amusa et al, 2022 [10]	Hybrid Sym6- Huffman coding	1.70
Gupta et al., 2022 [11]	Compressed wavelet tree	4.65
Wijaya et al., 2022 [12]	Unary Codes Algorithm	2.64
Kumar and Chatuverdi, 2021 [13]	RLE	2.53
Rahman and Hamada 2021 [14]	Bzip2	2.91
Sarker and Rahman 2021 [15]	Proposed Method	1.49
Iversen, 2020 [16]	ASCII Compression Module+GZİP	3.00
Ignatoski at al., 2020 [1]	LZW	3.33
Ibrahim and Gbolagade, 2023 [17]	Huffman+CRT(Chinese Remainder Theorem)	1.56
Reza et al., 2019 [18]	Huffman	2.30
Bulut, 2016 [19]	Huffman	2.94
Rincy and Rajesh, 2019 [20]	LZW	4.23
Horspool and Cormack, 1992 [21]	UNIX Compress	1.80
This study Pi Dataset	**BWT+Deflate**	**2.26**
This study Alice Dataset	**BWT+Deflate**	**3.28**
This study List Dataset	**BWT+Deflate**	**4.75**
This study Log Dataset	**BWT+Deflate**	**57.36**

Table 7 shows the success rates of similar studies in the literature and which algorithm is more successful. It is seen that the study is more successful than other studies.

4. Conclusion and Suggestions

In this experimental study, compression was performed on single and consecutive text files. In general, a certain amount of compression was achieved for all data sets and for all algorithms used. In the single compression process, the best results were obtained on the log data set. In this data set, it was observed that the Deflate algorithm achieved 96% data compression. One of the most successful results in terms of compression speed was achieved by compressing the log data set with the Deflate algorithm. The fact that the log data set is more successful than other data sets is due to the high similarity rate in the data set. For this reason, the Deflate algorithm was more successful than other algorithms in compressing log files.

Not all algorithms were successful in the dual, i.e. sequential compression process. Huffman-BWT, BWT-Huffman, Huffman-Deflate and BWT-Deflate algorithm pairs successfully compressed all data sets. The most successful result was obtained in BWT-Deflate dual compression. In the log data set, this success was achieved with a compression factor of 57.36. If we had performed the compression algorithm as Deflate-BWT in the log data set, this ratio would have been 29.21. The reason for achieving a higher compression ratio is that the blocks created by the BWT algorithm as a result of compression can be recompressed with the Deflate algorithm, which uses the tree structure. Therefore, it is very important which algorithm to use first in compression. Existing compression algorithms may have different sensitivity levels to different types of text data (e.g. news, articles, academic texts, poems, etc.). Thereby, we aim to perform sensitivity analyses to examine how compression performance varies according to the type of text. The development of compression algorithms optimized for specific types of texts is being considered.

Conflict of Interest Statement

There is no conflict of interest between the authors.

Statement of Research and Publication Ethics

The study is complied with research and publication ethics

References

[1] M. Ignatoski, J. Lerga, L. Stanković, and M. Daković, ‘Comparison of entropy and dictionary based text compression in English, German, French, Italian, Czech, Hungarian, Finnish, and Croatian’, *Mathematics*, vol. 8, no. 7, p. 1059, Jul. 2020, doi: 10.3390/MATH8071059.

[2] I. B. Ginzburg, S. N. Padalko, and M. N. Terentiev, ‘Short Message Compression Scheme for Wireless Sensor Networks’, *Moscow Work. Electron. Netw. Technol. MWENT 2020 - Proc.*, Mar. 2020, doi: 10.1109/MWENT47943.2020.9067371.

[3] M. R. Hasan, ‘Data Compression using Huffman based LZW Encoding Technique’, *Int. J. Sci. Eng. Res.*, vol. Volume 2, no. 11, pp. 1–7, 2011, Accessed: Mar. 20, 2023. [Online]. Available: http://www.ijser.org

[4] V. Ratnam Anappindi, ‘Issue 8 www.jetir.org (ISSN-2349-5162)’, *JETIREZ06012 J. Emerg. Technol. Innov. Res.*, vol. 8, 2021, doi: 10.1109/EDSSC.2017.8126506.J.

[5] A. Habib, M. J. Islam, and M. S. Rahman, ‘A dictionary-based text compression technique using quaternary code’, *Iran J. Comput. Sci.*, vol. 3, no. 3, pp. 127–136, Sep. 2020, doi: 10.1007/s42044-019-00047-w.

[6] S. S and R. L, ‘Text Compression Algorithms - a Comparative Study’, *ICTACT J. Commun. Technol.*, vol. 02, no. 04, pp. 444–451, 2011, doi: 10.21917/ijct.2011.0062.

[7] M. A. Rahman and M. Hamada, ‘Burrows–wheeler transform based lossless text compression using keys and Huffman coding’, *Symmetry (Basel).*, vol. 12, no. 10, pp. 1–14, Oct. 2020, doi: 10.3390/sym12101654.

[8] L. Barua, P. K. Dhar, L. Alam, and I. Echizen, ‘Bangla text compression based on modified lempel-Ziv-welch algorithm’, *ECCE 2017 - Int. Conf. Electr. Comput. Commun. Eng.*, pp. 855–859, Apr. 2017, doi: 10.1109/ECACE.2017.7913022.

[9] A. Fruchtman, Y. Gross, S. T. Klein, and D. Shapira, ‘Weighted Burrows–Wheeler Compression’, *SN Comput. Sci.*, vol. 4, no. 3, pp. 1–12, Mar. 2023, doi: 10.1007/s42979-022-01629-5.

[10] K. Amusa, A. Adewusi, T. Erinosho, S. Salawu, and D. Odufejo, 'On the application of wavelet transform and Huffman algorithm to Yorùbá language syntax text files compression', *Serbian J. Electr. Eng.*, vol. 19, no. 3, pp. 351–368, 2022, doi: 10.2298/sjee2203351a.

[11] S. Gupta, A. K. Yadav, D. Yadav, and B. Shukla, 'A scalable approach for index compression using wavelet tree and LZW', *Int. J. Inf. Technol.*, vol. 14, no. 4, pp. 2191–2204, Jun. 2022, doi: 10.1007/s41870-022-00915-y.

[12] B. A. Wijaya, S. Siboro, M. Brutu, and Y. K. Lase, 'Application of Huffman Algorithm and Unary Codes for Text File Compression', *SinkrOn*, vol. 7, no. 3, pp. 1000–1007, Jul. 2022, doi: 10.33395/sinkron.v7i3.11567.

[13] S. Kumar and A. Kumar Chaturvedi, 'A Generalized Digital Database Text Compression Scheme Compared Wıth Ascii', *Int. J. Adv. Technol. Eng. Res.*, vol. 11, no. 2, p. 12, 2021, Accessed: Mar. 29, 2023. [Online]. Available: www.ijater.com

[14] M. A. Rahman and M. Hamada, 'Lossless text compression using GPT-2 language model and Huffman coding', *SHS Web Conf.*, vol. 102, p. 04013, 2021, doi: 10.1051/shsconf/202110204013.

[15] P. Sarker and M. L. Rahman, 'Introduction to Adjacent Distance Array with Huffman Principle: A New Encoding and Decoding Technique for Transliteration Based Bengali Text Compression', *Adv. Intell. Syst. Comput.*, vol. 1299 AISC, pp. 543–555, 2021, doi: 10.1007/978-981-33-4299-6_45.

[16] S. Haldar-Iversen, 'Improving the text compression ratio for ASCII text Using a combination of dictionary coding , ASCII compression , and Huffman coding', no. November, Nov. 2020, Accessed: Mar. 29, 2023. [Online]. Available: https://munin.uit.no/handle/10037/20517

[17] M. B. Ibrahim and K. A. Gbolagade, 'Performance Comparison of Huffman Coding and Lempel-Ziv-Welch Text Compression Algorithms With Chinese Remainder Theorem', *Univ. Pitesti Sci. Bull. Ser. Electron. Comput. Sci.*, vol. 19, no. 2, pp. 7–12, Dec. 2019, Accessed: Mar. 29, 2023. [Online]. Available: http://bulletin.feccupit.ro/archive/view/2019_2_2.html

[18] M. S. Reza, S. A. Riya, S. A. Alam, and M. A. A. Hossain, 'Study on Text Compression', Feb. 2019, Accessed: Mar. 29, 2023. [Online]. Available: http://dspace.uiu.ac.bd/handle/52243/822

[19] F. BULUT, 'Huffman Algoritmasıyla Kayıpsız Hızlı Metin Sıkıştırma', *El-Cezeri Fen ve Mühendislik Derg.*, vol. 3, no. 2, May 2016, doi: 10.31202/ecjse.264192.

[20] T. A. Rincy and R. Rajesh, 'Preprocessed text compression method for Malayalam text files', *Int. J. Recent Technol. Eng.*, vol. 8, no. 2, pp. 1011–1015, 2019, doi: 10.35940/ijrte.B1806.078219.

[21] R. N. Horspool and G. V. Cormack, 'Constructing word-based text compression algorithms', *Data Compression Conf. Proc.*, vol. 1992-March, pp. 62–71, 1992, doi: 10.1109/DCC.1992.227475.

[22] B. Eren, Ü. Fen, B. Dergisi, and S. Keser, 'An Image Compression Method Based on Subspace and Downsampling', *Bitlis Eren Üniversitesi Fen Bilim. Derg.*, vol. 12, no. 1, pp. 215–225, Mar. 2023, doi: 10.17798/BITLISFEN.1225312.

[23] I. F. Ince, F. Bulut, I. Kilic, M. E. Yildirim, and O. F. Ince, 'Low dynamic range discrete cosine transform (LDR-DCT) for high-performance JPEG image compression', *Vis. Comput.*, vol. 38, no. 5, pp. 1845–1870, May 2022, doi: 10.1007/S00371-022-02418-0/FIGURES/3.

[24] M. ASLANYÜREK and A. MESUT, 'Kümeleme Performansını Ölçmek için Yeni Bir Yöntem ve Metin Kümeleme için Değerlendirmesi', *Eur. J. Sci. Technol.*, no. 27, pp. 53–65, 2021, doi: 10.31590/ejosat.932938.

[25] R. Leelavathi and M. N. Giri Prasad, 'High-Capacity Reversible Data Hiding Using Lossless LZW Compression', *EAI/Springer Innov. Commun. Comput.*, pp. 517–528, 2022, doi: 10.1007/978-3-030-86165-0_44.

[26] J. R. Jayapandiyan, C. Kavitha, and K. Sakthivel, 'Optimal Secret Text Compression Technique for Steganographic Encoding by Dynamic Ranking Algorithm', *J. Phys. Conf. Ser.*, vol. 1427, no. 1, p. 012005, Jan. 2020, doi: 10.1088/1742-6596/1427/1/012005.

[27] M. M. Aşşık and M. Oral, 'Kanonik Huffman kod sözcükleri uzunluklarının evrim stratejileri algoritması ile belirlenmesi', *Gazi Üniversitesi Mühendislik-Mimarlık Fakültesi Derg.*, vol. 38, no. 2, pp. 771–780, 2022, doi: 10.17341/gazimmfd.882745.

[28] M. Varol Arısoy, 'LZW-CIE: a high-capacity linguistic steganography based on LZW char index encoding', *Neural Comput. Appl.*, vol. 34, no. 21, pp. 19117–19145, Nov. 2022, doi: 10.1007/s00521-022-07499-5.

[29] D. Zhang, Q. Liu, Y. Wu, Y. Li, and L. Xiao, 'Compression and indexing based on BWT: A

surveyZhang, D., Liu, Q., Wu, Y., Li, Y., & Xiao, L. (2013). Compression and indexing based on BWT: A survey. Proceedings - 2013 10th Web Information System and Application Conference, WISA 2013, 61–64. https://doi', *Proc. - 2013 10th Web Inf. Syst. Appl. Conf. WISA 2013*, pp. 61–64, 2013, doi: 10.1109/WISA.2013.20.

[30] P. M. Fenwick, 'The Burrows–Wheeler Transform for Block Sorting Text Compression: Principles and Improvements', *Comput. J.*, vol. 39, no. 9, pp. 731–740, Jan. 1996, doi: 10.1093/COMJNL/39.9.731.

[31] D. Kempa and T. Kociumaka, 'Resolution of the burrows-wheeler transform conjecture', *Commun. ACM*, vol. 65, no. 6, pp. 91–98, Jun. 2022, doi: 10.1145/3531445.

[32] 'Alice's Adventures in Wonderland dataset | Kaggle'. https://www.kaggle.com/datasets/roblexnana/alice-wonderland-dataset (accessed May 23, 2023).

Bitlis Eren Üniversitesi Fen Bilimleri Dergisi
BİTLİS EREN UNIVERSITY JOURNAL OF SCIENCE
ISSN: 2147-3129/e-ISSN: 2147-3188
VOLUME: 12 NO: 3 PAGE: 797-807 YEAR: 2023
DOI:10.17798/bitlisfen.1311415

Enhancing Motorway Exit Efficiency: Determining the Ideal Number of Toll Booths

Göker AKSOY[1*]

[1]*Gebze Technical University, Institution of Transportation Technologies, 41400 Gebze, Kocaeli, Türkiye*
(ORCID: 0000-0003-4592-7048)

Keywords: Toll booth, Barrier control, Electronic toll collection, Manual toll collection, Service time.

Abstract

This study presents a model for determining the optimal number of toll booths at barrier-operated motorway exit toll booths in Istanbul, considering mixed traffic conditions and payment methods. In the past decade, Istanbul has experienced rapid growth in its road network due to public-private partnership (PPP) projects. However, despite relatively modest demand, long queues are frequently observed at the exit toll booths of newly constructed PPP motorways, which utilize barrier-controlled toll collection systems. These toll booths offer both electronic toll collection (ETC) and manual toll collection (MTC) options, with MTC users required to come to a complete stop for transactions, while ETC users experience reduced speeds. The presence of mixed payment methods leads to significant interactions between vehicles, resulting in longer service times and limited toll booth capacity. To evaluate the system, service times were measured considering four vehicle classes, payment methods of both the leading and serving vehicles, and whether the serving vehicle needed to wait for money exchange. The findings reveal that based on the current vehicle composition and considering only the utilization of the ETC system, 1.77 toll booths would be required to serve a demand of 1,800 veh/h/lane.

1. Introduction

Istanbul, as a megacity, faces challenges in terms of population growth and land use. To address the increasing demand for transportation, the public-private partnership (PPP) model has been implemented over the past decade, leading to significant transportation projects aimed at expanding the capacity of Istanbul's road network. However, the adoption of high-fee toll roads has not been fully realized. This limited adoption, along with a low user choice ratio, has resulted in constrained demand for the PPP motorway network in Istanbul.

In the context of PPP projects, private organizations initially finance road construction and subsequently charge tolls to recover their costs. To maximize revenue or prevent toll loss, barrier-controlled toll booths with both electronic toll collection (ETC) and manual (cash) toll collection (MTC) systems have been implemented. However, government-operated motorways utilize open tolling systems. In instances where drivers do not possess an ETC system, each exit toll booth is manned by a toll collector. Consequently, the number of operating toll booths fluctuates throughout the day due to the need for toll collectors with the MTC system. As a result, all types of vehicles utilize practically every toll gate, leading to a mixed use of toll booths by vehicles of varying sizes that employ either the MTC or ETC system. Despite the allocation of rightmost toll gates for heavy vehicles, regular cars frequently utilize these toll booths to bypass long queues.

The barrier-controlled exit motorway toll booths pose a significant bottleneck due to factors such as mixed payment options, mixed vehicle usage, and insufficient active toll booths. This leads to

*Corresponding author: gaksoy@gtu.edu.tr
Received: 08.06.2023, Accepted: 19.09.2023

extended delays for users. In general, the low demand for PPP motorways results in minimal or negligible congestion issues, despite the long service times at toll booths. However, during peak travel periods such as the start or end of long public holidays, incidents, road closures, or congestion on alternative routes can cause a surge in demand. This leads to long queues and increased service times, even when all dedicated toll booths are operational. Additionally, the rerouting of heavy-load vehicle traffic to the newly constructed PPP motorways contributes to longer service times for specific vehicle classes. This indicates the need for a reevaluation of the required number of toll booths. Typically, in the PPP motorways of Istanbul, the number of barrier-operated toll booths used to be 2-2.5 times the number of available lanes. For instance, a four-lane motorway would typically have ten toll booths on both the entrance and exit sides. However, this number of toll booths is clearly inadequate for a four-lane motorway with the characteristics mentioned above. Additionally, it is observed that entrance toll booths have statistically shorter service times [1], yet the same number of toll booths have been installed on Istanbul's PPP motorways. Service times are influenced by various external factors, and it is necessary to reconsider either the physical design or the number of toll booths. The objective of this paper is to evaluate the required number of toll booths from this perspective.

In this study, the service times at barrier-operated exit motorway toll booths were measured, and the required number of toll booths was determined by considering various external factors. Given that service times at entry toll booths are significantly shorter [1], this study focuses exclusively on exit toll booths. The service time refers to the duration during which drivers spend paying the toll fee. Technically, the ETC system should have no service time. However, regardless of the payment method, each vehicle needs to decelerate and pass through a physical toll gate equipped with a barrier. Even for ETC payers, a small amount of time is required for electronic payment, transaction procedures, and barrier opening. Thus, service time does exist in the real world, although it is minimal. Consequently, service time measurements were conducted at exit motorway toll booths, considering four different vehicle classes, leader (the vehicle in the front of a line) and serving vehicle (the vehicle at the toll both) payment methods, and whether the serving vehicle needed to exchange money.

Motorway toll booths play a crucial role in ensuring uninterrupted traffic flow for drivers. However, if they are inadequately designed, they can become bottlenecks leading to significant delays and reduced travel comfort. One major contributing factor to bottlenecks in toll booth areas is the lane discontinuity between upstream and downstream directions. The service time, which directly affects capacity and service efficiency, is a critical factor in toll booth operations. Barrier-operated toll booths further exacerbate the situation, intensifying the bottleneck effect [2]. Service times at toll booths vary depending on vehicle class and payment method [3]. Increasing the usage of ETC systems has been shown to decrease queue lengths and delays, thereby improving overall efficiency [4]. Numerous studies have demonstrated the negative impact of barrier-operated toll booths on road safety [5-7] and air pollution [8].

Many researchers have previously covered motorway toll booths from various perspectives. One notable finding is that service times at barrier-controlled toll booths tend to be significantly longer compared to those without barrier control [2]. Additionally, Abdelwahab [9] determined that to alleviate excessive delays, the optimal number of toll booths should range from 14 to 18 when cash payment is used by 50 percent or more of the vehicles, and the hourly demand reaches 4000 vehicles per hour for barrier-controlled toll booths. These studies highlight the importance of considering factors such as payment methods and demand levels when determining the appropriate number of toll booths to ensure efficient traffic flow and minimize delays.

Previous studies have extensively examined various aspects related to toll payment systems, vehicle classes, delays, and queues in the literature. Bari et al. [10] focused on mixed traffic conditions and utilized seven different vehicle classifications to determine the delay experienced by vehicles using the MTC system and queue waiting time found between 5.06 sec to 298.04 sec. Al-Deek [11] found that the exclusive use of the ETC system reduced service times by 5 seconds compared to MTC. Aksoy et al. [12], through a microsimulation study, demonstrated a direct correlation between the number of toll booths and delays. Aycin et al. [13] evaluated the capacity of toll booths with mixed payment options by considering successive pairings of payment types for vehicles, such as MTC-MTC, ETC-MTC, ETC-ETC, and MTC-ETC. Similarly, Bari et al. [14] analyzed the service times of the MTC system in mixed traffic scenarios, considering factors such as follower-leader pairs, vehicle type, and toll rates. Lima et al. [15] found that payment method and the sex of toll booth workers had the most significant influence on service times in the MTC system, along with vehicle type. Navandar et al. [3] developed a methodology for estimating service times in mixed traffic conditions

for seven different vehicle classes, highlighting that as the number of small-sized vehicles in the traffic stream increases, the service time decreases for those vehicles but increases for larger-sized vehicles. Deshmukh et al. [16] investigated service times for MTC systems in mixed traffic scenarios, considering seven distinct vehicle classes.

The comprehensive review of the literature highlights the significance of toll booth areas in terms of service time and capacity considerations, and various external factors. The payment method chosen by users and the presence of a barrier control system have a notable impact on service times. Similarly, user experiences are greatly influenced by increased delays and waiting times in queues. Moreover, the type of vehicle plays a crucial role in determining service times, which directly affects toll booth capacity. Additionally, the payment system and sequential pairings of vehicle payment methods also contribute to the overall operating conditions. The determination of the required number of toll booths was accomplished through the development of a service time estimation model, which took into account four distinct vehicle classes, the payment method of the leading vehicle, the payment method of the serving vehicle, and whether the serving vehicle needed to wait for money exchange (in the case of the MTC system). These data were collected from Istanbul's PPP highways, providing valuable insights for this study.

2. Material and Method

Service times were determined by analyzing video recordings of each payment transaction at the barrier operated Alemdag toll booth which is a part of Istanbul's PPP motorway. A total of 3,264 individual measurements were collected at this toll booth, covering various periods including weekdays and weekends. It is important to note that the data set excluded measurements taken during adverse weather conditions, focusing solely on bright days.

In this study, service time specifically refers to the time required to complete the toll payment transaction at the toll booth. Other factors such as queue waiting times and overall time spent on toll payment are influenced by arrival rates and various external variables. However, for the purpose of this study, the focus is solely on the time spent on the fee transaction itself, regardless of the queue length. The aim is to estimate service times based on the collected external parameters. The observed motorway segment includes four vehicle classifications, as given in Table 1: car (C), medium goods vehicle (MGV), truck & bus (TB), and articulated trucks (AT), with proportions of 70.82 percent, 11.85 percent, 8.24 percent, and 9.09 percent, respectively, out of the total 3,264 observations. ETC payment accounted for 86.73 percent of the transactions, while MTC accounted for the remaining 13.27 percent.

Table 1. Vehicle categories with their specifications.

Vehicle Class	Detail
1: Car (C)	Passenger car, pick-up, jeep, vehicles with up to 4-8 passenger capacity
2: Medium Goods Vehicle (MGV)	Vehicles with 8-25 person passenger capacity and trucks with 3.5 - 5 tonnes in weight
3: Truck & Bus (TB)	Vehicles with high load & passenger transport capability, 8-12 m in length.
4: Articulated Truck (AT)	Higher load capability with 10-18 m in length.

Service times at toll booths are influenced by multiple factors, including the payment amount, toll booth employee experience, payment method, and vehicle type [4]. Notably, there are significant variations in service times between cars and trucks [2]. However, it is worth noting that the literature lacks a standardized definition or implementation of service times. Mahdi et al. [1] measured service times at MTC toll booths as the duration between a vehicle's stop and start while considering ETC transactions to have a service time of zero in their microsimulation study. In contrast, Karim et al. [4] defined MTC service time as the time interval between a vehicle's stop and passing over a barrier. Interestingly, Karim et al. [4] assigned a service time of 5 seconds for ETC transactions. On the other hand, Lima et al. [15] defined MTC service times as the time interval between the start of a transaction and the complete departure of a vehicle. These variations in defining service times highlight the need for a standardized approach in toll booth studies.

Navandar et al. [3] provided a unique definition of service time, considering it as the sum of transaction time and travel time required to cover the vehicle's distance. Building upon this definition, the current study measured MTC service times from the

moment the vehicle stops for a transaction until it completely passes the barrier. As for ETC payments, which do not require vehicles to stop during the fee transaction, service times were determined based on the time taken by vehicles to travel their distance within the payment section. It is important to note that even for ETC customers, service times can be affected by factors such as the delayed opening of a barrier and the long and narrow physical toll booth section. These conditions can result in reduced vehicle speeds and, in some cases, significantly increased ETC service times.

2.1. Descriptive analysis of the data

The measured service times in this study were categorized into eight groups, considering the combination of four different vehicle classes and two payment alternatives, as shown in Table 2. It is observed that MTC service times exhibit a higher level of dispersion, as evidenced by the larger standard deviation of MTC service times. Each group has its distinct pattern, and the coefficient of variation (CV) can be used to assess the spread of the data. The CV for the ETC system ranges between 20.6 and 23.8 percent, while for the MTC system, it ranges between 39.9 and 57.2 percent. Initially, the MTC system appears to have a higher level of variability compared to the ETC system.

Table 2. Descriptive statistics for the service times.

Vehicle Class	Sample Size	Minimum (sec)	Maximum (sec)	Mean	Std. Dev	CV
C - ETC	2051	1.1	5.2	2.42	0.574	0.238
MGV - ETC	336	1.9	6.8	3.27	0.763	0.233
TB - ETC	213	3.0	9.4	4.95	1.077	0.218
AT - ETC	231	4.6	13.3	8.14	1.675	0.206
C - MTC	261	6.1	58.2	22.07	12.638	0.572
MGV - MTC	51	8.3	50.0	21.89	12.372	0.565
TB - MTC	55	10.3	57.0	27.84	11.814	0.424
AT - MTC	66	10.5	66.0	35.66	14.224	0.399

Service times were further analyzed by considering various scenarios experienced by drivers, which go beyond the scope of vehicle classes and payment type combinations. By disregarding vehicle classes, eight distinct main scenarios were identified based on the payment method of both the serving and leader vehicles, as well as whether the serving vehicle waits for money exchange or not. Consequently, three scenarios were observed for ETC payments (E1 to E3), and five scenarios were observed for MTC payments (M1 to M5), as indicated in Table 3.

Table 3. Observed cases from the field.

Case No	Condition	Number of Occurrence	Occurrence Percentage
Case E1	ETC payment. No leader vehicle.	1,925	58.98
Case E2	ETC payment. Leader vehicle makes ETC payments too.	671	20.56
Case E3	ETC payment. Leader vehicle makes MTC payment.	235	7.20
Case M1	MTC payment. No leader vehicle. No money exchange.	384	11.76
Case M2	MTC payment. Leader vehicle makes ETC payment. No money exchange.	12	0.37
Case M3	MTC payment. Leader vehicle makes MTC payments too. No money exchange.	5	0.15
Case M4	MTC payment. Leader vehicle makes ETC payment. Waiting for money exchange.	19	0.58
Case M5	MTC payment. Leader vehicle makes MTC payments too. Waiting for money exchange.	13	0.40
Total		3,264	100.00

During the field observations, a total of eight different cases were recorded, each varying in terms of their occurrence frequency. The most common case, observed frequently, is Case E1, which involves

ETC payments by the serving vehicle without the presence of a leader vehicle. This can be attributed to the widespread adoption of the ETC system. As mentioned earlier, the low demand for PPP motorways contributes to the prevalence of Case E1. Cases E2 and E3, on the other hand, involve the presence of a leader vehicle, either with ETC or MTC payments, and were observed 671 and 235 times, respectively. These cases are relatively less common compared to Case E1.

The MTC system exhibits clear discrimination in terms of service times and toll booth capacity, particularly when the serving vehicle needs to wait for money exchange. Among the observed cases for the MTC system, there are a total of five subcases, with Case M3 being the least common. This implies that instances, where two successive MTC payments are made without waiting for money exchange, are rarely encountered. On the other hand, there are 32 observations in the dataset where vehicles had to wait for money exchange, which can lead to increased service times (Cases M4 and M5). Similar to the ETC cases, the majority of observations fall under Case M1, indicating that 384 separate MTC payments were made by vehicles without the presence of a leader vehicle at the toll booth. This highlights the prevalence of such scenarios within the MTC system.

3. Results and Discussion

To estimate the service time of a single toll booth, a multiple linear regression model is constructed. The model incorporates independent variables such as vehicle class, serving, and leader vehicle payment method, and whether the serving vehicle waits for money exchange. The service time is considered the dependent variable in this model. Since the independent variables are categorical, they are encoded as dummy variables. To determine the coefficients of the model, appropriate reference categories are carefully selected. In this case, AT is chosen as the reference category for vehicle classes, MTC is selected as the reference for both the serving and leader vehicle payment methods, and not waiting for money exchange is chosen as the reference for the money exchange variable. The estimated linear regression model with its calculated parameters can be found in Table 4.

Table 4. Calculated model coefficients with their statistics.

	Unstandardized Coefficients		Standardized Coefficients	t	Sig.	95% Confidence Interval for B		Collinearity Statistics	
	B	Std. Error	Beta			Lower Bound	Upper Bound	Tolerance	VIF
(Constant)	19.216	0.479	-	40.098	0.000	18.276	20.155	-	-
Car (C)	-6.463	0.241	-0.325	-26.780	0.000	-6.937	-5.990	0.381	2.627
MGV (MGV)	-5.604	0.301	-0.201	-18.637	0.000	-6.194	-5.015	0.485	2.063
Truck & Bus (TB)	-3.925	0.326	-0.119	-12.035	0.000	-4.565	-3.286	0.571	1.751
Payment Method (PM)	-9.481	0.346	-0.356	-27.417	0.000	-10.159	-8.803	0.333	3.004
Leader Payment None (LPNo)	-1.059	0.257	-0.053	-4.121	0.000	-1.563	-0.555	0.335	2.986
Leader Payment ETC (LPETC)	-0.826	0.284	-0.038	-2.910	0.004	-1.382	-0.269	0.337	2.968
Money Exchange (ME)	16.821	0.406	0.539	41.431	0.000	16.025	17.617	0.332	3.012

Before discussing the model outcomes, the dummy variables in Table 1 have to be clarified. As mentioned earlier, AT is chosen as the reference category for vehicle classes. Therefore, in the regression model, the C, MGV, and TB variables should be zero to represent the selection of the reference category. For the payment method (PM) variable, MTC is selected as the reference category. There are three different alternatives for the leader payment (LP) variable: MTC, ETC (LPETC), and the absence of a leader vehicle (LPNo). Since the reference category is set to MTC, LPNo will take a value of 1 in the absence of a leader vehicle, LPETC will take a value of 1 when the leader pays with ETC, and both LP coefficients will be zero when the leader pays with MTC. Similarly, for the money exchange (ME) variable, it should be 1 if a serving vehicle is waiting for a money exchange, as indicated by the positive and high coefficient value of ME. Finally, the

service time estimation model is derived using multiple linear regression, as shown in Equation 1.

$$\boldsymbol{ST} = 19.216 + [-6.463 \times C - 5.604 \times MGV - 3.925 \times TB] + [-9.481 \times PM] + [-1.059 \times LPNo - 0.826 \times LPETC] + [16.821 \times ME] \quad (1)$$

In Equation 1, the constant is calculated as 19.216 seconds, and ST represents the service time in seconds. The signs of each coefficient in the regression model should be carefully analyzed. The negative signs for the C, MGV, and TB coefficients indicate that the reference category, AT, has a negative influence on service times. This means that if any of these dummy variables is one, the corresponding vehicle class will have a shorter service time compared to the reference category. Consequently, the reference category (AT) will have the highest service time. When comparing the dummy variables with one another, the C coefficient has the greatest reduction influence on service time compared to TB and MGV, while MGV is placed between them. This suggests that as the vehicle size increases, the service time also increases, regardless of the other parameters included in Equation 1. This finding is further supported by the standardized coefficients column, which represents the relative effect of each variable compared to the others.

The negative sign of the PM coefficient in Equation 1 indicates that MTC has a comparable disadvantage in terms of service times. Since the reference category is MTC, a value of one for PM implies that ETC payment is chosen, resulting in a reduction of service time by 9.481 seconds. In other words, regardless of the other parameters considered in the model, using the ETC system alone leads to a reduction in service time by 9.481 seconds compared to the MTC system.

The negative signs of the LPNo and LPETC dummy variables in Equation 1 demonstrate the disadvantage of the reference category. The presence of a leader vehicle with MTC payment significantly increases service times. On the other hand, when the leader vehicle pays with ETC, it slightly increases service time compared to the absence of a leader vehicle (1.059 > 0.826). Although the difference is relatively small, in real-world situations, service time will likely be lower when there is no leader vehicle ahead of the approaching vehicle. This observation is consistent with the results obtained from the regression model.

Since the reference category is selected as "no waiting for money exchange," the ME dummy variable has the highest and positive coefficient in Equation 1. This indicates that anticipating money exchange will increase the service time of a vehicle. The positive sign of the ME coefficient implies that, when all other factors are ignored, the variable alone increases the service time by 16.821 seconds. This finding highlights the significant impact of waiting for money exchange on overall service times.

Table 4 demonstrates that the model coefficients for all parameters are statistically significant, as indicated by the p-values (<0.05) associated with each independent variable. The tolerance values, which indicate the amount of variability shown by a specific independent variable in the model's collinearity statistics, were all found to be greater than 0.1. A smaller tolerance value would suggest redundancy among variables, but in the estimated model, all tolerance values are greater than 0.1, indicating that each independent variable contributes unique information to the model and that the variance in the dependent variable cannot be fully explained by the other independent variables. Additionally, the variance inflation factor (VIF) values were found to be less than 5, which is generally preferred to avoid issues of multicollinearity. Table 5 provides a summary of the model, presenting these findings.

Table 5. Model summary of service time estimation.

R	R Square	Adjusted R Square	Std. Error of the Estimate	Durbin-Watson
0.904	0.817	0.817	3.867	2.033

Table 5 presents an evaluation of the model's goodness of fit. The R-squared value, which indicates the proportion of variance in the dependent variable explained by the independent variables, is determined to be 81.7 percent. This means that 81.7 percent of the variability in the dependent variable (service times) can be accounted for by the independent variables included in the model. Consequently, it can be concluded that the constructed model is effective in estimating service times based on the selected independent variables.

3.1. Determination of the number of toll booths

The estimated model considers various external factors, including vehicle class, to estimate service times at a single toll booth. Based on Equation 1, service times can be calculated, allowing for the evaluation of the number of toll booths needed under different conditions. To assess this, service times were computed using Equation 1 for the observed cases listed in Table 3. The resulting service times are presented in Figure 1.

For each vehicle class, the shortest estimated service times were determined for cases E1, E2, and E3. The minimum service time for vehicle class C in case E1 is calculated to be 2.21 seconds. However, Figure 1 demonstrates that even when the ETC system is utilized, the vehicle class AT requires a considerably longer service time of 8.67 to 9.73 seconds for cases E1, E2, and E3. These extended service times undoubtedly lead to significant queues and congestion.

Figure 1 illustrates the impact of waiting for money exchange in cases M4 and M5. Interestingly, there are negligible differences between vehicle classes in terms of money exchange anticipation. The shortest calculated service time for these cases is 28.75 seconds for vehicle class C in case M4, while the highest is 36.04 seconds for vehicle class AT in case M5. On the other hand, due to the absence of waiting for money exchange, the service times for cases M1, M2, and M3 are lower compared to cases M4 and M5. Both Figure 1 and Equation 1 demonstrate the influence of vehicle size, waiting for money exchange, and other previously mentioned parameters on service times.

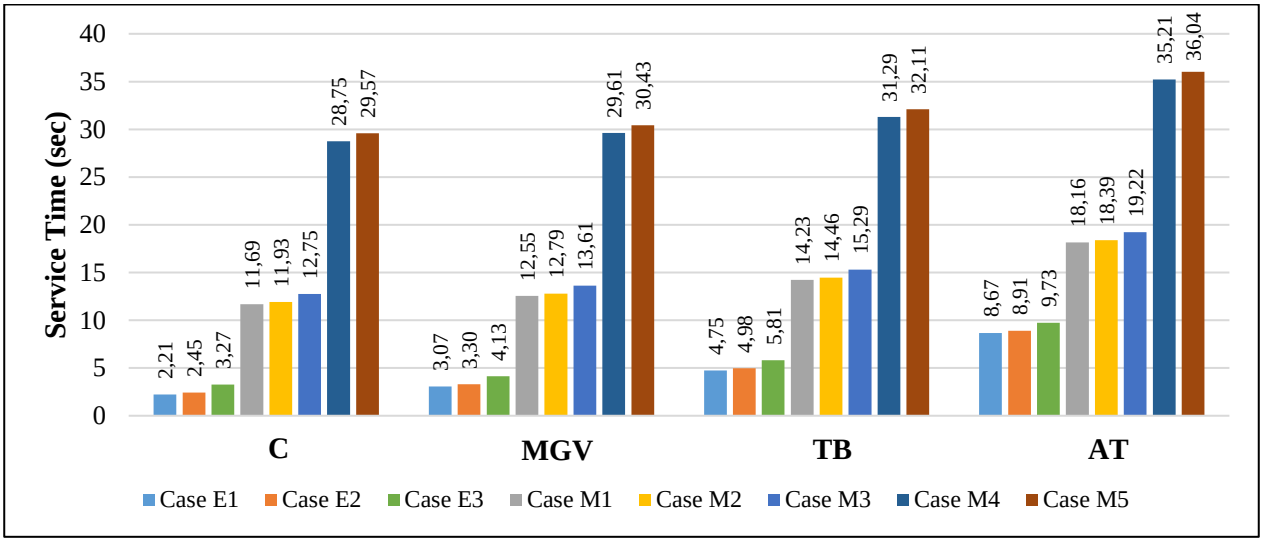

Figure 1. Service time estimates for observed cases.

Indeed, the prevalence of scenarios M1 through M5 at a toll booth will undoubtedly result in longer service times and the need for additional toll booths. Conversely, if the traffic flow primarily consists of cases E1 through E3, a lower number of toll booths might be sufficient. Additionally, vehicle class has a significant impact on service time, with larger-sized vehicles experiencing longer service times. Moreover, the overall volume of traffic on a motorway is a crucial factor in determining the appropriate number of toll booths required. In summary, the vehicle class, occurrence of the eight cases, and the volume of traffic all play a vital role in determining the necessary number of toll booths and managing motorway congestion effectively.

Table 3 presents the frequencies of cases observed during service time measurements, while Table 2 provides the distribution of vehicles across different classes. In this section, Equation 1 has been utilized to investigate the trends in MTC usage and changes in vehicle composition. Consequently, the number of required toll booths was estimated. It was found that only 13.27 percent of vehicles in the observed dataset used MTC, with the remaining composition consisting of 70.83 percent for class C, 11.86 percent for MGV, 8.21 percent for TB, and 9.10 percent for AT. These percentages reflect the proportions of each vehicle class within the dataset.

The computation methodology presented in Table 6 was utilized to calculate the number of toll booths needed. The vehicle arrivals were assumed to be deterministic, without any external stochastic influences. The total required service time was determined based on this assumption, and the number of toll booths required was obtained by dividing the total required service time by 3,600. Table 6 provides an illustrative example scenario, including the observed volume and the existing vehicle composition, to demonstrate the application of the methodology.

Table 6. Calculation procedure.

	Cases		X: Volume considering total volume (veh/h)				Y: Service time for dedicated cases (sec)				X*Y: Total required service duration (sec)				# toll booth
No	**#**	**%**	**C**	**MGV**	**TB**	**AT**	**C**	**MGV**	**TB**	**AT**	**C**	**MGV**	**TB**	**AT**	
E1	1925	58.98	1363.5	228.2	158.1	175.2	2.21	3.07	4.75	8.67	3015	701	751	1520	
E2	671	20.56	475.3	79.6	55.1	61.1	2.45	3.30	4.98	8.91	1162	263	275	544	
E3	235	7.20	166.5	27.9	19.3	21.4	3.27	4.13	5.81	9.73	544	115	112	208	
M1	384	11.76	272.0	45.5	31.5	34.9	11.69	12.55	14.23	18.16	3180	571	449	634	4.23
M2	12	0.37	8.5	1.4	1.0	1.1	11.93	12.79	14.46	18.39	101	18	14	20	
M3	5	0.15	3.5	0.6	0.4	0.5	12.75	13.61	15.29	19.22	45	8	6	9	
M4	19	0.58	13.5	2.3	1.6	1.7	28.75	29.61	31.29	35.21	387	67	49	61	
M5	13	0.40	9.2	1.5	1.1	1.2	29.57	30.43	32.11	36.04	272	47	34	43	
Total	3264	100	2312	387	268	297	-	-	-	-	8708	1790	1690	3038	-
Grand Total	-	-	3264				-	-	-	-	15226				-

To explain the calculation method, consider a total of 3,264 vehicles observed, consisting of 2,312 vehicles in class C, 387 in MGV, 268 in TB, and 297 in AT. It can be assumed that these numbers represent the hourly volume of the toll booth area, along with the observed case occurrences and percentages for each vehicle class. The "Volume" column (X) in Table 6 is computed by multiplying the case percentages with the total hourly volume of 3,264 vehicles. The "Service times for dedicated cases" column (Y) is derived using Equation 1, as shown in Figure 1. The total required service duration (X*Y) is obtained by multiplying the service times by the volume counts for each case and vehicle type. Consequently, the total required service duration is computed for each vehicle class and case. The overall necessary service duration for the provided hourly volume and case percentages is calculated as 15,226 seconds, with 8,708 seconds for class C, 1,790 seconds for MGV, 1,690 seconds for TB, and 3,038 seconds for AT. This means that if the vehicles arrive at the toll booth deterministically over an hour, 15,226/3,600 = 4.23 toll booths would be required for the 3,264 vehicles.

The same computation approach is employed to analyze different vehicle compositions and MTC payment percentages. This allows us to examine and explain the impact of both vehicle classes and the MTC system. Table 7 shows the number of toll booths required for a volume of 1,800 vehicles per hour, considering various vehicle compositions and the percentage of MTC system usage.

Table 7. Required number of toll booths for different vehicle compositions.

Volume (veh/h/lane)	MTC percent	Vehicle composition (percent for vehicle class 1 to 4)					
		Existing	**64-12-12-12**	**55-15-15-15**	**46-18-18-18**	**40-20-20-20**	**25-25-25-25**
1,800	0	1.77	1.91	2.06	2.21	2.31	2.55
	25	3.81	3.95	4.10	4.25	4.34	4.59
	50	5.84	5.99	6.13	6.28	6.38	6.63
	75	7.88	8.02	8.17	8.32	8.42	8.66
	100	9.92	10.06	10.21	10.36	10.46	10.70

In Table 7, the distribution of cases (E1 to M5) is assumed to be equal, unlike the observed case percentages in Table 3. This allows for a more straightforward evaluation of the effects of the MTC system and changes in vehicle composition. For the existing vehicle composition (70.83 percent C, 11.86 percent MGV, 8.21 percent TB, and 9.10 percent AT), it would require 1.77 toll booths if all drivers used ETC (600 vehicles for case E1, 600 for case E2, and 600 for case E3). However, if 100 percent of vehicles (360 vehicles for case M1, 360 for case M2, 360 for case M3, 360 for case M4, and 360 for case M5) used the MTC system, 9.92 toll booths would be needed. The transition from 0 percent to 100 percent MTC usage is quite significant, but the impact on vehicle compositions is less pronounced. The first group, composed of 64 percent C, 12 percent MGV, 12 percent TB, and 12 percent AT, would require

between 1.91 and 10.06 toll booths. The latter group, with equal distribution of vehicles (25 percent each), would require between 2.55 and 10.70 toll booths.

Toll booth capacity needs to be evaluated considering both changes in vehicle composition and the percentage of MTC usage. Therefore Figure 2 is generated by dividing the volume by the required number of toll booths from Table 7. When there is zero percent MTC usage and the existing vehicle composition is considered, the highest toll booth capacity is calculated as 1017 veh/h/lane. However, even if all drivers use the ETC system and vehicle composition is equally distributed among all vehicle classes (25 percent each), toll booth capacity decreases by approximately 30 percent from 1017 to 705 veh/h/lane. As the MTC usage percentage increases, toll booth capacities decrease, and the disparities in vehicle composition become almost negligible. When 100 percent of drivers prefer the MTC system, toll booth capacity is calculated as 181 veh/h/lane for the existing vehicle composition, and it decreases by 7 percent to 168 veh/h/lane for equally distributed (25 percent each) vehicle composition. As MTC usage grows, the differences between vehicle classes diminish significantly.

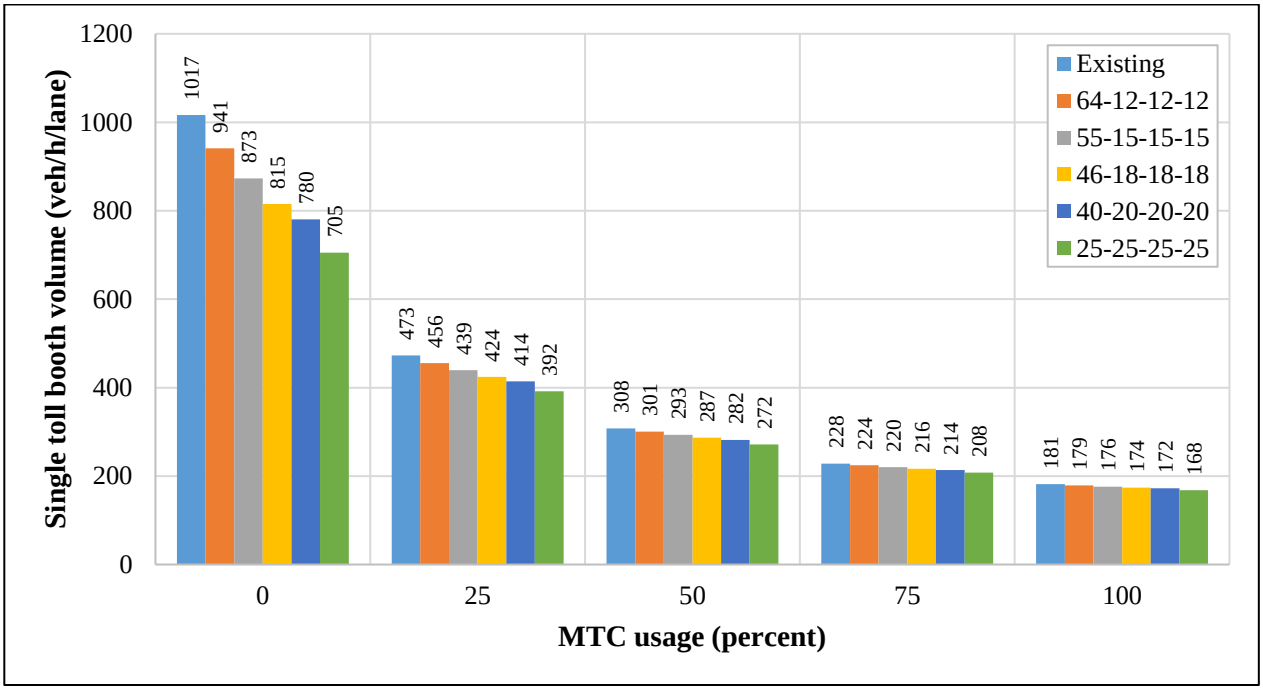

Figure 2. Single toll booth capacities.

Furthermore, the MTC system has a more significant impact on service times (and capacities) compared to changes in vehicle composition. In any scenario, toll booth capacity experiences a substantial decrease, highlighting the inefficiency of the MTC system. However, it is important to note that this model estimates service times for barrier operated toll booths. Even if 100 percent of drivers use the ETC system, at least two toll booths per lane are required for the existing composition because the capacity is lower than the demand (1,800>1,017 veh/h). Additionally, a significant impact on system performance is observed with only 25 percent MTC usage. When 25 percent of MTC is in use, toll booth capacity decreases from 1,017 veh/h/lane to 473 veh/h/lane for the existing vehicle composition, representing a 54 percent capacity loss. Capacity losses for the 50, 75, and 100 percent MTC usage conditions are computed as 70, 78, and 82 percent, respectively, for the existing traffic composition.

4. Conclusion and Suggestions

Motorways offer a seamless and convenient travel experience in exchange for toll fees. Various payment methods are available and widely accepted by motorway users. Advancements in technology have significantly reduced the time required for fee transactions. Electronic payment options enable fast and efficient transactions, eliminating the need for time-consuming cash transactions.

Cash (MTC), near field communications, and radio frequency identification (RFID) technologies are commonly used toll payment methods on motorways. While all these methods serve the purpose of toll collection, the emphasis is on ensuring

uninterrupted traffic flow during the payment process. Although the MTC system is considered outdated for state motorways, it still holds its appeal for fee collection on barrier-controlled public-private partnership (PPP) motorways, primarily due to financial considerations. In mixed traffic scenarios, where both ETC and MTC systems are in use, all vehicles must pass through the same toll booths. This can lead to driver inconvenience and confusion, as they need to make a decision on which toll gate to approach. Moreover, when combined with the presence of a leading vehicle using the MTC system, the complexity and difficulties are further amplified. Therefore, it is important to have a well-designed system in place that considers the required number of toll booths to minimize delays, and queues, and improve the overall level of service.

This article proposes a toll booth calculation model that considers various external variables, including different vehicle classes, payment methods of both the leader vehicle and serving vehicle, and whether the serving vehicle waited for money exchange. The model is developed based on 3,264 field observations, allowing for the calculation of the required service time for each vehicle and the determination of toll booth capacity. By considering the payment method and other relevant external parameters, the model approximates the service time of each vehicle class accurately.

The model provides valuable insights into the service times for different vehicle classes and payment methods. For ETC users without a leader vehicle, cars (C) have a minimum service time of 2.21 seconds, while articulated trucks (AT) have a minimum service time of 8.67 seconds. Medium goods vehicles (MGV) and truck & bus (TB) classes have minimum service times of 3.07 seconds and 4.75 seconds, respectively. In the worst-case scenario, where a vehicle approaches an occupied toll booth, uses MTC as the payment method, and waits for money exchange, the estimated service times are 29.57 seconds for cars (C) and 36.04 seconds for articulated trucks (AT). It is evident that the service times are influenced by both the payment method chosen by the serving vehicle and the leader vehicle's preferred payment method, as well as whether the serving vehicle waits for money exchange. This results in eight distinct cases based on the combinations of leader and serving vehicle payment methods and money exchange anticipation. The best-case scenario for an approaching vehicle is to encounter a completely empty toll booth, while the worst-case scenario involves approaching an occupied toll booth as an MTC user, with MTC payment and the anticipation of money exchange.

Using the developed model, the impact of vehicle composition and variations in vehicle composition is examined. Based on the current vehicle composition (70.83 percent C, 11.86 percent MGV, 8.21 percent TB, and 9.10 percent AT) and considering only the utilization of the ETC system, it is estimated that 1.77 toll booths would be required to serve a demand of 1,800 veh/h/lane. However, this number increases to 2.55 toll booths when the vehicle composition is evenly distributed (25 percent each) across all vehicle classes. As the usage of the MTC system increases, the number of required toll booths also tends to increase. For the existing vehicle composition, if 100 percent of drivers prefer the MTC system, it is estimated that 9.92 toll booths would be required to serve the demand of 1,800 veh/h/lane.

The capacity of a toll booth is directly influenced by service times, which in turn are affected by the percentage of MTC usage and the vehicle composition. Both factors play a comparable role in determining capacity and service times. When all drivers prefer the ETC system, the calculated capacity of a single toll booth is 1017 veh/h/lane for the existing traffic composition. However, for an equally distributed vehicle composition (25 percent for each vehicle class), the capacity decreases to 705 veh/h/lane. In the case where all drivers prefer the MTC system, the toll booth capacities range from 168 to 181 veh/h/lane. Interestingly, even with only 25 percent of drivers using the MTC system, the mixed usage of toll booths by MTC, and ETC customers results in a significant reduction in capacity. For the existing traffic composition, the toll booth capacity decreases to 473 veh/h/lane from the initial 1017 veh/h/lane, representing a 54 percent capacity reduction.

The toll booth areas play a vital role in ensuring efficient and satisfactory journeys for drivers. It is crucial to accurately determine the number of toll booths and design them appropriately to meet the needs of the traffic flow. The study's findings indicate that even with 100 percent ETC usage, service times still exceed 2 seconds. This suggests that to handle the capacity effectively, a minimum of two toll booths per motorway lane is necessary for the C vehicle class alone. It is evident that the precise estimation of the required toll booth number is essential, taking into consideration the projected demand and vehicle composition. In this regard, the presented model provides a clear estimation of the necessary toll booths in such scenarios.

Future research in this field will focus on incorporating the stochastic nature of traffic flow into the analysis. Recognizing the impact of randomness

on the overall system conditions, future efforts will aim to evaluate queue length while considering the stochastic characteristics of traffic flow and delays. Additionally, it will be important to develop estimation models for assessing the level of service in relation to the number of toll booths, taking into account the variability and unpredictability inherent in traffic patterns. By considering these factors, future studies can provide more comprehensive and accurate insights into toll booth operations and their impact on traffic flow.

Conflict of Interest Statement

On behalf of all authors, the corresponding author states that there is no conflict of interest.

Statement of Research and Publication Ethics

The study is complied with research and publication ethics.

References

[1] M. B. Mahdi, L. V. Leong, and A. F. M. Sadullah, "Use of microscopic traffic simulation software to determine heavy-vehicle influence on queue lengths at toll plazas," *Arab. J. Sci. Eng.*, vol. 44, no. 8, pp. 7297–7311, 2019.

[2] T. H. H. Woo and L. A. Ho EL, "Toll plaza capacity and level of service," Trb.org. [Online]. Available: https://onlinepubs.trb.org/Onlinepubs/trr/1991/1320/1320-015.pdf. [Accessed: 07-Jun-2023].

[3] Y. V. Navandar, H. D. Golakiya, A. Dhamaniya, and D. A. Patel, "Vehicle class wise service time prediction models for tollbooths under mixed traffic conditions," *in Urbanization Challenges in Emerging Economies*, 2018.

[4] Y. Liu, H. Liao, Z. Yu, and M. Cai, "Analysis of the operational impact of ETC lanes on toll station," *in ICCTP 2011*, 2011.

[5] H. Yang, K. Ozbay, and B. Bartin, "Effects of open road tolling on safety performance of freeway mainline toll plazas," *Transp. Res. Rec.*, vol. 2324, no. 1, pp. 101–109, 2012.

[6] M. Abuzwidah and M. Abdel-Aty, "Safety assessment of the conversion of toll plazas to all-electronic toll collection system," *Accid. Anal. Prev.*, vol. 80, pp. 153–161, 2015.

[7] M. Abuzwidah and M. Abdel-Aty, "Crash risk analysis of different designs of toll plazas," *Saf. Sci.*, vol. 107, pp. 77–84, 2018.

[8] C.-H. Lai, P.-K. Hsiao, Y.-T. Yang, S.-M. Lin, and S.-C. Candice Lung, "Effects of the manual and electronic toll collection systems on the particulate pollutant levels on highways in Taiwan," *Atmos. Pollut. Res.*, vol. 12, no. 3, pp. 25–32, 2021.

[9] H. T. Abdelwahab, "Traffic micro-simulation model for design and operational analysis of barrier toll stations," *Ain Shams Eng. J.*, vol. 8, no. 4, pp. 507–513, 2017.

[10] C. S. Bari, Y. V. Navandar, and A. Dhamaniya, "Delay modelling at manually operated toll plazas under mixed traffic conditions," *Int. J. Transp. Sci. Technol.*, vol. 11, no. 1, pp. 17–31, 2022.

[11] H. M. Al-Deek, A. A. Mohamed, and A. E. Radwan, "Operational benefits of electronic toll collection: Case study," *J. Transp. Eng.*, vol. 123, no. 6, pp. 467–477, 1997.

[12] G. Aksoy, H. B. Celikoglu, and E. Gedizlioglu, "Analysis of toll queues by micro-simulation: Results from a case study in Istanbul," *Procedia Soc. Behav. Sci.*, vol. 111, pp. 614–623, 2014.

[13] M. Aycin, K. Kiskel, V. Papayannoulis, and G. Davies, "Development of methodology for toll plaza delay estimation for use in travel demand model postprocessor," *Transp. Res. Rec.*, vol. 2133, no. 1, pp. 1–10, 2009.

[14] C. Bari, Y. V. Navandar, and A. Dhamaniya, "Service time variation analysis at manually operated toll plazas under mixed traffic conditions in India," *Journal of the Eastern Asia Society for Transportation Studies*, vol. 13, pp. 331–350, 2019.

[15] J. P. Lima, P. P. A. Inácio, and F. Leal, "Service levels of highway toll plazas: the influence of factors on manual customer service," *Production*, vol. 29, 2019.

[16] M. Deshmukh, Y. V. Navandar, and A. Dhamaniya, "Statistical distribution analysis of clearance time at manually operated toll plazas under mixed traffic conditions", *Proceedings of the Eastern Asia Society for Transportation Studies*, vol. 12, 2019.

Bitlis Eren Üniversitesi Fen Bilimleri Dergisi
BİTLİS EREN UNIVERSITY JOURNAL OF SCIENCE
ISSN: 2147-3129/e-ISSN: 2147-3188
VOLUME: 12 NO: 3 PAGE: 808-821 YEAR: 2023
DOI:10.17798/bitlisfen.1315117

Laboratory Modelling and Analysis of Displacement Pile in Different Geometries on Alluvial Soils

Taylan Ulas DINC[1], Inci DEVELIOGLU[1], Hasan Firat PULAT[1*]

[1]*Izmir Katip Celebi University, Civil Engineering Department, Cigli, Izmir, Turkey*
(ORCID: 0000-0001-7408-3740) (ORCID: 0000-0001-6594-8095) (ORCID: 0000-0002-8298-7106)

Keywords: Alluvial Soil, Cross-section area, Lateral area, Concrete pile, Pile geometry.

Abstract

Alluvial soils are weak soils that require precautions and have disadvantageous engineering characteristics such as low shear strength and bearing capacity, high void ratio, and settlement potential. Different foundation systems are preferred for structures built on these soils to transfer the load effects safely. Pile foundations as deep foundations are classified depending on various parameters such as; material property, application method, and load-bearing method. In this study, cylindrical and square concrete piles with different cross-sections and lateral areas were placed in the alluvial soil. The natural alluvial soil taken from İzmir province, Balatcik location was placed in a displacement-controlled pile model unit with a unit weight of ≈ 17 kN/m3. The manufactured concrete piles were driven into the soil with a Standard Proctor hammer. Tensile effects were applied at different time intervals to examine long-term and short-term behavior. As a result of experiments, load-displacement (p-y) and displacement-time (y-t) graphs were drawn. When the displacement piles were examined under long-term tension, it was seen that the cylindrical piles displaced the most. Square piles with the same cross-sectional area as cylindrical piles made less displacement. All studies were modeled 1:1 as numerical and compared with experimental results. Numerical investigations revealed that under long-term effects, the highest displacements were observed in cylindrical piles, while the lowest displacements were in square piles with equal cross-sectional area as cylindrical piles. Under short-term tension effects, investigations showed that the highest bearing capacity, according to both experimental and numerical results, was in square piles which have an equal cross-sectional area with cylindrical piles. Studies showed that the experimental and numerical results for pile behavior were compatible.

1. Introduction

With the assistance of advancing technology in the contemporary world, safer techniques have started to be employed in the construction of complex structures. Particularly in regions where weak bearing capacity soils are present, urbanization has increased and has contributed to the growth of the population. In terms of geotechnical engineering, alluvial soils, considered problematic and extensively studied by numerous researchers, exhibit distinct behavioral characteristics including weak bearing capacity, high void ratio, and low shear strength [1], [2]. In regions where weak soil layers such as alluvial soils, which are considered geological formations not yet fully formed, are present, there has been an increasing inclination towards deep foundations in planned constructions to ensure structural safety [3], [4], [5]. Pile foundations, which are a type of deep foundation, provide the opportunity for safe designs by transferring the superstructure load to soil layers with high bearing capacity, both under dynamic and static loads, thereby offering support to the superstructure [6]. This allows for secure designs under both dynamic and static loading conditions.

*Corresponding author: hfirat.pulat@ikcu.edu.tr
Received: 15.06.2023, Accepted: 20.09.2023

Piles, in general, is construction element used in situations such as taking part in; weak or compressible soil layers under the foundation, the failure to transfer the horizontal, compression, and tension loads on the foundation safely to the soil layers, the danger of shrinkage in the soil layers, excavation near an existing structure in the future, soil layers that are likely to swell or collapse within the effective depth [7]. Piled systems especially, are encountered in special applications where the structure is under tension loads, such as wind turbine foundations and offshore oil refineries [8] ,[9]. To ensure compliance checks of pile designs, field tests are conducted after construction to measure the performance of the pile. However, this practice can sometimes lead to issues due to time and economic constraints. As a result, numerical and laboratory-based model studies have gained momentum for determining pile behavior depending on various parameters [10], [11].

In studies conducted by various researchers on the behavior of piles under tensile loading, it has been understood that parameters such as; pile installation method, friction mechanism between the pile and the soil, duration of load application, pile surface roughness, and pile dimensions have significant effects on pile behavior [12], [13]. In the method, which is described as displacement pile and causes displacements within the soil during the application, laboratory studies have shown that the effect of the pile-soil friction mechanism increases, leading to a 1.33 times increase in shaft resistance [14]. It has been reported that as the duration of applied load on the pile increases, there is an increase in shaft resistance of the pile and subsequently an increase in pile bearing capacity [15]. This phenomenon highlights the significant role of the friction mechanism in pile behavior. When examining the behavior of piles with different surface roughness under tensile loading, it is observed that there is a proportional relationship between surface roughness and tensile load. Specifically, as the surface roughness of the pile increases, the tensile bearing load of the pile also increases [16].

Behavioral characteristics obtained from laboratory studies are also investigated on computer-based models using the Finite Element Method (FEM), which is a numerical analysis technique [17], [18]. This allows for exploring the behavior of the examined system in a computational environment. The similarity between the obtained laboratory data and the generated model validates the reliability and consistency of engineering designs. Nowadays, numerous engineering software utilize scientific foundations by drawing from existing studies and methods in the literature [19]. This approach helps to establish robust scientific frameworks for these software applications. Hence, the alignment of laboratory study results with models created in a numerical environment holds significant scientific importance.

In this study, the behaviors of concrete displacement piles with different geometries under tensile loading conditions within alluvial soils have been investigated by examining both laboratory and numerical model behaviors. Concrete piles with different cross-sectional properties were placed in a displacement-controlled pile model unit in the laboratory using a Standard Proctor hammer. The study examines the effect of cross-sectional properties on the behavior of piles with equal cross-sectional area and lateral area in different geometries. The importance of the duration of load on pile behavior was explored by analyzing long-term and short-term load effects. The data obtained from laboratory experiments were compared and interpreted with the results from a 1:1 scale experimental system created in a numerical environment.

2. Material and Method

2.1. Alluvial Soil

Alluvial soils are commonly found around geographical formations like rivers and streams. In terms of their composition, alluvial soils can contain clay, silt, sand, gravel, and even organic materials [20]. The alluvial soils used in this study were obtained from the Çiğli-Balatçık region. Çiğli district is located to the north of İzmir and is situated within the edge of the Gediz Delta. Due to the presence of the Gediz River, this region contains significant alluvial soil deposits. The location from which alluvial soils were obtained, the Balatçık region, is depicted in Figure 1.

Figure 1. Alluvial soil location

Alluvial soils were obtained through drilling conducted at İzmir Katip Çelebi University. During the drilling process, soil samples were extracted at every 1.50 meters of depth. These soil samples were packaged and brought to the Geotechnical Laboratory of İzmir Katip Çelebi University for further analysis.

2.2. Concrete Piles

Within the scope of the study, concrete piles with different cross-section properties and geometries were produced. The concrete mortar preparation process was carried out in the laboratories of İzmir Katip Çelebi University according to the relevant regulations and prescriptions. Plywood forms were suitable for predetermined pile dimensions used in the pile manufacture. Plastic pipe material (PVC) was used as a form in the production of cylindrical concrete piles. The information about the piles produced for model studies has been given in Table 1. (L: pile length, L': pile embedded length, D: diameter, L/D: pile length/diameter, L'/D: pile embedded length/diameter).

Table 1. Engineering properties of piles

Pile Type	Cylinder	Square Type 1	Square Type 2
Material	Concrete	Concrete	Concrete
Diameter / Side Length (mm)	45	35	40
L (mm)	400	400	400
L' (mm)	250	250	250
L'/D	5.5	6.3	5.5
L/D	8.9	10.1	8.9
Cross-section area (mm^2)	1600	1225	1600
Lateral area (mm^2)	56550	56000	64000
Frictional lateral area (mm^2)	35340	35000	40000

2.3. Displacement – Controlled Pile Model Unit

Within the scope of the study, a displacement-controlled pile model unit was produced in the laboratory. Plywood formwork materials were used in the manufacture of the pile model unit. During the pile application, horizontal displacements (stretches) were prevented by bonding the unit wall (Figure 2.). In this way, only vertical displacements were allowed to occur. Periodic checks were made to detect out-of-plane deformations that may occur in the pile model unit forms during the experiments. Information about the pile model unit manufactured within the scope of the study has been shown in Table 2.

Figure 2. Displacement-controlled pile model unit

Table 2. Pile model unit information

Parameters	Unit
Material	Timber plywood
Thickness (mm)	20
Width (mm)	400
Length (mm)	595
Height (mm)	577

2.4. Other Equipment

To conduct the tensile tests, a pulley-based tensile testing apparatus was manufactured. This apparatus was manufactured using components such as a steel cage element that was used as a framework, a pulley rail system, Medium-Density Fiberboard (MDF) support pieces, steel hooks, and anchors (Figure 3.).

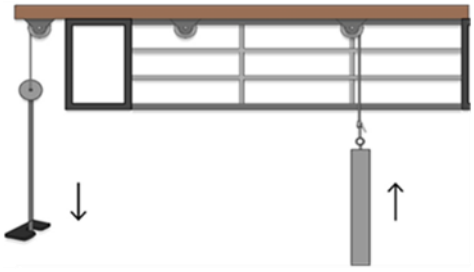

Figure 3. Tensile experiment apparatus

2.5. Laboratory Experiments

In order to determine the geotechnical index properties of alluvial soil; Specific Gravity Test, Fall Cone Test, Plastic Limit Test, Direct Shear Test, Sieve Analysis, Hydrometer, and Proctor Tests were conducted according to regulations. The specific gravity of alluvial soil was determined using the Pycnometer Method [21]. The specific gravity test involved using a 50g sample passing through a No. 4 sieve, along with distilled water and a vacuum pump. Dry and Wet Sieve Analyses were performed to obtain particle size distribution [22] ,[23]. The Hydrometer Test was conducted due to the high fine content of the soil [24]. The Standard Proctor Test was carried out to determine the optimum water content and maximum dry unit weight of the alluvial soil [25]. The results curve from the Standard Proctor Tests were generated using Method A. The Fall Cone Method was conducted to determine the liquid limit values of the alluvial soil [26]. The plastic limit value of the soil was determined using the method specified in the relevant regulation [27]. The soil classification of the alluvial soil was determined using the Unified Soil Classification System (USCS) [28].

2.6. Tensile Behavior Investigation

In order to examine pile behavior in a laboratory setting, various researchers have created small-scale models [29], [30]. The created systems generally consist of a sand tank, pile element, and loading apparatus. In this study, a soil model unit and concrete pile manufacturing were conducted to examine the behavior of piles under tensile effects. Using the established loading and monitoring system, the behavior of the piles under tensile loading was investigated.

Soil unit weight for soil placement in the pile model unit was adjusted at the level of approximately 17 kN/m3 (±0.20)) as the maximum dry unit weight corresponding to the optimum water content obtained as a result of the Standard Proctor Test. Before being placed in the soil model unit, the unit was divided into 50 mm equal layers. Since the target unit weight was 17 kN/m3 (±0.20), the required soil weight for each layer was calculated (Equation 1.).

$$17\frac{kN}{m^2} * 0.05 * 0.04 * 0.0595 * \frac{1000}{9.81\frac{m}{s^2}} = 0.2kN \quad (1)$$

A Standard Proctor hammer was used for the compaction of the soil. To achieve the compaction as described in Equation 1, 10 blows of the Standard Proctor hammer were applied to an area of 0.04 m2. In this way, an application was made by the determined soil unit volume weight. The piles were placed in the displacement-controlled pile model unit using the driving method (Figure 4). Considering the method of application, the piles were displacement piles. The piles placed in the soil were positioned in such a way that the distance from the pile center to the boundary edge in cohesive soils is at least 3 times the pile diameter [31]. During the application of the piles to the soil, it was checked whether there was any inclination in the pile axis at intervals each of 50 mm depth. The experiment was repeated if any inclination was detected during pile driving.

Figure 4. Displacement pile application process

It is known that the soil at the tip of the pile is somewhat compressed during pile placement due to the constant fall energy applied. In order not to affect the experimental results, the displacement-controlled pile model unit was emptied after each displacement pile test. The water content of the samples taken at every 50 mm depth from the test soil was checked. After the losses detected in the water content were compensated, the soil was recompressed and placed in the model unit by the calculations.

During the long-term tensile tests, the test piles were examined under constant stress for 24 hours. After the first 24 hours were completed, the tensile stress on the piles was increased and the displacement values were recorded. Reading of values during tensile tests; 5-minute intervals in the first 6 hours, 15-minute intervals in the 6-12 hour period, and 30-minute intervals in the 12-24 hour period. Pile tension tests were repeated at least 4 times for all piles, and continuity was ensured in the experimental results.

During the short-term tensile tests, incremental loads were applied to the test piles at frequent intervals. The piles were examined for 30 minutes under the applied tensile effects, and the start and end readings were obtained. Behavior results of piles under short-term effects were obtained with the pile tensile test carried out in the laboratory. Information about the short and long-term tensile tests within the scope of the study has been shared in Table 3.

Table 3. Short and long-term loading data

Parameters	Short term loading	Long term loading
Loading type	Tensile force	
Total phases	14	2
Stress duration (min)	30	1440
Stress increments (kPa)	3.1	12.3
Initial stress (kPa)	6.2	18.5
Final stress (kPa)	49.3	30.8

To facilitate comparison and interpretation of the displacement values obtained as a result of the pile tensile tests, normalization was performed (Equation 2). Normalized displacement values were obtained using Equation 2. Given in the formula; Δ (mm) represents the displacement as a result of the tensile effect, D (mm) represents the pile diameter and η represents normalized displacement. Since there are piles with different geometric shapes, the diameter value in the equation is calculated as the equivalent diameter for piles other than cylindrical piles.

$$\eta = \frac{\Delta}{D} \times 1000 \quad (2)$$

2.7. Numerical Analysis

The study system, which was modeled and tested in the laboratory, was modeled as a numerical using finite element method software, and numerical analyses were performed. The analysis model was on a 1:1 scale of the model used in the laboratory. The experimental soil was Mohr-Coulomb, and the experimental piles were modeled as volume elements. Experimental results in the laboratory were used to define the material parameters. The existing concrete parameters (C30) were used by modeling the pile elements with the 'Linear-Elastic' and 'Non-porous' material models accepted in the literature [32]. The model information of numerical analyses has been shared in Table 4. Boundary conditions for the numerical model to be compatible with the real model; the xz-plane was fixed in the y-direction, the yz-plane was fixed in the x-direction, the upper surface was free, and the bottom surface was fixed in all directions. In the analyses, the long-term tensile loads applied to the piles were examined by defining the dynamic function. Short-term tensile effects were defined as point load step by step by increasing the load. The solution of the analysis system was carried out using 'stage construction'. Experimental results were reported by obtaining time-normalized displacement and load-settlement curves.

Table 4. Numerical model information

Numerical Analyses		
Model	Scale	1:1
	Soil Mesh Size (cm)	3.5-4-4.5
	Pile Mesh Size (cm)	3.5-4-4.5
Soil	Material Model	Mohr-Coloumb
	Drainage Type	Drained
Concrete Pile	Pile Model	Volume Element
	Material Model	Linear-Elastic
	Drainage Type	Non-Porous

3. Results and Discussion

3.1. Geotechnical Index Parameters Experiment Results

The shear parameters, specific gravity, particle size distribution, limit values, optimum water content, and unit weight of alluvial soil were obtained through laboratory tests. Based on the test results, it was determined that the alluvial soil exhibits non-plastic (NP) behavior. From tests conducted to determine the particle size distribution of the soil, it was found that the finest content of the soil is 96%, and the soil composition is 5% sand, 25% clay, and 71% silt.

Considering the consistency limit values and particle size distributions, the classification of the alluvial soil was determined as “ML”, which stands for “ fine-grained less sandy, low plasticity clayey silt” according to the Unified Soil Classification System (USCS). The geotechnical parameters of the soil have been presented in Table 5.

Table 5. Alluvial soil geotechnical index parameters

Soil geotechnical parameters	
Liquid limit (LL)	29
Plastic limit (PL)	NP
Plasticity index (PI)	-
Fine content (-No.200) %	96
Maximum dry unit weight (kN/m^3)	17
Natural unit weight (kN/m^3)	19.8
Optimum water content (%)	16.5
Specific gravity (G_s)	2.7
Unified Soil Classification System (USCS)	ML
Cohesion (kPa)	28
Internal friction angle (°)	33

3.2. Pile Tension Test and Numerical Results

The behavior of displacement piles in various geometries with different cross-sectional and lateral areas under the effect of tension was investigated by long and short-term tension tests in the laboratory. Time-displacement curves were drawn to understand the behavior of piles under long-term effects. It aimed to find the ultimate capacities of the piles in the soil with short-term tensile tests. The experimental results were interpreted using the 'Tangent Method', which was accepted as a reliable approach [33]. By using finite element method software, 1:1 scale analyses of the study were carried out in the laboratory environment. Results; time-normalized displacement and load-displacement curves. The results obtained as a result of numerical analyses were compared with the results of experimental studies carried out in the laboratory. The time-dependent experimental normalized displacement values of concrete tension piles with displacement properties under long-term tensile effects have been shown as immediate and long-time displacement with phases in Figures 5, 6, and 7.

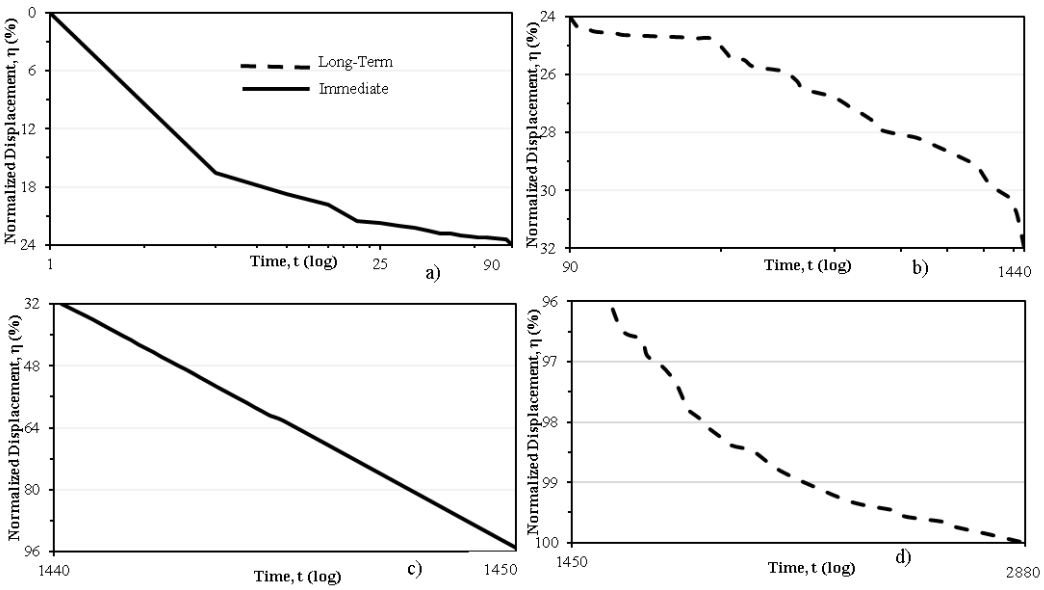

Figure 5. The log(t) – η (%) Curves of Cylinder Piles, a) 1st Phase (Immediate), b) 1st Phase (Long), c) 2nd Phase (Immediate), d) 2nd Phase (Long)

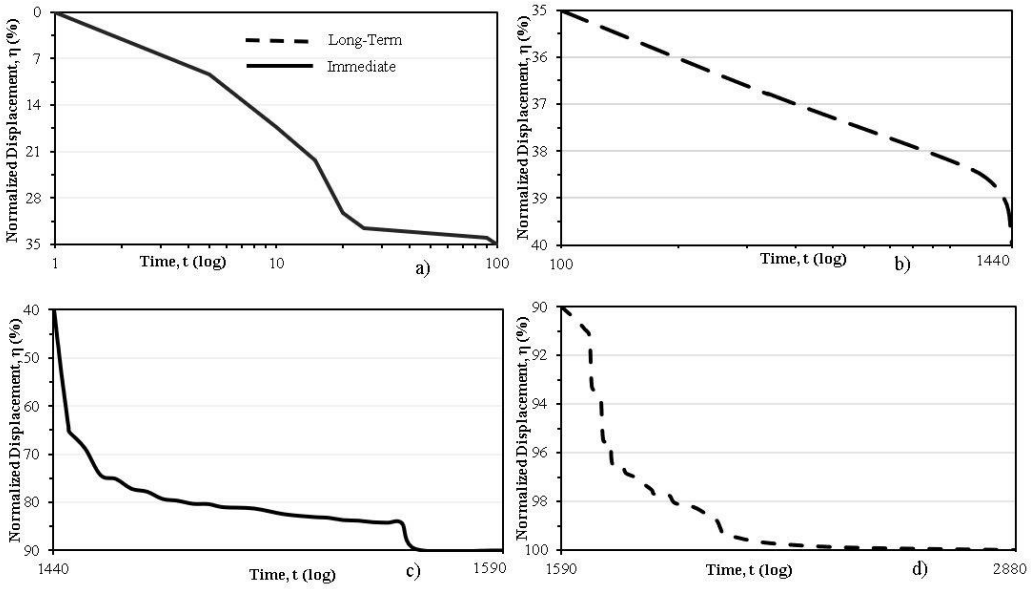

Figure 6. The log(t) – η (%) of 40x40mm Square Piles, a) 1st Phase (Immediate), b) 1st Phase (Long), c) 2nd Phase (Immediate), d) 2nd Phase (Long)

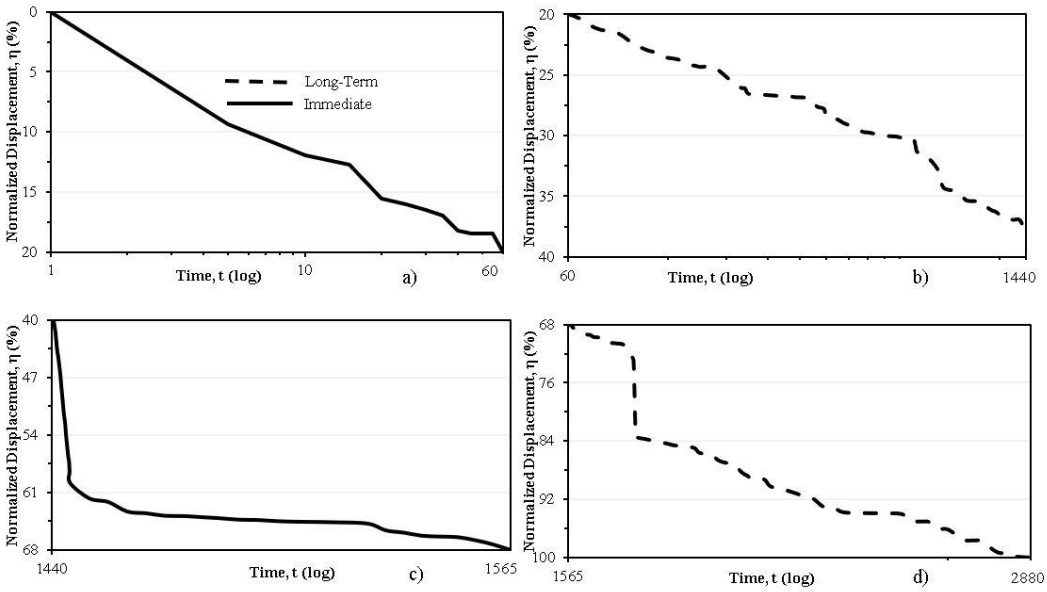

Figure 7. The log(t) – η (%) of 35x35mm Square Piles, a) 1st Phase (Immediate), b) 1st Phase (Long), c) 2nd Phase (Immediate), d) 2nd Phase (Long)

The numerical model results are shown in Figure 8. The data obtained as a result of experimental and numerical analyses were summarized in Table 6. When the time-dependent changes of the normalized displacement values of the piles are examined, it was seen that approximately 25% of the entire displacement occurs, especially in the first 90 minutes following the load increase. When comparing cylindrical and 40x40 mm square displacement piles with an equal cross-sectional area under long-term tension effects, it was revealed that 40x40 mm square piles were exposed to 56% lower displacement.

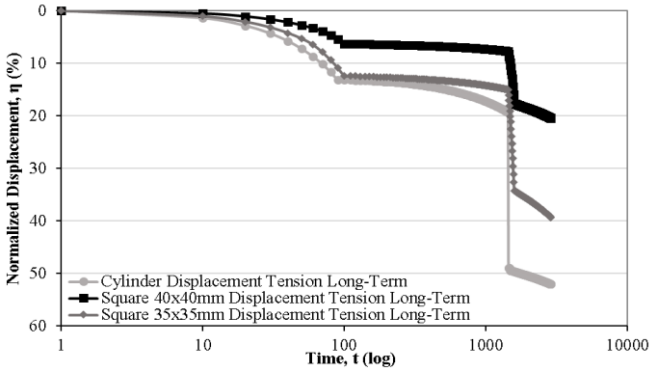

Figure 8. Displacement tension piles numerical results

Table 6. Long-term loading results

Results	Experimental results			Numerical results		
Pile	Cylinder	40x40 square	35x35 square	Cylinder	40x40 square	35x35 square
Tension stress (kPa)	30.84	30.84	30.84	30.84	30.84	30.84
Normalized displacement	48	21	37	52.2	20.2	39.6

It is seen that there were similar behaviors in the studies in the literature on cylindrical and square piles on the determination of the pile-bearing capacity [34]. In this examination, which was carried out by keeping the cross-sectional areas equal, it was understood that the geometric shape has a significant effect on pile behavior. In experimental studies on tension piles of the same geometric shape, it was seen that the increase in the cross-sectional area directly affects the pile-bearing capacity, and the increase in the cross-sectional area was directly proportional to the pile-bearing capacity [35].

When cylindrical and 35x35 mm square displacement piles with equal lateral area were compared, it was seen that 22.9% lower displacement occurs in 35x35 mm square piles. Although cylindrical piles had a larger cross-sectional area compared to 35x35 mm square piles, it was

understood that the geometric effect was one of the determining factors in piles under tension effect.

The short-term test results have been given in Figures 9, 10, and 11. As a result of the load capacity determinations of the cylinder and square piles accepted in the literature within the scope of the experiment, different results were obtained from long-term investigations. According to the test results, piles with cylindrical sections, which were exposed to the greatest displacement in long-term tensile effect, were in second place in terms of load-bearing capacity.

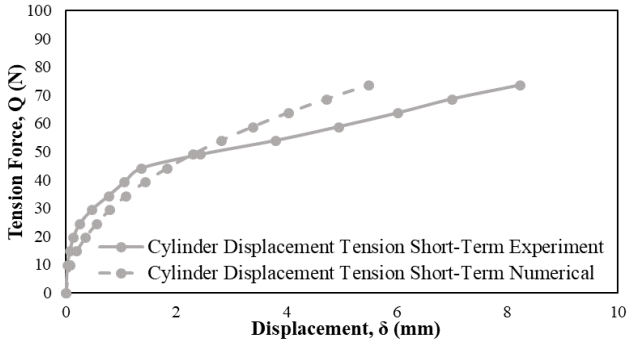

Figure 9. Cylinder displacement piles short-term results

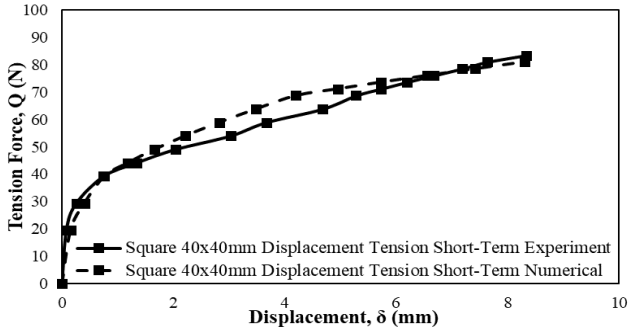

Figure 10. Square (40x40mm) displacement piles short-term results

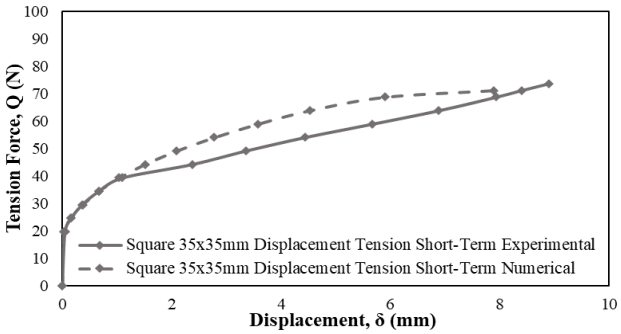

Figure 11. Square (35x35mm) displacement piles short-term results

Low displacement of piles under long-term stress effects compared to piles under short-term effects; could also be explained by the thixotropic property, which was observed in soils with high fine-grain ratio soils. The disturbance of the soil through compaction leads to the alteration of its original structure and can result in sudden drops in its mechanical properties. However, in soils that exhibit thixotropic behavior, ceasing the compaction process can lead to changes in the soil's mechanical properties and a gradual return to its previous strength values [36]. It's known that a significant portion of soils showing thixotropic behavior are constituted by sediment deposits [37].

As a result of numerical model studies, the displacements around the pile caused by the short and long-term tensile effect applied to the piles have been shown in Figures 12, 13, and 14. As indicated in Figures 13 and 14, it could be seen that under the short-term tensile effects of square piles, the acting load cannot spread around the embedded surface of the pile and the surface friction mechanism could not be activated throughout the embedded depth of the pile. In piles under long-term effects, displacements occurred on the pile surface along the pile embedded depth. This indicates that the long-term effects were transmitted to the pile surface perimeter and the effects were countered by spreading over a much larger area.

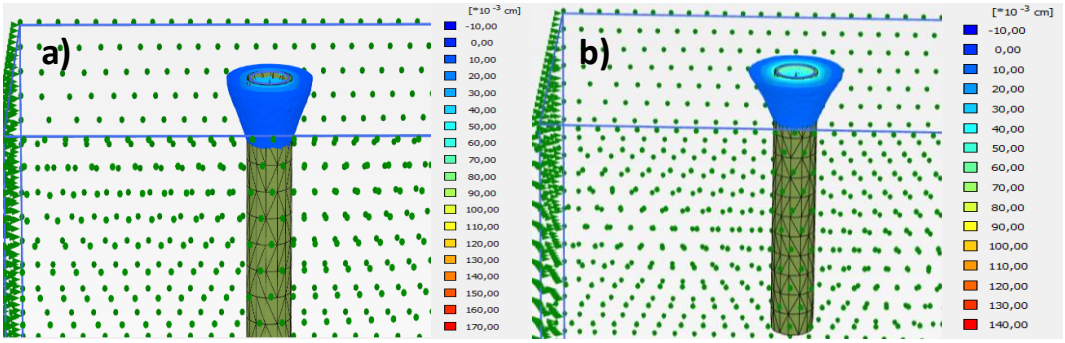

Figure 12. Numerical behavior model of cylinder piles under a) short-term and b) long-term loading

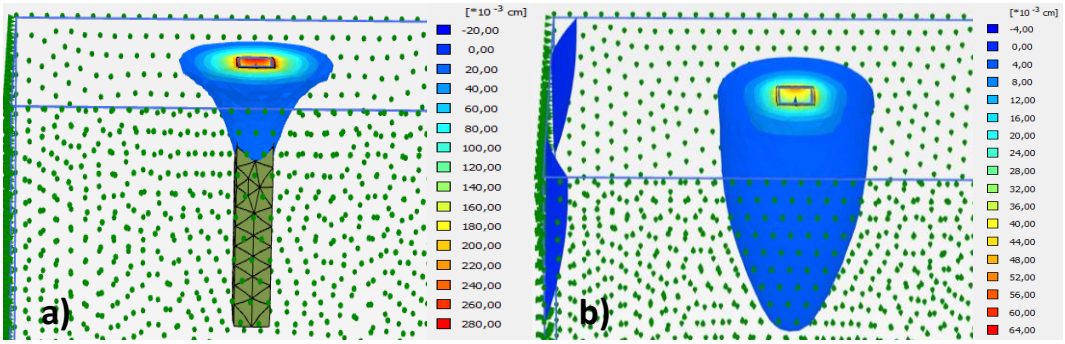

Figure 12. Numerical behavior model of square 40x40mm piles under a) short-term and b) long-term loading

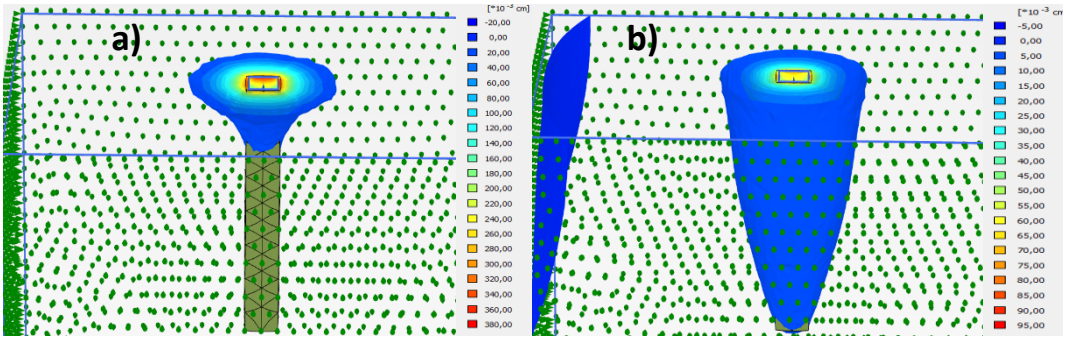

Figure 13. Numerical behavior model of square 35x35mm piles under a) short-term and b) long-term loading

As a result of numerical studies, the soil displacement around different piles, the distribution of soil movement along the length of the pile, and the affected soil surroundings have been examined. The obtained results are presented in Table 7. During the long-term effects, the disturbance range around the pile and disturbance length along the pile have increased compared to short-term loading.

Table 7. Numerical results of soil movement

Pile Type	Short - Term			Long - Term		
	Pile Around Normalized Displacement (η)	Disturbance Range (mm)	Disturbance Length (mm)	Pile Around Normalized Displacement (η)	Disturbance Range (mm)	Disturbance Length (mm)
Cylinder	15.5	250	60	13.33	230	80
40x40 Square	48.78	195	80	8.87	180	270
35x35 Square	65.82	220	120	12.15	180	300

3.3. Discussion

Based on experimental and numerical studies, it has been observed that under long-term tensile effects, the lowest displacements occurred at 40x40 square piles. The results of the numerical analysis support the findings of the experimental studies. When examining the behavior of piles with equal cross-sectional area and equal lateral area, it was observed that cylindrical piles exhibit the highest displacements among the studies.

When examining the effect of cross-sectional properties on the behavior of concrete piles under tensile effects, it was found that the displacement piles with corners had higher tensile load capacities. This observation indicates that the piles with corners exhibit stronger pile-soil interactions due to their shape. The results regarding long-term effects are presented in Table 8.

Table 8. Experimental and numerical comparison of long-term effect

	Equal Cross Section Area		Equal Lateral Area	
Pile	40x40 Square	Cylinder	35x35 Square	Cylinder
Experimental Normalized Displacement, η	21	48	37	48
Square - Cylinder Normalized Displacement Difference (%)	+132.5		+29.7	
Numerical Normalized Displacement, η	20.2	52.2	39.6	52.2
Square - Cylinder Numerical Normalized Displacement (%)	+144		+26.8	
Experimental - Numerical Normalized Displacement Change (%)	-1.06	+3.85	+6.2	+3.85

When comparing the results of pile behavior under short-term effects, it can be observed that 40x40 square-sectioned concrete piles have the highest tensile load capacity. The numerical analysis results were found to be similar to the experimental results. The highest resemblance between experimental and numerical results was observed in cylindrical piles. The results under short-term effects are shared in Table 9.

Table 9. Experimental and numerical comparison of short-term effect

Parameter	Equal Cross Section Area		Equal Lateral Area	
Pile	40x40 Square	Cylinder	35x35 Square	Cylinder
Experimental Q (N)	42	38	36	38
Experimental Q (N) Difference	-9.5		+5.5	
Numerical Q (N)	58	38	44	38
Numerical Q (N) Difference	-34.5		-13.6	
Experimental - Numerical Q (N) Change (%)	+38.1	0	+22.2	0

4. Conclusion and Suggestions

In this study, the behavior of concrete piles with different geometrical properties placed on the soil by the driving method under the effect of tension was investigated. As a result of the experiments, the following results were obtained.

- Studies show that the behavior of piles in long-term applications was different from short-term pile tensile tests. It was understood that the pile-bearing capacity increases with time. It has been observed that the adhesion between the pile surface and the soil increases in direct proportion to time in soils with a high fine grain ratio, and the grains bonding with the pile surface create a surface thickness on the pile surface, improving the surface friction effect over long periods.
- The thixotropic mechanism seen in fine-grained cohesive soils significantly affected the displacement and behavior of the piles depending on the load application time. Under long-term load

effects, the soil gained its initial strength in direct proportion to the time and this mechanism affects the relations between the pile-soil and increased pile bearing capacity.

• When the numerical analyses and experimental study results were compared, the model scale effect was examined. The lab model was a 5.6% scaled version of the field model. In this context, the scale effect directly affected the virtual surface thickness and surface stiffness, especially between the pile surface and the soil. Within the scope of numerical studies, the surface friction coefficient was used by decreasing it by the model scale.

Studies have revealed the effects of tensile load time on pile behavior and the importance of pile geometry. Since there are many parameters affecting the pile behavior, it is understood that results close to the real field behavior will only be possible with experiments to be carried out by focusing on specific points in the laboratory environment. It is understood that the interaction between pile-soil is directly dependent not only on soil shear parameters and pile surface roughness but also on the period of the tension effect and the geometry of the structural pile element. For the pile behavior to converge to the expected behavior in the field, it is of great importance to carry out detailed studies on the scale models to be created in the laboratory environment and to determine the parameters used in numerical analyses specific to the situation.

Contributions of the authors

All authors contributed equally to the study.

Conflict of Interest Statement

There is no conflict of interest between the authors.

Statement of Research and Publication Ethics

The study complies with research and publication ethics

References

[1] E. I. Stavridakis, “Assessment of anisotropic behavior of swelling soils on the ground and 551 construction work,” *in: Al-Rawas AA, Goosen MFA (eds) Expansive soils: recent advances in 552 characterization and treatment*. Taylor and Francis, London, pp. 371-384, 2006.

[2] D. Hyndman and D. Hyndman, “Natural hazards and disasters,” Cengage Learning, 2016.L. Liu and H. Miao, "A specification-based approach to testing polymorphic attributes," in *Formal Methods and Software Engineering: Proc. of the 6th Int. Conf. on Formal Engineering Methods, ICFEM 2004, Seattle, WA, USA, November 8-12, 2004*, J. Davies, W. Schulte, M. Barnett, Eds. Berlin: Springer, 2004. pp. 306-19.

[3] A. K. Yadav, K. Gaurav, R. Kishor, and S. K. Suman, “Stabilization of alluvial soil for subgrade using rice husk ash, sugarcane bagasse ash and cow dung ash for rural roads,” *International Journal of Pavement Research and Technology*, vol. 10, no. 3, pp. 254-261, 2017.T. J. van Weert and R. K. Munro, Eds., *Informatics and the Digital Society: Social, ethical and cognitive issues*: IFIP TC3/WG3.1&3.2 Open Conf.e on Social, Ethical and Cognitive Issues of Informatics and ICT, July 22-26, 2002, Dortmund, Germany. Boston: Kluwer Academic, 2003.

[4] R. Sundaram, S. Gupta, and S. Gupa, “Foundations for tall buildings on alluvial deposits—Geotechnical aspects,” Frontiers in Geotechnical Engineering, pp. 369-393, Springer, Singapore.

[5] M. A. Nunez, L., Briançon, and D. Dias, “Analyses of a pile-supported embankment over soft clay: Full-scale experiment, analytical and numerical approaches,” Engineering Geology, vol. 153, pp. 53-67, 2013.

[6] M. J. Cassidy, B. W. Byrne, and M. F. Randolph, “A comparison of the combined load behaviour of spudcan and caisson foundations on soft normally consolidated clay,” Géotechnique, vol. 54(2), pp. 91-106, 2004.

[7] A. S. Vesic, “Design of pile foundations,” *NCHRP Synthesis of Highway Practice*, vol. 42, 1977.

[8] S. Basack, i, G. Goswam, Z. H.Dai & Baruah, P. “Failure-mechanism and design techniques of offshore wind turbine pile foundation: Review and research directions”. *Sustainability*, vol. 14, no. 19, p. 12666, 2022.

[9] Chandrasekaran, S. *Advanced marine structures*. CRC Press, 2015.

[10] A. I. Al-Mhaidib "Experimental investigation of the behavior of pile groups in sand under different loading rates". *Geotechnical & Geological Engineering*, vol. 24, no. 4, p. 889, 2006

[11] K. Zarkiewicz, "Laboratory experiment of soil vertical displacement measurement near an axially loaded pile". *In IOP Conference Series: Materials Science and Engineering* Vol. 603, No. 3, p. 032012. IOP Publishing, 2019.

[12] F. S. Tehrani, F. Han, R. Salgado, M. Prezzi, R. D. Tovar, and A. G. Castro, "Effect of surface roughness on the shaft resistance of non-displacement piles embedded in sand," *Géotechnique*, vol. 66, no.5, pp. 386-400, 2016.

[13] W. R., Azzam & M. Al Mesmary, "The behavior of single tension pile subjected to surcharge loading". *NED Univ. J. Res*, vol. 7, no.1, pp. 1-12, 2010.

[14] A. S. Alawneh, A. I. H. Malkawi, & H. Al-Deeky, "Tension tests on smooth and rough model piles in dry sand" *Canadian geotechnical journal*, vol. 36, no. 4, pp. 746-753, 1999.

[15] J. Yannie, & C. Alén, "Field test of tension piles: on the long-term behaviour. Forskningsrapporter: tillämpad mekanik," 2015.

[16] R. Saravanan, P. D. Arumairaj, & T. Subramani, "Experimental model study on ultimate uplift capacity of vertical pile in sand". *Water and Energy International*, vol. 60, no. 1, pp. 58-66, 2017.

[17] S. F.Masouleh , & K. Fakharian, "Application of a continuum numerical model for pile driving analysis and comparison with a real case". *Computers and Geotechnics*, vol. 35, no.3, pp. 406-418, 2008.

[18] Tolun M., Laman M., *Eksenel yüklü tekil kazığın farklı yöntemlerle sayısal analizi*, Adana, 2006.

[19] Plaxis 2D-3D Scientific Manual, Bentley Advancing Infrasturcture

[20] EI. Stavridakis Assessment of anisotropic behaviour of swelling soils on ground and 551 construction work. *In: Al-Rawas AA, Goosen MFA* (eds) Expansive soils: recent advances in 552 characterization and treatment. Taylor and Francis, London, pp. 371-384, 2006.

[21] ASTM D854/D854-14, "Standard Test Methods for Specific Gravity of Soil Solids by Water Pycnometer," ASTM International, American Society for Testing and Materials, West Conshohocken, PA, 2014.

[22] ASTM D 6913 – 14: Standard Test Methods for Particle-Size Distribution (Gradation) of Soils Using Sieve Analysis. ASTM International, West Conshohocken, PA,USA;2009. [23] Plaxis 2D-3D Scientific Manual, Bentley Advancing Infrasturcture

[23] ASTM D 422 Standard Test Method for Particle-Size Analysis of Soils ASTM International, West Conshohocken, PA, ASTM International;2020. [25] Plaxis 2D-3D Scientific Manual, Bentley Advancing Infrasturcture

[24] ASTM D7928-16, Standard Test Method for Particle-Size Distribution (Gradation) of Fine-Grained Soils Using the Sedimentation (Hydrometer) Analysis, ASTM International, West Conshohocken, PA, 2016. [19] Plaxis 2D-3D Scientific Manual, Bentley Advancing Infrasturcture

[25] ASTM D 698-12: Standard Test Methods for Laboratory Compaction Characteristics of Soil Using Standard Effort. ASTM International, West Conshohocken, PA, USA ;2021.

[26] British Standard Institution BS 1377-1: Methods of test for soils for civil engineering purposes, London, UK. ; 2016.

[27] ASTM D4318-10 Standard Test Methods for Liquid Limit, Plastic Limit, and Plasticity Index of Soils. ASTM International, West Conshohocken, PA, USA ;2021

[28] ASTM D2487/D2487-11, "Standard Practice for Classification of Soils for Engineering Purposes (Unified Soil Classification System)," ASTM International, American Society for Testing and Materials, West Conshohocken, PA, 2011.

[29] Al-Mhaidib, A. I. "Experimental investigation of the behavior of pile groups in sand under different loading rates" *Geotechnical & Geological Engineering*, vol. 24, no. 4, p. 889, 2006.

[30] Nasr, A. M., Azzam, W. R., & Ebeed, K. E., "Bearing Capacity of Defective Reinforced Concrete Pile in Sand-model Study" *Advances in Geological and Geotechnical Engineering Research*, vol. 4, no. 3, pp. 1-11, 2022.

[31] K. W. Brown, *Design and Construction with the 2006 International Building Code*, Foundation Engineering Handbook, 2nd ed., McGraw-Hill Book Co., California, 2006.

[32] PLAXIS 2D Reference Manual, 2022, p. 157.

[33] M. Olgun, Y. Yenginar, and A. Hanati, "Interpreting Load-Settlement Curves of Pile Foundations by Graphical Methods," *Eurasian Journal of Civil Engineering and Architecture*, vol. 1, no. 2, pp. 1-10, 2017.

[34] J. M. Abbas and H. Q. Ibrahim, "The effect of pile cross section on the lateral behavior of piles under combined loading," *Journal of Engineering Science and Technology Review*, vol. 11, no.3, pp. 174-179, 2018.

[35] Y. Lai and G. F. Jin, "Uplift behavior and load transfer mechanism of prestressed high-strength concrete piles," Journal of Central South University of Technology, vol. 17(1), pp. 136-141, 2010.

[36] S. W. Jeong, J. Locat, J. K. Torrance, and S. Leroueil, "Thixotropic and anti-thixotropic behaviors of fine-grained soils in various flocculated systems," Engineering Geology, vol. 196, pp. 119-125, 2015.

[37] Boswell, P. G. H. (1948). A preliminary examination of the thixotropy of some sedimentary rocks. Q. J. Geol. Soc. 104, 499–526. doi: 10.1144/GSL.JGS.1948.104.01-04.23

Bitlis Eren Üniversitesi Fen Bilimleri Dergisi
BİTLİS EREN UNIVERSITY JOURNAL OF SCIENCE
ISSN: 2147-3129/e-ISSN: 2147-3188
VOLUME: 12 NO: 3 PAGE: 822-828 YEAR: 2023
DOI:10.17798/bitlisfen.1317907

Freezing and Thawing Resistance of Hemp Fiber Reinforced Clays

Zeynep Neşe KURT ALBAYRAK[1*], Bahattin ÖZDEMİR[1]

[1]*Atatürk Üniversitesi, Mühendislik Fakültesi, İnşaat Mühendisliği Bölümü, Erzurum.*
(ORCID: 0000-0002-6323-8652) (ORCID: 0000-0002-8854-7160)

Keywords: Clay, Freezing-thawing, Hemp fiber, Soil stabilization, Unconfined compressive strength.

Abstract

Clays are natural soils. In geotechnical engineering, clayey soils are problematic because of their volume-change properties when they interact with water. Additionally, they may lose strength when exposed to freezing and thawing. Various soil improvement methods are used to modify the clay soil's properties. One of these methods is by adding natural fibers. The aim of the study was to investigate the strength and freezing-thawing properties of a high-plasticity clay (CH) with hemp fiber. For this purpose, fiber-reinforced clay samples were prepared by adding hemp fiber at different percentages (0.5%, 1%, and 1.5%) and different lengths (2 mm, and 5 mm) to a CH clay from Erzurum, Turkey, and the consistency, unconfined compressive strength (UCS), and freezing-thawing properties of the samples were investigated. According to the consistency limits test results, liquid limit values increased as the fiber length and the hemp fiber addition ratio increased, and the plastic limits of the specimens varied depending on the hemp fiber addition. The unconfined compressive strength of the samples increased with the increase in the hemp fiber percentage, and improvements occurred in their unconfined compressive strengths after four freezing-thawing cycles compared to unreinforced clay. According to the test results, it is thought that hemp fibers could be an alternative for improving the freezing and thawing resistance of clay soils.

1. Introduction

The clay soils frequently encountered in geotechnical engineering are problematic because they display plastic behavior and because of their water absorption, shrinkage, swelling, and settlement properties. Additionally, freezing-thawing is also an important problem, especially on the clays in cold climatic regions. After freezing-thawing cycles, due to the change in soil structure, the soil's strength decreases [1]. Eliminating the unfavorable properties of problematic clay soils and improving their engineering properties have played an important role in geotechnical engineering. For this purpose, waste materials like fly ash, silica fume, lime, red mud, ground glass, and marble powder may be used as additives to modify the engineering properties of clay soils [2], [3], [4], [5].

Other materials used to improve clay soils include natural fibers. In the past, researchers looked at how coconut coir, rice straw, and Cannabis sativa fibers could be used in the field. They found that the natural fibers made from these plants improved tensile strength [6], [7]. Prabakar and Sridhar [8] used sisal fiber at different lengths and percentages as a reinforcement material for soils and investigated the strength properties. The triaxial compression test results showed that sisal fiber improves the strength of soils [8]. Güllü and Khudir [9] have treated fine-grained soil with jute fiber, steel fiber, and lime. And it was mentioned that adding jute fiber to low-plasticity clay improves the strength behavior after freezing-thawing cycles [9]. Hemp is a natural fiber that is extracted from the stalk of cannabis plants (Cannabis sativa). Cannabis is a ligneous plant from the family of Cannabinaceae, and its annual fiber

*Corresponding author: znkurt@atauni.edu.tr
Received: 21.06.2023, Accepted: 06.09.2023

yield is quite high; its homeland is Asia [10]. It is an annual plant with a height of 1-5 m, having generally single and specific leaves, and it is grown in fields with a high nitrogen content [11]. Natural hemp fiber is biodegradable and widely recyclable [12]. Ammar et al. [13] and Ammar et al. [14] conducted direct shear tests and single fiber pullout tests on the hemp fiber-reinforced sandy clay soils to investigate the interface shear strength between sandy clay and natural hemp fibers. The researchers thought that hemp fibers have a high water absorption capacity, and this could affect the clay-fiber interface [13], [14]. Najjar et al. [15] have conducted unconsolidated, undrained triaxial tests on the hemp fiber-reinforced clays to improve the load response of compacted clays. According to test results, the undrained shear strength of the hemp fiber-reinforced clays increased with hemp fiber content [15]. Abou Diab et al. [16] used hemp fiber to improve the strength properties of natural clay and indicated that hemp fibers improve the shear strength of compacted clay. With the addition of hemp fibers, clay gained a ductile structure [16].

There are scarcely any studies in the literature researching the effects of the freezing-thawing effect on the hemp fiber-reinforced clays. The aim of this study is to indicate the potential usability of natural hemp fiber in improving the freezing-thawing resistance of high-plasticity clays. In this study, natural clay from Erzurum, Turkey, was reinforced with hemp fiber in different lengths (2mm, 5mm) and percentages (0.5%, 1%, 1.5%) to show the effect of hemp fiber on the geotechnical properties of the clay. Tests of the consistency limits, unconfined compressive strength, and freezing-thawing properties were conducted on the clay specimens. Then the same tests were conducted on the clay specimens reinforced with hemp fiber. The test results obtained from the clay specimens reinforced with hemp fiber were compared with the results obtained with clay.

2. Material and Method

2.1. Clay

In the study, a clay specimen (C) from Erzurum, Turkey, was used. After the clay was brought to the laboratory, it was dried for 24 hours at 105 °C in an oven, ground in a Los Angeles abrasion device, and sieved through a number-40 sieve before being used in the tests. Some geotechnical properties of the clay are seen in Table 1, and its chemical content, determined by X-ray fluorescence (XRF) analysis, is seen in Table 2. The clay specimen's mineral content was determined to be quartz, plagioclase, clay mineral, and calcite. The clay's soil class was found to be high plasticity clay (CH) according to the Unified Soil Classification System (USCS).

Table 1. Geotechnical properties of the clay [17]

Geotechnical Properties	Clay
Clay content (< 0.002 mm) (%)	42
Specific gravity	2.64
Liquid limit (%)	60.8
Plastic limit (%)	26.5
Plasticity index (%)	34.3
Soil classification	CH
Optimum moisture content* (%)	25.5
Maximum dry unit weight* (kN/m^3)	15

*The results were obtained from samples compacted with standard proctor energy.

Table 2. Chemical composition of the clay (XRF analysis)

Item	Clay
SiO_2	59.3
Al_2O_3	16.5
Fe_2O_3	8.0
MgO	2.1
K_2O	1.6
CaO	1.5
Na_2O	1.4
TiO_2	0.6
P_2O_5	0.2
MnO	<0.1
SO_3	-
LOI	8.50

2.2. Hemp Fiber

The commercial hemp fiber (H) was supplied from a local hardware store in Erzurum. In the literature, it is seen that fibers were used in different lengths for the stabilization of soils [7], [16], [25]. In this study, hemp fiber was cut into lengths of 2 and 5 mm and used in the tests. Hemp's specific gravity is 1.50, and its moisture content is 10%. Table 3 and Table 4 list the chemical content and physico-mechanical properties of the hemp fiber, respectively. Figure 1 shows the appearance of the clay and hemp fiber used in the tests.

Table 3. The chemical composition of hemp fiber [18]

Item	Cellulose (%)	Hemi-cellulose (%)	Lignin (%)	Wax (%)
Hemp	70.2-74.4	17.9-22.4	3.7-5.7	0.8

Table 4. Physico-mechanical properties of hemp fiber [19]

Properties	Values
Tensile Strength (MPa)	690
Young's Modulus (GPa)	70
Elongation at break (%)	1.6

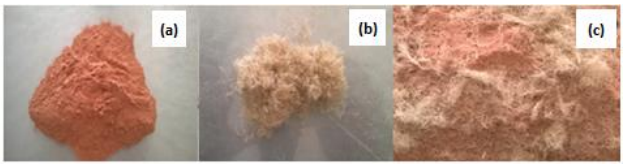

Figure 1. The materials (a) Clay, (b) Hemp fiber, (c) Hemp fiber-clay mixture

2.3. Preparation of Specimens

Cut hemp fiber was mixed with finely ground CH clay in amounts of 0.5%, 1%, and 1.5% of the weight of the clay. The mixture was then mixed evenly to make hemp fiber-reinforced clay specimens. The hemp fiber ratios have been chosen according to the literature focused on the natural fiber-reinforced clays [7], [25]. Figure 1 (c) shows the appearance of hemp fiber-reinforced clay. The addition percentages used in preparing the specimens are recorded in Table 5. Three identical specimens were prepared from each additive percentage.

Table 5. Additive percentages

Sample	Hemp fiber (%)	
	2 (mm)	5 (mm)
C	-	-
H1	0.5	-
H2	1	-
H3	1.5	-
H4	-	0.5
H5	-	1
H6	-	1.5

2.4. Testing Procedures

Liquid limit, plastic limit, unconfined compressive strength, and freezing-thawing tests were conducted on the clay and hemp fiber-reinforced clay samples. Liquid limit tests were conducted on the specimens through the fall cone method according to BS 1377, Part 2 [20]. Plastic limit tests were conducted on the samples according to ASTM D 4318 [21].

Unconfined compressive strength and freezing-thawing tests were conducted on 35 mm diameter and 70 mm height reinforced clay samples taken from specimens compacted under standard Proctor energy at the optimum moisture content of the clay specimens according to ASTM D 2166 [22]. In the freezing-thawing tests, to protect the water content of the prepared samples, the samples were wrapped in aluminum foil before they were put into the automatic freezing-thawing cabin. Additionally, vaseline has been used to prevent aluminum foil from adhering to samples. The number of cycles in the freezing-thawing tests was four, the temperature values were -20 °C for freezing and +25 °C for thawing, and the time interval selected for each process was six hours [23], [24]. The unconfined compressive strength values after freeze-thaw cycles were determined on the specimens taken from the cabin after the freezing-thawing cycles.

3. Results and Discussion

3.1. The Results of Consistency Limits Tests

Hemp fiber has a high water absorption capacity [13]. Table 6 shows the values of the liquid limits of the hemp fiber-reinforced clay specimens as measured by the increase in hemp fiber percentage. Liquid limit values increased as the fiber length (2 mm and 5 mm) and the hemp fiber addition ratio increased. It is thought that the increase in the liquid limit with the increase in fiber length and percentage is due to the high absorption capacity of hemp fiber. Due to the higher absorption capacity of hemp fiber, hemp fiber-reinforced clay specimens absorb more water, and the liquid limit values are increased. Furthermore, the plastic limits of the specimens varied depending on the hemp fiber addition. The consistency limits test results showed that the CH soil classification of clay changed to MH with hemp fiber addition according to USCS (Table 6).

Table 6. Consistency limits test results of specimens

	Liquid Limit (%)	Plastic Limit (%)	Plasticity Index (%)	Soil Classification
C	60.8	26.5	34.3	CH
H1	67.8	39.1	28.7	MH
H2	68.8	41.2	27.6	MH
H3	71.2	35.8	35.4	MH
H4	69.2	36.0	33.2	MH
H5	70.8	39.2	31.6	MH
H6	71.3	42.3	29.0	MH

3.2. The Results of UCS Tests

Figure 2 shows the values measured for UCS in the hemp fiber-reinforced clay specimens with the increase in hemp length and hemp percentage. The

specimens conducted to unconfined compression strength tests have been presented in Figure 3.

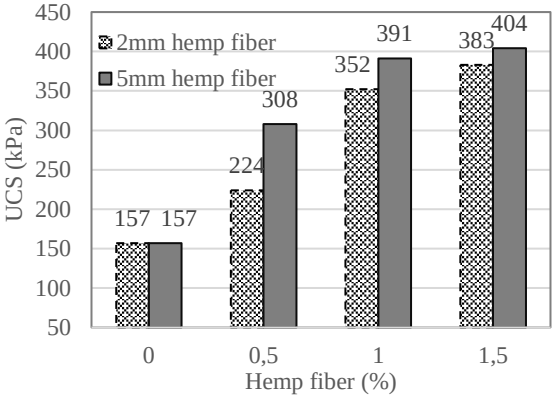

Figure 2. UCS values measured in the hemp fiber-reinforced clay specimens with increases in hemp length and hemp percentage

Figure 2 shows that the 2-mm hemp fiber-reinforced clay's unconfined compressive strength increased by 42.6%, 124%, and 144% when the hemp ratio was 0.5%, 1%, and 1.5%, respectively, compared to the clay's UCS (when the hemp ratio was 0%). The 5-mm hemp fiber-reinforced clay's UCS increased by 96%, 149%, and 157% compared to the clay's UCS when the hemp ratio was 0.5%, 1%, and 1.5%, respectively (Figure 2). The increase in strength with increasing hemp fiber percentage and hemp fiber length means there is good interaction between clay and hemp. The hemp fiber structure prevents the fiber from slipping into the clay, which increases its strength. Similarly, Sharma et al. [7] demonstrated that fibers increased the compressive strength of soils, and they attributed that behavior to better soil-fiber interaction and the resultant bond that did not allow slippage of fibers over each other.

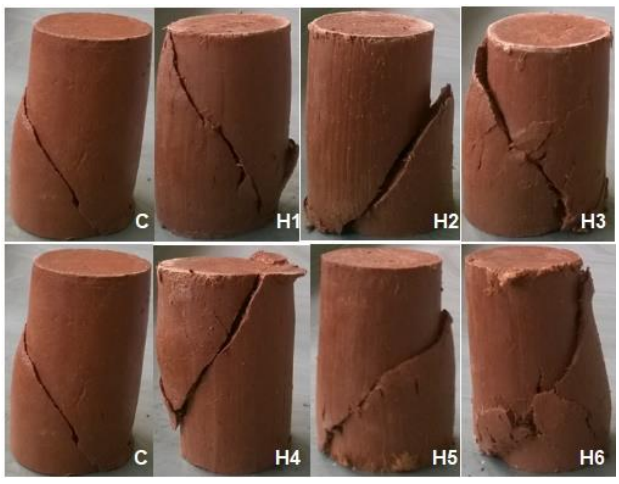

Figure 3. Specimens after UCS tests

The failure plains of samples have been obtained along the shear planes at an angle because of the ductility of hemp fiber (Figure 3). Similarly, Güllü and Khudir [9] found that the failure planes in the specimens reinforced with jute fiber have been obtained along the shear planes at an angle varying from 0 to 70° due to the ductility of jute fiber. Additionally, they thought that jute fiber being stretched still provides resistance; hence, post-peak strength retention is also increased.

3.3. The Results of Freezing-Thawing Tests

Figure 4 illustrates the variations that occurred in the UCS of hemp fiber-reinforced clay specimens after freezing-thawing tests. According to Figure 4, the UCS of the hemp fiber-reinforced clay specimens after freezing and thawing increased with increasing fiber percentage. The UCS values after freezing-thawing cycles of the 2-mm hemp fiber-reinforced clay increased by 20%, 178.8%, and 208.2% compared to the clay when the hemp fiber ratio was 0.5%, 1%, and 1.5%, respectively. Similarly, the UCS values after freezing-thawing cycles of 5-mm hemp fiber-reinforced clay increased by 144.7%, 183.5%, and 193% compared to the clay when the hemp fiber ratio was 0.5%, 1%, and 1.5%, respectively.

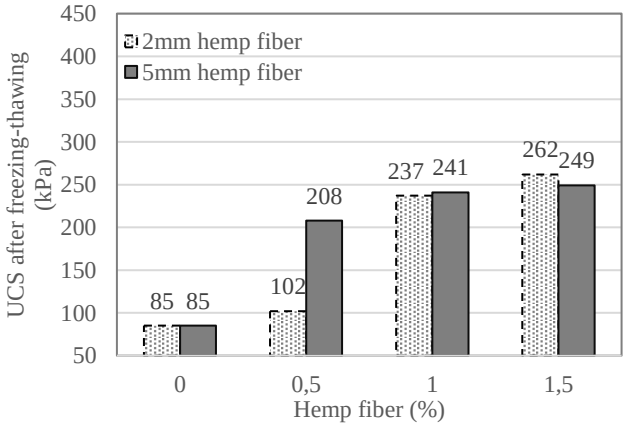

Figure 4. UCS values of the hemp fiber-reinforced clay specimens after freezing-thawing tests

In comparisons of the UCS of the hemp fiber-reinforced clay specimens (Figure 2) with their UCS after freezing-thawing tests (Figure 4), it is obvious that the UCS after freezing-thawing was lower. The clay specimen lost 45.8% of its strength after freezing-thawing cycles. The 2-mm 1.5% hemp fiber-reinforced clay specimen lost 31.6% of its strength after freezing-thawing cycles, and the 5-mm 1.5% hemp fiber-reinforced clay specimen lost 38.4%. The specimens subjected to the UCS tests after freezing-

thawing cycles have been presented in Figure 5. It is seen that with freezing and thawing, the failure mechanisms of samples have changed. Wei et al. [27] indicated that with freezing and thawing, the failure patterns of soils transformed from brittle failure to plastic failure, and the cracks were thin and short. Additionally, it is thought that freezing and thawing cycles can reduce the bonding and interlocking force between soil particles, and the stress-strain behaviors of soil have changed [27].

Due to the fact that the hemp fiber structure prevents the fiber from slipping in the clay, the UCS values of fiber-reinforced clay specimens exposed to freezing-thawing cycles are increased with the increase in hemp fiber percentage and hemp fiber length. Similarly, Zaimoglu et al. [26] investigated the effects of randomly distributed polypropylene fibers with different fiber lengths on soil and obtained that the peak stress value of the reinforced soil increases with the increase in fiber length. They demonstrated that randomly distributed fibers act as a bridge between soil grains which improves the load-deformation behavior. Ammar et al. [14] indicated that hemp fibers have a high water absorption capacity that may affect the fiber-clay interface interaction. According to this, it is thought that the structure of hemp fiber, which interacts with water, could be decomposed with freezing-thawing cycles. Due to the decomposition of hemp fiber, with increasing percentages of hemp fiber, unconfined compression strength values after freezing-thawing cycles of 2 mm and 5 mm hemp fiber lengths are close. When the hemp fiber percentage is 1.5%, the UCS after freezing-thawing cycles of a 5mm-long hemp fiber-reinforced clay sample is 5% lower than a 2mm-long hemp fiber-reinforced clay sample.

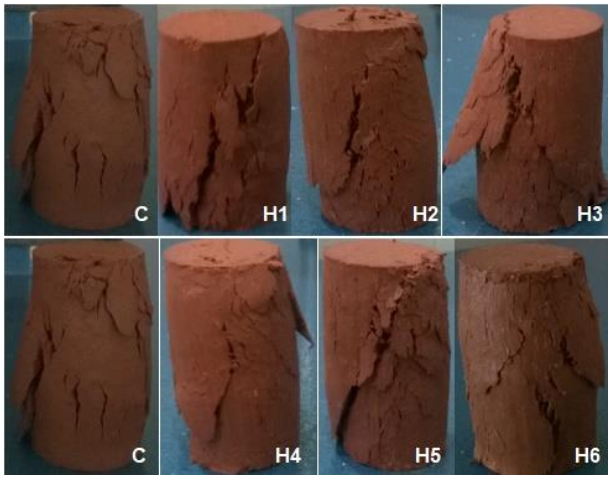

Figure 5. The specimens subjected to the UCS tests after freezing-thawing cycles

4. Conclusion and Suggestions

In this study, the potential usability of natural hemp fiber to improve the freezing-thawing resistance of high-plasticity clay has been investigated. The results obtained are listed below:

- The liquid limit values increased when fiber length and fiber percentage increased, and the plastic limits and plasticity indexes varied depending on the fiber additions.
- UCS tests conducted on the hemp fiber-reinforced clay specimens showed that UCS increased with increasing fiber percentage. The UCS of 5-mm hemp fiber-reinforced clay specimens was higher than that of 2-mm hemp fiber-reinforced clay specimens.
- Four-cycle freezing-thawing tests were conducted on the hemp fiber-reinforced clay specimens. The UCS of fiber-reinforced specimens after freezing and thawing was higher than the UCS after freezing and thawing of the clay alone.
- In the fiber-reinforced clay specimens, the UCS after freezing and thawing increased for the ratios of 0.5% and 1% of fiber but decreased by 4.9% for the ratio of 1.5%.

The addition of a natural hemp fiber increased CH clay's unconfined compressive strength both before and after freezing and thawing. As a contribution to the literature, it is thought that hemp fiber can be used as an alternative material, especially in cold climates, for reducing the effects of freezing and thawing on clay soils.

Contributions of the authors

Author 1: Methodology, writing, supervising, reviewing and editing.
Author 2: Experimental study.

Conflict of Interest Statement

There is no conflict of interest between the authors.

Statement of Research and Publication Ethics

The study is complied with research and publication ethics

References

[1] C. Liu, Y. Lv, X. Yu, and X. Wu, "Effects of freeze-thaw cycles on the unconfined compressive strength of straw fiber-reinforced soil," *Geotextiles and Geomembranes*, vol. 48, no. 4, pp. 581–590, 2020.

[2] F. Zha, S. Liu, Y. Du, and K. Cui, "Behavior of expansive soils stabilized with fly ash," *Natural Hazards*, vol. 47, pp. 509–523, 2008.

[3] Y. Zaika, A. Soeharjono, and R. Anwar, "Improving expansive soil by using combination of rice husk ash and fly ash," *EJGE*, vol. 20, no. 8, pp. 2055–2063, 2015.

[4] L. Abi Rekha, B. Keerthana, and H. Ameerlal, "Performance of fly ash stabilized clay reinforced with human hair fiber," *Geomechanics and Engineering*, vol. 10, no. 5, pp. 677–687, 2016.

[5] E. R. Sujatha, A. R. Geetha, R. Jananee, and S. R. Karunya, "Strength and mechanical behaviour of coir reinforced lime stabilized soil," *Geomechanics and Engineering*, vol. 16, no. 6, pp. 627–634, 2018.

[6] J. H. Kim, S. D. Cho, Y. S. Jang, and S. S. Kim, "Soft ground improvements using natural fiber," *Materials Science Forum*, vol. 544–545, pp. 629–632, 2007.

[7] V. Sharma, H. K. Vinayak, and B. K. Marhava, "Enhancing compressive strength of soil using natural fibers," *Construction and Building Materials*, vol. 93, pp. 943–949, 2015.

[8] J. Prabakar, and R. S. Sridhar, "Effect of random inclusion of sisal fibre on strength behaviour of soil," *Construction and Building Materials*, vol. 16, no. 2, pp. 123–131, 2002.

[9] H. Güllü and A. Khudir, "Effect of freeze–thaw cycles on unconfined compressive strength of fine-grained soil treated with jute fiber, steel fiber and lime," *Cold Regions Science and Technology*, vol. 106–107, pp. 55–65, 2014.

[10] E. Hodgson, "Toxins and venoms," in *Progress in Molecular Biology and Translational Science*, vol. 112, Academic Press, 2012, pp. 373-415.

[11] D. W. Pate, "Chemical ecology of cannabis," *Journal of the International Hemp Association*, vol. 2, no. 29, pp. 32–37, 1994.

[12] M. Syed, A. GuhaRay, and D. Goel, "Strength characterisation of fiber reinforced expansive subgrade soil stabilized with alkali activated binder," *Road Materials and Pavement Design*, vol. 23, no. 5, pp. 1037–1060, 2021.

[13] A. Ammar, S. Najjar, and S. Sadek, "Interface resistance between clays and natural hemp fibers," *IFCEE*, 2018, pp. 175-185.

[14] A. Ammar, S. Najjar, and S. Sadek, "Mechanics of the interface interaction between hemp fibers and compacted clay," *International Journal of Geomechanics*, vol. 19, no. 4, 2019.

[15] S. S. Najjar, S. Sadek, and H. Taha, "Use of hemp fibers in sustainable compacted clay systems," *Geo-Congress*, 2014.

[16] A. Abou Diab, S. Sadek, S. Najjar, and M. H. Abou Daya, "Undrained shear strength characteristics of compacted clay reinforced with natural hemp fibers," *International Journal of Geotechnical Engineering*, vol. 10, no. 3, pp. 263–270, 2016.

[17] B. Özdemir, "Doğal/sentetik lif ve uçucu kül katkılı killerin bazı geoteknik özelliklerinin araştırılması," Yüksek lisans tezi, Atatürk Üniversitesi, Erzurum, Türkiye, 2019.

[18] S. Kumar Ramamoorthy, M. Skrifvars, and A. Persson, "A review of natural fibers used in biocomposites: Plant, animal and regenerated cellulose fibers," *Polymer Reviews*, vol. 55, no. 1, pp. 107–162, 2015.

[19] O. Faruk, A. K. Bledzki, H. P. Fink, and M. Sain, "Biocomposites reinforced with natural fibers: 2000–2010," *Progress in Polymer Science*, vol. 37, no. 11, pp. 1552–1596, 2012.

[20] *Methods of test for soils for civil engineering purposes, classification tests*, BS 1377, 1990.

[21] *Standard test method for liquid limit, plastic limit, and plasticity index of soils*, ASTM D 4318, 2002.

[22] *Standard test method for unconfined compressive strength of cohesive soil*, ASTM D 2166, 2002.

[23] M. Ghazavi, and M. Roustaie, "The influenze of freeze thaw cycles on the unconfined compressive strength of fiber reinforced clay," *Cold Regions Science and Technology*, vol. 61, no. 2–3, pp. 125–131, 2010.

[24] A. Ş. Zaimoğlu, and R. K. Akbulut, "Effect of aspect ratio on the freezing thawing of a CH clay*," Selçuk Üniversitesi Mühendislik Bilim, ve Teknik Dergisi*, vol. 7, no. 1, pp. 66–74, 2019.

[25] A. E. M. K. Mohamed, "Improvement of swelling clay properties using hay fibers," *Construction and Building Materials*, vol. 38, pp. 242-247, 2013.

[26] A. S. Zaimoglu, Y. Calik, R. K. Akbulut, T. Yetimoglu, "A study on freeze-thaw behavior of randomly distributed fiber-reinforced soil," *Periodica Polytechnica Civil Engineering*, vol. 60, no. 1, pp. 3-9, 2016.

[27] L. Wei, S. Chai, M. Xue, P. Wang, F. Li, "Structural damage and shear performance degradation of fiber–lime–soil under freeze–thaw cycling," *Geotextiles and Geomembranes*, vol. 50, pp. 845-857, 2022.

Bitlis Eren Üniversitesi Fen Bilimleri Dergisi
BİTLİS EREN UNIVERSITY JOURNAL OF SCIENCE
ISSN: 2147-3129/e-ISSN: 2147-3188
VOLUME: 12 NO: 3 PAGE: 829-841 YEAR: 2023
DOI:10.17798/bitlisfen.1319038

Numerical Investigation of Mold Heating Power and Time in Metal Layered Composite Production

Muhammed Safa KAMER[1], Arif ÇUTAY[1*], Şemsettin TEMİZ[2] , Ahmet KAYA[1]

[1]*Kahramanmaraş Sutcu Imam University, Faculty of Engineering and Architecture, Mechanical Engineering Department, Kahramanmaraş, Turkey*
[2]*Inonu University, Faculty of Engineering, Mechanical Engineering Department, Malatya, Turkey*
(ORCID: 0000-0003-3852-1031) (ORCID: 0000-0002-0057-9417) (ORCID: 0000-0002-6737-3720) (ORCID: 0000-0001-9197-3542)

Keywords: Computational Fluid Dynamics (CFD), Epoxy resin curing time and energy, Heated mold, Laminate composite.

Abstract

The curing time of epoxy resin is an important phenomenon in the production of metal-layered composites. In this study, the heating time of the mold and epoxy resin was investigated by performing numerical analysis based on time to reduce the curing time. The most consistent mesh structure was chosen among five different mesh numbers in terms of the difference between temperature results. 10 different cases were created to examine different heater powers and different operating patterns. The results were examined by creating a temperature-time graph and contours showing the temperature distribution. As the number of cartridges and heater power increase, higher temperatures are reached in a shorter time. Even with the same heater power, different operating patterns can lead to differences in results in terms of temperature. The different operating pattern was seen as an independent parameter in heater power for obtaining a homogeneous temperature distribution.

1. Introduction

Composite materials have been used in many fields from the past to the present, and they are one of the most important alternatives that can replace traditional materials in terms of lightness and strength [1]-[4]. Composite materials have many advantages over traditional materials as well as disadvantages. The main disadvantages of the use of composite materials can be listed as molding, production time, and production costs. The most important factors affecting production costs are the cost of composite material components and molding costs. The most important factor affecting the production time is the resin curing time. Many experimental and numerical studies have been carried out in the literature to reduce the resin curing time, some of which are given below.

Liu et al. [5] simulated resin transfer molding to observe gate control, venting, and dry spot prediction process. The liquid Injection Molding Simulation program which is based on the finite element technique was used to solve the governing equation of the problem. As a result of simulation, they proved the benefit of numerical simulation in molding processes to make cost-effective manufacturing. Saouab et al. [6] investigated injection simulations of thick composite parts manufactured by the RTM process. Palardy et al. [7] simulated class A surface finish in the resin transfer molding process. Walczyk and Kuppers [8] studied the thermal distribution of composite laminar parts by utilizing COSMOS (Finite Element Analysis (FEA)) in thermal press curing. Pressure uniformity tests were done to validate the results of the FEA study. 12 discrete points of mold were selected to analyze pressure distribution. 32,000 tetragonal elements were created on the curing mold geometry tool surface. Laurenzi et al. [9] simulated a large composite aeronautic beam by resin transfer

*Corresponding author: arifcutay@ksu.edu.tr
Received: 23.06.2023, Accepted: 23.09.2023

modeling. The numerical analysis process was carried out with the help of a commercial Mold Flow program. The simulation aims to investigate the resin flow process during impregnation. Finite element-modified control volume analysis was utilized to solve governing equations. Triangular elements were chosen to mesh the discretization process. Mesh analysis was performed to make mesh independency. As a result of the simulation, it is concluded that numerical modeling of the resin transfer process was useful while experimental trial and error should be minimized. Rahman et al.[10] made an optimization study of an inorganic matrix material for high-temperature reinforced composites. They divided the resin into three different stages. As a result of this, it is stated that controlling the duration and humidity was facilitated. Also, improved thermos-dynamic stability was achieved at high temperatures. Keller et al. [11] studied the compression resin transfer molding process in terms of flow and heat transfer. The numerical processes were simulated in COMSOL Multiphysics 5.0 program. A triangular 0.68 mm mesh was utilized in this simulation. Maximum resin temperature was observed at different time intervals while using variable injection pressures. They concluded that the high exothermic reaction of epoxy can be controlled with the utilization of correct manufacturing and processing conditions. Liu et al. [12] studied ohmic heating curing of fiber/carbon nanofiber in an ultralow environment. They conclude that ohmic heating can give comparable results in terms of power and time requirement as compared to other heating methods. Chen et al. [13] monitored the temperature in laminated composite plates by utilizing FBG sensors. The time range required to reach maximum temperature (Nearly 180ºC) was between 255 and 266 min in their experimental study. Li et al. [14] investigated cure-induced temperature gradients in laminated composites in numerical and experimental ways. In this study, they concluded that mold thickness is a significant factor in heating time in laminated composite curing. Maximum temperature was achieved after 140 minutes for laminated composites in this study. Also, 180oC was the maximum temperature at the most heated point in their experimental results. Wu et al. [15] investigated experimentally high-quality plate-shaped A356 alloy casting by a combined ablation cooling and mold heating method. They concluded that the risk of shrinkage porosity can be reduced when the mold temperature is higher than 200 oC. Rosa et al. [16] conducted a CFD study of cyclic transient heating of a blank mold with a conformal channel for manufacturing glass containers. They produced novel blank molds for the glass industry to reduce the operating temperature. 100 C temperature decrease was achieved by a novel blank mold called as ShellMould.

In this study, heater cartridges were added to the pressing mold system used in the production of laminated composites to reduce the curing time of epoxy resin in metal-layered composite production. Thus, the mold and epoxy resin will be heated during the pressing stage in the production of layered composites, and the curing time of the epoxy resin will be reduced. For this purpose, time-dependent numerical analyses were carried out using different heater powers and operating schemes. Thus, the necessary parameters were investigated for the metal-layered composite materials placed between the molds to reach the desired temperature in the shortest time in a homogeneous manner. It has been revealed that some of the parameters determined to be investigated in this and similar studies can also be examined with numerical analysis programs without the need for experimentation. In this way, it is aimed to save time and cost.

2. Material and Method

Reducing the resin curing time in composite material production is important in terms of accelerating composite material production. For this reason, composite materials are first pressed under certain pressures during the production phase, and then the curing of the resin is accelerated by firing. In this study, pressing and heating of the resin were tried to be performed at the same time, thus minimizing the production time of metal-layered composite material was aimed. For this purpose, a mold, press, and external environment used in the production of laminated composite materials were designed in SolidWorks 2018 solid modeling program (Figure 1), and numerical analyzes were carried out in the Fluent module of the Ansys 18.1 program. Ansys Fluent is a proven computational fluid dynamics program that is utilized in the numerical analysis of heat and flow problems [17]-[20].

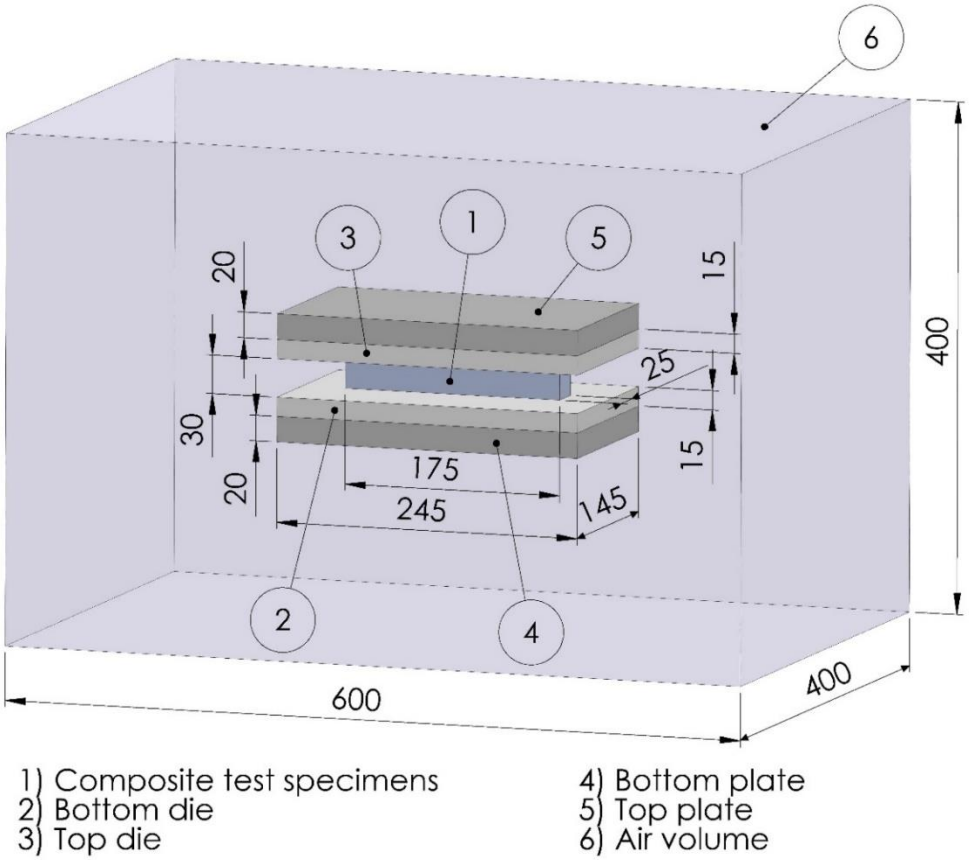

Figure 1. The design used in numerical analysis.

To heat the mold and resin during pressing in the production of composite materials, 6mm diameter, 17mm high, cylindrical heater cartridges with cylindrical geometry are placed on the lower plate and upper parts of the press. A total of 120 heater cartridges were utilized, 60 for the lower plate and 60 for the upper press. The layout of the heater cartridges is shown in Figure 2. Heater cartridges are defined to the Ansys-Fluent program in groups of twenty as separate for bottom plate and top press (bottom-inner, bottom-middle, bottom-outer, top-inner, top-middle, top-outer). Thus, in numerical analysis, different heater groups were operated together, and the effect of different heater operating patterns was examined.

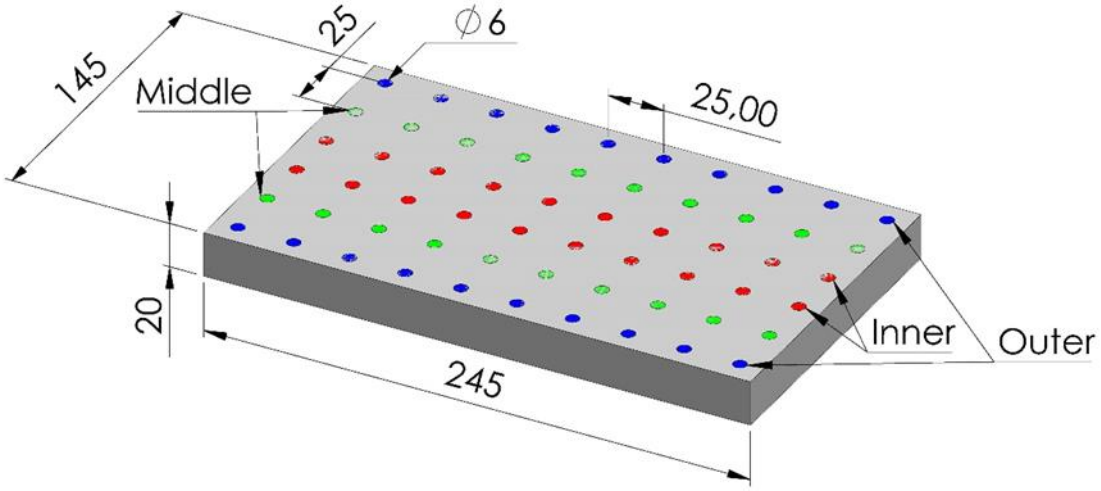

Figure 2. Heater cartridge layout.

Different heater powers and different heater operation patterns used in numerical analyzes are given in Table 1. Numerical analyzes were performed for 9 different cases using different powers and different operating schemes.

Table 1. Heater powers and operating arrangements used in numerical analysis

Numerical analysis ID	Heater cartridge usage status						Heater power	Number of active heaters	Total heater power	Heat flux
	Bottom plate			Top plate						
	Inner	Middle	Outer	Inner	Middle	Outer	(W)		(W)	(W/m^2)
Case-1	**On**	**On**	**On**	**On**	**On**	**On**	10	120	1200	31206.82
Case-2	**On**	**On**	**On**	**On**	**On**	**On**	20	120	2400	62413.72
Case-3	**On**	**On**	**On**	**On**	**On**	**On**	30	120	3600	93620.55
Case-4	**On**	**On**	**On**	**On**	**On**	**On**	40	120	4800	124827.4
Case-5	**On**	**On**	**On**	**On**	**On**	**On**	50	120	6000	156034.3
Case-6	**On**	**On**	**On**	Off	Off	Off	50	60	3000	156034.3
Case-7	Off	Off	Off	**On**	**On**	**On**	50	60	3000	156034.3
Case-8	**On**	Off	Off	**On**	Off	Off	50	40	2000	156034.3
Case-9	Off	**On**	Off	Off	**On**	Off	50	40	2000	156034.3
Case-10	**On**	**On**	Off	**On**	**On**	Off	50	80	4000	156034.3

As a result of numerical analysis, temperature values were taken from 5 different points (Figure 3) on the composite test sample placed between the molds, and the analysis results were compared. At these points, Y=0 and Z=0, and results were obtained such that only the positions of the points on the X-axis changed. In addition, as a result of the analysis, the temperature distribution contours on the composite test sample were also examined.

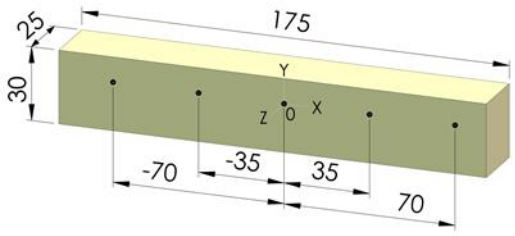

Figure 3. Composite test specimen temperature distribution measurement points.

In analyses using computational fluid dynamics, the correct determination of the solution mesh is of high importance in terms of the accuracy of the result. For this reason, using different variations, 5 different numbers of mesh structures were used to divide the flow volume into elements, and the mesh calculation time, which minimized the difference between the temperature results, was chosen considering the calculation time. Different element sizes and growth rates were given different values in the flow volume and mold, and solution mesh numbers from approximately 5 million to 13 million were created. Mass element dimensions were defined separately for all the masses in the design, and a separate element size definition was made for the part of the air volume between the upper and lower molds. The parameters used in the mesh independence studies are given in Table 2. In these analyses, 0.1s Times step size was used, and 3000 steps were solved. As a result, 300s solutions were obtained as a result of the analysis. Analyzes were performed while the heater cartridges were in the Case-4 state indicated in Table 1.

Table 2. Parameters used in mesh independence studies

Numerical analysis ID	Body element size (mm)					Grow rate	Number of mesh element	Max. Skewness	Min. Orthogonal quality
	Composite test specimens	Top and Bottom dies	Top and Bottom plates	Air volume	Air volume between dies				
Mesh-1	5	5	5	10	10	1.1	4,996,595	0.799	0.2
Mesh-2	2	5	5	10	2	1.1	6,542,234	0.799	0.2
Mesh-3	**2**	**2**	**2**	**10**	**10**	**1.2**	**7,622,720**	**0.83888**	**0.16112**
Mesh-4	2	2	2	5	5	1.2	11,519,731	0.82295	0.17705
Mesh-5	2	2	2	5	5	1.1	12,910,476	0.8225	0.17744

The results obtained from the mesh independence studies are given in Table 3. For each analysis, temperature values were taken from the points indicated in Figure 3 and the average of these temperature values was calculated and a table was created. When Table 3 is examined, it is seen that the results obtained from the mesh independence studies are very close to each other. For this reason, it was decided to use the solution mesh with the number of 7.6 million elements in the calculations with the most accurate result without increasing the calculation time and load too much (Mesh-3). In addition, numerical analyses were carried out at different time step size times (0.01s; 0.05s; 0.1s) using the selected mesh structure, and 300s solutions were obtained as a result of these analyses. The results obtained from the analysis are also given in Table 3. It is seen that the results obtained from time step size independence studies are also very close to each other, and in the following analyses (other cases specified in Table 1), Mesh-3 mesh structure, 0.1s time step size, and 3000-time step were used. The Mesh-3 mesh used in the numerical calculation is shown in Figure 4.

In the numerical calculation, in the nozzle design provided by the die heating, the inlet boundary condition was created by giving the heat flux to the wall boundary condition, and the pressure boundary condition was chosen as the atmospheric boundary condition at the outlet. The type of flow was chosen as laminar due to the nature of the problem.

Table 3. Results obtained from the studies of independence from mesh and time step

Numerical analysis ID	**Temperature (K)**									
	30s	**60s**	**90s**	**120s**	**150s**	**180s**	**210s**	**240s**	**270s**	**300s**
Mesh-1	310.21	326.01	342.78	359.82	376.94	394.08	411.32	428.41	445.40	462.74
Mesh-2	310.20	326.01	342.78	359.88	376.94	394.08	411.24	428.41	445.57	462.74
Mesh-3	**310.37**	**326.23**	**343.02**	**360.06**	**377.18**	**394.33**	**411.49**	**428.65**	**445.82**	**462.98**
Mesh-4	310.38	326.25	343.04	359.96	377.20	394.35	411.51	428.67	445.84	463.01
Mesh-5	310.37	326.23	343.02	360.06	377.18	394.33	411.49	428.66	446.02	462.99
Time Step Size 0.01s	310.36	326.23	343.02	360.06	377.18	394.32	411.48	428.65	445.81	462.97
Time Step Size 0.05s	310.37	326.23	343.02	360.06	377.18	394.33	411.33	428.65	445.82	462.98

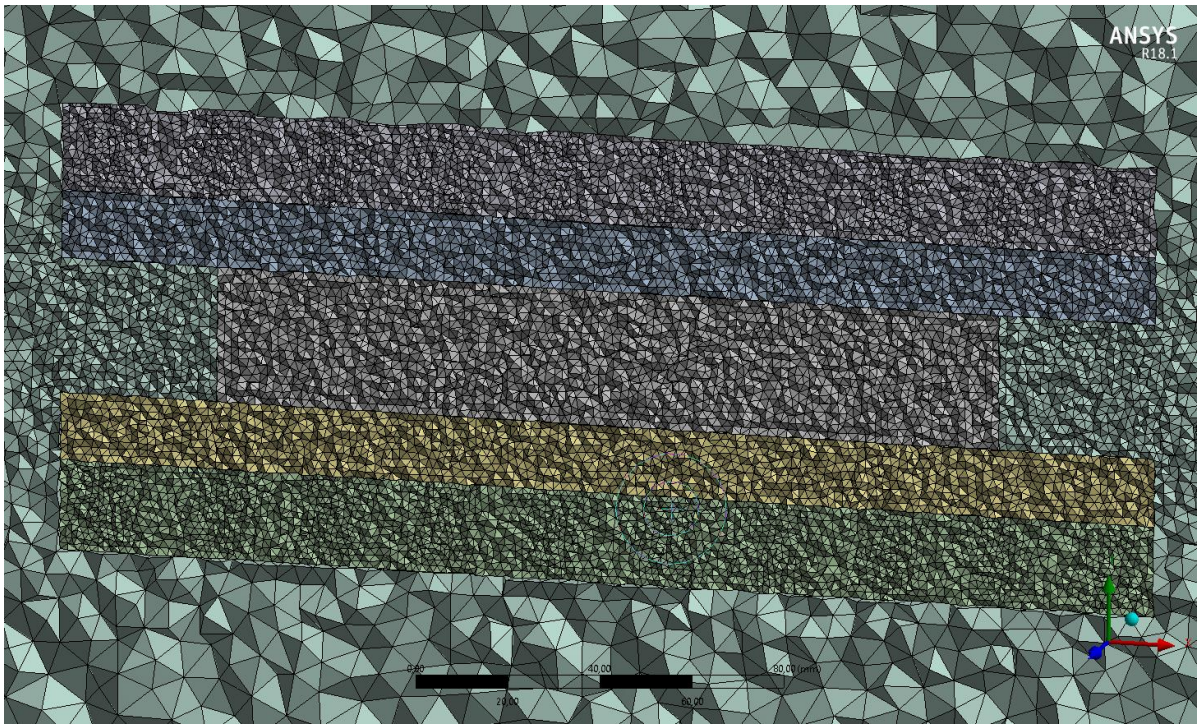

Figure 4. Mesh structure used in numerical studies.

3. Results and Discussion

In this study, the heating time and the maximum temperature are studied using numerical methods depending on time using different heater powers and nozzle configurations. The results are shown graphically and contoured in the figures below. Graphs showing the change of temperature over time are shown for 5 minutes of simulation for 5 different points (-70, -35, 0, 35, 70 mm) averages. Figure 5 (a) shows the time-dependent variation of the average temperature at the 5 different points with all nozzles open at 5 different heater powers. As expected, the highest heater power reaches the highest temperature value in the specified period in the Kelvin temperature unit. It is seen in the graphs that the effect of increasing heater power on temperatures increases over time. Increasing the heater power from 1200W to 6000W causes a 53.6% increase in the maximum temperature that will occur after 5 minutes. The maximum temperature value reached for 6000W was calculated as 504.583 K as a result of numerical simulations. The rate of increase between maximum and minimum power is calculated as 53.3% at the end of the 5 minutes. When the heater power is increased from 1200W to 2400W, the increase in Kelvin from the temperature value is calculated as 11.9%. The temperature difference between different heater power cases increases with time. The maximum temperature that can be reached for case 1 was calculated as 341 K, while case 5 passed this temperature in 120 seconds. Each 1200W heater power causes an increase of approximately 40 K maximum temperature, while this value is calculated as 50 K when increased from 4800 W to 6000 W. More heater power enables reaching the desired temperature in a shorter time and rising to higher temperatures as expected in our design.

In Figure 5(b), the time-dependent variation of the average temperature for 5 points is shown for 5 different operating cartridge patterns. In these cases, the heater power is changed while using different operating patterns. Even though similar heater powers were studied, the change in heater cartridge positions caused a significant difference in the average temperature graph. The maximum temperature reached by the lowest heater power, 367 K, reached case 5 in less than 120 seconds. Although the increased heater power is increased by using different heater patterns, it enables it to reach higher temperatures in a shorter time. Increasing the heater power from 2000W to 4000W increases the maximum achievable temperature for these cases by 17.95 %. Switching from the heater power of 4000 W to Case 5 is observed in the graph as an approximately 14.28 % increase in the maximum temperature. Although Case 8 and 9 have the same heating power, Case 8 appears to reach higher temperatures in a shorter time. Because while the middle heater cartridges are open in case 9, case 8 has an arrangement in which the inner heater cartridges are opened.

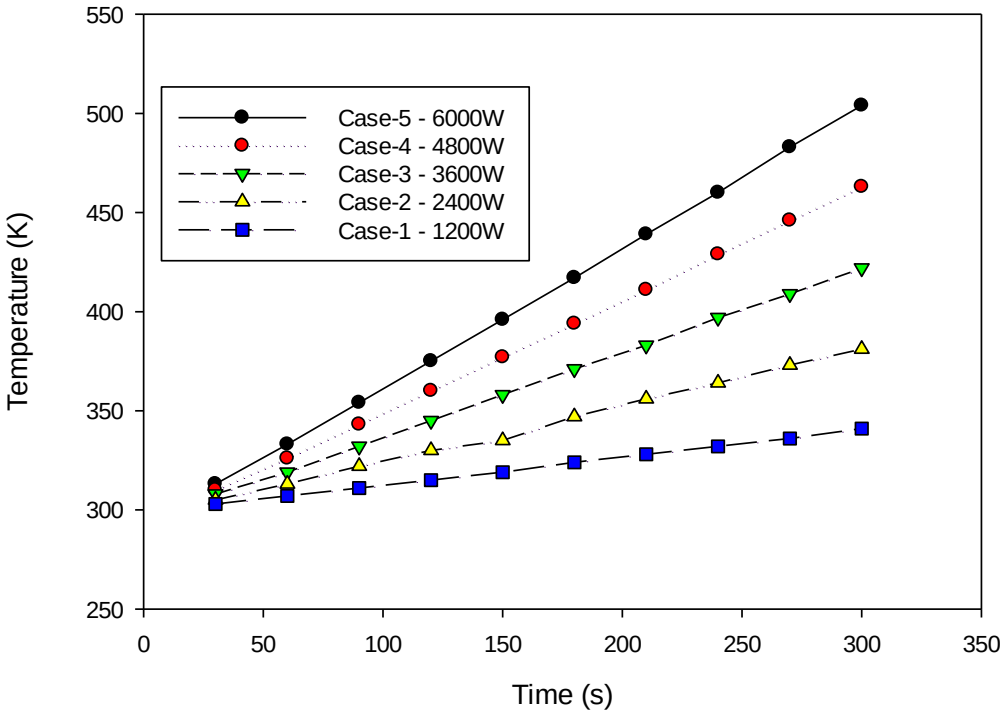

(a)

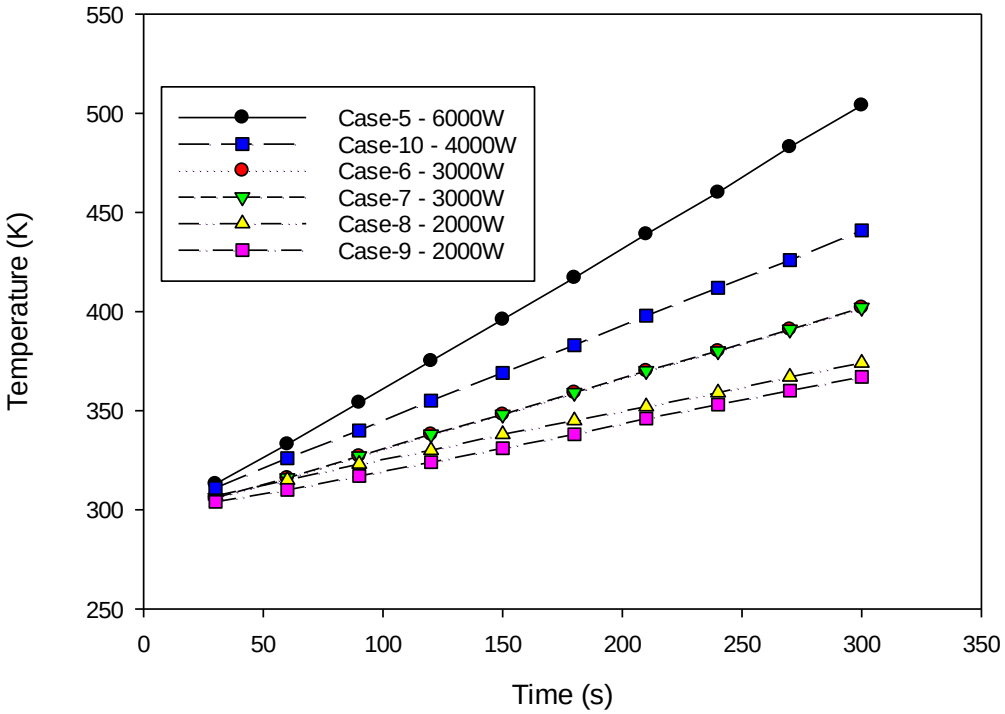

(b)

Figure 5. Temperature-time graphs created by numerical analysis results using different heater powers (a) and different operating patterns (b).

Figure 6 depicts the temperature contour as user-specified and local cases for different heater power at the end of 300 seconds. The minimum and maximum temperature is specified as 340K and 510 K. In the local case, the temperature is set only for the maximum and minimum values of these cases. For

this reason, there are color differences among contours. The effect of increased heater power on the temperature distribution is clearly shown in the contours created with the user-specified. The local contours depict in terms of color how the open and closed cartridge positions affect the maximum and minimum temperatures that will occur. As the temperature increases at the edge of the mold, a significant decrease towards the middle has occurred as a result of numerical analysis. Figure 7 shows the temperature contour as user-specified and local cases for different heater operating patterns at the end of 300 seconds. The effect of the increased heater power on the temperature is seen in the user-specified contours. The effect of the positions of the opened heater cartridges can be seen in the locally created contours. As expected, as seen in case 6, a temperature increase is observed close to that region when the lower cartridge is open, while a temperature increase is observed in the upper region when the upper cartridge is open. As it can be understood from these contours, besides the heater power, the position of the heater cartridges to be opened is a significant factor in obtaining a homogeneous temperature distribution. Figure 8 shows the temperature distribution of the analysis region from the top view using lower and upper separate operating patterns for XY and YZ planes. As expected, when all heater powers are turned on at the highest level, the amount of red area indicating the height of the temperature covers a lot of space for case 5 compared to the others for both planes. Case 7, where the top heater cartridges are opened, is compared to case 6, where only the bottom cartridges are opened, it seems for this mold design that case 7 affects a larger area in terms of heat increase. In addition, the areas close to the open heater cartridges in the mold show higher values in terms of temperature as expected.

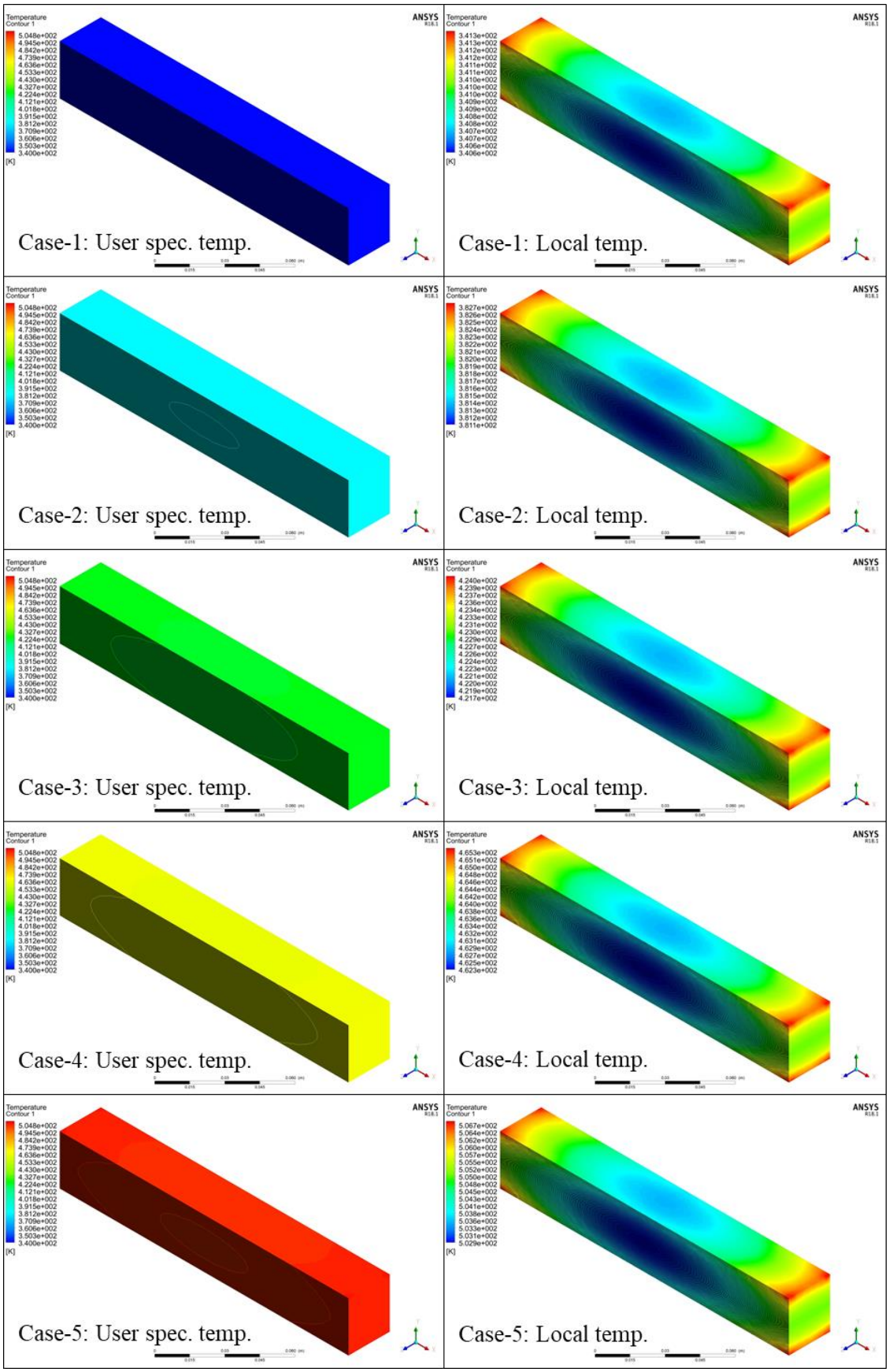

Figure 6. Temperature contours results using different heater powers and created on test samples.

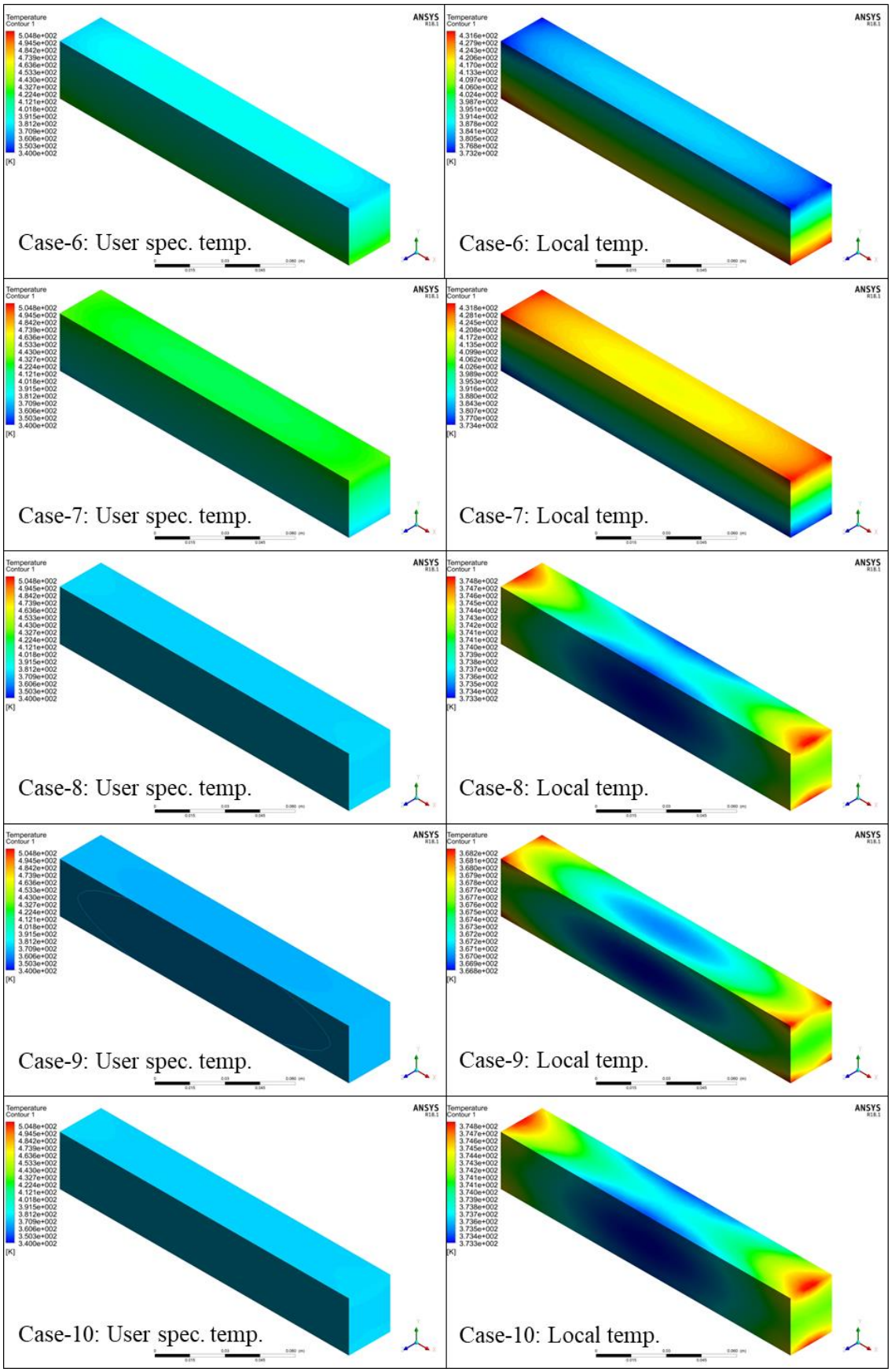

Figure 7. Temperature contours results using different operating patterns and created on test samples.

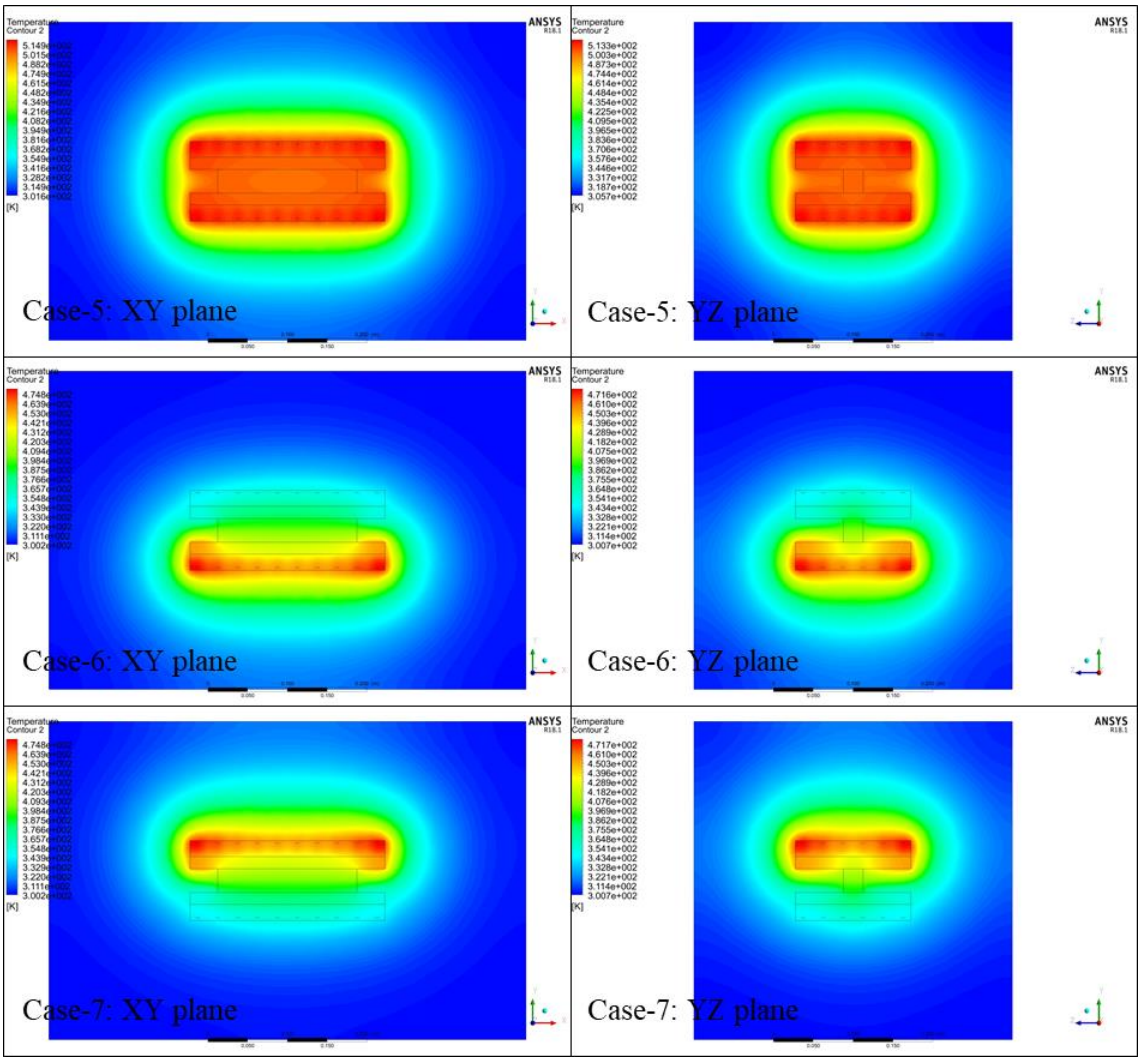

Figure 8. Temperature contours results using lower and upper separate operating patterns on the analysis region.

4. Conclusion

In this study, numerical simulation was performed at laminated composites in order to reduce the curing time of epoxy resin in metal layered composite production for different heater power and different operating patterns. According to different heater power and operating patterns, 10 different situations were created and analyzes were performed. The outputs obtained according to these numerical analyzes are as follows.

- The increased heater power causes higher temperatures to be reached in a shorter time, regardless of the different operating patterns.
- It is seen that choosing the heater cartridges according to the area to be heated provides more effective results.
- For this design, opening the upper heater cartridge provides a temperature increase in a wider area and it is seen to be more efficient.
- Although cases 8 and 9 have the same heater power, case 8 produced higher temperature results. This shows the importance of the heating pattern even though they are of the same power.
- Although case 5 differs from all other cases in terms of reaching higher temperatures in a shorter time, its use according to the desired temperature amount of time may cause unnecessary energy consumption.
- It is important to establish the operating pattern correctly to obtain a homogeneous temperature distribution.

Acknowledgment

The workstation and Ansys software used in the numerical analyses in this study were provided by the Scientific and Technological Research Council of Turkey (TUBITAK) grant number 217M865. The authors thank TUBITAK for their support.

Contributions of the authors

All the authors have accepted responsibility for the entire content of this submitted manuscript and approved the submission.

Conflict of Interest Statement

The authors declare no conflicts of interest regarding this article.

Statement of Research and Publication Ethics

The study is complied with research and publication ethics.

References

[1] S. Kaveloğlu and Ş. Temiz, "An experimental and finite element analysis of 3D printed honeycomb structures under axial compression," *Polymers & Polymer Composites*, vol. 30, p. 096739112211223, Jan. 2022.

[2] A. Saylik and Ş. Temiz, "Low-speed impact behavior of fiber-reinforced polymer-based glass, carbon, and glass/carbon hybrid composites," *MP MATERIALPRUEFUNG - MP MATERIALS TESTING*, vol. 64, no. 6, pp. 820–831, Jun. 2022.

[3] S. Kaveloğlu, Ş. Temiz, O. Doğan, and M. S. Kamer, "Investigation of Bending Strength of Honeycomb Sandwich Structures with Different Cell Diameters Produced by 3D Printer," *Çukurova Üniversitesi Mühendislik Fakültesi Dergisi*, vol. 37, no. 2, pp. 459–470, Jun. 2022.

[4] M. Yilmaz, N. F. Yilmaz, and M. F. Kalkan, "Rheology, crystallinity, and mechanical investigation of interlayer adhesion strength by thermal annealing of polyetherimide (PEI/ULTEM 1010) parts produced by 3D printing," *Journal of Materials Engineering and Performance*, vol. 31, no. 12, pp. 9900–9909, Jun. 2022.

[5] B. Liu, S. Bickerton, and S. G. Advani, "Modelling and simulation of Resin Transfer Moulding (RTM)—gate control, venting and dry spot prediction," *Composites Part A: Applied Science and Manufacturing*, vol. 27, no. 2, pp. 135–141, 1996.

[6] A. Saouab, J. Bréard, P. Lory, B. Gardarein, and G. Bouquet, "Injection simulations of thick composite parts manufactured by the RTM Process," *Composites Science and Technology*, vol. 61, no. 3, pp. 445–451, 2001.

[7] G. Palardy, P. Hubert, E. Ruiz, M. Haider, and L. Lessard, "Numerical simulations for class A surface finish in resin transfer molding process," *Composites Part B: Engineering*, vol. 43, no. 2, pp. 819–824, 2012.

[8] D. Walczyk and J. Kuppers, "Thermal press curing of Advanced Thermoset Composite Laminate Parts," *Composites Part A: Applied Science and Manufacturing*, vol. 43, no. 4, pp. 635–646, 2012.

[9] S. Laurenzi, A. Casini, and D. Pocci, "Design and fabrication of a helicopter unitized structure using resin transfer molding," *Composites Part A: Applied Science and Manufacturing*, vol. 67, pp. 221–232, 2014.

[10] A. S. Rahman and D. W. Radford, "Cure cycle optimization of an inorganic polymer matrix material for high-temperature fiber reinforced composites," *Composites Part A: Applied Science and Manufacturing*, vol. 85, pp. 84–93, 2016.

[11] A. Keller, C. Dransfeld, and K. Masania, "Flow and heat transfer during compression resin transfer molding of highly reactive epoxies," *Composites Part B: Engineering*, vol. 153, pp. 167–175, 2018.

[12] Y. Liu, M. Wang, W. Tian, B. Qi, Z. Lei, and W. Wang, "Ohmic heating curing of carbon fiber/carbon nanofiber synergistically strengthening cement-based composites as repair/reinforcement materials used in ultra-low temperature environment," *Composites Part A: Applied Science and Manufacturing*, vol. 125, p. 105570, 2019.

[13] J. Chen, J. Wang, X. Li, L. Sun, S. Li, and A. Ding, "Monitoring of temperature and cure-induced strain gradient in a laminated composite plate with FBG sensors," *Composite Structures*, vol. 242, p. 112168, 2020.

[14] X. Li, J. Wang, S. Li, and A. Ding, "Cure-induced temperature gradient in laminated composite plate: Numerical simulation and experimental measurement," *Composite Structures*, vol. 253, p. 112822, 2020.

[15] J. Wu, D. Sui, and Q. Han, "High quality plate-shaped A356 alloy casting by a combined ablation cooling and mold heating method," *Journal of Materials Processing Technology*, vol. 303, p. 117536, 2022.

[16] N. Rosa, J. Costa, and A. G. Lopes, "CFD study of transient heating and cooling of a blank mold with a conformal cooling channel for manufacturing glass containers," *Results in Engineering*, vol. 17, p. 100932, 2023.

[17] T. Karataş and İ. G. Aksoy, "Heat and Flow Analysis of Different Type Baffle in Shell and Tube Heat Exchanger," *Bitlis Eren Üniversitesi Fen Bilimleri Dergisi*, vol. 10, no. 3, pp. 973–986, 2021. doi:10.17798/bitlisfen.872465

[18] M. Yavuz, C. Yıldız, and G. Çakmak, "Numerical Analysis of Velocity and Temperature Distributions in Winter Air Conditioning of Cabin Type Offices," *Bitlis Eren Üniversitesi Fen Bilimleri Dergisi*, vol. 10, no. 3, pp. 958–972, 2021.

[19] S. Akçay, "Investigation of effects of Baffle Heights on flow and heat transfer in a trapezoidal channel with vertical baffles," *Bitlis Eren Üniversitesi Fen Bilimleri Dergisi*, vol. 11, no. 2, pp. 478–489, 2022. doi:10.17798/bitlisfen.1033852

[20] Y. Sayan, "Investigation of the effect of a different trapezoidal inclination angle in a reverse trapezoidal cross-section flow channel on the performance of the PEM fuel cell with the computational fluid dynamic (CFD) method," *Kahramanmaraş Sütçü İmam Üniversitesi Mühendislik Bilimleri Dergisi*, https://jes.ksu.edu.tr/en/pub/issue/77849/1180483 (accessed Aug. 15, 2023).

Bitlis Eren Üniversitesi Fen Bilimleri Dergisi
BİTLİS EREN UNIVERSITY JOURNAL OF SCIENCE
ISSN: 2147-3129/e-ISSN: 2147-3188
VOLUME: 12 NO: 3 PAGE: 842-852 YEAR: 2023
DOI:10.17798/bitlisfen.1323858

An Investigation of the Strength Properties of Fly Ash and Metakaolin-Based Geopolymer Mortars Containing Multi-Wall Carbon Nanotube, Nano Silica, and Nano Zinc

Maksut SELOĞLU[1*], Harun TANYILDIZI[2], Mehmet Emin ÖNCÜ[3]

[1]*Dicle University Institute of Science and Technology*
[2] *Firat University, Faculty of Technology, Department of Civil Engineering*
[3] *Dicle University Faculty of Engineering, Civil Engineering Department*
(ORCID: 0000-0002-0200-8423) (ORCID: 0000-0002-7585-2609) (ORCID: 0000-0001-6434-293X)

Keywords: Geopolymer mortar, MW-CNT, nano-SiO_2, nano-ZnO, compressive strength, flexural strength.

Abstract

In this study, the mechanical properties of geopolymer mortar composites containing different nanomaterials were investigated. Fly ash (FA) and metakaolin (MK) were used as binders in geopolymer mortar samples. Sodium silicate (Na_2SiO_3) and sodium hydroxide (NaOH) solutions (12 M) were used as alkali activators. Multi-walled carbon nanotubes (MW-CNT), nano-SiO_2 (NS), and nano-ZnO (NZ) were used in the study. Geopolymer mortar samples without nanomaterials were determined as control samples, and geopolymer mortar samples containing 0.5% by weight of MW-CNT, NS, and NZ were prepared. All prepared samples were cured at 20±2 °C in laboratory conditions for 7-day and 28 day. The curing geopolymer mortar samples were subjected to compressive strength and flexural strength tests. As a result of this study, the mechanical strength of all geopolymer mortar samples containing nanomaterials increased compared to the control samples. The highest compressive strength and flexural strength were obtained from geopolymer mortar samples containing MW-CNT. These samples were followed by geopolymer mortar samples containing NS and NZ, respectively.

1. Introduction

Concrete is the most frequently used building material in the world, especially in the construction industry. Cement, which is the main component and binder of concrete, causes 7% of CO_2 emissions in the world [1], [2]. In addition, since cement production can be carried out at high temperatures such as 1400-1500 °C, it also necessitates a significant energy requirement. The increase in energy prices also increases the cost of cement production. The amount, dosage, and technical properties of cement directly affect the cost, performance, and workability of concrete. In this case, fly ash, blast furnace slag, silica fume, rice husk ash, etc. are used in research to reduce the amount of cement used, and the cost of concrete, and make concrete more sustainable. The reuse of industrial waste materials that can increase mechanical properties and strength has been revealed [3], [4]. Due to economic and environmental reasons, the search for alternative binders to cement has gained serious importance recently. In this case, an alternative composite material to cement called geopolymer has come to the fore and has gained a place in the construction technology sector by finding widespread use day by day. Geopolymers are alumina silicate-type binder materials formed by activating natural and waste pozzolans with various alkali activators. It has been repeatedly stated in various sources that geopolymer production causes 80% fewer CO_2 emissions compared to cement production [5]-[7] and provides 60% energy savings [8], [9].

Geopolymer mortar or concrete is defined as a mortar or concrete that uses one or more of the material components considered waste during

*Corresponding author: mseloglu@firat.edu.tr
Received: 06.07.2023, Accepted: 05.09.2023

production and does not harm the environment. According to literature research, although geopolymer mortar, or concrete, is known as an environmentally friendly type of concrete, it also means cementless concrete. Geopolymers are three-dimensional Si-O-Al- framed inorganic materials made of alkali-soluble aluminum silicate [10]. The use of industrial wastes with pozzolanic properties and limited storage areas in the production of geopolymer mortar or concrete causes it to be known as environmentally friendly concrete. Geopolymer has become an alternative binder to cement in some applications because of its sustainability qualities, such as low energy consumption and low CO_2 emissions. In fact, after lime and cement, geopolymer has started to be considered the third-generation binder. The use of industrial wastes instead of cement reduces cement consumption and provides positive contributions to the physical and mechanical properties of mortar or concrete. It also has superior performance and longevity [11]. Geopolymer mortars, ground blast furnace slag, fly ash (FA), baked clays and shales, silica fume, heat-treated materials such as metakaolin (MK), natural pozzolans such as volcanic ash, trasses, and diatomite soils, industrial wastes, and volcanic glassy rock can be produced by activating materials such as pumice, also known as pumice, and ground perlite, a volcanic rock, with alkaline activators.

Nanotechnology is the expression of matter at the nanometer level (1-100 nm.) in order to produce materials with new properties and functions, and it is one of the emerging fields to develop new materials with superior properties and high performance [12]. The properties of building materials can be further improved using nanomaterials. Nano-sized materials improve the mechanical strength properties of geopolymer mortars due to their superior physical, chemical, and rheological properties, which are completely different from the same products with larger dimensions [13]. The addition of nanomaterials to geopolymer mortars has an effect similar to that of micro-based materials such as metakaolin (MK) and silica fume and improves the mechanical strength properties [14]. If a homogeneous distribution is provided, composite materials with high mechanical and durability properties can be produced, depending on the material type and ratio used. Nanomaterials with small particle sizes have very high chemical activities because they have very large, specific surface areas. High microstructure density is achieved thanks to this high reactivity feature and the mechanisms of filling the pores with the filler effect of the materials. The addition of nanomaterials increases both the early and advanced-age compressive strengths of mortars and improves the aggregate and cement paste interface. For this reason, it has been observed that nanomaterials lead to improvements in the mechanical properties of geopolymer mortars and concretes [15]-[17]. Nanomaterials have been added to geopolymer mortars to improve their mechanical properties. Many properties vary according to the different nanomaterials used. Theoretically, all materials in the aluminosilicate class can be activated by alkalis and show binding properties. However, the physical, chemical and rheological properties of nanomaterials directly affect the behavior of the geopolymer binder. In this respect, knowing the properties of the nanomaterial to be used is very important in terms of determining the performance of the geopolymer binder [18]. The nanomaterial most commonly added to geopolymer mortars is nano-SiO_2, which has high activity. Nano-SiO_2 (NS) improves the mechanical properties of geopolymer mortars by reacting with alkali activators in solution and forming gels to improve the pore structure [19] and prevent the calcification of geopolymer mortars [20]. The improvement of the mechanical properties of NS in geopolymer mortars is also due to its high pozzolanic activity and filler effect [21]. In the literature, there are many studies that have produced geopolymer mortar and concrete containing NS added to the composite by dry and wet mixing methods in different volumetric ratios [22], [23].

Geopolymer composites containing 1% NS by volume, especially affecting the initial stages of binder formation and thus mechanical performance, yielded high mechanical strength results [17], [24]-[28]. In some studies, geopolymer composites containing 2% by volume NS yielded high compressive strength results [15], [16], [29]-[34]. Fly ash shows pozzolanic properties because they are very fine-grained materials with a siliceous and aluminous amorphous structure. Metakaolin (MK), on the other hand, is widely used in the production of geopolymer mortar and concrete due to its high content of amorphous silica and its special production. MK reacts with $Ca(OH)_2$ and water and provides C-S-H gel formation, giving the geopolymer high strength. In the literature, studies comparing the mechanical strength of metakaolin (MK) and fly ash (FA) based geopolymer mortars containing different nanomaterials are limited.

In this study, geopolymer mortar samples were produced by using equal amounts of MK and FA, containing different nanomaterials in the same volumetric mixing ratios and activating with alkalis. For this purpose, geopolymer mortars were produced

by adding multi-walled carbon nanotubes (MW-CNT), nano silicon dioxide (nano-SiO2), and nano zinc oxide (nano-ZnO) to the composite at 0.5% volumetric ratios, and both among themselves and with control samples that did not contain nanomaterials mechanical strengths were compared. After curing the produced mortar samples at 20±2 °C in laboratory conditions for 7 and 28 days, their mechanical properties were investigated.

2. Materials and Method

2.1. Materials

The fly ash (FA) used in this study is classified as class F fly ash according to ASTM C 618 [35]. In this study, F-class fly ash produced by burning imported hard coal at the Sugözü thermal power plant in the Yumurtalık district of Adana was used. FA and MK were used as pozzolanic materials in the study. FA and MK specifications are given in Table 1.

Table 1. FA and MK characteristics

Chemical components	%	
	FA	MK
SiO_2	58.25	56.10
Al_2O_3	22.95	40.25
Fe_2O_3	7.25	0.85
CaO	2.58	0.19
MgO	2.42	0.16
Na_2O	0.92	0.24
K_2O	0.99	0.55
LOI (loss on ignition)	0.91	1.11
Blaine (cm^2/g)	3000	-
Specific gravity (g/cm^3)	2.31	2.52

As an aggregate, natural river sand was obtained from the Murat River in the Palu district of Elazig province. The alkali activator, which is often preferred for the activation of geopolymer raw materials, is sodium silicate (Na_2SiO_3) and sodium hydroxide (NaOH) solution, which is called glass water due to its easy availability and viscosity. In this study, solid NaOH was used to prepare an activator solution. The NaOH concentration was chosen as 12 M, and the solution was kept under laboratory conditions for 24 hours. Then, sodium hydroxide solution and sodium silicate were added to the geopolymer mortar mixture. Some physical and chemical properties of alkali activators are shown in Table 2.

Table 2. Chemical properties of Na_2SiO_3 and NaOH solution

Chemical properties	Na_2SiO_3	NaOH
Molecular weight (g/mol)	122.08	40
Density (g/cm^3)	1.39	2.13
H_2O (%)	64.8	–
SiO_2 (%)	28.7	–
Na_2O (%)	8.9	–
pH	-	13.5
Color	White	White

Metakaolin increases the water requirement of the mortar due to the clay structure it contains. For this reason, plasticizer additives were used in the study, and their ratio was chosen as 1% of the binder amount. The nanomaterials used in the study are multi-walled industrial grade carbon nanotube (MW-CNT), nano silicon dioxide (nano-SiO2), and nano oxide (nano-ZnO). These nanomaterials are expressed as M-CNT, NS, and NZ, respectively, and some of their technical properties are given in Table 3.

2.2. Preparation of Geopolymer Mortar Samples

While preparing the geopolymer mortar mixtures, the geopolymer mortar samples that do not contain nanomaterials were determined as control samples in the study and indicated with K.

Geopolymer mortar samples containing 0.5% nanomaterial were expressed as M-CNT, NS, and NZ, respectively. Geopolymer mortar samples were subjected to flexural strength and compressive strength tests after they were kept at 20±2 °C in laboratory conditions for 7 and 28 days. For the flexural strength test, 40×40×160 mm for all ages (7 and 28 days) and three for each sized prismatic samples were produced and tested separately for geopolymer mortar samples containing each nanomaterial. In addition to flexural strength, compressive strength analysis was also performed in accordance with ASTM C349 [37] on prismatic samples of the same age, which were subjected to flexural strength tests with the 3-point bending method according to ASTM C348 [36]. The samples used in the compressive strength tests are the samples subjected to the flexural strength test and divided into two for each sample.

Table 3. Properties of nanomaterials used

Nanomaterials Used	**M-CNT**	**NS**	**NZ**
Formula	MWCNT-OH^-	SiO_2	ZnO
Color	Black	White	White
Purity (%)	92	99.95	99.99
Average particle diameter (nm)	8-28	13-22	18
Length (μm)	10-35	-	-
Surface area (m_2/g)	220	165-195	20-65
Type	Industrial	Non-porous	-
Chemical structure	Stable	Amorphous	Crystal
Shape	-	Spherical	Near spherical

FA and MK were first mixed in a mixer for approximately one minute. Then, the fine aggregate was added to them and mixed for about three minutes. Nanomaterials were prepared by adding them to the alkali activator solution and mixing until homogeneous for about 1 hour in an ultrasonic bath with pure water at the bottom. Then, the alkali activator solution containing nanomaterials was added to the dry mixture. After the dry ingredients were added, mixing continued for four minutes. Then, a plasticizer was added to the geopolymer mortar mixture, and mixing was continued for about two more minutes. In total, the mixing time was about ten minutes.

In this study, the alkali activator solution/binder (AAS/B) ratio was kept at 0.8126 for all mixtures. The percentage of FA was determined to be 50% of the binder weight, added to the dosage, and used. Fine aggregate with a maximum aggregate size (Dmax) of 0.600 mm was used. The plasticizer ratios were chosen at 1% of the binder amount. Abbasi et al. [38] obtained the highest compressive strength results in samples containing 0.5% M-CNT in their study. Zidi et al. [39] also obtained the highest compressive strength results in samples containing 0.5% NZ compared to control samples. For this reason, a 0.5% volumetric ratio was determined in the study, and geopolymer mortar samples were produced by using each nanomaterial at this ratio. The casting parameters of the experimental study as a whole are given in Table 4.

Table 4. Raw materials used for geopolymer mortars by mass ratio

Binder	**FA**	**MK**	**Aggregate**	**SH***	**SM***	**AAS/B**	**Plasticizer**	**Nanomaterial**
1	0.5	0.5	2.57	0.25	0.5626	0.8126	0.01	0.005

SH*: Sodium Hydroxide solution, SM*: Sodium metasilicate

3. Experimental Results

In this study, fly ash-metakaolin based 40×40×160 mm sized geopolymer mortars were produced. The produced geopolymer mortar samples were cured at 20±2 °C in laboratory conditions for 7 and 28 days, and their mechanical strength properties were investigated. For this purpose, samples were subjected to bending and compressive strength tests. Prismatic specimens subjected to flexural strength tests with the 3-point flexural method according to ASTM C348 [36] were tested at the end of 7 and 28 days, with three samples from each series. The test results are shown in the study by taking the average of all three samples for each batch. In all of the samples, there was an increase in mechanical strength in the 28-day test results compared to the 7-day test results.

3.1. Flexural Strength Results of Geopolymer Mortars

The flexural strength test results of geopolymer mortar samples are given in Figure 1.

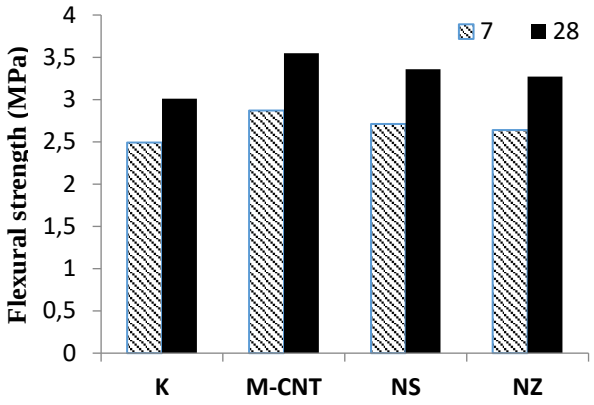

Figure 1. Flexural strength test results of geopolymer mortar samples

When Figure 1 is examined, the flexural strengths of the geopolymer mortar control samples at 7 and 28 days were found to be 2.49 and 3.01 MPa, respectively. The 7-day and 28-day flexural strengths of geopolymer mortar samples containing 0.5% volumetric multi-walled carbon nanotubes (M-CNT) were found to be 2.87 and 3.55 MPa, respectively. The 7-day and 28-day flexural strengths of the geopolymer mortar samples containing nano silicon dioxide (NS) and nano zinc oxide (NZ) were found to be 2.71, 3.36 MPa, and 2.64, 3.27 MPa, respectively. When the 7-day flexural strength results were examined, the flexural strengths of the samples containing nanomaterials showed an increase of 15.26%, 8.84%, and 6.02%, respectively, compared to samples containing 0% nanomaterials. When the 28-day flexural strength results were examined, compared to the samples without nanomaterials the flexural strengths of the samples containing nanomaterials (M-CNT, NS, and NZ) increased by 17.94%, 11.63%, and 8.64%, respectively. The highest flexural strength results were obtained from geopolymer mortar samples containing multi-walled carbon nanotubes (M-CNT) in both 7-day and 28-day test results. In the literature, similar flexural strength increase rates have been observed in composites containing multi-walled carbon nanotubes (M-CNT) [40], [41]. Kotop et al. [41] reported that in the 28-day flexural strength results, a 15.8% increase in strength was obtained in the samples containing M-CNT compared to the samples containing 0% nanomaterials, while an 18% increase in strength was obtained in this study. In the literature, similar rates of flexural strength increase have been observed in samples containing higher volumetric NS ratios [42]. These results were obtained using a 0.5% lower NS volume ratio in the study. Quercia et al. [43] achieved an increase of 9.1% in the 28-day flexural strength test results in samples containing 3.8% NS. Saini et al. [44] achieved an increase of approximately 7% in the 28-day flexural strength test results in samples containing 2% NS compared to samples containing 0% nanomaterials. But, in this study, with the use of one-fourth of the ratio NS, a 12% increase in the flexural strength test results compared to samples containing 0% nanomaterials was obtained. Nuaklong et al. [42] obtained a 19% increase in the 28-day flexural strength test results in samples containing 1% NS compared to the control samples, while using 0.5% NS in the study showed an increase of 12% in flexural strength compared to samples containing 0% nanomaterials. In all samples containing nanomaterials, the 28-day flexural strength results showed an increase of approximately 24% compared to the 7-day flexural strength results. The fact that nanomaterials fill the existing voids by creating a filler effect in geopolymer mortar mixtures and creating a more impermeable microstructure causes an increase in strength [14], [33].

In the geopolymer mortar samples containing three different nanomaterials, the flexural strength values were respectively M-CNT, NS, and NZ compared to the control mortar samples without nanomaterials. The 7-day and 28-day flexural strength results of the M-CNT-containing geopolymer mortar samples increased by approximately 5.9% and 5.65%, respectively, compared to the NS-containing geopolymer mortar samples. The 7-day and 28-day flexural strength results of the geopolymer mortar samples containing M-CNT were approximately 8.71 and 8.56% higher, respectively, than the geopolymer mortar samples containing NZ.

3.2. Compressive Strength Results of Geopolymer Mortars

Compressive strength test results of geopolymer mortar samples are given in Figure 2.

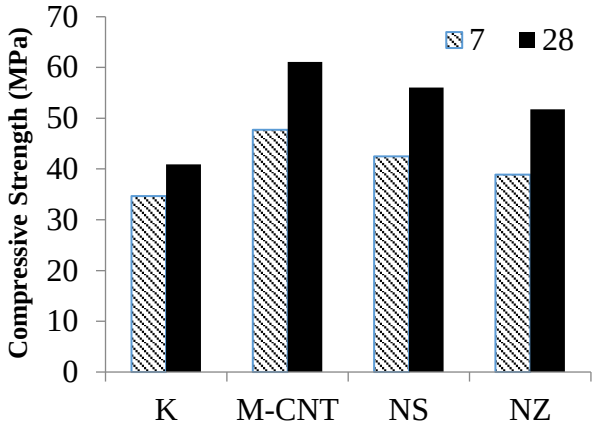

Figure 2. Compressive strength test results of geopolymer mortar samples

Compressive strength results showed parallelism with flexural strength results. As shown in Figure 2, the 7-day compressive strength of the geopolymer mortar control samples was found to be 34.69 MPa. The 7-day compressive strength results of geopolymer mortar samples containing multi-walled carbon nanotubes (M-CNT), nano silicon dioxide (NS), and nano zinc oxide (NZ) were found to be 47.75 MPa, 42.5 MPa, and 38.89 MPa, respectively. When the 7-day compressive strength results were examined, the compressive strengths of the samples containing nanomaterials showed an increase of 37.65%, 22.51%, and 12.11%, respectively, compared to the control samples. The 28-day compressive strength of geopolymer mortar samples without nanomaterials is given in Figure 2 as 40.94 MPa. The 28-day compressive strength results of geopolymer mortar samples containing nanomaterials were given as 61.07, 56.05, and 51.79 MPa, respectively. When the 28-day compressive strength results were examined, the compressive strengths of the samples containing M-CNT, NS, and NZ showed an increase of 49.18, 36.92, and 26.52%, respectively, compared to the samples without nanomaterials. The highest compressive strength results were obtained from geopolymer mortar samples containing multi-walled carbon nanotubes (M-CNT) in both 7-day and 28-day test results. In the literature, similar compressive strength increase rates have been observed in composites containing multi-walled carbon nanotubes (M-CNTs) [45], [46]. Alvi et al. [46] stated that it increased the 28-day compressive strength by 45.12% compared to samples containing 0% nanomaterials. Rovnanik et al. [45] achieved the highest compressive strength results in samples containing 0.5% M-CNT. The increase in strength in geopolymer mortar samples containing nanomaterials is due to the high specific surface area and high reactivity of the nano-sized material. In addition, it is observed that the strength increase of the nanomaterial-containing geopolymer mortar samples has become more evident over time as a result of the 28-day-long pozzolanic reactions. While the highest compressive strength was recorded at 61.07 MPa in geopolymer mortar samples containing multi-walled carbon nanotubes, the rate of increase in strength was 49.18%. According to many studies in the literature, the rate of increase in compressive strength was higher in geopolymer mortar samples containing multi-walled carbon nanotube (M-CNT) [47]-[49]. Collins et al. [49] obtained an average 25% increase in compressive strength compared to control samples in mortar samples containing 0.5% M-CNT; in the mortar samples produced in the study, with the same volumetric ratio of M-CNT, an increase in compressive strength was obtained almost twice as much as in this study.

In the literature, similar compressive strength increase rates have been observed in the samples produced using NS [26]. Adak et al. [50], in their study investigating the structural performance of NS-modified fly ash-based geopolymer concrete, increased the 28-day compressive strength of samples containing 1% NS by 34% compared to the control samples. Wu et al. [26] showed that the effect of NS and nano-CaCO3 on the mechanical properties of ultra-high performance concrete increased the 28-days compressive strength of the samples containing 1% NS by 35% compared to samples containing 0% nanomaterials in their study. With the use of 0.5% NS in the study, the 28-day compressive strength increase was 37% compared to samples containing 0% nanomaterials. Compared to many studies in the literature, the compressive strength performances of geopolymer mortar samples produced using a much lower volumetric ratio (0.5%) NS were much higher. Mustakim et al. [51] obtained the highest compressive strength test result of 63 MPa with samples containing 1.5% NS, in their study on increasing the fresh, mechanical, and microstructural properties of FA-blast furnace slag-based geopolymer concrete with the addition of nano and micro silicon dioxide. In the study, the compressive strength of 28 days was obtained as 56.05 MPa in the samples produced using 0.5% NS. Nuaklong et al. [42] stated that the 28-day compressive strength of the samples containing 2% NS increased by 29% compared to samples containing 0% nanomaterials. With samples containing 3% NS, Behfarnia et al. [52] increased the 28-day compressive strength by 12% compared to samples containing 0% nanomaterials, and Mahboubi et al. [53] increased the 28-day compressive strength

by 44% compared to samples containing 0% nanomaterials. 28-day compressive strength increases in the samples were 37% compared to samples containing 0% nanomaterials. While İbrahim et al. [54] increased the 28-day compressive strength by 25% with the samples containing 5% NS compared to samples containing 0% nanomaterials, this increase was 37% compared to samples containing 0% nanomaterials with only 0.5% NS content in the study. Assaedi et al. [55] found the compressive strengths of the samples formed by adding 1% and 2% NS to the samples without nanomaterials with a compressive strength of 37.2 MPa, to be 47.3 MPa, and 44.9 MPa, respectively. Patel et al. [56] increased the compressive strength by approximately 10% by adding 1.5% NS to the control samples, which did not contain NS and had a compressive strength of 39 MPa, and obtained a 28-day compressive strength of 43 MPa in samples containing 1.5% NS. In the study, the compressive strength value of the sample without nanomaterials, which was 40.94 MPa, increased to 56.05 MPa with the addition of 0.5% NS. Therefore, with the addition of fewer nanomaterials, higher strength was achieved in this study. While the 7-day and 28-day compressive strengths of samples containing 4% NS increased by 24% and 26%, respectively [57], in another study containing NS at the same volumetric ratio [58], they increased by 25% and 49%, respectively. The 7-day and 28-day compressive strengths of the samples containing 2% NS increased by approximately 25% [20], and in another study containing 1% NS [59], the 7-day and 28-day compressive strengths of the samples increased by 21% and 28%, respectively. In this study containing 0.5% NS, the 7-day and 28-day compressive strengths of the samples increased by 22% and 37%, respectively. This result is attributed to the high performance in the early wet compressive strength of the low NS content.

The number of studies investigating the mechanical properties of NZ-containing geopolymers is very limited in the literature. Zidi et al. [38] increased the compressive strength by 26.67% in samples containing 0.5% NZ compared to samples containing 0% nanomaterials. Strength increase rates and nanomaterial content showed similar results to our study. Zailan et al. [60] investigated the mechanical properties of the geopolymer mortar containing 2.5%-10% NZ in their study and obtained the highest 28-day compressive strength value of 51.61 MPa in the samples containing 2.5% NZ. In this study, a 28-day compressive strength of 51.79 MPa was obtained for the samples containing only 0.5% NZ at a much lower volumetric ratio.

28-day compressive strength results in samples containing nanomaterials (M-CNT, NS, and NZ) showed an increase of 27.9, 31.88, and 33.17%, respectively, compared to 7-day compressive strength results. In the geopolymer mortar samples containing three different nanomaterials in the same weight ratio, the mechanical performances of M-CNT, NS and NZ were respectively the highest to the lowest compared to the control mortar samples without nanomaterials. The 7-day and 28-day compressive strength results of the geopolymer mortar samples containing M-CNT were found to be approximately 12.35%, 22.78%, 8.96%, and 17.92% higher than the geopolymer mortar samples containing NS and NZ, respectively.

4. Conclusion

In this study, the strength properties of geopolymer mortars containing MW-CNT, NS, and NZ were investigated. Geopolymer mortar samples without nanomaterials were determined as control samples and geopolymer mortar samples containing 0.5% by weight of % MW-CNT, NS, and NZ were produced. The results obtained in this study are given below:

-When the flexural strength test results are examined, in both 7-day and 28-day strength results, flexural strengths increased in all samples containing nanomaterials and control samples. These increases were 15.26%, 8.84%, and 6.02% in the samples containing nanomaterials (M-CNT, NS, and NZ) compared to samples containing 0% nanomaterials in the 7-day strengths, respectively. At 28 days, it was 17.94%, 11.63% and 8.64% in the samples containing nanomaterials (M-CNT, NS, and NZ) compared to samples containing 0% nanomaterials, respectively.

-When the compressive strength test results were examined, both 7-day and 28-day strengths increased in all geopolymer mortar samples containing nanomaterials compared to the control samples without nanomaterials. This increase was 37.65%, 22.51%, and 12.11% in samples containing nanomaterials (M-CNT, NS, and NZ) compared to control samples cured at ambient conditions for 7 days, respectively. Compared with samples without nanomaterials cured for 28 days, samples containing nanomaterials (M-CNT, NS, and NZ) had an increase of 49.18%, 36.92%, and 26.52%, respectively. While the highest compressive strength value was obtained at 61.07 MPa in multi-walled carbon nanotube (M-CNT) geopolymer composites, the lowest compressive strength value was obtained at 51.79

MPa in geopolymer composites containing nano-ZnO (NZ).

When the data obtained are examined, it is seen that the use of different nanomaterials in very low volumetric ratios in the production of geopolymer mortars shows a good performance in the mechanical strength of geopolymer mortars. In addition, it is seen that more economical and higher-strength geopolymer mortars can be produced by mixing the expensive nanomaterials with the wet method and using them in lower volumetric ratios. Finally, it will be meaningful to carry out studies on the durability properties of the produced geopolymer mortars and to bring them to the literature by comparing the research made in terms of both strength and durability.

Contributions of the authors

Maksut SELOĞLU: Literature, Conceptualization, Methodology, Investigation, Writing-review& editing. Harun TANYILDIZI¸: Conceptualization, Methodology, Investigation, Writing-review& editing. Mehmet Emin ÖNCÜ¸: Methodology, Investigation, Writing-review& editing.

Conflict of Interest Statement

There is no conflict of interest between the authors.

Statement of Research and Publication Ethics

The study is complied with research and publication ethics.

References

[1] Y. M. Amran, R. Alyousef, H. Alabduljabbar, and M. El-Zeadani, "Clean production and properties of geopolymer concrete; A review", *Journal of Cleaner Production*, 251, 119679, 2020.

[2] A. B. Moradikhou, A. Esparham, and M. J. Avanaki, "Physical & mechanical properties of fiber reinforced metakaolin-based geopolymer concrete." *Construction and Building Materials*, 251, 118965, 2020.

[3] K. A. Komnitsas, "Potential of geopolymer technology towards green buildings and sustainable cities.", *Procedia Engineering*, 21, 1023-1032, 2011.

[4] M. A. Villaquirán-Caicedo, and R. M. de Gutiérrez, "Synthesis of ceramic materials from ecofriendly geopolymer precursors.", *Materials Letters*, 230, 300-304, 2018.

[5] Y. Wang, F. Aslani, and A. Valizadeh, "An investigation into the mechanical behaviour of fibre-reinforced geopolymer concrete incorporating NiTi shape memory alloy, steel and polypropylene fibres.", *Construction and Building Materials*, 259, 119765, 2020.

[6] A. C. Ganesh, and M. Muthukannan, "Development of high performance sustainable optimized fiber reinforced geopolymer concrete and prediction of compressive strength.", *Journal of Cleaner Production*, 282, 124543, 2021.

[7] E. Mohseni, "Assessment of Na2SiO3 to NaOH ratio impact on the performance of polypropylene fiber-reinforced geopolymer composites.", Construction and Building Materials, 186, pp.904-911, 2018.

[8] J. Davidovits, D. C. Comrie, J. H. Paterson, and D. J. Ritcey, "Geopolymeric concretes for environmental protection.", Concrete International, vol. 12, no. 7, pp. 30-40, 1990.

[9] S.M.A. El-Gamal, and F.A. Selim, "Utilization of some industrial wastes for eco-friendly cement production.", *Sustainable Mater.Technol*. 12, pp. 9-17, 2017.

[10] K. M. Liew, A. O. Sojobi, and L. W. Zhang, "Green concrete: Prospects and challenges.", *Construction and building materials*, 156, pp.1063-1095, 2017.

[11] B. Suhendro, "Toward green concrete for better sustainable environment.", *Procedia Engineering*, 95, pp. 305-320, 2014.

[12] F. Sanchez, and K. Sobolev, "Nanotechnology in concrete-a review", *Construction and building materials*, vol. 24, no. 11, pp. 2060-2071, 2010.

[13] A. W. Qarluq, R. Polat, and F. F. Karagöl, "Halloysit Nano-Kil, Nano-SiO2 ve Nano-CaO'in Tekli ve İkili Kullanımının Çimento Esaslı Harçların Özelliklerine Etkileri.", *Avrupa Bilim ve Teknoloji Dergisi*, vol. 20, pp.815-826, 2020.

[14] M.S.M. Norhasri, M.S. Hamidah, and A.M. Fadzil, "Applications of Using Nano Material in Concrete: A review", *Constr. Build. Mater*., vol:133, pp. 91-97, 2017.

[15] T. Phoo-ngernkham, P. Chindaprasirt, V. Sata, S. Hanjitsuwan, and S. Hatanaka, "The effect of adding nano-SiO2 and nano-Al2O3 on properties of high calcium fly ash geopolymer cured at ambient temperature", *Materials & Design*, 55, pp. 58-65, 2014.

[16] P. S. Deb, P. K. Sarker, and S. Barbhuiya, "Effects of nano-silica on the strength development of geopolymer cured at room temperature.", *Construction and building materials*, 101, pp. 675-683, 2015.

[17] K. Gao, K. L. Lin, D. Wang, H. S. Shiu, C. L. Hwang, and T. W. Cheng, "Effects of nano-SiO2 on setting time and compressive strength of alkali activated metakaolin-based geopolymer", *The Open Civil Engineering Journal*, vol. 7, no. 1, 2013.

[18] M. Tuyan, "Development of geopolymer mortar and concrete with natural and waste materials.", PhD Thesis, Ege University, Institute of Science and Technology, İzmir, 2017.

[19] M. Sumesh, U. J. Alengaram, M. Z. Jumaat, K. H. Mo, and M. F. Alnahhal, "Incorporation of nano-materials in cement composite and geopolymer based paste and mortar-A review.", *Construction and Building Materials*, 148, pp. 62-84, 2017.

[20] K. Sun, X. Peng, S. Wang, L. Zeng, P. Ran, and G. Ji, "Effect of nano-SiO2 on the efflorescence of an alkali-activated metakaolin mortar", *Construction and Building Materials*, 253, p.118952, 2020.

[21] N. Yaltay, "Investigation of the effect of nano silica on concrete compressive strength.", *Engineering Sciences*, vol. 12, no. 4, pp. 216-223, 2017.

[22] H. U. Ahmed, A. A. Mohammed, and A. S. Mohammed, "The role of nanomaterials in geopolymer concrete composites: A state-of-the-art review", *Journal of Building Engineering*, 49, p. 104062, 2022.

[23] N. B. Singh, S. K. Saxena, and M. Kumar, "Effect of nanomaterials on the properties of geopolymer mortars and concrete", *Materials today: proceedings*, vol. 5, no. 3, pp. 9035-9040, 2018.

[24] S. Ridha, M. Akmalludin, and S. S. Salehudin, "Microstructure investigations on nano-geopolymer cement cured under HPHT conditions", *ARPN Journal of Engineering and Applied Sciences*, vol. 11, no. 1, pp. 144-149, 2016.

[25] K. Gao, K. L. Lin, D. Wang, C. L. Hwang, H. S. Shiu, Y. M. Chang, and T. W. Cheng, "Effects SiO2/Na2O molar ratio on mechanical properties and the microstructure of nano-SiO2 metakaolin-based geopolymers.", *Construction and building materials*, 53, pp. 503-510, 2014.

[26] Z. Wu, K. H. Khayat, C. Shi, B. F. Tutikian, and Q. Chen, "Mechanisms Underlying the Strength Enhancement of UHPC Modified with Nano-SiO2 and Nano-CaCO3", *Cement and Concrete Composites*, vol. 119, p. 103992, 2021.

[27] F. U. A. Shaikh, S. W. M. Supit, and P. K. Sarker, "A study on the effect of nano silica on compressive strength of high volume fly ash mortars and concretes", *Materials & Design*, 60, pp. 433-442, 2014.

[28] S. M. A. El-Gamal, F. S. Hashem, and M. S. Amin, "Influence of carbon nanotubes, nanosilica and nano metakaolin on some morphological-mechanical properties of oil well cement pastes subjected to elevated water curing temperature and regular room air curing temperature", *Construction and Building Materials*, 146, pp. 531-546, 2017.

[29] J. Wang, P. Du, Z. Zhou, D. Xu, N. Xie, and X. Cheng, "Effect of nano-silica on hydration, microstructure of alkali-activated slag", *Construction and Building Materials*, 220, pp. 110-118, 2019.

[30] E. Ekinci, İ. Türkmen, F. Kantarci, and M. B. Karakoç, "The improvement of mechanical, physical and durability characteristics of volcanic tuff based geopolymer concrete by using nano silica, micro silica and Styrene-Butadiene Latex additives at different ratios", *Construction and Building Materials*, 201, pp. 257-267, 2019.

[31] X. Gao, Q. L. Yu, and H. J. H. Brouwers, "Characterization of alkali activated slag-fly ash blends containing nano-silica", *Construction and Building Materials*, 98, pp. 397-406, 2015.

[32] U. Durak, O. Karahan, B. Uzal, S. İlkentapar, and C. D. Atiş, "Influence of nano SiO2 and nano CaCO3 particles on strength, workability, and microstructural properties of fly ash-based geopolymer", *Structural Concrete*, 22, E352-E367, 2021.

[33] B. B. Jindal, "Investigations on the properties of geopolymer mortar and concrete with mineral admixtures: A review", *Construction and building materials*, 227, p. 116644, 2019.

[34] A. M. Rashad, and A. S. Ouda, "Thermal resistance of alkali-activated metakaolin pastes containing nano-silica particles.*", Journal of Thermal Analysis and Calorimetry*, 136, pp. 609-620, 2019.

[35] C. ASTM, "Specification for fly ash and raw or calcined natural pozzolana for use as a material admixture in Portland cement concrete", pp. 618-78, 1978.

[36] A. ASTM, "Test method for flexural strength of hydraulic mortar cement", *Annual Book of ASTM Standards* C348, 401, 2002.

[37] C. ASTM, "Standard Test Method for Compressive Strength of Hydraulic-Cement Mortars (Using Portions of Prisms Broken in Flexure)", ASTM International, pp. 349-02, 2002.

[38] Z. Zidi, M. Ltifi, Z. B. Ayadi, L. E. Mir, and X. R. Nóvoa, "Effect of nano-ZnO on mechanical and thermal properties of geopolymer", *Journal of Asian Ceramic Societies*, vol.8, no. 1, pp. 1-9, 2020.

[39] S. M. Abbasi, H. Ahmadi, G. Khalaj, and B. Ghasemi, "Microstructure and mechanical properties of a metakaolinite-based geopolymer nanocomposite reinforced with carbon nanotubes", *Ceramics International*, vol. 42, no. 14, pp.15171-15176, 2016.

[40] M. Saafi, K. Andrew, P. L. Tang, D. McGhon, S. Taylor, M. Rahman, and X. Zhou, "Multifunctional properties of carbon nanotube/fly ash geopolymeric nanocomposites", *Construction and Building Materials*, 49, pp. 46-55, 2013.

[41] M. A. Kotop, M. S. El-Feky, Y. R. Alharbi, A. A. Abadel, and A. S. Binyahya, "Engineering properties of geopolymer concrete incorporating hybrid nano-materials", *Ain Shams Engineering Journal*, vol. 12, no. 4, pp. 3641-3647, 2021.

[42] P. Nuaklong, V. Sata, A. Wongsa, K. Srinavin, and P. Chindaprasirt, "Recycled aggregate high calcium fly ash geopolymer concrete with inclusion of OPC and nano-SiO2", *Construction and Building Materials*, 174, pp. 244-252, 2018.

[43] G. Quercia, P. Spiesz, G. Hüsken, and H. J. H. Brouwers, "SCC modification by use of amorphous nano-silica", *Cement and Concrete Composites*, 45, pp. 69-81, 2014.

[44] G. Saini and U. Vattipalli, "Assessing properties of alkali activated GGBS based self-compacting geopolymer concrete using nano-silica", *Case Studies in Construction Materials*, 12, e00352, 2020.

[45] P. Rovnaník, H. Šimonová, L. Topolář, P. Schmid, and Z. Keršner, "Effect of carbon nanotubes on the mechanical fracture properties of fly ash geopolymer", *Procedia Engineering*, 151, pp. 321-328, 2016.

[46] M. A. A. Alvi, M. Khalifeh, and M. B. Agonafir, "Effect of nanoparticles on properties of geopolymers designed for well cementing applications", *Journal of Petroleum Science and Engineering*, 191, p.107128, 2020.

[47] M. Oualit, and A. Irekti, "Mechanical performance of metakaolin-based geopolymer mortar blended with multi-walled carbon nanotubes", *Ceramics International*, vol. 48, no.11, pp. 16188-16195, 2022.

[48] H. M. Khater, and H. A. Abd el Gawaad, "Characterization of alkali activated geopolymer mortar doped with MWCNT", *Construction and building materials*, 102, pp. 329-337, 2016.

[49] F. Collins, J. Lambert, and W. H. Duan, "The influences of admixtures on the dispersion, workability, and strength of carbon nanotube-OPC paste mixtures", *Cement and Concrete Composites*, vol. 34, no. 2, pp. 201-207, 2012.

[50] D. Adak, M. Sarkar, and S. Mandal, "Structural performance of nano-silica modified fly-ash based geopolymer concrete", *Construction and Building Materials*, 135, pp. 430-439, 2017.

[51] S. M. Mustakim, S. K. Das, J. Mishra, A. Aftab, T. S. Alomayri, H. S. Assaedi, and C. R. Kaze, "Improvement in fresh, mechanical and microstructural properties of fly ash-blast furnace slag based geopolymer concrete by addition of nano and micro silica", *Silicon*, 13, pp. 2415-2428, 2021.

[52] K. Behfarnia, and M. Rostami, "Effects of micro and nanoparticles of SiO2 on the permeability of alkali activated slag concrete", *Construction and building materials*, 131, pp. 205-213, 2017.

[53] B. Mahboubi, Z. Guo, and H. Wu, "Evaluation of durability behavior of geopolymer concrete containing Nano-silica and Nano-clay additives in acidic media", *Journal of civil Engineering and Materials Application*, vol. 3, no. 3, pp. 163-171, 2019.

[54] M. Ibrahim, M. A. M. Johari, M. Maslehuddin, and M. K. Rahman, "Influence of nano-SiO2 on the strength and microstructure of natural pozzolan based alkali activated concrete", *Construction and Building Materials*, 173, pp. 573-585, 2018.

[55] H. Assaedi, F. U. A. Shaikh, and I. M. Low, "Characteristics of nanosilica-geopolymer nanocomposites and mixing effect", *Int. J. Chem*, vol. 9, no.12, pp.1363-1370, 2015.

[56] Y. Patel, I. N. Patel, and M. J. Shah, "Experimental investigation on compressive strength and durability properties of geopolymer concrete incorporating with nano silica", *Journal Impact Factor*, vol. 6, no. 5, pp. 135-143, 2015.

[57] E. Rabiaa, R. A. S. Mohamed, W. H. Sofi, and T. A. Tawfik, "Developing geopolymer concrete properties by using nanomaterials and steel fibers", *Advances in Materials Science and Engineering*, pp. 1-12, 2020.

[58] B. Mehdikhani, B. Saeedi Razavi, J. Ahmadi, and A. Goharrokhi, "The effect of adding nano-silica on the ultrasonic pulse velocity of geopolymer concrete", *Journal of Particle Science and Technology,* vol. 7, no. 2, pp. 99-105, 2021.

[59] F. Shahrajabian, and K. Behfarnia, "The effects of nano particles on freeze and thaw resistance of alkali-activated slag concrete", *Construction and Building Materials*, 176, pp. 172-178, 2018.

[60] S. N. Zailan, A. Bouaissi, N. Mahmed, and M. M. A. B. Abdullah, "Influence of ZnO nanoparticles on mechanical properties and photocatalytic activity of self-cleaning ZnO-based geopolymer paste", *Journal of Inorganic and Organometallic Polymers and Materials*, 30, pp. 2007-2016, 2020.

Bitlis Eren Üniversitesi Fen Bilimleri Dergisi
BİTLİS EREN UNIVERSITY JOURNAL OF SCIENCE
ISSN: 2147-3129/e-ISSN: 2147-3188
VOLUME: 12 NO: 3 PAGE: 853-862 YEAR: 2023
DOI:10.17798/bitlisfen.1323976

A constructive heuristic for the heterogeneous drone delivery problem that considers packages' setups and battery capacity with the aim of minimizing weighted total waiting times of customers

Murat ŞAHİN[1*]

[1]*Celal Bayar University, Industrial Engineering, Manisa*
(ORCID: 0000-0003-3173-1749)

Keywords: Drone delivery problem, drone routing problem, energy consumption, unmanned aerial vehicles, route planning.

Abstract
This article considers the heterogeneous drone routing problem, which takes into account the setup times of customers' packages and aims to minimize the weighted total waiting times of customers. Cases where drones differ from each other in terms of battery capacity, carrying capacity, speed and load capacity have been handled. The battery capacity has been associated with the payload carried by the drone as long as it stays in the air. A constructive heuristic has been suggested and many test instances have been used to show how the efficiency of the algorithm changes when different priority values are used. As a result, it has been seen that good solutions can be obtained by assigning the light customer packages to the fast drones for the given test instances by using the suggested constructive heuristic.

1. Introduction

Along with technological improvements, there have been significant developments and applications in the field of unmanned aerial vehicles (UAVs) in recent years. The integration of online shopping into daily life has also increased the need for innovative solutions in logistics operations. In this context, businesses have started to prefer drone transportation for satisfying customer demands uninterruptedly and quickly. With drone transportation, it has become possible to make carriage to locations where access is difficult, traffic congestion is intense and infrastructure requirements have not been completed yet [1].

UAVs like as drones have the potential to significantly reduce the transportation cost and time required to deliver materials since they are less expensive than traditional delivery vehicles such as trucks and needs much lower energy requirements. In parallel with recent advancements in UAVs technology and the stated advantages, large companies like Amazon, DHL, Federal Express have start to package delivery with UAVs for their commercial services. Thanks to these developments a new delivery system has been emerged and, a new problem category arises, drone routing problem. Despite the increasing focus on UAVs and the field's status as an emerging technology, there is no comprehensive literature about the transportation characteristics and the methods used to solve drone routing problem in the current state [2]. The drone routing problem has very similar structures with vehicle routing problem in general. However, in many aspects drone routing problem can differ from the simple routing problem such as; the battery capacity; the ability to visit different charging stations; the ability to make only one tour from the depot as well as the ability to tour more than once; delivering the packages both drones and trucks and etc. Drone routing problem contains too much stochastic information in contrast to vehicle routing problem, as drones should be able to adapt, modify, and optimize their routes in delivering packages. In addition to the objectives used in general routing problems, many individual objectives may be used in drone routing problem such as minimizing the

*Corresponding author: sahin.murat@cbuu.edu.tr
Received: 07.07.2023, Accepted: 07.09.2023

customers' waiting times, reducing drone transportation costs, enhancing profitability, increasing safety in operations, minimizing the total delivery times and etc. Drone routing problems are affected many parameters in contrast to traditional vehicle routing problems. For instance drone routing should be in 3D environment and changing weather conditions (wind direction, air condition, loaded package weight, wind speed and etc.) should be considered in solutions [2].

Considering the given information, it is obvious that drone routing will have an important place in real life applications. When this routing problem is examined, it is possible to divide it into many different classes. Considering the literature review proposed by Macrina et al., [3] it is seen that drone routing can be divided into two different basic groups. In the first problem group drones and trucks perform the delivery, in the second one, only drones perform the delivery. It is possible to detail the first group of problems depending on the number of drones and trucks used and their synchronization with each other. It is possible to divide the type of problem in which the delivery is made only through drones, into two classes depending on whether trucks are used or not. In addition, it is possible to diversify all these types of problems according to the types of objective functions, the drone features used, the number of depots used, the number of tours that can be performed and etc..

It is known that the transportation costs are generally low in drone distribution, so customer satisfaction can come to the fore as the aim function. In this study, heterogeneous drone routing problem has been tried to be solved by using drones with different characteristics in terms of speed, transport and battery capacities in order to minimize the weighted total waiting times of the customers. In the problem, each customer has a weight in the objective function and it is desired that the customer with a high weight has no or low delay. Beside that a setup time is required for customer packages to be loaded into drones.

The problem addressed in this study is directly related to vehicle routing and drone routing problems. It is known that the vehicle routing problem has a large literature and it is seen that the studies on drone routing have intensified in recent years. Studies on drone routing are given in detail in the literature survey proposed by Macrina et al., [3].

Coelho et al. [4] suggested a multi-objective drone delivery problem for overcoming difficulties related to limited driving range, they addressed charging stations. For evaluating energy consumption, the authors presented a consumption rate only related to the speed of the drone. The handled problem was tried to solve by using a mathematical formulation and a metaheuristic. An important study was proposed by Dorling et al. [5] that solves drone delivery problems in which drones may perform multi-trips and serve more than one customer per route. They modelled energy consumption of the drones as a function of a battery and payload weight, considering a constant speed value. They tried to solve the problem by presenting a mixed integer linear programming formulation and a simulated annealing heuristic. Yadav and Narasimhamurthy [6] improved a heuristic for optimizing delivery schedule of drones that could serve one or several customers depending on the capacity constraints. In the problem handled by Troudi et al. [7], drones could perform multiple visits and multiple deliveries per day. An approximation model similar to that of Dorling et al. [5] has been proposed to calculate the energy consumption during a mission. Liu [8] considered an on-demand meal delivery process and suggested a dynamic drone's delivery model to optimize this process.

As in this problem, considering the drone routing problems which aim to minimize the total waiting times of customers; Moshref et al. [9] present a mathematical formulation and a heuristic solution approach for the optimal planning of delivery routes in a multi-modal system which combines truck and drone operations. The presented optimization model minimizes the waiting time of customers in the system. Moshref et al. [10] extend the traveling repairman problem by supposing a single truck that can stop at customer locations and launch drones multiple times to serve customers. The stated problem has been mathematically modelled, several bound analyses are developed to determine the maximum possible improvements in customer waiting times with an efficient hybrid tabu search-simulated annealing algorithm.

Cheng et al. [11] tried to solve a multi-trip drone routing problem, where drones' energy consumption was modelled as a nonlinear function of payload and travel distance. Logical cuts and sub gradient cuts were added in the solution process to tackle the more complex nonlinear (convex) energy function, instead of using the linear approximation method. A uniform framework to facilitate understanding different drone energy consumption models and the inter-relationships between key factors for drone delivery operations is presented by Zhang et al. [12]. Recently a literature review which considers advances in

drone technologies and their popularity has been suggested by Viloria et al. [13]. In the stated study academic contributions on drone routing problems have been analysed between 2005 and 2019 to state the research trends and recent improvements. Phalapanyakoon and Siripongwutikorn [14] considered route planning for rechargeable UAVs under the mission time constraint in cases where more than one trip can be done by drones due to limited battery capacities. Phalapanyakoon and Siripongwutikorn [15] handled with the route planning of multiple rechargeable heterogeneous UAVs with multiple trips under mission time and payload carrying constraints. They tried to detect the types and number of drones to be used and their flying paths that minimizes the monetary cost.

Literature review shows that there are many studies which take into account the waiting times of customers and heterogeneous drone routing problem separately. However, no study has been conducted on the heterogeneous drone routing problem, which tries to minimize the weighted total waiting times of customers yet. This article suggests a constructive heuristic for the heterogeneous drone routing problem to minimize the weighted total waiting times of customers. It is shown on many test instances how the efficiency of the algorithm changes when different priority values are used. The rest of the article as follows. In section 2 problem definition in detail is given while the solution method is presented in section 3. Computational experiments are given in section 4. Lastly, the conclusions and future research directions are presented in section 5.

2. Problem Definition

This article considers drone routing problem for minimizing the weighted total waiting times of customers. What needs to be decided in the problem is the order in which the customer packages will be delivered with which drone, based on the customers' and drones' information given. Customers' packages are requested to be delivered by a certain time which is named as *due time* (dt_i). If customer packages are delivered later than this time, a penalty, which is equal to multiplied by the customer's weight and the delay time (l_i), is added to the objective value. Delay time is depend on the difference between the service time (st_i) and due time (dt_i), and calculated as $l_i = \max(0, st_i - dt_i)$. The delivery of each customer's package has different degrees of importance and this value is defined as *customer weight* (cw_i). The objective value is computed as $z = \sum_{i \in N} cw_i \cdot l_i$ where N represents the set of customers.

In the studied problem, cases where drones differ from each other in terms of battery capacity, carrying capacity, speed and load capacity are considered. It has been stated by Dorling et al., (2016) that there is an almost linear relationship between the capacity of battery of a drone and the airtime depending on the load it carries. Therefore, in this study the battery capacity is associated with the payload carried by the drone as long as it stays in the air. In addition to all these, a setup time is required for customer packages to be loaded into drones. The main purpose is delivering the packages to the customers without exceeding the specified due times. If that is not possible, the weighted total delay time is tried to be minimized. The rest of the assumptions is given below:

1. There is only one of each type of drone.
2. Each customer has a weight in the objective function and the aim is minimizing the weighted total delay time.
3. Each drone has different carrying capacities in terms of load and quantity. Again, each drone has different battery capacity and speed.
4. The distances between customer locations are calculated in Euclidean.
5. It takes a certain time (setup time) for customer packages to be loaded on drones, and this time does not change depending on the drone to which the customer package is assigned.
6. Setup times do not cause a decrease in the battery capacity of the drone.
7. There is a linear relationship between the battery life of drones and the load carried by the drone itself and the time it stays in the air.
8. Each drone is initially in the depot and can only take 1 tour.
9. When assigning customer packages to drones, the drone carrying capacity, battery life and the load capacity of the drone should not be ignored.

Information about the example with 3 drones and 6 customers (there are 7 locations with depot) is given in Table 1.

Table 1. Information about the test instance.

(a) Information about the drones

Drone ID	Unit Capacity	Weight Capacity	Velocity	Battery Capacity	Energy Consumption	Drone Weight
1	3	6	300	5000	3*γ	2.0
2	4	8	275	5500	4*γ	2.5
3	5	10	250	6000	5*γ	3.0

(b) Information about the customers

Customer ID	$X_{Coordinate}$	$Y_{Coordinate}$	Package Weight (pw_i)	Due Time	Objective Weight	Package Setup Times
1 (Depot)	1500	1500	-	-	-	-
2	1813	2545	0.87	5	0.15	0.15
3	1934	4443	2.16	8	0.53	0.22
4	366	3316	1.62	10	0.44	0.20
5	692	2563	3.6	14	0.7	0.16
6	4148	348	0.63	12	0.2	0.33
7	555	28	0.25	8	0.08	0.14

From the Table 1 the Euclidian distances between the customer locations can be computed easily. In the stated table γ is a constant value used to determine the battery capacity that the drone consumes depending on the load and the time it stays in the air. A solution for this example is given in Figure 1.

As is seen in Figure 1 package 2 and 3 are assigned to the drone 1 and route for this drone must be 1-2-3-1. It shouldn't be ignored that the weight and unit capacities of drone 1 are sufficient for package 2 and 3. Euclidean distances from location 1 to 2, 2 to 3 and 3 to 1 are respectively equal to nearly 1091, 1902 and 2975. Total setup time for this drone is computed as (0.15 + 0.22) 0.37 and travel time is calculated as (3.63 + 6.34 + 9.91) 19.88. In this example drone 1 firstly flies from depot to location 2 in 3.63 time unit with 3.03 (0.87 + 2.16) package weight. Notice that package 2 and package 3 are uploaded to drone 1 at depot. The required battery capacity of drone 1 for flying from depot to location 2 is equal to multiplied total weight (the weight of drone and the weights of packages) with the flying duration and constant $\left((2 + 3.03)\cdot(3.63)\cdot 3\cdot\gamma = 54.77\gamma\right)$. γ is accepted as 10 for this example. Similarly required capacity from location 2 to location 3 and from location 3 to depot are respectively computed as 79.12γ and 59.46γ. Total required battery capacity for route 1-2-3-1 is equal to 193.35γ. If the value of γ was greater than 25.86 the battery capacity of drone 1 would be insufficient for the given assignments. Arrival times of location 2 and 3 are detected by considering flying and setup times as 0.37+3.63=4 and 0.37+3.63+ 6.34 = 10.34 respectively. Route of drone 2 is 1-4-5-1 and the flying time from location 1 to 4, location 4 to 5 and location 5 to 1 are respectively 7.78, 2.98 and 4.85. Similarly route of drone 3 is 1-6-7-1 and the flying time from location 1 to 6, location 6 to 7 and location 7 to 1 are respectively 11.55, 14.42 and 7. Consequently, arrival times of the drones to the customer locations are (4 – 10.34 – 8.14 – 11.12 – 12.02 – 26.44). Waiting time of each customer is computed considering due time and arrival time. These are (0 – 2.34 – 0 – 0 – 0.02 – 18.44) and weighted waiting times for each customer is (0 – 1.240 – 0 – 0 – 0.004 – 1.475). The value of the objective for this solution is computed as 2.719.

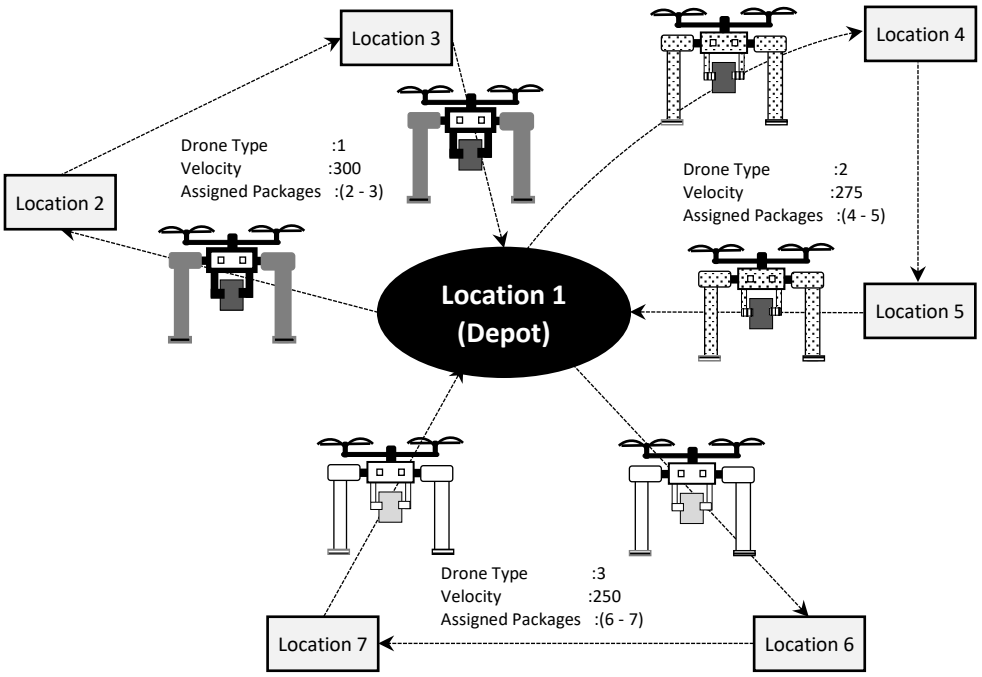

Figure 1. An illustrative example for heterogeneous drone routing problem with setup times.

To the author best knowledge the drone routing problem described above and illustrated on an example is not considered in the literature for the stated purpose. Therefore, in the following section, a new constructive heuristic method has been suggested for the solution of the problem is presented.

3. Solution Method

An effective constructive solution method has been suggested for solving the heterogeneous drone routing problem with setup times by using an array with (n + m) elements where n represents the number of customer and m shows the number of drones. In the similar studies from literature, permutation coding is generally used since it is more suitable for the structure of the problem. However, in this study, it is preferred to convert the continuous values to permutation representation later in order to use different priority values. For the example given in Figure 1 a continuous array and its conversion to permutation representation is given Figure 2. Note that location 1 is depot. As is seen in Figure 2 the customer or drone which has the highest value is assigned smallest position in the permutation encoding.

Location 2	Location 3	Location 4	Location 5	Location 6	Location 7	Drone 1	Drone 2	Drone 3
0,30	0,25	0,61	0,88	0,58	0,12	0,90	0,26	0,50
Customer Sequence *n*=6						Drone Sequence *m*=3		

(a) Array with continues numbers.

Position 1	Position 2	Position 3	Position 4	Position 5	Position 6	Position 1	Position 2	Position 3
5	4	6	2	3	7	1	3	2
Customer Sequence *n*=6						Drone Sequence *m*=3		

(b) Permutation encoding.

Figure 2. An illustrative example of an array with continuous numbers and its permutation encoding.

The steps of the constructive heuristic are given in Figure 3. The assignments of the customers' packages to the drone have been satisfied by using this algorithm. As is seen in this figure all routes of drone start from depot since drones are ready at depot.

Algorithm :Generating a solution from an array which shows assignment priorities for the drone and customers
Input : An array which shows assignment priorities, information about the drones and locations
Output : Objective function value and the routes for drones

Step 1. Set $\mathbf{DR} = \{dr_k = 0 \mid k \in \mathbf{K}\}$; $\mathbf{DW} = \{dw_k = 0 \mid k \in \mathbf{K}\}$; $\mathbf{DU} = \{du_k = 0 \mid k \in \mathbf{K}\}$; $Route_k = \{1\},\ k \in \mathbf{K}$.
Step 2. Generate the permutation encoding from the given array.

while (*all customers are not assigned to a drone*)
{
Step 3. Take current customer (*i*) from permutation encoding**,** and find the most appropriate drone which can take the customer package.

Step 3.1. Find the elements of **AD** set which shows the appropriate drones by controlling the drone unit capacity, drone weight capacity and drone battery capacity

$$\mathbf{AD} = \{k \mid (du_k + 1) \le uc_k,\ (dw_k + q_i) \le wc_k,\ RB_k(Route_k + i) \le bc_k\}$$

Step 3.2. ***If*** **(AD** = {**})** Add penalty value to the objective function value and Go to **Step 6**;
Else Find the selected drone (*k*) $k = \min_{k \in \mathbf{AD}} (dr_k)$ and *k* is the first drone element in the permutation encoding

Step 4. Update the $dr_k = dr_k + (d_{ji}/v_k)$ where *j* is the last location in $Route_k$
$dw_k = dw_k + q_i$;
$du_k = du_k + 1$; $Route_k = Route_k + i$

}
Step 5. Compute the objective function value considering setup times of drones.
Step 6. Output the objective function value and the routes for drones.

DR: set of ready times of drones; **DW**: set of the total weights of packages which are assigned to each drones; **DU**: set of the number of the packages which are assigned to each drones; $Route_k$: route of drone k; q_i: package weight of location *i*; d_{ji}: the distance between location *j* and *i*, v_k: velocity of drone *k*; $RB_k(Route_k + i)$: the required battery capacity for the new route which is formed by inserting the location *i* to the route of drone *k* ($Route_k$)

Figure 3. The main steps of the constructive heuristic.

In the first step of the algorithm, required sets are generated then in the second step continuous numbers are converted to permutation representation. It is requested that the package of the customer with the highest priority be assigned to the earliest available drone. If more than one drone is available at the earliest, the customer package is requested to be assigned to the drone with the highest priority value. When calculating the value of RB_k, it should not be ignored that the battery capacity required for the return of the drone to the depot is also calculated on the given route. Some permutations may form such that the capacity of the drones is not sufficient to carry customer packages. In such cases, the algorithm is stopped by giving a very high value (penalty) to the objective function. It shouldn't be ignored that the setup times of customer packages to the drones are added to the service times after the routes are obtained. An illustrative example for constructive heuristic with given array is presented in Figure 4.

Remaining Customers	*Selected Location*	*Appropriate Drones*	*Most Suitable Drones*	*Selected Drone*	*Drone Suitable Times* (dr_k)	*Drone Route Assignments*
5-4-6-2-3-7	5	1-2-3	1-2-3	1	{4.45} {0} {0}	{1-5} {1} {1}
4-6-2-3-7	4	1-2-3	2-3	3	{4.45} {0} {8.56}	{1-5} {1} {1-4}
6-2-3-7	6	1-2-3	2	2	{4.45} {18.68} {8.56}	{1-5} {1-6} {1-4}
2-3-7	2	1-2-3	1	1	{8.19} {18.68} {8.56}	{1-5-2} {1-6} {1-4}
3-7	3	1-2-3	1	1	{14.53} {18.68} {8.56}	{1-5-2-3} {1-6} {1-4}

7	7	2-3	3	3	{14.53}{18.68} {16.29}	{1-5-2-3} {1-6} {1-4-7}

Generated routes for drones	:{1-5-2-3-1} {1-6-1} {1-4-3-1}
Service time	: {0 – 9.12 – 15.06 – 8.09 – 4.98 – 20.68 – 16.63}
Lateness for customers	: {0 – 4.12 – 7.06 – 0 – 0 – 8.68 – 8.63}
Weighted Total Lateness	: (4.12 · 0.15) + (7.06 · 0.53) + (8.68 · 0.2) + (8.63 · 0.08) = 6.79

Figure 4. An illustrative example for the suggested constructive heuristic.

In the suggested constructive heuristic, nine different priority approaches for customers and three different priority approaches for drones are used to measure the effectiveness of the algorithm. Explanations of the priorities for customers are given in Table 2.

Table 2. Explanations of priority approaches for customers.

Priority ID for customer	Explanation
1	Random number between 0 and 1 [0-1]
2	$(1/dt_i)$
3	(cw_i)
4	$1/(setup_i)$
5	$1/(pw_i)$
6	(cw_i/dt_i)
7	(pw_i / dt_i)
8	(cw_i / pw_i)
9	$cw_i / (dt_i \cdot pw_i)$

dt_i: due time of customer i, cw_i: the objective weight of customer i, $setup_i$: setup time of package i, pw_i: package weight of customer i.

As is seen in Table 2 the first priority is generated randomly, and second one is related to the customers' due times. Logically, if a customer's due time is late, that customer's package can be delivered later. Therefore second priority is arranged as $1/dt_i$. Third priority is the customer objective function weight. While the fourth one gives the highest priority to the customer whose package has the smallest setup time, the fifth priority gives the highest priority to the customer whose package is the lightest. While sixth priority is obtained by dividing customer's objective function weight by the due time, seventh priority is obtained by dividing customer's package weight by the due time. Eighth priority value gives the highest priority to the customer who has the highest objective function weight for per package weight unit. The last priority is computed considering customer's objective function value weight, due time and package's weight. Explanations of priorities for drones are given in Table 3.

Table 3. Explanations of priority approaches for drones.

Priority ID for drone	Explanation
1	Random number between 0 and 1 [0-1]
2	Velocity of drone
3	Unit capacity of drone

As is seen in Table 3, first priority is generated randomly, and the second one gives the highest priority to the fastest drone. According to the last one, highest priority is given to the drone with the highest unit carrying capacity. 27 (9 · 3) different priority sequences have been created by crossing these drone and customer priority values. In the experimental study, these 27 different priority values are used as inputs in the constructive algorithm mentioned above. In the next section, computational experiments are given.

4. Computational Experiments

In order to measure the effectiveness of the suggested priority values on the proposed constructive heuristic, 34 different test problems, consisting of the smallest 5 customer 3 drones and

the largest 20 customer 7 drones, were used. These test instances have been generated for this study randomly. The constructive heuristic is coded in the C# programming language and the calculations took less than 1 second for each test instance. In order to compute the efficiency, the best solution obtained from 27 different priority values for these 34 samples was taken into account. Deviations from the best solution found were calculated for each priority as in equation (1).

$$\% \; gap = 100 \cdot \left(sol_i - sol_{Best} \right) \Big/ sol_i \qquad (1)$$

In equation (1) sol_i represents the objective function value of the solution obtained by using priority i and sol_{Best} shows the best objective function value obtained by using all priority approaches. The summary of the calculation results on the basis of the priorities of drones and customers is presented in Table 4.

Table 4. Summary of the computational study according to priorities of the customers and drones.

Priority for customer	Priority for drone	# of instances	Average *% gap*	#of best solution	# of no solution
1	1	34	53.742	0	5
1	2	34	30.969	2	6
1	3	34	58.343	0	5
2	1	34	43.022	0	5
2	2	34	35.612	2	6
2	3	34	46.678	0	**1**
3	1	34	50.136	1	2
3	2	34	24.447	**8**	6
3	3	34	48.645	0	2
4	1	34	45.502	2	3
4	2	34	25.892	5	2
4	3	34	51.292	0	3
5	1	34	40.572	0	8
5	2	34	**20.045**	3	**7**
5	3	34	47.812	1	9
6	1	34	45.622	0	3
6	2	34	37.839	0	2
6	3	34	47.741	0	2
7	1	34	51.222	0	3
7	2	34	49.889	1	2
7	3	34	50.154	0	**1**
8	1	34	49.129	1	4
8	2	34	22.261	6	4
8	3	34	49.492	0	6
9	1	34	43.556	1	3
9	2	34	32.578	1	7
9	3	34	46.654	2	3

Note: Bold values shows the best value among the column.

In Table 4, while the first and second column shows the priority IDs for customers and drones, third column states the number of instances. Forth column gives the average *% gap* of 34 test instances for the given priorities. Fifth column gives the number of best solution obtained by this priorities. For example any best solution could not obtain among the 34 test instances by using priority 1 approach in the suggested constructive heuristic. The last column shows the number of infeasible solution obtained by suggested priority values. When Table 4 is examined, it is seen that the best approach in terms of *% gap* value is the 5th priority approach for the customer and the 2nd priority approach for the drone. In other words, good solutions were obtained in parallel with the loading of the light ones from the customer packages to the fast drones. Similarly, it has been seen that good results can be obtained by loading customer packages with high objective function weight and lightest package weight priority into fast drones.

Considering the number of reaching the best solution, it is seen that the most effective method is the 3rd priority approach for customers and the 2nd priority approach for drones. In other words, it is seen that the probability of reaching the best solutions is higher by assigning the customer packages with a high objective function weight to the fast drones. The

summary of the computational study only according to the customer priority values is presented in Table 5.

Table 5. Summary of the computational study based on priorities for only customers.

Priority For Customer	# of instances	Average % gap	# of best solution	# of no solution
1	102	47.879	2	16
2	102	42.057	2	12
3	102	41.799	**9**	10
4	102	40.735	7	8
5	102	**35.787**	4	24
6	102	43.714	0	7
7	102	50.411	1	**6**
8	102	40.085	7	14
9	102	41.305	4	13

Note: Bold values shows the best value among the column.

As is seen in Table 5 the best priority approach for the customer is the 5th priority approach when only average *% gap* value is considered. However, the probability of obtaining an infeasible solution with the constructive heuristic is also quite high with this priority approach, since this approach obtained infeasible solutions in 24 of the 102 examples. Considering the number of best solution 3rd priority approach is quite effective. The summary of the computational study according to the drone priority values is presented in Table 6.

Table 6. Summary of the computational study based on priorities for only drones.

Priority For Drone	# of instances	Average % gap	# of best solution	# of no solution
1	306	47.045	5	36
2	306	**31.338**	**28**	42
3	306	49.596	3	**32**

Note: Bold values shows the best value among the column.

Not many priority approaches have been used in terms of drone priorities, but it is seen that the best method is to give the highest priority to the fastest drone. In order to increase the probability of obtaining a suitable solution, it seems logical to give the highest priority to the drone with a high carrying capacity.

5. Conclusions and Future Research Direction

In parallel with technological developments on UAVs, the use of these vehicles in package delivery systems has been increased. And the integration of online shopping into daily life has also increased the need for innovative solutions in logistics operations. Along with all these developments, innovative research on drone routing was needed. This article considers the heterogeneous drone routing problem, which takes into account the setup times of customers' packages to the drones and aims to minimize the weighted total waiting times of customers. A constructive heuristic has been suggested to solve the stated problem. 27 different priority approaches and 34 different test instances, consisting of the smallest 5 customers with 3 drones and the largest 20 customers with 7 drones have been used for evaluating the suggested constructive heuristic. Through the computational experiments it has been seen that good solutions can be obtained by assigning the light customer packages to the fast drones for the given test instances by using the suggested constructive heuristic.

As a result, in this study, a new variation of drone routing has been discussed and a constructive heuristic has been developed. Considering the drone routing area, it is seen that it is a new and open

research area and different solution methods are needed. Therefore, it is necessary to investigate the effectiveness of metaheuristic such as simulated annealing, tabu search, genetic algorithm and exact solution methods such as branch & bound, branch & cut, benders decomposition on the solution of the stated problem. In this study, it is assumed that all data are deterministic, but in many real-life applications, data are known may be stochastic. Considering this situation, new solution approaches can be developed for stochastic drone routing problems.

References

[1] M. Turgut, and B. Şeker, "An exploratory study on the use of unmanned aerial vehicles (UAVs) in transportation: drone transportation and its applications," *Journal of Intelligent Transportation Systems & Applications*, vol. 5, no. 2, pp. 169-187, 2022.

[2] A. Thibbotuwawa, G. Bocewicz, P. Nielsen, and Z. Banaszak, Z. "Unmanned aerial vehicle routing problems: a literature review," *Applied sciences*, vol. 10, no. 13, pp. 4504, 2020.

[3] G. Macrina, L. D. P. Pugliese, F. Guerriero, and G. "Laporte, Drone-aided routing: A literature review," *Transportation Research Part C: Emerging Technologies*, vol. 120, 2020.

[4] N. B. Coelho, V. N. Coelho, I. M. Coelho, L. S. Ochi, R. Haghnazar, D. Zuidema, and A. R. da Costa, "A multi-objective green UAV routing problem," *Computers & Operations Research*, vol. 88, pp. 306-315, 2017.

[5] K. Dorling, J. Heinrichs, G. G. Messier and S. Magierowski, "Vehicle routing problems for drone delivery", *IEEE Transactions on Systems, Man, and Cybernetics: Systems*, vol. 47, no. 1, pp. 70-85, 2016.

[6] Y. Yadav, and A. Narasimhamurthy, "Algorithms for solving the vehicle routing problem with drones", presented at the 2017 Ninth International Conference on Advances in Pattern Recognition (ICAPR), IEEE, Bangalore, India, 2017.

[7] A. Troudi, S. A. Addouche, S. Dellagi and A. E. Mhamedi, "Sizing of the drone delivery fleet considering energy autonomy," *Sustainability*, vol. 10, no. 9, 2018.

[8] Y., Liu, "An optimization-driven dynamic vehicle routing algorithm for on-demand meal delivery using drones," *Computers & Operations Research*, vol. 111, pp. 1-20, 2019.

[9] M. Moshref-Javadi, A. Hemmati and M. Winkenbach, "A truck and drones model for last-mile delivery: A mathematical model and heuristic approach," *Applied Mathematical Modelling*, vol. 80, pp. 290-318, 2020.

[10] M. Moshref-Javadi, S. Lee and M. Winkenbach, "Design and evaluation of a multi-trip delivery model with truck and drones," *Transportation Research Part E: Logistics and Transportation Review*, vol. 136, pp. 101887, 2020.

[11] C. Cheng, Y. Adulyasak and L. M. Rousseau, "Drone routing with energy function: Formulation and exact algorithm," *Transportation Research Part B: Methodological*, vol. 139, pp. 364-387, 2020.

[12] J. Zhang, J. F., Campbell, D. C. Sweeney and A. C. Hupman, "Energy consumption models for delivery drones: A comparison and assessment," *Transportation Research Part D: Transport and Environment*, vol. 90, p. 102668, 2021.

[13] D. Viloria Rojas, E. L. Solano-Charris., A. Muñoz-Villamizar and J. R. Montoya-Torres, "Unmanned aerial vehicles/drones in vehicle routing problems: a literature review," *International Transactions in Operational Research*, vol. 28, no. 4 pp. 1626-1657, 2021.

[14] K. Phalapanyakoon and P. Siripongwutikorn, "Route Planning of Unmanned Aerial Vehicles under Recharging and Mission Time Constraints," *International Journal of Mathematical, Engineering and Management Sciences*, vol. 6, no. 5, p. 1439, 2021.

[15] K. Phalapanyakoon and P. Siripongwutikorn, "Route planning of heterogeneous unmanned aerial vehicles under recharging and mission time with carrying payload constraints," *Journal of Industrial Engineering and Management*, vol. 16, no. 2, pp. 215-235, 2023

Bitlis Eren Üniversitesi Fen Bilimleri Dergisi
BİTLİS EREN UNIVERSITY JOURNAL OF SCIENCE
ISSN: 2147-3129/e-ISSN: 2147-3188
VOLUME: 12 NO: 3 PAGE: 863-870 YEAR: 2023
DOI:10.17798/bitlisfen.1330206

Birth and Various Period Live Weights of Hair Goat Kids

Ayhan YILMAZ[1*], Doğan DENİZ[2] Mehmet Emin VURAL[3]

[1] *Bitlis Eren University, Faculty of Health Sciences, Department of Nutrition and Dietetics*
[2]*Diyarbakır Damızlık Koyun ve Keçi Yetiştiricileri Birliği, Diyarbakır*
3 GAP Uluslararası Tarımsal Araştırma ve Eğitim Merkezi Müdüürlüğü, Diyrabakır

(ORCID: *0000-0002-5990-7550*) *(*ORCID: *0000-0002-0404-2975*) *(*ORCID: *0000-0002-6831-5071*)*

Keywords: Live Weight, Goat, Hair Goat, Growth, Kid.

Abstract

The animal material of this study consisted of 6000 goats and 300 goats, which were supported within the scope of the "Animal Breeding in the Hands of the Public National Project" in the province of Diyarbakir of Turkey. Within the scope of the project in which the research was included, the animals were identified and their records were kept. The records of goats in 2019, 2020, 2021 and 2022 formed the data of this research. The weights of birth, 30th day, 60th day, 90th day were determined in goats born in the specified years. Live weight of hair goat kids at various periods (birth, 30th, 60th, 90th) and daily body weight gains up to 90th day (birth-30, 30-60, 90th days). Statistical analysis of the data was made in the SPSS package program.

In the study, birth weight of Hair goat kids was 2.84±0.010; Body weight at day 30 was 6.97±0.028; Body weight at day 60 was determined as 11.06±0.065 and body weight at 90th day was determined as 14.49±0.058. In addition, daily live weight gains on the 30th day of birth in Hair goat kids was 136.84±0.884; body weight gain at birth-60th day 136.41±1.083; daily body weight gain at birth-90th day was determined as 129.08±0.640. When the effect of environmental factors examined in the study was evaluated, the effect of gender on live weights of all ages was found to be statistically significant. However, in the study, it was determined that the type of birth and the effect of birth month showed a difference only between birth and 30th day age. As a result, in the current thesis study, it was found that the findings obtained in terms of growth and development characteristics in Hair goat kids were compatible with the findings of other studies on the subject.

1. Introduction

Our country, both geographically and with its socio-economic characteristics, presents a suitable qualification for goat breeding. Goat breeding and production is suitable for breeders living in mountainous and rural areas. Goat raising is an important source of employment and livelihood. Periodic change in Turkey's goat population has a fluctuating structure. Social and economic problems in rural areas, migration, traditional agricultural production structure, lack of organization, deficiencies in livestock support, low demand for goat products, difficulties in finding shepherds and reluctance of young people are some of the reasons for the decline in goat breeding. [1]. In recent years, some measures have been taken to prevent this decline. Apart from the economic characteristics of the production line, projects are carried out by the relevant ministry in order to protect our cultural animal genetic resources [2].

Sustainability in animal production is closely related to the farming economy. In other words, it does not seem possible for non-economic animal

*Corresponding author: *ayilmaz1@beu.edu.tr*
Received: 20.07.2023, Accepted: 20.09.2023

production to be sustainable. Reproductive characteristics, birth weight, viability, growth and development characteristics of goats are very important indicators in terms of farming economy [3]. The yield of animal production is closely related to healthy young animal and their growth-development characteristics. Birth weight of kids and live weight gains in the following periods are important growth and development criteria for economic goat breeding. As in other animal production lines, the basis of goat breeding and sustainability is its profitability. Especially due to the traditional structure of our animal production and the ever-changing characteristics of the economy, change is necessary in animal production. In other words, an animal production based only on self-consumption and cheap input costs loses its value in contemporary production systems. Various projects are carried out by the related ministry in our country. The Ministry also adopts various approaches to use animal resources effectively. In recent years, projects have been carried out with the participation and support of breeders and long-term production plans are envisaged.

The aim of this study is to determine the birth weights and 30th, 60th and 90th day live weights of hair goat populations supported within the scope of the project in Diyarbakır in terms of various environmental factors.

2. Material and Method

The animal material of this study consisted of 6000 goats and 300 goats, which were supported within the scope of the "Animal Breeding in the Hands of the Public National Project" in the province of Diyarbakir of Turkey. Within the scope of the related project, the animals were given ear numbers and the animals were recorded. The records of hair goats for the years 2019, 2020, 2021 and 2022 formed the data of this research. Birth, 30th day, 60th day and 90th day live weights of kids obtained in the mentioned years were determined. Births were followed in the villages where the research was conducted. Birth weight of kids were determined by weighing in 24 hours with precision scales (sensitivity of 1 g). In addition, the type of birth, gender and date of birth were recorded. In order to determine the growth-development performance of the kids, their age-adjusted body weights were calculated in three different periods (birth, 30th day, 60th day, 90th day) from birth to 3 months. Calculations were made separately for males and females and no adjustment was made for birth weight. Body weights of hair goat kids at various periods (birth, 30th, 60th, 90th day) and daily body weight gains to 90th day (birth-30th, 30-60th, 90th day) were analyzed using the following statistical model:

In order to determine the growth-development performance of kids, age-adjusted live weights were calculated in 4 different periods (birth, 30th, 60th, and 90th days) from birth to weaning (90th day) and no adjustment was made for birth weight.

Live weights of kids at various periods (birth, 30th, 60th and 90th days) and daily average body weight gains up to 90th day (birth-30th, 60th and 90th days) were analyzed using the following statistical model:

$$Y_{ijkl} = \mu + a_i + b_j + c_k + d_l + e_{ijkl} \quad (1)$$

Formulation;

$\boldsymbol{Y_{ijkl}}$ = i. year, j. gender, k. in the birth type, the analyzed live weight/live weight gain of the lamb born in the 1st month of birth

μ = population mean,

a_i = i. effect of year (i=2019, 2020, 2021, 2022),

b_j = j. effect of gender (j = 1, 2; erkek ve dişi),

c_k = k. effect of birth type (k = 1, 2; tek ve ikiz),

d_l = l. effect of 1st month of birth (l = 1 (january), 2 (february), 3 (march)), 4 (april), 5 (may),

$\boldsymbol{e_{ijkl}}$ = Indicates independent and random error.

The data obtained from the research were processed into Microsoft Excel program and statistical analyzes were made using SPSS package program (SPSS, 2012). More than two subgroups of the factors determined to be important as a result of the analysis of variance were compared with the Duncan test.

3. Results

Averages of live weights of hair goat kids in various periods are given in Table 1.

Table 1. Average of least squares of live weights at birth, 30th, 60th and 90th days of hair goat kids

Characteristics	Birth weight		Live weight in 30th		Live weight in 60th		Live weight in 90th	
	n	X±Sx	n	X±Sx	n	X±Sx	n	X±Sx
Year								
2019	4479	2,51+0,013	4127	6,94+0,034	4064	11,31+0,073	3569	14,79+0,069
2020	4490	2,83+0,013	4473	6,68+0,034	4427	10,82+0,071	4125	13,85+0,070
2021	5139	3,06+0,013	4555	7,61+0,034	4300	12,14+0,075	3234	16,62+0,081
2022	5697	2,97+0,012	4806	6,63+0,033	4514	9,95+0,072	3356	12,70+0,075
Gender		*		*		*		*
Female	10090	2,77+0,011 b	9074	6,76+0,030 b	8714	10,71+0,068 b	7214	13,99+0,063 b
Male	9715	2,92+0,011 a	8887	7,17+0,030 a	8591	11,41+0,068 a	7070	14,99+0,063 a
Birth type		*		**		**		**
Twin	3048	2,68+0,014 b	2710	6,77+0,037 b	2658	10,84+0,077 b	2340	14,30+0,079 b
Single	16757	3,01+0,009 a	15251	7,16+0,025 a	14647	11,27+0,062 a	11944	14,68+0,052 a
Month of birth		**						
January	612	2,85+0,027 c	527	5,01+0,068	527	7,65+0,111	527	10,56+0,141
February	5962	2,81+0,009 b	5502	6,07+0,023	5502	9,69+0,038	5320	13,43+0,049
March	10109	2,91+0,008 a	9430	6,82+0,019	9302	10,91+0,031	7964	15,16+0,042
April	2708	2,85+0,014 a	2272	8,04+0,034	1900	12,60+0,060	473	18,81+0,144
May	414	2,81+0,032 a	230	8,90+0,099	74	14,44+0,284		
General	19805	2,84+0,010	17961	6,97+0,028	17305	11,06+0,065	14284	14,49+0,058

When the least squares averages of the birth, 30th, 60th and 90th day live weights of hair goat kids were evaluated, it was determined that the birth, 30th, 60th and 90th day live weights of the kids did not show a significant difference according to the year of birth ($p > 0,05$). On the other hand, when the comparisons made by gender are examined, it is seen that the weights of male kids at the 4 measurement times are significantly higher than female kids ($p < 0,05$). In the comparisons made according to the birth type, it was found that the weights of the single born kids at the time of 4 measurement were higher than the twin born kids ($p < 0,05$). Finally, when the weight values were compared according to the months of birth, significant differences were observed only according to the birth weight ($p < 0,01$). Accordingly, it can be said that the birth weights of the kids born in March, April and May are higher than the birth weights of the kids born in January and February. On the other hand, it was determined that the 30th, 60th and 90th day live weights did not show a statistically significant difference according to the month of birth ($p < 0,05$).

The least squares averages of daily live weight gains on the 30th, 60th and 90th days of birth in Hair goat kids are given in Table 2.

Table 1. The least squares averages of daily live weight gains on the 30th, 60th and 90th days of birth in Hair goat kids

Characteristics	Birth-30th CAA		Birth-60th CAA		Birth-90th CAA	
	n	X±Sx	n	X±Sx	n	X±Sx
Year						
2019	4127	147,35+1,098	4064	146,37+1,218	3569	136,16+0,764
2020	4473	127,97+1,077	4427	132,88+1,188	4125	122,29+0,776
2021	4555	151,39+1,101	4300	151,16+1,245	3234	150,71+0,899
2022	4806	120,66+1,071	4514	115,25+1,203	3356	107,18+0,835
Gender		**		*		*
Female	9074	132,40+0,951 b	8714	131,78+1,126 b	7214	124,39+0,698 b
Male	8887	141,28+0,955 a	8591	141,05+1,125 a	7070	133,78+0,701 a
Birth type		***		***		***
İkiz	2710	135,80+1,192 b	2658	135,61+1,284 b	2340	128,84+0,882 b
Tek	15251	137,89+0,800 a	14647	137,22+1,032 a	11944	129,33+0,582 a
Month of birth						
January	527	70,71+2,178	527	79,44+1,852	527	85,28+1,570
February	5502	108,30+0,736	5502	114,63+0,627	5320	118,03+0,546
March	9430	130,24+0,596	9302	133,27+0,510	7964	135,96+0,466
April	2272	173,06+1,087	1900	162,09+1,002	473	177,07+1,606
May	230	201,90+3,169	74	192,63+4,713		
General	17961	136,84+0,884	17305	136,41+1,083	14284	129,08+0,640

The least squares averages of the birth-30th, 60th and 90th day live weight gains in hair goat kids were evaluated and the data on the birth-30th day, birth-60th day and birth-90th day live weight gains were compared statistically. According to the findings, it was determined that the 30-day, 60-day and 90-day live weight gains of the kids did not show a significant difference according to the year of birth ($p > 0,05$). On the other hand, it is seen that the 30-day, 60-day and 90-day live weight gains of male kids are significantly higher compared to female kids ($p < 0,05$). In the evaluation made according to the birth type, it was seen that the 30-day, 60-day and 90-day live weight gains of the single born kids were significantly higher than the live weights of the twin born kids ($p < 0,01$). Finally, when the weight values were compared according to the months of birth, it was determined that the 30-day, 60-day and 90-day live weight gains of the kids did not show a significant difference according to the birth month ($p > 0,05$).

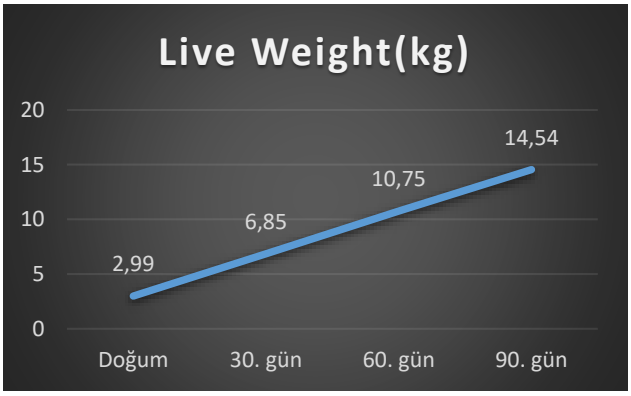

Figure 1. Growth curve of kids for various periods of body weight

The average live weight of all kids examined in the study was 2.99±0.005 kg at birth. On the 30th day, it was measured as 6.85±0.013 kg on average. It is seen that it is 10.75±0.021 kg on the 60th day and 14.54±0.031 kg on the 90th day.

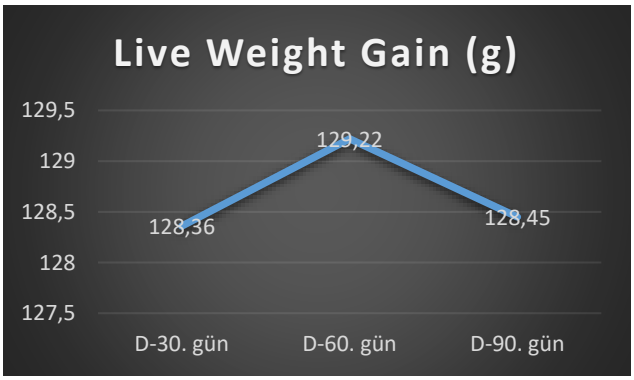

Figure 2. Growth curve of kids for live weight gains in various periods

The live weight gains of all kids examined in the study were 128.36±0.408 g per day from birth to the 30th day. It was determined as 129.22±0.353 g per day until the 60th day and 128.45±0.340.

4. Discussion, Conclusion and Suggestions

In this study, the birth weight of hair goat kids and the values related to hair goat live weights in various periods were determined. In the study, the birth weight of hair goat kids was measured as 2.84±0.010. On the 30th day, the live weight is 6.97±0.028. The live weight on the 60th day was 11.06±0.065 and the live weight on the 90th day was determined as 14.49±0.058. In addition, daily live weight gain between birth and 30th days in hair goat kids is 136.84±0.884. Live weight gain at birth-60th day is 136.41±1.083 and daily live weight gain at birth-90th day is 129.08±0.640. When the effect of environmental factors examined in the study was evaluated, the effect of gender on live weights of all ages was found to be statistically significant.

Growth and development characteristics of kids are important in terms of animal production economy. Growth is one of the important practical and economic physiological characteristics in livestock raising [4]. Birth weight in kids affects postnatal growth and viability characteristics of kids [3,5].

In the study, the average birth weight of hair goat kids was found to be 2.99±0.005 kg and the minimum weight was 1.03 kg and the maximum weight was 4.97 kg. The coefficient of variation (%) was found to be 22.95%. This value, which was determined as 4.97, has a place between the values 2.85 kg reported by Kırk [6]; 2.58 kg reported by Oral and Altınel [7]; 2.6 kg reported by Öztürk [8]; reported 2.63 kg by Sengonca et al. [9]; 2.18 kg reported by Şimşek et al. [10]; 2.77 kg reported by Şimşek and Bayraktar [11]; 2.99 kg reported by Şimşek [12]; 3.89 kg reported by Darcan [13] (2000); 3.8 kg reported by Daş and Savaş [14]; 3.31 kg by Montenegro [15]; and 3.72 kg reported by Tozlu [16].

In the study, the weight of the hair goat kids on the 30th day was found to be 6.85±0.013 kg. Compared to the studies conducted for this purpose, this value was reported as 6.29 kg in females and 6.89 kg in males for Angora goat kids [17]. In other studies, conducted for Angora goat kids, the 30th day live weight was reported as 9.669 kg [18] and 5.5 kg [19, 20]. In a study conducted for colored Angora goats, the live weight was found to be 4.34 kg on the 30th day [21]. In another study conducted for Angora goat and colored Angora goat hybrids, the live weight was 4.30 kg [21], 5.78 kg for Norduz goats [22], 6.36 kg for hair goats [7], 8.68 kg [23], 6.49 kg [24]. The value of 6.85±0.013 kg, which was determined as the 30th day weight in hair goat kids in the study, is among the values reported especially for hair goats.

In this study, the average live weight of hair goat kids on the 60th day was found to be 10.75±0.002 kg. In the researches, Öztekin and Akçapınar [17] determined the 60th day weight of Angora goats as 9.60 kg for females and 10.60 kg for males; Yurtseven et al. [18] 4,158 kg (overall average); Özdemir and Dellal [19] 8.2 kg; Yeni [20] 8.20 kg and Özel [22] 0.51 kg for Norduz Goats. In the research conducted for hair goats, Oral and Akınel [7] 9.75 kg; Şimşek and Bayraktar [11] 11.80 kg; Atay et al. [23]13.98 kg; Erten and Yılmaz [24] 9.81 kg; Şimşek and Bayraktar [11] 11.04 kg in Saanen x hair goat hybrids; Şengonca et al. [25] 14.38 kg in Bornova goats; Salman [26] 9.86 kg in Kilis goats; Salman [26] determined 8.66 kg in Kilis x Saanen goat hybrids. In this study, the 90th day weight of hair goat kids was determined as 14.54±0.0031. In other studies, Öztekin and Akçapınar [6] found 10.4 kg in females and 13.1 kg in males in Angora goats; Yurtseven et al. [18] 19,647 kg; Özdemir and Dellal [19] 11.7 kg; Yeni [20] 11.70 kg; Özel [22] 14.82 kg for Norduz goats; Oral and Altınel [7] 13.58 kg for hair goats; Şimşek and Bayraktar [11] 16.05 kg; Atay et al. [23] 19.18 kg; Erten and Yılmaz [24] 12.32 kg; Şimşek and Bayraktar [11] 14.14 kg for Saanen x hair goat hybrids; Gök et al. [27] 24.1 kg for Honamlı goats. Keskin et al. (2016) 10.7 kg for Kilis x hair goat

hybrids; Salman (2009) 12.38 kg for Kilis x Saanen hybrids and Keskin et al. [28] 10.1 kg for Damascus goats.

In addition, daily live weight gain on the 30th day of birth in hair goat kids was 128.36±0.408; daily live weight gain at birth-60th day was 129.22±0.353; daily body weight gain on the 90th day of birth was determined as 128.45±0.340. When the effect of environmental factors examined in the study was evaluated, the effect of gender on live weights of all ages was found to be statistically significant. In research, Şimşek and Bayraktar[11] found live weight gain of birth-90th 147 g for hair goats; Erten and Yılmaz [24] 102.51 g; Şimşek and Bayraktar [11] 124 g for Saanen x Hair Goat hybrids; Salman [26] 125.6 g for Kilis Goats; Salman [26] 103.2 g for Kilis x Saanen hybrids; Gök et al. [27] 218g; Özel [22] 132.1 g for Norduz goats was reported.

As a result, live weights at birth, 30th, 60th and 90th days of hair goat kids supported within the scope of the project in this study are consistent with the findings in the literature. When the environmental factors examined were evaluated, it was revealed that gender had a statistically significant effect in all periods.

4.1. Suggestions

1) In order to get efficiency in goat breeding in Turkey, an effective improvement and breeding program should be implemented.

2) In Turkey, goat breeding studies were delayed and an effective model could not be developed in goat breeding. A breeding program involving hair goat and Angora goat breeder communities, relevant public institutions (TİGEM, Faculty of Veterinary Science and Faculty of Agriculture) and producers should be put into effect. These studies should be continued through a sustainable and auditable structure.

3) The breeding model should be applicable in the field. Different studies should be done for the most suitable breeding model. This model should cover all components of production.

4) Livestock support for small cattle breeding should be continued. Incentive programs should be developed.

5) Collaboration between research institutes, universities and small farmers is needed to increase goat production and productivity. All stakeholders of goat development (national and international development organisations, research institutes and universities, the private sector, government agencies and smallholder farmers) should jointly meet the nutritional-income needs of small farmers in a public-private-producer-partnership model, while achieving higher production and creating sustainable goat markets.

6) The problem of insufficiency of pasture areas should be eliminated. This is one of the important studies to be done for the development of hair goat breeding. With the effective use of pasture areas, the problems in animal nutrition are eliminated, operating costs are reduced and the profit of the enterprise increases.

7) In goat breeding, support should be provided that will contribute to the growth of small-scale enterprises and to increase living standards.

8) Especially in Hair goat enterprises, the structure that offers the surplus to the market needs to be changed. The change of this structure is highly dependent on the integration of production and industry. In recent years, the increasing demand due to some characteristics of goat milk reveals that it would be beneficial for the dairy industry to take some initiatives to meet this demand.

9) For this purpose, an integration model should be established that will process goat milk and turn it into a product, and that will pay for the labor of the producer while doing this.

10) Hair goat breeding, which is the most done and inexpensive in Turkey, should be evaluated in the best way. Goat cheese and yogurt are also known to be delicious. Hair goats, which are the most common goat breeds, need to be supported in order to be effective in the country's economy and specially to reduce foreign dependency. The current structure and problems of manufacturers and enterprises should be determined. After these determinations, it will be useful to carry out the necessary studies.

11) Similar to the contract model applied in different livestock sectors, it can be considered as a practicable and beneficial experience for goat breeding. Increasing interest in organic products and widespread use will increase the demand for products made from hair and Angora goats in the near future.

With the steps and initiatives to be taken, goat breeding and goat products can be turned into an attractive production area again.

12) Although the intensification of agricultural production is the reason for feeding the increasing population, the demand for organic or ecological products has increased in parallel with the awareness of the society in recent years. In animal production branches where traditional production systems are applied, the transition to organic animal production can be easy.

13) In our country, classical methods are generally used in slaughterhouse and laniary. This type of businesses to be established for hair goat breeding regions can be established in accordance with the legislation. Thanks to the use of vehicles suitable for transporting animals and the training of butchers, slaughterhouses will meet the appropriate conditions. With the common facilities to be established in the region, long-term transportation of animals will be prevented.

Contributions of the authors

The authors confirm that the contribution is equally for this paper

Conflict of Interest Statement

There is no conflict of interest between the authors.

Statement of Research and Publication Ethics

The study is complied with research and publication ethics.

References

[1] M. Ertuğrul, T. Savaş, G. Dellal, T. Taşkın, M. Koyuncu, F. Cengiz, B. Dağ, S. Koncagül, E. Pehlivan, "Improving small ruminant breeding in Turkey. *In: Turkey" Agricultural Engineering VII. Technical Congress*, Ankara, Turkey, pp. 667-685, 2010.

[2] İ. Güngör, K. Alkoyak, S. Öz, S. Koncagül, "Growth, survival rate, and some reproductive characteristics of Hair goat under breeder conditions in Kahramanmaraş Province", *Turk J Vet Anim Sci*, vol. 45 no. 6, pp. 1022-1029, 2021

[3] E. Demirören, T. Taşkın, A. Alçiçek, N. Koşum, "İnek sütü ile emiştirilen oğlaklarda gelişme", *Ege Üniversitesi Ziraat Fakültesi Dergisi*, vol. 36 no.1-2-3, pp. 89-96, 1999.

[4] H. Akçapınar and C. Özbeyaz,. *Hayvan Yetiştiriciliği Temel Bilgileri*, Kariyer Matbaacılık Ltd. Şti. 1. Baskı, Ankara, 1999.

[5] S.S. Husain, P. Horst, A.B.M.M, Islam, "Effect of Different Factors on Preweaning Survivability of Black Engal Kids", *Small Rum Res*, vol. 18, no. 1, pp. 1-5, 1995.

[6] K. Kırk, "Doğu Anadolu Bölgesi Yerli Keçi Irklarının Islahının Orman ve Korulukların Korunması ve Alternatif Hayvansal Üretim Modellerinin Geliştirilmesi Üzerine Etkileri", *GAP IV. Tarım Kongresi*, 21-23 Eylül 2005, Şanlıurfa, Türkiye, vol. 2, pp. 1253-1258.

[7] D.H. Oral and A. Altınel, "The phenotypic correlations among some production traits of the Hair goats bred on the private farm conditions in Aydın province", *Journal of Veterinary Faculty of Istanbul University*, vol . 32 no. 3, pp. 41-52. 2006

[8] D. Öztürk, "The characteristics of goat farming systems in Kahramanmaraş in the North Eastern Mediterranean region of Turkey", *7th International Conference on Goat*, France, 15-21 May, pp. 360-36, 2000.

[9] M. Şengonca, T. Taşkın, N. Koşum, "A simultaneous study on the determination of some yield characteristics of Saanen x hair goat hybrids and pure hair goats", Turk J Vet Anim Sci,, vol. 27 no. 6, pp. 1319-1325, 2003

[10] Ü.G. Şimşek and M. Bayraktar, "Kıl keçisi ve Saanen x Kıl keçisi (F1) melezlerine ait büyüme ve yaşama gücü özelliklerinin araştırılması", *F.Ü. Sağlık Bilimleri Veteriner Dergisi*, vol. 20 no. 3, pp. 229-238, 2006.

[11] Ü.G. Şimşek, M. Bayraktar, M. Gürses, "Saanen x Kıl Keçisi F1 ve G1 melezlerinde büyüme ve yaşama gücü özelliklerinin araştırılması", *F.Ü. Sağlık Bilimleri Veteriner Dergisi*, vol. 21 no. 1, pp. 21-26. 2007.

[12] Ü.G. Şimşek, "Kıl keçisi ve Saanen x Kıl keçisi (F1) melezlerinde büyüme, besi performansı ve karkas özelliklerinin araştırılması", Doktora Tezi, Fırat Üniversitesi Sağlık Bilimleri Enstitüsü Zootekni Anabilim Dalı, Elazığ, Türkiye, 2005.

[13] N. Darcan, "Çukurova Bölgesi Subtropik İklim Koşullarında Geliştirilen Bazı Keçi Genotiplerinin Bu Koşullardaki Adaptasyon Mekanizmaları Üzerinde Karşılaştırmalı Araştırmalar", Doktora Tezi, Çukurova Üniversitesi Fen Bilimleri Enstitüsü Zootekni Anabilim Dalı, Adana, Türkiye, 2000.

[14] G. Daş, ve T. Savaş, "Keçilerde bir batında doğum ağırlığı ve varyasyonu seleksiyon ölçütü olarak kullanılabilir mi?" *Hay. Üret.*, vol. 43 no. 2, pp. 86-90, 2002.

[15] H. Tozlu, "Amasya İli Kıl Keçisi Islah Projesi Kapsamında Elde Edilen Saanen X Kıl Keçisi (F1) Melezleri ile Saf Kıl Keçilerinin Büyüme ve Diğer Yetiştiricilik Özellikleri Bakımından Mukayesesi" Yüksek Lisans Tezi, Ondokuz Mayıs Üniversitesi, Fen Bilimleri Enstitüsü Zootekni Anabilim Dalı, Samsun, Türkiye, 2006.

[16] R. Yurtseven, A. Öztürk, Ü. Köseoglu, B. Ankarali, "Farkli genotipteki Ankara keçisi oğlaklarının çeşitli verim özelliklerinin karşılaştırılması" *Lalahan Hay. Arast. Enst. Derg*., vol. 38 no. 2 pp. 32-40, 1998.

[17] H. Özdemir and G. Dellal, "Determination of growth curves in young Angora goats", *Tarim Bilimleri Dergisi*, vol. 15, pp. 358–362, 2009.

[18] H. Yeni, "Genç Ankara Keçilerinde Büyüme Fonksiyonunun Belirlenmesi", Yüksek Lisans Tezi, Ankara Üniversitesi Fen Bilimleri Enstitüsü Zootekni Anabilim Dalı, Ankara, Türkiye, 2003.

[19] F. Odabaşıoğlu, M. Küçük, O. Yılmaz, "Renkli Tiftik Keçisi ve Ankara Keçisi x Renkli Tiftik Keçisi F1 Oğlaklarında Yaşama Gücü ve Büyüme Performanslarının Araştırılması", *YYÜ Vet Fak. Derg*, vol. 8 no. 1 pp. 29-36, 2007.

[20] O.Atay, and O. Gokdal, "Some production traits and phenotypic relationships between udder and production traits of Hair goats", *Indian J. Anim. Res.*, vol. 50 no. 6, 983-988, 2016.

[21] Ö. Erten, and O. Yılmaz, "Investigation of Survival Rate and Growth Performances of Hair Goat Kids Raised Under Extensive Conditions", *YYÜ Vet. Fak. Derg*, vol. 24 no. 3, pp. 109-112, 2013.

[22] M. Şengonca, T. Taşkın, N. Koşum "Saanen x Kıl keçi melezlerinin ve saf Kıl keçilerinin kimi verim özelliklerinin belirlenmesi üzerine eş zamanlı bir araştırma", *Turk J Vet Anim Sci*, vol. 27 no. 6, pp. 1319-1325, 2003.

[23] S. Salman,. "Saanen melezi ve Kilis Keçilerde Bazı Döl Verimi Özellikleri ile Oğlaklarda Büyüme ve Yaşama Gücü" Yüksek Lisans Tezi, KSÜ Fen Bilimleri Enstitüsü Zootekni Anabilim Dalı, Kahramanmaraş, Türkiye, 2009.

[24] B. Gök, A.H. Aktaş, Ş. Dursun, "Honamlı Goat: rising star of the Taurus mountains", *RBI 8th Global Conference on the Conservation of Animal Genetic Resources*, Tekirdağ, p. 65-72, 2011.

[25] M. Keskin, S. Gül, E. Can, Z. Gündüz, "Yarı Entansif Koşullarda Yetiştirilen Şam Keçileri ile Kilis x Kıl Keçisi Melez Genotipinin Süt ve Döl Verim Özellikleri". *Lalahan Hay. Araşt. Enst. Derg*, vol. 56 no. 1 pp. 20-24, 2016.

Bitlis Eren Üniversitesi Fen Bilimleri Dergisi
BİTLİS EREN UNIVERSITY JOURNAL OF SCIENCE
ISSN: 2147-3129/e-ISSN: 2147-3188
VOLUME: 12 NO: 3 PAGE: 871-886 YEAR: 2023
DOI:10.17798/bitlisfen.1331310

Breast Cancer Segmentation from Ultrasound Images Using ResNext-based U-Net Model

Oğuzhan KATAR[1*], Özal YILDIRIM[1]

[1]*Department of Software Engineering, Faculty of Technology, Firat University, Elazig, Turkey (ORCID: 0000-0002-5628-3543) (ORCID: 0000-0001-5375-3012)*

Keywords: Breast cancer, Ultrasound images, Semantic segmentation, U-Net, Disease detection, Deep learning.

Abstract

Breast cancer is a type of cancer caused by the uncontrolled growth and proliferation of cells in the breast tissue. Differentiating between benign and malignant tumors is critical in the detection and treatment of breast cancer. Traditional methods of cancer detection by manual analysis of radiological images are time-consuming and error-prone due to human factors. Modern approaches based on image classifier deep learning models provide significant results in disease detection, but are not suitable for clinical use due to their black-box structure. This paper presents a semantic segmentation method for breast cancer detection from ultrasound images. First, an ultrasound image of any resolution is divided into 256×256 pixel patches by passing it through an image cropping function. These patches are sequentially numbered and given as input to the model. Features are extracted from the 256×256 pixel patches with pre-trained ResNext models placed in the encoder network of the U-Net model. These features are processed in the default decoder network of the U-Net model and estimated at the output with three different pixel values: benign tumor areas (1), malignant tumor areas (2) and background areas (0). The prediction masks obtained at the output of the decoder network are combined sequentially to obtain the final prediction mask. The proposed method is validated on a publicly available dataset of 780 ultrasound images of female patients. The ResNext-based U-Net model achieved 73.17% intersection over union (IoU) and 83.42% dice coefficient (DC) on the test images. ResNext-based U-Net models perform better than the default U-Net model. Experts could use the proposed pixel-based segmentation method for breast cancer diagnosis and monitoring.

1. Introduction

Cancer is a disease resulting from the accumulation of genetic mutations or aberrant alterations in cellular genes [1]. In a healthy body, cells follow a regulated cycle, but mutations can disrupt this balance, leading to uncontrolled cell growth [2]. These mutations can be inherited or occur due to environmental factors like radiation, chemicals, or viruses [3].

When a gene loses its normal function or gains a new abnormal function due to a mutation, it can disrupt the complex signaling pathways that regulate cell growth and division. As a result, the affected cells gain the ability to divide uncontrollably and form a mass of abnormal cells called a tumor [4]. Tumors can be broadly classified into two main categories: benign tumors and malignant tumors [5]. Benign tumors are usually not cancerous and do not pose an immediate threat to health. The cells in benign tumors are very similar to normal cells and their growth rate tends to be relatively slow. Importantly, they do not invade nearby tissues or spread to other parts of the body [6]. Benign tumors are therefore considered localized and do not usually lead to life-threatening conditions. In contrast, malignant tumors become cancerous and have the potential to cause

*Corresponding author: okatar@firat.edu.tr
Received: 22.07.2023, Accepted: 13.09.2023

serious harm to an individual's health. If left untreated, malignant tumors can invade surrounding tissues and organs and have the ability to metastasize, meaning they can spread to distant parts of the body through the bloodstream or lymphatic system [7].

Breast cancer is the most frequently diagnosed cancer among women worldwide [8]. It originates in the cells of the breasts, particularly in the ducts or lobules. As the disease progresses, malignant cells derived from these areas possess the ability to invade neighboring healthy tissues. Moreover, if cancer cells infiltrate the lymph nodes, they can easily spread via the lymphatic system to distant organs such as the bones, lungs, liver, or brain [9]. Detecting breast cancer in its early stages is therefore crucial for successful treatment and improved outcomes [10]. Specialists use radiological images to assess the structure of breast tissue and possible tumor findings. However, manual evaluation of radiologic images is time-consuming and involves subjective decision depending on the experience and training of the specialist. To overcome these challenges, it is a popular research topic to use artificial intelligence methods to detect breast cancer findings from radiological images. Michael et al. [11] proposed a LightGBM-based method for breast cancer detection from ultrasound images. The proposed method is validated on a dataset of 912 samples. To classify malignant and benign tumors, 185 features were extracted manually. Using these features, LightGBM achieved 99.86% accuracy. González-Luna et al. [12] proposed a method for classifying breast ultrasound images as benign or malignant. The dataset used in the study contains 2032 samples, of which 1341 are benign lesions and 691 are malignant lesions. Linear discriminant analysis (LDA) outperformed other classifiers by classifying the test samples with 89.00% accuracy, 82.00% sensitivity and 93.00% specificity. Wei et al. [13] proposed a method for automatic classification of cancer from breast ultrasound images. The proposed method is based on benign and malignant lesion features. Validated on a total of 1061 different ultrasound images, the support vector machine (SVM) classifier achieved 75.94% accuracy, 66.37% sensitivity, 86.87% specificity and 85.23% precision.

The traditional machine learning approach to breast cancer detection involving feature extraction from radiological images requires feature engineering and performs poorly on complex datasets. Modern deep learning approaches based on convolutional neural networks (CNN) provide significant results for image classification studies. Atrey et al. [14] proposed a hybrid method (CNN+LSTM) for the classification of benign and malignant breast cancer tumors. They used 43 mammogram images and 43 ultrasound images. Dataset samples were increased by using data augmentation techniques. The proposed model achieved a classification accuracy of 97.16% for mammography images and 98.84% for ultrasound images. Raza et al. [15] proposed the DeepBraestCancerNet model for breast cancer detection and classification. In the training and validation of the model, 1030 samples obtained from two different publicly available ultrasound datasets were used. The proposed model achieved 99.35% classification accuracy. Gupta et al. [16] proposed a modified ResNet-50 model that can classify breast ultrasound as normal, benign or malignant. Validated on a publicly available dataset, the model achieved 97.8% accuracy, 97.68% recall, 99.21% precision and 98.44% F1-score.

CNN models have demonstrated promising results in classification studies. However, their black box structure renders them unsuitable for clinical implementation. The primary challenge lies in the inability to identify which pixel areas in the image are crucial for predictions. To overcome this limitation, CNN models can be made explainable using class activation mapping (CAM) algorithms that visualize the feature maps from the last convolutional layer as heat maps. Nonetheless, CAM algorithms employ a coarser approach when locating objects at the region level. Therefore, the output of the CAM algorithm is less accurate compared to sharp and precise pixel-based segmentation results. Byra et al. [17] proposed a deep learning-based method for automatic segmentation of breast cancer tumor areas in ultrasound images. The proposed method was evaluated on 882 different ultrasound images. Of the 882 images, 632 images were used for training, 100 images for validation and 150 images for testing. The trained U-Net and SK-U-Net models made mask predictions on the 150 images allocated for testing. As a result of the predictions, the SK-U-Net model achieved a Dice Score (DS) of 82.60%. Sannasi and Rajaguru [18] proposed a deep learning-based approach to segment tumor areas from breast cancer ultrasound images. They used a publicly available dataset containing 780 ultrasound images collected from 600 different female patients. An adaptive median filtering algorithm was used to remove the noise in the images. FCN16s, FCN8s, SegNet, SegNet, U-Net, SK-U-Net and SKMAT-U-Net models built specifically for this study were trained for 60 epochs with 224×224 input resolution and batch size of 12. As a result of the completed training stages, the SKMAT-U-Net model is the most successful model among the tested models, reaching a DS value of 92.90%.

Segmentation studies have shown high precision and high accuracy. However, since segmentation models can process input images at a fixed resolution, the proposed methods are usually based on image resizing. Information loss is inevitable in resized images. In addition, given the availability of different radiological devices and technologies today, the scope of methods that expect a fixed input size is quite limited.

This paper proposes a ResNext-based U-Net model for segmenting benign and malignant breast cancer tumors from ultrasound images. The proposed model first cropping the input image into 256×256 pixel patches and then extracts features with the encoder blocks (ResNext) of the U-Net model. The model processes the output of the encoder network in the default decoder network of the U-Net model to obtain the prediction mask image. The sequentially processed patches are merged again in the same order to reach the original size. The approach proposed in this study has the potential to be applied clinically for computer-aided automatic breast cancer detection due to its flexible structure. The main contributions of this study can be summarized as follows:

- Semantic segmentation was performed with the ResNext-based U-Net model using a public dataset.
- A method is proposed to process different and high resolution images in the U-Net model.
- Hardware requirements are reduced by using input images divided into 256×256 pixel patches.
- The proposed model outperforms the default U-Net model.

2. Material and Method

A segmentation system was developed to identify benign and malignant tumor regions in ultrasound images using a deep learning model based on ResNext and U-Net. The block diagram illustrating the system is given in Figure 1.

The use of images with high and non-constant resolution poses challenges that can hamper the efficiency and practicality of the model. In order to overcome these challenges, a method is proposed that involves cropping the original images into smaller and more manageable patches. In this way, high-resolution images can be utilized without imposing the memory constraints of the hardware.

2.1. Ultrasound Dataset

In this study, we used a publicly available dataset [19] of ultrasound images of female patients, with corresponding mask images showing tumor areas marked by an expert. The dataset was compiled in 2018 and consists of samples from 600 different patients ranging from 25 to 75 years old. The dataset consists of a total of 780 different images, all stored in PNG file format. The images have different resolutions with non-fixed sizes ranging from 190×335 pixels to 1048×578 pixels. The images in the dataset are categorized into three different classes: normal, benign and malignant.

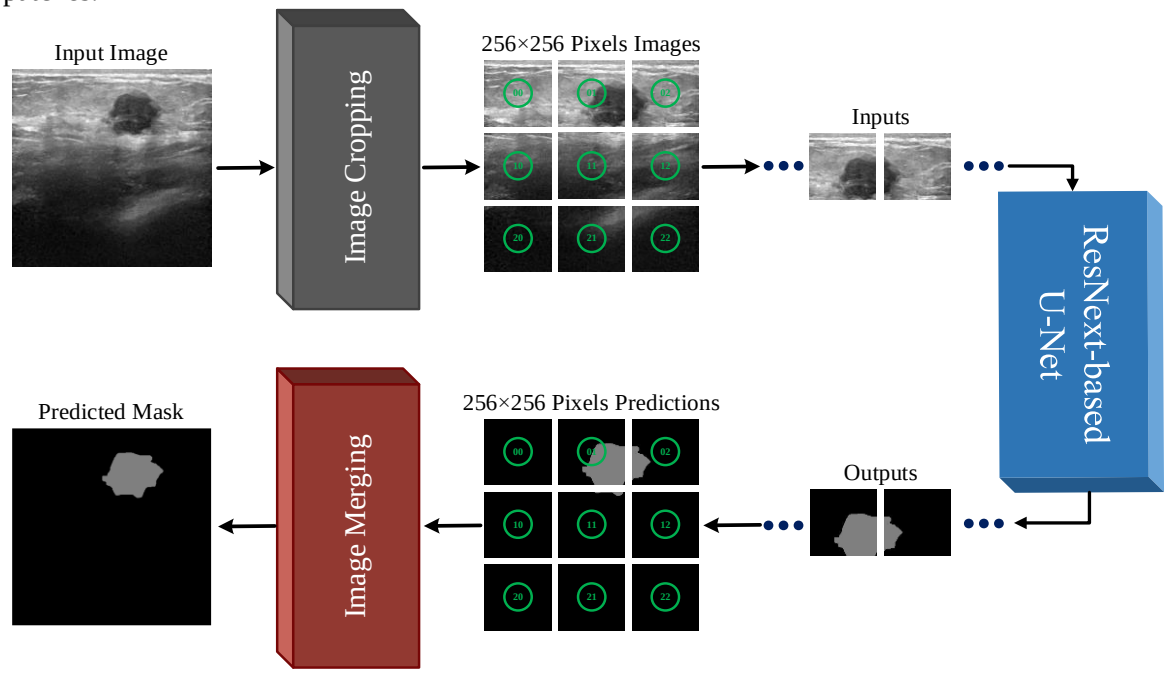

Figure 1. Block diagram of the proposed method

These classes serve to classify ultrasound images according to the presence and nature of tumors. To provide a better understanding of the structure of the dataset, the distribution of images into the three classes is summarized in Table 1.

Table 1. Classes and distributions of dataset samples

Class Name	Number Of Samples
Benign	437
Malignant	210
Normal	133
Total	780

Typically, in medical imaging, different tumor or tissue types are assigned different pixel values or color codes to facilitate easier identification and analysis [20]. In this particular dataset, however, mask images do not use different pixel values to distinguish between benign and malignant tumors. Instead, mask images mark the regions where tumors are present in ultrasound images, regardless of their specific structure. Figure 2 shows a randomly selected set of dataset examples and their corresponding mask images.

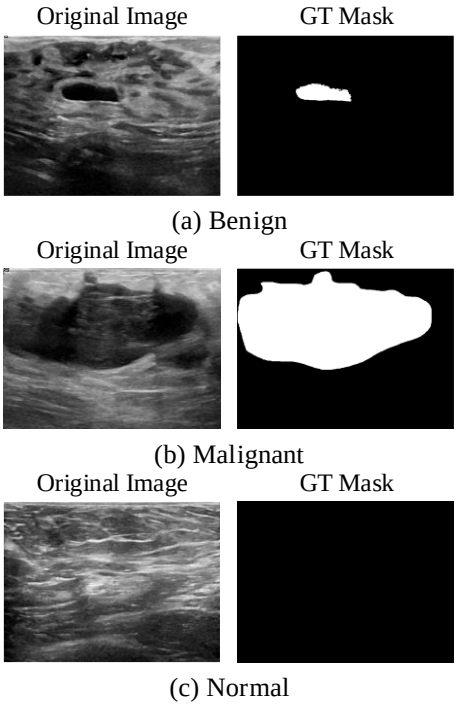

Figure 2. Dataset samples

2.2. Pre-processing

In the dataset samples, some images contain multiple tumor areas. To accurately represent these multiple tumor regions, separate mask images were initially created for each different area in an image. However, having multiple mask images for a single ultrasound image can lead to challenges and may not be ideal for certain analyses or applications. To address this issue, a preprocessing step was applied to the dataset samples. This pre-processing involves merging the individual mask images associated with multiple tumor areas within a single ultrasound image. This results in a merged mask image that covers all tumor regions in the image. The goal of this pre-processing step is to ensure that each ultrasound image in the dataset is associated with a single mask image, eliminating the complexity and potential complications of having multiple mask images for a single image. Figure 3 shows an example of a dataset with multiple mask images and the composite mask image generated after the pre-processing step.

Pixel values are numerical representations of the intensity or color of each pixel in an image. If benign and malignant tumors have the same pixel values, it becomes problematic to create a reliable segmentation model that can accurately classify and distinguish between these two classes. To overcome this issue, a technique called pixel-based value substitution was employed. This technique involves replacing the original pixel values with new values that correspond to specific classes. In this case, a value of '1' was assigned to denote regions representing benign tumor areas, a value of '2' was assigned for malignant tumor areas, and a value of '0' was designated for areas defined as the background that do not contain tumor regions. The result of the pixel-based value substitution process is shown in Figure 4.

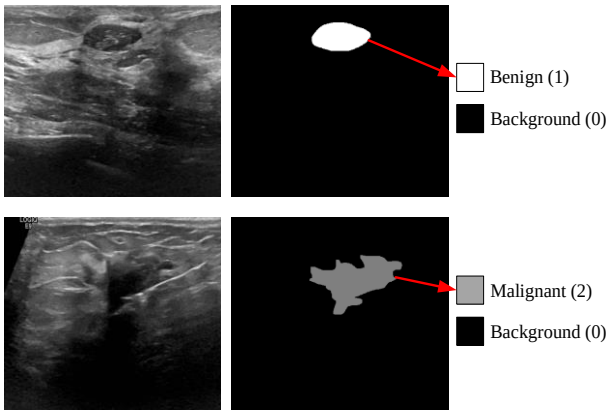

Figure 4. Class-based pixel value assignment

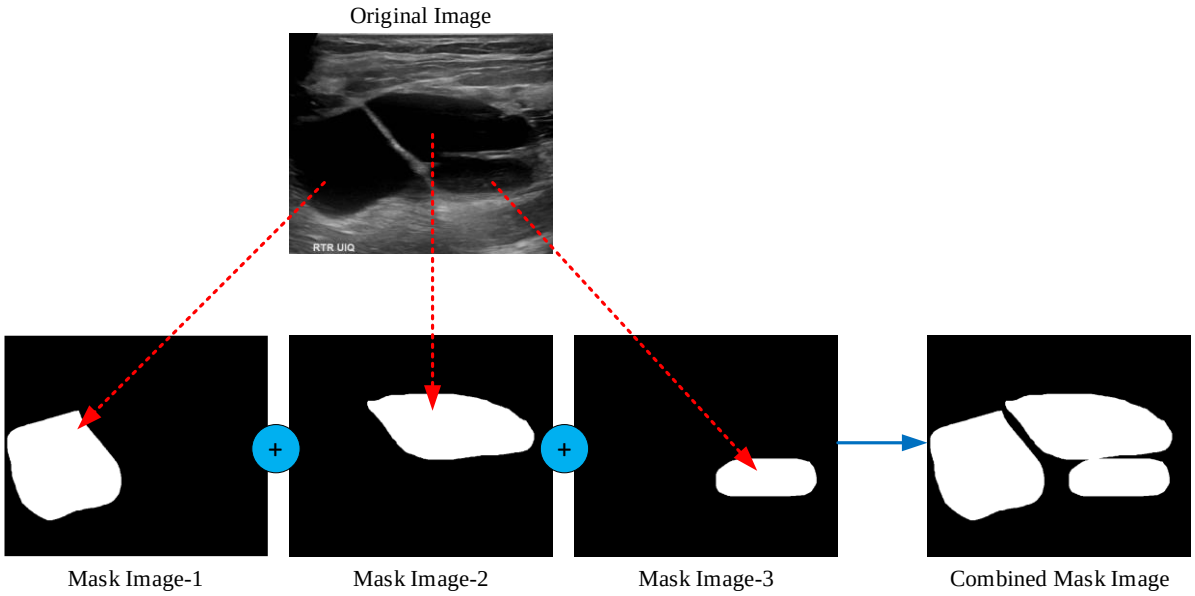

Figure 3. Combining multiple mask images into a single mask image

The use of deep learning models for image segmentation often requires fixed input sizes to ensure consistent processing. However, in the case of the dataset used in this study, the samples did not have a fixed resolution, which posed a challenge for training a deep learning model. To address this issue, a decision was made to employ a deep learning model with an input size of 256×256 pixels, which is a commonly chosen size for various segmentation tasks. In order to adapt the original images and corresponding mask images to the desired input size, a cropping process was applied. This involved dividing the images into smaller sub-images, each with a size of 256×256 pixels. By cropping the images, it became feasible to train a deep learning model that expects fixed-size inputs. During the cropping process, some of the original images might not perfectly fit the 256×256 pixel size due to their inherent dimensions. In such cases, a padding method was utilized to address this discrepancy. The details of the image cropping and padding process are shown in Figure 5. After the padding and cropping operations are completed for the original images, the same operations are repeated for the mask images. In this way, there is no loss in the matching of the original image and the mask image.

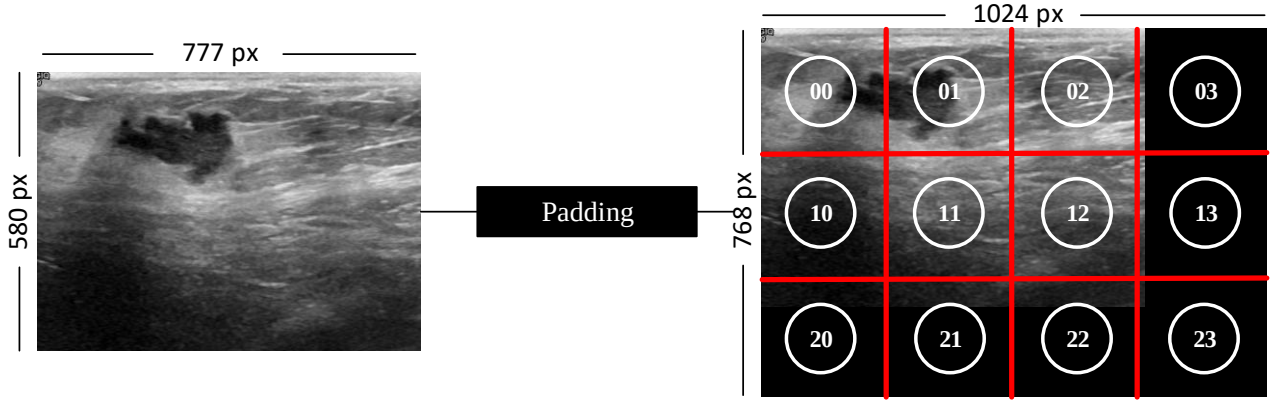

Figure 5. The proposed padding process

2.3. Segmentation Model

The U-Net architecture is a popular CNN architecture that is widely used for image segmentation tasks, particularly in the field of biomedical image analysis [21]. The U-Net architecture derives its name from its shape, which resembles the letter "U". A block diagram of the U-Net architecture is given in Figure 6. It is designed to address the challenges of pixel-wise image segmentation, where the goal is to assign a label to each pixel in an image, indicating the class or category it belongs to.

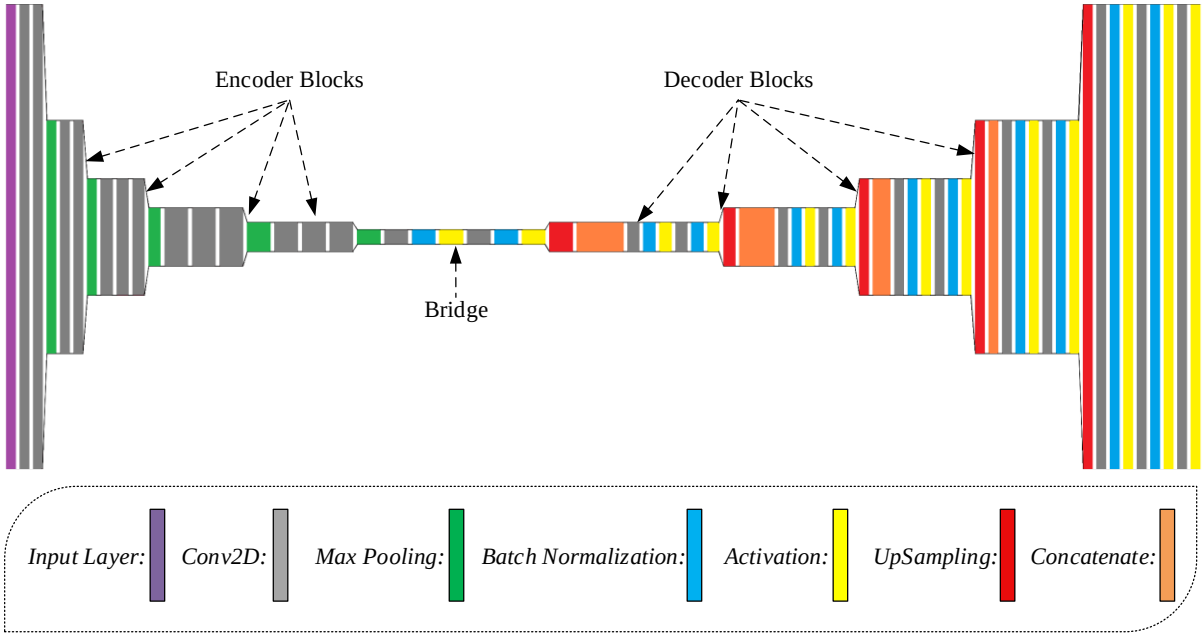

Figure 6. The default U-Net architecture

This is particularly useful in applications such as medical image segmentation, where identifying and delineating specific structures or regions within an image is crucial [22]. The key characteristic of the U-Net architecture is its use of an encoder-decoder structure combined with skip connections.

To enhance the performance and efficiency of the U-Net model, pre-trained CNN networks can be utilized in the encoder layer [23]. These networks are models trained on large-scale datasets, such as ImageNet [24], and have learned to recognize a wide range of low-level and high-level features from images. The main advantage of using pre-trained CNN networks in the encoder layer is transfer learning. It allows us to leverage the knowledge and feature representations learned by the pre-trained models on a large dataset and apply it to a different task or domain with limited data. By using pre-trained CNN networks, we can benefit from their generalization capabilities and feature extraction power [25]. In many studies, these networks are used as feature extractors in the encoder layer of the U-Net model [26], [27]. The input images are passed through the pre-trained CNN network, and the output feature maps are then fed into the subsequent layers of the U-Net model. The pre-trained CNN networks can capture generic features like edges, corners, textures, and object parts, which are beneficial for a wide range of computer vision tasks. By utilizing these pre-trained networks, the U-Net model can achieve better performance, even when training data is limited. Moreover, using pre-trained networks in the encoder layer can help speed up the training process since the initial layers are already well-initialized with meaningful filters.

In this study, pre-trained ResNext-50 and ResNext-101 models are integrated into the encoder network of the U-Net models. The ResNeXt architecture is an extension of the ResNet architecture. It introduces a cardinality parameter to ResNet blocks, enabling increased model capacity and performance without significantly increasing computational complexity. The block diagram of the first encoder block of the ResNext-50 based U-Net model is given in Figure 7.

In this study, three different models are compiled to study the effect of CNN architecture on the performance of the encoder network. These models are the default U-Net, ResNext-50 based U-Net and ResNext-101 based U-Net (Models are available at (github.com/oguzhankatar/BCSeg).

2.4. Performance Metrics

In order to assess the performance of a segmentation algorithm, various metrics, including true positive (TP), true negative (TN), false positive (FP), and false negative (FN), are employed. To comprehensively evaluate segmentation algorithms, pixel-based evaluation techniques have been developed. These methods are pivotal in determining the algorithm's effectiveness in identifying and distinguishing malignant, background, and benign regions. They quantify the reate of overlap between the predicted segmentation and the ground truth. Several commonly utilized pixel-based evaluation methods can be summarized as follows.

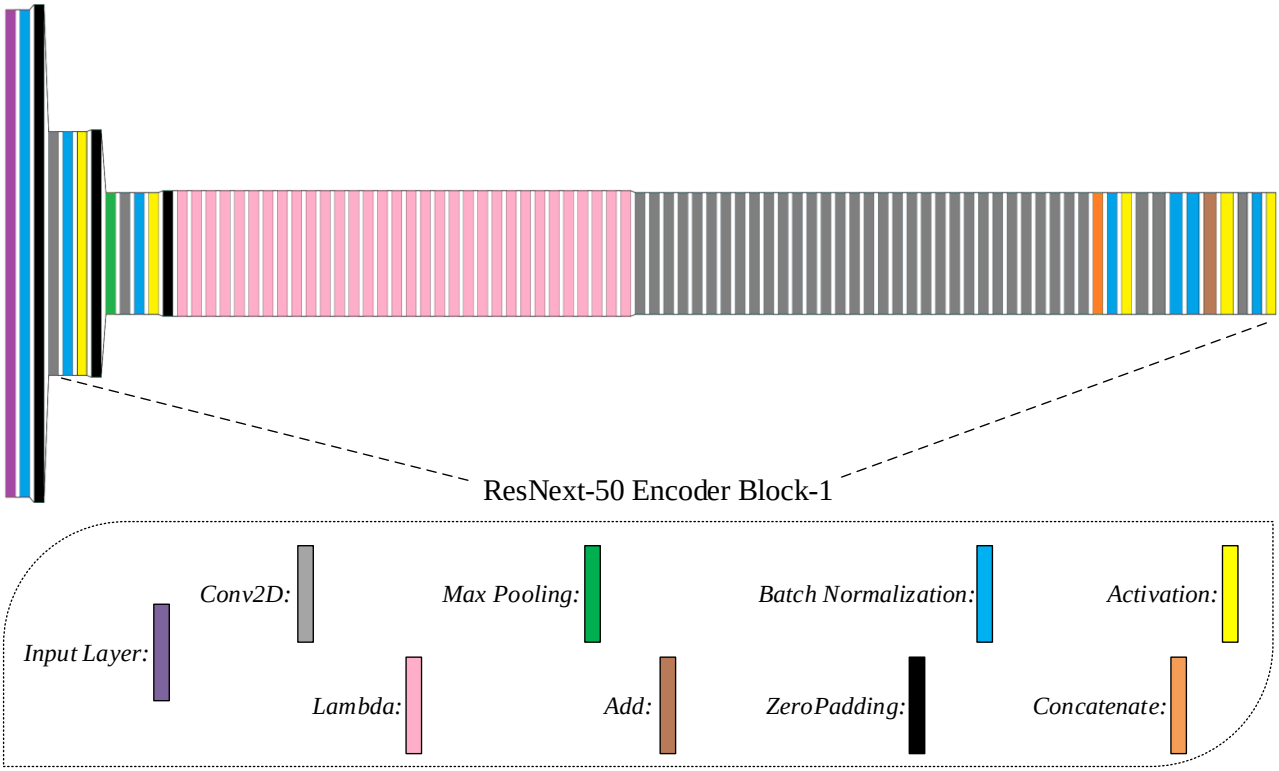

Figure 7. The first encoder block of the ResNext-50 based U-Net

- Pixel accuracy (PA) measures the proportion of correctly classified pixels over the total number of pixels in the image [28].
- Intersection over Union (IoU) measures the overlap between the predicted and ground truth segmentation masks for each class [29].
- Dice coefficient (DC) is another metric that evaluates the overlap between the predicted and ground truth masks. The DC ranges from 0 to 1, with 1 indicating a perfect match [30].

The equations used to calculate these methods and the advantages and disadvantages of each method are given in Table 2.

Table 2. Performance metrics and details

Method	Equation	Advantages	Disadvantages
PA	$\frac{(TP+TN)}{(TP+FP+FN+TN)}$	A simple and straightforward metric. Effective for similar distributions of two classes.	It can be misleading in unbalanced class distributions.
IoU	$\frac{TP}{(TP+FP+FN)}$	Resilient to class imbalance. Clearly shows the difference between correct and incorrect predictions.	Poor performance on objects with sharp edges.
DC	$\frac{2\times TP}{(2\times TP+FP+FN)}$	Resilient to class imbalance. Performs well in object segmentation.	Can be complex when there are multiple classes.

3. Results

The results of the U-Net models trained for segmentation of benign, malignant and background areas in ultrasound images are presented in this section. In addition, various evaluation metric values of the experimental findings are shown in the following sections.

3.1. Experimental Setups

After the preprocessing steps on the images were completed, 70% of the images in the dataset were divided for training, 20% for validation and 10% for testing. The dividing process was randomized in such a way that the original image and the mask image were kept together. The setup of the data dividing process is given in Figure 8.

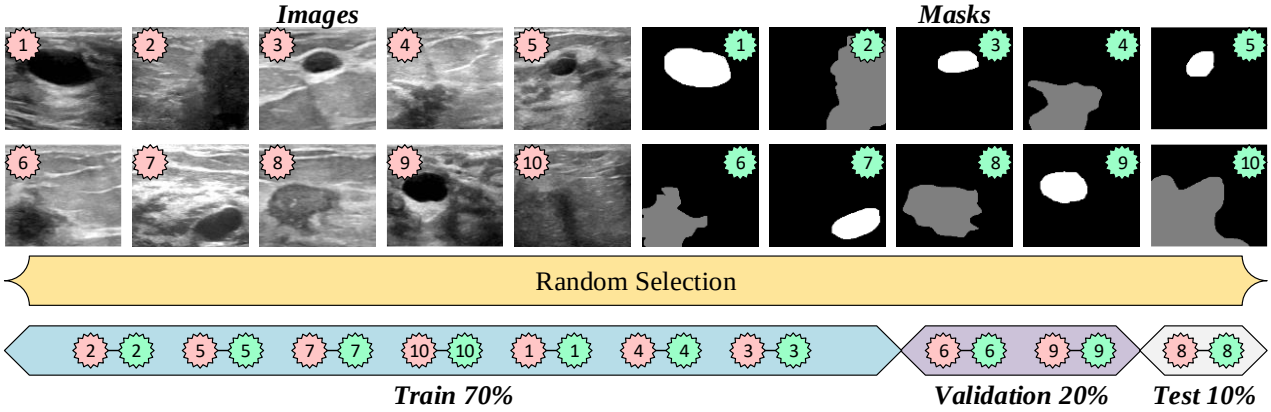

Figure 8. Dividing of training, validation and test subsets

U-Net models with 256×256×3 input size were included in the training thanks to the 'Segmentation Models' library. Models were created by integrating pre-trained ResNext-50 and pre-trained ResNext-101 models into the encoder network of the default U-Net model. In order to accurately compare the performance of the default U-Net, ResNext-50 based U-Net and ResNext-101 based U-Net models, the parameters in the training and validation processes were kept identical. Each model was compiled with Adam optimization and a learning rate of 0.0001. In Adam optimization, the weights are updated by the mathematical process given in Equation 1. w_t represents the updated weights at step t, w_{t-1} represents the weights at step $t-1$, η is the constant known as the learning rate, $\hat{m}_t$ represents the moving average of the gradients, $\hat{v}_t$ represents the moving average of the squares of the gradients, ∈ represents a small positive value added to avoid division by zero error.

$$w_t = w_{t-1} - \eta \frac{\hat{m}_t}{\sqrt{\hat{v}_t} + \in} \quad (1)$$

The batch size was 16 and the models were trained for 100 epochs with the Dice Loss function. The mathematical equation used to calculate the Dice Loss value is given in Equation 2. In this equation, p_{true} represents the ground truth mask, p_{pred} represents the model's prediction mask, and ∈ represents a small positive value added to avoid a division by zero error.

$$Loss_{Dice} = \frac{2 * \sum p_{true} * p_{pred}}{\sum p^2_{true} + \sum p^2_{pred} + \in} \quad (2)$$

All experimental phases were carried out on the A100 GPU in the Google Colab environment using the Python programming language.

3.2. Experimental Results

The number of trainable parameters in a model is a crucial factor that greatly influences the training and validation process. For the proposed models aimed at segmenting benign, malignant, and background areas from ultrasound images, the number of trainable parameters is as follows: 23,748,531 for the default U-Net, 31,993,270 for the ResNext-50 based U-Net, and 51,142,070 for the ResNext-101 based U-Net. The duration of each epoch in training the models directly correlates with the number of trainable parameters. Throughout the training process, the IoU and loss values were recorded at each epoch on both the train and validation sets. The IoU value represents the model's accuracy in segmenting correctly, while the loss value quantifies the discrepancy between the model's predictions and the true values. Figure 9 illustrates the IoU and loss graphs for each model during the training and validation phases.

The performance discrepancy observed between the default U-Net model and the models incorporating pre-trained ResNext-50 and pre-trained ResNext-101 architectures can be attributed to the differences in the feature extraction capabilities of these architectures. The default U-Net model typically consists of simple convolutional layers, while the pre-trained ResNext-50 and ResNext-101 architectures are based on deeper and more complex networks, pre-trained on large-scale datasets.

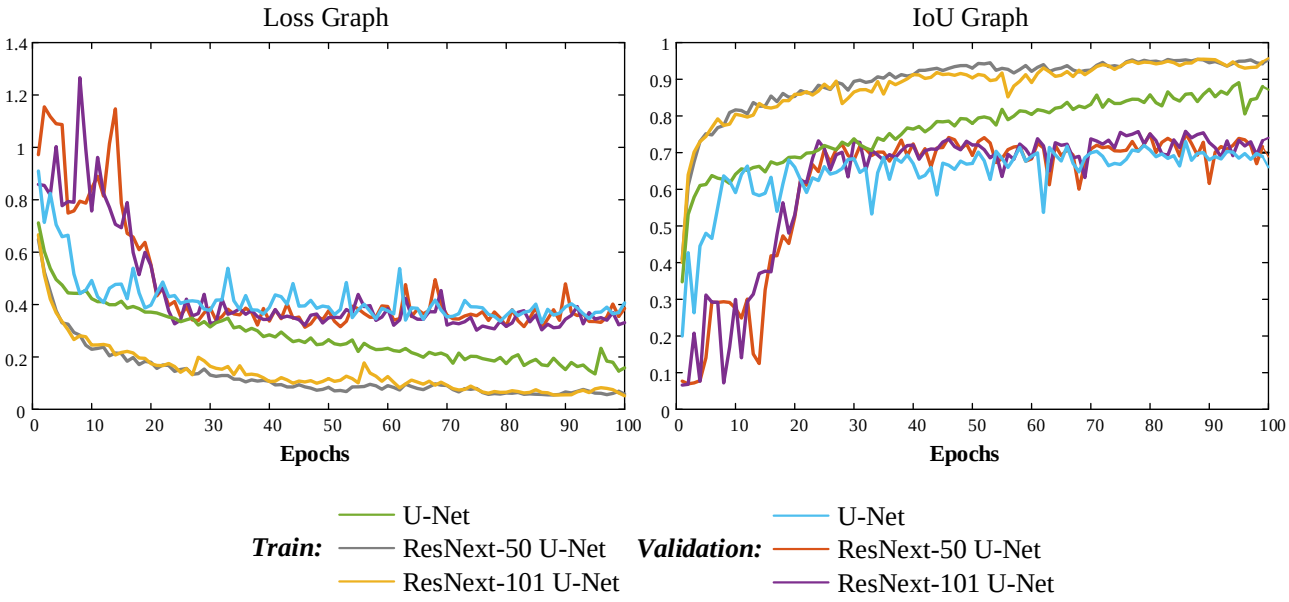

Figure 9. Train and validation graphs

By leveraging the knowledge encoded in the pre-trained ResNext-50 and ResNext-101 architectures, the U-Net models with these architectures as encoders benefit from transfer learning. The pre-trained models have already learned generalizable features from a large and diverse dataset, allowing them to extract relevant information for the segmentation task more effectively. This transfer of knowledge gives the models a head start during training, resulting in improved segmentation performance compared to the default U-Net model. Therefore, the lower performance of the default U-Net model can be attributed to its relative simplicity and limited ability to capture intricate image features compared to the more advanced pre-trained ResNext-50 and ResNext-101 architectures, which good at feature extraction tasks. The weights obtained by the models after training were saved in 'hdf5' format. Using these weights, the models were tested on the test set samples. The samples randomly selected among the predictions made by the models in the test phase are given in Figure 10.

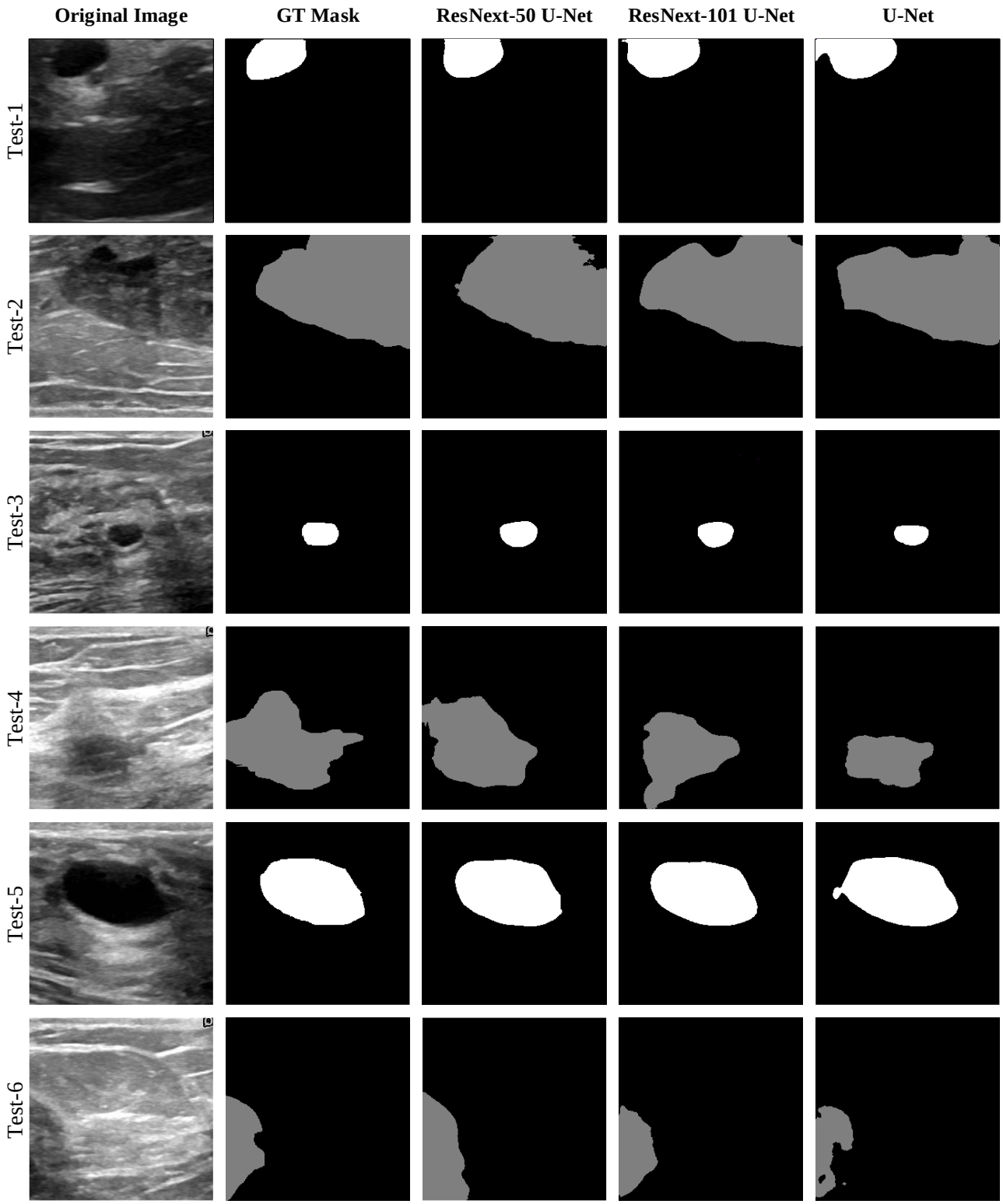

Figure 10. Test samples and predicted masks

Performance metrics were calculated by comparing the predictions with the ground truth mask images on a pixel basis. The bar graph of these metrics is given in Figure 11.

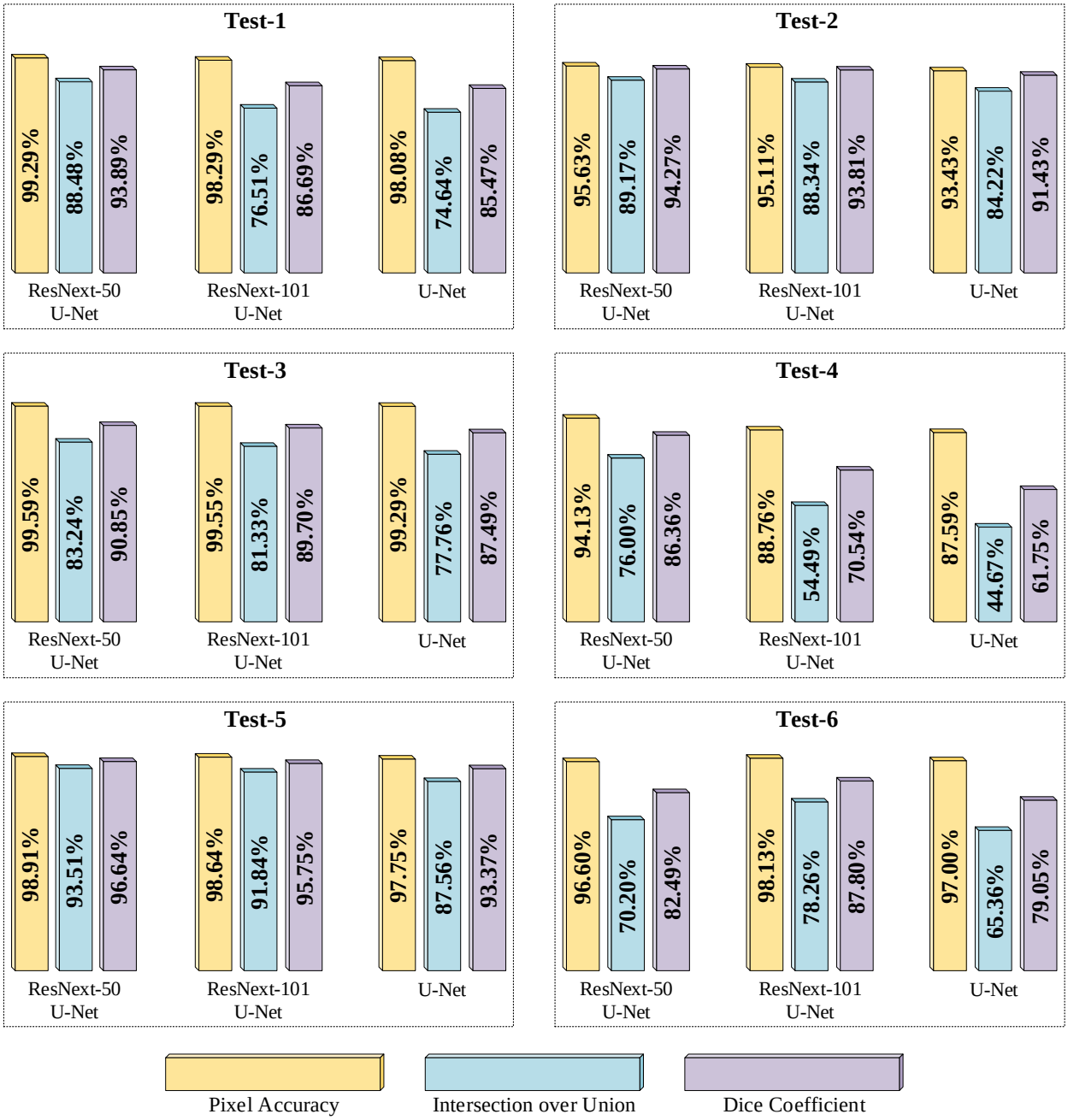

Figure 11. The performance values of test predictions

When the performance of the models on the random test images is analyzed, it is seen that the models achieve high pixel accuracy rates. However, it is not sufficient to make a comparison between the models based on pixel accuracy alone. For this reason, the class-based IoU values of the models were analyzed on each test sample. The class-based IoU values obtained by the models in their predictions on the test images are presented in Table 3.

Table 3. The IoU values obtained on test images

Classes	ResNext-50 U-Net	ResNext-101 U-Net	U-Net
Background (0)	89.06%	87.27%	84.10%
Benign (1)	71.44%	68.34%	65.33%
Malignant (2)	59.01%	61.11%	54.79%
Mean IoU	73.17%	72.24%	68.07%

The models performed worse than the other classes in classifying malignant areas in the test images. The main reasons for this are the visual similarity of malignant areas to background areas and the insufficient number of samples in the dataset. Even though the ResNext-50 based U-Net model classified malignant areas with an IoU rate of 59.01%, it is the model with the highest mean IoU value due to its superior performance over other classes. The ResNext-50 based U-Net model proposed in this study can only predict on 256×256 pixel images. However, thanks to the image cropping and image merging functions, it can produce predictions for images of any size without being bound to any resolution value. The proposed method for the model to produce predictions on all images without depending on any resolution value is given in Figure 12.

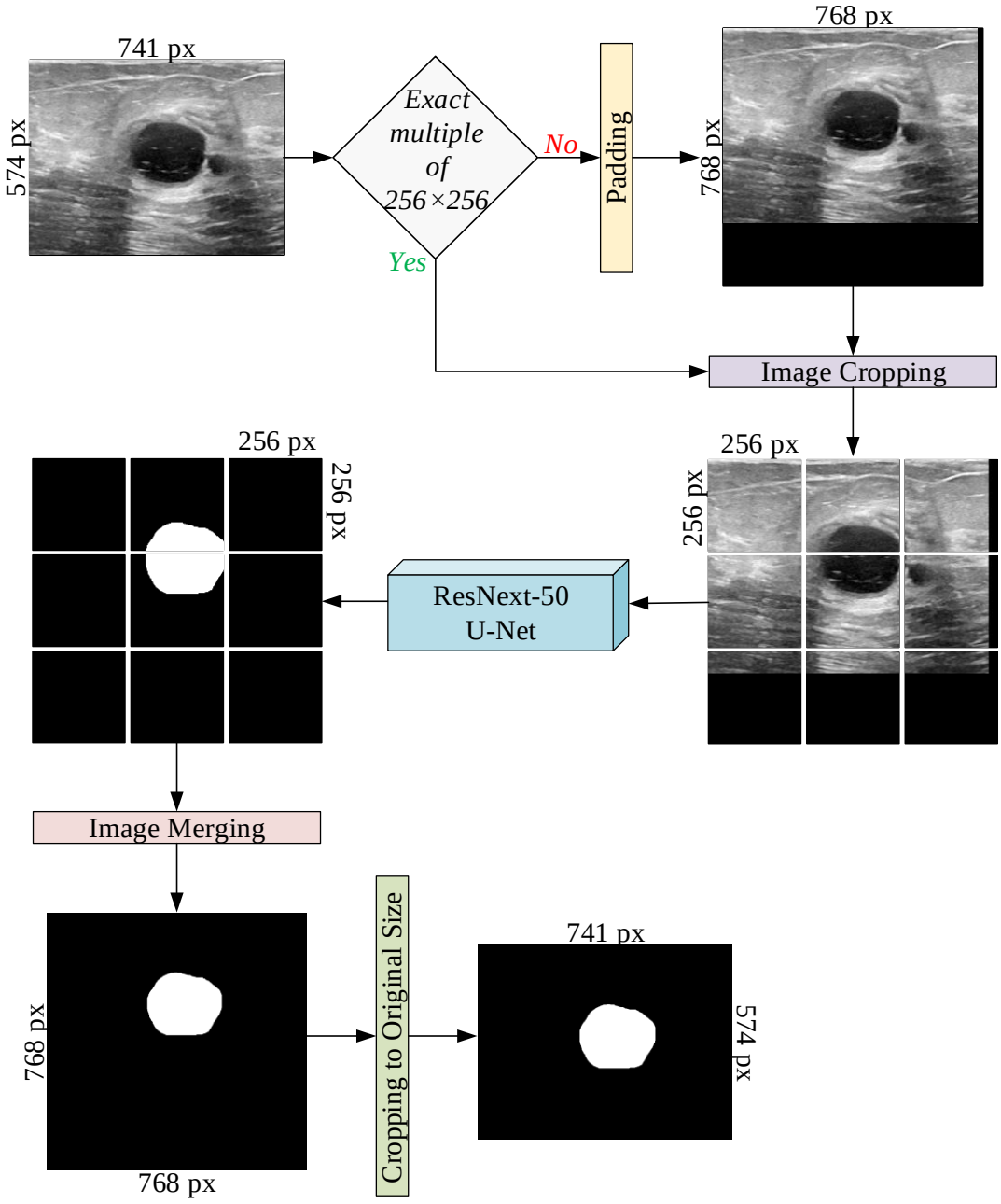

Figure 12. The proposed method for input images of different resolutions

Different radiological devices used today produce images of various resolutions for medical imaging. With the proposed method, it is possible to directly feed images of different resolutions obtained from radiological devices into the model. This provides more flexibility to the experts, allowing them to evaluate images from various devices on the same model. The predictions of the ResNext-50-based U-Net on ultrasound images with different resolutions are presented in Figure 13.

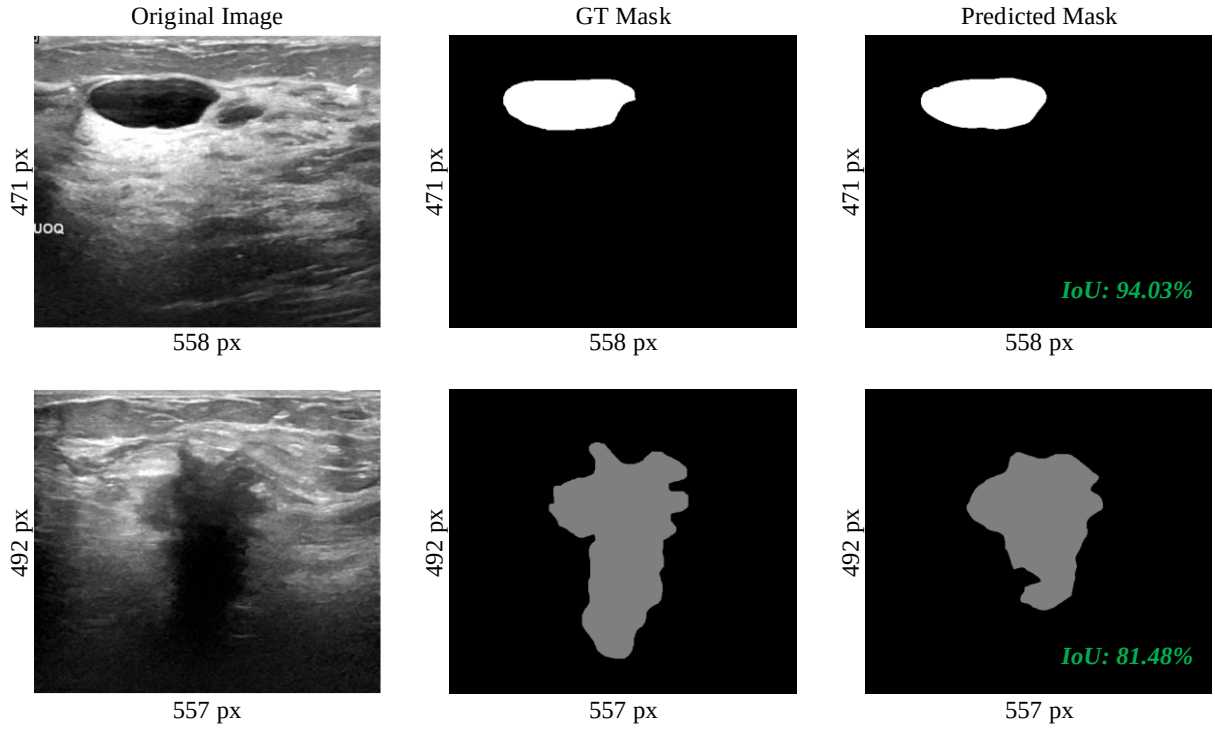

Figure 13. The predictions on images of different resolutions

4. Discussion

Breast cancer segmentation using radiologic images is an active research topic. Table 4 provides details of research studies developed using the same dataset. Kai et al. [31] proposed the swin-transformerv2-UNet (S2UNet) model. The S2Unet model achieved 73.26% DC and 58.30% IoU on the test set. Inan et al. [32] proposed a U-Net and VGG-16 based method for classification and segmentation of benign and malignant tumor areas on ultrasound images. Simple Linear Iterative Clustering (SLIC) algorithm was applied to the dataset samples in the preprocessing stages. The proposed model was trained for 300 epochs and achieved a DC of 63.40% in the test phase. Bal-Ghaoui et al. [33] proposed a DenseNet-121 based U-Net model for automatic segmentation of breast cancer lesions. This model achieved a DC of 73.70%. Azam et al. [34] proposed the Efficient-Net based Atrous Spatial Pyramid Pooling (Efficient-Net ASPP) model for breast cancer segmentation. Only 210 malignant samples were used in the training and testing processes of the model consisting of EfficientNetV2B3 backbone. The proposed model achieved 62.00% DC on 42 test images.

Table 4. Comparison of studies using the same dataset

Study	Year	Model	Fixed Input Size	Number of Classes	Performance
Kai et al. [31]	2022	S2UNet	Yes	3 (benign, malignant, background)	IoU=58.30% DC=73.26%
Inan et al. [32]	2022	U-Net	Yes	3 (benign, malignant, background)	DC=63.40%
Bal-Ghaoui et al. [33]	2023	DenseNet-121 U-Net	Yes	3 (benign, malignant, background)	DC=73.70%
Azam et al. [34]	2023	Efficient-Net ASPP	Yes	2 (malignant, background)	DC=62.00%
The proposed study	**2023**	**ResNext-50 U-Net**	**No**	**3 (benign, malignant, background)**	**IoU=73.17%** **DC=83.42%**

In this study, a pre-trained ResNext-50 based U-Net model is used for automatic segmentation of benign and malignant tumor areas from ultrasound images. The model was able to predict three different classes of pixel values in its output and achieved 73.17% test IoU. Compared to the studies listed in Table 4, we obtained higher performance rates. In addition, the constraint of processing on fixed resolution images, which is included in other studies, is not included in our study. Thus, our model is capable of predicting on input images of any resolution and has a wider scope compared to other studies. The advantages of our explainable model can be summarized as follows:

- Since the ResNext-50 model was pre-trained on large datasets, it performed well on the tumor segmentation problem with a low training cost.
- The proposed method has an end-to-end CNN architecture and can perform segmentation without any manual feature extraction.
- In clinical settings, experts can effortlessly utilize the proposed model, facilitating easy interpretation and understanding of the results.
- Due to its flexible structure, it can be fine-tuned with datasets of varying resolutions and effectively employed in diverse tasks.

The limitations of our study are outlined as follows. The dataset used in the study is a publicly available dataset with unbalanced distribution. The performance of the study on images in different formats for integration into real-time applications has not been verified. In future studies, the number of dataset samples will be increased by collaborating with clinical radiologists. Optimization studies will be carried out on the hyper parameters of the model.

5. Conclusions

Detection of benign and malignant tumors is a vital step in the accurate diagnosis of breast cancer. Current detection methods are time-consuming and error-prone due to human factors. Detection of breast cancer cells using artificial intelligence techniques is an active area of research. Studies using CNN-based classifier models achieve high accuracy. However, due to the black box structure of the models, the pixels they focus on in their predictions are not explained. This creates a lack of confidence in the clinical use of classifier models. This study proposes to perform pixel-based segmentation of breast cancer tumors using ResNext-50 based U-Net model. The proposed method includes image cropping and image merging functions that segment the size of the input images into 256×256 pixel patches and reassemble them after performing model predictions on these images. A mean IoU value of 73.17% was obtained on the test images. Although the proposed method is only applied on ultrasound images, it can be easily fine-tuned for different types of radiological imaging such as mammography. In the future, we plan to expand the dataset and process data from different devices with the support of an expert radiologist. The proposed method can be tested to reduce the hardware requirements for segmentation of high-resolution radiological images.

Contributions of the Authors

The authors confirm that the contribution is equally for this paper.

Conflict of Interest Statement

There is no conflict of interest between the authors.

Statement of Research and Publication Ethics

The study is complied with research and publication ethics.

References

[1] J. S. You and P. A. Jones, “Cancer genetics and epigenetics: two sides of the same coin?,” *Cancer Cell*, vol. 22, no. 1, pp. 9–20, 2012.

[2] S. Gómez-López, R. G. Lerner, and C. Petritsch, “Asymmetric cell division of stem and progenitor cells during homeostasis and cancer,” *Cellular and Molecular Life Sciences*, vol. 71, pp. 575–597, 2014.

[3] N. Parsa, “Environmental factors inducing human cancers,” *Iran J Public Health*, vol. 41, no. 11, p. 1, 2012.

[4] M. Hejmadi, Introduction to cancer biology. *Bookboon*, 2014.

[5] M. Amrane, S. Oukid, I. Gagaoua, and T. Ensari, "Breast cancer classification using machine learning," in *2018 electric electronics, computer science, biomedical engineerings' meeting (EBBT)*, IEEE, 2018, pp. 1–4.

[6] J. Boutry et al., "The evolution and ecology of benign tumors," *Biochimica et Biophysica Acta (BBA)-Reviews on Cancer*, vol. 1877, no. 1, p. 188643, 2022.

[7] K. Soda, "The mechanisms by which polyamines accelerate tumor spread," *Journal of Experimental & Clinical Cancer Research*, vol. 30, pp. 1–9, 2011.

[8] L. Wilkinson and T. Gathani, "Understanding breast cancer as a global health concern," *Br J Radiol*, vol. 95, no. 1130, p. 20211033, 2022.

[9] K. Mortezaee, "Organ tropism in solid tumor metastasis: an updated review," *Future Oncology*, vol. 17, no. 15, pp. 1943–1961, 2021.

[10] O. Ginsburg et al., "Breast cancer early detection: A phased approach to implementation," *Cancer*, vol. 126, pp. 2379–2393, 2020.

[11] E. Michael, H. Ma, H. Li, and S. Qi, "An optimized framework for breast cancer classification using machine learning," *Biomed Res Int*, vol. 2022, 2022.

[12] F. A. González-Luna, J. Hernández-López, and W. Gomez-Flores, "A performance evaluation of machine learning techniques for breast ultrasound classification," in *2019 16th International Conference on Electrical Engineering, Computing Science and Automatic Control (CCE)*, IEEE, 2019, pp. 1–5.

[13] M. Wei, Y. Du, X. Wu, and J. Zhu, "Automatic classification of benign and malignant breast tumors in ultrasound image with texture and morphological features," in *2019 IEEE 13th International Conference on Anti-counterfeiting, Security, and Identification (ASID)*, IEEE, 2019, pp. 126–130.

[14] K. Atrey, B. K. Singh, N. K. Bodhey, and R. B. Pachori, "Mammography and ultrasound based dual modality classification of breast cancer using a hybrid deep learning approach," *Biomed Signal Process Control*, vol. 86, p. 104919, 2023.

[15] A. Raza, N. Ullah, J. A. Khan, M. Assam, A. Guzzo, and H. Aljuaid, "DeepBreastCancerNet: A Novel Deep Learning Model for Breast Cancer Detection Using Ultrasound Images," *Applied Sciences*, vol. 13, no. 4, p. 2082, 2023.

[16] S. Gupta, S. Agrawal, S. K. Singh, and S. Kumar, "A Novel Transfer Learning-Based Model for Ultrasound Breast Cancer Image Classification," in *Computational Vision and Bio-Inspired Computing: Proceedings of ICCVBIC 2022*, Springer, 2023, pp. 511–523.

[17] M. Byra et al., "Breast mass segmentation in ultrasound with selective kernel U-Net convolutional neural network," *Biomed Signal Process Control*, vol. 61, p. 102027, 2020.

[18] S. R. Sannasi Chakravarthy and H. Rajaguru, "SKMAT-U-Net architecture for breast mass segmentation," *Int J Imaging Syst Technol*, vol. 32, no. 6, pp. 1880–1888, 2022.

[19] W. Al-Dhabyani, M. Gomaa, H. Khaled, and A. Fahmy, "Dataset of breast ultrasound images," *Data Brief*, vol. 28, p. 104863, 2020.

[20] F. Oztekin et al., "Automatic semantic segmentation for dental restorations in panoramic radiography images using U-Net model," *Int J Imaging Syst Technol*, vol. 32, no. 6, pp. 1990–2001, 2022.

[21] O. Ronneberger, P. Fischer, and T. Brox, "U-net: Convolutional networks for biomedical image segmentation," in *Medical Image Computing and Computer-Assisted Intervention–MICCAI 2015: 18th International Conference*, Munich, Germany, October 5-9, 2015, Proceedings, Part III 18, Springer, 2015, pp. 234–241.

[22] J. Zhang, Y. Zhang, Y. Jin, J. Xu, and X. Xu, "MDU-Net: multi-scale densely connected U-Net for biomedical image segmentation," *Health Inf Sci Syst*, vol. 11, no. 1, p. 13, 2023.

[23] A. Abedalla, M. Abdullah, M. Al-Ayyoub, and E. Benkhelifa, "Chest X-ray pneumothorax segmentation using U-Net with EfficientNet and ResNet architectures," *PeerJ Comput Sci*, vol. 7, p. e607, 2021.

[24] J. Deng, W. Dong, R. Socher, L.-J. Li, K. Li, and L. Fei-Fei, "Imagenet: A large-scale hierarchical image database," in *2009 IEEE conference on computer vision and pattern recognition*, IEEE, 2009, pp. 248–255.

[25] X. Zhong and H. Ban, "Pre-trained network-based transfer learning: A small-sample machine learning approach to nuclear power plant classification problem," *Ann Nucl Energy*, vol. 175, p. 109201, 2022.

[26] M. H. BENDIABDALLAH and N. SETTOUTI, "A comparison of U-net backbone architectures for the automatic white blood cells segmentation," *WAS Science Nature*, vol. 4, no. 1, 2021.

[27] A. Abedalla, M. Abdullah, M. Al-Ayyoub, and E. Benkhelifa, "The 2ST-UNet for pneumothorax segmentation in chest X-Rays using ResNet34 as a backbone for U-Net," *arXiv preprint* arXiv:2009.02805, 2020.

[28] M. Xi, J. Li, Z. He, M. Yu, and F. Qin, "NRN-RSSEG: A deep neural network model for combating label noise in semantic segmentation of remote sensing images," *Remote Sens*, vol. 15, no. 1, p. 108, 2022.

[29] A. N. Gajjar and J. Jethva, "Intersection over Union based analysis of Image detection/segmentation using CNN model," in *2022 Second International Conference on Power, Control and Computing Technologies (ICPC2T)*, IEEE, 2022, pp. 1–6.

[30] A. M. H. Mahran, W. Hussein, and S. E. D. M. Saber, "Automatic Teeth Segmentation Using Attention U-Net," *Preprint*, 2023.

[31] H. Kai, Z. Y. Feng, H. Meng, F. Y. Baoping, and Y. R. Han, "Ultrasound Image Segmentation of Breast Tumors Based on Swin-transformerv2," in *Proceedings of the 2022 10th International Conference on Information Technology: IoT and Smart City*, 2022, pp. 106–111.

[32] M. S. K. Inan, F. I. Alam, and R. Hasan, "Deep integrated pipeline of segmentation guided classification of breast cancer from ultrasound images," *Biomed Signal Process Control*, vol. 75, p. 103553, 2022.

[33] M. Bal-Ghaoui, M. H. E. Y. Alaoui, A. Jilbab, and A. Bourouhou, "U-Net transfer learning backbones for lesions segmentation in breast ultrasound images," *International Journal of Electrical and Computer Engineering (IJECE)*, vol. 13, no. 5, pp. 5747–5754, 2023.

[34] K. Azam, M. A. Azam, M. A. Qureshi, K. B. Khan, and M. A. Azam, "Efficient-Net ASPP Deep Network for Malignant Ultrasound Breast Cancer Segmentation," in *2023 IEEE International Conference on Emerging Trends in Engineering, Sciences and Technology (ICES&T)*, IEEE, 2023, pp. 1–6.

Bitlis Eren Üniversitesi Fen Bilimleri Dergisi
BİTLİS EREN UNIVERSITY JOURNAL OF SCIENCE
ISSN: 2147-3129/e-ISSN: 2147-3188
VOLUME: 12 NO: 3 PAGE: 887-893 YEAR: 2023
DOI:10.17798/bitlisfen.1333113

Determination of Energy Absorption Capabilities of Shear Thickening Fluid Impregnated Aramid Fiber Fabrics for Ballistic Applications

Ali İmran AYTEN[1*]

[1]*Yalova University, Faculty of Engineering, Department of Polymer Materials Engineering, Yalova, 77200, TURKEY*
(ORCID: 0000-0002-3948-3690)

Keywords: Drop weight impact test, Energy absorption capability, Shear thickening fluid, Para-aramid fabric.

Abstract

The low-velocity impact behavior of shear thickening fluid (STF) impregnated aramid fabric having different numbers of layers was investigated throughout this study to determine a relationship between the number of layers and perforation energy. Firstly, STF solutions, including polyethylene glycol, silica nanoparticles, and ethanol, were prepared by mixing with a homogenizer. Solutions containing 5%, 10%, and 20% silica nanoparticles by weight were prepared, and rheological analysis was performed. 20% weight fraction solution showed the optimum thickening behavior among the three solutions. After thickening behavior and the critical shear rate were determined from rheological analysis, the solution was impregnated into the aramid fabric. Then, specimens with different numbers of layers, from 1 to 8, were prepared for low-velocity impact experiments. A drop-weight impact test was applied at different energy levels from 20 J to 240 J, and perforation energy was determined. Finally, an equation that has a form of power function was fitted to use it for potential energy absorption applications such as ballistic impact.

1. Introduction

Shear thickening fluids (STF) are the solutions in which nanoparticles are dispersed in a polymer phase. They can be defined as non-Newtonian fluids that do not follow Newton's viscosity law. In Newtonian fluids, viscosity remains constant as the shear rate increases, whereas in shear thickening fluids, viscosity increases with an increasing shear rate, and the fluid behaves like a solid for an instant. The fundamental reason for this behaviour is that the silica nanoparticles in STF are dispersed and homogeneous when no stress is applied. When the shear stress is applied, silica nanoparticles come together and show agglomeration behaviour, due to the polymer phase in the solution. There are various applications of shear thickening fluids in the literature [1]-[21]. One of the most common applications of STF is the impregnation of the aramid fabric to increase its energy absorption capability.

The first study on the impregnation of aramid fabric was conducted by Lee et al.[22]. STF, including silica nanoparticles with a diameter of 450 nm particles impregnated with woven Kevlar fabric, was tested by shooting with a bullet having a speed of 244 m/s. They found that the 2 ml STF-impregnated Kevlar fabric, consisting of 4 layers, showed 42% less deformation compared to the bare 4-layer Kevlar fabric.

Avila et al. [23] achieved a dual-phase formation by dispersing calcium carbonate and nanosilica fillers in polyethylene glycol (PEG) and ethanol, and they enabled the spread of these fillers into aramid fiber fabric. This method increased the inter-yarn friction and bullet deformation. They found that a composition of 25% nanosilica and 75% calcium carbonate by weight yielded the best results. They observed that the ballistic performance of a 32-layer aramid fabric was equivalent to that of a 19-

*Corresponding author: aiayten@yalova.edu.tr
Received: 26.07.2023, Accepted: 18.09.2023

layer aramid fabric impregnated with a nanosilica/calcium carbonate solution.

Gürgen and Kuşhan [24] synthesized multi-phase STFs by adding varying amounts of silicon carbide (SiC) to a silica- and PEG-based solution. They conducted ballistic tests on aramid fabrics impregnated with multi-phase STFs using lead-core bullets at a speed of 330 m/s. Rheology tests revealed that single-phase STF samples exhibited more thickening behavior compared to multi-phase STF samples. However, aramid fabrics impregnated with multi-phase STFs provided significant benefits, especially in reducing trauma depth. They mentioned that the potential drawback of multi-phase STF samples was their increased areal density.

In another study by Gürgen and Kuşhan [25], three different ceramic fillers, namely silicon carbide, aluminum oxide, and boron carbide, were added to STFs in various weight percentages within the composite. The researchers investigated the rheological effects of these added fillers on the STFs. They found that these additions significantly influenced the thickening behavior of the STFs. For instance, at 60°C and with a 5% weight of filler, the composite containing aluminum oxide exhibited the highest thickening behavior.

Khodadadi et al. [26] prepared STFs containing silica nanoparticles at weight percentages of 15%, 25%, 35%, and 45%. They examined the energy dissipation performance of solutions. In ballistic tests, they observed that fabric impregnated with STFs showed increased energy dissipation values, but STFs with a high percentage of nanosilica filler started to have negative effects. They determined that the specific energy dissipation value of the Kevlar fabric impregnated with 15% filler STFs was lower than that of the bare Kevlar fabric. On the other hand, the Kevlar fabric impregnated with 35% filler STFs exhibited a 2.3 times higher specific energy dissipation value compared to the neat Kevlar fabric.

Qin et al. [27] synthesized a new type of STF and impregnated it into Kevlar fabric, then subjected it to a dynamic penetration resistance test. They found that the new type of STF, containing silica microspheres and ionic liquid, exhibited a unique double-continuous shear thickening behavior. They achieved the optimum dynamic penetration resistance with 34.89% by weight of STF-impregnated fabric. They observed that the newly synthesized STF significantly increased inter-yarn friction.

In this study, three different solutions with different silica nanoparticle weight ratios (5%, 10%, and 20%) were prepared and their rheological behaviors were examined. According to the results, in the final step of the rheological analysis, STF with 20% silica concentration was prepared and soaked into aramid fabric. Additionally, 20% silica concentration is the optimum rate in most published studies because the high amount of silica in STF may create an agglomeration problem at the preparation stage of the fluid. After the impregnation process is completed, different numbers of layers of aramid fabric are subjected to a drop-weight impact test to determine their energy absorption capabilities. After determining the "number of layers-perforation energy" relationship, the equation was obtained by the curve fitting method. This equation may be used to determine how many layers of fabric are needed for ballistic protection at different ballistic protection levels.

2. Material and Method

Shear thickening fluid solution was prepared by using polyethylene glycol (PEG) 200 (Merck), ethanol, and hydrophilic fumed silica nanoparticles, which have a 12 nm diameter particle size (Aerosil 200, Evonik). First, PEG and ethanol were mixed by homogenizer (IKA T18 Basic Ultra Turrax) for 15 min at 3000-3500 rpm (Figure 1a). After they were completely mixed, Aerosil 200 silica nanoparticles were manually added to prevent agglomeration as the mixing continued. When the addition of silica nanoparticles was ended, mixing of all components continued for 1 h.

Three mixtures were prepared with three different Aerosil 200/PEG200 weight ratios, namely 5%, 10%, and 20%. STF solution was poured into a container, and aramid fabric was soaked into the solution (Figure 1b). Twaron CT709 plain weave aramid fabric (Teijin Ltd.), having a 200 g/m2 real weight, was used throughout this study. Both sides of the fabric were left in solution to provide impregnation for 2 min. The fabric was hung on the rope and left for 1 day to evaporate the ethanol (Figure 1c). Finally, specimens with two or more layers were stitched to prevent slipping throughout low-velocity impact experiments.

Rheology analysis was carried out by a rotational dynamic oscillatory hybrid rheometer (TA Instruments, Discovery HR-1) with 25 mm diameter parallel plates within a shear strain rate of 1 to 2250 s^{-1} at room temperature.

The Instron Ceast 9350 drop tower impact system was used to perform low-velocity impact (LVI) tests at different energy levels depending on the number of fabric layers. A series of LVI experiments

were performed from 1 layer to 8 layers of STF-impregnated aramid fabrics. A hemispherical impactor tip with 10 mm diameter was used as an impactor (Figure 2). Extra mass was added to adjust the impact energy. Different initial energies, from 20 J to 240 J, were set for different numbers of fabric layers.

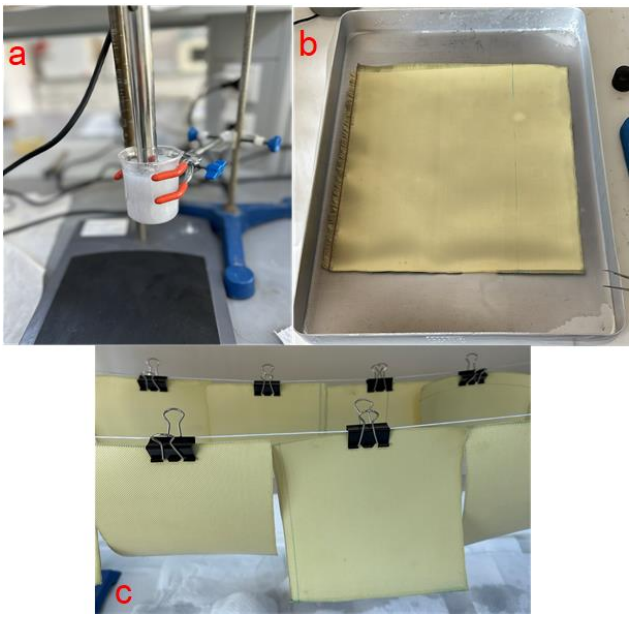

Figure 1. Preparation of STF and impregnate it to the aramid fabric. a) Mixing the solution components by homogenizer, b) Impregnation of the STF into the aramid fabric, c) Drying fabric for evaporating ethanol.

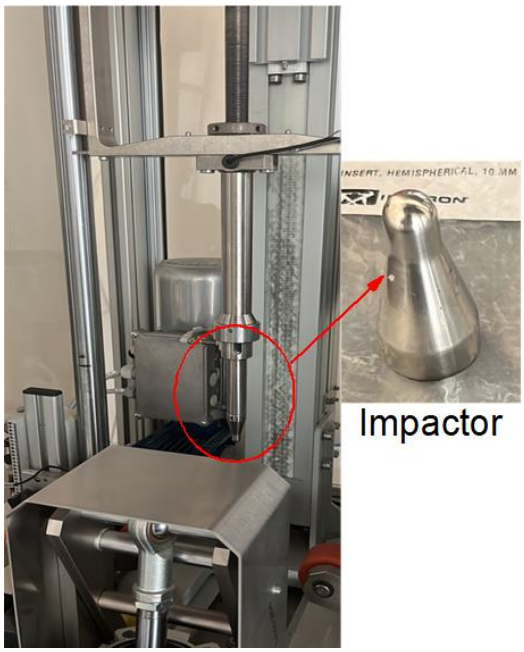

Figure 2. Drop tower impact system and impactor.

3. Results and Discussion

3.1. SEM Results

SEM images were captured to understand the impregnation of STF on the surface of aramid fiber. Figure 3 shows the images of neat and STF-impregnated fabric at different magnifications. When Figures 3a and 3b were compared, the difference between two of them could be clearly observed. The surface of the aramid fibers was covered by the STF solution. Herein, PEG plays a crucial role in sticking to the surface. Figures 3c and 3d have a difference in terms of the fabric being covered by STF homogeneously.

3.2. Rheological Analysis Result

Rheological analysis was carried out with an increasing shear rate between 1 and 2250 s^{-1}. PEG has a Newtonian characteristic, but its behavior has been changing by adding silica nanoparticles [24]. In Figure 4, the viscosity curve includes three zones according to the viscosity change. Firstly, the solution showed a thinning behavior until the 250 s^{-1} shear rate value, and then shear thickening behavior was observed because silica nanoparticles aggregated in the polymer phase. At the final step, agglomerated parts of nanoparticles suddenly crashed at the high shear rate, and shear thinning behavior was observed again.

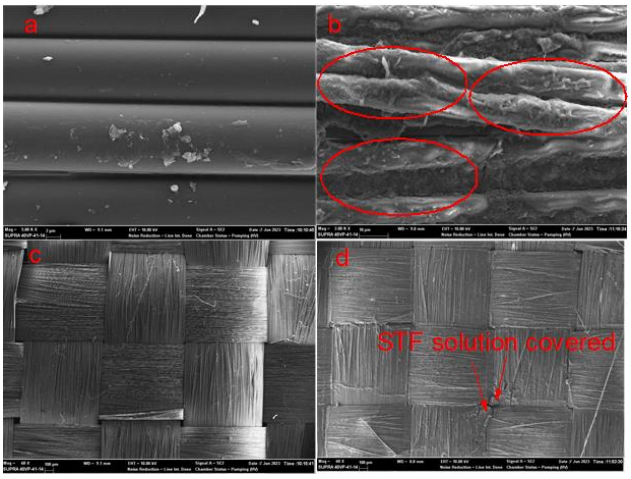

Figure 3. SEM images of a) neat fabric at 2 µm scale, b) STF impregnated fabric at 10 µm scale, c) neat fabric at 100 µm scale, d) STF impregnated fabric at 100 µm scale.

Figure 5 presents a comparison of different solutions, including different amounts of silica nanoparticles. The 5% silica concentration solution did not show any thickening behaviour. Its viscosity

increased 0.74 times between 6.42 and 1534.78 s^{-1} shear rates. The viscosity value of a 10% silica concentration solution increased 9.575 times (957.5%) between 100 and 250 s^{-1} shear rate values. The greatest viscosity increase was observed in the 20% solution. It showed viscosity increasing 11.02 times (1102%) between 100 and 640.37 s^{-1} shear rate.

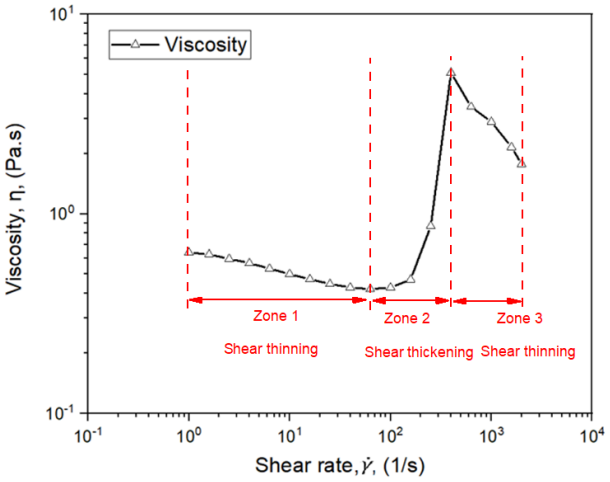

Figure 4. Viscosity-shear rate relationship for Aerosil 200/PEG 200 STF solution.

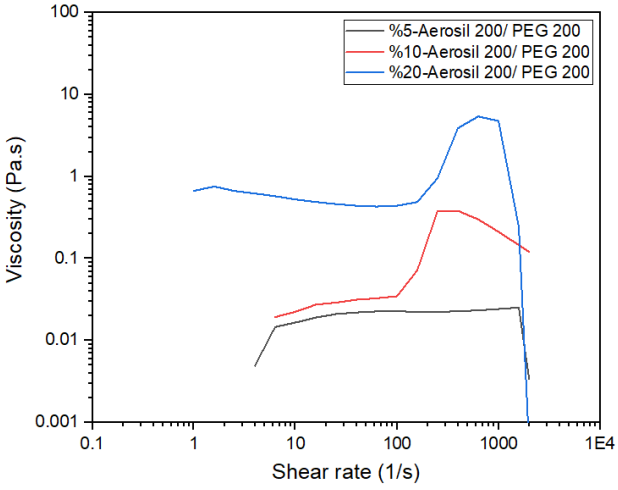

Figure 5. Comparison of Aerosil 200/PEG200 solution at different silica nanoparticle concentrations.

3.3. Low Velocity Impact Test Results

Figure 6 compares the low-velocity impact response of 3 layers of neat and STF-impregnated aramid fabric. There is an 18.5% difference in terms of maximum loading. Figure 7 presents force-displacement curves for 1 layer to 8 layers of aramid fabric. The curves include noise because the soft structure of the fabric causes contact problems between the impactor and the specimen. When the first 10 mm displacement value part of the curves is investigated, it can be seen that the stiffness value is increasing proportionally with the number of fabric layers. 'V' shape in the curve of all specimens can be seen around 42 mm displacement values. This behavior may be associated with the damage pattern of the fabric in Figure 9. After the first load drop occurred, the fabric structure became bulkier, which increased the contact force again.

$$Absorbed\ energy = \int_0^{\delta} F.d\delta \quad (1)$$

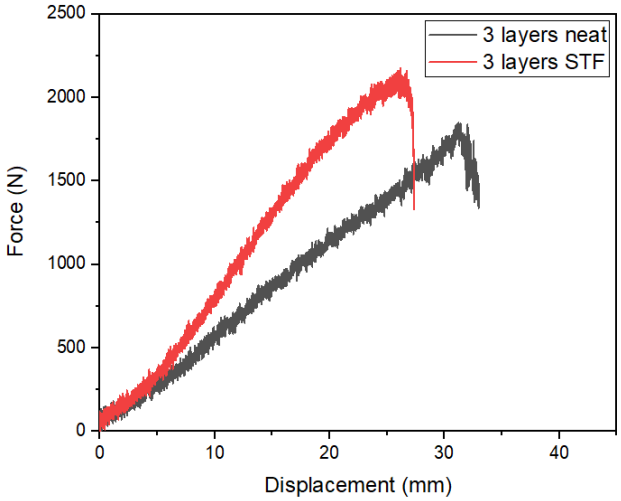

Figure 6. A comparison of low velocity impact response between neat aramid and STF impregnated aramid fabric for 3 layers specimens.

The amount of absorbed energy by fabric specimens was calculated by integrating under the area of the force-displacement curve as shown in Equation 1. Herein, 'F' is the contact force, and 'δ' is displacement. Calculated values were listed in Table 1 and plotted in Figure 8 to fit a curve. Table 1 also shows that maximum contact force values depend on the number of layers. The increasing rate of maximum contact force has decreased with the increasing number of layers. For instance, the ratio in contact force between 1-layer and 2-layers specimens is 1.92, while this value is 1.16 for 7- and 8-layers specimens. This situation can be explained by the fact that the rigidity of specimens does not increase critically after a certain level of layering.

Equation 2 is the curve-fitting equation, which shows the relationship between the number of layers and the amount of absorbed energy. In this equation, 'x' implies the number of layers, while 'y' represents absorbed energy.

Figure 9 presents the damage mechanisms and damage areas for a 2-layer STF-impregnated aramid fabric specimens. Two different damage zones were observed in specimens: primary and secondary. In the primary damage zone, both the geometrical pattern of the fabric and the fibers were subjected to damage, while in the secondary damage zone, only the geometrical distortion was distorted. Ruptured yarns on the right side of Figure 9 play a key role in mitigating impact energy.

Table 1. Relationship between number of fabric layers and energy absorption values

Number of layers	Absorbed Energy (J)	Maximum Contact Force (N)
1	16.3	487.13
2	24	935.34
3	40	1747.74
4	70	2715.76
5	90	3277.60
6	115	3851.87
7	150	4230.05
8	180	4888.37

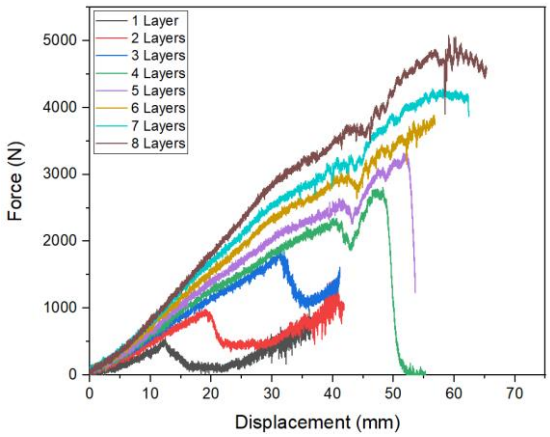

Figure 7. A comparison of low velocity impact response between neat aramid and STF impregnated aramid fabric for 3 layers specimens.

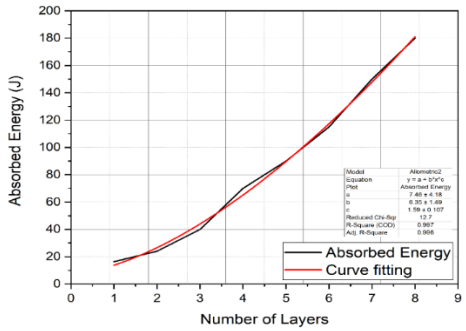

Figure 8. Curve fitting equation for relationship between absorbed energy and number of layers.

$$y = 7.46 + 6.35(x^{1.59}) \quad (2)$$

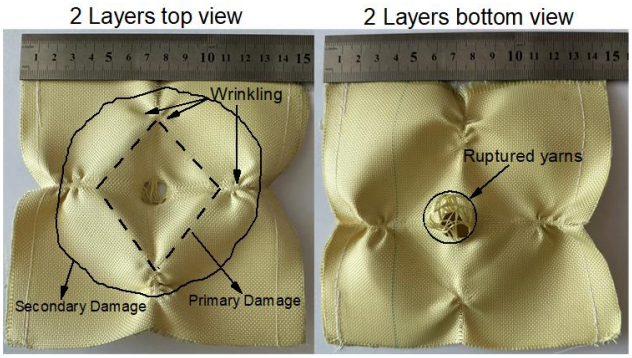

Figure 9. Damage mechanisms and regions for a 2 layers STF impregnated aramid fabric

4. Conclusion and Suggestions

Shear thickening fluids having 5%, 10%, and 20% silica concentrations were prepared and analysed by a rheometer to determine their thickening behaviors. There was a 15% difference in terms of the viscosity increase rate between 10% and 20% concentration solutions. Then, STF-impregnated aramid fabric specimens were examined by LVI test at different impact energies from 20 J to 240 J. Table 1 presents energy absorption, the number of layers relationship, and maximum contact force values. Finally, an equation in power function form (Eq.2) was obtained from Figure 8 as a curve-fitting equation. This relationship may be used for different energy absorption applications. As an example of the usage of this equation, a type IIA-level ballistic threat has a kinetic energy of around 555 J depending on ammo type- according to the NIJ 0101.06 standard. To absorb this level of kinetic energy, the needed number of fabric layers can be found at 16 layers.

Acknowledgment

This work was supported by Yalova University Scientific Research Projects Unit (BAP) (Project No: 2020/AP/0013). The author would like to express his thanks for funding.

Statement of Research and Publication Ethics

The study is complied with research and publication ethics.

References

[1] T. A. Hassan, V. K. Rangari, and S. Jeelani, "Synthesis, processing and characterization of shear thickening fluid (STF) impregnated fabric composites," *Materials Science and Engineering: A*, vol. 527, no. 12, pp. 2892-2899, 2010.

[2] A. Majumdar, B. S. Butola, and A. Srivastava, "Optimal designing of soft body armour materials using shear thickening fluid," *Materials & Design (1980-2015)*, vol. 46, pp. 191-198, 2013.

[3] A. Haris, H. P. Lee, T. E. Tay, and V. B. C. Tan, "Shear thickening fluid impregnated ballistic fabric composites for shock wave mitigation," *International Journal of Impact Engineering*, vol. 80, pp. 143-151, 2015.

[4] W. Na *et al.*, "Shear behavior of a shear thickening fluid-impregnated aramid fabrics at high shear rate," *Composites Part B: Engineering*, vol. 97, pp. 162-175, 2016.

[5] N. Asija, H. Chouhan, S. A. Gebremeskel, and N. Bhatnagar, "High strain rate characterization of shear thickening fluids using Split Hopkinson Pressure Bar technique," *International Journal of Impact Engineering*, vol. 110, pp. 365-370, 2017.

[6] S. Cao, Q. Chen, Y. Wang, S. Xuan, W. Jiang, and X. Gong, "High strain-rate dynamic mechanical properties of Kevlar fabrics impregnated with shear thickening fluid," *Composites Part A: Applied Science and Manufacturing*, vol. 100, pp. 161-169, 2017.

[7] M. Hasanzadeh, V. Mottaghitalab, M. Rezaei, and H. Babaei, "Numerical and experimental investigations into the response of STF-treated fabric composites undergoing ballistic impact," *Thin-Walled Structures*, vol. 119, pp. 700-706, 2017.

[8] A. Majumdar, A. Laha, D. Bhattacharjee, and I. Biswas, "Tuning the structure of 3D woven aramid fabrics reinforced with shear thickening fluid for developing soft body armour," *Composite Structures*, vol. 178, pp. 415-425, 2017.

[9] K. Fu, H. Wang, L. Chang, M. Foley, K. Friedrich, and L. Ye, "Low-velocity impact behaviour of a shear thickening fluid (STF) and STF-filled sandwich composite panels," *Composites Science and Technology*, vol. 165, pp. 74-83, 2018.

[10] K. Fu, H. Wang, S. Wang, L. Chang, L. Shen, and L. Ye, "Compressive behaviour of shear-thickening fluid with concentrated polymers at high strain rates," *Materials & Design*, vol. 140, pp. 295-306, 2018.

[11] A. Haris, H. P. Lee, and V. B. C. Tan, "An experimental study on shock wave mitigation capability of polyurea and shear thickening fluid based suspension pads," *Defence Technology*, vol. 14, no. 1, pp. 12-18, 2018.

[12] Q. He, S. Cao, Y. Wang, S. Xuan, P. Wang, and X. Gong, "Impact resistance of shear thickening fluid/Kevlar composite treated with shear-stiffening gel," *Composites Part A: Applied Science and Manufacturing*, vol. 106, pp. 82-90, 2018.

[13] X. Wu, K. Xiao, Q. Yin, F. Zhong, and C. Huang, "Experimental study on dynamic compressive behaviour of sandwich panel with shear thickening fluid filled pyramidal lattice truss core," *International Journal of Mechanical Sciences*, vol. 138-139, pp. 467-475, 2018.

[14] V. A. Chatterjee, S. K. Verma, D. Bhattacharjee, I. Biswas, and S. Neogi, "Enhancement of energy absorption by incorporation of shear thickening fluids in 3D-mat sandwich composite panels upon ballistic impact," *Composite Structures*, vol. 225, 2019.

[15] S. Sen, N. B. Jamal M, A. Shaw, and A. Deb, "Numerical investigation of ballistic performance of shear thickening fluid (STF)-Kevlar composite," *International Journal of Mechanical Sciences*, vol. 164, 2019.

[16] C. Caglayan, I. Osken, A. Ataalp, H. S. Turkmen, and H. Cebeci, "Impact response of shear thickening fluid filled polyurethane foam core sandwich composites," *Composite Structures*, vol. 243, 2020.

[17] L. Liu, Z. Yang, Z. Zhao, X. Liu, and W. Chen, "The influences of rheological property on the impact performance of kevlar fabrics impregnated with SiO2/PEG shear thickening fluid," *Thin-Walled Structures*, vol. 151, 2020.

[18] C. Huang, L. Cui, Y. Liu, H. Xia, Y. Qiu, and Q.-Q. Ni, "Low-velocity drop weight impact behavior of Twaron® fabric investigated using experimental and numerical simulations," *International Journal of Impact Engineering*, vol. 149, 2021.

[19] M. R. Sheikhi and S. Gürgen, "Anti-impact design of multi-layer composites enhanced by shear thickening fluid," *Composite Structures*, vol. 279, 2022.

[20] V. Mahesh, D. Harursampath, and V. Mahesh, "An experimental study on ballistic impact response of jute reinforced polyethylene glycol and nano silica based shear thickening fluid composite," *Defence Technology*, vol. 18, no. 3, pp. 401-409, 2022.

[21] C.-H. Shih, C.-P. Chang, Y.-M. Liu, Y.-L. Chen, and M.-D. Ger, "Ballistic Performance of Shear Thickening Fluids (STFs) Filled Paper Honeycomb Panel: Effects of Laminating Sequence and Rheological Property of STFs," *Applied Composite Materials*, vol. 28, no. 1, pp. 201-218, 2021.

[22] Y. S. Lee, E. D. Wetzel, and N. J. Wagner, "The ballistic impact characteristics of Kevlar woven fabrics impregnated with a colloidal shear thickening fluid," *Journal of Materials Science*, vol. 38, pp. 2825-2833, 2003.

[23] A. F. Ávila, A. M. de Oliveira, S. G. Leão, and M. G. Martins, "Aramid fabric/nano-size dual phase shear thickening fluid composites response to ballistic impact," *Composites Part A: Applied Science and Manufacturing*, vol. 112, pp. 468-474, 2018.

[24] S. Gürgen and M. C. Kuşhan, "The ballistic performance of aramid based fabrics impregnated with multi-phase shear thickening fluids," *Polymer Testing*, vol. 64, pp. 296-306, 2017.

[25] S. Gürgen, W. Li, and M. C. Kuşhan, "The rheology of shear thickening fluids with various ceramic particle additives," *Materials & Design*, vol. 104, pp. 312-319, 2016.

[26] A. Khodadadi, G. Liaghat, S. Vahid, A. R. Sabet, and H. Hadavinia, "Ballistic performance of Kevlar fabric impregnated with nanosilica/PEG shear thickening fluid," *Composites Part B: Engineering*, vol. 162, pp. 643-652, 2019.

[27] J. Qin, B. Guo, L. Zhang, T. Wang, G. Zhang, and X. Shi, "Soft armor materials constructed with Kevlar fabric and a novel shear thickening fluid," *Composites Part B: Engineering*, vol. 183, 2020.

Bitlis Eren Üniversitesi Fen Bilimleri Dergisi
BİTLİS EREN UNIVERSITY JOURNAL OF SCIENCE
ISSN: 2147-3129/e-ISSN: 2147-3188
VOLUME: 12 NO: 3 PAGE: 894-910 YEAR: 2023
DOI:10.17798/bitlisfen.1334583

Studies on the Ennominae Fauna and Taxonomy of the Dağlıca (Geometridae, Lepidoptera)*

Hanife UÇAK[1†], Muhabbet KEMAL[2]

[1]*Van Yüzüncü Yıl University, Institute of Science, Biology PhD student, 65100 Van, Turkey*
[2]*Van Yüzüncü Yıl University, Faculty of Science, Department of Biology, 65100 Van, Turkey*

(ORCID: 0000-0002-3148-6678) (ORCID: 0000-0003-0183-4050)

Keywords: Dağlıca, Ennominae, Geometridae, Hakkari, Taxonomy, Türkiye.

Abstract

Ennominae is an important group in the Geometridae family that contains problematic species with very similar external morphological characters. In this study, Ennominae species collected from Yüksekova Dağlıca town of Hakkari Province between April and September 2017 were evaluated from a faunistic and taxonomic perspective. 28 species were identified in the study. *Charissa onustaria*, *C. subtaurica* and *Crocallis tusciaria* species were identified for the first time from Hakkari Province. *C. loebeli*, *Neognopharmia cataleucaria*, and *Ramitia kufrana* were detected in the region are also important endemic taxa for the Turkish fauna. *Rhoptria mardinata* and *Eumera hoferi*, known only in Türkiye and Iran, are other rare species found in the region. *R. mardinata* was presented with photographs of male genitalia for the first time. Morphological and taxonomic aspects of the species under the genera *Dicrognophos*, *Gnopharmia*, *Crocallis*, *Bellachima*, *Charissa*, *Synopsia* and *Nychiodes* are discussed.

1. Introduction

Hakkari is a rich region of Türkiye in biodiversity. The first entomological research in the area was started by Koçak in 1972, the results [1-3] and the rich biological diversity of the region attracted the attention of many foreign entomologists. On this subject, Görgner [4] wrote in his article: “Lediglich im letzten Jahrzehnt dehnten die in der Türkei tätigen Entomologen ihr Arbeitsgebiet auf diese entlegene und früher fast unzugängliche Provinz aus. So bereiste zuerst A. Ö. KOÇAK (Universität Ankara) 1973 dieses Gebiet und wies aus der Provinz Hakkari sechs Lepidopterenarten für das Staatsgebiet der Türkei neu nach.” (*Only in the last decade have entomologists working in Turkey expanded their field of work to this remote and previously almost inaccessible province. So first A. Ö. KOÇAK (University of Ankara) studied this area in 1973 and identified six lepidopteran species from the province of Hakkari for the national territory of Turkey*.). Dağlıca village, a former sub-district center of Hakkari, Yüksekova district, as one of Türkiye's easternmost border outposts, remained a truly inaccessible, and hard-to-reach settlement due to security reasons for many years. In recent years, some studies on Lepidoptera species [5-8] have been carried out in and around Yüksekova, Dağlıca village. Dağlıca is located in a geography with high potential in terms of biodiversity and also in the Buzul (Glacier) and İkiyaka Mountains (DOG066 code in ÖDA) regions, which should be followed up by additional studies to determine the Important Natural Areas (ÖDA) of Türkiye [9]. Following the first lepidoptera list of Hakkari [10], second, more comprehensive study including 985 species was published [11].

Geometridae, which is in the Lepidoptera order, is one of the richest groups in the with

†Corresponding author: uck_hanife@hotmail.com
Received: 29.07.2023, Accepted: 19.09.2023

23,872 species. Approximately 80 new species have been defined annually between 2000-2022 [12]. This number shows that the family in question is a moth group with a high potential in terms of species diversity. Geometrids are represented by 687 species in Türkiye's Lepidoptera checklist [11], 193 of them belong to Ennominae. This number includes a new genus that has been added in recent years, *Bellachima* Kemal et al., 2018 [13] and species such as *Ramitia kufrana* Seven, 2015 [14], and *Wehrliola inexpectata* Kemal & Uçak, 2018. After this article, *Charissa adjectaria* Staudinger, 1898, from Batman, *Charissa annubilata* (Christoph, 1885) and *Gnophos sacraria* Staudinger, 1895 were added to the fauna of Türkiye from Siirt Province [15]. In Türkiye, while the genus *Tephronia* is represented by *oppositaria* Mann, 1864 and *sepiaria* (Hufnagel, 1767) species [11], the species *lepraria* Rebel, 1909 is also included in the fauna of Türkiye in European Ennominae [16]. *Eupithecia opistographata* was given from Siirt [17] as a new record for Türkiye, but was omitted in the Koçak and Kemal [11] list. A new species *Eupithecia nemrutica* has been described from Bitlis Province [18]. *Protorhoe centralisata* from Batman and Siirt Provinces and *Perigune jordanaria* from Batman were added together with the genus for the Turkish fauna. A new subspecies *Perigune jordanaria anatolica* was also described in the study [19]. *Kresnaia beschkovi* (Ganev, 1987), previously known only from Iran in the Irano-Turanian Geographical Region, the first record of the fauna of Türkiye was given by Seven from Batman Province [20]. Finally, with *Nychiodes eberti* Wanke, Hausmann & Rajaei, 2020, detected in Erzurum, Türkiye's Geometrids increased to 694 species and the *Ennominae* subfamily increased to 197.

It is suggested that approximately 11,100 species identified in this subfamily worldwide and another 7000 taxa clustered at the species level according to the barcoded genetic data await identification [12]. It should be said that the studies for Türkiye also, especially the Irano-Turanian Geographic Region which has a rich potential in terms of *Ennominae* species, are still at the beginning stage. As a matter of fact, the genetic barcoding studies we have started are very late compared to Europe and our opportunities are extremely limited. Despite these conditions, we anticipate that new species will be discovered in the fauna of Türkiye. In the current study carried out in this context, the number of *Ennominae* species of Dağlıca village has increased to 31. On the other hand, knowing the habitat and food plants they live in is also important ecologically, in terms of agriculture and forestry, of this group, which plants nutrition both in early development stages and when they are adults.

2. Material and Method

The study material consists of samples collected at night with automatic light traps placed in natural areas in Dağlıca village of the research area between April-October 2017. Samples prepared in the laboratory were photographed with a Canon 60D-250D 35-155 lens camera, genital preparations were made according to Robinson [21] for definitive diagnosis, and photographed with a computer-equipped microscope at Leica S8APO, DFC290 resolution.

The noun combinations of the species listed in the study and the taxonomic hierarchy were arranged according to Koçak and Kemal [11], Müller et al., [16] and Wanke et al., [22-23] studies. For the distribution of the species in the world in Türkiye, Koçak and Kemal [11, 24] is based. The records about the specimens collected from the research area are given in Table 1. This table includes the names of the species identified from the area in alphabetical order, their vertical distribution together with the collection dates and the total number of male and female specimens collected from each species. In Table 2, the distribution of the species in the Palearctic Region and Türkiye is presented with country and traffic codes. Accordingly, based on the frequency of occurrence of the species throughout Türkiye, the species were evaluated in 5 categories: endemic if known only in Türkiye, rare if recorded in less than 5 provinces, little known if known between 5 and 10 provinces, well known if known from more than 10 provinces and less than 20 provinces, and common if known from more than 20 provinces. In addition, additional species for Hakkari fauna are marked with '*'. These assessments are based on current literature and information identified in the field study. At the end of the study, a checklist of Dağlıca Ennominae species is presented according to the taxonomic hierarchy under the tribus to which each genus belongs.

Table 1. Material examined from Dağlıca.

	Species identified in the area	Altitude and collection date	Number of specimens
1	*Bellachima diaphanaria*	2♂, 1515m, 23.09.2017; 3♂, 1505m, 15.10.2017; 2♂1♀, 1505, 16.10.2017; 1♀, 1785m, 17.10.2017; 1♀, 1520m, 20.10.2017; 1♂, 1520m, 23.10.2017.	8♂3♀
2	*Charissa annubilata*	1♂, 1505m, 15.10.2017.	1♂
3	*Charissa dubitaria*	1♀, 1505m, 15.10.2017.	1♀
4	*Charissa onustaria*	1♂, 1865m, 22.05.2017; 2♂, 1865m, 23.05.2017; 3♂, 1490m, 24.05.2017; 1♂, 1765m, 25.05.2017; 1♂, 1530m, 19.10.2017.	8♂
5	*Charissa subtaurica*	3♂, 2085m, 22.05.2017; 1♂, 1520m, 24.07.2017;1♂, 1505m, 15.10.2017; 1♂, 1520m, 20.10.2017;	6♂
6	*Chiasmia clathrata*	2♂, 1865m, 23.05.2017; 2♂, 1457m, 24.05.2017; 1♂, 1865m, 23.05.2017; 1♂, 1765m, 25.05.2017.	6♂
7	*Crocallis loebeli*	1♂, 1520m, 22.09.2017; 3♂, 1515m, 23. 09. 2017.	4♂
8	*Crocallis tusciaria*	1♂, 1505m, 15.10.2017	1♂
9	*Dasycorsa modesta*	3♂, 1650m, 24.04.2017.	3♂
10	*Dyscia innocentaria*	1♂, 1865m, 22.05.2017; 12♂2♀ 1865m 23.05.2017; 8♂1♀, 1457m, 24.05.2017; 1♂, 1765m, 25.05.2017; 1♂, 1515m, 19.09.2017; 1♂, 1520m, 20.09.2017; 1♂, 1520m, 22.09.2017; 1♂, 1515m, 23.09.2017.	26♂3♀
11	*Eilicrinia cordiaria*	1♂, 2085m, 22.06.2017; 1♂, 1525m, 23.04.2017.	2♂
12	*Ennomos fraxineti*	1♂, 1560m, 31.08.2017; 3♂, 1505m, 15.10.2017; 2♂, 1505m, 16.10.2017; 2♂, 1520m, 20.10.2017.	8♂
13	*Ennomos quercarius*	1♂, 1480m, 21.07.2017; 1♂, 1700m, 24.08.2017; 1♂, 1505m, 15.10.2017; 2♂, 1♀, 1505m, 15.10.2017; 2♂, 1505m, 16.10.2017; 1♂, 1720m, 18.10.2017; 2♀, 1520m, 20.10.2017.	8♂3♀
14	*Eumera hoeferi*	2♂, 1520m, 22.09.2017; 3♂, 2♀, 1515m, 23.09.2017; 1♂, 1505m, 16.10.2017.	6♂
15	*Gnopharmia colchidaria*	4♂, 1865m, 22.05.2017; 5♂, 1865m, 23.05.2017; 5♂, 4♀, 1457m, 24.05.2017; 1♀, 1765m, 25.05.2017; 1♂, 2075m, 21.06.2017; 7♂, 2♀, 2085m, 22.06.2017; 1♂, 1♀, 1410m, 23.06.2017; 1♂, 1550m, 22.07.2017; 1♀, 1490m, 24.07.2017.	24♂9♀
16	*Gnopharmia irakensis*	6♂, 1♀, 1865m, 22.05.2017; 3♂, 1865m, 23.05.2017; 8♂, 3♀, 1457m, 24.05.2017; 1♂, 1♀, 1765m, 25.05.2017; 4♂, 1♀, 2075m, 21.06.2017; 7♂, 7♀, 2085m, 22.06.2017; 1♂, 2♀, 1410m, 23.06.2017; 1♂, 1♀, 1520m, 24.06.2017; 7♂, 3♀, 1480m, 21.07.2017; 1♂, 3♀, 1550m, 22.07.2017; 1♀, 1520m, 24.07.2017.	39♂22♀
17	*Gnophos gorgatus*	5♂, 4♀, 2075m, 21.06.2017; 6♂, 4♀, 2085m, 22.06.2017; 3♀, 1410m, 23.06.2017; 2♀, 1480m, 21.07.2017; 2♀, 1520m, 24.07.2017; 2♂, 1♀, 1730m, 3.08.2017; 1♂ 1715m, 28.08.2017.	14♂12♀
18	*Gnophos sartatus*	2♂, 2075m, 21.06.2017; 3♂, 2085m, 22.06.2017; 1♀, 1520m, 24.06.2017; 1♂, 2♀, 1515m, 22.09.2017; 1♂, 1♀,1720m, 18.10.2017; 1♀ 1530m, 19.10.2017; 1♂, 1♀, 1520m, 20.10.2017.	8♂4♀
19	*Heliomata glarearia*	4♀, 1865m, 22.05.2017; 11♂, 4♀, 1865m, 23.05.2017; 11♀ 1457m, 24.05.2017; 1♂, 1490m, 1♂, 1♀, 1715m, 28.08.2017.	13♂20♀

Table 1. Material examined from Dağlıca (continue).

	Species identified in the area	Altitude and collection date	Number of specimens
20	*Neognopharmia cataleucaria*	1♂, 1♀, 1865m, 22.05.2017; 4♂, 1865m, 23.05.2017; 7♂, 1♀,1457m, 24.05.2017; 2♂, 1765m, 25.05.2017; 1♂, 3♀, 2075m, 21.06.2017; 1♂, 3♀, 2075m, 21.06.2017; 4♂, 4♀, 2085m, 22.06.2017; 1♂, 1410m, 23.06.2017; 2♀, 1520m, 24.06.2017; 1♀, 1730m, 23.08.2017; 1♀, 1835m, 24.08.2017; 1♀, 1715m, 28.08.2017; 2♀, 1520m, 30.08.2017.	21♂19♀
21	*Nychiodes divergaria*	1♂, 1♀, 1865m, 22.05.2017; 1♂, 1865m, 23.05.2017; 3♂, 1♀, 1457m, 24.05.2017; 3♂, 2♀, 2075m, 21.06.2017; 12♂, 1♀, 2085m, 22.06.2017; 6♂, 1410m, 23.06.2017; 3♂, 1520m 24.06.2017; 3♂, 1730m, 23.08.2017; 5♂, 1835m, 24.08.2017; 2♂, 1830m, 26.08.2017; 4♂, 1715m, 28.08.2017; 1♂, 1520m, 30.08.2017; 1♂, 1560m, 31.08.2017	45♂5♀
22	*Peribatodes rhomboidarius*	1♀, 1490m, 24.05.2017; 2♂, 2075m,21.06.2017; 1♂, 2085m, 22.06.2017; 2♂, 1410m, 23.06.2017; 2♂, 1715m, 28.08.2017; 2♂, 1520m, 22.09.2017; 2♂, 2♀, 1515m, 23.09.2017.	11♂3♀
23	*Peribatodes umbrarius*	2♀, 1765m, 25.05.2017.	2♀
24	*Pseudopanthera syriacata*	2♂, 1♀, 1865m, 22.05.2017; 6♂, 1865m, 23.05.2017; 1♀, 1457m, 24.05.2017; 1♀, 1765m, 25.05.2017.	8♂3♀
25	*Ramitia kufrana*	1♂1650m, 24.04.2017; 1♀ 1457m, 24.05.2017.	1♂1♀
26	*Rhoptria mardinata*	1♂, 1525m, 23.04.2017; 1♂, 1650m, 24.04.2017.	2♂
27	*Synopsia phasidaria*	1♂, 2085m, 22.06.2017.	1♂
28	*Wehrliola inexpectata*	1♂, 1515m, 19.09.2017; 1♀, 1520m, 22.09.2017; 1♂, 1505m, 15.10.2017; 1♂, 1505m, 16.10.2017; 1♂, 1520m, 20.10.2017.	4♂1♀

Table 2. Distribution of Dağlıca *Ennominae* species in the Palearctic Region and Türkiye.

Species list	World distribution with geographic codes [11, 24]	Distribution on Türkiye with province traffic codes [11], [24-26]	Frequency of
Bellachima diaphanaria	TM IR TR AM	04 12 13 30 51 56 65	little known
Charissa annubilata	TR AZ GG IR	53 56 65 73	rare
Charissa dubitaria	TR LB AM IR TR Cc	13 21 23 30 33 38 47 56 65 72	little known
*Charissa onustaria**	ES FR IT RO YU AL BG GR TR GG Cc AZ AM IQ IL JO IR	05 07 14 16 23 31 33 44 46 52 56 61 65 67	well known
*Charissa subtaurica**	GR TR LB IL CY JO	01 05? 07 16? 21 31 33 42 46 48 56? 65?	?well known
Chiasmia clathrata	MA DZ PT ES FR IT IE GB BE NL LU DE CH AT PL CZ SK HU RO YU AL BG GR TR Cc GG AZ AM DK NO SE FI EE LV LT RU MD UA BY Ui KG	02 05 06 10 13 14 16 18 21 22 30 31 33 34 36 42 46 49 50 56 65 71 75 80 81	common

Table 2. Distribution of Dağlıca *Ennominae* species in the Palearctic Region and Türkiye (continue).

Species list	World distribution with geographic codes [11, 24]	Distribution on Türkiye with province traffic codes [11], [24-26]	Frequency of
Crocallis loebeli	TR	02 07 30 38 44 50 58 62 65 70	endemic
*Crocallis tusciaria**	PT ES FR IT DE CH AT PL CZ SK HU RO YU BG GR TR Cc GG Kir AZ AM RU MD UA BY	01 05 17 31 34 42 46 56 58	little known
Dasycorsa modesta	RO YU BG GR CY TR LB IL IQ IR	01 05 14 17 21 22 30 31 33 34 39 42 44 46 48 49 56 59 65 71 73	well known
Dyscia innocentaria	IT YU HV AL MK BG RO GR RU MD UA TR IQ IR TM JO IL SY CY GG AZ AM AF KG UZ CN Ui	01 05 06 07 13 14 16 17 18 20 21 25 27 30 34 35 36 38 42 44 45 46 47 50 56 65 71	common
Eilicrinia cordiaria	AT SK HU RO YU BG GR RU MD UA BY TR Cc AZ AM GG IQ IR FA IN	01 02 05 06 09 13 14 16 18 22 24 30 36 38 42 44 45 46 51 56 58 59 61 65 71 73	common
Ennomos fraxineti	TÜRKİYE, IRAN, IRAQ	13 30 42? 44? 56 65 80	little known
Ennomos quercarius	PT ES FR IT CH AT PL SK HU RO YU MK AL BG GR Cr TR Cc GG AZ AM IR IQ RU MD UA BY CY LB IL JO	05 07 14 30 31 33 34 42 47 55 56 60 65	well known
Eumera hoeferi	TR IQ Cc AZ IR	30 38 44 56 63	rare
Gnopharmia colchidaria	TR Cc GG IL TM IQ AZ AM IR PK	13 21 23 27 30 31 46 56	little known
Gnopharmia irakensis	TR IQ IR PK AF	02 30 44 47 56 63 65	little known
Gnophos gorgatus	TR, IR	30 65	rare
Gnophos sartatus	IT HV YU AL BG GR TR Cc GG AZ AM LB RU MD UA BY SY IR IL CY	02 05 06 14 16 17 20 21 27 30 31 34 35 42 45 46 56 65 80	well known
Heliomata glarearia	FR IT DE CH AT PL CZ SK HU RO YU AL BG GR TR Cc GG AZ AM IR RU MD UA BY Ui	01 05 06 13 14 16 29 30 36 37 39 43 49 56 60 65 71 75 76	well known
Neognopharmia cataleucaria	TR	30 47	endemic
Nychiodes divergaria	TR LB IL RU Cc IR IQ	13 21 23 30 47 56 65	little known
Peribatodes rhomboidarius	MA PT ES FR IT IE GB BE NL LU DE CH AT PL CZ SK HU RO YU AL BG GR TR Cc AZ GG IQ IR DK SE FI RU MD UA BY IL LB CY	01 05 08 14 15 16 17 22 30 31 33 34 36 37 42 44 45 46 48 52 56 57 59 60 61 65 77 81	common
Peribatodes umbrarius	MA DZ PT ES FR IT CH SK HU RO YU AL BG GR TR IQ IR RU MD UA BY IL LB CY	05 12 14 30 31 42 44 45 46 56 65 71	well known
Pseudopanthera syriacata	TR LB IL IQ	01 02 13 21 30 31 33 44 46 47 56 65 73 80	well known

Table 2. Distribution of Dağlıca *Ennominae* species in the Palearctic Region and Türkiye (continue).

Species list	World distribution with geographic codes [11, 24]	Distribution on Türkiye with province traffic codes [11], [24-26]	Frequency of
Ramitia kufrana	TR	30 56 65 73	endemic
Rhoptria mardinata	TR, IR	30 47 56	rare
Synopsia phasidaria	Cc GG AF IR TM AZ TR	04 13 30 65 73	rare
Wehrliola inexpectata	TR	30	endemic

3. Results

In this study, Dağlıca Ennominae species were investigated faunistically and taxonomically. As a result, 28 species were identified from the area. Distribution information of the species in Türkiye and in the world [11, 24], [25-26] together with the collection records are presented (Table 1). *Charissa onustaria*, *C. subtaurica* and *Crocallis tusciaria* species were added to the fauna of Hakkari, and it was also understood that these species spread to the easternmost part of Türkiye. As a result of the research, *Neognopharmia cataleucaria*, *Crocallis loebeli* and *Ramitia kufrana* species endemic to the fauna of Türkiye were identified along with *Wehrliola inexpectata* which is described from Dağlıca. *Charissa annubilata*, *Synopsia phasidaria*, *Gnophos gorgatus*, *Rhoptria mardinata* and *Eumera hoeferi* are rare species throughout Türkiye and have been located during the field work. Additionally *R. mardinata* and *E. hoeferi*, according to the available data, are taxa known only from Türkiye and Iran and have a narrow distribution area throughout the world [11], [16], [27]. The genus *Eumera* Staudinger,1892 is represented in Türkiye by the species *regina* Staudinger, 1892, *turcosyrica* Wehrli, 1932 and *hoeferi* Wehrli, 1934. However, in previous taxonomic studies, the tribus of this genus was not yet clear [16], while Wanke et al. [23] stated that this genus belongs to the *Prosopolophini* Warren, 1894 tribus. The general morphological characteristics of *E. hoeferi* from the area are similar to Malatya specimens examined in Wanke et al. [23].

Bellachima diaphanaria, *Gnopharmia colchidaria*, *G. irakensis*, *Crocallis tusciaria*, *Ennomos fraxineti*, *Nychiodes divergaria* and *Pseudopanthera syriacata* are species identified in the research that are little known in Türkiye, and are also elements of the Irano-Turanian Geographical Region, not found in Europe. *Dyscia innocentaria*, *Chiasmia clathrata*, *Eilicrinia cordiaria*, *Ennomos quercarius*, *Heliomata glarearia*, *Peribatodes rhomboidarius* and *P. umbrarius* are taxonomically well known species that are widespread in Türkiye from Europe, Caucasus and Middle East to Central Asia [11], [24-26].

Seven [8] recorded the species *Odontognophos zacharius*, *Gnophos pseudosnelleni* and *Crocallis elinguaria* from Dağlıca. Thus, the number of Ennominae species in Dağlıca increased to 31.

4. Discussion

Ennominae are both rich in species diversity and difficult to distinguish by external morphological features, such as wing patterns and coloration. This has at times led to misdiagnosis. External morphological characters and even the structure of the genital organs that enable gene exchange have not been sufficient to distinguish some taxa (as in *Nychiodes* spp). This has led to the division into numerous subgenera in systematic and taxonomic studies, especially in the genera *Charissa*, *Gnophos* and *Gnopharmia*.

The genus *Charissa* is currently represented by 53 species from Palaearctic and Orientalic regions [16]. In the fauna of Türkiye, a total of 29 species are known from the following taxonomic groups, *Cnestrognophos*, Wehrli, 1951; *Euchrognophos*, Wehrli, 1951; *Kemtrognophos* Wehrli, 1951; *Neognophina* Wehrli, 1946; *Organognophos* Wehrli, 1951; *Rhopalognophos* Wehrli, 1951 and 7 subgenus including the nominant subgenus *Charissa* Curtis, 1826 [11]. *Charissa annubilata*, *C. dubitaria*, *C. onustaria* and *C. subtaurica* species were identified from the area. The first two

species are distributed in Türkiye and its eastern neighbors [28], but are not known from the European fauna [11], [24-26]. The male genitalia of the *subtaurica* from Dağlıca differ from those of Anamur [29] and Müller et al., [16]. For example, the chitinous structure on the costal margin of the valve is relatively thick, the saccus is round, the ampulla is inclined outward, the aedeagus spine is relatively wide at the base, and the juxta reaches the tip of the uncus (Figure 4. 8: a-b). In the specimen of this species from Diyarbakır (Hazro) [5], the juxta does not reach to the tip of the uncus. Whether these differences are within the limits of variation can only be resolved by future molecular research. *Charissa subtaurica* is distributed in Greece only on the island of Samos, Cyprus and along the Eastern Mediterranean coast [16]. In Türkiye, apart from the Mediterranean region, it is recorded as suspected in Amasya, Bursa, Siirt and Van, and is also known from Diyarbakır and Konya [11, 24]. In a study on the *Gnophini* tribus in Türkiye, it is based on molecular results that *Charissa dubitaria staudingeri,* formerly considered a subspecies, is a taxon at the species level and sister to *C. assoi* and *C. corsica* [30]. As a matter of fact, *C. staudingeri* was later presented at species level in Volume 6 of European Geometrids, and its distribution in the coastal Aegean region of Türkiye was mapped [16]. *Charissa subtaurica* and *C. staudingeri* are difficult to distinguish in terms of appearance. However, male and female genital structures can be easily distinguished [16]. The *subtaurica* examined in the Dağlıca study differs easily from the closest species *staudingeri* in terms of genital structure (Figure 5. 3). Another important species in Dağlıca fauna is *Charissa dubitaria* (Staudinger, 1892). The distribution of this species suggests that there are intermittent records from İçel (Anamur) in the Mediterranean region and from the East and Southeast of Türkiye [11]. Most recently, there have been records from Batman, Elazığ and Diyarbakır [25-26], [31]. This species while there is no European record yet [16] it is known to be distributed in the Caucasus, Lebanon, Armenia and Iran [11, 24], [25-26]. Two male and one female specimens of this species were previously examined from Van (Cesa coll.: GP2407♂, GP2418♂, GP2926♀). The genital characters of the specimens are shorter in the male than in the aedeagus spines *staudingeri* species, while in the female the ductus bursae is relatively long and the corpus bursae is rounded, prominently concave on one side, 1/3 membranous towards the free end. These characters are similar to those of a female from Dağlıca (Figure 5. 4).

Charissa annubilata (Christoph, 1885) is included in the Türkiye checklist under the subgenus *Euchrognophos* Wehrli, 1951. However, Müller et al. [16] transferred it to the subgenus *Cnestrognophos* Wehrli, 1951. While this species is rare in Türkiye, it is also a poorly known taxon in neighboring Azarbeijan, Georgia and Iran [11], [27]. *Charissa onustaria* (Herrich-Schäffer, [1852]) is a well-known species distributed from Europe to Iran and Iraq [11], [16]. It is better represented in the area than the other three species. The genitalia of two male individuals of this species were examined, but some significant differences were detected in the genital structures. The genitalia of the first male (GP22♂), collected in the same habitat and on the same dates are very close to those of Seven [32] and Müller et al. [16]. The other specimen (GP56♂) differs in that the uncus and gnathos are wider and shorter, and the length and width of the thumb-shaped juxta are similar to the saccus (Figure 4. 9: a-b). Whether these differences are variation or a separate taxon will be clarified by future molecular studies.

The genus *Gnopharmia* Staudinger,1892 is represented by 7 species in Türkiye, Middle East, Caucasus, Iran and Iraq [11], [12], [33], distributed outside Europe and a member of the Irano-Turanian Geography. Recorded in Türkiye with *colchidaria*, *irakensis* and *rubraria* species [11], [32], [34-35]. The first two species are distributed in eastern and southeastern Türkiye and are little known. *G. rubraria* is more common in Western, Central and Southeastern Anatolia. Numerous specimens of *G. colchidaria* and *irakensis* species were examined from the study area (Table 1). Among the materials examined, some differences in the male genitalia of the specimens belonging to *colchidaria* are noteworthy. Namely, the proximal projection of sacclus being relatively thick, but a pair of sternite extensions looks like nominate subspecies *colchidaria* [33]. The female genitalia is to some degree similar to the subspecies *colchidaria colchidaria* (Figure 4. 3: a-b-c) [33]. However, the lateral arms of lamellae postvaginalis structure, antrum, ductus bursae and cingum are different to some degree (Figure 5. 2: a-b).

Perhaps these differences are reported by Rajaei et al. [33] photograph may be due to the fact that it is not very clean and unclear.

One of the lesser known species in this genus in Türkiye is *irakensis*. Rajaei et al. [33] also included Köprüköy [Kırıkkale], Kahramanmaraş from Türkiye and Afghanistan from the Middle East countries in its distribution area. According to Koçak and Kemal [11], it is distributed in Türkiye, Iran, Iraq and Pakistan. The above information was confirmed once again in the latest European Geometrid study [16]. This species, described from Erbil in northern Iraq, is very different from the Dağlıca specimen in terms of external morphological characters. The external morphology and structures of the male genitalia of the syntype specimen of this taxon are presented in Rajaei et al. [33]. The genitalia of 5 males and 3 females of this taxon from Dağlıca were examined. These specimens were previously identified as *irakensis*, but differ from the syntype in the structures described below. They also have some differences among themselves. In the Dağlıca *G. irakensis* specimens, the upperside of the wing is darker, the distal spots of the forewing and hindwing are more prominent on the underside than on the upperside. The postdistal line, bordering the broad brown submarginal band on the upperside, is composed of orange spots and continues intermittently to the hindwing. Forewing apical patch is quadrangular and light yellowish cream in color. The thick submarginal band on the underside is dark brown and slightly concave medially on the hindwing (Figure 2.a-b). In male genitalia of GP6♂, GP7♂ and GP11♂ specimens, gnathos and uncus structure, distal and proximal projection of sacculus (except GP34♂), valva, slightly arcuate aedeagus (with GP34, except GP7♂) and abdominal 8th sternite (except GP34♂) are almost the same structure. Differences: GP7♂ has a distinctly outwardly membranous structure up to halfway up the valva. Juxta base is rounded (straight on GP11♂ and GP7♂), aedeagus is almost straight, slightly curved at the tip. Sacculus is similar to that of the syntype [33], in the other specimens (GP11♂, GP6♂ and GP34♂) the sacculus is wider on both wings and distinctly square. The sternite projections of the GP34♂ specimen are thicker and relatively short. Also, the distal and proximal projection of sacculus is relatively thick (Figure 4. 2: a-b-c). In females, the apophyses anterior and apophyses posterior are thin and relatively long in GP74♀ and thick and relatively short in GP53♀ and GP54♀. Lamaella post vaginalis, antrum and ductus bursae are similar in GP53♀ and GP54♀, but different in GP74♀. The signums on all three female genitalia are oval and star-shaped. However, the spines in the center of the signum are separate in GP74♀, relatively separate in GP53♀ and not separate in GP54♀. Furthermore, the signum is relatively rounded in GP74♀ and the lateral spines are longer (Figure 5. 1: a-b). The above-mentioned structural features suggest that *irakensis*-like taxa in Türkiye should be revisited.

Neognopharmia cataleucaria (Staudinger, 1901), whose type locality is Mardin, was originally proposed as a subspecies in the original study as *Gnophos stevenaria* var. *cataleucaria* Staudinger, 1901, and later elevated to species level. The genus is represented by 3 species including *stevenaria* (Boisduval, 1840), *cataleucaria* (Staudinger, 1901) and *horhammeri* (Brandt, 1941) [16], [36]. In the Türkiye checklist, *stevenaria* is distributed in Europe, Caucasus, Türkiye, Iran and Iraq, while *cataleucaria* is an endemic species found only in Türkiye [11]. *Neognopharmia horhammeri* (Brandt, 1941) is known only from Iran according to current records [14], [27].

The genus *Rhoptria* Guenée, [1858] is represented worldwide by the species *Rhoptria asperaria* (Hübner, [1817]), *R. dolosaria* (Herrich-Schäffer, [1848]), *R. mardinata* (Staudinger, 1900) and *R. erebata* (W. Warren, 1897). The first two species are distributed in some European countries including Türkiye, while *mardinata* was described in Mardin and is only known from Türkiye and Iran. In this study, it is presented for the first time with male genital photographs (Figure 4. 4: a-b). In the 123 years since it was described, the research shows that the species has remained as a taxon in the endemic to Irano-Turanian geographic region. The *R. erabata* is known from Brazil in the Neotropical region [10-11]. Only *asperaria* and *dolosaria* are listed in the European Geometrids of the 6th volume [16].

The genus *Crocallis* Treitschke, 1825 is represented by 19 species in the Palearctic region [16], [36]. In Türkiye, the number of species increased to 8 with the study of Stadie & Fiebig [37], as it is on the Koçak & Kemal [11] checklist. According to Skou & Sihvonen [36],

transcaucasica Wehrli, 1940 is a subspecies of *tusciaria* that distribution in Türkiye and the Caucasus. However, it is presented at the species level in recent studies [11], [16], [27]. Thus, the fauna of Türkiye today includes *elinguaria* (Linnaeus,1758), *tusciaria* (Borkhausen,1793), *inexpectata* Warnecke,1940; *elingomorpha* Stadie & Fiebig, 2014; *loebeli* Stadie & Fiebig, 2014 (type locality: Sivas, Gürün), *rothei* Stadie & Fiebig, 2014 (type locality: Hakkari, Merkez [Durankaya]) and *sylvana* Fiebig, 2014 (type locality: Tunceli, Ovacık). The last three species seem to be endemic species distributed only in Türkiye for now. Specimens of *tusciaria* (GP47♂) and *loebeli* (GP19♂) were examined from Dağlıca. *Crocallis loebeli* (Figure 4. 6: a-b) (GP436♂) external morphology has some differences. Fore and hind wing ground color is pale yellow, antemedian and postmedian fascia is very faint, difficult to determine (Figure 2. g-h). Anterior wing discal spot is very small, very weak. This species has been recorded from 10 provinces in Türkiye [11], [37]. In this study, even if we evaluate it in the category of lesser-known species whose distribution is limited only to Türkiye, it is likely to be found in countries neighboring Türkiye in the future. According to the available data *Crocallis tusciaria* (Borkhausen, 1793), distribution intermittently in Western Anatolia, Mediterranean region and Central Anatolia [11]. The data in the thesis study has been added to the Eastern Anatolia fauna [11, 24], [25-26]. Examined material wing color and patterns, genital structures also have some differences in Skou & Sihvonen [36]. Uncus tapers abruptly in the 2/3 part. Annelus is short, projecting laterally at the base. Clasper process is closer to the tip, large and perpendicular to the clasper. Annelus short, protruding laterally at base (Figure 4.5: a-b). This is also observed in Siirt populations [32].

Eilicrinia Hübner,[1823] is known in the palearctic region with the species *cordiaria* (Türkiye, Iran, Iraq, Eastern Europe and Caucasus region), *subcordiaria* (Türkiye: only Van and Igdir; Caucasus region and central Asia) and *trinotata* (Türkiye, Eastern Europe, Caucasus region) [11, 36]. Two specimens (GP41♂ and GP423♂) of *cordiaria* (Hübner, 1790) from Dağlıca were examined. In both male specimens, unlike Skou and Sihvonen [36], the uncus is long pointed, and the base of the furca connected to the juxta is prominently lobed on both sides. A pair of furca arms are long and thin and the right side is slightly long. Valva is wider, costa and the anal margin is slightly convex. The aedeagus vesica teeth are small and sparse (Figure 4.7: a-b).

Ennomos Treitschke,1825, according to the by Koçak and Kemal [10], is represented by 12 species in the palaearctic region. However, 9 species are listed in the 6th volume of European Geometrids [16]. *E. fuscantaria ssp. efractaria* Freyer, [1842] from the European part of Russia; *E. quercaria ssp. freidbergi* Hausmann, 1997 is presented as subspecies from the eastern Mediterranean region. On the other hand *zandi* Wiltshire 1947, listed in Koçak & Kemal [10] from Iran, but not included in the *Ennominae* checklist [16]. This may be due to the hesitant definition of the genre as "... may be an aberration or a race ..." [38]. But this species has been listed in the last Iranian Lepidoptera catalog [27].

In Türkiye, the genus *Ennomos* is represented by a total of 5 species together with the following two species [11], *Ennomos fraxineti* Wiltshire, 1947 and *Ennomos quercarius* (Hübner, [1813]). The first species is distributed in Türkiye, Iran and Iraq. It is probably endemic to the Irano-Turanian geographic region. It is little known species in Türkiye [11]. Distribution of the species in Müller et al. [16] is limited to Southern Turkmenistan and Iran. However, the examined material and previous records strongly support the distribution of the species in Türkiye. The second species, *E. quercaria*, is well known and occurs in the Palearctic region.

Dicrognophos Wehrli, 1951 is transferred from *Gnophini* to *Abraxini* + *Cassymini* + *Eutoeini* group, tentatively in *Cassymini* [16]. The species *amanensis* (endemic for Türkiye), *sartatus*, *anophaeus*, *choristus*, *orthogonius* and *pseudosnelleni*, as well as the newly described species *siciliana* (from Italy, Sicily), were revised under this genus. However, *choristus* and *pseudosnelleni* differ significantly from the other species in terms of their genital structures [32]. The species presented in the thesis with the name combination *Gnophos (Dicrognophos) gorgatus* Brandt,1938 was added to the fauna of Hakkari (Figure 4. 1: a-b). *Gnophos* (*Dicrognophos*) *sartatus* Treitschke, 1827 is well known in Eastern Europe, Caucasus, Middle East and Türkiye, and Müller et al. [16] and Rajaei et al. [27] listed this species in the genus *Dicrognophos*.

The previously valid genera *Synopsia* Hübner, 1825 and *Synopsidia* Djakonov, 1935 were represented by one species each in the palearctic region [11], [16]. Wanke et al. [22], based on morphological characters, molecular data and distribution records, *Synopsidia* Djakonov, 1935 is downgraded to synonym with *Synopsia* Hübner, 1825. Accordingly, *Synopsidia phasidaria* (Rogenhofer, 1873) was transferred to the genus *Synopsia* as *Synopsia phasidaria* (Rogenhofer, 1873). Thus, in the fauna of Türkiye, the genus *Synopsia* is represented by *sociaria* and *phasidaria* species. The first species is distributed in Europe, including Türkiye, the Caucasus, the Urals and Central Asia (Kazakhstan, Uyghur Province) and Iran [11], [22], while *phasidaria* is distributed in eastern Türkiye (Ağrı, Bitlis, Hakkari, Van, Şırnak), the Caucasus, Afghanistan, Azerbaijan, Iran and Turkmenistan. The s*ubsp*. *centralis* Wiltshire, 1966, formerly described as a subspecies of *Synopsidia phasidaria*, was elevated to species level and the name combination was changed to *Synopsia centralis* (Wiltshire, 1966) [22]. This species is only known from Iran [22], [27].

In thesis study, a male of this species, listed as *Synopsidia phasidaria*, was examined. The genital structure of the specimen is generally consistent with Wanke et al., [22] (the Türkiye population was excluded from the genetic analysis). However, the free end of the harp is rounded and the spiny process dorsal to the apex of the valva is distinctly lobed (stand out budge). These characters may not change the results of the aforementioned study. However, the need for extensive genetic research on Türkiye populations remains important. In this context, we tentatively accept the Dağlıca sample in the combination presented by Wanke et al., [22] and transferred the taxon *phasidaira* (Rogenhofer, 1873) to the genus *Synopsia* Hübner, 1925.

The genus *Wehrliola* is represented by a single species in the subfamily Ennominae. While *Revocaria* Staudinger, 1892, described from Lebanon, is known from Mersin, Konya and Kahramanmaraş Provinces in Türkiye [11], the second species of the genus was revealed by examining the specimens collected from Dağlıca. With the external morphological features and genital structure characters of the taxon, it was easily be distinguished from *recorvaria* and defined as *Wehrliola inexpectata* Kemal & Uçak, 2018 and took its place in the scientific world [39]. In Volume 6, Part 1 of the Geometrids of Europe, the genus *Wehrliola* is temporarily placed in the *Gnophini* tribus, while its classification in the higher categories remains uncertain [16].

The genus *Apochima*, founded by Agassiz in 1847, is known in the Western Palearctic region with the species *flabellaria* (Heeger,1838) and *diaphanaria* (Püngeler, 1904) [13]. There are faunistic records of these two species in Türkiye [11]. When the individuals belonging to the *diaphanaria* species among the Dağlıca materials were examined morphologically, it was revealed that they had different structural characters at the genus level from *flabellaria*. This was also supported by molecular research, and a new genus *Bellachima*, the type species of which is *diaphanaria*, was defined [13]. In the study of Europe Ennominae, the molecular analysis was based only on the mtCOI gene and was not compared with the subspecies *A. diaphora rjabovi* and the genus *Chondrosoma* (this genus is represented only by *fiducaria*, with wingless females, and is morphologically very different) [16, 40], suggesting that they are not considered as separate genera [16]. However, the morphological characters of *Bellachima diaphanaria* (Püngeler, 1904) from the genus *Apochima* have been detailed, and the genetic distance between the two species has been determined to be at the level of a separate lineage in the genus category, well above a species distinction [13]. According to available data, the species is distributed in Türkiye, Iran, Armenia and Turkmenistan [11, 16, 41]. However, the specimen in the Turkmenistan record differs from the Dağlıca specimen with features such as clasper in the genital structure, aedeagus spine and short caecum [41]. Based on these characters, it would be appropriate to evaluate the species in another study covering the distribution areas of the species.

The genera *Nychiodes* and *Peribatodes* are included in the tribus *Boarmini* Duponchel, 1845 according to the latest systematic arrangements [16]. *Nychiodes* Lederer, 1853 is represented by 8 species in the fauna of Türkiye [11]. In recent years, the non-European species of the genus *Nychiodes* have been revised [22]. Accordingly, the previously listed species of *amygdalaria, divergaria, rayatica, waltheri* and with the newly described *eberti* Wanke,

Hausmann and Rajaei, 2020 (type locality Erzurum, Kopdağı Pass) increased to 5 species in Türkiye. Based on genetic data in the study, variabila became synonymous with *divergaria*. Thus, the specimen from Dağlıca, which was previously diagnosed as *variabila*, is presented in this study with the combination *Nychiodes divergaria* (Staudinger, 1892). The *rhomboidarius* and *umbrarius* species belonging to the genus *Peribatodes* were also identified from the research area. Research on these species is also in progress.

Ennominae taxa are highly variable in terms of external morphological characters and show high variation. This situation becomes more complicated especially for the species represented in genera such as *Charissa*, *Gnophos*, *Gnopharmia* and. The fauna of the Irano-Turanian Geographical Region, which is still at the beginning of research, is in need of comprehensive research. Even if the differences in genital structure, which provide gene transfer in morphological studies, are helpful to some extent, they are not sufficient to solve the problem. The data obtained by molecular methods and genetic differences at the species and subspecies level contribute to the solution of the problem in taxonomic and phylogenetic studies. In this study, genetic research is needed to clarify the taxonomic status of some species.

Tentative checklist of Dağlıca Ennominae Species

Tribus **Abraxini** Warren, 1893
1) *Odontognophos zacharius* (Staudinger, 1879)

Tribus **Cassymini** Holloway, 1994
2) *Dicrognophos sartatus* Treitschke, 1827 (sensu Müller et al., [16])
3) *Dicrognophos pseudosnelleni* Rjabov, 1964 (sensu Müller et al., [16])
4) *Dicrognophos gorgatus* Brandt, 1938 (sensu Rajaei et al., [27])

Tribus **Macariini** Guenée, 1858
5) *Heliomata glarearia* (Brahm, 1791)
6) *Neognopharmia cataleucaria* (Staudinger, 1901)
7) *Gnopharmia irakensis* Wehrli, 1938
8) *Gnopharmia colchidaria* (Lederer, 1870)
9) *Chiasmia clathrata* (Linnaeus, 1758)
10) *Rhoptria mardinata* (Staudinger, 1900)

Epionini of uncertain association (sensu Müller et al., [16])
11) *Pseudopanthera syriacata* (Guenée, 1858)
12) *Eilicrinia cordiaria* (Hübner, 1790)

Tribus **Ennomini** Duponchel, 1845
13) *Ennomos (Deuteronomos) quercarius* (Hübner, [1813])
14) *Ennomos (Deuteronomos) fraxineti* Wiltshire, 1947
15) *Crocallis (s.str.) tusciaria* (Borkhausen, 1793)
16) *Crocallis elinguaria* (Linnaeus, 1758)
17) *Crocallis (s.str.) loebeli* Stadie & Fiebig, 2014

Tribus **Prosopolophini** Warren, 1894
18) *Bellachima diaphanaria* (Püngeler, 1904)
19) *Dasycorsa modesta* (Staudinger, 1879
20) *Eumera hoeferi* Wehrli, 1934 (sensu Wanke et al., [22])

Tribus **Theriini** Herbulot, 1963
21) *Ramitia kufrana* Seven, 2015

Tribus **Gnophini** Duponchel, 1845
22) *Charissa (Euchrognophos) dubitaria* (Staudinger, 1892)
23) *Charissa (Euchrognophos) annubilata* (Christoph, 1885)
24) *Charissa (Euchrognophos) subtaurica* (Wehrli, 1934)
25) *Charissa (Kemtrognophos) onustaria* (Herrich-Schäffer, [1852])
26) *Synopsia phasidaria* (Rogenhofer, 1873)
27) *Dyscia (Calodyscia) innocentaria* (Christoph, 1885)

Gnophini of uncertain association (sensu Müller et al., [16])
28) *Wehrliola inexpectata* Kemal & Uçak, 201

Tribus **Boarmiini** Duponchel, 1845
29) *Nychiodes (Eunychiodes) divergaria* (Staudinger, 1892)
30) *Peribatodes rhomboidarius* ([Denis & Schiffermüller], 1775)
31) *Peribatodes umbrarius* (Hübner, [1809]

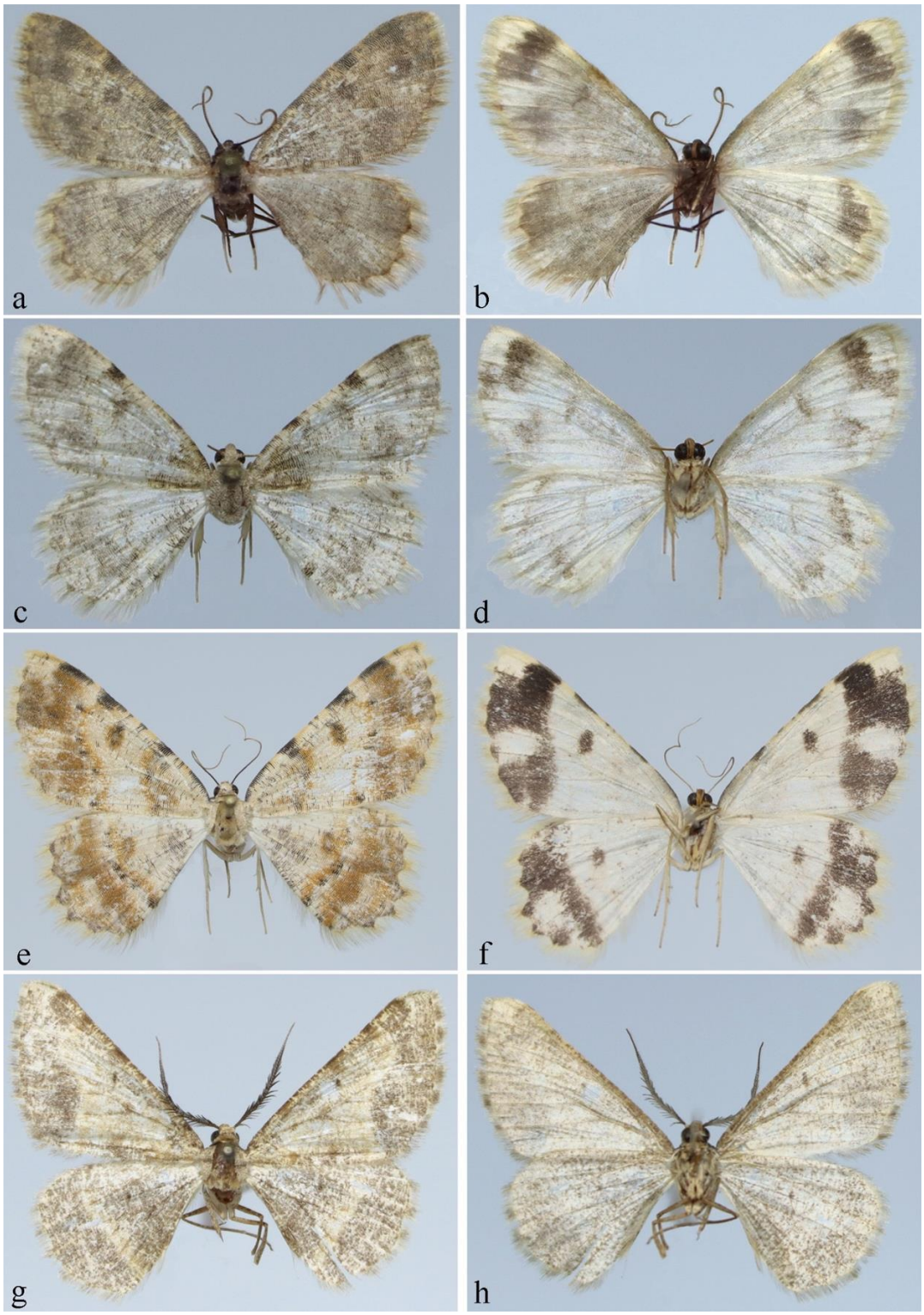

Figure 1. a-b. *Charissa annubilata* **a.** upperside **b.** underside. **c-d**. *Charissa subtaurica* **c.** upperside **d.** underside. **e-f**. *Charissa dubitaria* **e.** upperside **f.** underside. **g-h**. *Gnopharmia colchidaria* **g.** upperside **h.** underside.

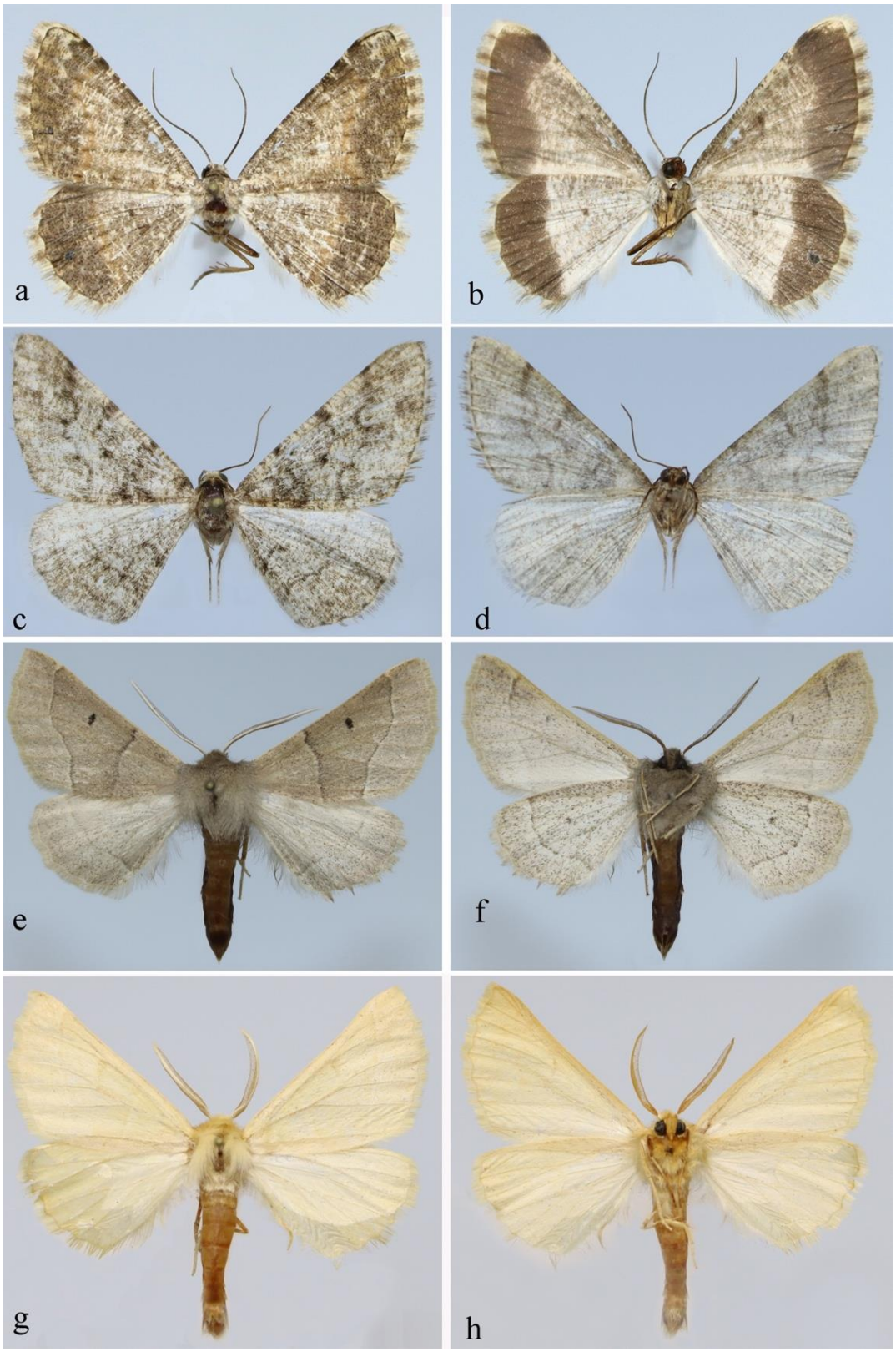

Figure 2. a-b. *Gnopharmia irakensis* **a.** upperside **b.** underside. **c-d**. *Rhoptria mardinata* **c.** upperside **d.** underside. **e-f.** *Crocallis tusciaria* **e.** upperside **f.** underside. **g-h**. *Crocallis loebeli*. **h.** upperside. **g.** underside

Figure 3. a-b. *Eilicrinia cordiaria* **a.** upperside. **b.** underside

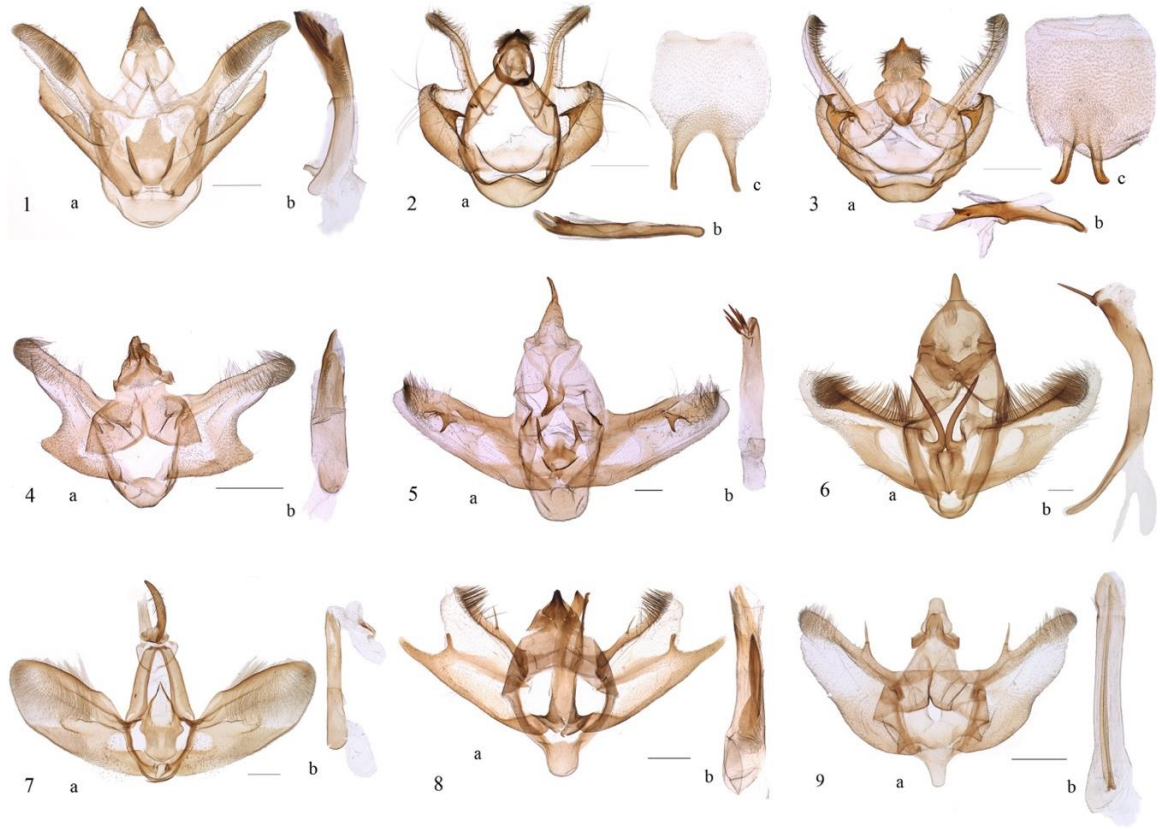

Figure 4. Genitalia Structures. **1.** *Gnophos gorgatus*. **a.** Male genitalia (17GP♂). **b.** Aedeagus. **2.** *Gnopharmia irakensis* (GP34♂). **a.** Male genitalia. **b.** Aedeagus. **c.** Sternite. **3.** *Gnopharmia colchidaria* **a.** Male genitalia (GP9♂). **b.** Aedeagus. **c.** Sternite. **4.** *Rhoptria mardinata* **a.** Male genitalia (GP42♂). **5.** *Crocallis tusciaria*. **a.** Male genitalia (GP47♂). **b.** Aedeagus. **6.** *Crocallis loebeli*, **a.** Male genitalia (GP436♂). **b.** Aedeagus. **7.** *Eilicrinia cordiaria*, **a.** Male genitalia (GP423♂). **b.** Aedeagus. **8.** *Charissa subtaurica.* **a.** Male genitalia (GP27♂). **b.** Aedeagus. **9.** *Charissa onustaria*, **a.** Male genitalia (GP56♂). **b.** Aedeagus. (Scale bar: 1mm).

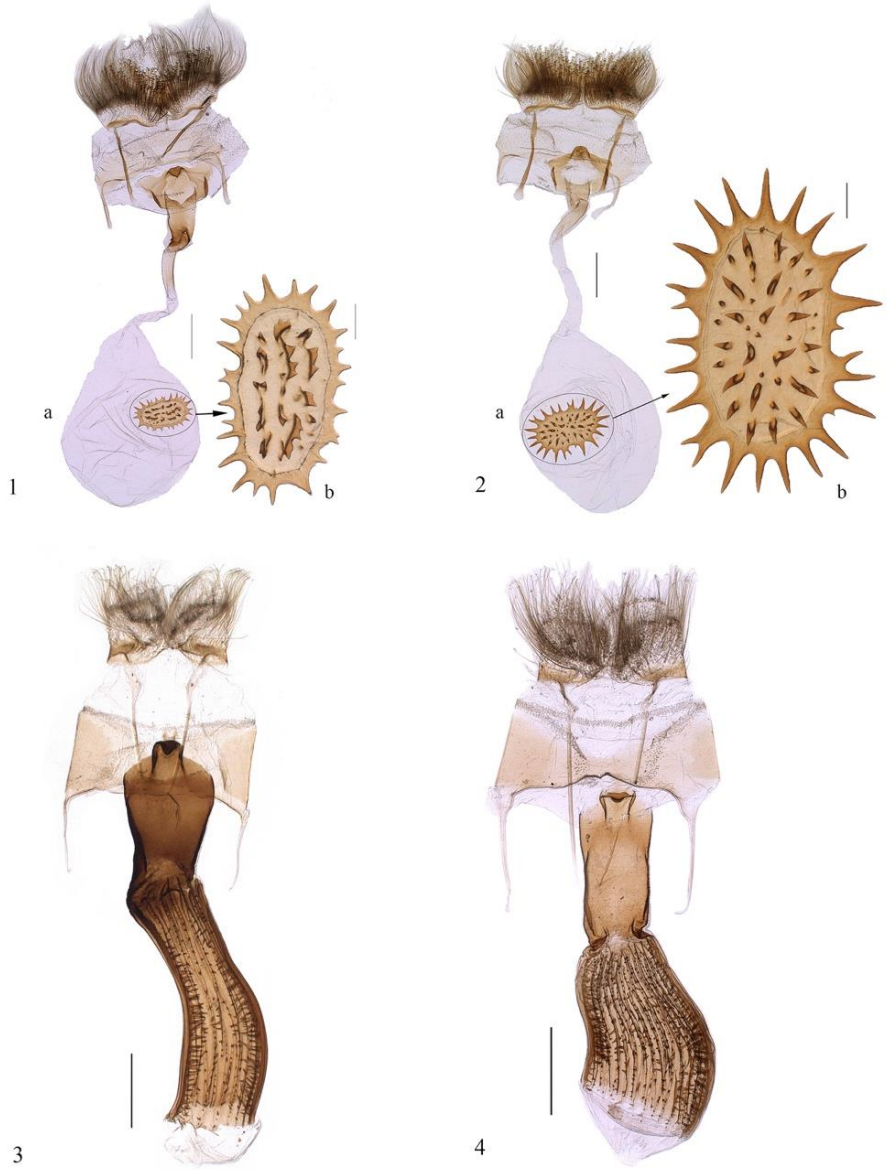

Figure 5. Genital Structures. **1.** *Gnopharmia irakensis*, **a.** Female genitalia (GP54♀). **b.** Signum **2.** *Gnopharmia colchidaria*, **a.** Female genitalia (GP33♀). **b.** Signum (Scale bar: 0.5mm). **3.** *Charissa subtaurica*, Female genitalia GP26♀). **4.** *Charissa dubitaria* Female genitalia (GP48♀). (Female genitalia: Scale bar: 1mm, Signum: Scale bar: 0.5mm).

Acknowledgment

We always feel Prof. Dr. Koçak's guidance and support through his knowledge and experience engrained onto us. We remember him with respect and longing, and would like to express our deepest gratitudes.

* This article is a part of the study, which was accepted as a master's thesis at Van Yüzüncü Yıl University, Institute of Science in 2019 with the same title.

Author's Contributions

All authors contributed equally to the study.

Statement of Conflicts of Interest

No potential conflict of interest was reported by the authors.

References

[1] A. Ö., Koçak, "New Lepidoptera from Turkey-I." *Atalanta* vol.6 pp.24-30, 1975.

[2] A. Ö., Koçak, "New Lepidoptera from Turkey V." *Atalanta* vol.7, no.2, 1pp. 26-147, 1977.

[3] A. Ö., Koçak, "Studies on the family Lycaenidae (Lep.) I. New taxa and records from East Turkey." *Atalanta* vol. 8, no.1, pp. 41-62, 1977.

[4] E., Görgner, "Beiträge zur Kenntnis der Lepidopteren der südosttürkischen Provinz Hakkari" *Nachr. Ent. Ver Apollo,* vol.4 pp.77-94, 1985.

[5] M. Kemal and A. Ö., Koçak, "Preliminary list of the Pterygota of Varegöz-Yeşiltaş area (Yüksekova, Hakkari Province, SE Turkey)", *Cesa News*, pp. 1-26, 2015.

[6] M. Kemal, A. Ö., Koçak, and H. Uçak, "On a collection of Lepidoptera from Dağlıca (South-East Turkey, Hakkari Province)", *Cesa News*, pp. 1-24, 2017.

[7] M. Kemal and A. Ö., Koçak, and H. Uçak, "List of the Lepidoptera species of Dağlıca (Hakkari Province, SE Turkey)", *Cesa News*, pp. 1-21, 2018.

[8] E. Seven, "Contributions to the knowledge autumnal Lepidoptera of Dağlıca (Hakkari) with two poorly known noctuid species", *Eur J For Sci*, vol. 6, no. 4, pp. 48-57, 2018.

[9] A. İ., Gökçen, *Buzul ve İkiyaka Dağları 422-425 (Cilt II). Türkiye'nin Önemli Doğa Alanları*. Doğa Derneği, Ankara. 2006.

[10] A. Ö., Koçak and M. Kemal, "Annotated list of the Lepidoptera of Hakkari Province (SE Turkey).", *Cesa News* 116, pp. 1-146, 2015.

[11] A. Ö., Koçak and M. Kemal, "A synonymous and distributional list of the species of the Lepidoptera of Turkey", *Memoirs* 8, pp. 1-487, 2018.

[12] H., Rajaei, A., Hausmann, M., Scoble, D., Wanke, P., Plotkin, G., Brehm, L., Murillo-Ramos and P., Sihvonen, "An online taxonomic facility of Geometridae (Lepidoptera), with an overview of global species richness and systematics" *Stuttgart Contributions to Natural History.*vol. 5, no. 2, pp. 145-192, 2022.

[13] M. Kemal, I. Yildiz, S. Kızıldağ, H. Uçak, and A. Ö., Koçak, "Taxonomical and molecular evaluation of Apochima Agassiz in East Turkey, with a description of a new genus (Lepidoptera, Geometridae, Ennominae)," *Misc. Pap.*, pp. 1–13, 2018.

[14] E., Seven, "Ramitia kufrana sp. n., A New Species from Turkey (Lepidoptera: Geometridae)". *Journal of the Kansas Entomological Society* vol. 88, no.4, pp. 430-433, 2015.

[15] E. Seven, "Notes on some species of gnophini (ennominae, geometridae, lepidoptera) from Turkey, with new records", *Journal of the Entomological Research Society*, vol, 20, pp. 53-58, 2018.

[16] B. Müller, S. Erlacher, A. Hausmann, H. Rajaei, P. Sihvonen and P. Skou, "Ennominae II: (Boarmiini, Gnophini, additions to previous volumes)", in *Ennominae II*, Brill, 2019.

[17] E. Seven, "A new record and three little-known Eupithecia Curtis species from Turkey (Lepidoptera: Geometridae)", *Turk J Zool.*, vol. 41, pp. 583-586, 2017.

[18] E. Seven, V. Mironov and K. Akin, "A new species of Eupithecia Curtis (Lepidoptera: Geometridae, Larentiinae) from Turkey", *Zootaxa*, vol. 4668, pp. 443-447, 2019.

[19] E. Seven, A. Hausmann, and A. Aykal, "Redescription of the little-known geometrid moth *Perigune jordanaria* (Staudinger, 1901), with description of a new subspecies (Lepidoptera: Geometridae)", *Zoology in the Middle East*., vol. 67, no. 1, pp. 65-72, 2021.

[20] E. Seven, "A New Genus and Species Record of Geometrid Moth (Lepidoptera) from Turkey", *Journal of the Entomological Research Society,* vol. 23, pp. 153-156, 2021.

[21] G.S., Robinson, "The Preparation of slides of Lepidoptera genitalia with special reference to the Microlepidoptera." *Entomologist's Gazette*, vol. 27, 127-132, 1976.

[22] D. Wanke, A. Shirvani, A. Hausmann, L. Murillo-Ramos, and P. Sihvonen, "Tribal assignment of the genus Eumera Staudinger, 1892, using multi-gene analysis, with description of a new species from Iran (Lepidoptera: Geometridae: Ennominae)," *Zootaxa*, vol. 5270, no. 1, pp. 92-104, 2023.

[23] D. Wanke, A. Hausmann, L. Krogmann, G. Petrányi, and H. Rajaei, "Taxonomic revision of the genus Nychiodes Lederer, 1853 (Geometridae: Ennominae: Boarmiini) with description of three new species-an integrative approach," *Zootaxa*, vol. 4812, no. 1, 2020.

[24] A. Ö., Koçak and M. Kemal, "First updated geographical codes used in the publications of the Cesa". *Priamus* vol. 17, no. 4, pp. 319-360, 2019.

[25] E. Seven, "First Comprehensive Faunistic List On The Lepıdoptera Species of Batman Province (Southeastern Turkey)", *Munis Entomology & Zoology*, vol. 14, no. 2, pp. 439-447, 2019.

[26] E. Seven, "New Records of Geometrid Moths (Lepıdoptera: Geometridae) From Southeast of Turkey," *Art. sy*, vol. 1, 2020.

[27] H. Rajaei, L. Aarvik, W. Arnscheid, G. Baldizzone, and B. Daniel, "Catalogue of the Lepidoptera of Iran," *Integrative Systematics*, vol. 6, no. 7, pp. 121-459, 2023.

[28] M.A., Rjabov and S.A., Vardikyan, "Kavkazkie vidy roda Gnophos Tr. Akad nauk rmjanskoj SSR," Zool. Inst., Zool. sbornik, vol. 13, pp.105-147, 1964.

[29] M. Kemal and A. Ö., Koçak, "Annotated list of the moth fauna of Anamur district (İçel Prov., South Turkey), with descriptions of new species (Lepidoptera).", *Miscellaneous Papers*, vol. 167, pp. 1-45, 2018.

[30] M., Kemal, S., Kızıldağ and A. Ö. Koçak, "Some molecular phylogenetic and taxonomical remarks on the Gnophini of Turkey, with faunistical notes (Lepidoptera, Geometridae, Ennominae)." *Misc. Pap*. vol 172, pp 1-15, 2018.

[31] E. Seven and A. Çakır, "A faunistic study on the geometrid moths (Lepidoptera) of Maden (Elâzığ) district"," *Eurasian Journal of Forest Science*, vol. 7, no. 3, pp. 225-236, 2019.

[32] E. Seven, *Eco-faunistic studies on the Macroheterocera species in Şirvan district of Siirt (Lepidoptera). PhD*. Van, Turkey, 2014.

[33] H. Rajaei, D. Stüning, and R. Trusch, "Taxonomic revision and zoogeographical patterns of the species of Gnopharmia Staudinger, 1892 (Geometridae, Ennominae)," *Zootaxa*, vol. 3360, pp. 1-52, 2012.

[34] M. Kemal and A. Ö., Koçak, "On the moths of Mutki district (Bitlis Province, East Turkey (Lepidoptera)," *Cesa News*, vol. 150, pp. 2-46, 2017.

[35] M. Kemal and A. Ö., Koçak, "On the vernal Lepidoptera fauna of Nizip-Birecik districts-Euphrates region in South Turkey," *Cesa News*, vol. 137, pp. 1-20, 2017.

[36] P. Sihvonen and P. Skou, *Ennominae I*. Brill, 2015.

[37] D. Stadie and R. Fiebig, *Taxonomic notes on the morphology, ecology and distribution of the Crocallis elinguaria (Linnaeus, 1758) species lineage of Asia Minor and the eastern adjacent territories with description of five new species and one new subspecies*. 2014.

[38] E. P. Wiltshire, "Middle East Lepidoptera, VIII. Some more new species and forms from Iran," *Entomologist's rec. j. var*, vol. 59, pp. 125-127, 1947.

[39] M. Kemal and H. Uçak, "Description of a new species of the genus Wehrliola Strand in East Turkey (Lepidoptera, Geometridae)"," *Miscellaneous Papers*, pp. 1-4, 2018.

[40] K. Nupponen and P. Sihvonen, "Dorsispina furcicornaria, a new geometrid species and new genus from Kazakhstan (Lepidoptera: Geometridae: Ennominae)"," *Nota Lepidopterologica, c*, pp. 179-186, 2013.

[41] E. A. Beljaev and S. V. Vasilenko, "New and little known Ennominae from Turkmenistan with the description of two new species (Lepidoptera, Geometridae)," *Atalanta*, vol. 28, no. 3/4, pp. 315-326, 1998.

Bitlis Eren Üniversitesi Fen Bilimleri Dergisi
BİTLİS EREN UNIVERSITY JOURNAL OF SCIENCE
ISSN: 2147-3129/e-ISSN: 2147-3188
VOLUME: 12 NO: 3 PAGE: 911-924 YEAR: 2023
DOI:10.17798/bitlisfen.1336357

Human Energy Expenditure in High-Level Order Picking

Murat BİNİCİ[1,2*], Mehmet Mutlu YENİSEY[2]

[1]*Bitlis Eren University, Faculty of Engineering and Architecture, Bitlis, Türkiye*
[2]*Istanbul University-Cerrahpaşa, Faculty of Engineering, Istanbul, Türkiye*
(ORCID: 0000-0003-1814-438X) (ORCID: 0000-0002-4532-344X)

Keywords: Order Picking, High-Level Warehouse, Human Energy Expenditure, Order Batching and Routing, Tchebychev distance.

Abstract

Order picking is one of the most significant components of the warehouse management. More than 50% of the cost incurred in warehouses is due to the order picking process. Although this process has mostly been considered within the framework of economic objectives, in recent years the ergonomic perspective has become increasingly visible. Order picking studies regarding ergonomic objectives have mostly focused on low-level order picking systems, but the human factor has been ignored in high-level order picking. In order to fill this gap, this study focuses on the order picking process of a single block high-level warehouse with a special focus on human factor. For this purpose, a capacity-constrained mathematical model based on order batching and routing for the minimization of human energy expenditure is proposed. In this three-dimensional (3D) warehouse system, the distances and travel times between locations were first determined using Manhattan distance-based Tchebychev formulas in order to calculate the human energy expenditure between order locations. Then, human energy matrices between order locations were created using human energy calculation formulas based on time and item weight. These matrices, which were created for three different randomly generated sample data sets, were used in the mathematical model solution and the optimum batches and routes were determined. In order to compare the results, First-come First-serve (FCFS) batching and S-shaped routing, which are simple and common batching and routing methods used in practice, were applied for the sample problem data sets and it was observed that the mathematical model gave better results.

1. Introduction

In today's world of intense competition, companies can achieve a solid competitive structure with the successful implementation of supply chain management and one of the most important components of the supply chain is warehouses [1]. More than 50% of the total cost incurred in a warehouse is due to the order picking process [2]. Order picking refers to the process by which orders are collected from warehouse locations and returned to the customer, and this process consists of labor-intensive and costly activities [3].

Various order picking systems are used in warehouses. The most common of these is the picker-to-parts order picking system. In this system, the order picker picks items from the order list by walking or driving an order picking vehicle. Moreover, this system is divided into low-level and high-level order picking. In low-level order picking, the order picker picks the items on the order list from low-level shelves in the warehouse where a person can comfortably reach. In high-level order picking, the order picker picks the items on the order picking list using order picking tools that can reach high shelf levels. In low-level order picking, only horizontal distance is considered, while in high-level order

*Corresponding author: mbinici@beu.edu.tr
Received: 01.08.2023, Accepted: 15.09.2023

picking, horizontal and vertical distance calculations are used together [3]. Low-level warehouses can therefore be referred to as two-dimensional (2D) warehouses, while high-level warehouses can be referred to as three-dimensional (3D) warehouses [4]. The majority of order picking studies have focused on low-level warehouses, but studies on high-level warehouses, which provide efficiency in space utilization in warehouses, have been neglected [5,6].

In the order picking process, four different approaches have been developed to improve efficiency through the minimization of order picking time or travel distance [1]. The first one is to minimize the travel time by using a suitable order picking route. The second is the division of the warehouse into zones. Order pickers are assigned to these zones and only pick orders in their zone. The third approach is storage location assignment, i.e. assigning items to locations on the shelves within the warehouse. The fourth approach is the batching of orders. All of the batched orders are picked at once within their own batch. Among all these methods, the most important approaches are storage location assignment, order batching and routing [1]. Batching has a great impact on reducing the order picking time [2], and it can improve system performance [7]. Routing also has a great impact on optimizing the order picking system [8].

Although the order picking process is generally addressed by considering economic objectives such as time and distance minimization, human factor is also one of the important issues to be studied in this field [9]. The necessity of including the human factor in the order picking process has been emphasized in recent studies [6,10]. Despite of the fact that technological developments related to the automation of warehouse processes have increased in recent years due to Industry 4.0, humans are still at the center of this process [11]. However, the human factor has been ignored in most order picking studies [9]. By including ergonomic objectives related to the human factor in these studies, health risks can be minimized. This can reduce the loss of employees and absenteeism due to illness. In this way, both economic goals can be achieved and a positive contribution to the work-life balance of the employee can be achieved [9].

There are some studies regarding the human factor in order picking. In one of these, a human energy-based storage location assignment policy that minimizes total order picking time and human energy expenditure in a low-level warehouse system were proposed [12]. A heuristic model is proposed to analyze the optimal rack design and storage location assignment policy for a low-level order picking system that takes into account order picking cost, human energy expenditure and worker posture [13]. In another storage location assignment study based on human energy expenditure, a low-level order picking system was considered and a mathematical model was proposed [14]. A simulation study was conducted for a low-level order picking system using hybrid order picker humans and robots, taking into account cost, efficiency and human energy expenditure, in order to determine the optimal storage location assignment policies [15]. In another study where economic and ergonomic objectives were used together, a two-stage methodology was presented to determine the storage location assignment policy in a low-level warehouse [16]. In a low-level order picking study in which a multi-objective linear programming model was proposed for the minimization of the order picking time, human energy expenditure and health risk, different scenarios were considered to determine the storage location assignment policy and optimum shelf locations [17].

Considering the studies in this field, there is no study that deals with the human factor in the batching and routing of high-level order picking. Therefore, in this study, in order to fill a gap in this field, human energy expenditure in high-level order picking is considered and a batching and routing based mathematical model minimizing human energy expenditure is proposed.

In the second part of the study, the warehouse and problem is defined. In the third section, the solution method is stated. While the implementation of the method and the results are given in the fourth section, the last two sections include discussion and conclusions respectively.

2. Warehouse and Problem Definition

The warehouse in this study is single block and high-level (Figure 1). The order picker starts its movement from the input/output (I/O) point. The I/O point is located at the bottom left corner of the warehouse [4, 18]. In total there are 10 rows of shelves from left to right. The first and last shelves are single rows and the other shelves are back to back. The shelves have a depth of 1 meter. Each row of shelves consists of 10 divisions and each division has 5 layers. There are 50 locations in a single row of shelves and the total number of locations in the warehouse is 500. In addition to the front and rear cross aisles, there are five picking aisles in the warehouse. Locations are numbered in sequence from 1 to 500, starting from the first floor of the shelf row on the far left of the warehouse to the fifth floor on the upper right corner

of the shelf row on the far right. For example, the number 5 in Figure 1 refers to locations 1, 2, 3, 4 and 5 starting from the first floor to the 5th floor. The following number 10 refers to locations 6, 7, 8, 9 and 10 from the first floor to the fifth floor respectively. Of these, locations 1 and 6 are located on the first floor, locations 2 and 7 on the second floor, locations 3 and 8 on the third floor, locations 4 and 9 on the fourth floor and locations 5 and 10 on the fifth floor. For all other locations, the last digit of the location number corresponds to the floor number of the first 9 locations. Locations with the last digit ending in 0 indicate that they are on the fifth floor. The I/O point is at floor height and has a height of zero. The lengths of the warehouse are shown in Figure 1.

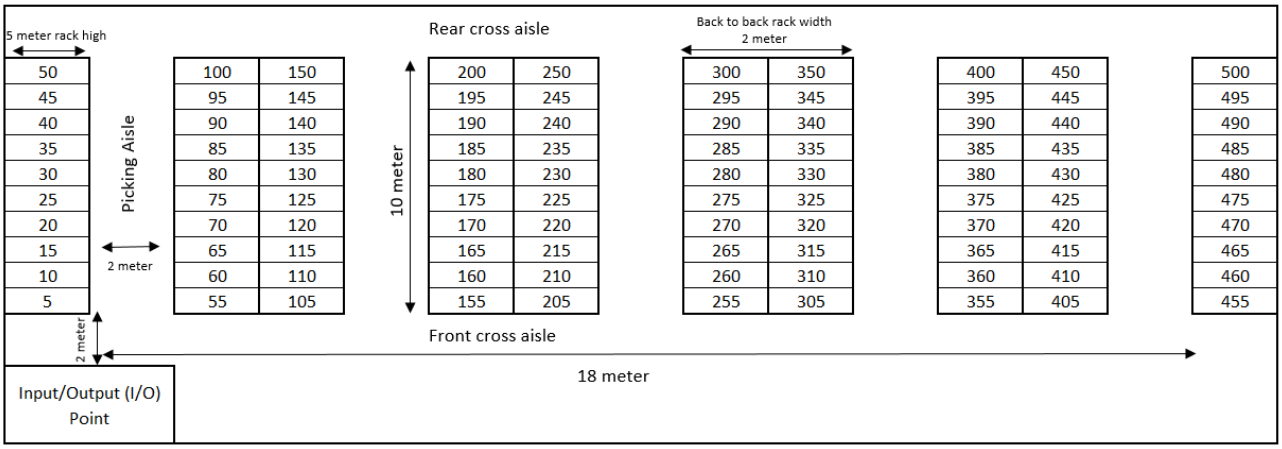

Figure 1. Top view of a single block and high-level warehouse

The horizontal and vertical speeds of the order picking vehicle are different, while the horizontal and vertical movements are simultaneous. No reference height when crossing the aisles is considered in this study. In other words, the movement from the height of the location in one aisle to the height of the location in the other aisle continues without interruption. The speed of the order picker when lifting and lowering, with or without load, is the same.

Each location has a single item type. Items have different weights. The maximum weight of an item is considered to be 20 kg [13]. The capacity of the order picker is determined on the basis of the number of items, which is 5 in this study.

Each order consists of a single item. Incoming orders will be picked by the order picker using the order picking vehicle. The number of orders to be picked is either the total number of orders reached in a given time interval or a predetermined target number of orders reached. Incoming orders are batched according to the capacity of the order picking vehicle and the order picking route is determined for each batch. The order picker expends energy during the order picking. This energy expenditure consists of both the energy expended when the order picker is not lifting any load in the order picker, i.e., when it is just standing while driving, and the energy expenditure that occurs when lifting items with a certain weight at the locations. The aim of this study is to batch and route incoming orders in a way that minimizes human energy expenditure.

3. Methodology

The overall objective of the batching and routing problem in order picking is to minimize the travel distance or time. The order picking routing problem can be modeled as a classical Steiner traveling salesman problem by computing an LxL matrix where i,j is the minimum travel distance or minimum travel time from storage location i to storage location j [4]. By adding batch capacity constraints to the routing problem, the batching and routing problem can be expressed as an integer programming model [1]. In this study, since human energy minimization will be performed, the human energy matrix LxL between locations will be used instead of distance or time between locations.

In this study, a mixed integer linear programming (MILP) mathematical model based on order batching and routing is proposed to minimize the human energy expended during the picking of orders from warehouse locations.

Assumptions:

- Each order contains one item.
- Each item has a weight and the maximum weight is 20 kg.
- Each location has only one item type and there are always items in the locations.

- The warehouse has a random location assignment policy. That is, items are randomly assigned to empty locations in the warehouse [19].
- Order picker capacity is expressed in terms of the number of items [1].
- The distance, time, and human energy expenditure between the locations are known in advance.
- Each tour starts from the I/O point and returns to the I/O point.
- Aisles are wide enough for two vehicles to pass through comfortably and there is no congestion.
- From the I/O point, the movement starts at zero height.
- There is no reference height at aisle entrances and exits.
- In aisle turns, the movement is linear and the turn angle is not considered.
- Horizontal and vertical speeds of the order picker vehicle are different and standard.
- The speed of the order picker is constant throughout the horizontal and vertical movements.
- The speeds of the order picker when lifting and lowering are the same and independent of the load.
- The order picker is standing on the vehicle while picking orders.
- The order picker is a male at the age of 30 and has a body weight of 75 kg [12].
- In all locations, the handling time of the order picker is the same and does not vary depending on the weights of items. It is assumed that the order picker carries the item during this time.

3.1. Notations

The indices, variables and parameters used in the mathematical model are explained in this section.

Indicies:
p: 1, 2,…..,P for locations.
l: 1, 2,…..,L for locations.
b: 1,2,.....,B for batches.

Decision Variables:
x_{bp}: 1 if location p is assigned to batch b, 0 otherwise.
y_{pl}^{b}: 1 if location p is immediately after location l in batch b, 0 otherwise.

Parameters:
C: Capacity of order picking truck vehicle (number of items)
G: Number of batches
S: Subset of set V
v_h: Horizontal speed of the order picker vehicle (m/s)
v_v: Vertical speed of the order picker vehicle (m/s)
t_{pl}: Travel time between locations p and l (sec)
h_l: Item handling time at location l (sec)
he_{pl}: Amount of human energy expended from location l to location p (kcal)
E_{stand}: Human energy expenditure of standing for 1 second (kcal/s)
BW: Order picker body weight (kg)
w_l: weight of the item at location l (kg)
ΔE: Energy to hold 1 kg for 1 second (kcal/s)

3.2. Mathematical Model

The mixed integer linear programming mathematical model based on batching and routing that minimizes human energy in order picking is as follows:

Objective Function:

$$OBJ_{min} = \sum_b^B \sum_p^P \sum_l^L y_{pl}^b * he_{pl} \quad (1)$$

Constraints:

$$\sum_p^P x_{bp} \leq C \qquad \forall b, \quad p > 1 \quad (2)$$

$$\sum_{b=1}^B x_{bp} = 1 \qquad \forall p, \quad p > 1 \quad (3)$$

$$\sum_{b=1}^B x_{bp} = G \qquad \forall p, \quad p = 1 \quad (4)$$

$$\sum_l^L y_{pl}^b = x_{bp} \qquad \forall b, p, \quad p \neq l \quad (5)$$

$$\sum_l^L y_{lp}^b = x_{bp} \qquad \forall b, p, \quad p \neq l \quad (6)$$

$$\sum_{i,j \in S} y_{pl}^b \leq |S| - 1 \qquad \forall S \in V, \quad p \neq l \quad (7)$$

$$x_{bp}, y_{pl}^b = \{0,1\} \qquad \forall b, p, l \quad (8)$$

Equation (1) gives the objective function and minimizes the human energy expenditure. Equation (2) is the capacity constraints of the order picking vehicle. The number of items picked in a single batch cannot exceed this capacity. According to Equation (3), each location is assigned to a batch, except for the I/O point represented by location number 1 in the solution of the model. Equation (4) states that each batch must have an I/O point. The number of batches (G) is the total number of orders divided by the capacity of the order picker (C). Equation (5) and Equation (6) state that in each batch b, there can be only one way from location p to location l and only one way from location l to location p. Equation (7) is the subtour eliminating constraints [20]. Equation (8) is 0-1 binary constraints.

3.3. Manhattan Distance-based Tchebychev Metrics and Travel Time Between Locations

The coordinates of the locations i and j of a 3D warehouse can be expressed as (x_i, y_i,z_i) and (x_j,

y_j,z_j) [4]. Figure 2 shows an example of the representation of the coordinates of locations i and j.

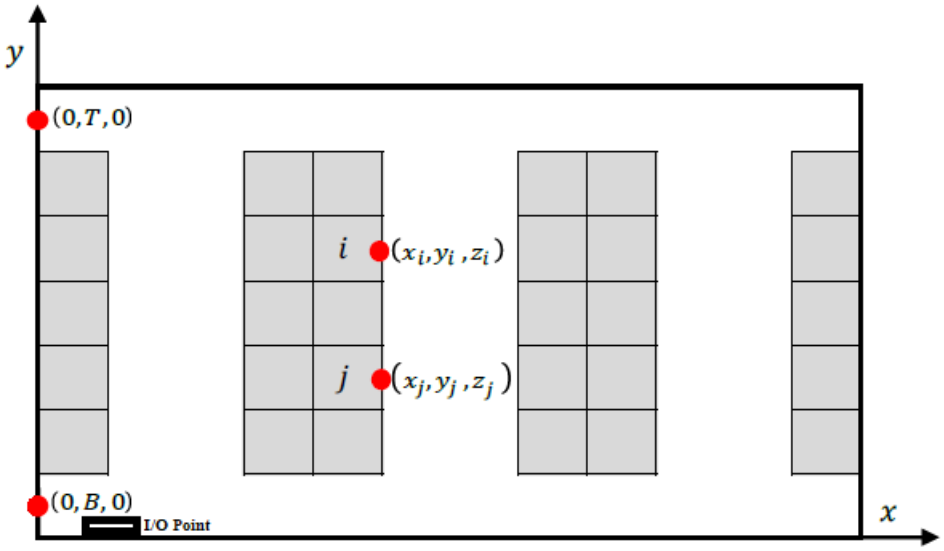

Figure 2. Top view of a single block high-level warehouse in X and Y Axis [4].

Points B and T are located on the y-axis and represent the upper and lower coordinates used to cross from one aisle to another, respectively. Also, x and y are the horizontal coordinates while z is the vertical coordinate. The minimum distance (d_{ij}) between locations i and j in the same aisle and the minimum distance from the I/O point to the locations within the warehouse are calculated by Equation (9). If the locaations are on different aisles, Equation (10) is used [4].

$$d_{ij} = |z_i - z_j| + |x_i - x_j| + |y_i - y_j| \quad (9)$$

$$d_{ij} = |z_i - z_j| + |x_i - x_j| + min\{|y_i - T| + |T - y_j|, |y_i - B| + |B - y_j|\} \quad (10)$$

Since the horizontal and vertical speeds of the order picking vehicles used in 3D warehouses are different, time calculation formula can be used instead of the distance formula. The travel time of a sequentially moving order picker between two locations in the same aisle and from the I/O point to the locations in the warehouse can be found using Equation (11). If the locations are on different aisles, Equation (12) is used [4].

$$t_{ij} = \frac{|y_i - y_j| + |x_i - x_j|}{v_h} + \frac{|z_i - z_j|}{v_v} \quad (11)$$

$$t_{ij} = \frac{|x_i - x_j|}{v_h} + min\left\{\frac{|y_i - T| + |T - y_j|}{v_h} + \frac{|z_i - z_j|}{v_v}, \frac{|y_i - B| + |B - y_j|}{v_h} + \frac{|z_i - z_j|}{v_v}\right\} \quad (12)$$

For order picking vehicles that perform simultaneous horizontal and vertical movements, the maximum travel time in horizontal and vertical movements is taken into account. Since the order picking vehicle considered in this study moves both horizontally and vertically simultaneously and at different speeds, the maximum travel time in horizontal and vertical movements can be found using the Tchebychev formula [4]. Equation (13) is used to calculate the travel time between locations within the same aisle and the travel time from the I/O point to a location within the warehouse, while the travel time between locations on different aisles can be found using Equation (14) [4].

$$t_{ij} = max\left\{\frac{|y_i - y_j| + |x_i - x_j|}{v_h}, \frac{|z_i - z_j|}{v_v}\right\} \quad (13)$$

$$t_{ij} = min\left\{max\left\{\frac{|y_i - T| + |T - y_j| + |x_i - x_j|}{v_h}, \frac{|z_i - z_j|}{v_v}\right\}, max\left\{\frac{|y_i - B| + |B - y_j| + |x_i - x_j|}{v_h}, \frac{|z_i - z_j|}{v_v}\right\}\right\} \quad (14)$$

3.4. Human Energy Expenditure

When calculating the human energy expenditure between two locations, both the time between locations and the weight of the items in the locations are taken into account. The order picker is standing on the order picking vehicle and therefore expends energy. Equation (15) gives the energy expended by a human in 1 second while standing depending on body weight, while Equation (16) gives the human energy caused by holding a load weighing w_p kg for 1 second [21]. Equation (17) gives the total human energy expenditure of travelling from location p to location l and putting the item from location l into the order picking vehicle.

$$E_{stand} = \frac{0.024*BW}{60}(kcal/s) \quad (15)$$

$$\Delta E_l = \frac{0.062*w_l}{60}(kcal/s) \quad (16)$$

$$he_{pl} = E_{stand} * t_{pl} + \Delta E_l * h_l \quad (17)$$

4. Implementations and Results

In this part of the study, three sample data sets were generated for the solution of the mathematical model. The proposed mathematical model for the problem was solved using the CPLEX solver in GAMS. Sample data sets of 5, 10 and 20 orders are shown in Table 1. Distance and human energy matrices were created for the locations of the orders. Equations (13), (14), (15), (16) and (17) were used to find the human energy expenditure between the locations. The average horizontal speed $\boldsymbol{v_h}$ of the order picking vehicle was taken as 3.33 m/s and the average vertical speed $\boldsymbol{v_v}$ as 0.40 m/s [22]. To compare the results of the mathematical model, FCFS batching and S-Shaped routing were applied using the same data sets.

Table 1. Number of orders and location numbers of orders

Sample data set	Number of orders	Location numbers of orders
1	5	443, 9, 22, 463, 367
2	10	196, 63, 192, 293, 311, 14, 202, 183, 447, 493
3	20	378, 194, 286, 249, 332, 63, 259, 4, 162, 215, 470, 117, 294, 166, 11, 110, 385, 483, 33, 305

4.1. Distance, Time and Human Energy Calculations

For the solution, it is first necessary to determine the distances between locations, and accordingly the time and energy expenditure. The solution will be explained in detail based on the sample data set 1. First, a 6x6 distance matrix consisting of 6 locations with I/O point 1 is created. The locations where the orders are located are numbered from 2 to 6 according to the arrival order. The distance matrix including horizontal and vertical distances calculated using Equations (9) and (10) is given in Table 2.

The calculation of the distance between locations 22 and 463, which are located on different aisles, is performed as follows: First, the x, y, z coordinates of both locations are found. Location 22 is on the second floor in the fourth shelf division of the first row of shelves in the picking aisle one. This location is at the zero meter according to the x coordinate, at the 7th meter according to the y coordinate, and the z coordinate, which expresses the shelf height, is at the 2nd meter. Location 463 is on the third floor in the third shelf division of the tenth shelf row in the fifth picking aisle. This location is at 18 meters according to the x coordinate, 5 meters according to the y coordinate and 3 meters according to the z coordinate. The x, y, z coordinates of locations 22 and 463 are (0,7,2) and (18,5,3) respectively. The coordinates of the crossing points B and T on the y-axis are 1 and 13 respectively. In this case, the shortest distances between locations 22 and 463 are calculated using Equation (10).

$$d_{22,463}(horizontal, vertical) = |x_{22} - x_{463}| + min\{|y_{22} - T| + |T - y_{463}|, |y_{22} - B| + |B - y_{463}|\}, |z_{22} - z_{463}|$$

$$= |0 - 18| + min\{|7 - 13| + |13 - 5|, |7 - 1| + |1 - 5|\}, |2 - 3|$$

$$= |-18| + min\{14, 10\}, |-1|$$

$$= 28, 1$$

In this case, the order picker will travel 28 meters horizontally and 1 meter vertically. Since the order picking vehicle moves horizontally and vertically simultaneously, the maximum of the horizontal and vertical travel times is found. For this reason, Equations (13) and (14) are used to calculate the travel times between the order locations. To find the travel time between the locations 22 and 463, Equation (14) is used since they are on different aisles.

Table 2. Horizontal and vertical distance matrix for the sample data set 1

Horizontal and Vertical Distances (meter)												
Locations	I/O (1)		443 (2)		9 (3)		22 (4)		463 (5)		367 (6)	
I/O (1)	0	0	27	3	4	4	7	2	23	3	20	2
443 (2)	27	3	0	0	27	1	24	1	8	0	11	1
9 (3)	4	4	27	1	0	0	3	2	25	1	22	2
22 (4)	7	2	24	1	3	2	0	0	28	1	25	0
463 (5)	23	3	8	0	25	1	28	1	0	0	13	1
367 (6)	20	2	11	1	22	2	25	0	13	1	0	0

$$t_{22,463} = min\left\{\begin{matrix} max\left\{\frac{|y_{22}-T|+|T-y_{463}|+|x_{22}-x_{463}|}{v_h}, \frac{|z_{22}-z_{463}|}{v_v}\right\}, \\ max\left\{\frac{|y_{22}-B|+|B-y_{463}|+|x_{22}-x_{463}|}{v_h}, \frac{|z_{22}-z_{463}|}{v_v}\right\} \end{matrix}\right\}$$

$$= min\left\{\begin{matrix} max\left\{\frac{|7-13|+|13-5|+|0-18|}{3.33}, \frac{|2-3|}{0.40}\right\}, \\ max\left\{\frac{|7-1|+|1-5|+|0-18|}{3.33}, \frac{|2-3|}{0.40}\right\} \end{matrix}\right\}$$

$$= min\begin{Bmatrix} max\{9.6, 2.5\}, \\ max\{8.4, 2.5\} \end{Bmatrix} = t_{22,463} = 8.4\ s$$

Table 3. Travel time matrix between the locations of the sample data set 1

Travel time between the order locations (s)						
	I/O (1)	443 (2)	9 (3)	22 (4)	463 (5)	367 (6)
I/O	0.0	8.1	10	5	7.5	6
443	8.1	0.0	8.1	7.2	2.4	3.3
9	10	8.1	0.0	5	7.5	6.6
22	5	7.2	5	0.0	8.4	7.5
463	7.5	2.4	7.5	8.4	0.0	3.9
367	6	3.3	6.6	7.5	3.9	0.0

Once the travel times between locations are determined, the human energy expenditure due to time can be found using Equations (15), (16) and (17). Since the travel times between locations given in Table 3 are the times when the order picker does not lift any item on the vehicle, only the energy caused by standing is calculated. In order to calculate the energy due to weight lifting at the locations, the weight of the items at these locations (w_l) and how long this weight is carried must be known (h_l) (Table 4). These

weights are randomly assigned to the items with a maximum of 20 kg [13]. It was also assumed that the lifting time (h_l) of each location was 6 seconds and the body weight (BW) of the order picker was 75 kg [12]. In this case, an order picker going from location 22 to 463 expends energy both in the process of reaching location 463 and in the process of lifting the weight of the item (w_l= 10.2 kg) at this location. The total energy is the energy spent between these two locations. The matrix of human energy expenditure between order locations for the sample data set 1 is given in Table 5. Table 5 demonstrates that the human energy matrix based on the order locations is not symmetric. This is mainly due to the different weight of the items in each location. Even though the energy expenditure on both sides is the same during travel between any two locations, the human energy expenditure during lifting and placing the items in the order picking vehicle at order locations is not the same due to the different weight of the items in each location.

$$E_{stand} = \frac{0.024 * BW}{60} = \frac{0.024 * 75}{60} = 0.03\ (kcal/s)$$

$$\Delta E_{463} = \frac{0.062 * w_l}{60} = \frac{0.062 * 10.2}{60} = 0.01054\ (kcal/s)$$

$$he_{22,463} = E_{stand} * t_{22,463} + \Delta E_{463} * o_{463} = 0.03 * 8.4 + 0.01054 * 6 = 0.315\ kcal$$

Table 4. Item weights and handling times at locations

	I/O	443	9	22	463	367
w_l	0	17 kg	12.9 kg	17.4 kg	10.2 kg	19.5 kg
h_l	0 s	6 s	6 s	6 s	6 s	6 s

Table 5. Human energy matrix between the order locations of the sample data set 1

Locations	I/O (1)	443 (2)	9 (3)	22 (4)	463 (5)	367 (6)
I/O (1)	0	0.348	0.380	0.258	0.288	0.301
443 (2)	0.243	0	0.323	0.324	0.135	0.220
9 (3)	0.300	0.348	0	0.258	0.288	0.319
22 (4)	0.150	0.321	0.230	0	0.315	0.346
463 (5)	0.225	0.177	0.305	0.360	0	0.238
367 (6)	0.180	0.204	0.278	0.33	0.180	0

4.2. Solution of the Mathematical Model

GAMS optimization software was used to solve the mathematical model. Solutions for the three sample data sets were also performed. The item capacity of the order picking vehicle was set to 5 [23]. In each batch, travel starts from the I/O point and returns to the I/O point. Optimum batches, routes (by location number) and total human energy expenditures are given in Table 6. Also, the optimal route determined for the sample data set 1 is shown in Figure 3.

For the sample data set 1, only one batch was created and the picking sequence is specified in Table 6. The total human energy expenditure for the sample data set 1 was 1,353 kcal. In the analysis of the sample data set 2, the locations were divided into two batches and within each batch, the picking sequence for each batch takes place in Table 6. The minimum human energy expended for the sample data set 2 was 2,167 kcal. Finally, for the sample data set 3, the order locations were divided into four batches and picking sequence for each batch is given in Table 6. The minimum total human energy expenditure for the sample data set 3 was 4,253 kcal.

Table 6. Results of the mathematical model

Sample Data Set	Order Size	Batches and Routes	Total Energy Expenditure (kcal)	Throughput time (s)
1	5	Batch 1: I/O-22-9-463-443-367-I/O	1.353	59.2
2	10	Batch 1: I/O-196-192-183-14-63-I/O Batch 2: I/O-202-293-493-447-311-I/O	2.167	108.9
3	20	Batch 1: I/O-483-470-305-385-378-I/O Batch 2: I/O-194-249-294-332-286-I/O Batch 3: I/O-11-63-117-162-166-I/O Batch 4: I/O-33-4-110-215-259-I/O	4.253	224.3

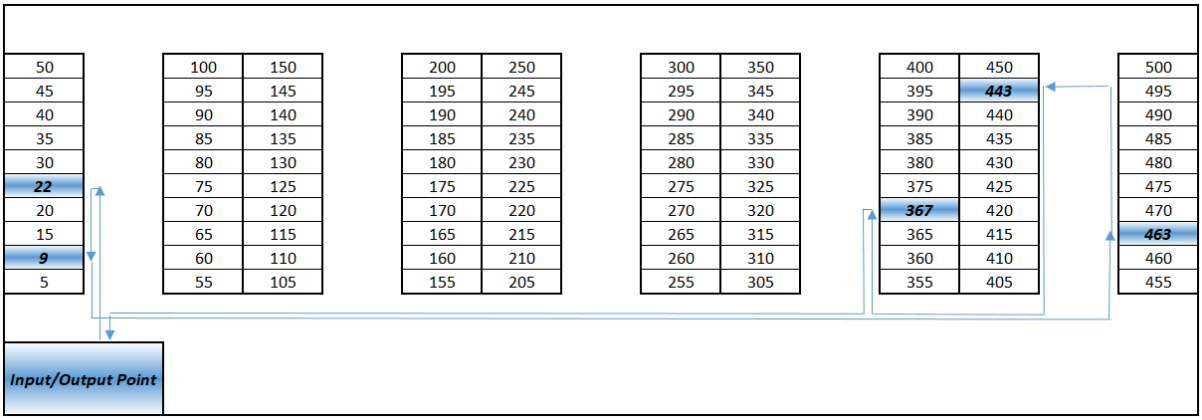

Figure 3. Optimum route for the sample data set 1

```
**** REPORT SUMMARY :          0     NONOPT
                               0 INFEASIBLE
                               0  UNBOUNDED
GAMS 43.1.0  203303bb Apr 27, 2023          WEX-WEI x86 64bit/MS Windows - 07/29/23 00:58:52 Page 8
G e n e r a l   A l g e b r a i c   M o d e l i n g   S y s t e m
E x e c u t i o n


----     96 VARIABLE y.L  1 if location l in group b is immediately after location p otherwise 0

               1           2           3           4           5           6

1.1                                                1.000
1.2                                                                    1.000
1.3                                                            1.000
1.4                                    1.000
1.5                        1.000
1.6         1.000


----     96 VARIABLE x.L  1 if location p is assigned to group b otherwise 0

              1           2           3           4           5           6

1         1.000       1.000       1.000       1.000       1.000       1.000


----     96 VARIABLE OBJ.L                  =        1.353  minimization of human energy expenditure

EXECUTION TIME       =        0.438 SECONDS      4 MB  43.1.0 203303bb WEX-WEI
```

Figure 4. GAMS screen display for the results of the sample data set 1

As can be seen in Figure 3, the order picker starts its movement from the I/O point at ground floor height and goes to location 22 on the second floor. From there, it moves along the same aisle to location 9 at the fourth floor height. The next travel point is location 463 and the order picker moves horizontally while simultaneously descending from the fourth floor to the third floor. From here the order picker travels to location 443 and does not move vertically but only horizontally. Travelling to location 367, where the last order in the order list is located, the order picker descends one floor to pick this order, which is located on the second floor. After all the orders have been picked, the order picker returns to the I/O point and at the same time moves down two floors to the ground floor.

4.3. Implementation of FCFS Batching and S-Shaped Routing

Warehouse managers prefer methods that are easier to implement for warehouse workers [6]. FCFS batching is a widely used method in practice and in many studies [3, 24, 25]. Similarly, the s-shaped (traversal) routing method is widely used in many warehouses due to its simplicity in terms of implementation [2]. For this reason, FCFS batching and s-shaped routing were applied to the same data sets to compare the results obtained with the mathematical model.

The capacity for each batch is 5 orders. If this number is not reached in the first aisle entered, the order picker crosses to the next aisle containing orders. If the capacity is reached in this aisle, the order picker returns to the I/O point to unload the orders. If there are still unpicked orders, the order picker moves to the nearest aisle containing orders and starts picking and returns to the I/O point when the capacity is reached.

FCFS batching and s-shaped routing results for the sample data sets are given in Table 7. In addition, the s-shaped route for the sample data set 1 is also shown in Figure 5.

Tablo 7. The results of FCFS batching ve S-shaped routing for the Sample Data Sets

Sample Data Set	Order Size	Batches and Routes	Total Human Energy Expenditure (kcal)	Throughput time (s)
1	5	Batch 1: I/O-9-22-367-463-443-I/O	1.602	67.5
2	10	Batch 1: I/O-63-196-192-293-311-I/O Batch 2: I/O-14-183-202-447-493-I/O	2.746	128.2
3	20	Batch 1: I/O-194-249-286-378-332-I/O Batch 2: I/O-4-63-162-259-215-I/O Batch 3: I/O-11-117-166-294-470-I/O Batch 4: I/O-33-110-305-385-483-I/O	5.327	260.1

The sample data set 1 consists of only one batch and the energy expenditure is 1,602 kcal as a result of s-shaped routing. The picking sequence for the Sample Data Set 1 is given in Table 7. In the batching and routing for the sample data set 2, the locations were divided into two batches and their picking sequence are given in Table 7. The total human energy expenditure of these two batches as a result of order picking was 2,746 kcal. Finally, as a result of FCFS batching and s-shaped routing for the sample data set 3, the order locations were divided into four batches and routes are given for each batch in Table 7. The total human energy expenditure for the sample data set 3 was 5,327 kcal.

Looking at Figure 5, in s-shaped routing, the order picker starts its movement by entering the first aisle closest to the I/O point, since it has orders in this aisle. While the horizontal movement towards location 9 continues, it also makes a four-meter upward movement from ground floor to the fourth floor towards this location, which is located on the fourth floor in its devision. After receiving the order at this location, it moves to location 22 on the second floor in the same picking aisle and makes a descending movement of two meters. The closest picking aisle where the order is located is the fourth picking aisle. Leaving the first picking aisle from the direction opposite to the direction it entered, it enters the fourth picking aisle and reaches location 367 on the second floor. There are two more orders in the last picking aisle. It goes to the first one, the closest location 463. Finally, after receiving the order at the last location 443, it exits from the direction it entered this aisle and returns to the I/O point.

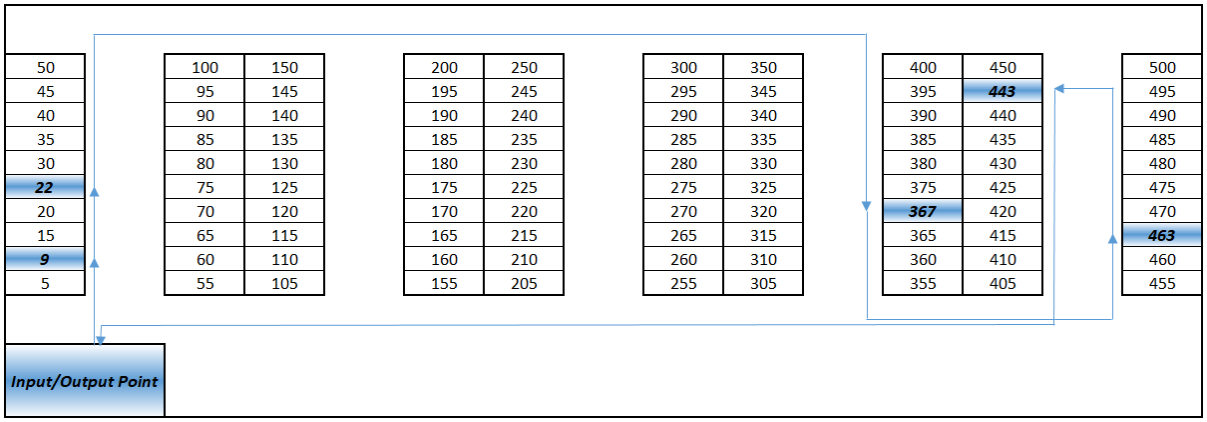

Figure 5. S-shaped route for the sample data set 1

5. Discussion

In this study, the order picking process in a sample single block high-level warehouse system was investigated from an ergonomic point of view. Firstly, human energy expenditures were calculated using the distance, time and human energy formulas. Then, human energy expenditure was minimized using a mathematical model based on order batching and routing for the three different sample data sets that were created for the analysis.

For the solution, three-dimensional (x, y, z) coordinates of the locations were determined to calculate the distances between the order locations in the high-level warehouse and the minimum distances were found. Since the high-level order picking vehicle travels simultaneously at different speeds horizontally and vertically, the travel times to the target locations were calculated. For this, Tchebychev formulas were used to find the maximum of the horizontal and vertical travel times. Since the human energy calculation depends on both the time between locations and the weights at the locations, the human energy matrices of the order locations were created using the standing and weight lifting human energy formulas. In order to compare the results of the mathematical model, FCFS batching and s-shaped routing methods, which are widely applied in warehouses, were also applied to the same sample data sets.

The mathematical model based on batching and routing was applied for the three different sample data sets and the results are given in Table 6. The results of FCFS and s-shaped routing method are given in Table 7. The results are also given comparatively in Table 8. Looking at Table 8, in all cases, both human energy expenditure and throughput time decreased when the human energy based mathematical model was used.

Table 8. Comparison of the results

Order Size	Batch Size	Batching and Routing	Total Human Energy Expenditure (kcal)	Throughput time (s)
5	1	FCFS and S-haped	1.602	67.5
		Human Energy Based Mathematical Model	1.353	59.2
10	2	FCFS and S-haped	2.746	128.2
		Human Energy Based Mathematical Model	2.167	108.9
20	4	FCFS and S-haped	5.327	260.1
		Human Energy Based Mathematical Model	4.253	224.3

In high-level warehouses, the distance, time and energy calculations differ from low-level warehouses. While low-level storages are 2D, high-level storages are 3D. For this reason, only horizontal movements are calculated in low-level order picking, while vertical movements should also be taken into account in high-level order picking. However, the fact that the horizontal and vertical speeds of the high-level order picking vehicles are different, but their movements are simultaneous, implies that special calculations are required. In the low-level warehouse, distance and time measurements between locations can be made on the (x, y) coordinate plane, while the high-level warehouse is similar to the (x, y, z) coordinate plane due to its 3D structure and calculations are made according to the three-dimensional coordinates of the locations. The use of Tchebychev formulas would be more accurate for 3D warehouses due to the simultaneous horizontal and vertical movement of the order picker. Because when moving from one location to another, the horizontal movement may end, but the vertical movement may still continue. Conversely, the destination may have been reached in the vertical, but the movement in the horizontal may still continue. For this reason, if order picking vehicles moving simultaneously are used in 3D warehouses, it would be a more accurate analysis to calculate time rather than distance. Since horizontal and vertical travel times may be different, using Tchebychev formulas that find the maximum of these times would be a better approach for high-level warehouses.

6. Conclusions and Suggestions

In this study, in which the human factor is considered in a single block high-level order picking, human energy expenditures based on the time between order locations and item weight were analyzed and the optimum human energy batches and routes were determined with the order batching and routing based mathematical model aiming at human energy minimization. Using three different data sets of 5, 10 and 20 orders, the mathematical model based on batching and routing gave better results than FCFS batching and s-shaped routing. The use of the Tchebychev formula to calculate the time between order locations for the order picker vehicle moving simultaneously horizontally and vertically in the high-level warehouse was significant in obtaining accurate results. In addition, using the (x, y, z) coordinate plane to find the distances between locations in high level (3D) warehouses has facilitated the achievement of accurate results.

In a future study to improve this work, meta-heuristic methods can be used for big data sets. Studies with more than one block and larger numbers of locations can also be conducted. Traffic congestion was not taken into account in this study, so a study that takes this into account can also be carried out. A study that takes into account the reference height at the aisle enters and exits can also be conducted. Finally, this study could be improved by taking into account the angle of rotation when crossing aisles.

Contributions of the authors

The authors confirm that the contribution is equally for this paper.

Conflict of Interest Statement

There is no conflict of interest between the authors.

Statement of Research and Publication Ethics

The study is complied with research and publication ethics.

References

[1] S. Ene and N. Öztürk, "Storage location assignment and order picking optimization in the automotive industry," *The International Journal of Advanced Manufacturing Technology*, vol. 60, no. 5–8, pp. 787–797, Aug. 2011. doi: https://doi.org/10.1007/s00170-011-3593-y.

[2] C. G. Petersen and G. Aase, "A comparison of picking, storage, and routing policies in manual order picking," *International Journal of Production Economics*, vol. 92, no. 1, pp. 11–19, Nov. 2004. doi: https://doi.org/10.1016/j.ijpe.2003.09.006.

[3] M. B. M. De Koster, E. S. Van der Poort, and M. Wolters, "Efficient order batching methods in warehouses," *International Journal of Production Research*, vol. 37, no. 7, pp. 1479–1504, May 1999. doi: https://doi.org/10.1080/002075499191094.

[4] J. A. Cano, P. Cortés, J. Muñuzuri, and A. Correa-Espinal, "Solving the picker routing problem in multi-block high-level storage systems using metaheuristics," *Flexible Services and Manufacturing Journal*, Feb. 2022. doi: https://doi.org/10.1007/s10696-022-09445-y.

[5] J. C.-H. Pan, M.-H. Wu, and W.-L. Chang, "A travel time estimation model for a high-level picker-to-part system with class-based storage policies," *European Journal of Operational Research*, vol. 237, no. 3, pp. 1054–1066, Sep. 2014. doi: https://doi.org/10.1016/j.ejor.2014.02.037.

[6] S. Vanheusden, T. van Gils, K. Ramaekers, T. Cornelissens, and A. Caris, "Practical factors in order picking planning: state-of-the-art classification and review," *International Journal of Production Research*, pp. 1–25, Apr. 2022, doi: https://doi.org/10.1080/00207543.2022.2053223.

[7] L. C. Tang and E.-P. Chew, "Order picking systems: Batching and storage assignment strategies," *Computers & Industrial Engineering*, vol. 33, no. 3–4, pp. 817–820, Dec. 1997, doi: https://doi.org/10.1016/s0360-8352(97)00245-3.

[8] F. Caron, G. Marchet, and A. Perego, "Routing policies and COI-based storage policies in picker-to-part systems," *International Journal of Production Research*, vol. 36, no. 3, pp. 713–732, Mar. 1998, doi: https://doi.org/10.1080/002075498193651.

[9] E. H. Grosse, C. H. Glock, M. Y. Jaber, and W. P. Neumann, "Incorporating human factors in order picking planning models: framework and research opportunities," *International Journal of Production Research*, vol. 53, no. 3, pp. 695–717, Jun. 2014, doi: https://doi.org/10.1080/00207543.2014.919424.

[10] G. Casella, A. Volpi, R. Montanari, L. Tebaldi, and E. Bottani, "Trends in order picking: a 2007–2022 review of the literature," *Production and Manufacturing Research: An Open Access Journal*, vol. 11, no. 1, Mar. 2023, doi: https://doi.org/10.1080/21693277.2023.2191115.

[11] T. De Lombaert, K. Braekers, R. De Koster, and K. Ramaekers, "In pursuit of humanised order picking planning: methodological review, literature classification and input from practice," *International Journal of Production Research*, vol. 61, no. 10, pp. 3300–3330, Jun. 2022, doi: https://doi.org/10.1080/00207543.2022.2079437.

[12] D. Battini, C. H. Glock, E. H. Grosse, A. Persona, and F. Sgarbossa, "Human energy expenditure in order picking storage assignment: A bi-objective method," *Computers & Industrial Engineering*, vol. 94, pp. 147–157, Apr. 2016, doi: https://doi.org/10.1016/j.cie.2016.01.020.

[13] M. Calzavara, C. H. Glock, E. H. Grosse, and F. Sgarbossa, "An integrated storage assignment method for manual order picking warehouses considering cost, workload and posture," *International Journal of Production Research*, vol. 57, no. 8, pp. 2392–2408, Sep. 2018, doi: https://doi.org/10.1080/00207543.2018.1518609.

[14] F. Zangaro, S. Finco, D. Battini, and I. Zennaro, "An optimization model for the storage assignment of the reference under ergonomics constraints," *Proceedings of the Summer School Francesco Turco*, September 11–13, 2019. [Online]. Available: https://www.summerschool-aidi.it/edition-2019/cms/extra/papers/116.pdf. [Accessed: Sep. 12, 2023.]

[15] M. Zhang, S. Winkelhaus, and E. H. Grosse, "Evaluation of human workload in a hybrid order picking system," *IFAC-PapersOnLine*, vol. 54, no. 1, pp. 458–463, 2021, doi: https://doi.org/10.1016/j.ifacol.2021.08.053.

[16] J. A. Larco, R. de Koster, K. J. Roodbergen, and J. Dul, "Managing warehouse efficiency and worker discomfort through enhanced storage assignment decisions," *International Journal of Production Research*, vol. 55, no. 21, pp. 6407–6422, Apr. 2016, doi: https://doi.org/10.1080/00207543.2016.1165880.

[17] B. Gajšek, S. Šinko, T. Kramberger, M. Butlewski, E. Özceylan, and G. Đukić, "Towards Productive and Ergonomic Order Picking: Multi-Objective Modeling Approach," *Applied Sciences*, vol. 11, no. 9, p. 4179, May 2021, doi: https://doi.org/10.3390/app11094179.

[18] D. Dukic, and D. Oluio, "Order-picking routing policies: Simple heuristics, advanced heuristics or optimal algorithm." *Strojniski Vestnik*, vol. 50, no. 11, pp. 530-535, Jan. 2004. [Online]. Available: https://www.researchgate.net/publication/296803926_Order-picking_routing_policies_Simple_heuristics_advanced_heuristics_or_optimal_algorithm. [Accessed: Sep. 12, 2023.]

[19] P. Parikh and R. D. Meller, "A travel-time model for a person-onboard order picking system," *European Journal of Operational Research*, vol. 200, no. 2, pp. 385–394, Jan. 2010, doi: https://doi.org/10.1016/j.ejor.2008.12.031.

[20] R. Wang, L. Zang, and X. Tan, "An Optimal Routing Model of High-level Picker-to-part System," *Lecture notes in electrical engineering*, pp. 371–383, Sep. 2012, doi: https://doi.org/10.1007/978-1-4471-4600-1_32.

[21] A. Garg, D. B. Chaffin, and G. D. Herrin, "Prediction of metabolic rates for manual materials handling jobs," *American Industrial Hygiene Association Journal*, vol. 39, no. 8, pp. 661–674, Aug. 1978, doi: https://doi.org/10.1080/0002889778507831.

[22] "BT Optio 1t Yüksek Seviye," *Toyota*. https://toyota-forklifts.com.tr/ueruenlerimiz/siparis-toplama-makineleri/yueksek-seviye-toplama/bt-optio-1t-yueksek-seviye/ (accessed Sep. 12, 2023).

[23] S. Ene, İ. Küçükoğlu, A. Aksoy, and N. Öztürk, "A genetic algorithm for minimizing energy consumption in warehouses," *Energy*, vol. 114, pp. 973–980, Nov. 2016, doi: https://doi.org/10.1016/j.energy.2016.08.045.

[24] J. Won and S. Olafsson *, "Joint order batching and order picking in warehouse operations," *International Journal of Production Research*, vol. 43, no. 7, pp. 1427–1442, Apr. 2005, doi: https://doi.org/10.1080/00207540410001733896.

[25] C.-C. Lin, J.-R. Kang, C.-C. Hou, and C.-Y. Cheng, "Joint order batching and picker Manhattan routing problem," *Computers & Industrial Engineering*, vol. 95, pp. 164–174, May 2016, doi: https://doi.org/10.1016/j.cie.2016.03.009.

Bitlis Eren Üniversitesi Fen Bilimleri Dergisi
BİTLİS EREN UNIVERSITY JOURNAL OF SCIENCE
ISSN: 2147-3129/e-ISSN: 2147-3188
VOLUME: 12 NO: 3 PAGE: 925-940 YEAR: 2023
DOI:10.17798/bitlisfen.1346730

3BResNet: A Novel Residual Block-Based ResNet Model Approach for COVID19 Detection

Ekrem Eşref KILINÇ[1*], Fahrettin AKA[2], Sedat METLEK[3]

[1]*Burdur Mehmet Akif Ersoy University, Vocational School of Ağlasun, Department of Computer Technology and Programming, Burdur / Türkiye*
[2]*Isparta University of Applied Sciences, Vocational School of Atabey, Department of Computer Technologies, Isparta / Türkiye*
[3]*Burdur Mehmet Akif Ersoy University, Vocational School of Technical Sciences, Department of Electronics and Automation, Burdur / Türkiye*
(ORCID: 0000-0003-1806-4937) (ORCID: 0000-0003-1449-2969) (ORCID: 0000-0002-0393-9908)

Keywords: Deep Neural Network, Residual Block, Resnet, 3BResNet.

Abstract

In recent years, upper respiratory tract infections that have affected the whole world have caused the death of millions of people. It is predicted that similar infections may occur in the coming years. Therefore, it is necessary to develop methods that can be used widely, especially during epidemic periods. The study developed a decision support system for use in upper respiratory tract infections. At this stage, first, the ResNet models in the literature were examined and an application was developed on the SARS-CoV-2 Ct dataset. Next stage, the block structure in the ResNet models in the literature was changed, the number of layers was reduced, and a new model was proposed that provides higher success with fewer parameters. With the proposed model, the values 0.97, 0.97, 0.94, and 0.98 were achieved for accuracy, F1 score, precision and sensitivity on the SARS-CoV-2 Ct dataset, respectively. When the obtained values are compared to state of the art methods in the literature, it has been determined that they are at a competitive level with much fewer parameters. Hardware-related problems encountered in the training of ResNet models at low hardware levels were solved with the proposed model, resulting in a higher success rate. Furthermore, the proposed model can be widely used in different decision support systems that are urgently needed in adverse conditions such as pandemics due to its lightweight structure and high-performance results. As a result of the study, a new model that can provide higher performance with much lower layer structure than existing ResNet models has been introduced into the literature with the proposed model.

1. Introduction

The easy transmission of upper respiratory tract diseases causes regional or worldwide outbreaks. Recently, one of these epidemics emerged in the city of Wuhan, China and affected the whole world [1]. As a result, the World Health Organization (WHO) announced this situation as a pandemic due to the risk of spreading the disease easily to the masses [2]. During the pandemic, the authorities reported about 600 million cases and about 7 million deaths [3].

Due to the deaths that occurred during the pandemic period, health facilities such as emergency rooms and intensive care units were also overcrowded. This situation caused significant labor and financial difficulties [4]. In order to prevent these difficulties at least one step, it has become an extremely vital issue to detect diseases that may pose a risk of epidemic and to take the necessary precautions. For this reason, many studies have been conducted in the literature to detect disease [5]. One of the most fundamental studies is the Real-Time

*Corresponding author: ekilinc@mehmetakif.edu.tr
Received: 21.08.2023, Accepted: 16.09.2023

Polymerase Chain Reaction (RT-PCR) method [6]. Thanks to the RT-PCR method, which was used extensively during the Covid19 pandemic period, numerous patients were diagnosed with the disease. However, one of the biggest obstacles to the efficient use of the system is that the method used gives results after a long time. In addition, some inconsistencies in the results of RT-PCR testing have called into question the reliability of this method. Despite the disadvantages of this method, it was the most preferred method because there were not many alternatives during the pandemic. However, delivering diagnostic test kits using the RT-PCR method over a wide geographic area during the pandemic period presented a different problem.

The use of technology to provide diagnosis and treatment to large populations is critical during such epidemics. Therefore, researchers have focused on rapid response systems as an alternative to test kits in disease diagnosis [7]. Radiological images are one of the most important of these. Radiological images are used in the detection of many diseases because they can be easily obtained from X-ray machines commonly found in hospitals [8]. However, since the soft tissues cannot be fully detected with X-ray images, Computed Tomography (CT) scans, which give faster results, are preferred [9]. This method was preferred because it is both safer and gives faster results than other test kits. It is considered a safer method than many other diagnostic methods, especially when evaluated in terms of maintaining physical distance between the patient and the doctor. Machine learning methods that use CT images for faster and more reliable disease detection have also begun to be developed. One of the leading machine learning methods is deep learning (DL) algorithms. Ancillary decision support systems created with DL algorithms can help experts make more accurate decisions faster [10]. Transfer learning methods are at the forefront of DL algorithms that are commonly used in auxiliary decision support systems. Transfer learning methods are based on using the weight values of pre-trained models on new datasets. This approach greatly decreases the training time for models and simplifies the determination of weight values for the layers utilized in deep neural network models [11].

In the literature, it is claimed that models based on the transfer learning method give better results than basic convolutional neural networks (CNN) or other machine learning models in classifying images in datasets consisting of medical images [12]. For this reason, numerous research studies in the literature employ transfer learning techniques to train neural network models on limited-sized datasets [13] – [16].

Studies that use DL methods and CT images together for disease detection are commonly found in the literature. Residual Network (ResNet) based methods are used in many of these studies. But in general, ResNet-based models have some disadvantages. There are several gaps in the literature that need to be filled to overcome these disadvantages. The major gaps identified in the literature are:

- At higher depth levels, semantic gaps occur. The most important factor that causes this semantic gap is the vanishing or exploding. Although increasing the number of layers in ResNet models is done to improve performance, this can produce low-performance results depending on the dataset. For this reason, when reviewing the studies in the literature, it is generally found that different ResNet models produce more successful results on different datasets. This situation can lead to problems concerning the comparison of ResNet models.
- In the literature, a limited number of ResNet models and different models are compared on the same dataset in studies conducted to measure the performance of ResNet models. The datasets used in these studies are generally datasets with access problems [17]. For this reason, it is necessary to carry out new studies in which ResNet models will be compared with each other using publicly available datasets.
- The process of transferring filters obtained from a pre-trained model to a new model is called transfer learning. This method allows the model to be trained quickly and allows for better results. In addition, when randomly selected filters are used for training, the time required for training the models increases excessively. In this case, training can take days, especially when training is done on a low-equipped level. Therefore, new solutions are needed that can be trained and operated in low-equipped systems are needed.

To fill the similar gaps mentioned in the literature, a study was conducted to categorize patients infected with Covid19 using different ResNet models on the publicly accessible dataset "The severe acute respiratory syndrome coronavirus 2 (SARS-CoV-2) Ct-Scan". A novel approach is presented, utilizing convolutional and residual blocks, which eliminates the disadvantages of ResNet models for the classification of individuals with Covid19 infection. The study's contribution to the literature is briefly summarized below.

- In the proposed model (3BResNet), a competitive alternative has been developed that can operate on platforms with lower hardware capacity by reducing the layer count, the parameter count, and the computational cost.
- A different residual block structure has been developed for the issue of overfitting, which is the primary problem of ResNet models. The developed structure has been used in the 3BResNet model and compared with other ResNet models in the literature.
- The block structure used in the ResNet18, ResNet34, ResNet50, ResNet101, ResNet152, and ResNet202 models in the literature and the effect of the 3BResNet block structure on the model success are presented in detail in the study.
- In the study, instead of increasing the number of layers as in ResNet models, it has been determined that the use of the proposed block structure has a greater effect on success. Therefore, a model has been proposed that can be trained and run for Covid19 classification on low-equipped systems.

The following section two of the study presents studies in the literature in general. In section three, ResNet models that are widely used in the literature and the model proposed in the study are shared. In section four, the experimental study is described in detail. In section five, the findings and results of the experimental study are presented. In section six, the results of the study are evaluated and information about future studies is presented.

2. Literature

Researchers have conducted many experimental and theoretical studies to detect diseases of the upper respiratory tract due to the global pandemic in the 21st century [18]-[21]. Among these studies, the most popular are DL-based studies. DL-based approaches are also used in medical image analysis due to their success in classification and prediction. Researchers used X-ray and tomography images to detect Covid19, which is a respiratory illness that affects the upper respiratory system. In the literature section of the study, some of the studies performed with X-ray images are presented in detail below.

Chowdhury et al. conducted their study using a dataset of chest X-rays from 423 Covid19 patients, 1485 viral pneumonia patients, and 1579 healthy individuals. The researchers also used data augmentation methods in addition to the existing dataset. In their study, they tested eight different models that are generally preferred in the field of DL. As a result of the study, they emphasized that the ResNet18 and CheXNeT models achieved the highest success in disease detection with an accuracy rate of 99.41% [2]. Additionally, they found that data augmentation methods directly affect the success of the model.

Farooq and Hafeez proposed a new model called COVID-ResNet, which consists of 4 classes using the COVIDx dataset containing 5941 chest X-rays. Using a three-step technique on the ResNet50 architecture, they achieved a 96.23% success rate with the COVID-ResNet model [22]. Kana et al. achieved a 99.0% success rate in detecting Covid19 in their chest X-rays study using ResNet50 [23].

For the detection of pneumonia and Covid19, Keles et al. developed two models in their study called COV19-CNNet and COV19-ResNet. They used viral pneumonia (350), Covid19 (210), and healthy chest X-rays (350) in their study. They achieved 94.28% and 97.61% classification success for the COV19-CNNet and COV19-ResNet models, respectively. In their study, they emphasized that pre-trained models are less successful in medical images. In the two proposed models, they did not use a pre-trained model, taking a different approach from many studies in the literature. In this sense, it is one of the studies that inspired the present paper [24].

Zhang et al. developed COVID34XrayNet, a ResNet19-based model that uses a two-stage transfer learning approach. The developed model was tested on chest X-rays images and succeeded with 91.8% accuracy in Covid19 detection. The highlight of the model is the addition of a feature smoothing layer (FSL) and a feature extraction layer (FEL) to the 32 layers of the ResNet34 model [25]. Rahaman et al. tested 15 different CNN models and achieved the most classification success (89.3%) with VGG-19 [26].

Asnaoui and Chawki used models with different types of architectural structures in their study. They applied DenseNet201, InceptionResNetV2, InceptionV3, ResNet50, MobilenetV2, VGG16 and VGG19 models on the same dataset. They achieved the highest accuracy with InceptionResNetV2 at 92.18% [27]. The use of different types of DL models by Asnaoui and Chawki is one of the points that inspired our study. This is because it is expected that the success results of models with different types of architecture will be quite different from each other. Examining the success results of models with similar architectures is a very important to show the effect of the preferred layer structure in the development of these models on success. Therefore, in this study, the effect of the number of layers on the success of ResNet models with similar architecture is analyzed.

CT images are also frequently preferred in Covid19 detection with DL applications. For this reason, in the next section of the literature, studies consisting of applications in which CT scan images are preferred are presented. Xu et al. designed a classification network using the ResNet18 model to distinguish Covid19 from the influenza A virus on a dataset of 618 CT images. The images in the dataset were classified by segmentation. In their study, they achieved an accuracy rate of 86.7% [28]. Zheng et al. proposed a CNN-based 3D model named DeCovNet. In their proposed model, they used a total of 630 CT images obtained on different dates. The researchers also used data augmentation techniques to train their proposed model. They detected Covid19 disease using the model they developed and CT images. The performance of the model they developed was measured using the ROC AUC metric and they obtained a value of 0.95 [29]. Hu et al. succeeded in detecting Covid19 disease with 89% accuracy using a weakly supervised DL model with data obtained from CT images. In their study, unlike other studies in the literature, they were able to achieve a higher accuracy rate in disease detection by determining the exact location of the lesions or inflammation caused by Covid19 [30]. Li et al. developed a 3D DL model called COVNet for the detection of Covid19. In their model, they used a dataset of 4352 chest CT images from 3322 patients. With the model they developed using the ResNet50 backbone, the images were first pre-processed. Then, using a UNet-based segmentation method, the infected region was detected from the lung region and classification was performed. With the COVNet model, they obtained AUC values of 0.96, 0.95, and 0.98 for the detection of Covid19, pneumonia, and healthy individuals, respectively [31]. Song et al. developed the DRENet model including VGG16, DenseNet and ResNet models to detect Covid19 causing pneumonia, and localize the main lesions. With the model developed, they achieved a 93% accuracy rate in the classification of CT images obtained from Covid19, healthy individuals and pneumonia [32]. Shah et al., in their study using 738 CT images, suggested a DL model called CTnet10 with an accuracy rate of 82.1%. CTnet10 is compared with DenseNet-169, VGG-16, ResNet-50, InceptionV3, and VGG-19 models in the literature. As a result of the comparison, they determined that although the proposed model has a lower accuracy rate compared to other models, the model has the least duration for training and testing. After the comparison, it is observed that the CTnet10 has a lower accuracy rate than the other models. However, the CTnet10 was found to have the shortest training and testing duration compared to the duration required for training and testing other models [33]. This situation shows that evaluating the proposed models by the success rate alone may not be sufficient. For this reason, success rates and training times were also taken into account in the development of the CTnet10 in the article.

As can be seen from these studies in the literature, it is necessary to develop models that can work with maximum accuracy, especially in minimum training duration [34]. To fill this gap in the literature, a new DL model called 3BResNet has been proposed.

3. Methods

In this section, the general layer structure of CNN-based models, which are commonly used among DL models, the ResNet models used in the study, and the 3BResNet DL model inspired by these models are presented.

3.1. CNN's Basic Layers

CNNs are DL algorithms that usually use two-dimensional images as input and perform convolution with filters to extract features from the image [34]. CNNs are designed to isolate visual components and reduce images to lower dimensions while preserving the essential features of the image [25]. CNN is likened to traditional ANNs, especially because of the structure of its last layer. The determination of the features used in ANN models is usually done by the designer. In CNNs, on the other hand, this structure is different from traditional ANNs. Because the system performs the feature extraction process with the filters used in CNNs. For this reason, it is used as a very popular DL model in the literature [35]. A classical CNN model usually has three different types of layers. These are convolution, pooling, and fully connected layers. These layers are briefly summarized below.

3.1.1. Convolution Layer

One of the most fundamental parts of the CNN architecture is the convolution layer. In general, it performs automatic feature extraction with the filters used during forward propagation. The filter structure used at this stage also constitutes the basic structure of the CNN model. Thanks to the convolution layer, new feature maps are created over the two-dimensional data from the previous layer. This process repeats as many times as the number of convolution blocks added one after the other [36], [37].

3.1.2. Pooling Layer

The overall purpose of the pooling layer is to reduce the number of parameters and the computational complexity of the model. For this, it gradually reduces the representation size [35],[38]. The pooling is usually done by applying filters of different sizes. These filters can be 2x2, 3x3, ..., nxn in size. The most common types of used pooling methods are max, min, and mean pooling. Mean pooling reduces the input size by averaging the pixel values within the pooling region. Max-pooling, on the other hand, reduces the input size by taking the largest value within a pooling zone. This layer increases the learning capacity of the network in the feature extraction process and helps to learn the features of the data [39].

3.1.3. Fully Connected Layer

The fully connected layer is often employed as the output layer at the end of CNN models. Gives the latest output values of CNN models [25]. The feature maps originating from the final convolution or other layers are transformed into a one-dimensional array and passed on to the fully connected layer. In the fully connected layer, each input value is bound to a weighting factor. The number of outputs in the fully connected layer usually contains as many nodes as the number of classes. In the literature, a non-linear (ReLU) activation function is also used after each fully connected layer [36].

3.2. Resnet Models

There is a general belief that more layers should be used in CNN models to improve performance. However, increasing the depth, that is, the number of layers, can cause various problems such as gradient burst or disappearance [40]. The ResNet architecture was developed to overcome these problems. This architecture has become a remarkable architecture in the computer vision sector, winning first awards in the ImageNet Large Scale Visual Recognition Challenge (ILSVRC, 2015) and Microsoft Common Objects in Context (MS COCO, 2015) competitions in 2015 [41].

ResNet models use residual blocks in their layers. These blocks are used to improve the performance of deep networks [42]. Residual blocks possess a general structure that establishes a connection between the input of the layer and the output of the next layers. This structure is shown in detail in Figure 1.

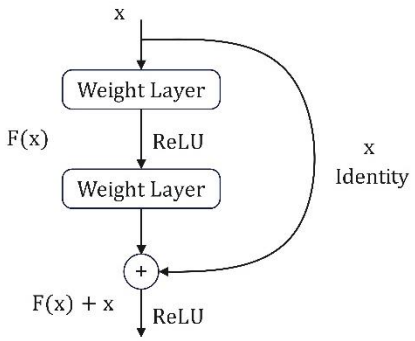

Figure 1. Residual block structure [41]

In Figure 1, x and F(x) refer to the input value of the first layer and the output value of the next layer, respectively. The ReLU between the two layers is the activation function used to reduce the values at the output of the first layer to the desired range [43]. The residual blocks shown in Figure 1 are used to prevent the new values obtained as a result of the convolution process from changing excessively compared to the initial values. Therefore, new ResNet models were developed using different numbers of residual blocks and convolution values. In these architectures, although input images of different sizes can be used, resizing is performed at the input of the models to reduce the images to the appropriate size for the model. This study is based on the ResNet18, ResNet34, ResNet50, ResNet101, ResNet152, and ResNet202 models commonly used in the literature. In these models, five main convolution layers are used: conv1, conv2, conv3, conv4, and conv5 [41]. The content and number of filters used in these layers can be different from each other. The layers of the models used in the study, the blocks belonging to these layers, the matrices used in these blocks and their output dimensions are presented in detail in Table 1.

Table 1. ResNet model family architecture [41]

Layer Name	Output Size	18layer	34layer	50layer	101layer	152layer
conv1	112x112	7x7, 64, stride 2				
conv2x	56x56	3x3 max pool, stride 2				
		$2x\begin{bmatrix}3x3,64\\3x3,64\end{bmatrix}$	$3x\begin{bmatrix}3x3,64\\3x3,64\end{bmatrix}$	$3x\begin{bmatrix}1x1,64\\3x3,64\\1x1,256\end{bmatrix}$	$3x\begin{bmatrix}1x1,64\\3x3,64\\1x1,256\end{bmatrix}$	$3x\begin{bmatrix}1x1,64\\3x3,64\\1x1,256\end{bmatrix}$
conv3x	28x28	$2x\begin{bmatrix}3x3,128\\3x3,128\end{bmatrix}$	$4x\begin{bmatrix}3x3,128\\3x3,128\end{bmatrix}$	$4x\begin{bmatrix}1x1,128\\3x3,128\\1x1,512\end{bmatrix}$	$4x\begin{bmatrix}1x1,128\\3x3,128\\1x1,512\end{bmatrix}$	$8x\begin{bmatrix}1x1,128\\3x3,128\\1x1,512\end{bmatrix}$
conv4x	14x14	$2x\begin{bmatrix}3x3,256\\3x3,256\end{bmatrix}$	$6x\begin{bmatrix}3x3,256\\3x3,256\end{bmatrix}$	$6x\begin{bmatrix}1x1,256\\3x3,256\\1x1,1024\end{bmatrix}$	$23x\begin{bmatrix}1x1,256\\3x3,256\\1x1,1024\end{bmatrix}$	$36x\begin{bmatrix}1x1,256\\3x3,256\\1x1,1024\end{bmatrix}$
conv5x	7x7	$2x\begin{bmatrix}3x3,512\\3x3,512\end{bmatrix}$	$3x\begin{bmatrix}3x3,512\\3x3,512\end{bmatrix}$	$3x\begin{bmatrix}1x1,512\\3x3,512\\1x1,2048\end{bmatrix}$	$3x\begin{bmatrix}1x1,512\\3x3,512\\1x1,2048\end{bmatrix}$	$3x\begin{bmatrix}1x1,512\\3x3,512\\1x1,2048\end{bmatrix}$
	1x1	average pool, 1000-d fc, softmax				
FLOPs		1.8 x 109	3.6 x 109	3.8 x 109	7.6 x 109	11.3 x 109

In the ResNet models, 64 filters of size 7x7 are used in the conv1 convolution layer in all models to quasi the size of the input images. In the conv2 convolution layer, a 3x3 pooling layer is first used for data size reduction. As a result of this process, the size of the data is quasi-ed again. For the remaining operations of the conv2 convolution layer and for operations in other convolution layers, different numbers and sizes of filters are used according to different ResNet models. In the final stage, all outputs are converted into a single vector using the global mean pooling layer. This vector is then sent to the classification layer.

ResNet models have some disadvantages in themselves. Analyzing the FLOPs values presented in Table 1, it is seen that the processing capacity directly increases with increasing the number of layers. When the layer structure in the ResNet18 and ResNet152 models is analyzed, there is approximately six times the computational cost between both models. However, when both models are compared on a similar dataset, the ratio of the accuracy values obtained, and the ratio of the computational cost values cannot be obtained the same. Therefore, when evaluating the performance of the models, they also need to be evaluated in terms of computational cost and training time. Based on this point, this study aims to develop models with less training time.

3.3. Proposed Model

In the developed model, unlike the classical residual blocks used in ResNet models, the block structure shown in Figure 2 is used. In classical residual blocks, there may be anomalous differences between the input data and the output data obtained at the end of the block. Therefore, in the last part of the classical residual block, the initial input data and the final data obtained after the convolution operations are summed with each other. However, if there are small details or small changes between pixels in the images used, these attributes can be lost in classical residual blocks. The loss or inability to obtain these features can cause irreversible problems, especially in healthcare studies using CT-based images. Therefore, in this study, a new structure for the residual blocks is proposed. The 3BResNet residual block structure is shown in detail in Figure 2.

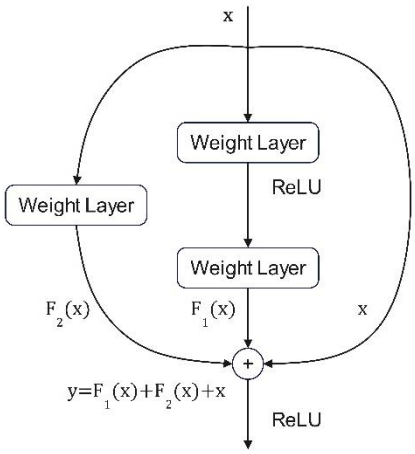

Figure 2. Proposed residual block structure

Data from 3 different branches are combined in the residual block structure proposed in Figure 2. Due to the use of data from 3 branches in the residual block structure, the proposed model is named 3BResNet. In this structure, the data of the first branch represent the input data (x), the data from the second branch represent the data obtained as a result of the sequential convolution operation F1 (x), and the data from the third branch represent the data obtained as a result of the single convolution operation F2 (x). The value denoted by y represents the output of the proposed residual block structure. The mathematical expression of the performed operation is presented in Equation 1.

$$y = (x) + F_1(x) + F_2(x) \quad (1)$$

Due to the structure presented in Equation 1, sudden and large changes between the first image and the last image are prevented, and small details in the image can be captured. Using the proposed residual block, a new 14-layer architecture was created as shown in Figure 3 and Table 2. As it can be understood from this architecture, fewer convolution layers are used than the ResNet18, ResNet34, ResNet50, ResNet101, ResNet152, and ResNet202 models in the literature.

Table 2. 3BResNet architecture

Layer Name	Output Size	14-layer
conv1	112 x 112	7 x 7, 64, stride 2
conv2	56 x 56	[3 x 3], max pool, stride 2
		$\begin{bmatrix} 3x3, 64 \\ 3x3, 64 \end{bmatrix} x2$, stride 1
conv3	28 x 28	$\begin{bmatrix} 3x3, 128 \\ 3x3, 128 \end{bmatrix}$, stride 2 / stride 1
		$\begin{bmatrix} 3x3, 128 \\ 3x3, 128 \end{bmatrix}$, stride 1 / stride 1
conv4	14 x 14	$\begin{bmatrix} 3x3, 256 \\ 3x3, 256 \end{bmatrix}$, stride 2 / stride 1
		$\begin{bmatrix} 3x3, 256 \\ 3x3, 256 \end{bmatrix}$, stride 1 / stride 1
	1x1	average pool, 1000-d fc, softmax
FLOPs		$1{,}9x10^9$

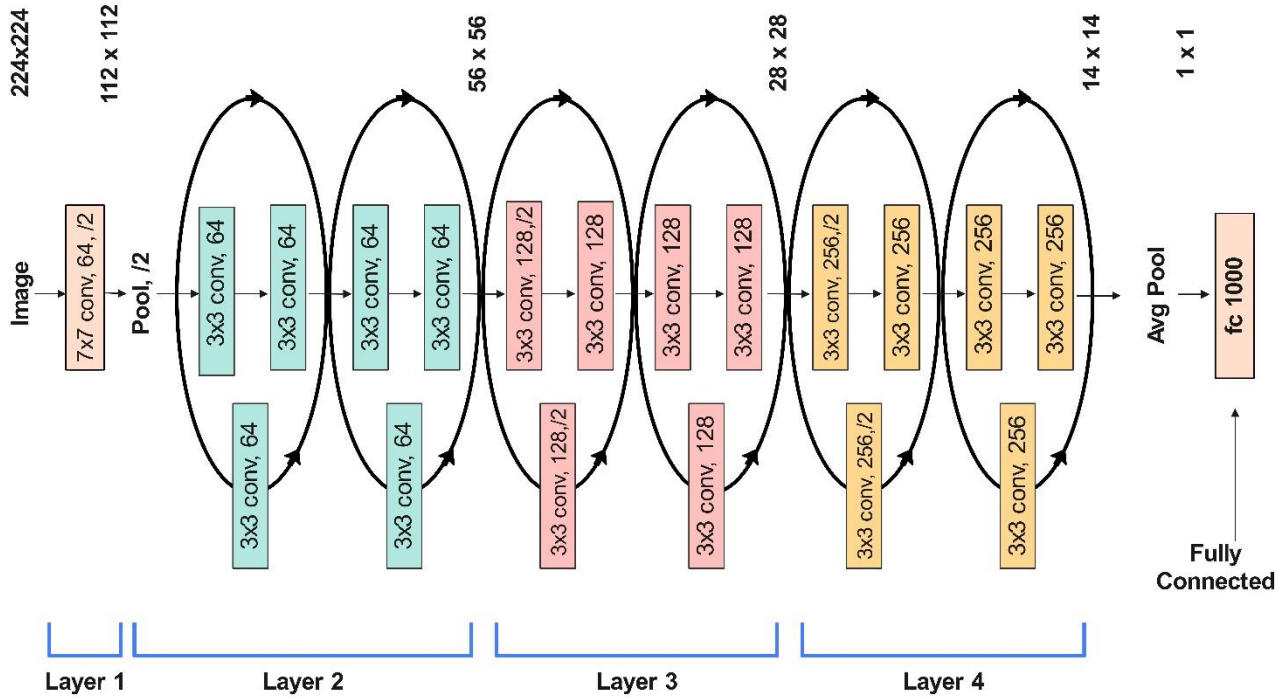

Figure 3. Architecture of the 3BResNet model

4. Experimental Study

The experimental study carried out consists of 4 steps as shown in Figure 4. These steps are data pre-processing, model selection, implementation, and testing. The results of the experimental study are compared in Table 5 with the results of other studies in the literature using the same dataset.

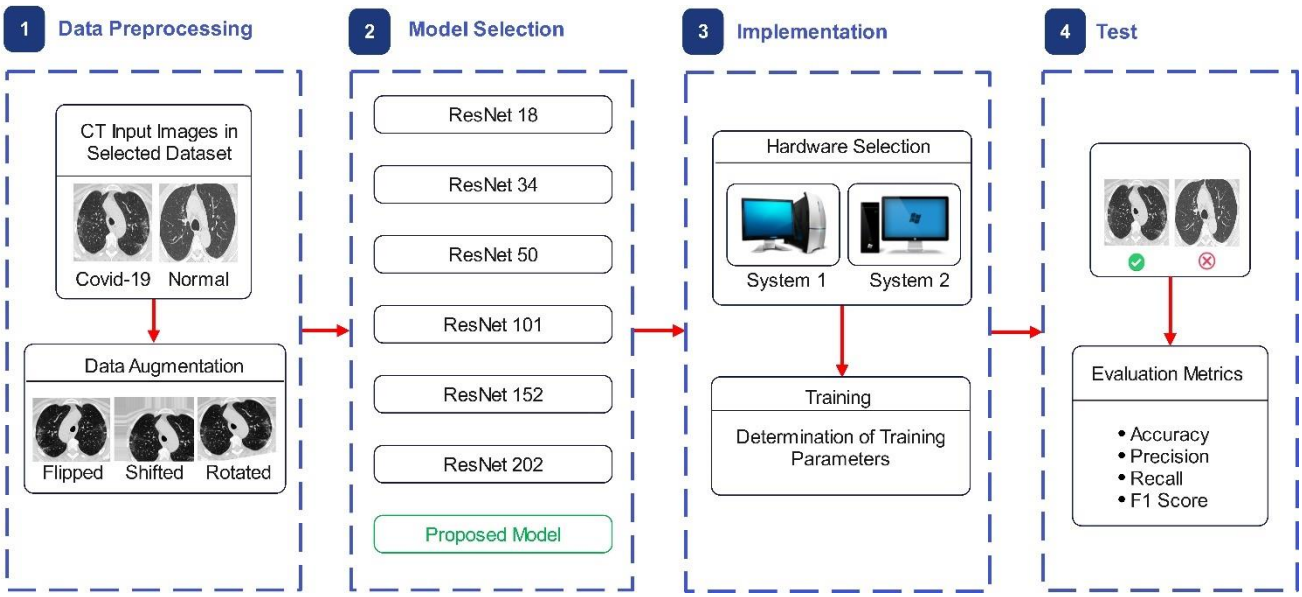

Figure 4. Experimental study diagram

4.1. Data Pre-Processing

This section of the study, information about the dataset used is given and the steps followed for data augmentation are presented.

4.1.1. Selected Dataset

Within the scope of the study, the SARS-CoV-2 CT dataset, which is used in many different studies in the literature, was used to evaluate the performance of the ResNet models and the 3BResNet model together with other studies in the literature [44]. The dataset used was obtained from CT images of patients in hospitals in Sao Paulo, Brazil, by Soares et al., to be used in the diagnosis of SARS-CoV-2 (COVID19) infection. There are 1252 positive and 1230 negative CT images in the dataset. The examples of positive and negative Covid19 chest CT scans shown in Figure 5.

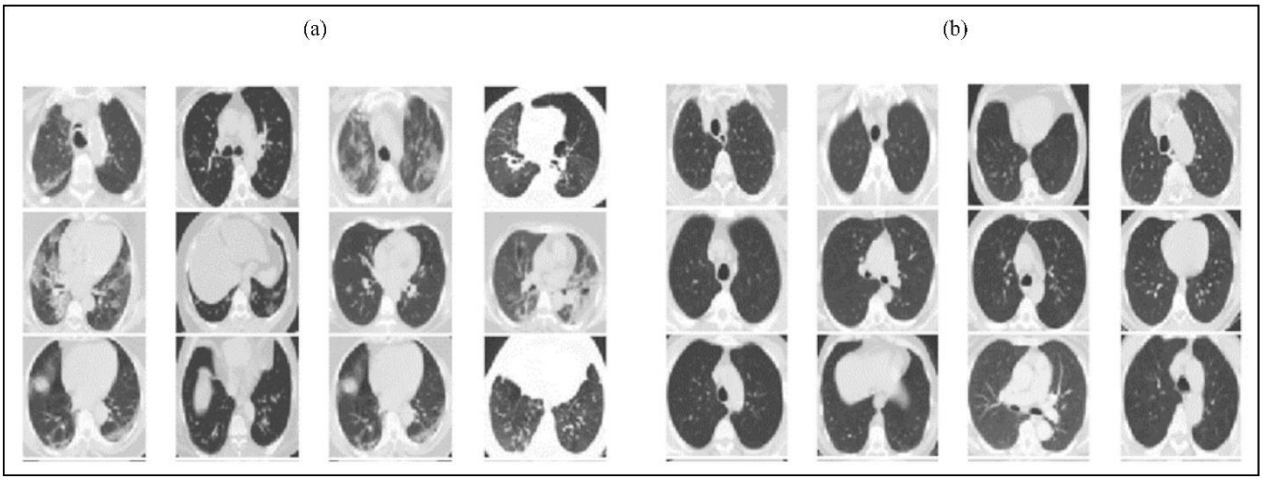

Figure 5. a) Positive COVID19 chest CT scans b) Negative COVID19 chest CT scans

4.1.2 Data Augmentation Processing

Data augmentation processing is a strategy that aims to generate more samples by applying different transformations to the available training data [45]. By ensuring that the network encounters different data in each training round, the aim is to prevent the problem of overfitting and, accordingly, increase the generalization performance of the model. Deep neural networks need high-quality training examples to get accurate results. However, biomedical image datasets often contain fewer images than publicly available image datasets. Many biomedical datasets, including the dataset used in this study, contain fewer than 10,000 images.

For this reason, three different data augmentation techniques were applied to increase the number of images in the study. The data augmentation methods preferred in the study are image rotation, image shift, and flip. 90-degree angles were used for image rotation. In the image shift process, 0.2, 0.4, and 0.6 values are preferred as the shift value, and horizontal flipping is preferred in the flipping process. As the images obtained by these methods are variants of the original images and have similar patterns, they can be considered reliable data. An example of the images obtained because of the data augmentation process is shown in Figure 6.

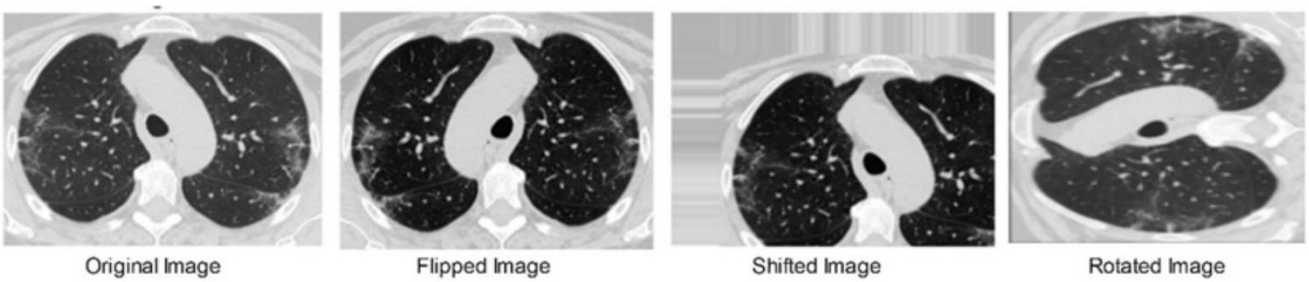

Figure 6. Examples of augmented images

In the study, the augmented data were separated into two groups as 80% training and 20% test data according to the cross-validation 5 value. The images in the dataset used in this study have different dimensions. For this reason, all images were resized to 224x224 to be suitable for the input of the models to be used in the next stages of the study.

4.2. Model Selection

The general structure of the model proposed in the study is presented in detail in Section 3.3. The DL models ResNet202, ResNet34, ResNet152, ResNet101, ResNet150, and ResNet18, which are widely used in the literature with similar parameters, are other preferred models in the study. The number of layers and the contents of these models used are discussed in detail in Section 3.3. To compare the performance of ResNet models, it is very important to use the same dataset and train with the same training parameters. As can be seen in Figure 4, whichever model is selected in the experimental study, the whole system is run on that model and results are produced. This step is repeated to train and test each model.

4.3. Implementation

In this step of the study, the hardware options and training parameters used in the experimental study are presented.

4.3.1. Hardware

To measure the effect of different DL models applied in the study on different hardware, it was aimed at performing training and testing processes on two different hardware systems. For this reason, detailed specifications of the hardware used in the study are shown in Table 3.

Table 3. Details of hardware and software used

	Hardware			Software		
	CPU	**GPU**	**RAM**	**Operating System**	**Programming Language**	**Library**
System 1	Intel Core i7 7500U 2.70GHz 2 Core	Intel HD Graphics 620	8 GB	Windows 10 Enterprise 64-bit	Python 3.8	TensorFlow v2.11.0
System 2	Intel Core i7 10750H 2,60 GHz 16 Core	NVIDIA GeForce GTX 1650 TI	64 GB	Windows 10 Enterprise 64-bit	Python 3.8	TensorFlow v2.11.0

4.3.2. Training

In this study, the training parameters of the ResNet models were determined taking into account the GPU memory limit of the system hardware to be used and the size of the data stacks to be used during training. Therefore, the batch size value is 64. A slow value is preferred for the learning rate of the network. Therefore, 0.001 was used as the learning parameter. Adam optimizer is preferred to optimize the parameters of the system. All models were trained using 500 epochs. In the study, the data were divided into two groups, training, and testing, according to the cross-validation value of 5. Data separated according to this value was used in the training phase. The metrics used to measure training and testing performance are presented in detail in section 4.4.

4.4. Evaluation Metrics

In order to analyze the performances of the DL architectures used in the study and the 3BResNet model, the confusion matrix, which is widely used in classification applications in the literature, was used [46]. Confusion matrix is a construct designed to evaluate the prediction accuracy of classification algorithms. With the Confusion matrix, information about the errors of the classification models used, the types of errors, and the performance of the model, in general, can be obtained.

The confusion matrix has four different values. These are True Positive (TP), True Negative (TN), False Positive (FP), and False Negative (FN). Sample values that the system predicts positively and that are actually positive are denoted by TP. Sample values that the system predicts negatively and are

actually negative are denoted by TN. Sample values that the system predicts as positive but are actually negative are represented by FP. Sample values that the system predicts negatively but are actually positive are compared with FN. Expressed. Equation 2-5 evaluates the overall performance of the system using these parameters.

$$\text{Accuracy;}\ \frac{(TN+TP)}{(TP+TN+FP+FN)} \quad (2)$$

$$\text{Precision;}\ \frac{(TP)}{(FP+TP)} \quad (3)$$

$$\text{Recall;}\ \frac{(TP)}{(FN+TP)} \quad (4)$$

$$\text{F1 Score;}\ 2x\left(\frac{Recall * Precision}{Recall + Precision}\right) \quad (5)$$

The criterion used to evaluate the success of the classification model is defined as accuracy. This metric, presented in Equation 2, is expressed as the ratio of the number of correctly classified samples to the total number of samples. The criterion used to evaluate how many of the positive classes predicted by the classification model are actually positive is defined as precision. This metric, presented in Equation 3, is calculated by dividing the number of correct positive predictions by the number of all positive predictions in the matrix. The criterion used to evaluate how accurately the classification model classifies true positive samples is defined as sensitivity. This metric, presented in Equation 4, is calculated by dividing the number of true positive predictions in the matrix by the number of true positive samples. The F1 Score presented in Equation 5, on the other hand, expresses the balance between the accuracy and precision of the model. It is calculated as the harmonic mean of the accuracy and precision criteria.

5. Result and Discussion

The results of the experimental studies and discussions are shared in detail in this section. The results are then compared with other previous studies in the literature using the same dataset.

5.1. Performance Analysis

Despite the difficulties in diagnosing upper respiratory tract infections, there is a trend toward DL models due to the high performance of machine learning methods [47]. For this reason, DL models were preferred in the study. All preferred models and the 3BResNet model were tested separately on the same data set and performance evaluation was made. Due to the preferred dataset, there has been a classification as positive or negative for Covid19.

The training and testing procedures for all models used in this study were carried out using System 2, which is presented in Table 3. In the training phase of the study, the accuracy, precision, sensitivity, F1 score, training duration, and flops obtained separately for all models are presented in detail in Table 4.

Table 4. Analysis results

Model	Flops	Accuracy	Precision	Recall	F1 Score	Duration
ResNet18	$1.8x10^9$	0.94	0.94	0.96	0.95	610 sec
ResNet34	$3.6x10^9$	0.95	0.98	0.92	0.95	868 sec
ResNet50	$3.8x10^9$	0.95	0.92	0.96	0.94	1361 sec
ResNet101	$7.6x10^9$	0.95	0.96	0.95	0.95	2057 sec
ResNet152	$11.3x10^9$	0.90	0.95	0.87	0.91	2842 sec
ResNet202	$14.8x10^9$	0.92	0.95	0.90	0.93	3732 sec
Proposed Model(3BResNet)	$1.9x10^9$	0.97	0.96	0.98	0.97	675 sec

Although in the literature thought that increasing the number of layers used in CNN-based models will increase success, the opposite is found in this study. When the training results of the system in Table 4 are analyzed, it is seen that the accuracy does not change at the same rate and direction with the number of layers. In addition, it was found that the number of parameters used, and

the time required to train the models increased due to the increase in the number of layers. It has been observed that the accuracy obtained from ResNet152 and ResNet202 models, which have a greater number of layers, is lower than other models.

In this study, inspired by ResNet models, the 3BResNet model achieved a classification success much superior to other ResNet models, reaching an accuracy value of 0.97, despite reducing the number of layers and modifying its structure. The residual block structure used in the 3BResNet model has been found to shorten the training time and increase the success rate.

When the training time and the number of parameters of all models were examined, it was determined that the proposed model completed the training process faster than all other ResNet models except ResNet18. In the 3BResNet model, more parameters are used than the number of parameters used in ResNet18. This is due to the increase of convolution operations in the block structure of the 3BResNet model. As a result of this, the training duration of the ResNet18 model was shorter than that of the 3BResNet model.

In addition, the 3BResNet model was trained and tested with the lower hardware System 1 presented in Table 3. Training of the 3BResNet model with System 1 was completed in 2342 seconds. On the other hand, the same model was trained with System 2 for 675 seconds. Thus, the low-equipped system was compared with the high-equipped system, and it was determined that the 3BResNet model could also work in low-equipped systems by compromising the training time. When the results are examined in general, it is seen that the training time of the 3BResNet model is much shorter than the training times of the ResNet152 and ResNet202 models.

5.2. Comparison With State of The Art

In order to present a realistic evaluation of the 3BResNet model and other ResNet models used in the study, a comparison was made with the state of the art (SOTA) latest technology studies using the same data set in the literature. The comparison made is presented in Table 5 in detail. In the evaluation, it is detected that especially the Inception ResNet model performs lower than many studies in the literature. The success rates of the ResNet models used in the study and the VGG and DenseNet models are seen to be close to each other. The 3BResNet model showed a 97% classification success. This result shows that the 3BResNet model has the potential to compete with other models in the existing literature.

Table 5. Comparison with the SOTA in literature

References	Pre-trained model	Accuracy
[48]	VGG-16	0.94
[49]	DenseNet201	0.96
	VGG-16	0.95
	ResNet 152V2	0.94
	Inception ResNet	0.90
[13]	DenseNet201	0.97
	VGG-16	0.94
	ResNet50V2	0.96
	MobileNet	0.95
[50]	VGG-19	0.94
[51]	VGG-19 with LR	0.94
	VGG-19 with KNN	0.94
	VGG-16 with LR	0.94
	VGG-16 with KNN	0.94
[52]	ResNet50	0.95
Our Study	ResNet18	0.94
	ResNet34	0.95
	ResNet50	0.95
	ResNet101	0.95
	ResNet152	0.90
	ResNet202	0.92
	Proposed(3BResNet)	0.97

6. Conclusion

The ResNet models used in the literature are open to improvement and new models can be developed by adding different layers. However, in DL models, semantic gaps can occur when high depth levels are reached. There may be different reasons for these semantic gaps. Although increasing the number of layers in ResNet models is done to increase performance, this may produce low performance

results depending on the dataset. For this reason, a new model called 3BResNet with a new layer and block structure is proposed in this study, inspired by the ResNet models in the literature. In the 3BResNet model, instead of increasing the number of layers, the residual block structure used in ResNet models is modified, and the number of layers is reduced to 14 layers.

The 3BResNet model is also aimed to solve the gradient vanishing and explosion problem, which is commonly encountered in ResNet models in the literature. To objectively evaluate the performance, different ResNet models were also trained and tested using the same dataset.

The confusion matrix, which is commonly used in the literature, was used in the training and testing processes. In addition, two different hardware configurations were also created to measure the performance of the system at different hardware levels. The 3BResNet model can run on a high-equipped level as well as on a much lower-equipped level. Therefore, the proposed model is considered a suitable solution to deal with hardware problems commonly encountered in DL models. With this study, a method that can be widely used at all levels of hardware during epidemic periods, such as a pandemic, has been developed.

With the 3BResNet model proposed in the study, a more successful result was obtained than other ResNet models in the literature, reaching an accuracy rate of 0.97 in classifying people infected with Covid19. In addition, the training time of the model was completed in 675 seconds. This time is much less than the ResNet models used in the study. Training of the 3BResNet model on machines of different hardware levels has also been tested. As a result of the test, it has been seen that training can be performed on systems with low hardware levels. System 1 was used as an example of a low-equipped system in the study. The training process on System 1 was completed in 2342 seconds. It has been observed that the proposed model can be trained on a low-equipped system, with some sacrifice of training time. In light of the results obtained, it was determined that the 3BResNet model performed better than the ResNet models used in the study.

Considering the success of the proposed model in image classification, it is anticipated that it can be applied not only to medical image datasets, but also to various datasets from different fields. It has been concluded that the focus of the studies planned to be carried out on the basis of ResNet models in the future is to develop models that can provide higher success with shorter training time by developing different block structures, rather than increasing the number of layers. This approach will provide a different perspective to overcome current limitations and achieve higher accuracy rates. The model proposed in the study is capable of contributing to future studies to make the education process faster and more efficient.

Contributions of the authors

The authors confirm that the contribution is equally for this paper.

Conflict of Interest Statement

There is no conflict of interest between the authors.

Statement of Research and Publication Ethics

The study is complied with research and publication ethics.

References

[1] A. A. Ardakani, A. R. Kanafi, U. R. Acharya, N. Khadem, ve A. Mohammadi, "Application of deep learning technique to manage COVID-19 in routine clinical practice using CT images: Results of 10 convolutional neural networks", *Comput Biol Med*, vol. 121, Haz. 2020, doi: 10.1016/j.compbiomed.2020.103795.

[2] M. E. H. Chowdhury *vd.*, "Can AI Help in Screening Viral and COVID-19 Pneumonia?", *IEEE Access*, vol. 8, pp. 132665-132676, 2020, doi: 10.1109/ACCESS.2020.3010287.

[3] Z. hui Chen, S. ping Wan, ve J. ying Dong, "An integrated interval-valued intuitionistic fuzzy technique for resumption risk assessment amid COVID-19 prevention", *Inf Sci (N Y)*, vol. 619, pp. 695-721, Oca. 2023, doi: 10.1016/j.ins.2022.11.028.

[4] X. Li, C. Li, ve D. Zhu, "Covid-mobilexpert: On-device covid-19 screening using snapshots of chest x-ray", *arXiv preprint arXiv:2004.03042*, 2020.

[5] Çalışkan, A. (2023). "Diagnosis of malaria disease by integrating chi-square feature selection algorithm with convolutional neural networks and autoencoder network", *Transactions of the Institute of Measurement and Control*, vol. 45, no. 5, pp. 975-985. https://doi.org/10.1177/01423312221147335.

[6] M. P. Cheng *vd.*, "Diagnostic Testing for Severe Acute Respiratory Syndrome–Related Coronavirus 2", *Ann Intern Med*, vol. 172, no 11, pp. 726-734, Nis. 2020, doi: 10.7326/M20-1301.

[7] X. He *vd.*, "Sample-efficient deep learning for COVID-19 diagnosis based on CT scans", in *IEEE Transactions on Medical Imaging*, p. 10, 2020. doi: 10.1101/2020.04.13.20063941.

[8] T. B. Chandra, K. Verma, B. K. Singh, D. Jain, ve S. S. Netam, "Coronavirus disease (COVID-19) detection in Chest X-Ray images using majority voting based classifier ensemble", *Expert Syst Appl*, vol. 165, p. 113909, 2021, doi: https://doi.org/10.1016/j.eswa.2020.113909.

[9] A. Bernheim et al., "Chest CT findings in coronavirus disease 2019 (COVID-19): Relationship to duration of infection", *Radiology*, vol. 295, no 3, pp. 200463, 2020. doi: 10.1148/radiol.2020200463.

[10] O. Gozes *et al.*, "Rapid AI Development Cycle for the Coronavirus (COVID-19) Pandemic: Initial Results for Automated Detection & Patient Monitoring using Deep Learning CT Image Analysis", 2020, [Çevrimiçi]. Erişim adresi: http://arxiv.org/abs/2003.05037

[11] R. Chelghoum, A. Ikhlef, A. Hameurlaine, and S. Jacquir, "Transfer learning using convolutional neural network architectures for brain tumor classification from MRI images", in *IFIP Advances in Information and Communication Technology*, Springer International Publishing, 2020, pp. 189-200. doi: 10.1007/978-3-030-49161-1_17.

[12] S. Metlek, "A new proposal for the prediction of an aircraft engine fuel consumption: a novel CNN-BiLSTM deep neural network model", *Aircraft Engineering and Aerospace Technology*, vol. 95, no 5, pp. 838-848, 2023, doi: 10.1108/AEAT-05-2022-0132.

[13] A. Halder and B. Datta, "COVID-19 detection from lung CT-scan images using transfer learning approach", *Mach Learn Sci Technol*, vol. 2, no 4, p. 0450013, 2021. doi: 10.1088/2632-2153/abf22c.

[14] M. Usman, T. Zia, and A. Tariq, "Analyzing transfer learning of vision transformers for interpreting chest radiography", *J Digit Imaging*, vol. 35, no. 6, pp. 1445-1462, 2022.

[15] C. Srinivas et al., "Deep transfer learning approaches in performance analysis of brain tumor classification using MRI images", *J Healthc Eng*, vol. 2022, 2022.

[16] H. Aljuaid, N. Alturki, N. Alsubaie, L. Cavallaro, and A. Liotta, "Computer-aided diagnosis for breast cancer classification using deep neural networks and transfer learning", *Comput Methods Programs Biomed*, vol. 223, p. 106951, 2022.

[17] M. Aly and N. S. Alotaibi, "A novel deep learning model to detect COVID-19 based on wavelet features extracted from Mel-scale spectrogram of patients' cough and breathing sounds", *Inform Med Unlocked*, vol. 32, p. 101049, 2022, doi: https://doi.org/10.1016/j.imu.2022.101049.

[18] L. K. Butola, R. Ambad, P. K. Kute, R. K. Jha, A. D. Shinde, and W. DMIMS, "The pandemic of 21st century-COVID-19", *Journal of evolution of medical and dental Sciences-JEMDS*, vol. 9, no 39, pp. 2913-2918, 2020.

[19] Y. Zhao, B. R. Dong, and Q. Hao, "Probiotics for preventing acute upper respiratory tract infections", *Cochrane Libr*, no. 8, 2022, doi: 10.1002/14651858.CD006895.pub4.

[20] A. Bianco, F. Licata, C. G. A. Nobile, F. Napolitano, ve M. Pavia, "Pattern and appropriateness of antibiotic prescriptions for upper respiratory tract infections in primary care paediatric patients", *Int J Antimicrob Agents*, vol. 59, no 1, p. 106469, 2022. doi: https://doi.org/10.1016/j.ijantimicag.2021.106469.

[21] A. W. Bartlow *vd.*, "Comparing variability in diagnosis of upper respiratory tract infections in patients using syndromic, next generation sequencing, and PCR-based methods", *PLOS Global Public Health*, vol. 2, no 7, pp. e0000811, 2022. https://doi.org/10.1371/journal.pgph.0000811

[22] M. Farooq and A. Hafeez, "Covid-resnet: A deep learning framework for screening of covid19 from radiographs", *arXiv preprint arXiv:2003.14395*, 2020.

[23] E. B. G. Kana, M. G. Z. Kana, A. F. D. Kana, and R. H. A. Kenfack, "A web-based Diagnostic Tool for COVID-19 Using Machine Learning on Chest Radiographs (CXR)", *medRxiv*, s. 2020.04.21.20063263, 2020. doi: 10.1101/2020.04.21.20063263.

[24] A. Keles, M. B. Keles, and A. Keles, "COV19-CNNet and COV19-ResNet: diagnostic inference Engines for early detection of COVID-19", *Cognit Comput*, pp. 1-11, 2021.

[25] R. Zhang *et al.*, "COVID19XrayNet: A Two-Step Transfer Learning Model for the COVID-19 Detecting Problem Based on a Limited Number of Chest X-Ray Images", *Interdiscip Sci*, vol. 12, no 4, pp. 555-565, 2020. doi: 10.1007/s12539-020-00393-5.

[26] M. M. Rahaman *et al.*, "Identification of COVID-19 samples from chest X-Ray images using deep learning: A comparison of transfer learning approaches", *J Xray Sci Technol*, vol. 28, no. 5, pp. 821-839, 2020, doi: 10.3233/XST-200715.

[27] K. El Asnaoui and Y. Chawki, "Using X-ray images and deep learning for automated detection of coronavirus disease", *J Biomol Struct Dyn*, vol. 39, no 10, pp. 3615-3626, 2021.

[28] X. Xu *et al.*, "A deep learning system to screen novel coronavirus disease 2019 pneumonia", *Engineering*, vol. 6, no 10, pp. 1122-1129, 2020.

[29] C. Zheng *et al.*, "Deep Learning-based Detection for COVID-19 from Chest CT using Weak Label", *IEEE Trans Med Imaging*, pp. 1-13, 2020, doi: 10.1101/2020.03.12.20027185.

[30] S. Hu *et al.*, "Weakly supervised deep learning for covid-19 infection detection and classification from ct images", *IEEE Access*, vol. 8, pp. 118869-118883, 2020.

[31] L. Li *et al.*, "Using Artificial Intelligence to Detect COVID-19 and Community-acquired Pneumonia Based on Pulmonary CT: Evaluation of the Diagnostic Accuracy", *Radiology*, vol. 296, no 2, pp. E65-E71, Mar. 2020, doi: 10.1148/radiol.2020200905.

[32] Y. Song *et al.*, "Deep learning enables accurate diagnosis of novel coronavirus (COVID-19) with CT images", *IEEE/ACM Trans Comput Biol Bioinform*, vol. 18, no 6, pp. 2775-2780, 2021.

[33] V. Shah, R. Keniya, A. Shridharani, M. Punjabi, J. Shah, and N. Mehendale, "Diagnosis of COVID-19 using CT scan images and deep learning techniques", *Emerg Radiol*, vol. 28, no 3, pp. 497-505, 2021.

[34] S. Metlek, "Forecasting of Dow Jones sukuk index prices using artificial intelligence systems.", *Econ Comput Econ Cybern Stud Res*, vol. 56, no 1, 2022.

[35] K. O'Shea ve R. Nash, "An Introduction to Convolutional Neural Networks", *CoRR*, c. abs/1511.0, 2015, [Çevrimiçi]. Erişim adresi: http://arxiv.org/abs/1511.08458

[36] R. Yamashita, M. Nishio, R. K. G. Do, and K. Togashi, "Convolutional neural networks: an overview and application in radiology", *Insights into Imaging*, vol. 9, no 4. pp. 611-629, 2018. doi: 10.1007/s13244-018-0639-9.

[37] J. Gu *et al.*, "Recent advances in convolutional neural networks", *Pattern Recognit*, vol. 77, pp. 354-377, 2018. doi: 10.1016/j.patcog.2017.10.013.

[38] S. Albawi, T. A. Mohammed, ve S. Al-Zawi, "Understanding of a convolutional neural network", in *2017 International Conference on Engineering and Technology, (ICET)* 2017. doi: 10.1109/ICEngTechnol.2017.8308186.

[39] A. Arı and D. Hanbay, "Bölgesel Evrişimsel Sinir Ağları Tabanlı MR Görüntülerinde Tümör Tespiti", *Gazi Üniversitesi Mühendislik-Mimarlık Fakültesi Dergisi*, vol. 2018, no 18-2, 2018. doi: 10.17341/gazimmfd.460535.

[40] M. Tokmak and A. Kıraç, "Classification of Some Species of Shrikes Family by Convolutional Neural Networks", *Bilge International Journal of Science and Technology Research*, vol. 5, no. 1, pp. 72-79 2021, doi: 10.30516/bilgesci.886291.

[41] K. He, X. Zhang, S. Ren, ve J. Sun, "Deep residual learning for image recognition", in 2016 *IEEE Conference on Computer Vision and Pattern Recognition (CVPR)*, 2016. doi: 10.1109/CVPR.2016.90.

[42] Z. Lu *et al.*, "The classification of gliomas based on a Pyramid dilated convolution resnet model", *Pattern Recognit Lett*, vol. 133, pp. 173-179, 2020, doi: https://doi.org/10.1016/j.patrec.2020.03.007.

[43] Q. A. Al-Haija ve A. Adebanjo, "Breast cancer diagnosis in histopathological images using ResNet-50 convolutional neural network", in 2020 IEEE *International IOT, Electronics and Mechatronics Conference (IEMTRONICS)*, 2020. doi: 10.1109/IEMTRONICS51293.2020.9216455.

[44] E. Soares, P. Angelov, S. Biaso, M. H. Froes, ve D. K. Abe, "SARS-CoV-2 CT-scan dataset: A large dataset of real patients CT scans for SARS-CoV-2 identification", *medRxiv*, s. 2020.04.24.20078584, Oca. 2020, doi: 10.1101/2020.04.24.20078584.

[45] K. Maharana, S. Mondal, ve B. Nemade, "A review: Data pre-processing and data augmentation techniques", *Global Transitions Proceedings*, vol. 3, no 1, pp. 91-99, 2022, doi: https://doi.org/10.1016/j.gltp.2022.04.020.

[46] O. Turk, D. Ozhan, E. Acar, T. C. Akinci, & M. Yilmaz, (2022). "Automatic detection of brain tumors with the aid of ensemble deep learning architectures and class activation map indicators by employing magnetic resonance images," *Z. Med. Phys.*, 2022. https://doi.org/10.1016/j.zemedi.2022.11.010.

[47] S. Siddiqui *vd.*, "Deep Learning Models for the Diagnosis and Screening of COVID-19: A Systematic Review", *SN Computer Science*, vol. 3, no 5, 2022. doi: 10.1007/s42979-022-01326-3.

[48] E. Soares, P. Angelov, S. Biaso, M. H. Froes, ve D. K. Abe, "SARS-CoV-2 CT-scan dataset: A large dataset of real patients CT scans for SARS-CoV-2 identification", *medRxiv*, p. 2020.04.24.20078584, Oca. 2020, doi: 10.1101/2020.04.24.20078584.

[49] A. Jaiswal, N. Gianchandani, D. Singh, V. Kumar, ve M. Kaur, "Classification of the COVID-19 infected patients using DenseNet201 based deep transfer learning", *J Biomol Struct Dyn*, vol. 39, no 15, pp. 5682-5689, 2021, doi: 10.1080/07391102.2020.1788642.

[50] H. Panwar, P. Gupta, M. K. Siddiqui, R. Morales-Menendez, P. Bhardwaj, ve V. Singh, "A Deep Learning and Grad-CAM based Color Visualization Approach for Fast Detection of COVID-19 Cases using Chest X-ray and CT-Scan Images", *Chaos Solitons Fractals*, vol. 140, no. 110190, p. 110190, Ağu. 2020, doi: 10.1016/j.chaos.2020.110190.

[51] S. Gupta, P. Aggarwal, N. Chaubey, and A. Panwar, "Accurate prognosis of Covid-19 using CT scan images with deep learning model and machine learning classifiers", *Indian Journal of Radio &Space Physics*,vol.50, no. 1, pp.19-24, 2021.

[52] K. L. Kohsasih ve B. H. Hayadi, "Classification SARS-CoV-2 Disease based on CT-Scan Image Using Convolutional Neural Network", *Scientific Journal of Informatics*, vol. 9, no 2, pp. 197-204, Kas. 2022, doi: 10.15294/sji.v9i2.36583.